Journal of Heat Transfer

Published Monthly by ASME

VOLUME 132 • NUMBER 2 • FEBRUARY 2010

GUEST EDITORIAL

RESEARCH PAPERS

Radiative Properties

Solution Methods

(Contents continued on inside back cover)

This journal is printed on acid-free paper, which exceeds the ANSI Z39.48-1992 specification for permanence of paper and library materials. ♾™
♲ 85% recycled content, including 10% post-consumer fibers.

SETTING THE STANDARD

Editor, **YOGESH JALURIA** (**2010**)
Assistant to the Editor, **S. PATEL**

Associate Editors
Yutaka Asako, Tokyo Metropolitan University, Japan (2010)
Cho Lik Chan, The University of Arizona (2010)
Louis C. Chow, University of Central Florida (2010)
Frank J. Cunha, Pratt & Whitney (2011)
Ali Ebadian, Florida International Univ. (2011)
Ofodike A. Ezekoye, Univ. of Texas-Austin (2011)
Srinivas Garimella, Georgia Institute Technology (2012)
Kenneth Goodson, Stanford University (2012)
Satish G. Kandlikar, Rochester Inst. of Tech. (2010)
Sung Jin Kim, KAIST, Korea (2010)
Giulio Lorenzini, University of Bologna (2012)
Jayathi Y. Murthy, Perdue University (2010)
Pamela M. Norris, Univ. of Virginia (2011)
Patrick H. Oosthuizen, Queens University, Canada (2012)
Patrick E. Phelan, National Science Foundation (2011)
Roger R. Schmidt, IBM Corporation (2010)
S. A. Sherif, University of Florida (2010)
Heping Tan, Harbin Institute of Technology (2011)
Wen Q. Tao, Xi'an University, China (2012)
Wei Tong, Danaher Corporation (2012)
Robert Tzou, University of Missouri-Columbia (2012)
Peter Vadasz, Northern Arizona University (2010)
Walter W. Yuen, Univ. of California–Santa Barbara (2011)

Past Editors
V. DHIR
J. R. HOWELL
R. VISKANTA
G. M. FAETH
K. T. YANG
E. M. SPARROW

HEAT TRANSFER DIVISION
Chair, **V. CAREY**
Vice Chair, **L. GRITZO**
Past Chair, **CHANG OH**

PUBLICATIONS COMMITTEE
Chair, **BAHRAM RAVANI**

OFFICERS OF THE ASME
President,
AMOS E. HOLT
Executive Director,
THOMAS G. LOUGHLIN
Treasurer,
WILBUR MARNER

PUBLISHING STAFF

Managing Director, Publishing
PHILIP DI VIETRO

Manager, Journals
COLIN McATEER

Production Coordinator
JUDITH SIERANT

Transactions of the ASME, Journal of Heat Transfer (ISSN 0022-1481) is published monthly by The American Society of Mechanical Engineers, Three Park Avenue, New York, NY 10016. Periodicals postage paid at New York, NY and additional mailing offices. POSTMASTER: Send address changes to Transactions of the ASME, Journal of Heat Transfer, c/o THE AMERICAN SOCIETY OF MECHANICAL ENGINEERS, 22 Law Drive, Box 2300, Fairfield, NJ 07007-2300. **CHANGES OF ADDRESS** must be received at Society headquarters seven weeks before they are to be effective. Please send old label and new address.

STATEMENT from By-Laws. The Society shall not be responsible for statements or opinions advanced in papers or ... printed in its publications (B7.1, Para. 3).

COPYRIGHT © 2010 by The American Society of Mechanical Engineers. For authorization to photocopy material for internal or personal use under those circumstances not falling within the fair use provisions of the Copyright Act, contact the Copyright Clearance Center (CCC), 222 Rosewood Drive, Danvers, MA 01923, tel: 978-750-8400, www.copyright.com. Request for special permission or bulk copying should be addressed to Reprints/Permission Department.

Canadian Goods & Services Tax Registration #126148048

Downloaded 05 Feb 2011 to 141.219.44.39. Redistribution subject to ASME license or copyright; see http://www.asme.org/terms/Terms_Use.cfm

(**Contents continued**)

Journal of Heat Transfer **Volume 132, Number 2** **FEBRUARY 2010**

Applications

TECHNICAL BRIEFS

The ASME Journal of Heat Transfer is abstracted and indexed in the following:

Applied Science and Technology Index, Chemical Abstracts, Chemical Engineering and Biotechnology Abstracts (Electronic equivalent of Process and Chemical Engineering), Civil Engineering Abstracts, Compendex (The electronic equivalent of Engineering Index), Corrosion Abstracts, Current Contents, E & P Health, Safety, and Environment, Ei EncompassLit, Engineered Materials Abstracts, Engineering Index, Enviroline (The electronic equivalent of Environment Abstracts), Environment Abstracts, Environmental Engineering Abstracts, Environmental Science and Pollution Management, Fluidex, Fuel and Energy Abstracts, Index to Scientific Reviews, INSPEC, International Building Services Abstracts, Mechanical & Transportation Engineering Abstracts, Mechanical Engineering Abstracts, METADEX (The electronic equivalent of Metals Abstracts and Alloys Index), Petroleum Abstracts, Process and Chemical Engineering, Referativnyi Zhurnal, Science Citation Index, SciSearch (The electronic equivalent of Science Citation Index), Theoretical Chemical Engineering

Journal of Heat Transfer

Guest Editorial

Foreword to the Special Issue on Radiative Heat Transfer

It is with great pleasure that we present this special issue of the *Journal of Heat Transfer*. Dating back to its inception, the *Journal of Heat Transfer* has been one of the premier journals in heat transfer to publish ground-breaking work on radiative heat transfer and related applications. Therefore, the journal is an appropriate home for a special issue on radiative heat transfer. We thank the Editor, Professor Yogesh Jaluria, for recognizing this opportunity, and graciously agreeing to publish this issue.

Through the publication of this special issue, we also celebrate the 65th birthday of Professor Michael F. Modest, an internationally recognized scholar and educator in the area of radiative heat transfer. Professor Modest's seminal contributions, spanning more than three decades, have laid the foundation for several aspects of radiative heat transfer and its applications, ranging from radiation in molecular gases and plasmas to laser processing of materials. The *Journal of Heat Transfer* has been home to a large fraction of his more than 200 publications. His textbook, *Radiative Heat Transfer*, now in its second edition, is widely recognized as a model of clarity and knowledge to students, teachers, and professional alike. Professor Modest has also served both as an Associate Technical Editor and as a Senior Associate Technical Editor of the *Journal of Heat Transfer*. The publication of this special issue closely follows the Symposium on Radiative Heat Transfer in Honor of Professor Michael Modest, held at the 2009 Summer Heat Transfer Conference in July in San Francisco, California. While a large majority of the contributors to this issue were in attendance at the Symposium, the publication of this issue provides another opportunity for those authors who were unable to attend to present their work and pay tribute to Professor Modest.

This special issue brings to light the state of the art in the area of radiative heat transfer through compilation of a collection of papers contributed by experts across the world—researchers who are working on various aspects of radiative heat transfer and its applications. Many of these researchers have worked directly under Professor Modest's supervision, others have worked with him in a collaborative capacity, and some simply share interest and work in technical areas of common interest. The 21 full-length Research Papers and 2 Technical Briefs contained in this special issue were contributed by authors from 9 different countries. They were all peer-reviewed in compliance with the rigorous review standards of the *Journal of Heat Transfer*. The papers represent a broad spectrum of research in the field, covering topics such as radiation in plasma systems, radiation in fires, radiation in porous media, radiation transport at small scales, novel finite-element and finite-volume method based approaches for solution of the radiative transfer equation, and Monte Carlo methods. As such, the papers have been classified into three broad sub-categories: (1) radiative properties, (2) solution methods, and (3) applications.

We sincerely thank all contributors for their overwhelming response to the call for papers for this special issue, and all reviewers for devoting their precious time to review the papers. Finally, we deeply appreciate the strong and responsive editorial assistance of Shefali Patel.

We are pleased to celebrate the career and contributions of Professor Michael F. Modest, and we hope that this special compilation of papers will be beneficial to researchers in the area of radiative heat transfer for years to come.

Sandip Mazumder
Ohio State University

Brent W. Webb
Brigham Young University

Infrared Radiative Properties of Heavily Doped Silicon at Room Temperature

S. Basu

B. J. Lee[1]

Z. M. Zhang[2]
Fellow ASME
e-mail: zhuomin.zhang@me.gatech.edu

George W. Woodruff School of Mechanical Engineering,
Georgia Institute of Technology,
Atlanta, GA 30332

This paper describes an experimental investigation on the infrared radiative properties of heavily doped Si at room temperature. Lightly doped Si wafers were ion-implanted with either boron or phosphorus atoms, with dosages corresponding to as-implanted peak doping concentrations of 10^{20} and 10^{21} cm^{-3}; the peak doping concentrations after annealing are 3.1×10^{19} and 2.8×10^{20} cm^{-3}, respectively. Rapid thermal annealing was performed to activate the implanted dopants. A Fourier-transform infrared spectrometer was employed to measure the transmittance and reflectance of the samples in the wavelength range from 2 μm to 20 μm. Accurate carrier mobility and ionization models were identified after carefully reviewing the available literature, and then incorporated into the Drude model to predict the dielectric function of doped Si. The radiative properties of doped Si samples were calculated by treating the doped region as multilayer thin films of different doping concentrations on a thick lightly doped Si substrate. The measured spectral transmittance and reflectance agree well with the model predictions. The knowledge gained from this study will aid future design and fabrication of doped Si microstructures as wavelength selective emitters and absorbers in the midinfrared region. [DOI: 10.1115/1.4000171]

Keywords: microscale, doped silicon, radiative properties, thin films

1 Introduction

Doped Si is extensively used in the semiconductor and microelectronics industry such as in tunnel diodes [1], semiconductor injection lasers, backward diodes, transistor emitters, and a host of other devices [2]. Thin films made of heavily doped Si are also used as filters for improving the performance of thermophotovoltaic devices, due to their metallic behavior [3]. Recently, Fujii et al. [4,5] showed the possibility of controlling the photoluminescence of Si nanocrystals by codoping them with boron and phosphorus. Doped Si gratings were proposed as coherent infrared light sources by exciting surface plasmon polaritons [6,7]. Near-field heat transfer between heavily doped Si surfaces was also studied for applications such as radiative cooling of Si devices [8,9]. As a matter of fact, knowledge of the radiative properties of doped Si is very important for microstructured surfaces, accurate temperature measurement of Si wafer during rapid thermal processing, and for investigating nanoscale radiative heat transfer between doped Si surfaces.

Radiative properties of doped Si have been extensively studied by several research groups. Engstrom [10] measured the infrared transmittance and reflectance of *p*-type laser annealed Si in the spectral range from 2.5 μm to 20 μm. However, the author fitted the experimentally measured radiative properties with the modeling results, based on the Drude model with scattering rate and carrier resistivity as the fitting parameters. Barta and Lux [11] used the Kramers–Kronig analysis to obtain the optical constants of heavily doped silicon from reflectance measurements. Using values of the optical constants, analytical expressions for relaxation time as a function of carrier concentration were obtained, which are valid only in the spectral region above 5 μm. Ehsani et al. [3] characterized the radiative properties of arsenic, boron, and phosphorus-doped Si films at different doping concentrations for their applications as filters in thermophotovoltaic devices. A detailed investigation was performed regarding the effect of annealing on the radiative properties of doped Si. However, their experimental results have not been validated, and the model used for simulating the performance of the filters is overly simplified. Recently, Fu and Zhang [9] examined the dielectric function of doped Si at different temperatures and doping concentrations in order to predict the near-field heat transfer between doped Si surfaces. However, the ionization and mobility models used in this study, for predicting the dielectric function of doped Si, may provide incorrect values of the radiative properties at doping concentrations greater than 10^{19} cm^{-3}.

The objectives of the present study are to identify more accurate carrier mobility and ionization models, before incorporating them in the Drude model for predicting the radiative properties of heavily doped Si at room temperature, and to validate the calculated radiative properties with experiments in the infrared. Heavily doped Si samples were prepared by ion bombardment of lightly doped Si wafer with boron and phosphorus atoms. The ion-implanted wafers were then annealed at different temperatures for dopant activation. Hereafter, unless otherwise mentioned, all the doped Si samples will be referred to by their as-implanted peak doping concentration. A Fourier-transform infrared (FTIR) spectrometer was employed to measure the radiative properties of the samples in the wavelength range from 2 μm to 20 μm. The doped Si samples were modeled as a multilayer structure of heavily doped Si thin films on a thick lightly doped Si substrate. The doping profile, as a function of depth, was obtained from secondary ion mass spectrometry (SIMS) measurements. The radiative properties of the doped Si samples were calculated using the doping profile obtained from SIMS and the optical constants from the Drude model. The calculated results were then compared with the experimental measurements.

---

[1] Present address: Department of Mechanical Engineering and Materials Science, University of Pittsburgh, PA 15261.

[2] Corresponding author.

Contributed by the Heat Transfer Division of ASME for publication in the JOURNAL OF HEAT TRANSFER. Manuscript received February 8, 2008; final manuscript received February 20, 2009; published online November 30, 2009. Assoc. Editor: Yogesh Jaluria.

2 Dielectric Function of Doped Si

For heavily doped Si at room temperature, ionized donors or acceptors produce free carriers, which can greatly enhance the absorption in the infrared region. The Drude model, originally developed to describe the frequency-dependent conductivity of metals, was employed to model the free-carrier absorption of doped Si in many studies [7,8]. For doped silicon in the infrared region ($\lambda > 2\ \mu$m), the Drude model gives the dielectric function or relative permittivity as follows:

$$\varepsilon(\omega) = (n + i\kappa)^2 = \varepsilon_\infty - \frac{\omega_p^2}{\omega(\omega + i\gamma)} \tag{1}$$

where ω is the angular frequency, ε_∞ is the limiting value of the dielectric function at high frequencies and is ≈ 11.7 [8], ω_p is the plasma frequency, and γ is the scattering rate. Note that the dielectric function is the square of the complex refractive index $n + i\kappa$, where n and κ are the refractive index and extinction coefficient, respectively. The plasma frequency and scattering rate can be expressed as $\omega_p = \sqrt{Ne^2/m^*\varepsilon_0}$ and $\gamma = e/m^*\mu$, respectively, where ε_0 is the permittivity of free space, e is the electron charge, N is the carrier concentration, m^* is the carrier effective mass, and μ is the mobility [12]. Notice that for heavily doped Si at room temperature, the scattering process is dominated by impurity scattering. Hence, lattice or phonon scattering is neglected in the present study. The effective mass, in general, depends on the carrier concentration and frequency. In the case of heavily doped silicon, the effective mass is independent of carrier concentration, unless it exceeds $5 \times 10^{20}\ \mathrm{cm^{-3}}$ [13–15]. The effective mass of electron or hole is taken as $0.27m_0$ or $0.37m_0$, respectively, where m_0 is the free electron mass in vacuum [16]. The effective mass is assumed to be independent of frequency. In order to obtain the optical constants of heavily doped silicon, it is very important to accurately model the mobility and carrier concentration at a given doping concentration. Hence, different mobility and ionization models are examined in the following. Hereafter, phosphorus and boron implanted Si is referred to as n-type and p-type Si, respectively.

Caughey and Thomas [17] proposed an empirical model for the carrier mobility of Si in the doping range from $10^{15}\ \mathrm{cm^{-3}}$ to $10^{21}\ \mathrm{cm^{-3}}$, by fitting the measured resistivity of Si with both p-type and n-type dopants. Using a different fitting procedure for the same expression, Baccarani and Ostoja [18] obtained different coefficients for n-type Si. On the other hand, Wagner [19] and Antoniadis et al. [20] obtained different coefficients for p-type Si. Masetti et al. [21] improved the above-mentioned mobility model in order to fit the experimental data more accurately at higher carrier concentrations. The mobility expression for n-type Si is given as

$$\mu = \mu_1 + \frac{\mu_{\max} - \mu_1}{1 + (N_e/C_r)^\alpha} - \frac{\mu_2}{1 + (C_s/N_e)^\beta} \tag{2}$$

Here, $\mu_1 = 68.5\ \mathrm{cm^2/V\ s}$, $\mu_{\max} = 1414\ \mathrm{cm^2/V\ s}$, $\mu_2 = 56.1\ \mathrm{cm^2/V\ s}$, $C_r = 9.2 \times 10^{16}\ \mathrm{cm^{-3}}$, $C_s = 3.41 \times 10^{20}\ \mathrm{cm^{-3}}$, $\alpha = 0.711$, $\beta = 1.98$, and N_e is the electron concentration [21]. The mobility for p-type Si is

$$\mu = \mu_1 \exp(-p_c/N_h) + \frac{\mu_{\max}}{1 + (N_h/C_r)^\alpha} - \frac{\mu_2}{1 + (C_s/N_h)^\beta} \tag{3}$$

Here, $\mu_1 = 44.9\ \mathrm{cm^2/V\ s}$, $\mu_{\max} = 470.5\ \mathrm{cm^2/V\ s}$, $\mu_2 = 29.0\ \mathrm{cm^2/V\ s}$, $C_r = 2.23 \times 10^{17}\ \mathrm{cm^{-3}}$, $C_s = 6.10 \times 10^{20}\ \mathrm{cm^{-3}}$, $\alpha = 0.719$, $\beta = 2$, $p_c = 9.23 \times 10^{16}\ \mathrm{cm^{-3}}$, and N_h is the hole concentration [21].

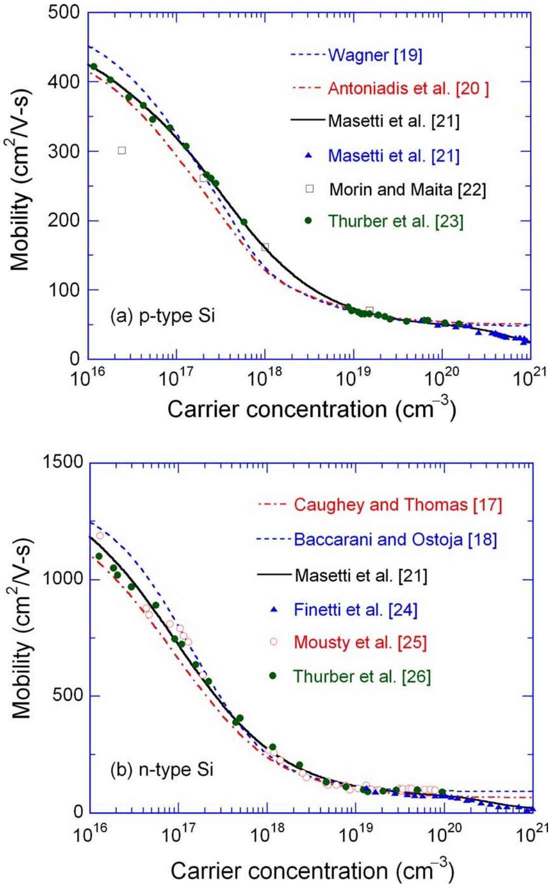

Fig. 1 Comparison of different mobility models for (*a*) *p*-type and (*b*) *n*-type Si at room temperature with experimental data

A comparison of different mobility models with the experimentally measured values is shown in Figs. 1(*a*) and 1(*b*) for p- and n-type Si, respectively. The data are taken from Refs. [21–26]. The solid lines refer to the models, while the symbols refer to the experimental data. It can be clearly seen that while the mobility model used in Refs. [17–20] predict a constant value beyond the carrier concentration of $5 \times 10^{19}\ \mathrm{cm^{-3}}$, the model suggested in Ref. [21] can accurately fit the experimental data at higher carrier concentrations. While the first two terms in Eqs. (2) and (3) exhibit a trend similar to the mobility expressions in Refs. [17–20], the third term accounts for the decreasing mobility at higher doping concentrations. Since this term is negligible for carrier concentrations lower than $5 \times 10^{19}\ \mathrm{cm^{-3}}$, the different mobility models exhibit a similar trend at lower carrier concentrations. Hence, the mobility model proposed in Ref. [21] is adopted in the present study for the calculation of the carrier mobility.

Marquier et al. [8] assumed complete impurity ionization over the entire doping concentration range in their calculation of the radiative properties of doped Si. Similar assumptions were also made in some previous studies by different researchers [17,18,27]. Fu and Zhang [9] on the other hand, considered complete ionization for doping concentrations below $10^{17}\ \mathrm{cm^{-3}}$, and partial ionization beyond $10^{17}\ \mathrm{cm^{-3}}$. They had adopted the ionization model proposed by Gaylord and Linxwiler [28] in their analysis. Recently, Park et al. [29] reported a doping density model, which was accurate to 8% of the measured values for doping concentration lower than $10^{18}\ \mathrm{cm^{-3}}$ within the temperature range of 50–300 K. However, for concentrations greater than $10^{19}\ \mathrm{cm^{-3}}$, the model generated considerable error. Previous experimental results on doped Si have indicated that only in the doping range from about $10^{17}\ \mathrm{cm^{-3}}$ to $10^{19}\ \mathrm{cm^{-3}}$, the dopant atoms are not completely ionized, and the majority carrier concentration can be lower than the doping concentration [23,26,30,31]. Between $10^{16}\ \mathrm{cm^{-3}}$ and $10^{18}\ \mathrm{cm^{-3}}$, the Fermi level is located close to the doping level; this results in the dopant states being occupied, and leads to incomplete ionization [32]. However, beyond $10^{18}\ \mathrm{cm^{-3}}$, the donor energy band gets broadened, and merges with the conduction

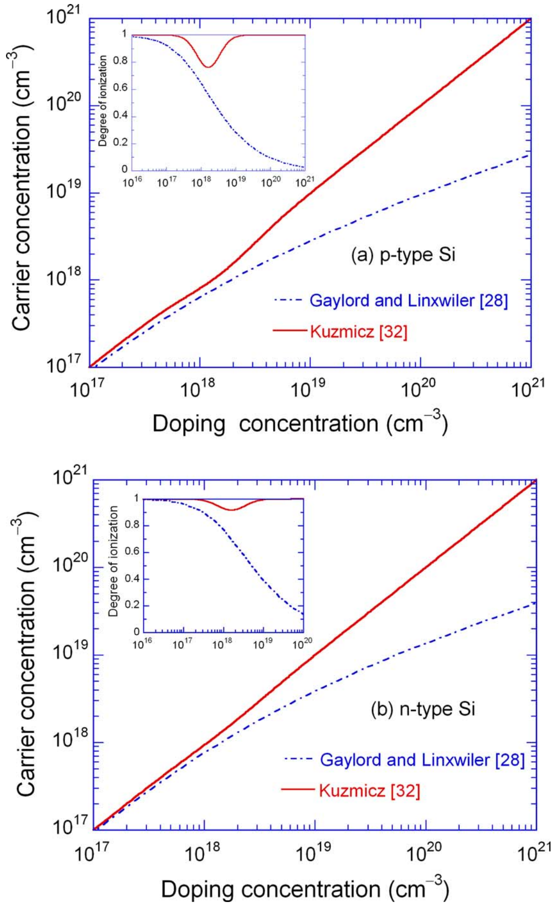

Fig. 2 Carrier concentration versus doping level calculated from two models for (*a*) *p*-type and (*b*) *n*-type Si at room temperature. The insets show the degree of ionization.

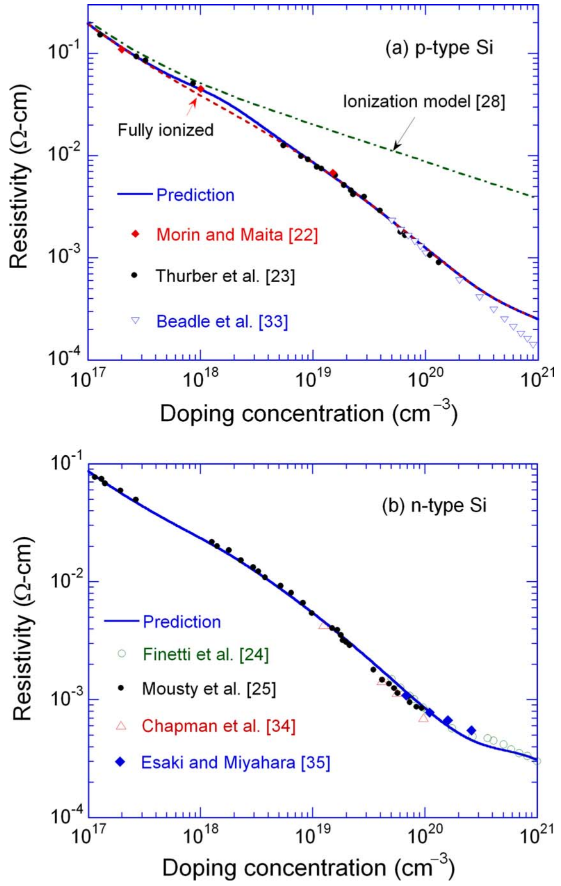

Fig. 3 Comparison of calculated resistivity with measurements from different studies for (*a*) *p*-type and (*b*) *n*-type Si, for different doping levels at room temperature

band; this generates more free carriers, and increases the degree of ionization as the doping level further increases [29]. As a result of the two competing effects, the degree of ionization is the lowest around 10^{18} cm^{-3}. Kuzmicz [32] included this effect of partial ionization while considering a wide range of doping concentrations for both *p*- and *n*-type Si, and developed an empirical model. Figures 2(*a*) and 2(*b*) compare the different ionization models for *p*- and *n*-type Si, respectively. The degree of ionization has been presented as insets in the two figures. For the model proposed in Ref. [32], the degree of ionization first reduces to 0.75 for *p*-type Si, and 0.9 for *n*-type Si around 10^{18} cm^{-3}, and then increases to almost unity at doping concentrations greater than 10^{19} cm^{-3}, suggesting partial ionization in the doping range from 10^{17} cm^{-3} and 10^{19} cm^{-3}, for both *p*- and *n*-type Si. On the other hand, the model predicted in Ref. [28] suggests incomplete ionization for both *p*- and *n*-type Si over the entire doping range, and the carrier concentration is only 5% of the doping concentration at doping levels exceeding 10^{21} cm^{-3}. For the complete ionization model, the degree of ionization is always 1. Using the different ionization models, the carrier concentrations can be obtained, which, when multiplied by mobility expressions in Eqs. (2) and (3), will yield resistivity.

The dc resistivity is a function of the carrier concentration and mobility, given as $\rho=(Ne\mu)^{-1}$. Figures 3(*a*) and 3(*b*) compare the measured resistivity values, taken from Refs. [22–25,33–35], with those calculated from different ionization models. The solid lines represent the resistivity predicted with the carrier concentration obtained from Ref. [32], and mobility from Eqs. (2) and (3), for *p*- and *n*-type Si, respectively. For comparison, the resistivity for *p*-type Si, calculated using the ionization model from Ref. [28], is shown as the dash-dotted line, and the resistivity, calculated by assuming complete ionization, is shown as the dashed line in Fig. 3(*a*). Clearly, the model from Ref. [28] results in an overprediction of the resistivity beyond 10^{18} cm^{-3}. On the other hand, the full ionization model yields an underprediction of the resistivity in the doping range between 10^{17} cm^{-3} and 10^{19} cm^{-3}. The resistivity obtained from the ionization model of Kuzmicz [32] agrees very well with the experimental measurements over a wide range of doping concentrations and, hence, is adopted in the present work. Beyond 10^{20} cm^{-3}, the data from Ref. [33] do not match well with the prediction for *p*-type Si, as can be seen from Fig. 3(*a*). At doping concentrations greater than 10^{20} cm^{-3}, the carrier mobility and the degree of ionization depend on the doping and annealing methods. The measurement data are often not very reliable [33].

The empirical expression for the ionization model of Ref. [32] gives the degree of ionization ζ, i.e., the ratio of the number of ionized dopant atoms to the total number of impurities, as

$$\zeta = 1 - A\exp\{-[B\ln(N/N_0)]^2\} \tag{4}$$

where N is the doping concentration, and the constants A, B, and N_0 are determined as follows. For *n*-type Si: $A=0.0824\Theta^{-1.622}$, $N_0=1.6\times10^{18}\Theta^{0.7267}$, and $B=0.4722\Theta^{0.0652}$ for $N<N_0$, and $B=1.23-0.3162\Theta$ for $N\geq N_0$. Here, $\Theta=T/300$ is a reduced temperature, and T is expressed in Kelvin. On the other hand, for *p*-type Si: $A=0.2364\Theta^{-1.474}$, $N_0=1.577\times10^{18}\Theta^{0.46}$, and $B=0.433\Theta^{0.2213}$ for $N<N_0$, and $B=1.268-0.338\Theta$ for $N\geq N_0$. With these parameters, Eq. (4) agrees with the numerical solution

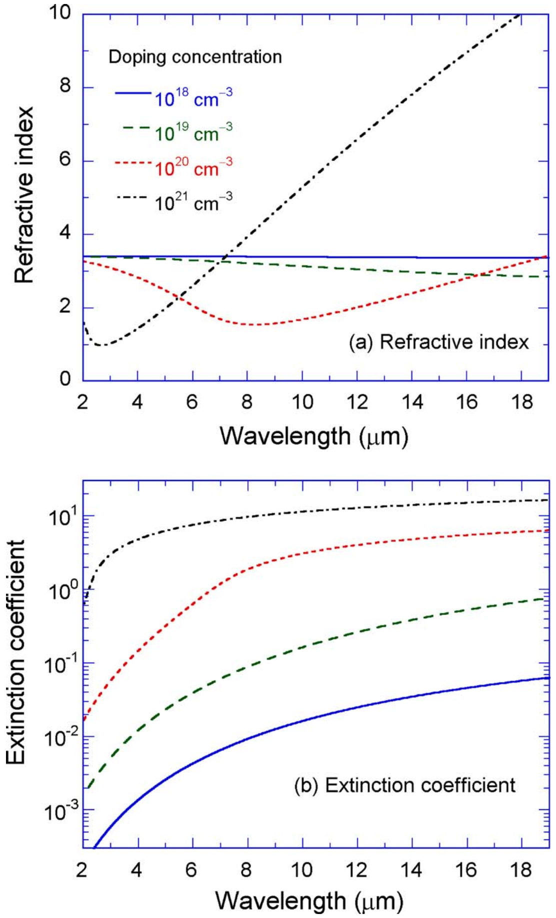

Fig. 4 Optical constants of *p*-type silicon for different doping concentrations calculated using the Drude model, including accurate values of carrier mobility and ionization: (*a*) refractive index, and (*b*) extinction coefficient. The legends are the same for both figures.

of the charge neutrality equations within 3% in the temperature range of 250–400 K [32].

Using the values for carrier concentration and resistivity, the optical constants of heavily doped Si can be calculated using the Drude model. Figure 4 shows the calculated refractive index and extinction coefficients of *p*-type Si for different doping concentrations. The optical constants of *n*-type Si show similar trends as those of *p*-type Si, and hence, have not been plotted. From Fig. 4(*a*), it can be seen that the refractive index of 1×10^{18} cm^{-3} doped Si remains constant in the spectral range from 2 μm to 20 μm. However, at higher doping concentrations, due to the greater number of free carriers, the refractive index initially decreases from that for 1×10^{18} cm^{-3}, attains a minimum, and then increases again. From Fig. 4(*b*), it is observed that an order of magnitude increase in the doping concentration of Si results in a tenfold increase in the extinction coefficient for the different doped samples. With increasing doping concentrations, the extinction coefficients become comparable to the refractive index, especially at longer wavelengths, which results in increased metallic behavior of the doped Si samples. Also, as the doping concentration increases, the location of the minimum in the refractive indices shifts to shorter wavelengths, and is close to the plasma frequency, as seen in Fig. 4(*a*). As the frequency increases towards the plasma frequency, the real part of the dielectric function becomes negative, which implies that the extinction coefficient becomes greater than the refractive index. Hence, due to the strong dependence of the optical constants of doped Si on the carrier concentrations, care must be taken while selecting the accurate ionization model for predicting the degree of ionization.

3 Sample Preparation and Characterization

Ion implantation is a standard technique being used in the Si microelectronics industry for introducing dopants into Si wafers due to its more precise control and lower processing temperature, as compared with diffusion [3]. In the present study, lightly doped (10^{15} cm^{-3}) Si wafers (400 μm thick) were ion-implanted by a commercial vendor, using 70 keV boron and 160 keV phosphorus atoms, with dosage of 6.4×10^{14} cm^{-2} and 6.4×10^{15} cm^{-2}, respectively. These dosages correspond to as-implanted peak doping concentrations of 1.0×10^{20} cm^{-3} and 1.0×10^{21} cm^{-3}, respectively, at a depth of approximately 300 nm from the surface. To activate the implanted ions, subsequent annealing is required at appropriate combinations of time and temperature [36].

Rapid thermal annealing was selected in order to prevent substantial dopant diffusion into the sample. Before annealing, the doped Si wafers were diced into 25×25 mm^2 samples, and a 500-nm thick silicon dioxide layer was deposited on the wafers using low-pressure chemical vapor deposition at 300°C, in order to prevent out-diffusion of boron and phosphorus ions during annealing. Different temperatures were selected for studying the influence of temperature on activation of the implanted ions. The *p*-type wafers were annealed at 850°C, 950°C, and 1100°C for 60 s, while the *n*-type wafers were annealed at 850°C, 950°C, and 1050°C for 60 s in vacuum. The annealing temperature and time are similar to those in Refs. [3,37,38]. The ramp time required to attain the annealing temperature was set to 10 s, consistent with the furnace specifications. The wafers were allowed to cool below 100°C before being taken out of the annealing chamber. The temperature of the wafers was constantly monitored using thermocouples. After annealing, the deposited oxide layer was etched away using dilute hydrofluoric acid.

Transmittance and reflectance for the doped Si samples were measured by a commercial FTIR spectrometer, equipped with a globar source and a pyroelectric detector [39]. The spectra were measured at room temperature with a spectral resolution of 4 cm^{-1} in the spectral range from 500 cm^{-1} to 5000 cm^{-1}. For the transmittance measurements, the sample holder with an aperture of 6 mm in diameter limits the beam diameter on the sample. The spectrometer and sample compartment were purged with N_2 gas for about 30 min to reduce the absorption by water vapor and CO_2 molecules in air. An average of over 64 scans was used. The uncertainty was estimated to be 0.01 with 95% confidence level [39]. Reflectance was measured at an incidence angle of 10 deg, using a specular reflectance accessory with an Au mirror as the reference. The reflectance of the Au mirror was calculated using the tabulated optical constants [40]. The measurement equation for the sample reflectance $R_s(\lambda)$ is

$$R_s(\lambda) = \frac{V_s(\lambda) - V_b(\lambda)}{V_{\mathrm{Au}}(\lambda) - V_b(\lambda)} R_{\mathrm{Au}}(\lambda) \tag{5}$$

$R_{\mathrm{Au}}(\lambda)$ is the reflectance of the gold mirror, and $V_s(\lambda)$, $V_{\mathrm{Au}}(\lambda)$, and $V_b(\lambda)$ are the reflected signals from the sample, gold mirror, and backside of the sample holder, respectively. The sample holder has a hole, which is smaller than the beam diameter. As a result, part of the beam is reflected back from the sample holder for measurements of both the sample and the reference. The reflectance from the backside of the holder was measured by removing the samples, and is always less than 0.02. The overall uncertainty for reflectance measurements was estimated to be 0.02 with 95% confidence level, taking into account the instrument effects (such as beam divergence and alignment error), Au mirror reflectance, and repeatability of measurements.

Figure 5 compares the transmittance of both *p*- and *n*-type Si wafers when annealed to different temperatures. Without annealing, both the *p*- and *n*-type as-implanted samples behave like

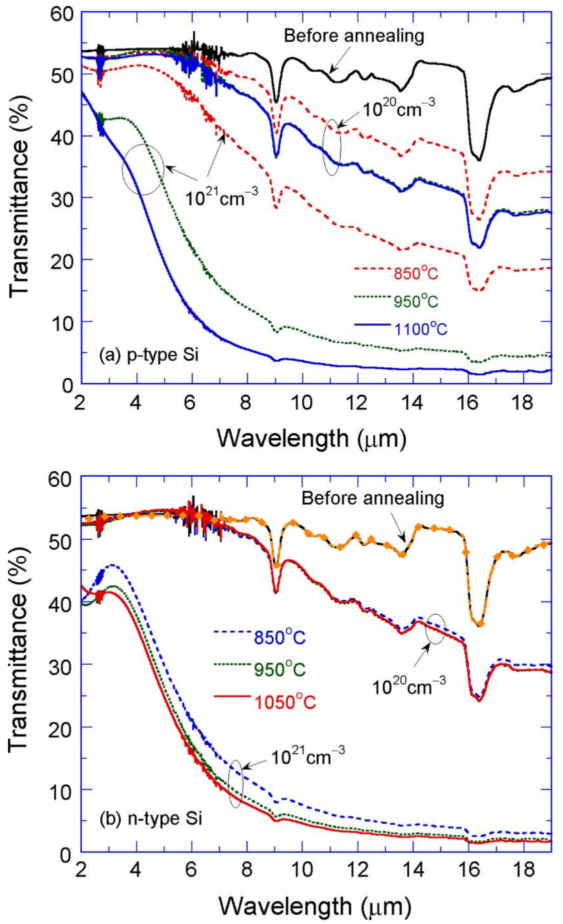

Fig. 5 Measured transmittance of (*a*) *p*-type and (*b*) *n*-type Si annealed at different temperatures. The dashed line with symbols in (*b*) refers to the transmittance calculated based on the refractive index of Si obtained from Ref. [40] and the extinction coefficient extracted from the measured transmittance at 4 cm^{-1} resolution. The doping concentration refers to the peak concentration before annealing of the samples.

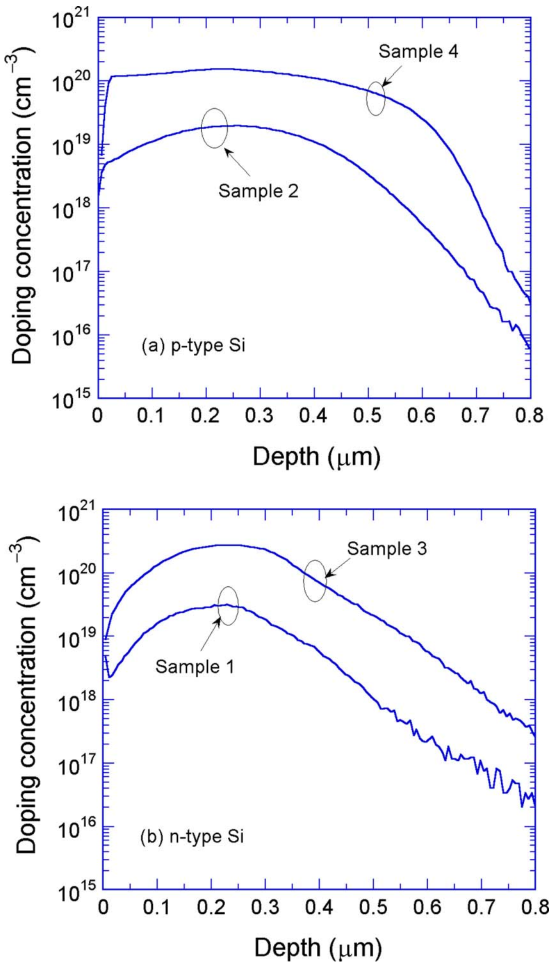

Fig. 6 Comparison of the doping profiles obtained from SIMS for (*a*) *p*-type Si (Sample 2 and 4) and (*b*) *n*-type Si (Sample 1 and 3)

lightly doped Si, as seen from the transmittance measurements, indicating that annealing is required in order to activate the dopants. For the 10^{20} cm^{-3} *p*-type Si, it is observed that the samples attain full dopant activation at 950°C, since there is no further change in the transmittance when annealed to 1100°C. However, for the 10^{21} cm^{-3} *p*-type Si, higher temperature is required to activate the majority of the dopants, as seen in Fig. 5(*a*). For *n*-type Si samples, there is not much difference between the transmittance for the samples annealed to three different temperatures for both the doping concentrations. These results are consistent with those observed in previous studies [3]. The dashed line with symbols in Fig. 5(*b*) shows the calculated transmittance of the lightly doped Si substrate used in this study, to be discussed in detail in Sec. 4. Based on the transmittance measurements, the four fully activated samples were selected for SIMS analysis. Table 1 tabulates the as-implanted and post-annealing peak doping concentration of the fully activated samples, along with the corresponding annealing temperatures. Hereafter, these four samples will be referred by their numbers.

SIMS analysis was provided by a commercial supplier for the four selected samples. In the SIMS technique, an ion beam sputters material off the surface of a semiconductor, and the ion component is detected and mass analyzed [36]. Since SIMS is a destructive test, one of the wafers was used for SIMS measurements while optical measurements were performed on the other sample but from the same batch. Due to the formation of a native-oxide layer of a few nanometers on the surface of Si, the doping concentration in the skin layer close to the surface is not accurate, as is seen from the SIMS profile, and this layer was subtracted from the total film thickness during modeling. Figure 6 shows the dop-

Table 1 Samples for SIMS analysis and spectrometric measurements

Sample number	Dopant type	As-implanted peak doping concentration (cm^{-3})	Annealing temperature (°C)	Peak doping concentration after annealing (cm^{-3})
1	Phosphorus	1.0×10^{20}	950	3.1×10^{19}
2	Boron	1.0×10^{20}	1100	3.8×10^{19}
3	Phosphorus	1.0×10^{21}	950	2.8×10^{20}
4	Boron	1.0×10^{21}	1100	1.5×10^{20}

ing profiles obtained from SIMS measurements for different samples.

4 Modeling of the Radiative Properties of a Multilayer Structure

The doped Si samples can be treated as a multilayer structure of thin films of varying doping concentrations on a thick Si substrate. For the Si substrate, the refractive index was obtained from the tabulated data in Ref. [40]. The extinction coefficient for the Si substrate was extracted from the measured transmittance at 4 cm^{-1} resolution. The tabulated values of the extinction coefficient from Ref. [40] cannot account for the absorption, due to the interstitial oxygen at around 9 μm [41], and the lattice absorption around 16 μm for the lightly doped Si substrate used in the present study. The transmittance, calculated using the refractive index from Ref. [40], and the extracted extinction coefficients, is shown in Fig. 5(*b*) as the dashed line with symbols. The doping profile down to a doping concentration of 1×10^{17} cm^{-3}, obtained from SIMS measurements, was approximated by a step function, and broken into 10 nm thin films. The film thickness was also reduced to 5 nm, and the difference in modeling results was observed to be less than 0.03%. The carrier concentrations were obtained from the doping concentrations using the ionization model of Ref. [32], and consequently, the optical constants could be calculated for each layer using the Drude model, as discussed in Sec. 2. For the structure of thin films on a thick substrate, radiation inside the film can be treated as coherent, and that in the substrate as incoherent. Since the substrate is semitransparent in the infrared, the reflectance depends on whether the radiation is incident on the film side or the substrate side. The transmittance, however, is independent on the side, on which radiation is incident. The transmittance and reflectance for the radiation incident on the substrate, as well as the film, were calculated from the following expressions [42]:

$$T_\lambda = \frac{\tau_a\tau_s\tau_i}{1-r_s r_b \tau_i^2} \tag{6a}$$

$$R_{\lambda,f} = r_a + \frac{r_s\tau_a^2\tau_i^2}{1-r_s r_b \tau_i^2} \tag{6b}$$

$$R_{\lambda,s} = r_a' + \frac{r_s'\tau_a'^2\tau_i^2}{1-r_s' r_s \tau_i^2} \tag{6c}$$

where T_λ is the transmittance, and $R_{\lambda,f}$ and $R_{\lambda,s}$ are the reflectance for the radiation incident on the film and substrate, respectively. Here, r_a and τ_a refer to the reflectance and transmittance at the air-film interface for rays incident from air, while r_b refers to the reflectance at the substrate-film interface for rays incident from the substrate, assuming that the substrate is semi-infinite. Also, r_s and τ_s represent the reflectance and transmittance at the air-substrate interface for rays incident from the substrate. Furthermore, r_a' and τ_a' refer to the reflectance and transmittance at the air-substrate interface for rays incident from air, and r_s' is the reflectance at the substrate-film interface for rays incident from substrate. These expressions can be calculated using the transfer-matrix formulation by neglecting absorption in the Si substrate [42]. It should be noted that absorption is accounted for in the expression for the internal transmissivity of the substrate given by $\tau_i=\exp(-4\pi\kappa_s d_s/\lambda)$, where κ_s and d_s are the extinction coefficient and thickness of the Si substrate, respectively.

5 Measurement Results and Comparison With Modeling

Figure 7 shows the measured transmittance and reflectance compared with theoretical modeling results for Sample 1 to 4. The transmittance and reflectance is calculated from Eq. (6) using the doping profiles obtained from SIMS measurements. In the calculation, the doped Si region is considered up to the doping level of 10^{17} cm^{-3} with a total of 65 layers, each 10 nm thick. For Sample 1, the calculated results, based on the Drude model, agree very well with the experimental measurements for both transmittance and reflectance. The reflectance for radiation incident on both the film and the substrate is close to that of the lightly doped Si substrate up to 8 μm. Beyond 8 μm, however, the reflectance for radiation incident on the substrate changes little, while the reflectance from the film increases with wavelength. This can be explained based on the optical constants of doped silicon, as shown in Fig. 4. For a doping concentration of 2×10^{19} cm^{-3}, the penetration depth increases with wavelength and, at 8 μm, the penetration depth is about 15 μm, which is much greater than the thickness of the doping region. As the wavelength further increases, the penetration depth continues to decrease, while the refractive index of the doping region decreases with the wavelength. Both effects contribute to the reduction in the reflectance for the incidence on the film. Note that the decreased refractive index of the film results in an antireflection effect. Generally speaking, the transmittance and reflectance for Sample 1 and 2 follow the same trends, due to the similar optical constants as a result of the similar doping concentrations. For Sample 2, however, the measured transmittance is lower than that predicted. The difference significantly exceeds the uncertainty of FTIR measurements. While the model may have some limitations, this discrepancy may also be caused by the nonuniformity in the dopant distribution during the ion bombardment, as well as the annealing process.

For Sample 3 and 4, the heavily doped region causes significant absorption, especially at longer wavelength, and results in a reduction in the transmittance. The measured and predicted radiative properties agree fairly well, except for the transmittance at shorter wavelengths. The reflectance is much higher for the incidence on the film, due to the metallic behavior of the heavily doped silicon. The location of the reflectance minima matches with that in the refractive index for the average doping concentration. Sample 3 has a slightly higher peak doping concentration, and the reflectance minimum is shifted to a slightly shorter wavelength than that for Sample 4. Note that the minimum value of the reflectance at around 4 μm for the incidence on the film is less than that for the incidence on the substrate. This implies that the absorptance is greater for the incidence on the film. At longer wavelengths, however, the reflectance for the incidence on the substrate is smaller, indicating a higher absorptance than the incidence on the film. While the transmittance for Samples 1 and 2 shows dips at 9 μm and 16 μm, due to lattice vibration, these dips are essentially not observable for Sample 3 and 4, due to the screening effect of the film. In fact, the reflectance for the incidence on the film does not show dips at all, because the penetration depth is much less than the thickness of the doping layer. Due to multiple reflections, the absorption at 9 μm and 16 μm is greatly enhanced for the incidence on the substrate, as can be seen by the magnitude of the dips in the reflectance. This can be understood as an optical cavity effect.

6 Conclusions

We have measured the transmittance and reflectance of heavily doped Si up to a doping concentration of 10^{21} cm^{-3} in the wavelength region from 2 μm to 20 μm. The Drude model was employed for modeling the dielectric function of doped Si, based on the selected carrier mobility and ionization models. It should be emphasized that the mobility and ionization models were adopted from studies performed by two different research groups, and the parameters suggested in their original publications have been strictly retained in this study. The doped Si samples were modeled as the multilayer structure of heavily doped Si thin films deposited on a thick lightly doped Si substrate. The calculated results are in good agreement with transmittance and reflectance

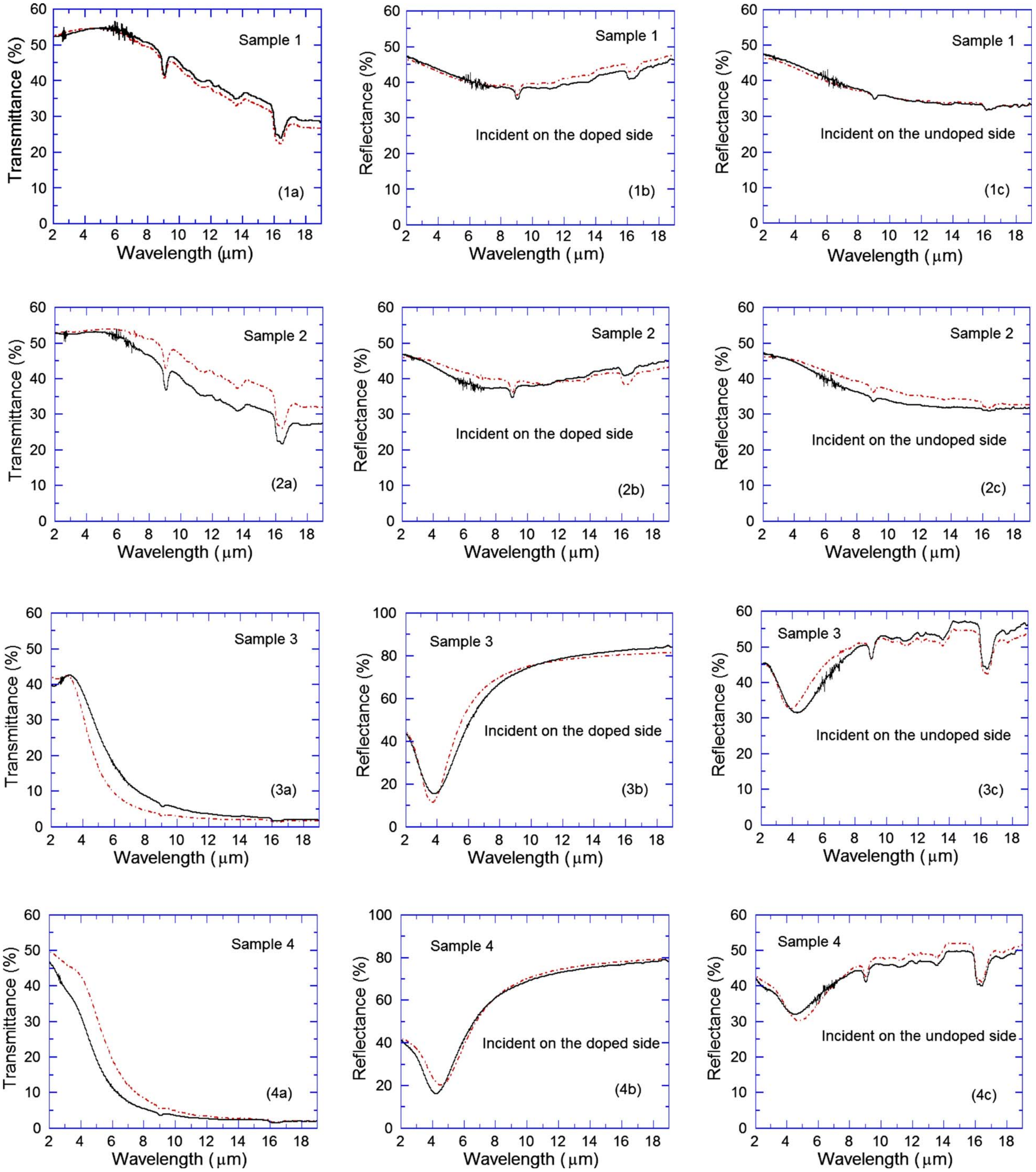

Fig. 7 Comparison of measured (solid lines) and calculated (dash-dotted lines) transmittance and reflectance (for incidence from either side) of all four samples

measurements, suggesting that the Drude model developed in this study is appropriate in predicting the radiative properties of heavily doped Si near room temperature.

Acknowledgment

The authors thank Dr. Keunhan Park for sharing references on various ionization and mobility models, as well as for valuable discussions. Partial financial support for S.B. from the National Science Foundation (Contract No. CBET-0500113) and that for B.J.L. and Z.M.Z. from the Department of Energy (Grant No. DE-FG02-06ER46343) are much appreciated.

Nomenclature

d = thickness (m)
e = electron charge (1.602×10^{-19} C)
m^* = carrier effective mass (kg)
m_0 = electron mass (9.109×10^{-31} kg)
n = refractive index
N = carrier concentration (cm^{-3})
R_λ = spectral reflectance
T = temperature (K)
T_λ = spectral transmittance

Greek Symbols

γ = scattering rate (rad/s)
ε = relative electrical permittivity, i.e., dielectric function
ε_0 = permittivity of vacuum (8.854×10^{-12} $\mathrm{C}^2/\mathrm{N\,m}^2$)
ε_∞ = dielectric function at high frequencies
κ = extinction coefficient
λ = wavelength in vacuum (m)
μ = carrier mobility ($\mathrm{cm}^2/\mathrm{V\,s}$)
ρ = dc resistivity (Ω cm)
ω = angular frequency (rad/s)

Subscripts

e = electron
f = film
h = hole
s = substrate

References

[1] Logan, R. A., and Rowell, J. M., 1964, "Conductance Anomalies in Semiconductor Tunnel Diodes," Phys. Rev. Lett., **13**, pp. 404–406.
[2] Soref, R. A., 1993, "Silicon-Based Optoelectronics," Proc. IEEE, **81**, pp. 1687–1706.
[3] Ehsani, H., Bhat, I., Borrego, J., Gutmann, R., Brown, E., Dziendziel, R., Freeman, M., and Choudhury, N., 1997, "Radiative Properties of Degenerately Doped Silicon Films for Applications in Thermophotovoltaic Systems," J. Appl. Phys., **81**, pp. 432–439.
[4] Fujii, M., Yamaguchi, Y., Takase, Y., Ninomiya, K., and Hayashi, S., 2004, "Control of Photoluminescence Properties of Si Nanocrystals by Simultaneously Doping *n*- and *p*-Type Impurities," Appl. Phys. Lett., **85**, pp. 1158–1160.
[5] Fujii, M., Yamaguchi, Y., Takase, Y., Ninomiya, K., and Hayashi, S., 2005, "Photoluminescence From Impurity Codoped and Compensated Si Nanocrystals," Appl. Phys. Lett., **87**, p. 211919.
[6] Marquier, F., Laroche, M., Carminati, R., and Greffet, J.-J., 2007, "Anisotropic Polarized Emission of a Doped Silicon Lamellar Grating," ASME J. Heat Transfer, **129**, pp. 11–16.
[7] Hesketh, P. J., Zemel, J. N., and Gebhart, B., 1988, "Polarized Spectral Emittance From Periodic Micromachined Surfaces. II. Doped Silicon—Angular Variation," Phys. Rev. B, **37**, pp. 10803–10813.
[8] Marquier, F., Joulain, K., Mulet, J.-P., Carminati, R., and Greffet, J.-J., 2004, "Engineering Infrared Emission Properties of Silicon in the Near Field and the Far Field," Opt. Commun., **237**, pp. 379–388.
[9] Fu, C. J., and Zhang, Z. M., 2006, "Nanoscale Radiation Heat Transfer for Silicon at Different Doping Levels," Int. J. Heat Mass Transfer, **49**, pp. 1703–1718.
[10] Engstrom, H., 1980, "Infrared Reflectivity and Transmissivity of Boron-Implanted, Laser-Annealed Silicon," J. Appl. Phys., **51**, pp. 5245–5249.
[11] Barta, E., and Lux, G., 1983, "Calculated and Measured Infrared Reflectivity of Diffused Implanted *p*-Type Silicon Layers," J. Phys. D, **16**, pp. 1543–1553.
[12] Ashcroft, N. W., and Mermin, N. D., 1976, *Solid State Physics*, Saunders, Philadelphia.
[13] Howarth, L. E., and Gilbert, J. F., 1963, "Determination of Free Electron Effective Mass of *n*-Type Silicon," J. Appl. Phys., **34**, pp. 236–237.
[14] Riffe, D. M., 2002, "Temperature Dependence of Silicon Carrier Effective Masses With Application to Femtosecond Reflectivity Measurements," J. Opt. Soc. Am. B, **19**, pp. 1092–1100.
[15] Miyao, M., Motooka, T., Natsuaki, N., and Tokuyama, T., 1981, "Change of the Electron Effective Mass in Extremely Heavily Doped *n*-Type Si Obtained by Ion-Implantation and Laser Annealing," Solid State Commun., **37**, pp. 605–608.
[16] Spitzer, W. G., and Fan, H. Y., 1957, "Determination of Optical Constants and Carrier Effective Mass of Semiconductors," Phys. Rev., **106**, pp. 882–890.
[17] Caughey, D. M., and Thomas, R. E., 1967, "Carrier Mobilities in Silicon Empirically Related to Doping and Field," Proc. IEEE, **55**, pp. 2192–2193.
[18] Baccarani, G., and Ostoja, P., 1975, "Electron-Mobility Empirically Related to Phosphorus Concentration in Silicon," Solid-State Electron., **18**, pp. 579–580.
[19] Wagner, S., 1972, "Diffusion of Boron From Shallow Ion Implants in Silicon," J. Electrochem. Soc., **119**, pp. 1570–1576.
[20] Antoniadis, D. A., Gonzalez, A. G., and Dutton, R. W., 1978, "Boron in Near-Intrinsic ⟨100⟩ and ⟨111⟩ Silicon Under Inert and Oxidizing Ambients—Diffusion and Segregation," J. Electrochem. Soc., **125**, pp. 813–819.
[21] Masetti, G., Severi, M., and Solmi, S., 1983, "Modeling of Carrier Mobility Against Carrier Concentration in Arsenic-Doped, Phosphorus-Doped, and Boron-Doped Silicon," IEEE Trans. Electron Devices, **30**, pp. 764–769.
[22] Morin, F. J., and Maita, J. P., 1954, "Electrical Properties of Silicon Containing Arsenic and Boron," Phys. Rev., **96**, pp. 28–35.
[23] Thurber, W. R., Mattis, R. L., Liu, Y. M., and Filliben, J. J., 1980, "Resistivity-Dopant Density Relationship for Boron-Doped Silicon," J. Electrochem. Soc., **127**, pp. 2291–2294.
[24] Finetti, M., Negrini, P., Solmi, S., and Nobili, D., 1981, "Electrical-Properties and Stability of Supersaturated Phosphorus-Doped Silicon Layers," J. Electrochem. Soc., **128**, pp. 1313–1317.
[25] Mousty, F., Ostoja, P., and Passari, L., 1974, "Relationship Between Resistivity and Phosphorus Concentration in Silicon," J. Appl. Phys., **45**, pp. 4576–4580.
[26] Thurber, W. R., Mattis, R. L., Liu, Y. M., and Filliben, J. J., 1980, "Resistivity-Dopant Density Relationship for Phosphorus-Doped Silicon," J. Electrochem. Soc., **127**, pp. 1807–1812.
[27] Sze, S. M., and Irvin, J. C., 1968, "Resistivity Mobility and Impurity Levels in GaAs, Ge and Si at 300 K," Solid-State Electron., **11**, pp. 599–602.
[28] Gaylord, T. K., and Linxwiler, J. N., 1976, "Method for Calculating Fermi Energy and Carrier Concentrations in Semiconductors," Am. J. Phys., **44**, pp. 353–355.
[29] Park, K., Marchenkov, A., Zhang, Z. M., and King, W. P., 2007, "Low Temperature Characterization of Heated Microcantilevers," J. Appl. Phys., **101**, p. 094504.
[30] Pearson, G. L., and Bardeen, J., 1949, "Electrical Properties of Pure Silicon and Silicon Alloys Containing Boron and Phosphorus," Phys. Rev., **75**, pp. 865–883.
[31] Lee, T. F., and Mcgill, T. C., 1975, "Variation of Impurity-to-Band Activation-Energies With Impurity Density," J. Appl. Phys., **46**, pp. 373–380.
[32] Kuzmicz, W., 1986, "Ionization of Impurities in Silicon," Solid-State Electron., **29**, pp. 1223–1227.
[33] Beadle, W. E., Tsai, J. C. C., and Plummer, R. D., 1985, *Quick Reference Manual for Silicon Integrated Circuit Technology*, Wiley, New York.
[34] Chapman, P. W., Tufte, O. N., Zook, J. D., and Long, D., 1963, "Electrical Properties of Heavily Doped Silicon," J. Appl. Phys., **34**, pp. 3291–3295.
[35] Esaki, L., and Miyahara, Y., 1960, "A New Device Using the Tunneling Process in Narrow *p-n* Junctions," Solid-State Electron., **1**, pp. 13–21.
[36] May, G. S., and Sze, S. M., 2004, *Fundamentals of Semiconductor Fabrication*, Wiley, New York.
[37] Michel, A. E., Rausch, W., Ronsheim, P. A., and Kastl, R. H., 1987, "Rapid Annealing and the Anomalous Diffusion of Ion-Implanted Boron Into Silicon," Appl. Phys. Lett., **50**, pp. 416–418.
[38] Mokhberi, A., Griffin, P. B., Plummer, J. D., Paton, E., McCoy, S., and Elliott, K., 2002, "A Comparative Study of Dopant Activation in Boron, BF_2, Arsenic, and Phosphorus Implanted Silicon," IEEE Trans. Electron Devices, **49**, pp. 1183–1191.
[39] Lee, B. J., Khuu, V. P., and Zhang, Z. M., 2005, "Partially Coherent Spectral Transmittance of Dielectric Thin Films With Rough Surfaces," J. Thermophys. Heat Transfer, **19**, pp. 360–366.
[40] Palik, E. D., 1985, *Handbook of Optical Constants of Solids*, Academic, Orlando.
[41] Zhang, Z. M., Hanssen, L. M., Datla, R. U., and Drew, H. D., 1996, "An Apparatus for Infrared Transmittance and Reflectance Measurements at Cryogenic Temperatures," Int. J. Thermophys., **17**, pp. 1441–1454.
[42] Zhang, Z. M., 2007, *Nano/Microscale Heat Transfer*, McGraw-Hill, New York.

S. Basu
George W. Woodruff School of Mechanical Engineering,
Georgia Institute of Technology,
Atlanta, GA 30332

B. J. Lee
Department of Mechanical Engineering and Materials Science,
University of Pittsburgh,
Pittsburgh, PA 15261

Z. M. Zhang[1]
Fellow ASME
George W. Woodruff School of Mechanical Engineering,
Georgia Institute of Technology,
Atlanta, GA 30332
e-mail: zhuomin.zhang@me.gatech.edu

Near-Field Radiation Calculated With an Improved Dielectric Function Model for Doped Silicon

This paper describes a theoretical investigation of near-field radiative heat transfer between doped silicon surfaces separated by a vacuum gap. An improved dielectric function model for heavily doped silicon is employed. The effects of doping level, polarization, and vacuum gap width on the spectral and total radiative transfer are studied based on the fluctuational electrodynamics. It is observed that increasing the doping concentration does not necessarily enhance the energy transfer in the near-field. The energy streamline method is used to model the lateral shift of the energy pathway, which is the trace of the Poynting vectors in the vacuum gap. The local density of states near the emitter is calculated with and without the receiver. The results from this study can help improve the understanding of near-field radiation for applications such as thermophotovoltaic energy conversion, nanoscale thermal imaging, and nanothermal manufacturing.

[DOI: 10.1115/1.4000179]

Keywords: doped silicon, lateral shift, near-field radiation

1 Introduction

Near-field radiation between two bodies can exceed blackbody radiation by several orders of magnitude due to photon tunneling and wave-interference effects, especially at nanometer distances [1,2]. This phenomenon is a subject of great interest due to its potential applications in near-field thermophotovoltaics [3,4], near-field thermal microscopy [5,6], and nanomanufacturing [7,8]. A large number of studies have been devoted to determining near-field radiative transfer between two closely spaced media, both theoretically and experimentally, for different materials with different geometries. The most commonly studied geometries are between two semi-infinite media with parallel surfaces [9–14], a sphere near the surface of semi-infinite medium [5,14,15], and two spheres [16].

Doped Si has been extensively used in microelectronics and optoelectronics industries. The optical properties of doped Si can be tuned by changing the doping concentration. Hence, the study of near-field radiation between doped Si is of great significance. Marquier et al. [17] studied near-field radiative transfer between doped silicon plates near room temperature using a simplified Drude model, without considering the effect of doping level. Fu and Zhang [10] calculated the radiative energy transfer between two plates of doped silicon at different temperatures for various doping levels and vacuum gap widths. However, the employed ionization and mobility models may not be appropriate for heavily doped silicon near room temperature, which in turn, may cause inaccuracies in the prediction of energy transfer.

Recently, Basu et al. [18] developed a more accurate dielectric function model that was validated in the infrared at room temperature. This model is expected to be valid in the temperature range from 250 K to 400 K. A comprehensive analysis of the near-field radiative heat transfer between closely spaced doped silicon surfaces is performed based on the new dielectric function model. As shown in Fig. 1, a vacuum gap of width d separates the two parallel and smooth surfaces of the semi-infinite media made of doped silicon at temperatures T_1 and T_2, respectively. Each medium is assumed to be at thermal equilibrium. In the calculation, it is always assumed that medium 1 (emitter) is at a higher temperature than medium 2 (receiver). More detailed discussion of Fig. 1 is provided in Sec. 2. The effects of doping, polarization, and vacuum gap width on the energy transfer are examined using fluctuational electrodynamics. In the near-field, most of the energy is transmitted via evanescent waves for which the z-component of the wavevector in vacuum (γ_0) is imaginary. The waves are essentially propagating along the surface. However, the energy propagation direction can be visualized using the energy streamline method based on the Poynting vectors [19,20]. This method is employed in the present study to trace the direction of energy pathway and to estimate the lateral shift of the energy streamline when it crosses the vacuum gap. The local density of states (LDOS) near the emitter is calculated in the case with the receiver and compared with that toward free space.

2 Theory

Thermal radiation in the near-field is dominated by photon tunneling and wave-interference effects, and hence, cannot be predicted by the traditional radiative transfer equation. Nevertheless, the radiative heat transfer can be modeled by fluctuational electrodynamics developed in 1950s [1,2]. For any material at a temperature above absolute zero, charges such as electrons in metals or ions in polar crystals undergo random thermal motion. The random motion of charges, or dipoles inside the medium represented as ellipses in Fig. 1, would result in time-dependent electric currents in the whole space, which in turn generate electric and magnetic fields. However, the electromagnetic waves generated due to charges deep inside the medium will attenuate due to absorption inside the medium. While the time-average of the induced field is zero at any location and frequency, there exists a nonzero energy density and the resulting electromagnetic waves can carry energy away from the surface. The statistical properties of the electromagnetic field can be fully determined, provided that the statistical properties of the random currents and the transmission properties of the radiation from the emitting medium are known. The fluctuation-dissipation theorem describes the correlations of random currents at thermal equilibrium and the dyadic

---

[1] Corresponding author.

Contributed by the Heat Transfer Division of ASME for publication in the Journal of Heat Transfer. Manuscript received September 18, 2008; final manuscript received March 16, 2009; published online November 30, 2009. Assoc. Editor: Yogesh Jaluria.

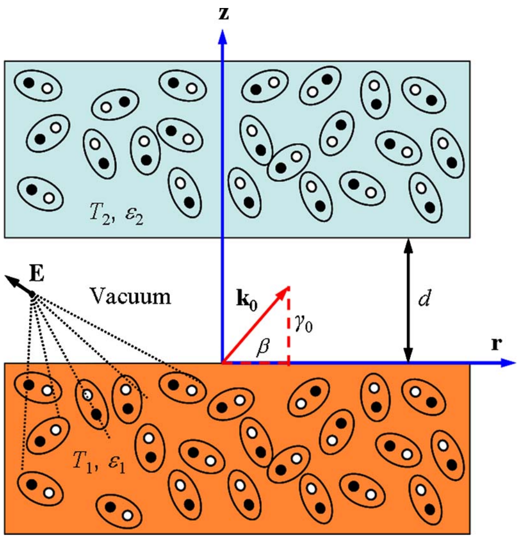

Fig. 1 Schematic for near-field radiation between two closely placed parallel plates at temperatures T_1 and T_2 separated by a vacuum gap of width d. The random motion of the dipoles, represented as ellipses in the figure, result in a space time-dependent fluctuating electric field.

Green's tensor is usually used to model the transmission properties of the system [2]. The spectral energy flux is given by

$$\langle \mathbf{S}(\mathbf{x},\omega)\rangle = \int_0^\infty \frac{1}{2}\langle \mathrm{Re}[\mathbf{E}(\mathbf{x},\omega)\times\mathbf{H}^*(\mathbf{x},\omega')]\rangle \mathrm{d}\omega' \tag{1}$$

where $\langle\ \rangle$ represents the ensemble average, $\mathbf{S}$ is the spectral Poynting vector, $\mathbf{E}$ and $\mathbf{H}$ are, respectively, the electric and magnetic fields at given locations and angular frequency, ω and ω' are the angular frequency, and * denotes the complex conjugate. The expressions for $\mathbf{E}$ and $\mathbf{H}$ can be obtained in terms of the fluctuating current, based on the dyadic Green's function [1,2] and Maxwell's equations. On the other hand, the spatial and spectral correlations of the fluctuating currents are obtained using the fluctuation-dissipation theorem [2]. The final form of the net energy flux between the two surfaces is given by [10]

$$q''_{\mathrm{net}} = \frac{1}{\pi^2}\int_0^\infty \mathrm{d}\omega[\Theta(\omega,T_1)-\Theta(\omega,T_2)]\int_0^\infty s(\omega,\beta)\mathrm{d}\beta \tag{2}$$

Here, $\Theta(\omega,T)=\hbar\omega/[\exp(\hbar\omega/k_BT)-1]$ is the mean energy of the Planck oscillator, where $\hbar$ is the Planck constant divided by 2π and k_B is the Boltzmann constant. Expression of $s(\omega,\beta)$ is different for propagating ($\beta<\omega/c$) and for evanescent ($\beta>\omega/c$) waves, namely,

$$s_{\mathrm{prop}}(\omega,\beta) = \frac{\beta(1-\rho_{01}^s)(1-\rho_{02}^s)}{4|1-r_{01}^s r_{02}^s e^{i2\gamma_0 d}|^2} + \frac{\beta(1-\rho_{01}^p)(1-\rho_{02}^p)}{4|1-r_{01}^p r_{02}^p e^{i2\gamma_0 d}|^2} \tag{3a}$$

and

$$s_{\mathrm{evan}}(\omega,\beta) = \frac{\mathrm{Im}(r_{01}^s)\mathrm{Im}(r_{02}^s)\beta e^{-2\,\mathrm{Im}(\gamma_0)d}}{|1-r_{01}^s r_{02}^s e^{-2\,\mathrm{Im}(\gamma_0)d}|^2} + \frac{\mathrm{Im}(r_{01}^p)\mathrm{Im}(r_{02}^p)\beta e^{-2\,\mathrm{Im}(\gamma_0)d}}{|1-r_{01}^p r_{02}^p e^{-2\,\mathrm{Im}(\gamma_0)d}|^2} \tag{3b}$$

In Eq. (3), the first term on the right-hand side refers to the contribution of s-polarization or TE wave (when the electric field is perpendicular to the plane of incidence) while the second term refers to the contribution of p-polarization or TM wave (when the magnetic field is perpendicular to the plane of incidence). As shown in Fig. 1, cylindrical coordinate system is used so that the space variable $\mathbf{x}=\mathbf{r}+\mathbf{z}$, with r-direction being parallel to the interface and z-direction perpendicular to the interface. Note that β and γ_j refer to the r-component and z-component of the wavevector $\mathbf{k}_j$, respectively. Thus, $\mathbf{k}_j=\beta\hat{\mathbf{r}}+\gamma_j\hat{\mathbf{z}}$ and $k_j^2=\beta^2+\gamma_j^2$ where $j=0$, 1, and 2. The magnitude of $\mathbf{k}$ is related to the dielectric function by $k_0=\omega/c$, $k_1=\sqrt{\varepsilon_1}\omega/c$, and $k_2=\sqrt{\varepsilon_2}\omega/c$ with c being the speed of light in vacuum and ε_1 and ε_2 being the dielectric function (or relative permittivity) of medium 1 and 2, respectively. Note that $r_{0j}^s=(\gamma_0-\gamma_j)/(\gamma_0+\gamma_j)$ and $r_{0j}^p=(\varepsilon_j\gamma_0-\gamma_j)/(\varepsilon_j\gamma_0+\gamma_j)$ are the Fresnel reflection coefficients for s- and p-polarization, respectively, at the interface between vacuum and medium j (medium 1 or medium 2). On the other hand, $\rho_{0j}=|r_{0j}|^2$ is the far-field reflectivity at the interface between vacuum and medium j.

The spectral energy density in the vacuum space between the two semi-infinite surfaces [1,2] is given by

$$\langle u(\mathbf{x},\omega)\rangle = \int_0^\infty \left[\frac{\varepsilon_0}{4}\langle \mathbf{E}(\mathbf{x},\omega)\bullet\mathbf{E}^*(\mathbf{x},\omega')\rangle + \frac{\mu_0}{4}\langle \mathbf{H}(\mathbf{x},\omega)\bullet\mathbf{H}^*(\mathbf{x},\omega')\rangle\right]\mathrm{d}\omega' \tag{4}$$

where ε_0 and μ_0 are the permittivity and permeability of vacuum, respectively. The somewhat modified expressions of Eqs. (1) and (4) compared with earlier publications [4,10] do not change the final results, as long as the Dirac delta function $\delta(\omega-\omega')$ is included in the correlation function of the currents for emission from medium 1

$$\langle j_m(\mathbf{x}',\omega)j_n(\mathbf{x}'',\omega')\rangle = \frac{4}{\pi}\omega\varepsilon_0\,\mathrm{Im}(\varepsilon_1)\Theta(\omega,T_1)\delta_{mn}\delta(\mathbf{x}'-\mathbf{x}'')\delta(\omega-\omega') \tag{5}$$

Here, m and n refer to each component of the coordinates, Im denotes imaginary part, and δ_{mn} is the Kronecker delta. The spectral energy density can be looked upon as the electromagnetic energy per unit volume per unit angular frequency. It is the product of the LDOS $D(z,\omega)$ and the mean energy of the Planck oscillator, i.e.,

$$\langle u(z,\omega)\rangle = D(z,\omega)\Theta(\omega,T) \tag{6}$$

The LDOS is the number of modes per unit frequency interval per unit volume. It is a fundamental quantity and can provide a qualitative understanding of the enhanced near-field radiation. In Eq. (6), the LDOS is expressed as a function of z only due to the continuous translation symmetry of the system in the radial direction. Several studies discussed the LDOS for a free-emitting surface, i.e., without medium 2 [2,10]. When the emission from the receiver is neglected, the LDOS can be expressed as the sum of electric and magnetic density of states, thus

$$D(z,\omega) = D_E(z,\omega) + D_M(z,\omega) \tag{7}$$

It can be shown that

$$D_E(z,\omega) = \frac{\omega\,\mathrm{Im}(\varepsilon_1)}{16\pi^2c^2}\int_0^\infty \left[(|\gamma_0 t_1^p|^2+|\beta t_2^p|^2)\frac{\beta^2+\gamma_1\gamma_1^*}{k_1k_1^*} + |k_0t_2^s|^2\right]\frac{\beta}{|\gamma_1|^2\mathrm{Im}(\gamma_1)}\mathrm{d}\beta \tag{8a}$$

and

$$D_M(z,\omega) = \frac{\omega\,\mathrm{Im}(\varepsilon_1)}{16\pi^2c^2}\int_0^\infty \left(|k_0t_2^p|^2\frac{\beta^2+\gamma_1\gamma_1^*}{k_1k_1^*} + |\gamma_2t_1^s|^2 + |\beta t_2^s|^2\right)\frac{\beta}{|\gamma_1|^2\mathrm{Im}(\gamma_1)}\mathrm{d}\beta \tag{8b}$$

In the above expressions, $t_1=t_+-t_-$ and $t_2=t_++t_-$, where

$$t_+ = \frac{t_{10}e^{i2\gamma_0 z}}{1 - r_{02}r_{01}e^{i2\gamma_0 d}} \tag{9a}$$

and

$$t_- = \frac{t_{10}r_{02}e^{i2\gamma_0 (d-z)}}{1 - r_{02}r_{01}e^{i2\gamma_0 d}} \tag{9b}$$

where $t_{10}=1+r_{10}$ is the Fresnel transmission coefficient for a given polarization. Note that subscripts + and − represent the forward and backward waves (due to multiple reflections from both surfaces), respectively, in the vacuum gap.

In addition to the net energy transfer, the direction of energy flow between the surfaces should be known since it gives an idea about the lateral dimensions of the surfaces in order for them to be considered as semi-infinite. Due to the random fluctuation of charges, the Poynting vectors are decoupled for different values of β (i.e., the parallel vector component) [20,21]. By tracing the Poynting vector at a given β in the vacuum region, the energy streamlines (ESLs) provide the direction of energy propagation [19]. For propagating waves, ESLs are nearly straight. However, for evanescent waves, the ESLs are curved due to photon tunneling. The ESLs are laterally displaced as they reach the receiver surface after crossing the vacuum gap. This lateral displacement, referred to as the *lateral shift*, may be important for determining the necessary lateral dimension of the emitter and receiver in order for them to be approximated as infinitely extended since real surfaces are always finite.

In order to analyze the nanoscale thermal radiation for doped Si, it is important to first understand the optical properties of Si at different doping levels. Due to the large number of free carriers in doped Si, the Drude model can be used to determine its dielectric function in the infrared region. For doped silicon in the infrared region, the Drude model is given as

$$\varepsilon(\omega) = \varepsilon' + i\varepsilon'' = \varepsilon_{\mathrm{bl}} - \frac{\omega_p^2}{\omega(\omega + i/\tau)} \tag{10}$$

In Eq. (10), the first term on the RHS accounts for contribution from the lattice vibration and band gap transitions while the second term accounts for free carrier absorption. For heavily doped Si in the infrared ($\lambda > 2$ μm), $\varepsilon_{\mathrm{bl}}$ may be taken as a constant equal to 11.7 [10]. The plasma frequency is $\omega_p = \sqrt{Ne^2/m^*\varepsilon_0}$ and the relaxation time is $\tau = m^*\mu/e$. Here, N, e, m^*, and μ are the carrier concentration, effective mass, charge, and mobility defined as the ratio of the carrier drift velocity to the field strength, respectively. For heavily doped silicon, the effective mass depends little on temperature, the doping concentration, or frequency. Hence, the electron and hole effective masses can be taken as $0.27m_e$ and $0.37m_e$, respectively, where m_e is the free-electron mass in vacuum [10]. Accurate carrier mobility and ionization models are needed in order to determine the optical constants of silicon. Fu and Zhang [10] combined the interband absorption, lattice vibration, and free-electron absorption to model the dielectric function of doped Si at temperatures from 300 K to 1000 K over the entire spectrum. However, the ionization model adopted in their study results in an underprediction of the carrier concentrations for doping concentrations greater than 10^{17} cm^{-3}. Hence, the dielectric function developed in Ref. [10] is not applicable for heavily doped Si ($>10^{18}$ cm^{-3}). On the other hand, Basu et al. [18] examined several models for the ionization and carrier mobility of heavily doped Si and compared the predicted optical properties with those measured with a Fourier-transform infrared spectrometer at room temperature. This experimentally validated Drude model is used in the present study to determine the optical constants of doped Si. The mobility model used in Ref. [18] was originally developed at room temperature (300 K). For heavily doped Si near room temperature, the scattering process is mostly dominated by impurity scattering, thus, the lattice scattering can be neglected. For impurity scattering, the temperature-dependent mobility [10] can be obtained by

$$\mu(T) = \mu_{300}(T/300)^{1.5} \tag{11}$$

where μ_{300} is the mobility calculated at 300 K and T is in kelvin.

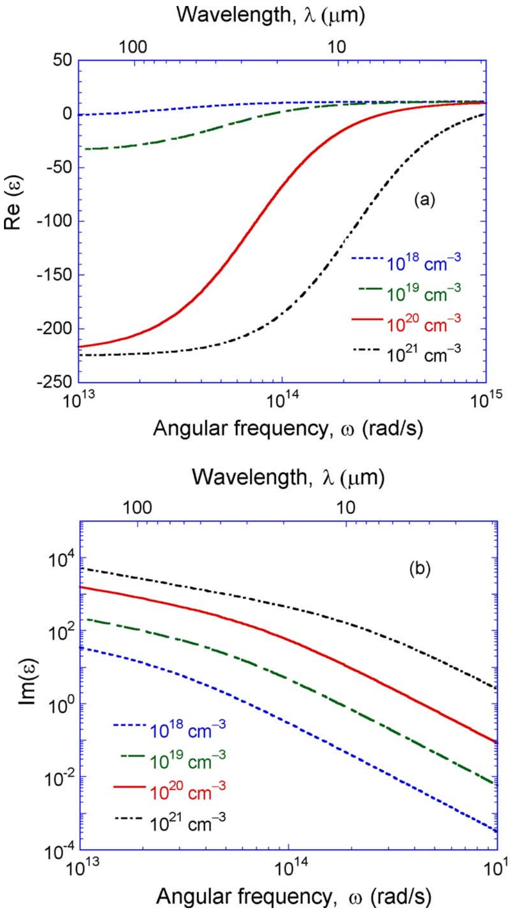

Fig. 2 Predicted dielectric function of *n*-type silicon for different doping concentrations at 400 K: (*a*) real part and (*b*) imaginary part

Figure 2 shows the real and imaginary parts of the dielectric function of n-type Si for different doping levels at 400 K. It is observed that with increase in the doping level, the real part of dielectric function $\varepsilon' = \mathrm{Re}(\varepsilon)$ decreases while the imaginary part $\varepsilon'' = \mathrm{Im}(\varepsilon)$ increases due to increased free carrier concentration. An order of magnitude increase in the doping concentration of Si results in a tenfold increase in ε''. A negative ε' with simultaneously very large ε'' results in metallic behavior of heavily doped silicon. The dielectric function in Ref. [10] fails to capture the metallic behavior of Si at doping levels greater than 10^{20} cm^{-3} due to lesser number of free carriers. On the other hand, the simple model used in Ref. [17] cannot accurately predict the dielectric function for Si in the doping range from 10^{17}–10^{19} cm^{-3} since it assumes that all the dopant atoms in Si are fully ionized irrespective of doping level.

3 Results and Discussion

In this section, near-field radiative heat transfer between two semi-infinite doped silicon plates, as shown in Fig. 1, will be presented. Surface roughness and tilting effects are not considered. The emitter is maintained at 400 K while the receiver is maintained at 300 K. Only n-doped Si is considered in this study since the results for p-doped Si would be similar.

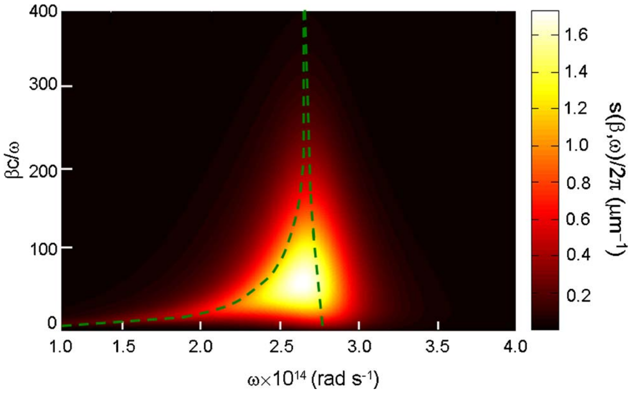

Fig. 3 Contour plot of $s(\omega,\beta)$ for doping concentration of 10^{20} cm^{-3} in both the emitter (at 400 K) and receiver (at 300 K) when the vacuum gap width $d=10$ nm. Note that the angular frequency is shown in the range from 10^{14} rad/s to 4×10^{14} rad/s and the parallel wavevector component is normalized to the frequency. The dashed curves represent the two branches of the surface-polariton dispersion.

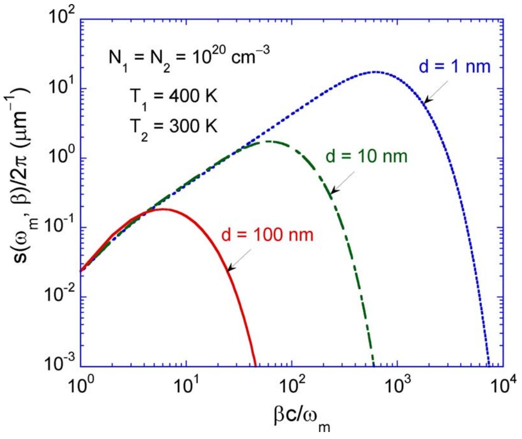

Fig. 4 Graph of $s(\omega_m,\beta)$ as a function of β for different vacuum gap widths

3.1 Effect of Surface Waves. As can be seen from Eq. (2), the net energy transfer involves integration over both ω and β. The function $s(\omega,\beta)/2\pi$ is illustrated in Fig. 3 as a contour plot for 10^{20} cm^{-3} doped Si plates separated by a 10 nm vacuum gap. It should be noted that Fig. 3 is for TM waves since the contribution from TE waves is negligible for doping levels between 10^{18} cm^{-3} and 10^{20} cm^{-3}. The color bar on the right shows the scale for $s(\omega,\beta)/2\pi$ with the brightest color representing the peak value at $\omega_m=2.67\times10^{14}$ rad/s, corresponding to $\lambda_m=7$ μm and $\beta_m=62\omega/c$. Most of the energy transfer will occur around this peak and there will be negligible energy transfer at $\beta>400\omega/c$ for a given ω and at $\omega>4\times10^{14}$ rad/s for any β. Note that the contribution of propagating waves ($\beta<\omega/c$) is also negligible. The resonance energy transfer in the near-field is a result of surface plasmon polaritons (SPPs), which can greatly enhance the radiative transfer. A SPP is a localized electromagnetic wave that propagates along the interface of two different media and decays exponentially away from the interface. SPPs can be excited at the vacuum-silicon interface. Furthermore, SSPs at both interfaces can be coupled, yielding two different branches of the dispersion relations. Following the work of Lee and Zhang [21], the dispersion relation is calculated between doped Si plates and plotted as dashed curves in Fig. 3. The lower-frequency branch corresponds to the symmetric mode and the higher-frequency branch represents the asymmetric mode. The dispersion curves match well with the peak in $s(\omega,\beta)$. Compared with SiC (see Ref. [21]) the peak is much broader due to the large ε'' of doped silicon.

The vacuum gap width d has a significant effect on near-field heat transfer. This can be understood by plotting $s(\omega,\beta)$ at ω_m as a function of β for different d values, as shown in Fig. 4, where β is normalized with respect to ω_m/c. Note that ω_m changes little for $d<100$ nm. As the gap width decreases, the peak of $s(\omega,\beta)$ increases and shifts toward larger β values. The area underneath is proportional to the spectral energy flux and the volume under the curved surface of $s(\omega,\beta)$ in Fig. 3 is proportional to the total energy flux that tends to be inversely proportional to d^2 as noted in previous studies [2,10]. An alternative view would be to consider the ratio s/β, which was called transfer function according to Fu and Zhang [10]. As d decreases, the peak value of $s(\omega,\beta)/\beta$ remains nearly unchanged but its location will shift toward larger β values. As a consequence, there will be a significant increase in the number of modes for energy transfer because the integration of s/β over $2\pi\beta d\beta$, i.e., the area in the x-y plane of the wavevector-space, is directly proportional to the energy transfer. Therefore, the transfer function can be viewed as the contribution per unit area in the parallel plane of the wavevector.

3.2 Effect of Doping Level. When different doping levels are considered, the location of the peak in $s(\omega,\beta)$ shifts toward higher frequencies with increased doping level. For example, $\omega_m=2.67\times10^{13}$ rad/s, 8.5×10^{13} rad/s, and 2.67×10^{14} rad/s for doping concentrations of 10^{18} cm^{-3}, 10^{19} cm^{-3}, and 10^{20} cm^{-3}, respectively. The integration of $s(\omega,\beta)$ over β gives a weighted function to modify the Planck blackbody distribution function. The spectral energy transfer per unit area q''_ω can be obtained as

$$q''_\omega = \frac{1}{\pi^2}[\Theta(\omega,T_1)-\Theta(\omega,T_2)]\int_0^\infty s(\omega,\beta)\mathrm{d}\beta \qquad (12)$$

so that $q''_{net}=\int_0^\infty q''_\omega \mathrm{d}\omega$. This function is plotted against ω for different doping concentrations in Fig. 5 for $T_1=400$ K and $T_2=300$ K. It can be seen from Fig. 5(a) that, for $d=100$ nm, a strong spectral peak occurs near the SPP resonance frequency for each doping level. The peaks for doped silicon, however, are much broader than that for SiC and for metals because of the large losses. In addition to the peaks caused by SPPs, there exists a broadband spectral distribution due to thermal fluctuation as described by the Planck's oscillator model. As discussed in Ref. [12], Wien's displacement law no longer holds for near-field radiative transfer. There may be two or more peaks in the spectral radiative flux. When the vacuum gap width is reduced to 10 nm, the spectral energy flux is increased by two orders of magnitude around the SPP resonance frequencies, as shown in Fig. 5(b). Away from the resonance frequencies, the energy is essentially transferred by propagating waves and the spectral energy flux does not increase as the d decreases. This is why some traces (away from the peaks) in Fig. 5(a) do not show up in Fig. 5(b). It is the area under these curves that determines the total energy transfer.

The predicted radiative heat transfer between two doped Si plates is plotted in Fig. 6 as a function of the vacuum gap width. Both plates are maintained at the same doping level, which is varied from 10^{18} cm^{-3} to 10^{21} cm^{-3}. The dotted line with circles is the radiation heat flux between two blackbodies given by $\sigma(T_1^4-T_2^4)$, where σ is the Stefan–Boltzmann constant. At $d=1$ nm, the net heat flux between 10^{19}cm^{-3} or 10^{20} cm^{-3} doped Si plates can exceed, by five orders of magnitude, that between two blackbodies because of photon tunneling and surface waves. It is interesting to note that while the energy flux spectra are very different between doping concentrations of 10^{19} cm^{-3} or 10^{20} cm^{-3}, the total energy flux is about the same when $d<30$ nm. As can be seen from Fig. 5, the peak is sharper and

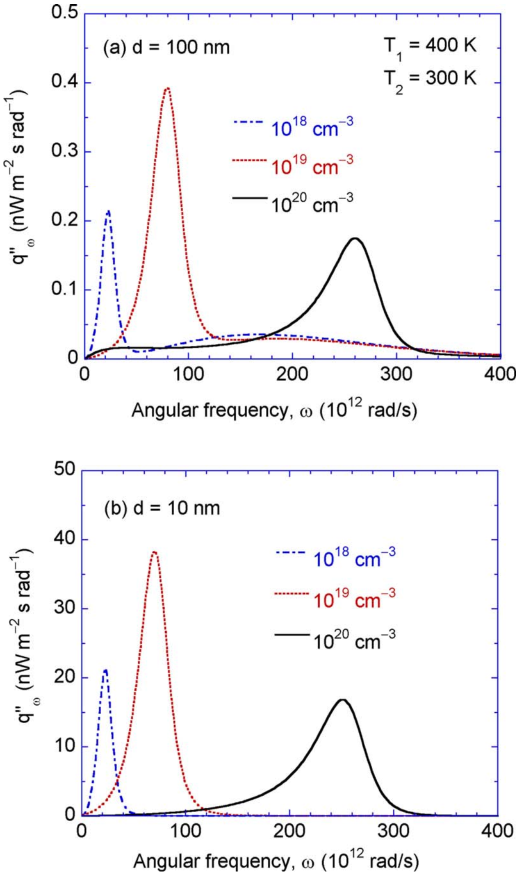

Fig. 5 Spectral energy flux for different doping levels at (*a*) *d* =100 nm and (*b*) *d*=10 nm

narrower for doping concentration of 10^{19} cm^{-3} than that for 10^{20} cm^{-3}. This explains why the nanoscale radiation between doped Si plates can be enhanced to the same order of magnitude as that between SiC plates; the latter case has an extremely high peak in a very narrow spectral band [15,16]. In the present study, the nonlocal effect, i.e., the spatial dependence of the dielectric function was not considered [2]. The nonlocal effect, however, is negligible at vacuum gap width $d > 1$ nm [11].

It should be noted that near room temperature, increase in the doping level of Si does not always enhance the energy transfer. In fact, the radiative heat transfer is smallest for 10^{21} cm^{-3} doped Si plates as compared with other doping levels as shown in Fig. 6. The main reason for this is that at the doping concentration of 10^{21} cm^{-3}, ω_m is too high and due to the exponential term in the denominator of the mean energy of Planck's oscillator, the spectral energy flux is not significantly enhanced as compared with other doping levels. Another way to view it is that at smaller d, the net spectral heat flux is proportional to product of $\mathrm{Im}[(\varepsilon_1 - 1)/(\varepsilon_1 + 1)]$ and $\mathrm{Im}[(\varepsilon_2 - 1)/(\varepsilon_2 + 1)]$ [2,10]. Hence, very large values of ε'', as for 10^{21} cm^{-3} doped Si, will significantly reduce the energy transfer. This is also the case for good metals in the infrared region such as Al and Cu [2]. At $d > 200$ nm, doping concentrations between 10^{18} cm^{-3} or 10^{19} cm^{-3} yield the largest radiative heat transfer. Note that surface wave coupling becomes weaker as d increases to beyond 100 nm. The above calculations assumed that the doping concentrations are the same for both media.

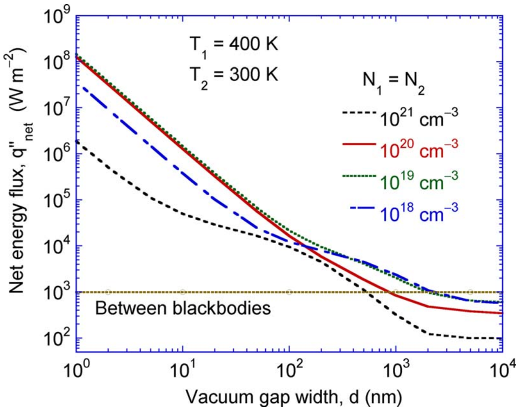

Fig. 6 Net energy flux between medium 1 at 400 K and medium 2 at 300 K at different doping levels versus gap width. The dash-dotted line refers to the net energy transfer between two blackbodies maintained at 400 K and 300 K, respectively.

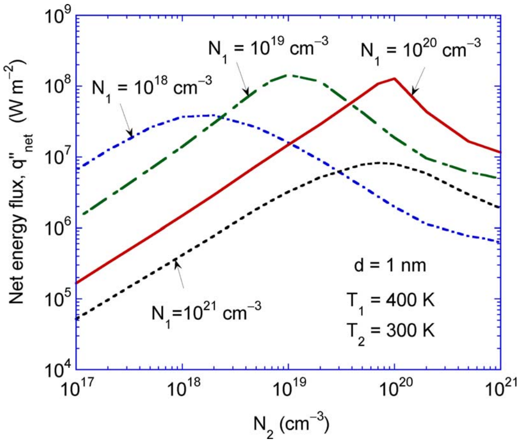

Fig. 7 Effect of doping on the net energy transfer between two doped Si plates separated by 1 nm vacuum gap

Figure 7 illustrates the effect of doping concentration on nanoscale radiation when the vacuum gap width is fixed at $d = 1$ nm. The doping level of medium 1 is represented as N_1 while that for medium 2 is represented by N_2. Generally speaking, surface waves are better coupled when the two media have similar dielectric functions. The results are that there exist peaks when $N_1 \approx N_2$ at doping levels up to 10^{20} cm^{-3}. A decrease in the energy transfer is observed when the doping level of one or both of the silicon plates exceeds 10^{20} cm^{-3}. In general, the model used in Ref. [10] does not correctly predict the net radiative transfer near room temperature for doping levels greater than 10^{18} cm^{-3} because it was assumed that a large portion of the doping sites are not ionized to free carriers. It should be noted that the dielectric function model used in the present study did not consider band gap absorption and cannot be used at wavelengths shorter than 1.3 μm. Furthermore, the Drude model proposed by Basu et al. [18] is not applicable at temperatures much higher than 400 K.

3.3 Effect of Polarization.

So far, all the discussions are for TM waves because the contributions by TE waves are negligible in most cases, except for doping concentration of 10^{21} cm^{-3} in the region $d > 5$ nm. As can be seen from Fig. 6 that the curve for the net energy transfer (calculated for both polarizations) for $N_1 = N_2 = 10^{21}$ cm^{-3} exhibits different trend as the other curves. Figure 8 shows the contribution of different polarization states to the net energy transfer for two doping levels. It is seen from Fig. 8(*a*) that TM wave contribution dominates the net energy transfer for 10^{20} cm^{-3} doped Si, although the TE wave contribution increases as d increases to beyond 100 nm. This is expected since surface waves are strongly coupled at the nanometer scales as discussed earlier. On the other hand, there is a significant TE wave contri-

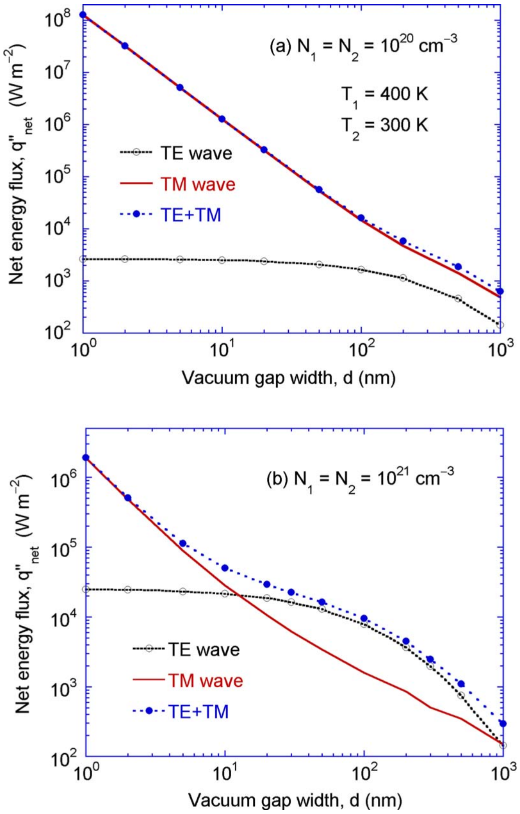

Fig. 8 Contribution of TE and TM waves to the net energy transfer for (*a*) 10^{20} cm^{-3} and (*b*) 10^{21} cm^{-3} doped Si at different gap widths

bution for 10^{21} cm^{-3} doped Si at vacuum gap $d > 10$ nm. The TE wave contribution does not increase when the gap is reduced further from about $d = 50$ nm or so. Most of the TE wave contributions are limited to smaller β values because Im(r^s_{01}) and Im(r^s_{02}) decreases quickly as β increases and become negligible when $\beta > 5\omega/c$. When $\beta < 5\omega/c$ and $d < 50$ nm, the term $\exp[-2\,\mathrm{Im}(\gamma_0)d] \approx 1$ in Eq. (3). Hence, $s(\omega,\beta)$ becomes independent of d resulting in the nearly constant total energy flux for the TE wave. Similar results were observed between two metallic surfaces [2,11].

3.4 Lateral Shift. Having calculated the net energy transfer between two surfaces, it is important to trace the direction of energy pathways as well as to estimate their lateral shifts from the emitter to the receiver. Figure 9 plots $s(\omega_m,\beta)/2\pi$ together with the lateral shift δ (at $\omega = \omega_m$) as functions of β for 10^{20} cm^{-3} doped Si at $d = 10$ nm. The inset in Fig. 9 illustrates the concept of lateral shift for near-field radiative transfer. The lateral shift provides an estimate of how large the surface should be in order for it to be considered infinitely extended in the parallel plane for calculation of the near-field energy transfer. Note that the lateral shift is obtained after taking the ratio of the Poynting vector components in *r*- and *z*-directions and hence is not directly related to the emitter temperature except through the materials properties. It is seen that δ increases sharply when β exceeds $200\omega_m/c$, where $\delta = 10d$. From calculation, about 14% of the energy flux is carried by evanescent waves with $\beta > 200\omega_m/c$, i.e., the shaded area. Although, the lateral shift is around $200d$ at $\beta = 400\omega_m/c$, the contribution to the energy flux by evanescent waves with $\beta > 400\omega_m/c$ is negligible. Generally speaking, the diameter of the plates should be greater than $100d$ for them to be treated as infinite. While, there are dielectric functions are very different the lateral shift for 10^{20} cm^{-3} doped Si is of the same order as that for SiC [20].

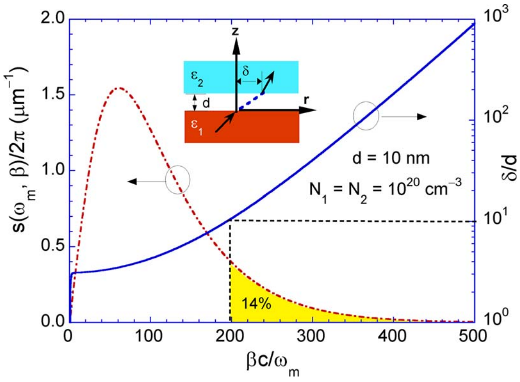

Fig. 9 Graphs of $s(\omega_m,\beta)$ and lateral shift versus β for 10^{20} cm^{-3} doped Si media with a gap width of 10 nm. The lateral shift δ is normalized with respect to d.

3.5 Local Density of States. The LDOS is calculated when both media are doped silicon with the same doping concentration of 10^{20} cm^{-3}. Only the LDOS for TM waves is considered since the contribution of TE waves is negligibly small. Here, the LDOS is calculated in the vacuum gap for the case when the emitter is at 400 K and the receiver is at 0 K. In other words, the emission from the receiver is not considered in this analysis. If the receiver is not at 0 K, the LDOS must be separately considered by assuming that the other medium is at 0 K. Since the electromagnetic fields from the emitter and the receiver are not correlated, the LDOS from each surface can be separately calculated, however, they cannot be added since the sum does not have any physical meaning. On the other hand, in terms of energy density, the local energy density will be sum of the energy densities from the emitter and the receiver and hence can be added together. As seen from Eqs. (6), (7), (8*a*), and (8*b*), the density of states is a function of the material properties of the emitter and the receiver. Other than the temperature dependence of the dielectric function, LDOS is not a function of temperature. Figure 10(*a*) plots the spectral variation in LDOS at three different locations inside the vacuum gap when $d = 10$ nm. At the surface wave resonance $\omega = \omega_m$, LDOS is strongly amplified and displays a peak in the spectra. Figure 10(*b*) compares the spatial variation in LDOS in the gap with and without the receiver at $\omega = \omega_m$. It can be seen from Fig. 10 that the receiver has little influence on the LDOS close to the emitter, e.g., $z < 0.5d$, where LDOS is almost the same as that of free emission from medium 1 into vacuum. As $z \to 0$, LDOS diverges as z^{-3}, which was observed by others without the receiver [2,10]. On the other hand, the presence of the receiver starts to modify the LDOS when $z > 0.5d$. At $z = d$, the LDOS calculated considering the receiver is nearly twice of the LDOS without the receiver. Multiple reflections of the evanescent waves result in a strong coupling that enhances the density of states near the receiver surface.

4 Conclusions

A theoretical investigation is performed on the near-field radiative energy transfer between heavily doped Si (10^{18} cm^{-3} to 10^{21} cm^{-3}) plates near room temperature, using an improved dielectric function model. The effect of surface wave is examined, and the ranges of ω and β that dominate the heat transfer are identified for different doping levels. Increasing in the doping level for Si does not necessarily increase the energy transfer. The lateral shift across the vacuum gap of the energy pathway is estimated using the energy streamline method. It is observed that the diameter of the receiver should be around 100 times the vacuum gap for the surfaces to be considered infinite in the lateral dimensions. The effect of the receiver on the local density of states in the vacuum gap is negligibly small except near the surface of the

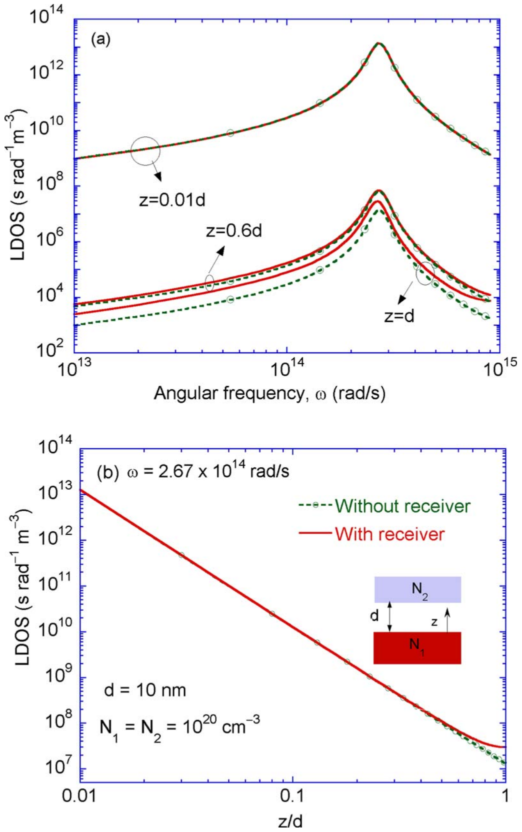

Fig. 10 Local density of states for 10^{20} cm^{-3} doped Si plates separated by a 10 nm vacuum gap: (*a*) spectral variation in LDOS at $z=0.01d$, $z=0.6d$, and $z=d$ (b) spatial variation in LDOS at $\omega_m=2.67\times10^{14}$ rad/s

receiver. The results obtained from this study will facilitate future design of experiments and applications of nanoscale thermal radiation.

Acknowledgment

This work was supported by the Department of Energy (Contract No. DE-FG02-06ER46343).

Nomenclature

c = speed of light in vacuum, 2.998×10^{8} m s^{-1}
d = vacuum gap thickness, m
$\mathbf{E}$ = electric field vector
$\mathbf{H}$ = magnetic field vector
$\hbar$ = Planck constant divided by 2π, 1.055×10^{-34} J s
$\mathbf{k}$ = wavevector, m^{-1}
k_B = Boltzmann constant, 1.381×10^{-23} J K^{-1}
q'' = heat flux, W m^{-2}
$\mathbf{r}$ = vector in the radial direction, m
r = Fresnel reflection coefficient
T = temperature, K
t = Fresnel transmission coefficient
$\mathbf{S}$ = spectral Poynting vector, W m^{-2} s rad^{-1}
$\mathbf{z}$ = vector in the direction normal to surfaces, m

Greek Symbols

β = parallel wavevector component, m^{-1}
γ = wavevector component in the z-direction, m^{-1}
ε = relative permittivity (i.e., dielectric function)
ε_0 = permittivity of vacuum, 8.854×10^{-12} F m^{-1}
Θ = mean energy of the Planck oscillator, J
λ = wavelength in vacuum, m
μ = mobility, cm^{2} V^{-1} s^{-1}
μ_0 = permeability of vacuum, $4\pi\times10^{-7}$ H m^{-1}
τ = relaxation time, s
ω = angular frequency, rad s^{-1}

Superscripts

p = p-polarization
s = s-polarization

Subscripts

0 = vacuum
1 = medium 1
2 = medium 2
E = electric
evan = evanescent wave
M = magnetic
m = maximum
prop = propagating waves

References

[1] Zhang, Z. M., 2007, *Nano/Microscale Heat Transfer*, McGraw-Hill, New York, Chap. 10.
[2] Joulain, K., Mulet, J.-P., Marquier, F., Carminati, R., and Greffet, J.-J., 2005, "Surface Electromagnetic Waves Thermally Excited: Radiative Heat Transfer, Coherence Properties and Casimir Forces Revisited in the Near-Field," Surf. Sci. Rep., **57**, pp. 59–112.
[3] Narayanaswamy, A., and Chen, G., 2003, "Surface Modes for Near-Field Thermophotovoltaics," Appl. Phys. Lett., **82**, pp. 3544–3546.
[4] Park, K., Basu, S., King, W. P., and Zhang, Z. M., 2008, "Performance Analysis of Near-Field Thermophotovoltaic Devices Considering Absorption Distribution," J. Quant. Spectrosc. Radiat. Transf., **109**, pp. 305–316.
[5] Kittel, A., Muller-Hirsch, W., Parisi, J., Biehs, S. A., Reddig, D., and Holthaus, M., 2005, "Near-Field Heat Transfer in a Scanning Thermal Microscope," Phys. Rev. Lett., **95**, p. 224301.
[6] De Wilde, Y., Formanek, F., Carminati, R., Gralak, B., Lemoine, P. A., Joulain, K., Mulet, J.-P., Chen, Y., and Greffet, J.-J., 2006, "Thermal Radiation Scanning Tunnelling Microscopy," Nature (London), **444**, pp. 740–743.
[7] Chimmalgi, A., Choi, T. Y., Grigoropoulos, C. P., and Komvopoulos, K., 2003, "Femtosecond Laser Aperturless Near-Field Nanomachining of Metals Assisted by Scanning Probe Microscopy," Appl. Phys. Lett., **82**, pp. 1146–1148.
[8] Wang, L., Uppuluri, S. M., Jin, E. X., and Xu, X., 2006, "Nanolithography Using High Transmission Nanoscale Bowtie Apertures," Nano Lett., **6**, pp. 361–364.
[9] Polder, D., and Vanhove, M., 1971, "Theory of Radiative Heat Transfer Between Closely Spaced Bodies," Phys. Rev. B, **4**, pp. 3303–3314.
[10] Fu, C. J., and Zhang, Z. M., 2006, "Nanoscale Radiation Heat Transfer for Silicon at Different Doping Levels," Int. J. Heat Mass Transfer, **49**, pp. 1703–1718.
[11] Chapuis, P. O., Volz, S., Henkel, C., Joulain, K., and Greffet, J.-J., 2008, "Effects of Spatial Dispersion in Near-Field Radiative Heat Transfer Between Two Parallel Metallic Surfaces," Phys. Rev. B, **77**, p. 035431.
[12] Francoeur, M., and Menguc, M. P., 2008, "Role of Fluctuational Electrodynamics in Near-Field Radiative Heat Transfer," J. Quant. Spectrosc. Radiat. Transf., **109**, pp. 280–293.
[13] Hu, L., Narayanaswamy, A., Chen, X. Y., and Chen, G., 2008, "Near-Field Thermal Radiation Between Two Closely Spaced Glass Plates Exceeding Planck's Blackbody Radiation Law," Appl. Phys. Lett., **92**, p. 133106.
[14] Volokitin, A. I., and Persson, B. N. J., 2001, "Radiative Heat Transfer Between Nanostructures," Phys. Rev. B, **63**, p. 205404.
[15] Mulet, J.-P., Joulain, K., Carminati, R., and Greffet, J.-J., 2001, "Nanoscale Radiative Heat Transfer Between a Small Particle and a Plane Surface," Appl. Phys. Lett., **78**, pp. 2931–2933.
[16] Narayanaswamy, A., and Chen, G., 2008, "Thermal Near-Field Radiative Transfer Between Two Spheres," Phys. Rev. B, **77**, p. 075125.
[17] Marquier, F., Joulain, K., Mulet, J.-P., Carminati, R., and Greffet, J.-J., 2004, "Engineering Infrared Emission Properties of Silicon in the Near-Field and the Far Field," Opt. Commun., **237**, pp. 379–388.
[18] Basu, S., Lee, B. J., and Zhang, Z. M., 2010, "Infrared Radiative Properties of Heavily Doped Silicon at Room Temperature," ASME J. Heat Transfer, **132**(2), p. 023301.
[19] Zhang, Z. M., and Lee, B. J., 2006, "Lateral Shift in Photon Tunneling Studied by the Energy Streamline Method," Opt. Express, **14**, pp. 9963–9970.
[20] Lee, B. J., Park, K., and Zhang, Z. M., 2007, "Energy Pathways in Nanoscale Thermal Radiation," Appl. Phys. Lett., **91**, p. 153101.
[21] Lee, B. J., and Zhang, Z. M., 2008, "Lateral Shift in Near-Field Thermal Radiation With Surface Phonon Polaritons," Nanoscale Microscale Thermophys. Eng., **12**, pp. 238–250.

A Quasidependent Scattering Radiative Properties Model for High Density Fiber Composites

Siu-Chun Lee
Applied Sciences Laboratory, Inc.,
Baldwin Park, CA 91706

This paper presents a theoretical model for the radiative properties of fiber composites fabricated of spatially oriented fiber strands that contain closely spaced fibers in the Mie scattering regime. Dependent scattering within the dense fiber strands is accounted for by utilizing the solution of Maxwell's equations that included the near field interaction of cylindrical waves. Scattering between strands is shown to be uncorrelated due to their macroscopic dimensions compared with the wavelength of the incident radiation. The model is called quasidependent scattering approximation (QDA), as the radiative properties are formulated as the uncorrelated sum of the dependent scattering properties of the constituent fiber strands. The extinction coefficient, scattering coefficient, and scattering phase function are derived for fiber composites of arbitrary internal architecture. The application of the QDA model is demonstrated by means of numerical analyses on two types of fiber composites. [DOI: 10.1115/1.4000186]

Keywords: dependent scattering, fiber, thermal insulation, fiber composite, woven fabric, heat shield, radiative properties, infinite cylinder

1 Introduction

Fiber insulations are used in many commercial and aerospace applications over a wide temperature range. These include building insulations for ambient environments, woven fabric heat shields for atmospheric entry vehicles, and fiber reinforced composites for refractory systems, and so on. Building insulations are high porosity fiber batts that do not have much resistance to compression. Reusable surface insulations such as the space shuttle thermal protection tiles are also high porosity media, yet they contain bonded fibers that form a semirigid matrix. Fiber reinforced composites contain multidirectional dense fiber strands, which exhibit considerable structural integrity.

The effectiveness of a fiber thermal insulation is due to absorption and scattering of radiation by fibers. The ability of fiber insulations to suppress radiation is a function of the fiber material, diameter, orientation, and solid volume fraction. As fibers in insulation materials are typically millimeters in length and micrometers in diameter, the large aspect ratio renders their scattering characteristics similar to those of an infinite cylinder [1]. Therefore, fibers are commonly modeled as an infinite cylinder, for which the scattering solution is well known [2,3]. The scattering properties of the fiber medium are strongly influenced by the solid volume fraction, as it dictates whether scattering is independent or dependent. Dependent scattering occurs when particles are located in the near field of other particles. This is because scattered waves in the near field are nonplane waves, which recover to plane waves in the far field. Interaction with nonplane waves causes the scattering properties of the particles to deviate from those for independent scattering, for which particles are located in the far field of each other where they interact only with plane waves. A map demarcating the scattering regimes as a function of the fiber solid volume fraction is given in Ref. [4].

Dependent scattering must be distinguished from multiple scattering, as the latter concerns the transport of radiation through the particulate medium via all scattering paths. More detailed discussions on multiple scattering of particles can be found in Refs. [5,6]. Dependent scattering affects the radiative properties of the medium, whereas multiple scattering governs radiative transfer through the medium. Within the phenomenology of the radiative transfer equation (RTE), multiple scattering is accounted for by the scattering phase function, which represents the in-scattering contribution. Multiple scattering is, therefore, inherently included in the solution of the RTE. On the other hand, dependent scattering can only be accounted for by considering the near field interactions of nonplane waves in the solution of Maxwell's equations.

Radiative properties in the independent scattering regime are based on the Mie theory for spheres and the solution for a single infinite cylinder for fibers. In the dependent scattering regime the radiative properties must be derived by a solution of Maxwell's equations that includes the near field interaction of the particles. While considerable research has been conducted on scattering involving spherical particles, the corresponding problem on two-dimensional particles such as infinite cylinders has received much less attention. This is evident in the database compiled by Mishchenko et al. [7], which collected over 700 references from 1965 to 2004 on electromagnetic scattering solution of particles, of which only 12 concerned cylindrical particles. This database provides an extensive repertoire for an in-depth exploration of the topics.

Fundamental studies on dependent scattering by closely spaced infinite cylinders can be categorized into those for unbounded [8–11] and bounded [12–21] domains. The former refers to cylinders located in an infinite homogeneous medium, and the latter concerns cylinders embedded in a semi-infinite or finite dielectric medium. For cylinders in an unbounded domain, only near field interaction of cylindrical waves needs to be considered. For cylinders in a bounded domain, discontinuity of the medium refractive index across the boundaries of the domain gives rise to boundary reflected waves that must be accounted for in the formulation. All of these studies, except those by Lee and co-worker [10,14,15,20], are restricted to normal incidence with respect to the fibers, i.e., the incident wave propagates in the plane perpendicular to the axes of the fibers. At normal incidence the polarization of the incident and scattered waves remains invariant. However, the scattered waves become depolarized at oblique incidence, which give rise to scattered waves of both transverse

---

Contributed by the Heat Transfer Division of ASME for publication in the Journal of Heat Transfer. Manuscript received October 29, 2008; final manuscript received May 14, 2009; published online December 1, 2009. Assoc. Editor: Yogesh Jaluria.

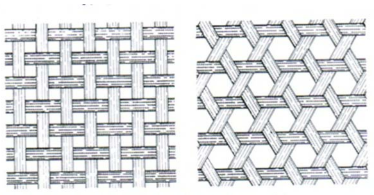

Bi-directional Tri-directional

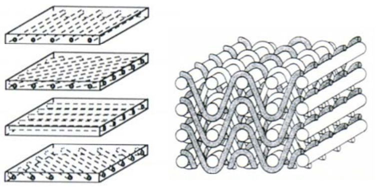

Laminated layers Textile preform

Fig. 1 Schematic diagrams of various types of high density fiber composites [32]

magnetic (TM) and transverse electric (TE) modes even for a single mode incident wave. The cross mode contributions that occur at oblique incidence are accounted for in formalisms for unbounded [10] and bounded [15,20] domains by Lee and in the formalism for a bounded domain by Lee and Grzesik [14].

For fiber media that contain densely packed fibers, the amount of fundamental studies is quite limited [22–28]. The large number of fibers necessitated the treatment of conditional averaging [29] and effective field [30]. These studies were concerned with the propagation of coherent waves and the derivation of the dispersion relation. The latter is the governing equation for the effective propagation constant that is proportional to the extinction efficiency. Most of the studies [22–26,28] were limited to normal incidence on the fibers, as they were concerned with the mechanical properties of fiber composites. The mechanical properties are dictated by shear and compression waves that propagate only in the plane normal to the fiber axes. An approximate model for the scattering coefficient of woven fabrics was given in Ref. [31] assuming normal incidence and Rayleigh–Gans limit, which are seldom satisfied in real applications. None of the studies can treat the general types of fiber composites as those shown in Fig. 1 [32], which contain interweaving, multidirectional fiber strands. Each strand contains closely spaced fibers in the Mie scattering regime. It is evident that dependent scattering is dominant inside the strand due to the high solid volume fraction. The vast quantity of fibers in each strand precludes the application of theoretical formulations for a finite configuration of closely spaced fibers. This is because the system of governing equations is of size $2N^*(2M+1)$, where N is the total number of fibers and M is the truncation order. As the fiber strands contain numerous fibers in the Mie regime, for which the truncation order usually exceeds ten, the number of equations can easily exhaust the resources of even mainframe computers.

An accurate knowledge of the radiative properties is essential to the analysis of radiative transfer through the fiber composite. This paper presents a theoretical model for the radiative properties of fiber composites that accounts for their internal architecture. The model does not place any restriction on the fiber size, refractive index, solid volume fraction, as well as the size and geometric configuration of the fiber strands. In Sec. 2.1, we present a brief overview of the scattering solution for a dense layer of infinite cylinders, which provides the theoretical basis for modeling a fiber strand. Theoretical consideration of the scattering interaction between fiber strands is described in Secs. 2.2.1 and 2.2.2, followed by the formulation to account for the orientation of the strands in Secs. 2.3 and 2.4. The application of the theoretical model is demonstrated in Sec. 3 by means of numerical examples.

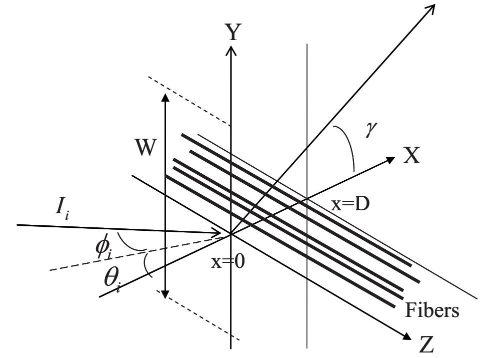

Fig. 2 Radiation incident on a layer containing a dense distribution of parallel fibers

2 Theory

The evaluation of the radiative properties of fiber composites, as those depicted in Fig. 1, requires a theoretical model that accounts for the geometric arrangement and physical characteristics of the fiber strands. In Secs. 2.1–2.4, we shall discuss successively the scattering solution for a single fiber strand, the interaction between strands, the geometric configuration of fiber strands, and the formulation of radiative properties.

2.1 Scattering Properties of a Fiber Strand.

A fiber strand is typically millimeters or centimeters in thickness and width, whereas the fibers are several micrometers in diameter. The macroscopic size of the fiber strand dictates that each strand would contain hundreds of thousands of fibers even for a cross section of only 1 mm^2. As the thickness and width of a fiber strand are orders of magnitude greater than the fiber diameter, a fiber strand can be modeled as a layer containing closely spaced infinite cylinders, for which the scattering solution has been developed [33]. The pertinent formulas to be used in the present paper are summarized below.

A schematic diagram of a fiber strand of width W and thickness D is depicted in Fig. 2. The extinction cross section per unit length is given by

$$C_{e,\psi} = -4\alpha_D W\, \mathrm{Im}(K_{\psi D}/k_i) \tag{1}$$

where the subscript $\psi(=I, II)$ denotes the TM and TE modes, respectively, Im refers to the imaginary part, $\alpha_D(=k_i D/2)$ is the strand size parameter based on thickness, k_i is the propagation constant or wave number of the medium in which the fibers reside, and $K_{\psi D}$ is the effective propagation constant of the fiber strand in the thickness direction. The scattering cross section per unit length is given by

$$C_{s,\psi} = \frac{8 f_v \alpha_D W}{\pi \alpha^2} C_{\psi o} \tag{2}$$

where $\alpha = k_i r$ is the fiber size parameter, r is the fiber radius, and

$$\begin{aligned} C_{\psi o} = \sum_{\tau,\tau'=\pm 1} \sum_{n,s=-\infty}^{\infty} & \frac{1-\exp[-i(\tau K_{\psi D} - \tau' K_{\psi D}^*)D]}{i(\tau K_{\psi D} - \tau' K_{\psi D}^*)D} (X_{\psi n}^{\tau} X_{\psi s}^{\tau'^*} \\ & + Y_{\psi n}^{\tau} Y_{\psi s}^{\tau'^*}) \cdot \Bigg\{ \delta_{sn} + 8 f_v \tau'^{s-n} \exp[i\tau'(s \\ & - n)\theta_{\psi}^*] \int_1^{\infty} J_{s-n}(2\ell_i r R) J_{s-n}(2L_{\psi}^* r R)[g(R)-1] R dR \Bigg\} \end{aligned} \tag{3}$$

In the above expression $(X_{\psi n}^{\tau}, Y_{\psi n}^{\tau})$ are the amplitudes of the effective waves; J_n is the integer order Bessel function; H_n is the Hankel function of the second kind; δ_{sn} is the Kronecker delta function; f_v is the solid volume fraction; in $\ell_i = k_i \cos \phi_i$, ϕ_i is the polar angle of incidence; in $L_\psi = K_\psi \cos\phi_\psi$, ϕ_ψ and θ_ψ are the complex propagation angles inside the strand; superscript * denotes the complex conjugate; and $g(R)$ is the radial distribution function. The extinction and scattering efficiencies are obtained by normalizing the respective cross sections by the total geometric cross section of the fibers. They are given by

$$\hat{Q}_{e,\psi} = -\frac{\pi\alpha}{f_v}\mathrm{Im}\left(\frac{K_{\psi D}}{k_i}\right) \tag{4}$$

$$\hat{Q}_{s,\psi} = \frac{2}{\alpha}C_{\psi o} \tag{5}$$

respectively. The difference between the extinction and scattering cross sections/efficiencies gives the absorption cross section/efficiency. It should be obvious that the radiative cross sections and efficiencies vary with both the polar (ϕ_i) and azimuth (θ_i) angles of incidence because a fiber strand is two-dimensional layer.

For an incident radiation in the direction of ϕ_i and θ_i, the angular distribution of the scattered radiation is prescribed by

$$\boldsymbol{I}_\psi(\gamma) = \frac{4 f_v \alpha_D W}{\pi^2 \alpha^2 \cos\phi_i R_p} i_\psi(\gamma)\boldsymbol{e}_s \tag{6}$$

where R_p is the radial distance

$$\begin{aligned} i_\psi(\gamma) = \sum_{\tau,\tau'=\pm 1} & \frac{1-\exp[-i(\tau K_{\psi D} - \tau' K_{\psi D}^*)D]}{i(\tau K_{\psi D} - \tau' K_{\psi D}^*)D}(X_\psi^\tau X_\psi^{\tau'^*} \\ & + Y_\psi^\tau Y_\psi^{\tau'^*}) \cdot \left\{ 1 + 8 f_v \sum_{m=-\infty}^{\infty} \tau'^m \exp[im(\gamma \right. \\ & \left. + \tau' \theta_\psi^*)] \int_1^\infty J_m(2\ell_i rR) J_m(2L_\psi^* rR)[g(R)-1]RdR \right\} \end{aligned} \tag{7}$$

and

$$\boldsymbol{e}_s = \cos\phi_i \cos\gamma \boldsymbol{e}_x + \cos\phi_i \sin\gamma \boldsymbol{e}_y + \sin\phi_i \boldsymbol{e}_z \tag{8}$$

The unit vector indicates that the scattered radiation propagates along the generators of a cone with half apex angle $\pi/2 - \phi_i$. This directional characteristic resembles that of a single fiber.

All of the above scattering properties are wavelength dependent, but the subscript λ that denotes the spectral dependence has been omitted for brevity. For unpolarized radiation the radiative properties are calculated as the average of the TM and TE modes

$$f = (f_I + f_{II})/2 \tag{9}$$

where $f \in \{C_e, C_s, Q_e, Q_s, i(\gamma)\}$. The scattering properties of a fiber strand provide the basis for formulating the radiative properties of a fiber composite.

2.2 Scattering Interaction Between Fiber Strands. As high density fiber composites contain interweaving fiber strands, the radiative properties of the fiber composite are influenced by the interactions between fiber strands in the near field due to (1) scattered waves from adjacent fiber strands and (2) scattered waves from various fiber strands in the far field. These effects are considered in Secs. 2.2.1 and 2.2.2.

2.2.1 Scattering Interaction in the Near Field. The interaction between adjacent fiber strands is due to secondary incident waves that arise from the scattered waves from other strands. The total Hertz potential in the vicinity of a fiber strand consists of the incident wave, scattered wave, and secondary incident waves as

$$\Psi_j = \Psi_j^o + \Psi_j^s + \sum_{k \neq j} \Psi_{kj}^s \tag{10}$$

where $\Psi \in (u, v)$ represents both the TM and TE modes. The Hertz potentials of the incident and scattered waves are given by

$$\Psi_j^o = \sum_{n=-\infty}^{\infty} (-i)^n \varepsilon_j \exp(in\gamma_{jp}) J_n(\ell_i R_{jP}) \tag{11}$$

$$\Psi_j^s \sim Z_j \exp(-i\mathbf{k}_i \cdot \boldsymbol{R}_{jP}) \tag{12}$$

respectively, where the former is the usual plane wave representation and the latter follows from Ref. [33]. In the above expressions ε_j is the phase shift at strand j, $Z \in (X, Y)$ is the amplitude of the respective modes, and $\boldsymbol{R}_{jP}$ is a radial vector from strand j to point P in space.

The scattered-incident wave from strands k to j is derived by first expanding Eq. (12) for strand k in an infinite series of integer order Bessel functions, followed by utilizing the addition theorem for Bessel functions. After some manipulations we get

$$\Psi_{kj}^s \sim Z_k \sum_{s,n=-\infty}^{\infty} F_n (-i)^{s-n} \exp[i(s-n)\gamma_{kj}] J_{s-n}(\ell_i R_{jk}) J_n(\ell_i R_{jp}) \tag{13}$$

where $F_n = (-i)^n \exp(in\gamma_{jp})$ and γ_{kj} is the azimuth angle from strands k to j. Substituting Eqs. (11)–(13) into Eq. (10) yields

$$\begin{aligned} \Psi_j = \sum_n F_n \Bigg[\varepsilon_j + \sum_{k\neq j} \sum_s Z_k \exp[i(s-n)(\gamma_{kj} \\ + \pi)] J_{s-n}(\ell_i R_{jk}) \Bigg] J_n(\ell_i R_{jp}) + \Psi_j^s \end{aligned} \tag{14}$$

As the distance traversed by the scattered waves is shortest at normal incidence, i.e., $\phi_i = 0$, it represents the limiting case for the greatest effect due to secondary incident waves. Equation (14) for normal incidence is obtained by simply setting $\ell_i (= k_i \cos\phi_i)$ to k_i.

Because fiber strands are macroscopic compared with the individual fibers, $k_i R_{jk}$ is generally large between a pair of fiber strands. For example, $k_i R_{jk} \sim \mathrm{O}(10^3)$ for millimeter thick strands in the thermal radiation regime. In the asymptotic limit of large argument, the integer Bessel function varies as

$$\lim_{k_i R_{jk} \to \infty} J_{s-n}(k_i R_{jk}) \sim 1/\sqrt{k_i R_{jk}} \to 0 \tag{15}$$

which causes the scattered-incident waves to vanish. Equation (14) becomes

$$\Psi_j = \Psi_j^o + \Psi_j^s \tag{16}$$

which indicates that the near field interaction between fiber strands is negligible.

2.2.2 Scattering Interaction in the Far Field. The correlation effect of far field interaction is assessed by utilizing the approach of conditional averaging [29]. The conditional average of Hertz potentials of scattered waves with fiber strands j and k fixed is given by

$$\langle \Psi^s \rangle_{jk} = \int \Psi^s p(\boldsymbol{R}_1 \boldsymbol{R}_2 \ldots \boldsymbol{R}_N) dV_1 \ldots dV_i \ldots dV_N, \quad i \neq j,k \tag{17}$$

where $p(\boldsymbol{R}_1 \boldsymbol{R}_2 \ldots \boldsymbol{R}_N)$ is the probability distribution function and dV_i is the differential volume about fiber strand i. The joint probability distribution of a pair of fiber strands is given by

$$p(\boldsymbol{R}_j, \boldsymbol{R}_k) = \begin{cases} g(R_{jk})/V & |\boldsymbol{R}_j - \boldsymbol{R}_k| > D \\ 0 & |\boldsymbol{R}_j - \boldsymbol{R}_k| \leq D \end{cases} \tag{18}$$

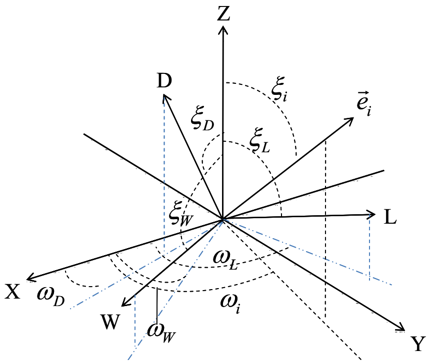

Fig. 3 Orientation of the *DWL* axes relative to the *XYZ* axes

where $g(R_{jk})$ is the radial distribution of a pair of fiber strands and D is the average thickness of strands j and k.

As the fiber strands are nonpenetrating, the interstrand separation is always greater than the strand thickness. The radial distribution function $g(R_{jk})$ is then unity, as the probability of locating another strand is definite. Equation (17) becomes

$$\lim_{R_{jk}>D} \langle \Psi^s \rangle_{jk} \sim \Psi_j^s \tag{19}$$

which indicates negligible correlation between scattered waves from various strands. The total scattered field from all fiber strands follows as:

$$\sum_{j=1}^{N} \langle \Psi^s \rangle_{jk} = \sum_{j=1}^{N} \Psi_j^s \tag{20}$$

which is the same as that for independent scattering. Consequently, the radiative properties of a collection of fiber strands are equal to the uncorrelated sum of those for each strand.

2.3 Orientation of Fiber Strands. As fiber composites contain spatially oriented fiber strands, the orientation of the strands must be accounted for in the formulation of radiative properties. Because each fiber strand is a two-dimensional layer, its orientation can be defined by the direction of two orthogonal vectors on the strand. We prescribe a coordinate system, designate it as *DWL*, on the fiber strand such that the *D*, *W*, and *L* axes coincide with the thickness, width, and length directions, respectively. The coordinate system of the fiber composite is specified as *XYZ*, and its boundaries are parallel to the *XY* plane.

Figure 3 depicts the orientation of a fiber strand in the composite. The spatial orientation of a fiber strand is defined by six angles as

$$\boldsymbol{\Omega} \in (\xi_D, \xi_W, \xi_L, \omega_D, \omega_W, \omega_L) \tag{21}$$

where (ξ_D, ξ_W, ξ_L) and $(\omega_D, \omega_W, \omega_L)$ are the polar and azimuth angles, respectively, relative to the *XYZ* axes. The orthogonality of the unit vectors along the *DWL* axes provides three equations

$$\cos \xi_L \cos \xi_D + \sin \xi_L \sin \xi_D \cos(\omega_L - \omega_D) = 0 \tag{22}$$

$$\cos \xi_D \cos \xi_W + \sin \xi_D \sin \xi_W \cos(\omega_D - \omega_W) = 0 \tag{23}$$

$$\cos \xi_L \cos \xi_W + \sin \xi_L \sin \xi_W \cos(\omega_L - \omega_W) = 0 \tag{24}$$

which reduce the number of independent angles to three.

The transformation between the *DWL* and *XYZ* coordinates can be obtained from geometric consideration. It can be shown that

$$[\boldsymbol{e}_{DWL}] = T_{DWL\text{-}XYZ}[\boldsymbol{e}_{XYZ}] \tag{25}$$

where $[\boldsymbol{e}_{DWL}]$ and $[\boldsymbol{e}_{XYZ}]$ are column unit vectors in the respective coordinate systems, and

$$T_{DWL\text{-}XYZ} = \begin{bmatrix} \sin \xi_D \cos \omega_D & \sin \xi_D \sin \omega_D & \cos \xi_D \\ \sin \xi_W \cos \omega_W & \sin \xi_W \sin \omega_W & \cos \xi_W \\ \sin \xi_L \cos \omega_L & \sin \xi_L \sin \omega_L & \cos \xi_L \end{bmatrix} \tag{26}$$

The inverse transform is

$$[\boldsymbol{e}_{XYZ}] = T_{XYZ\text{-}DWL}[\boldsymbol{e}_{DWL}] \tag{27}$$

where $T_{XYZ\text{-}DWL}$ is the transpose of $T_{DWL\text{-}XYZ}$.

The scattering properties of a fiber strand are given in terms of the incident and scattering angles $(\phi_i, \theta_i, \gamma)$ with respect to the *DWL* axes. The equivalence of the incident direction in the *DWL* and *XYZ* systems yields

$$\sin \phi_i = \sin \xi_i \sin \xi_L \cos(\omega_i - \omega_L) + \cos \xi_i \cos \xi_L \tag{28}$$

$$\tan \theta_i = \frac{\cos \xi_i \cos \xi_W - \sin \xi_i \sin \xi_W \cos(\omega_i - \omega_W)}{\cos \xi_i \cos \xi_D + \sin \xi_i \sin \xi_D \cos(\omega_i - \omega_D)} \tag{29}$$

Equation (6) indicated that the scattered radiation from a fiber strand propagates along the surface of a cone whose axis is along the *L*-axis. The scattered direction in space is, however, a function of the strand orientation and direction of the incident radiation. The scattered directions relative to the fiber strand and fiber composite are related by

$$\cos(\gamma + \theta_i) = [\sin \xi_i \sin \xi_s \cos(\omega_i - \omega_s) + \cos \xi_i \cos \xi_s - \sin^2 \phi_i]/\cos^2 \phi_i \tag{30}$$

which follows from the equivalence of the included scattering angle, i.e., $\boldsymbol{e}_i \cdot \boldsymbol{e}_s$, in the *DWL* and *XYZ* systems. Equation (30) describes the locus of scattered radiation for the incident radiation that propagates in the direction (ξ_i, ω_i) and makes an angle of incidence ϕ_i with the strand.

2.4 Radiative Properties of a Fiber Composite. We have demonstrated in Sec. 2.2 that the interaction between fiber strands is uncorrelated. As a result, the radiative properties of a fiber composite can be formulated by summing up the scattering properties of all the strands. We designate this theoretical approach that combines dependent scattering within a fiber strand and uncorrelated interaction between fiber strands as the QDA.

2.4.1 General Spatial Distribution of Fiber Strands. For composites that contain spatially oriented fiber strands, the extinction and scattering coefficients are obtained by integrating over a generalized size and orientation distribution d^2F as

$$\{\sigma_{e\psi}(\boldsymbol{e}_i), \sigma_{s\psi}(\boldsymbol{e}_i)\} = \int\int \{C_{e\psi}(\boldsymbol{e}_i, \boldsymbol{\Omega}), C_{s\psi}(\boldsymbol{e}_i, \boldsymbol{\Omega})\} d^2F \tag{31}$$

where $\boldsymbol{\Omega} \in (\boldsymbol{e}_D, \boldsymbol{e}_W, \boldsymbol{e}_L)$ denotes the strand orientation. The absorption coefficient is equal to the difference between the extinction and scattering coefficients

$$\sigma_a(\boldsymbol{e}_i) = \sigma_e(\boldsymbol{e}_i) - \sigma_s(\boldsymbol{e}_i) \tag{32}$$

To derive the scattering phase function, we note that the integration of the scattered radiation over all directions yields the scattering cross section

$$C_{s\psi} = \int_0^{2\pi} \boldsymbol{I}_\psi(\gamma) \cdot \boldsymbol{e}_R R_P d\gamma = \frac{8 f_v \alpha_D W}{\pi^2 \alpha^2 \cos^2 \phi_i} \int_0^{\pi - 2\phi_i} \hat{i}_\psi(\eta) \sin \eta d\eta \tag{33}$$

where $\eta = \cos^{-1}(\boldsymbol{e}_i \cdot \boldsymbol{e}_s)$ is the included angle between the incident and scattered directions, and

$$\hat{i}_\psi(\eta) = i_\psi(\gamma)/\sin(\gamma + \theta_i) \tag{34}$$

arises from the transformation of integration from γ to η. If the scattered intensity $\hat{i}_\psi$ were isotropic, Eq. (33) yields

$$\hat{i}_{\psi,\mathrm{iso}} = \frac{\pi^2 \alpha^2 \cos^2 \phi_i}{16 f_v \alpha_D W} C_{s\psi} \tag{35}$$

where the upper limit of integration has been extended to π to encompass the entire range.

The scattering phase function of a fiber strand is defined as the actual distribution of scattered radiation normalized by the corresponding value if scattering were isotropic

$$p_\psi(\boldsymbol{e}_i, \boldsymbol{e}_s, \boldsymbol{\Omega}) = \hat{i}_\psi(\eta, \boldsymbol{\Omega}) / \hat{i}_{\psi,\mathrm{iso}} \tag{36}$$

The phase function satisfies

$$\frac{1}{4\pi} \int_{4\pi} p_\psi(\boldsymbol{e}_i, \boldsymbol{e}_s, \boldsymbol{\Omega}) d\Omega_s = 1 \tag{37}$$

$$\frac{1}{4\pi} \int_{4\pi} C_{s\psi}(\boldsymbol{e}_i, \boldsymbol{\Omega}) p_\psi(\boldsymbol{e}_i, \boldsymbol{e}_s, \boldsymbol{\Omega}) d\Omega_s = C_{s\psi}(\boldsymbol{e}_i, \boldsymbol{\Omega}) \tag{38}$$

where $d\Omega_s (= \sin \xi_s d\xi_s d\omega_s)$ is the solid angle about the scattering direction.

The scattering phase function of a fiber composite is obtained by integrating the product of the scattering cross section and phase function of a fiber strand over the size and orientation distribution function

$$\overline{\sigma_{s\psi} P_\psi}(\boldsymbol{e}_i, \boldsymbol{e}_s) = \int\int C_{s\psi}(\boldsymbol{e}_i, \boldsymbol{\Omega}) p_\psi(\boldsymbol{e}_i, \boldsymbol{e}_s, \boldsymbol{\Omega}) d^2F \tag{39}$$

The product satisfies

$$\frac{1}{4\pi} \int_{4\pi} \overline{\sigma_{s\psi} P_\psi}(\boldsymbol{e}_i, \boldsymbol{e}_s) d\Omega_s = \sigma_{s\psi}(\boldsymbol{e}_i) \tag{40}$$

as integration over all scattered directions must yield the scattering coefficient. The overstrike emphasizes that the scattering coefficient and phase function must appear as a group, as the magnitude of scattered radiation from a strand is dictated by its scattering cross section.

2.4.2 Fiber Strands in Discrete Orientations. For composites that contain fiber strands oriented in discrete directions, the integration in Eqs. (31) and (39) can be replaced by a summation as

$$\{\sigma_{e\psi}(\boldsymbol{e}_i), \sigma_{s\psi}(\boldsymbol{e}_i)\} = \sum_p n_p \{C_{e\psi,p}(\boldsymbol{e}_i, \boldsymbol{\Omega}_p), C_{s\psi,p}(\boldsymbol{e}_i, \boldsymbol{\Omega}_p)\} \tag{41}$$

$$\overline{\sigma_{s\psi} P_\psi}(\boldsymbol{e}_i, \boldsymbol{e}_s) = \sum_p n_p C_{s\psi,p}(\boldsymbol{e}_i, \boldsymbol{\Omega}_p) p_{\psi,p}(\boldsymbol{e}_i, \boldsymbol{e}_s, \boldsymbol{\Omega}_p) \tag{42}$$

where n_p is the areal number density of strands oriented in the direction $\boldsymbol{\Omega}_p$. As each fiber strand can have a different solid volume fraction and geometric cross section, the above equations can be expressed in terms of the characteristics of the constituent strands

$$\begin{Bmatrix} \sigma_{e\psi}(\boldsymbol{e}_i) \\ \sigma_{s\psi}(\boldsymbol{e}_i) \end{Bmatrix} = \frac{F_{va}}{\sum_p x_p D_p W_p} \sum_p x_p D_p W_p \frac{2 f_{vp}}{\pi r_p} \begin{Bmatrix} \hat{Q}_{e\psi,p}(\boldsymbol{e}_i) \\ \hat{Q}_{s\psi,p}(\boldsymbol{e}_i) \end{Bmatrix} \tag{43}$$

$$\overline{\sigma_{s\psi} P_\psi}(\boldsymbol{e}_i, \boldsymbol{e}_s) = \frac{F_{va}}{\sum_p x_p D_p W_p} \sum_p x_p D_p W_p \frac{2 f_{vp}}{\pi r_p} \hat{Q}_{s\psi,p} p_{\psi,p}(\boldsymbol{e}_i, \boldsymbol{e}_s, \boldsymbol{\Omega}_p) \tag{44}$$

where the subscript p refers to strand p, $x_p (= n_p / n_c)$ is the fraction oriented in the direction $\boldsymbol{\Omega}_p$, and n_c is the total areal number density. In addition, we have

$$\begin{aligned} &\hat{Q}_{s\psi,p} p_{\psi,p}(\boldsymbol{e}_i, \boldsymbol{e}_s, \boldsymbol{\Omega}_p) \\ &\quad = \frac{4}{\pi \alpha_p \cos^2 \phi_i \sin(\gamma + \theta_i)} \\ &\quad \cdot \sum_{\tau, \tau' = \pm 1} \frac{1 - \exp[-i(\tau K_{\psi D} - \tau' K^*_{\psi D}) D]}{i(\tau K_{\psi D} - \tau' K^*_{\psi D}) D} (X^\tau_\psi X^{\tau' *}_\psi + Y^\tau_\psi Y^{\tau' *}_\psi) \\ &\quad \cdot \left\{ 1 + 8 f_{vp} \sum_{m=-\infty}^{\infty} \tau'^m \exp[im(\gamma + \tau' \theta^*_\psi)] \right. \\ &\quad \left. \times \int_1^\infty J_m(2\ell_i r_p R) J_m(2L^*_\psi r_p R)[g(R) - 1] R dR \right\} \end{aligned} \tag{45}$$

and

$$F_{va} = \sum_p n_p D_p W_p = n_c \sum_p x_p D_p W_p \tag{46}$$

is the apparent solid volume fraction of the composite based on the envelope dimension of the fiber strand. The actual solid volume fraction of the fiber composite is

$$F_v = n_c \sum_p x_p f_{vp} D_p W_p \tag{47}$$

2.4.3 Identical Fiber Strands in Discrete Orientations. For the special case that all the fiber strands have the same thickness and width, Eqs. (43) and (44) become

$$\begin{Bmatrix} \sigma_{e\psi}(\boldsymbol{e}_i) \\ \sigma_{s\psi}(\boldsymbol{e}_i) \end{Bmatrix} = F_{va} \sum_p x_p \frac{2 f_{vp}}{\pi r_p} \begin{Bmatrix} \hat{Q}_{e\psi,p}(\boldsymbol{e}_i) \\ \hat{Q}_{s\psi,p}(\boldsymbol{e}_i) \end{Bmatrix} \tag{48}$$

$$\overline{\sigma_{s\psi} P_\psi}(\boldsymbol{e}_i, \boldsymbol{e}_s) = F_{va} \sum_p x_p \frac{2 f_{vp}}{\pi r_p} \hat{Q}_{s\psi,p} p_{\psi,p}(\boldsymbol{e}_i, \boldsymbol{e}_s, \boldsymbol{\Omega}_p) \tag{49}$$

3 Numerical Examples

The radiative properties of a fiber composite are governed by two sets of parameters that characterize the fiber strands and the fiber composite, respectively. The former includes the diameter and refractive index of the fibers, as well as the solid volume fraction, thickness, and width of the fiber strand. The latter refers to the number density and orientation distribution of the strands. The strand parameters are needed for the determination of the basic characteristics of the fiber strands, i.e., the effective propagation constant K_ψ / k_i and scattering amplitudes $(X^\tau_{\psi m}, Y^\tau_{\psi m})$. These characteristics are dictated by the dispersion relations and a set of governing equations in Ref. [33], which must be evaluated for the entire range of polar and azimuth angles of incidence (ϕ_i, θ_i) for both the TM and TE modes. They are then applied to calculate the radiative properties of the strand. The fiber composite parameters, on the other hand, are utilized in conjunction with the single strand properties to calculate the radiative properties of the fiber composite. This process needs to be performed for each wavelength of interest.

The purpose of the numerical analyses is to demonstrate the application of the QDA model to calculate the radiative properties of fiber composites. The following fiber strand parameters are assumed: refractive index $\tilde{m} = 1.45 - i0.1$, fiber size parameter $\alpha = 1$, identical fiber strands with size parameter $\alpha_D = 200$, and solid volume fraction is 40%. Wood's radial distribution function for an isothermal-isobaric ensemble at the reduced pressure of 1.25 is used for the 40% volume fraction [34]. These size parameters give $D/r = 400$, which encompasses a wide range of fiber and strand sizes. For example, the ratio corresponds to 2-mm thick fiber strands and 10 μm diameter fibers, or 1-mm thick strand and 5 μm diameter fiber, and so on. For the purpose of illustration,

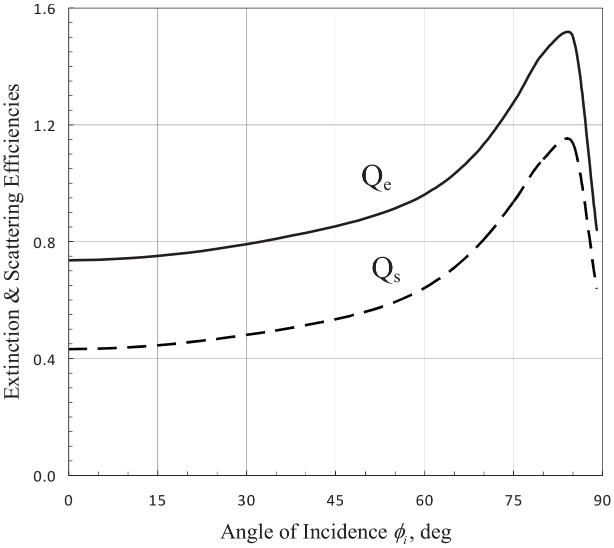

Fig. 4 Extinction and scattering efficiencies of a single fiber

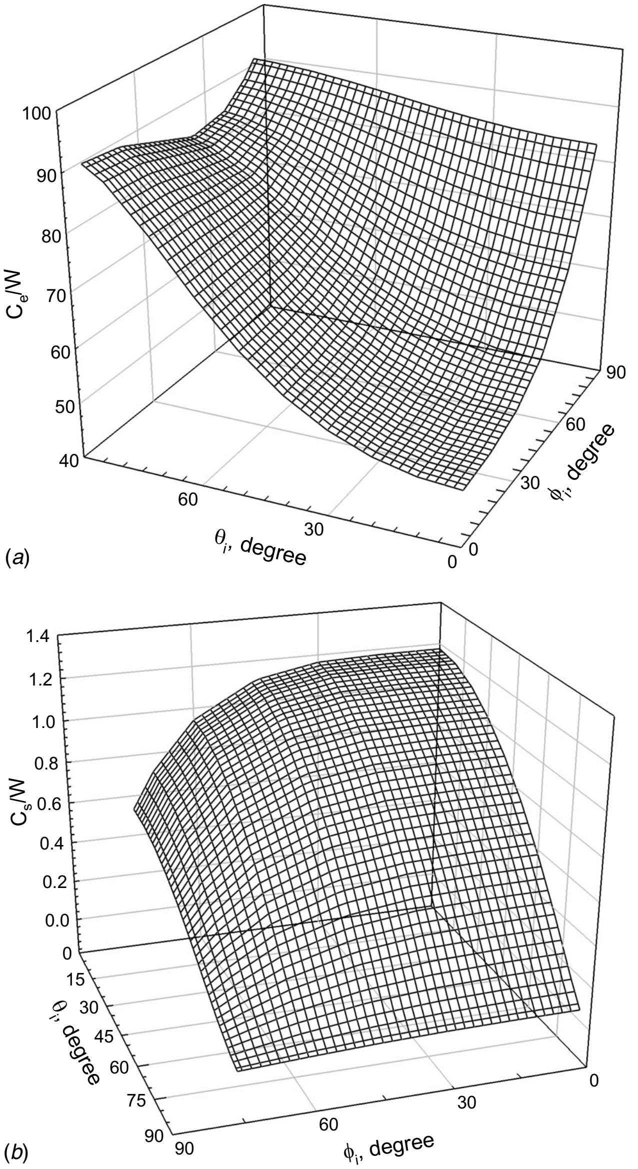

Fig. 5 (*a*) Variation in the extinction cross section of a fiber strand with angles of incidence and (*b*) variation in the scattering cross section of a fiber strand with angles of incidence

we consider two types of 2D fiber composites, i.e., fiber strands oriented parallel to the boundaries to explore the effect of weave pattern. The weave patterns are designated by 90/90 and 0/60/120, where the numeric values denote the azimuth angles of the *L* axes of the strands measured from the *X*-axis. The number of strands is evenly distributed in each direction. The designation 90/90 denotes that all fiber strands are aligned at 90 deg from the *X*-axis, i.e., parallel to the *Y*-axis, and 0/60/120 indicates that 1/3 each of the total number of strands is aligned at 0 deg, 60 deg, and 120 deg from the *X*-axis. The thickness direction (*D*-axis) is parallel to the *Z*-axis. The extinction and scattering characteristics are shown successively for a single fiber, fiber strand, and fiber composite to illustrate the effect of the constituents on the properties of a fiber composite.

Figure 4 shows the extinction and scattering efficiencies of a single fiber, which vary only with the polar angle of incidence ϕ_i due to cylindrical symmetry. A fiber strand, on the other hand, is a two-dimensional layer with a thickness and width. Its extinction and scattering cross sections then vary with both the polar and azimuth angles of incidence, as shown in Figs. 5(*a*) and 5(*b*). Normal incidence on a strand refers to the condition that both ϕ_i and θ_i are zero, whereas normal incidence on a fiber requires only $\phi_i=0$ and θ_i is arbitrary. The extinction cross section increases as the incident direction approaches grazing angles, i.e., $\phi_i,\theta_i \rightarrow 90$ deg, due to longer pathlength and thus greater attenuation. The longer pathlength also reduces the forward scattering component, thus causing the scattering cross section to decrease. The radiative properties of a fiber strand provide the basis for calculating the radiative properties of fiber composites, which are given in Figs. 6 and 7.

As a fiber composite contains multidirectional fiber strands, its radiative properties are strongly influenced by the geometric configuration of the fiber strands. This is illustrated by two examples of 2D fiber composites. Figures 6(*a*) and 6(*b*) show the nondimensional extinction and scattering coefficients for the unidirectional composite 90/90. These radiative coefficients are independent of the azimuth angle ω_i at normal incidence, i.e., $\xi_i=0$. For a given azimuth angle the extinction coefficient increases as the polar angle ξ_i approaches grazing incidence due to longer pathlength. The scattering coefficient, on the other hand, decreases due to reduction in the forward scattering cross section. Note that at the azimuth angle $\omega_i=0$, the incident direction lies in the plane perpendicular to the *L*-axis of the fiber strands. This is evident from the local maxima that coincide with the direction of the *L*-axis. When the incident direction is confined to this plane, the angle of incidence on the fiber layer varies from grazing to normal incidence with respect to the layer, while it remains at normal incidence on the fibers.

The effect of multiple weave directions is illustrated by a tri-ply composite designated as 0/60/120. The nondimensional extinction and scattering coefficients for this type of composite are shown in Figs. 7(*a*) and 7(*b*). Because the strands are oriented parallel to the boundaries, the effect of strand orientation becomes more pronounced only toward grazing incidence. The effect of additional strand direction is evident in the maxima in the extinction and scattering coefficients that occur at the azimuth directions of 30 deg, 90 deg, and 150 deg. These maxima arise from the fiber strands aligned at 120 deg, 0 deg, and 60 deg, respectively, due to perpendicular incidence. For example, radiation propagating in the azimuth direction of 30 deg lies in the plane perpendicular to the longitudinal axis of the fiber strands aligned at 120 deg, thus giving rise to maxima at this azimuth angle.

Although numerical results have been shown for only one set of fiber parameters, they served the purpose of illustrating the progression of scattering properties from a single fiber to composites

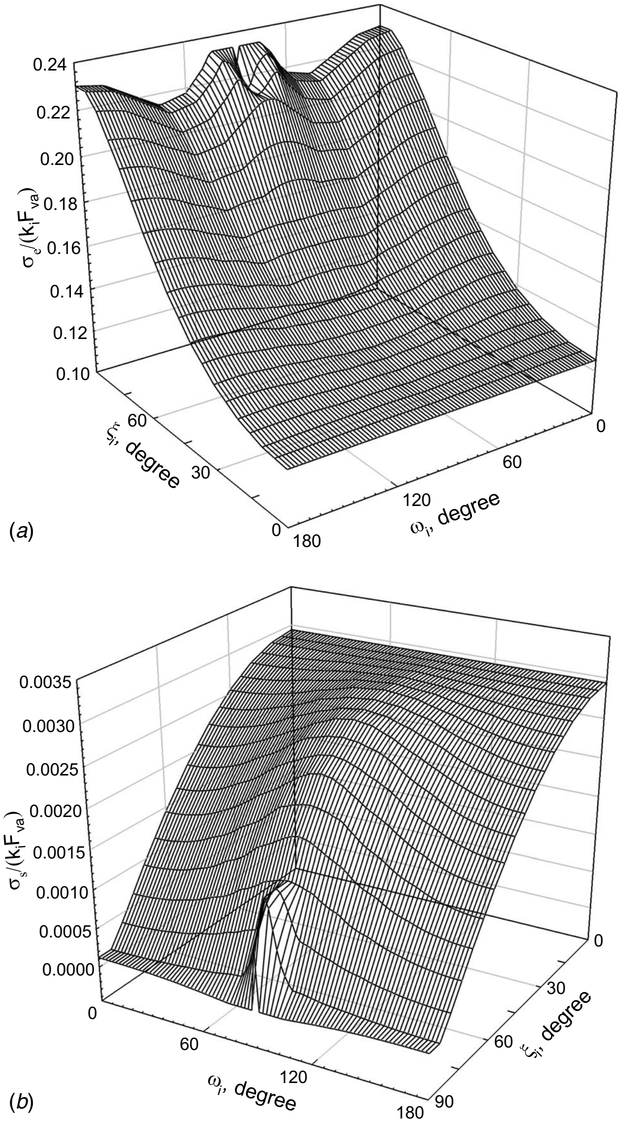

Fig. 6 (*a*) Extinction coefficient of a fiber composite containing unidirectional fiber strands and (*b*) scattering coefficient of a fiber composite containing unidirectional fiber strands

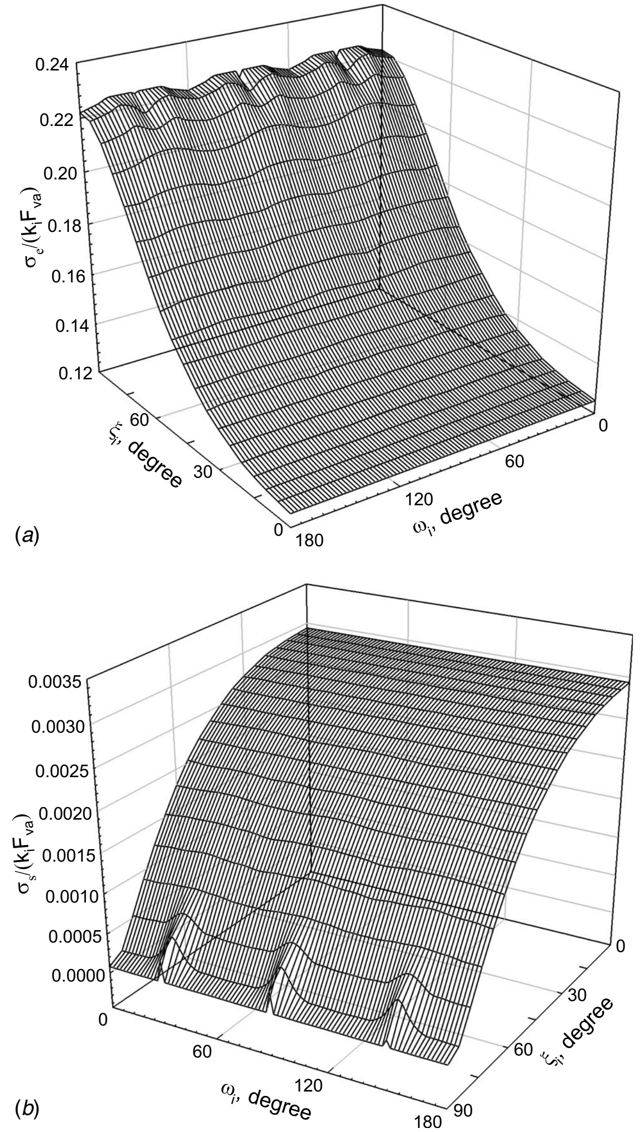

Fig. 7 (*a*) Extinction coefficient of a fiber composite containing 0/60/120 fiber strands and (*b*) scattering coefficient of a fiber composite containing 0/60/120 fiber strands

that contain dense fiber strands in multiple directions. The scattering properties of a single fiber are a function only of the angle that the incident radiation makes with the fiber axis due to cylindrical symmetrical. Because a fiber strand is a two-dimensional layer containing numerous closely spaced fibers, the absence of cylindrical symmetry causes its scattering properties to vary with both the polar and azimuth angles of incidence. As a fiber composite contains spatially oriented fiber strands dictated by its design, the angular variation in its radiative properties is then strongly influenced by the orientation of the fiber strands. The present QDA model provides the theoretical basis for predicting the radiative properties of fiber composites utilizing only fundamental design parameters.

4 Conclusion

Radiative analysis of high density fiber composites is a very complicated problem due to the complex internal architecture of the materials. These composites consist of spatially oriented, interweaving fiber strands that contain densely packed fibers in the Mie scattering regime. The fiber strand is modeled as a dense layer of infinite cylinders, for which a rigorous solution of Maxwell's equation is available [33]. The scattering solution captures the unique characteristics due to dependent scattering, which include the change in the effective refractive index with solid volume fraction, refraction of waves inside the fiber strand, coherent reflection and transmission, shifting of the forward peak of the scattered radiation, and so on. The interaction between fiber strands is shown to be uncorrelated based on theoretical consideration. Consequently, the radiative properties of a fiber composite are formulated as the sum of the scattering properties of all the strands accounting for their orientation. This theoretical model is designated as the QDA, as it incorporates both the dependent and uncorrelated scattering formalisms of the spatially oriented fiber strands. The model does not place any restriction on the size and refractive index of the fibers, or on the solid volume fraction and spatial orientation of the fiber strands. The application of the QDA model was demonstrated by numerical results on two types of 2D fiber composites.

Nomenclature

C_e, C_s = extinction and scattering cross sections
D = thickness of a fiber strand
f_v = solid volume fraction of a fiber strand

F_v = solid volume fraction of a fiber composite
F_{va} = apparent solid volume fraction of a fiber composite
H_n = Hankel function of the second kind
J_n = integer order Bessel function
k_i = propagation constant of the medium containing the fibers
K_ψ = effective propagation constant
ℓ_i = $k_i \cos \phi_i$
L = length of a fiber strand
L_ψ = $K_\psi \cos \phi_\psi$
n_c = areal number density of a fiber composite
n_p = areal number density of fiber strands oriented in $\boldsymbol{\Omega}_p$
p_ψ = scattering phase function of a fiber strand
P_ψ = scattering phase function of a fiber composite
$\hat{Q}_e, \hat{Q}_s$ = extinction and scattering efficiency
r = fiber radius
R = radial distance
W = width of a fiber strand
x_p = fraction of fiber strands oriented in $\boldsymbol{\Omega}_p$

Greek Symbols

α = fiber size parameter, $k_i r$
α_D = fiber strand thickness parameter, $k_i D/2$
δ = Kronecker delta function
ϕ = polar angle with respect to a fiber strand
γ = azimuth scattering angle relative to a fiber strand
η = included angle between the incident and scattered directions
θ = azimuth angle with respect to a fiber strand
σ = radiation coefficient
ω = azimuth angle with respect to a fiber composite
$\boldsymbol{\Omega}$ = coordinate triad prescribing the orientation of a fiber strand
ξ = polar angle with respect to a fiber composite
Ψ = Hertz potential

Subscripts

ψ = mode of radiation, I=TM and II=TE
D = thickness direction of a fiber strand
e = extinction
i = incident
L = longitudinal direction of a fiber strand
p = strand p
s = scattering
W = width direction of a fiber strand

References

[1] Cohen, L. D., Haracz, R. D., Cohen, A., and Aquista, C., 1983, “Scattering of Light From Arbitrarily Oriented Finite Cylinders,” Appl. Opt., **22**, pp. 742–748.
[2] Kerker, M., 1969, *The Scattering of Light and Other Electromagnetic Radiation*, Academic, New York.
[3] van de Hulst, H. C., 1981, *Light Scattering by Small Particles*, Dover, New York.
[4] Lee, S. C., 1994, “Dependent vs Independent Scattering in Fibrous Composites Containing Parallel Fibers,” J. Thermophys. Heat Transfer, **8**(4), pp. 641–646.
[5] van de Hulst, H. C., 1980, *Multiple Light Scattering: Tables, Formulas, and Applications*, Academic, New York.
[6] Mishchenko, M. I., Travis, L. D., and Lacis, A. A., 2006, *Multiple Scattering of Light by Particles: Radiative Transfer and Coherent Backscattering*, Cambridge University Press, Cambridge, England.
[7] Mishchenko, M. I., Videen, G., Babenko, V. A., Khlebtsov, N. G., and Wriedt, T., 2004, “T-Matrix Theory of Electromagnetic Scattering by Particles and Its Applications: A Comprehensive Reference Database,” J. Quant. Spectrosc. Radiat. Transf., **88**, pp. 357–406.
[8] Twersky, V., 1952, “Multiple Scattering of Radiation by an Arbitrary Configuration of Parallel Cylinders,” J. Acoust. Soc. Am., **24**, pp. 42–46.
[9] Oloafe, G. O., 1970, “Scattering by an Arbitrary Configuration of Parallel Cylinders,” J. Opt. Soc. Am., **60**, pp. 1233–1236.
[10] Lee, S. C., 1992, “Scattering by Closely-Spaced Radially Stratified Parallel Cylinders,” J. Quant. Spectrosc. Radiat. Transf., **48**(2), pp. 119–130.
[11] Felbacq, D., Tayeb, G., and Maystre, D., 1994, “Scattering by a Random Set of Parallel Cylinders,” J. Opt. Soc. Am. A Opt. Image Sci. Vis., **11**, pp. 2526–2538.
[12] Rao, T. C., and Barakat, R., 1994, “Plane Wave Scattering by a Finite Array of Conducting Cylinders Partially Buried in a Ground Plane: TM Polarization,” Pure Appl. Opt., **3**, pp. 1023–1048.
[13] Borghi, R., Gori, F., Santarsiero, M., Frezza, F., and Schettini, G., 1996, “Plane-Wave Scattering by a Set of Perfectly Conducting Circular Cylinder in the Presence of a Plane Surface,” J. Opt. Soc. Am. A Opt. Image Sci. Vis., **13**, pp. 2441–2456.
[14] Lee, S. C., and Grzesik, J. A., 1998, “Light Scattering by Closely Spaced Parallel Cylinders Embedded in a Semi-infinite Dielectric Medium,” J. Opt. Soc. Am. A Opt. Image Sci. Vis., **15**, pp. 163–173.
[15] Lee, S. C., 1999, “Light Scattering by Closely Spaced Parallel Cylinders Embedded in a Finite Dielectric Slab,” J. Opt. Soc. Am. A Opt. Image Sci. Vis., **16**(6), pp. 1350–1361.
[16] Radzevicius, S. J., and Daniels, J. J., 2000, “Ground Penetrating Radar Polarization and Scattering From Cylinders,” J. Appl. Geophys., **45**(2), pp. 111–125.
[17] Borghi, R., Frezza, F., Santarsiero, M., and Schettini, G., 2000, “Electromagnetic Scattering by Cylindrical Objects on Generic Planar Substrates: Cylindrical-Wave Approach,” *Light Scattering From Microstructures*, F. Moreno and F. González, eds., Springer, Berlin, pp. 97–111.
[18] Di Vico, M., Frezza, F., Pajewski, L., and Schettini, G., 2005, “Scattering by a Finite Set of Perfectly Conducting Cylinders Buried in a Dielectric Half-Space: A Spectral-Domain Solution,” IEEE Trans. Antennas Propag., **53**(2), pp. 719–727.
[19] Jia, H., and Yasumoto, K., 2005, “Scattering and Absorption Characteristics of Multilayered Gratings Embedded in a Dielectric Slab,” Int. J. Infrared Millim. Waves, **26**(8), pp. 1111–1126.
[20] Lee, S. C., 2006, “Optical Extinction by Closely Spaced Parallel Cylinders Inside a Finite Dielectric Slab,” J. Opt. Soc. Am. A Opt. Image Sci. Vis., **23**(9), pp. 2219–2232.
[21] Frezza, F., Pajewski, L., Ponti, C., and Schettini, G., 2009, “Scattering by Perfectly Conducting Circular Cylinders Buried in a Dielectric Slab Through the Cylindrical Wave Approach,” IEEE Trans. Antennas Propag., **57**(4), pp. 1208–1217.
[22] Bose, S. K., and Mal, A. K., 1973, “Longitudinal Shear Waves in Fiber-Reinforced Composite,” Int. J. Solids Struct., **9**, pp. 1075–1085.
[23] Mal, A. K., and Chatterjee, A. K., 1977, “The Elastic Moduli of a Fiber-Reinforced Composite,” ASME J. Appl. Mech., **44**, pp. 61–67.
[24] Varadan, V. K., Varadan, V. V., and Pao, Y.-H., 1978, “Multiple Scattering of Elastic Waves by Cylinders of Arbitrary Cross Section. I. SH Waves,” J. Acoust. Soc. Am., **63**, pp. 1310–1319.
[25] Varadan, V. K., 1979, “Scattering of Elastic Waves by Randomly Distributed and Oriented Scatterers,” J. Acoust. Soc. Am., **65**(3), pp. 655–657.
[26] Varadan, V. K., Ma, Y., and Varadan, V. V., 1986, “Multiple Scattering of Compressional and Shear Waves by Fiber-Reinforced Composite Materials,” J. Acoust. Soc. Am., **80**, pp. 333–339.
[27] Lee, S. C., 1992, “Effective Propagation Constant of Fibrous Media Containing Parallel Fibers in the Dependent Scattering Regime,” ASME J. Heat Transfer, **114**, pp. 473–478.
[28] Liu, W., 1997, “Multiple Wave Scattering and Calculated Effective Stiffness and Wave Properties in Unidirectional Fiber-Reinforced Composites,” Ph.D. thesis, Virginia Polytechnic Institute and State University, Blacksburg, VA.
[29] Foldy, L. L., 1945, “The Multiple Scattering of Waves, I. General Theory of Isotropic Scattering by Randomly Distributed Scatterers,” Phys. Rev., **67**(3–4), pp. 107–119.
[30] Lax, M., 1952, “Multiple Scattering of Waves. II. The Effective Field in Dense Systems,” Phys. Rev., **85**, pp. 621–629.
[31] Kumar, S., and White, S., 1995, “Dependent Scattering Properties of Woven Fibrous Insulations for Normal Incidence,” ASME J. Heat Transfer, **117**(1), pp. 160–166.
[32] Chou, T.-W., 1992, *Microstructural Design of Fiber Composites*, Cambridge University Press, Cambridge, England.
[33] Lee, S. C., 2008, “Scattering by a Dense Layer of Infinite Cylinders at Oblique Incidence,” J. Opt. Soc. Am. A Opt. Image Sci. Vis., **25**(10), pp. 2489–2498.
[34] Wood, W. W., 1970, “NpT-Ensemble Monte Carlo Calculations for the Hard Disk Fluid,” J. Chem. Phys., **52**, pp. 729–741.

Experimental and Computational Characterization of High Heat Fluxes During Transient Blackbody Calibrations

Amanie N. Abdelmessih
Department of Mechanical Engineering,
Saint Martin's University,
5300 Pacific Avenue, S.E.
Lacey, WA 98503-1297
e-mail: abdelmessih@stmartin.edu

Thomas J. Horn
National Aeronautics and Space Administration,
Dryden Flight Research Center,
P.O. Box 273,
MS 48202A Edwards, CA 93523;
e-mail: thomas.j.horn@nasa.gov

High heat fluxes are encountered in numerous applications, such as on the surfaces of hypersonic vehicles in flight, in fires, and within engines. The calibration of heat flux gauges may be performed in a dual cavity cylindrical blackbody. Insertion of instruments into the cavity disturbs the thermal equilibrium resulting in a transient calibration environment. To characterize the transient heat fluxes, experiments were performed on a dual cavity cylindrical blackbody at nominal temperatures varying from 800°C to 1900°C in increments of 100°C. The pre-insertion, steady state, axial temperature profile is compared experimentally and numerically. Detailed transient thermal models have been developed to simulate the heat flux calibration process at two extreme fluxes: the high flux is 1 MW/m^2 and the relatively low is 70 kW/m^2. Based on experiments and numerical analysis, the optimum heat flux sensor insertion location as measured from the center partition was determined. The effect of convection (natural and forced) in the blackbody cavity during the insertion is calculated and found to be less than 2% at high temperatures but reaches much higher values at relatively lower temperatures. The transient models show the effect of inserting a heat flux gauge at room temperature on the thermal equilibrium of the blackbody at 1800°C and 800°C nominal temperatures. Also, heat flux sensor outputs are derived from computed sensor temperature distributions and compared with experimental results. The numerical heat flux agreed with the experimental results to within 5%, which indicates that the numerical models captured the transient thermal physics during the calibration. Based on numerical models and all experimental runs the heat transfer mechanisms are explained. [DOI: 10.1115/1.4000187]

Keywords: cylindrical blackbody calibration, blackbody calibration furnace, transient blackbody calibration, blackbody cavity, heat flux calibration, heat flux measurement, temperature measurement, temperature calibration, numerical or computational calibration, experimental calibration

1 Introduction

High heat fluxes are generated on the surfaces of hypersonic vehicles in flight and on the surfaces of space vehicles during reentry. Other applications in which high heat fluxes are generated are reciprocating engines, gas turbine engines, scramjet engines, and fires. It is important to determine what these heat fluxes are in order to properly design hardware to survive high heat flux environments. Heat flux gauges can be used to measure heat fluxes but these gauges need to be properly calibrated before they are put into service. Additionally, the furnace used to calibrate heat flux gauges must be characterized in order to determine its effect on the accuracy of the calibration.

The calibration system considered in this study consists of a cylindrical dual cavity blackbody for calibrating a reference heat flux gauge. The blackbody temperature at the center of the middle partition is measured with an optical pyrometer facing one cavity. The National Institute of Standards and Technology (NIST) performs calibrations by locating the heat flux gauges outside the opposite cavity of the blackbody at a distance (≥ 1.25 cm), which avoids creating any disturbances to the thermal equilibrium of the blackbody. Calibrating by locating the heat flux gauge outside the blackbody can reach heat fluxes up to 50 kW/m^2 as reported by Holmberg and co-workers [1,2], Grosshandler and Blackburn [3], Murthy and co-workers [4–9], and Tsai et al. [10]. These heat fluxes are below the heat fluxes that can be generated in hypersonic flight; the latter can be in excess of 1 MW/m^2.

The heat flux gauge can be inserted into the blackbody cavity for a few seconds to achieve higher heat fluxes. The process of inserting the heat flux gauge, or any other measuring device, affects the internal thermal equilibrium of the blackbody creating transient conditions. In the last 10 years, research has begun to quantify the uncertainties associated with the blackbody calibration system. Abdelmessih [11] experimentally studied the effects due to the various boundary conditions such as conduction, radiation, convection, and the effect of axial temperature gradients on the blackbody cavity. Then Horn and Abdelmessih [12] performed experimental and numerical characterization of the blackbody cavity under steady state conditions followed by the effect of transient conditions on the blackbody [13]. Abdelmessih and Horn [14] then studied the effects of the transient insertion on the heat flux gauge, which ultimately affects the blackbody cavity; they reported heat fluxes of approximately 200 kW/m^2. Recently, Murthy et al. [15] experimentally inserted heat flux gauges into the blackbody cavity and used Monte Carlo simulations; they reported heat fluxes up to 500 kW/m^2.

This research addresses the optimum heat flux position inside the blackbody cavity based on experimental values between blackbody nominal temperatures of 800°C to 1900°C in incre-

---

Contributed by the Heat Transfer Division of ASME for publication in the JOURNAL OF HEAT TRANSFER. Manuscript received October 30, 2008; final manuscript received April 7, 2009; published online December 1, 2009. Assoc. Editor: Yogesh Jaluria.

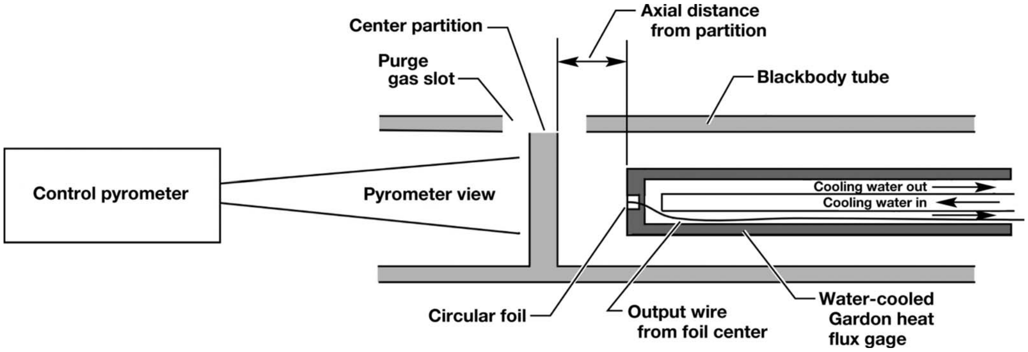

Fig. 1 Schematic of blackbody calibration system with location of instruments

ments of 100°C. The steady state axial temperature profile for insulated and uninsulated is shown experimentally and compared with numerical models. Two extreme heat fluxes of 70 $\mathrm{kW/m^2}$ and 1 $\mathrm{MW/m^2}$ at nominal temperatures of 800°C and 1800°C, respectively, were analyzed. Heat fluxes and temperatures were derived from the numerical models and compared with the experimental data resulting in better characterization of the calibration process.

2 Experimental Setup

The calibration system consists of a 28.9 cm cylindrical graphite blackbody. The blackbody is dual cavity with an inside diameter of 2.57 cm and a 5.4 mm thick partition at the middle. At the top center of the graphite tube is an oval slot 9.4 mm long and 3.1 mm wide, which serves as a bleed port for argon purge gas during pretest purging of the blackbody cavities. The graphite tube is held in place at each end by a graphite bushing assembly installed in a copper ring. The copper rings are cooled with water and have ports for introduction of argon gas. A quartz tube, which serves as a containment barrier for the argon purge gas, is held between the copper rings. The space between the outer surface of the blackbody and the quartz tube is insulated with graphite felt and foil when temperatures at 1100°C or above are desired (insulated configuration). The space is left uninsulated when the temperature does not exceed 1100°C (uninsulated configuration) as recommended by the manufacturer [16]. An aluminum water-cooled reflector surrounds the quartz cylinder. Unheated graphite extension tubes, 15.2 cm long, are installed at both ends of the blackbody. Argon gas is used to purge the interior and exterior of the graphite tube to minimize or avoid oxidation of the graphite. Creeping laminar flow of argon gas exiting the extension tubes prevents air from diffusing into the heated graphite tube. A schematic of the blackbody assembly calibration system is shown in Fig. 1.

The copper rings are placed atop two electrodes, which are connected to a power supply. The furnace temperature is closed loop controlled via computer. An optical pyrometer views the center of the midpartition from one end of the blackbody and provides temperature feedback to the control system. The thermal control system maintains the indicated temperature within ±0.5°C of the desired steady state set point from 800°C to 2200°C, by passing regulated electric current from the power supply through the blackbody assembly.

The electrical current passing through the blackbody assembly was measured using a current transformer. The output from the current transformer was connected to a current transducer, which converted the reduced current to a dc voltage. This dc voltage was then acquired by the data acquisition system and converted into the value of the blackbody assembly current. The measurement uncertainty of the current transformer and transducer combination was ±13 A (~1.3% and 3.3% of the maximum and minimum measured current, respectively) and the response time was 0.1 s.

Optical pyrometers were utilized during the experimental characterization of the blackbody cavity. A control pyrometer and a reference pyrometer measured blackbody temperature. These pyrometers are identical radiation pyrometers for measuring temperatures between 800°C and 3100°C. Their measurement spot covers approximately one-fourth of the diameter of the blackbody partition. The temperature measurements of the center partition with the reference pyrometer will be referred to as the nominal blackbody temperature throughout this paper.

Once the blackbody temperature was stabilized at the desired temperature according to the control pyrometer, the blackbody temperature was checked with the calibrated reference pyrometer. These temperatures were measured on opposite sides of the center partition and were within the uncertainty of the reference pyrometer calibration of ±0.4°C. The reference pyrometer was then moved away from the blackbody axis in order to provide a clear view for the infrared pyrometer and the emissivity measurement was taken.

Axial surface temperature profiles of the blackbody cavity were obtained using an *optical fiber thermometer* (OFT) [17]. The OFT system includes a sapphire lightpipe with a 90 deg bend at the tip, which is exposed to the heated region. The lightpipe is inserted into the blackbody cavity. The light is transmitted from the lightpipe to a receiving unit through a fiber optic cable. The receiving unit senses the incoming infrared energy and converts that energy into a dc voltage proportional to temperature, which is routed to a data acquisition system. The OFT system is capable of measuring temperatures from 400°C to 1900°C with a resolution of 0.4°C. The response time of the OFT system is 0.04 s. The OFT mount was locally designed and built to include the capability to rotate the sensor to measure the axial temperature distribution at various locations around the interior circumference of the blackbody cavity at angle increments of 45 deg.

A *Gardon heat flux gauge* was used to measure heat fluxes. The sensor is a circular foil of constantan connected at the outer edge to a copper cylinder. The heat flux gauge is 12.7 mm in diameter and is situated at the end of a water-cooled probe. The heat flux incident on the sensor surface flows radially from the center of the foil to the copper. The manufacturer's calibration was used to convert the heat flux gauge output to engineering units. A generic sketch of a Gardon type heat flux gauge is included in Fig. 1.

The OFT and the heat flux gauge were mounted on a slide track and crossbar assembly. The position of the heat flux gauge and optical fiber thermometer sensing tips were measured using a *deflection measurement potentiometer*. The range of the device was 0–1080 mm with an accuracy of ±1.6 mm. The measurement system was calibrated such that 0 mm was indicated when the surface of the measuring instrument was in contact with the center partition of the blackbody. The locations were nominally 4 mm, 15 mm, 40.6 mm, 66 mm, 91 mm, 117 mm, 129 mm, 136 mm, and 142 mm from the center partition.

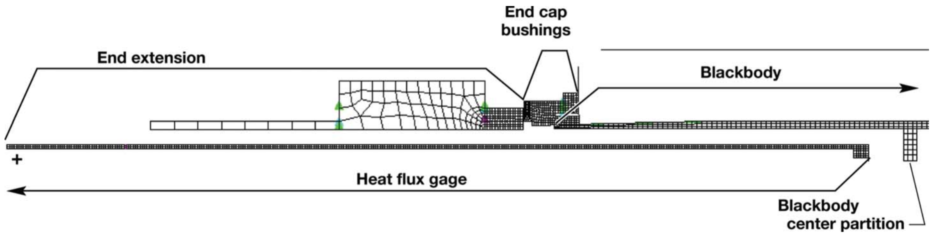

Fig. 2 Axisymmetric mesh of the left cavity of the blackbody assembly and heat flux gauge

The OFT or the heat flux gauge was then plunged (<1 s of motion) into the blackbody while its tip location and temperature or heat flux measurement were recorded by the data acquisition system. The slide track on which the heat flux gauge was mounted was pushed against a stop for the full insertion at 4 mm; this axial position was repeated within the measurement uncertainty stated above. The sensor was left at maximum depth of approximately 4 mm for approximately 3–6 s (until the sensor stabilized) and then removed from the blackbody. Similarly, measurements were recorded for the remainder of the repose axial locations indicated above.

Experiments were performed in the range of 800–1100°C for the uninsulated cylindrical blackbody and from 1100°C to 1900°C for the insulated cylindrical blackbody, in increments of 100°C.

After all experiments were performed, we used a type K thermocouple to measure the temperature of the argon gas that was exiting the extension. Also, the core temperatures at the center axis of the cavity were measured at the same repose locations mentioned above. A more detailed explanation of the experimental setup is found in Refs. [12–14].

3 Thermal Modeling

Numerical steady and transient thermal analysis models of the insulated ($1000\ \mathrm{kW/m^2}$) and uninsulated ($70\ \mathrm{kW/m^2}$) blackbody configurations were developed to aid in understanding the relevant heat transfer mechanisms occurring during the calibration process. The steady state models of the blackbody developed at the required nominal temperatures (800°C and 1800°C) formed the basis of the transient models.

Computational models of the blackbody assembly with and without the heat flux gauge were represented as thin slices of an axisymmetric geometry, which presents the cylindrical shapes on rotation about the axis. The blackbody assembly includes the graphite tube, end cap bushings, and extensions. Commercially available thermal analysis software [18] was used. Figure 2 shows half of the model during transient calibration, with the heat flux gauge inserted.

The node spacing in the blackbody wall was nominally 2 mm axial by 1 mm radial. The spacing was reduced to 1 mm axial at the connection to the bushing. The radial spacing was varied in the tapered region of the blackbody to maintain four nodes in the radial direction. Node spacing was 2 mm × 2 mm in the center partition. The bushings, where higher thermal gradients were expected, were meshed with a nominal 1 mm × 1 mm node spacing. Variable node spacing was used in the mesh of the end extensions. This mesh was approximately 1 mm × 1 mm near the bushings and expanded to 9 mm × 9 mm as distance from the bushings increased. The copper body of the heat flux gauge was meshed with 0.9 mm quad elements, while the sensing constantan foil was meshed with 0.01 mm quad elements.

The thermal solver computed the volumetric heat generation in the blackbody based on the experimentally measured current passing through the blackbody assembly, the local geometry of the assembly, and the temperature dependant electrical resistivity.

Thermal contact resistance is a significant factor affecting the conduction heat transfer at the material interfaces in both end caps. These interfaces include blackbody-to-bushing, bushing-to-copper-ring, and between bushing components. However, it is difficult to estimate the contact resistance with high reliability. Consequently, isothermal fixed boundary temperatures (based on experimental results) were forced on the points of contact between the water-cooled copper end caps and bushings for the steady state and transient models and the radiation exchange gaps were used between the bushings and blackbody. The main internal boundary condition in the blackbody cavities was radiation exchange between the surfaces.

The water-cooled copper ring at each end cap and the water-cooled aluminum reflector were represented as surfaces at fixed temperatures for the uninsulated model (low heat flux). These surfaces were modeled as isothermal at the nominal experimental cooling water temperature of 38°C. A surface temperature assumption for these surfaces was used in lieu of a more complex analysis and unfeasible experimental measurements since high precision simulation of these temperatures was not necessary. The thermal analysis was correlated with measured temperatures of the internal blackbody surface from both the light pipe (blackbody side wall) and control pyrometer (center partition opposite the heat flux gauge.)

The copper caps and aluminum reflector were included as constant temperature (38°C) boundaries in the model to properly define the radiant heat exchange between these surfaces and the external surface of the uninsulated graphite tube. Rings and reflector emissivities of 0.278 were used [12–14]. The heat transfer on the exterior of the uninsulated blackbody is dominated by the emissive power of the blackbody outer surface ($7.5\ \mathrm{W/cm^2}$ at 800°C and $105\ \mathrm{W/cm^2}$ at 1800°C) and not by the emissive power of the reflector or copper ring ($0.05\ \mathrm{W/cm^2}$ at 38°C, 0.7% of the 800°C outer blackbody surface emissive power.) The reflector and copper ring emissive powers at a hypothetical 100°C are only 1.5% of the 800°C blackbody emissive power. The relatively high reflectivity of the end caps and reflector also contribute to the blackbody temperature being the dominant heat transfer driver. The effect of reflector and copper ring temperature variation has therefore been neglected since such variations are expected to result $\sim 1\%$ or less change in the exterior blackbody heat transfer.

Graphite felt surrounds the blackbody tube in the insulated configuration (high heat flux). The effect of the insulation was modeled as an adiabatic boundary condition on the exterior graphite tube wall. Some of the electric current passing through the blackbody assembly passed through the graphite felt and foil insulation instead of the graphite tube in the insulated configuration. Horn and Abdelmessih [12] indicated that 49.3% of the total measured current passed through the insulated portion of the blackbody for the nominal blackbody temperature of 1100°C steady state case. In this research for the 1800°C case, 47.8% of the current passed through the blackbody.

The quartz tube, being essentially transparent to infrared radiation, was assumed to have little effect on the radiant heat transfer between the external surface of the graphite tube, the reflector, and

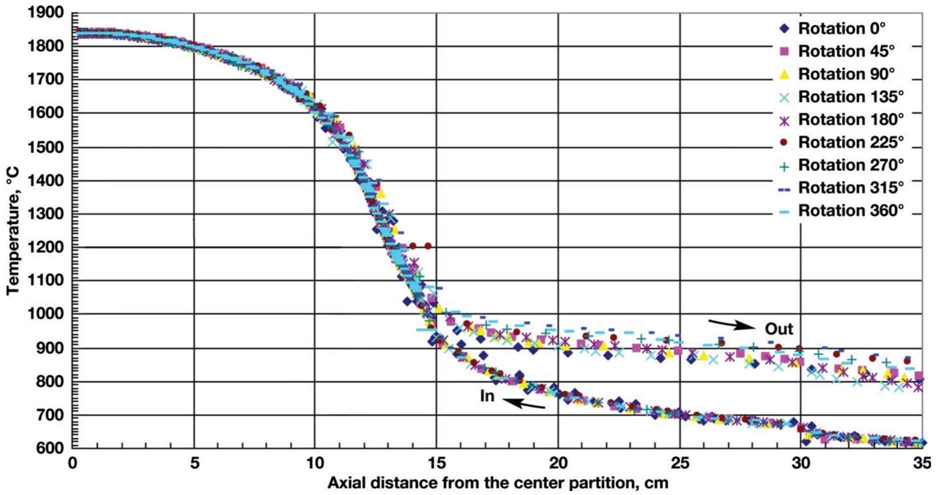

Fig. 3 Axial temperature distribution at a nominal temperature of 1800°C for an insulated blackbody configuration

the copper end caps in the uninsulated configuration. Similarly, the quartz was considered to have no effect on the heat transfer from the graphite tube in the insulated configuration. Therefore, the quartz tube was not included in either the insulated or uninsulated models.

Natural convection boundary conditions were applied to the external surfaces of the blackbody extensions at both ends of the blackbody.

Internal and external boundary conditions are symmetrical around the axis of the center partition for the steady state case. The nodal temperatures of the steady state blackbody models were used as the initial nodal temperatures for each of the transient models. The geometry, material properties, and boundary conditions from the steady state models (except internal blackbody radiation and electrical current) were used in the transient models. The transient models include the inserted heat flux sensor in the cavity and the experimental time varying electric current utilized in the heat generation calculation.

For the transient models, the internal boundary conditions were asymmetric about the partition due to the presence of the heat flux gauge in one cavity. The heat flux gauge model was stationary in the blackbody cavity resulting in an assumption that the temperature distribution in the blackbody did not change significantly during the rapid insertion of the gauge while experimenting. The model includes time varying current as measured during each heat flux gauge plunge beginning with first motion of the heat flux gauge. The copper surface of the heat flux gauge has an emissivity of 0.15 while most of the disk face of the heat flux gauge is painted with a flat black paint having an emissivity of 0.92. The heat flux gauge was internally cooled with water. The initial temperature of the heat flux gauge was chosen to be the temperature of the water cooling the gauge. The inside cylindrical copper wall and the toroid copper wall of the top of the heat flux gauge were subjected to water cooling (convection), while the inside surface of the foil and copper perpendicular to it were kept as adiabatic surfaces.

Detailed discussion of the material properties used in the analysis is given by Horn and Abdelmessih [12].

4 Results and Discussion

Blackbody calibrations were performed at nominal temperatures from 800°C to 1900°C in increments of 100°C. When the blackbody is subjected to 1100°C or higher it must be insulated; at lower temperatures the blackbody is not insulated.

4.1 Axial Temperature Profile Inside the Blackbody. For all runs, we observed that from the center partition to the end of the blackbody cavity (14.18 cm) and including the coupling to the electrodes (total 17.0 cm from the partition), a curved axial temperature profile exists followed by a linear temperature profile as shown for two extreme cases in Figs. 3 and 4 for the insulated at a nominal temperature of 1800°C and the uninsulated at a nominal temperature of 800°C, respectively. The axial temperature profiles, from the center partition to the end of the connection of the electrodes, are consistent with temperature profiles observed for heat generation.

The temperature data taken between the electrodes to the end of the extension (17.0–30.56 cm from the center partition) is unreliable due to the nature of the OFT instrument. It is likely that the data taken in this region at 1800°C is significantly contaminated by stray light entering at the bend in the lightpipe during the inbound transit. The outbound transit has the added possibility of measurement error due to internal radiation from the now-hot lightpipe. Both of these effects are small in comparison to the energy received by the instrument when viewing the hot blackbody interior but are noticeable when viewing the relatively cool extensions. The data shown in Fig. 4 between ∼17.5 cm and 30.5 cm from the partition indicates that the actual hardware temperatures were below the minimum detectable temperature capability of the OFT instrument.

A close look at both Figs. 3 and 4 shows that the uninsulated cavity had a flatter axial temperature profile when compared with the insulated blackbody. The reason for the flatter profile for the uninsulated configuration is that there are heat losses by radiation from both sides of the blackbody cylinder, in contrast to the insulated blackbody, which radiates to the interior cavities only. The radiation exchange between the outside boundary (reflector and copper ring close to room temperature), with the outside surface of the blackbody is proportional to the forth power of the outer blackbody surface temperatures. These findings are consistent with the experimental results of Horn and Abdelmessih [12] in which the researchers compared experimentally and numerically the difference between the temperature profiles for the insulated and uninsulated configurations at a nominal blackbody temperature of 1100°C.

4.2 Location for Optimum Axial Insertion of the Heat Flux Gauge. The heat flux gauge is inserted in the blackbody cavity to a specific axial depth from the center partition, left in location for a few seconds to stabilize the heat flux reading then removed. Figure 5 is a typical run showing the insertion process

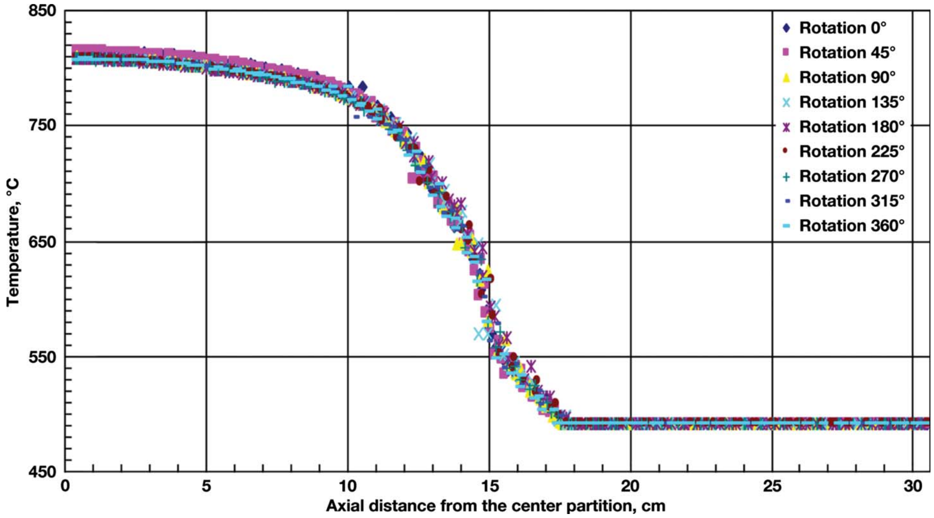

Fig. 4 Axial temperature distribution at a nominal temperature of 800°C for an uninsulated blackbody configuration

for each location (starting with 142 mm from the center partition) into which the heat flux gauge was inserted at a blackbody nominal temperature of 1800°C. When the heat flux gauge was inserted too close to the center partition, the radiation environment changed due to the slot and lowered the heat flux incident on the heat flux gauge face. Lower heat fluxes are observed during insertion and higher fluxes when withdrawing the heat flux gauge, as shown by the lines connecting the data points. The increase in heat flux during withdrawal is likely due to the response time of the heat flux gauge, deflection sensor, and data acquisition system during the highly transient insertion and removal motions. The total time to insert or remove the gauge from the blackbody was on the order of one second. The thermal response of the heat flux gauge during the transient insertion would tend to cause the indicated heat flux to lag the actual level during insertion and to indicate a high heat flux during removal. Therefore, no conclusions regarding blackbody state should be gleaned from the transient insertion and removal data.

The optimum position for the 2.57 cm inside diameter cylindrical blackbody was determined by examining all runs. We found that the maximum heat fluxes begin anywhere from a dimensionless distance (L/D_i) of 0.4 from the center partition to 1.0 and extend up to 2 for the uninsulated runs or slightly less than 1.6 for the insulated runs. Figures 6 and 7 show the variation in the heat flux with axial dimensionless distance from the center partition for the insulated (nominal temperatures 1100–1900°C) and uninsulated (nominal temperatures 800–1100°C) configurations, respectively. Consequently, the optimum insertion depth of approximately one (1/2 to $1\frac{1}{2}$) dimensionless diameter from the center partition should give the optimum results. All points were taken from experimental pseudosteady state data points, i.e., the heat flux gauge was left in position for a few seconds to reach equilibrium, except for the one dimensionless distance. The one dimensionless distance heat flux was estimated from the experimental data by interpolating between the closest two points. The scatter in the data is within the accuracy of the deflection measurement potentiometer (1.6 mm). Murthy et al. [10] using Monte Carlo simulations found that the optimum location for the measuring instrument is approximately one cavity radius from the partition of the cavity for a 2.57 cm cylindrical blackbody cavity, which confirms our experimental findings.

4.3 Effect of Convection in the Blackbody Cavity. The effect of natural convection between the heat flux gauge and the cavity environment of the blackbody was hand calculated for the blackbody at 1800°C nominal temperature. We assumed that the heat flux gauge front surface was a vertical plate at room temperature (30°C), and the argon gas in the cavity was at a temperature

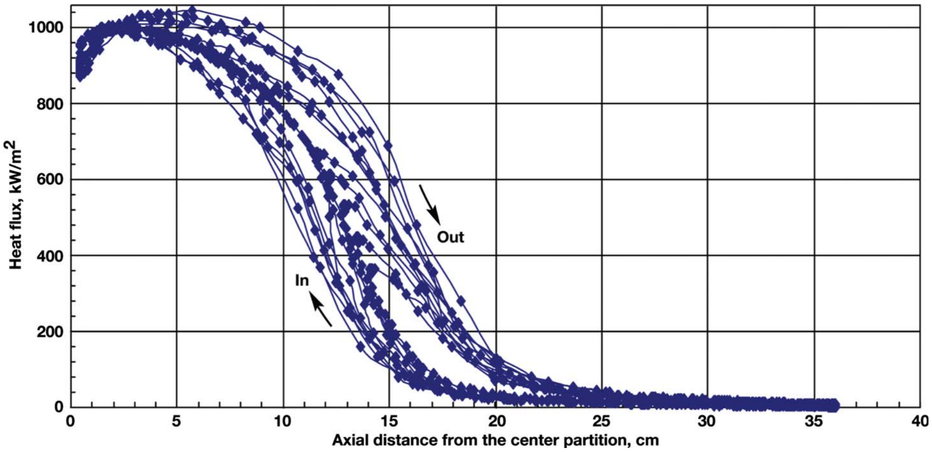

Fig. 5 Axial heat flux measurements during insertion in the blackbody at 1800°C nominal temperature

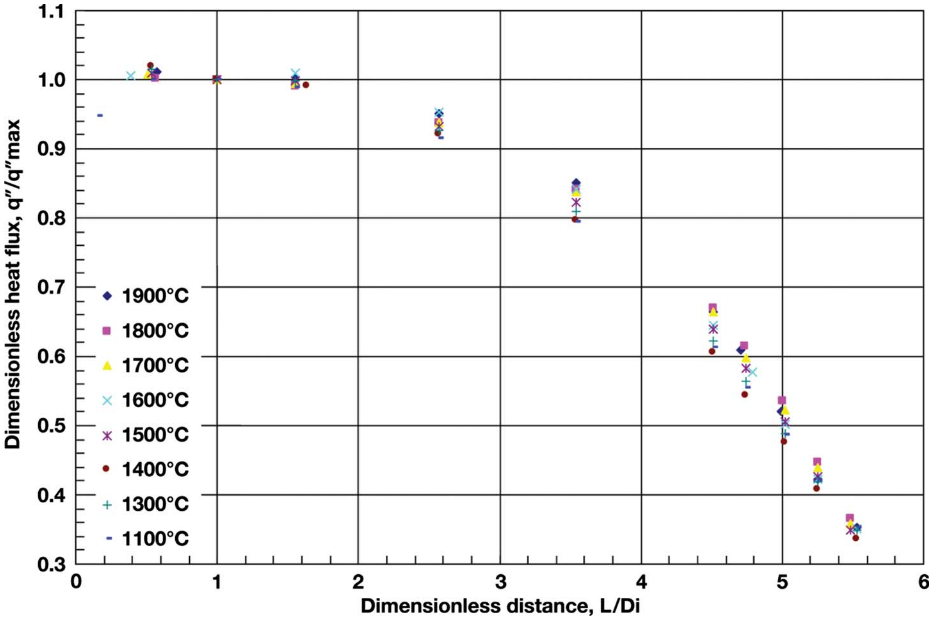

Fig. 6 Variation in heat flux with axial distance inside the insulated blackbody cavity for temperatures varying between 1100°C to 1900°C

of 1800°C (a bounding assumption). The properties of argon gas were extrapolated from Bolz and Tuve [19]. The natural convection from a vertical surface for this extreme condition was calculated to be less than 17 kW/m^2, which is less than 2% of the total heat flux. A forced convection estimate was also attempted, base on the Reynolds number on relative speed of motion of the heat flux gauge, using average temperature for properties; that value was also less than 2%. The Abdelmessih–Bell [20] correlation for mixed convection was applied, and that too gave less than 2% for the mixed convection. When hand calculations were repeated for the lower end of the experiments at nominal blackbody temperature of 800°C and gauge sensing surface at 30°C, the possible heat transfer due to natural convection was less than 11%. The physical properties of argon gas were interpolated between two points 500°C apart. Thus, the decrease in density in that range was 33% and the increase in viscosity was 61%. These crude estimations emphasize that the value of the absolute convection at the higher temperature is higher than that at the lower temperature, although the percentage is lower.

4.4 Steady State Numerical Models. We chose the extremes of the experimental range (blackbody nominal temperatures of 800°C and 1800°C) to show the effects of inserting the heat flux gauge on the equilibrium of both the blackbody and the gauge. The details of the numerical models are given in Sec. 3.

Comparisons between the axial experimental temperatures measured by the OFT and the numerical analysis are shown in Figs. 8 and 9 for the uninsulated (800°C) and insulated (1800°C) steady state blackbody configurations, respectively. The numerical models capture the trends, although between 7 cm and 12 cm from the partition, the models deviate from the measured local blackbody temperature as seen in Figs. 8 and 9, respectively. Similar trends

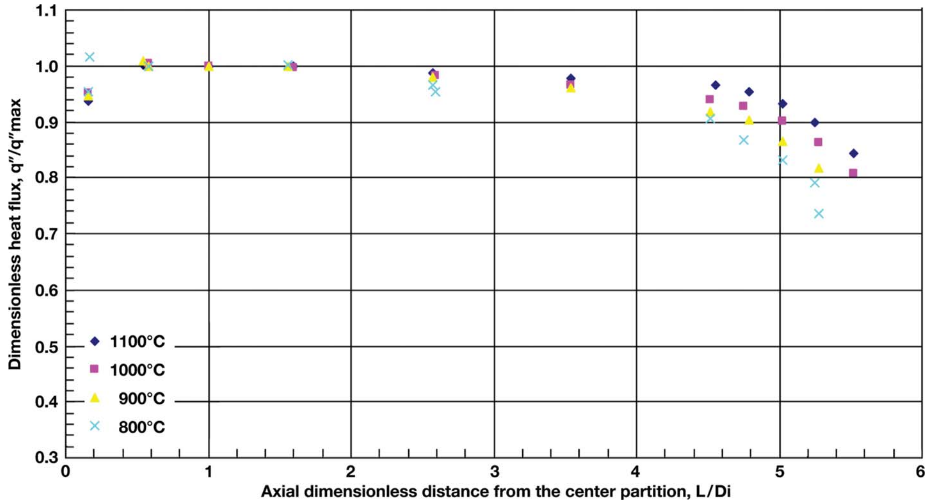

Fig. 7 Variation in heat flux with axial distance inside the uninsulated blackbody cavity for temperatures varying between 800°C to 1100°C

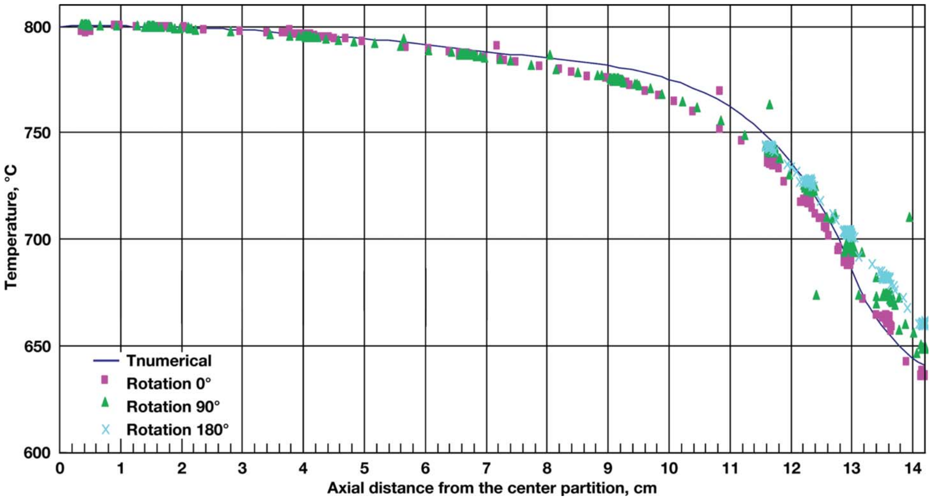

Fig. 8 Comparison of experimental numerical temperatures for the blackbody cavities at nominal 800°C steady state

with lesser magnitude were observed for the numerical analysis performed at 1100°C for both uninsulated and insulated configurations by Horn and Abdelmessih [12]. Consequently, it is believed that blackbody models at nominal temperatures above 800°C and below 1800°C will have smaller deviations between 8 cm and 12 cm than those shown in Figs. 8 and 9. It is important to note that these differences are in a region with negligible impact on the calculation of incident heat flux at the heat flux gauge face. The numerical results represent good agreement for models that were unchanged from analyses at other temperatures except for electrical current passing through the blackbody and the electrode temperature boundary conditions.

4.5 Effect of Insertion of Instruments in the Blackbody Cavity on Equilibrium. Room temperature instruments, when inserted into the hot blackbody cavity, disturb the thermal equilibrium. The cooler instrument starts heating while cooling the surrounding cavity. The heat exchange takes place for the most part by radiation (convection has been shown to be relatively small). As the instrument approaches the center partition, the surface of the partition cools due to radiation and convection, then conduction through the partition cools the opposite surface of the cavity. As the partition cools, the control pyrometer on the other side of the partition senses the decrease in temperature. Immediately, the control pyrometer sends a signal to the power controller to increase the power causing fluctuations until equilibrium is restored. These power variations have been recorded over the temperature range of all experiments. Figure 10 shows the time histories of blackbody current indicating changes in power commanded by the temperature control system and measured heat flux during a heat flux gauge insertion at a blackbody nominal temperature of 1800°C. Shortly after the power increases, the temperature in the blackbody increases as shown by the increase in the temperature recorded by the control pyrometer in Fig. 11. Note that the total temperature drop recorded by the control pyrometer was only ~4°C but the current passing through the blackbody nearly doubled. This phenomena was first reported by Abdelmessih [11]. Later, Abdelmessih and Horn [13,14] used this phenomenon and actual experimental current variations in the development of their transient thermal numerical models at set temperatures of 1100°C. Also, Murthy et al. [15] reported variations in the blackbody cavity partition temperature when heat flux gauges were placed at various locations inside the opposite cavity of a blackbody at a nominal temperature of 1100°C.

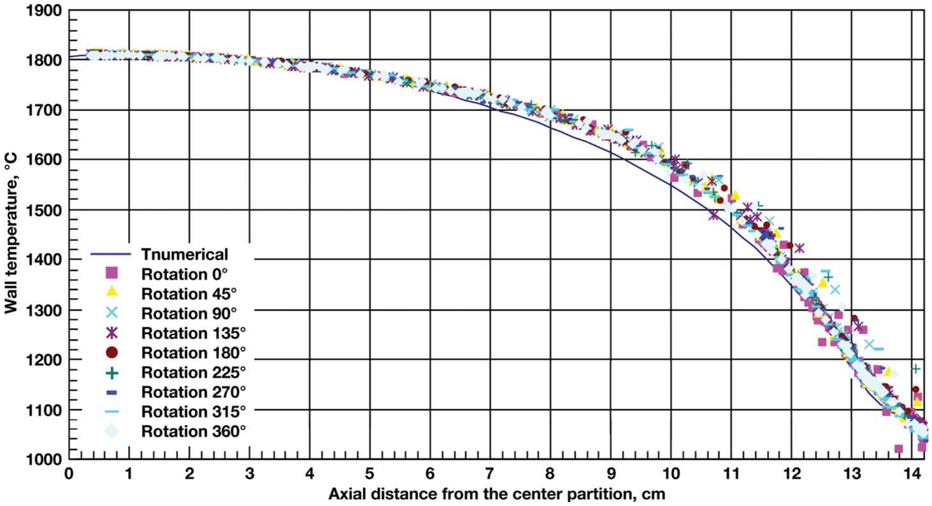

Fig. 9 Comparison of experimental numerical temperatures for the blackbody cavities at nominal 1800°C steady state

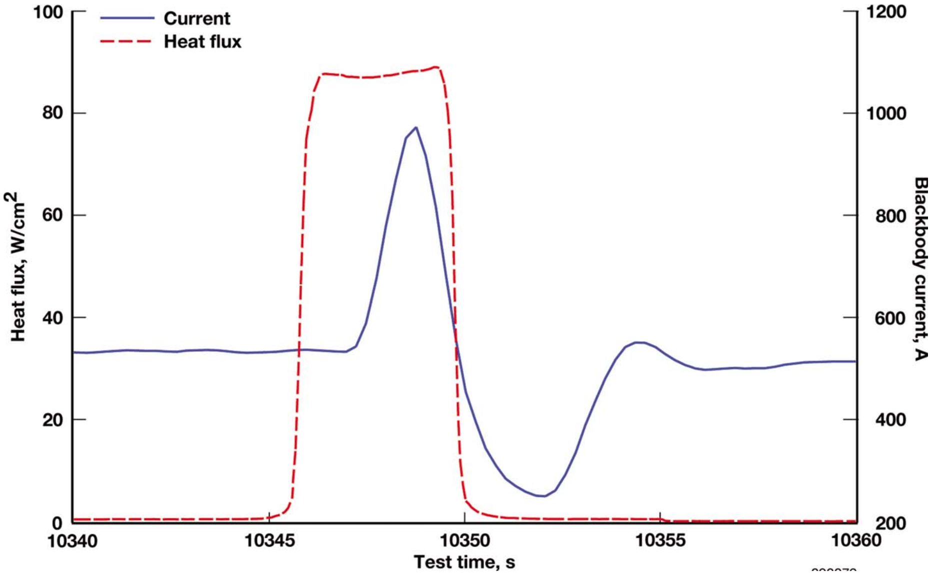

Fig. 10 Effect of inserting the heat flux gauge in one side of the cavity on the power input for a blackbody at a nominal 1800°C

4.6 Effect of Insertion of the Heat Flux Gauge on the Blackbody. The numerical models represent the transient insertion of the heat flux gauge into the blackbody cavity to a distance of 1.44 cm (0.56 dimensionless distance) from the center partition. This is the least axial distance from the center to give the maximum heat flux but not be affected by the slot. The models clarified the mechanisms involved in the transient calibration as explained in the rest of this section and Secs. 4.7 and 4.8.

4.6.1 Effect of Insertion of the Heat Flux Gauge on the Cylindrical Cavities. The models quantify the decrease in the blackbody axial temperature with time during the first 3 s after insertion due to the presence of the cooled heat flux gauge as shown in Figs. 12 and 13 for 800°C (uninsulated) and 1800°C (insulated) configurations, respectively. The effect of insertion of the heat flux gauge was less drastic in the opposite cavity for both blackbody models at 800°C (uninsulated) and 1800°C as shown in Figs. 14 and 15, respectively, because the effect was through the partition and not direct. The most noticeable transient effect due to direct insertion is at the highest blackbody temperature as shown in Fig. 13.

4.6.2 Effect of Insertion of the Heat Flux Gauge on the Blackbody Center Partition. At steady state when the blackbody model is at a nominal temperature of 1800°C, the center of the partition at both left and right cavities is 1801°C, as seen in Figs. 16 and 17, respectively. When the heat flux gauge is inserted in the left cavity of the blackbody, the temperature of the center of the partition (as calculated in the numerical models) decreases to 1787°C after 1 s. Then by conduction through the partition, the center of the opposite (right) partition decreases to 1798°C. Similarly, after 3 s the temperature at the center of the left partition drops to 1779 compared with 1791°C at the opposite side (right) indicating that the opposite (right) partition is not as drastically affected as the partition (left) facing the heat flux gauge. Similarly, for a blackbody model at a nominal temperature of 800°C, the

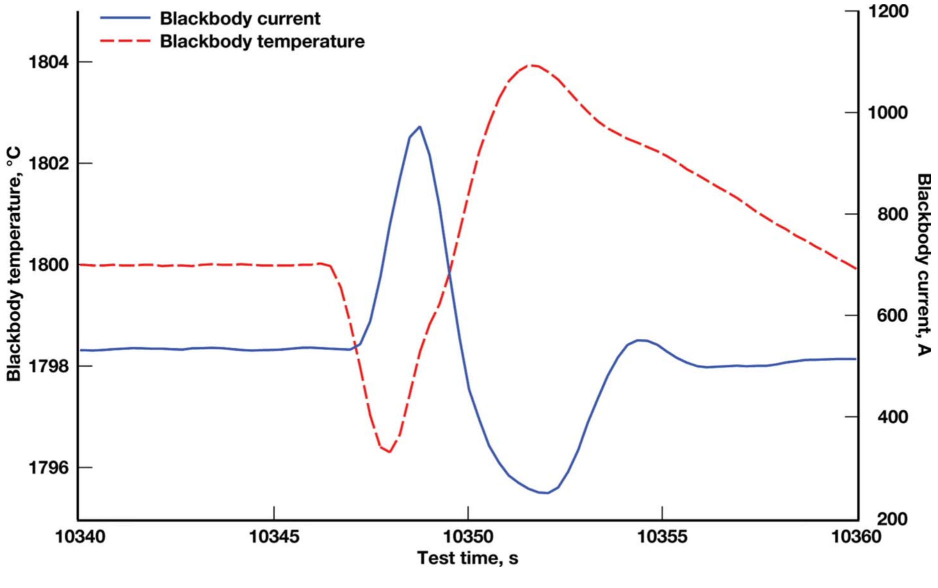

Fig. 11 Effect of inserting the heat flux gauge in one cavity on the control pyrometer in the other cavity

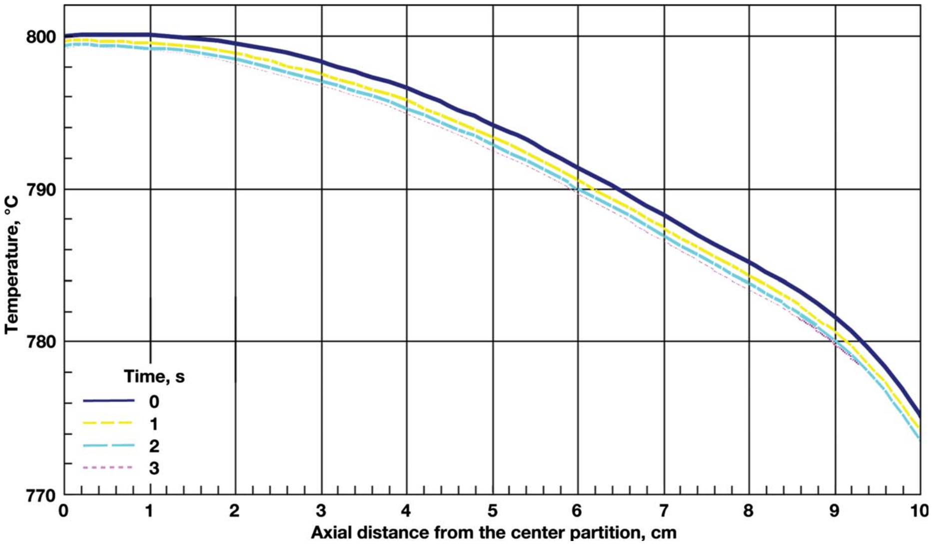

Fig. 12 Transient axial blackbody temperatures, due to insertion of the heat flux gauge in the same cavity (left) at 800°C

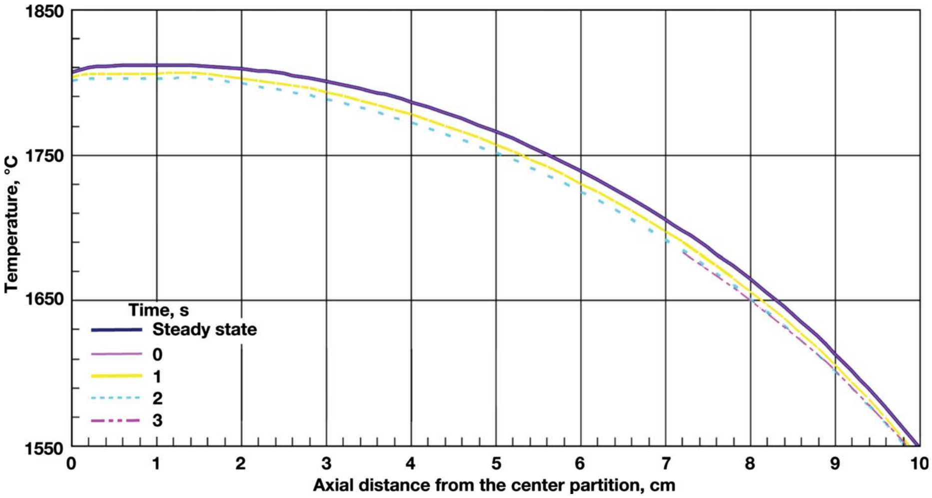

Fig. 13 Transient axial blackbody temperatures, due to insertion of the heat flux gauge in the same cavity (left) at 1800°C

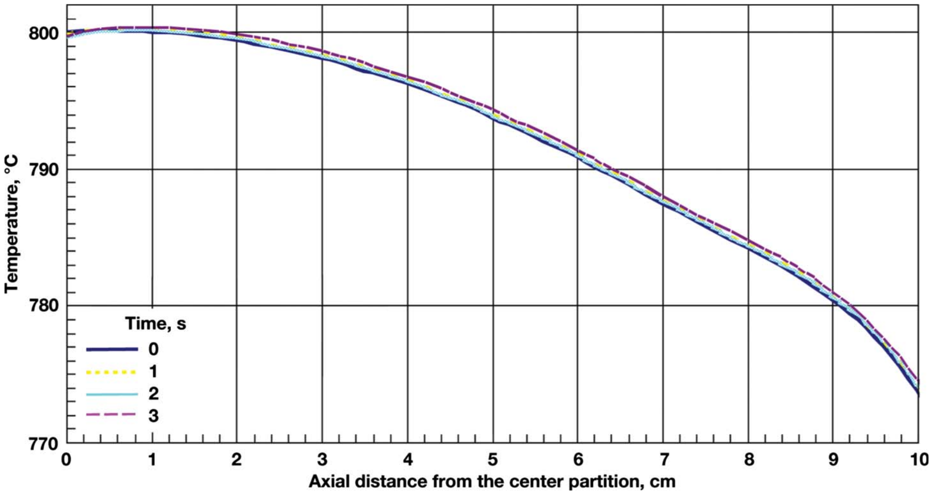

Fig. 14 Transient axial temperatures due to insertion of a heat flux gauge in the opposite cavity of a blackbody at 800°C

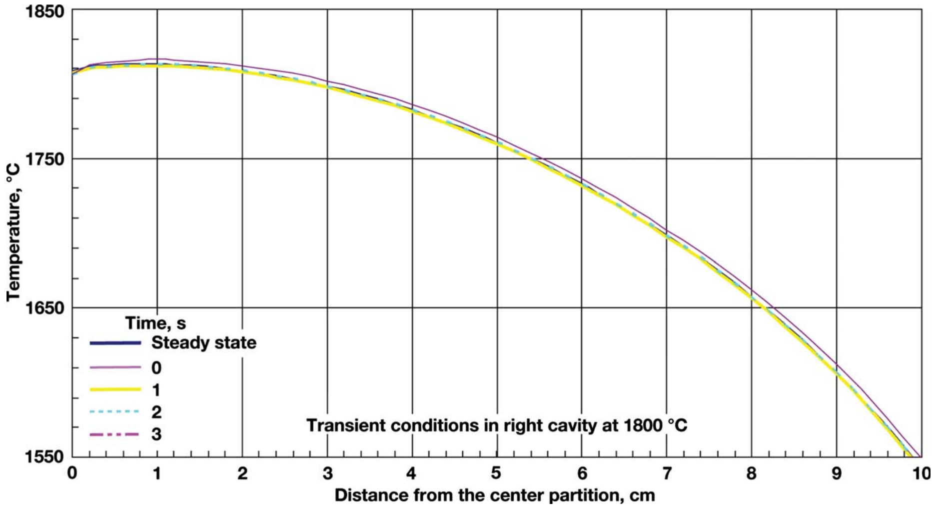

Fig. 15 Transient axial temperatures due to insertion of a heat flux gauge in the opposite cavity of a blackbody at 1800°C

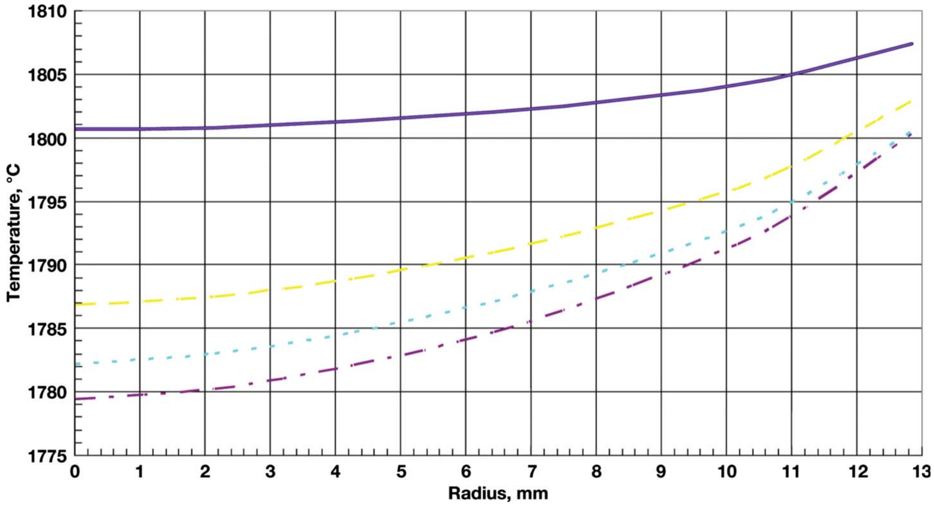

Fig. 16 Effect of inserting the heat flux gauge on the partition at 1800°C

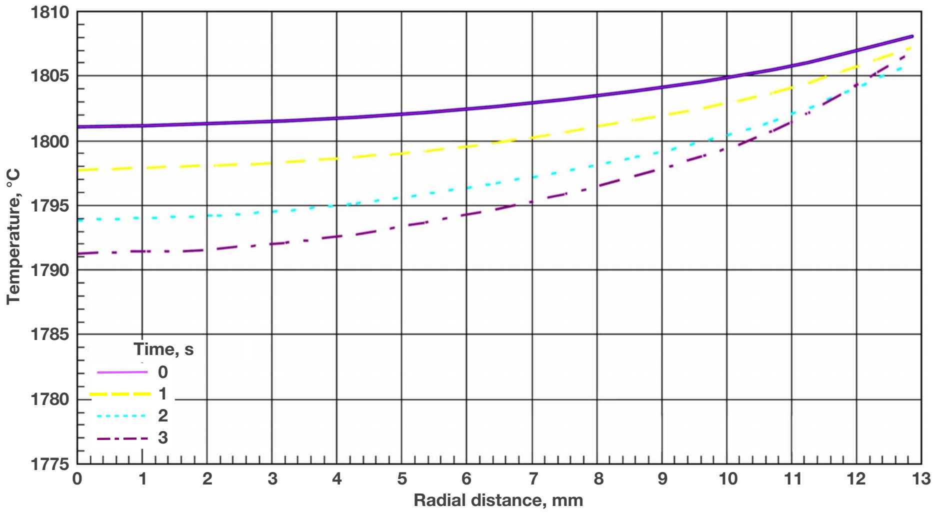

Fig. 17 Effect of inserting the heat flux gauge on the partition facing the opposite cavity at 1800°C

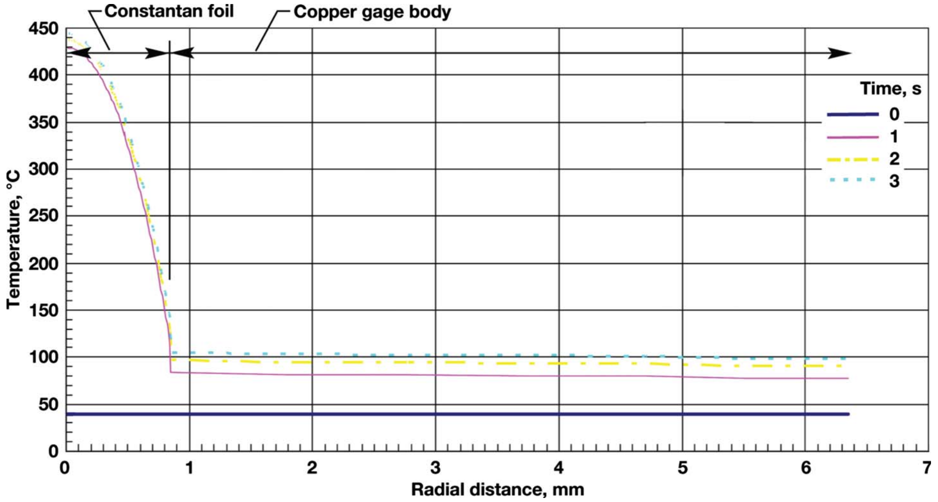

Fig. 18 Effect of inserting the heat flux gauge in the blackbody cavity on the sensing surface of the gauge at 1800°C

same effects of decreased temperature at the center of the left partition, followed by conduction through the partition and less decrease in temperature at the opposite (right) side of the partition. The blackbody temperature control pyrometer senses the temperature drop and commands additional power in order to recover the blackbody to the set control temperature.

4.7 Effect of Inserting the Heat Flux Gauge in the Blackbody on the Sensing Surface of the Gauge. The transient numerical models accounted for the insertion of the water-cooled heat flux gauge into the high temperature blackbody cavity. The initial temperature of the heat flux gauge was approximately room temperature. After the first second, the temperatures almost stabilized. The center of the constantan foil experiences the highest temperature up to 450°C for the blackbody at a nominal temperature of 1800°C as shown in Fig. 18. The temperature increase in the constantan foil is very sharp, followed by a very small linear increase in temperature in the copper. The sharp increase in the constantan temperature compared with the relatively small change in the copper is due to the small thermal mass, relatively low thermal conductivity, and limited heat conduction path of the thin foil constantan compared with that of relatively thick, conductive, water-cooled copper. The combination of geometry and thermal properties in the constantan limit the heat conducted out of the foil and result in the large temperature gradient across the foil radius. Similar profile trends were observed for the 800°C model, although the highest temperature reached at the center of the foil was 73.5°C (Fig. 19). The computed copper gauge body surface temperatures in Figs. 18 and 19 are reasonable given measured temperatures taken on the inside copper wall close to the foil were 76°C for the gauge inserted into the 1800°C blackbody and 40°C for the 800°C insertion, respectively.

The heat flux gauge face temperatures shown in Fig. 18 were utilized to calculate an estimate for the electrical output of the heat flux gauge. This calculation estimated the gauge output to be ~9.9 mV. The actual output of the gauge during insertion was approximately 6 mV. This appears to be a large discrepancy; however, the wire welded to the center of the heat flux gauge foil was omitted from the analysis. This small wire will reduce the foil center temperature by some amount and thereby decrease the voltage generated by the gauge. This simplification of the model along

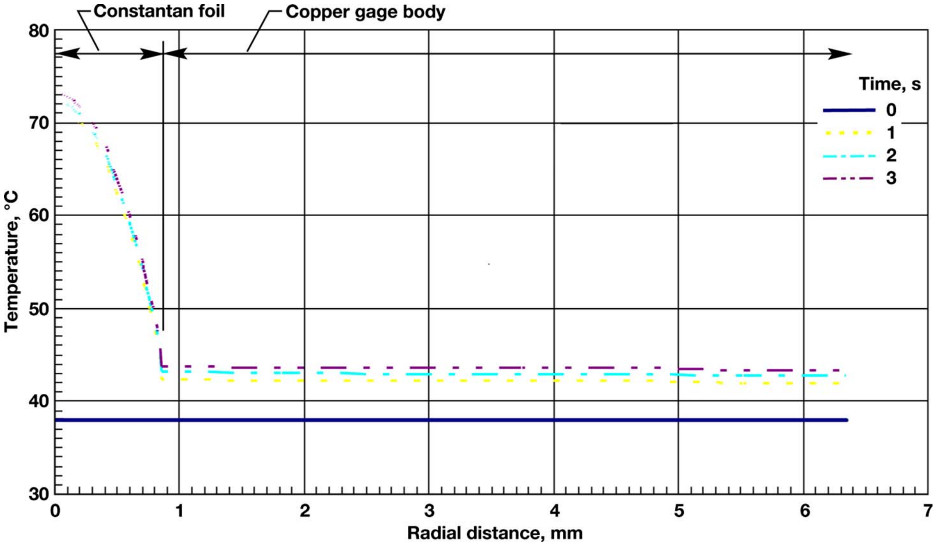

Fig. 19 Effect of inserting the heat flux gauge in the blackbody cavity on the sensing surface of the gauge at 800°C

Table 1 Comparison of experimentally measured heat fluxes $(\mathrm{kW/m^2})$ with predicted heat fluxes as a function of time for three models

	Time	Heat flux using manufacturer's calibration	Computed	Irradiance heat flux, nominal temperature	$T_{\mathrm{experimental}}$	Irradiance heat flux, measured temperature
Model	(s)	Measured	Model	$\sigma T^4_{\mathrm{nominal}}$	(c)	$\sigma T^4_{\mathrm{experimental}}$
Uninsulated	1	74.3	71.1	75.2	799.9	75.1
800	2	74.6	71.0	75.2	799.8	75.1
$\varepsilon = 0.89$	3	74.3	71.0	75.2	799.7	75.1
Insulated	1	989.6	994.3	1047.1	1798.8	1044.7
1800	2	991.8	987.0	1047.1	1796.8	1040.6
$\varepsilon = 0.98$	3	1004.5	985.2	1047.1	1798.8	1044.7

Table 2 Percent error between measured and computed heat flux

		Computed	Irradiance	
Model	Time	Model	$\sigma T^4_{\mathrm{nominal}}$	$\sigma T^4_{\mathrm{experimental}}$
Uninsulated	1	4.17	1.16	1.12
800	2	4.69	0.75	0.67
$\varepsilon = 0.89$	3	4.44	1.16	1.04
Insulated	1	0.48	5.81	5.56
1800	2	0.48	5.57	4.92
$\varepsilon = 0.98$	3	1.92	4.24	4.00

with material and manufacturing tolerance variations that affect the gauge output could account for this rather large discrepancy.

4.8 Error Analysis. An estimate of the incident heat flux at the sensing surface of the gauge was generated by applying a correlation for a disk in a cylinder, as reported by Leuenberger and Person [21], to the numerical results of the models. Table 1 shows comparisons between the measured heat flux using the heat flux gauge manufacturers calibration, the heat flux computed from the numerical model, the irradiance heat flux computed using the nominal blackbody temperature assuming the cavity emissivity of 1.0 and the irradiance heat flux computed using measured temperature assuming the cavity emissivity of 1.0 as recommended by the furnace manufacturer. The results, shown in Table 1, indicate that the detailed transient thermal model captures the trends of the experimental data and agree with the heat flux indicated by the gauge within less than 5%, as seen in Table 2, for the uninsulated configuration and less than 2% for the insulated model. These errors are attributed to neglecting the effects of convection inside the blackbody for all configurations and between the blackbody, aluminum reflector, and copper rings for the uninsulated configuration. All models accounted for convection from the blackbody extensions. The highest error is at the lowest blackbody nominal temperature (800°C), where convection effects are prominent. At a blackbody nominal temperature of 1100°C, Abdelmessih and Horn [14] reported an error of less than 2%; they also neglected the effects of convection.

5 Conclusion

The insertion of room temperature instruments in the high temperature blackbody cavity disturbs the thermal equilibrium. One would expect this disturbance to cause calibration errors. The results are based on experiments and computations at 800°C and 1800°C. The error in incident heat flux between numerical computations neglecting convection and experimental measurements was less than 5%. This error is for the most part due to the effects of convection inside the blackbody. The main heat transfer mode from the blackbody is radiation due to the blackbody's high temperatures during calibration.

The optimum location for the heat flux gauge is approximately equal to one inside diameter ($1/2$ to $1\frac{1}{2}$) from the end of the center partition, for the 2.57 cm blackbody and 1.27 cm diameter heat flux gauge. This location is valid for both insulated and uninsulated configurations, although the uninsulated configuration is more forgiving (up to 2) due to the more uniform axial blackbody temperature profile.

This study shows that the errors associated with the insertion of a heat flux gauge are relatively small. Natural convection tends to increase the net heat flux at the gauge face and increases the gauge's output compared with the numerical models but becomes less of an effect as heat flux (and blackbody temperature) are increased. Inserting a water-cooled heat flux gauge into a cylindrical blackbody cavity appears to be a viable method for increasing the heat flux available for heat flux gauge calibrations derived from temperature measurements.

Acknowledgment

This work was supported by the Dryden Flight Research Center Educational Programs for NASA Summer Faculty Research. The experiments were performed in the Flight Loads Laboratory, at NASA's Dryden Flight Research Center, Edwards, CA. Thanks are due to Dr. M. Rodon and the Flight Loads Laboratory staff.

Nomenclature

D = diameter, cm
L = axial length starting from the end of the center partition, cm
q'' = heat flux, $\mathrm{kW/m^2}$
T = temperature, °C, and K for radiation

Greek Symbols

σ = Stephan Boltzman constant
ε = percent emissivity

Subscripts

i = inside
max = maximum at any point
maxss = maximum after steady state is attained

References

[1] Holmberg, D., Steckler, K., Womeldorf, C., and Grosshandler, W., 1997, "Facility for Calibrating Heat Flux Sensors in a Convective Environment," ASME J. Heat Transfer, **119**, pp. 165–171.
[2] Holmberg, D. G., Womeldorf, C. A., and Grosshandler, W. L., 1999, "Design and Uncertainty Analysis of a Second-Generation Convective Heat Flux Calibration Facility," ASME J. Heat Transfer, **121**, pp. 65–70.
[3] Grosshandler, W. L., and Blackburn, D., 1997, "Development of a High Flux Conduction Calibration Apparatus," ASME J. Heat Transfer, **3**, pp. 153–158.
[4] Murthy, A. V., Tsai, B. K., and Gibson, C. E., 1997, "Calibration of High Heat Flux Sensors at NIST," J. Res. Natl. Inst. Stand. Technol., **102**, pp. 479–488.
[5] Murthy, A. V., Tsai, B. K., and Saunders, R. D., 1997, "Radiative Calibration of Heat Flux Sensors at NIST—An Overview," ASME J. Heat Transfer, **119**, pp. 159–164.
[6] Murthy, A. V., Tsai, B. K., and Saunders, R. D., 1998, "High-Heat-Flux Sensor

Calibration Using Black-Body Radiation," Metrologia, **35**, pp. 501–504.

[7] Murthy, A. V., Tsai, B. K., and Saunders, R. D., 1999, "Comparative Calibration of Heat Flux Sensors in Two Blackbody Facilities," J. Res. Natl. Inst. Stand. Technol., **104**, pp. 487–494.

[8] Murthy, A. V., Tsai, B. K., and Saunders, R. D., 2000, "Radiative Calibration of Heat-Flux Sensors at NIST: Facilities and Techniques," J. Res. Natl. Inst. Stand. Technol., **105**, pp. 293–305.

[9] Murthy, A. V., Tsai, B. K., and Saunders, R. D., 2001, "Transfer Calibration Validation Tests on a Heat Flux Sensor in the 51 mm High-Temperature Blackbody," J. Res. Natl. Inst. Stand. Technol., **106**, pp. 823–831.

[10] Tsai, B., Gibson, C., Murthy, A., Early, E., Dewitt, D., and Saunders, R., 2004, "Heat-Flux Sensor Calibration," U.S. Department of Commerce Technology Administration, National Institute of Standards and Technology, NIST Special Publication 250-65.

[11] Abdelmessih, A. N., 1998, "Experimental Measurements of Temperature and Heat Flux in a High Temperature Black Body Cavity," NASA Technical Reports, Report No. NGT 2-52212, Document ID 19990021026, pp. A:1–A:3.

[12] Horn, T., and Abdelmessih, A. N., 2000, "Experimental and Numerical Characterization of Steady State Cylindrical Blackbody Cavity at 1100°C," *Proceedings of the 34th National Heat Transfer Conference*, Pittsburgh, PA.

[13] Abdelmessih, A. N., and Horn, T., 2006, "Experimental and Numerical Characterization of Transient Insertion of Heat Flux Gages in a Cylindrical Blackbody Cavity at 1100°C," 13th International Heat Transfer Conference, Sydney, Australia.

[14] Abdelmessih, A. N., and Horn, T., 2007, "Effect of Insertion of Heat Flux Gages in a High Temperature Cylindrical Blackbody Cavity on the Gauge," draft submitted IMECE, Seattle, WA.

[15] Murthy, A. V., Fraser, G. T., and DeWitt, D. P., 2006, "Experimental In-Cavity Radiative Calibration of High-Heat-Flux Meters," J. Thermophys. Heat Trans-fer., **20**, pp. 327–335.

[16] Thermogage Inc., 1991, *Thermogage Operation Manual for Model 48 kW Calibration Furnace*, Forstburg, MD.

[17] Luxtron Inc., 1990, *Accufiber Models 10 &100 Optical Fiber Thermometers Manual*, Santa Clara, CA.

[18] MacNeal-Schwendler Corporation, 2003, *MSC/Patran Thermal Users Guide*, Vols, 1 and 2, Software Version is Patran 2005.

[19] Bolz, R. E., and Tuve, G. L., 1985, *CRC Handbook of Tables for Applied Engineering, Science*, 2nd ed., CRC Press, Boca Raton, FL.

[20] Abdelmessih, A. N., and Bell, K. J., 1999, "Effect of Mixed Convection and U-Bends on the Design of Double-Pipe Heat Exchangers," Heat Transfer Eng., **20**(3), pp. 25–36.

[21] Leuenberger, H., and Person, R. A., 1956, "Compilation of Radiation Shape Factors for Cylindrical Assemblies," ASME Paper No. 56-A-144.

Sophia Haussener
Department of Mechanical and Process Engineering,
ETH Zurich,
8092 Zurich, Switzerland

Patrick Coray
Solar Technology Laboratory,
Paul Scherrer Institute,
5232 Villigen, Switzerland

Wojciech Lipiński
Department of Mechanical Engineering,
University of Minnesota,
Minneapolis, MN 55455

Peter Wyss
Department of Electronics/Metrology,
EMPA Material Science and Technology,
Überlandstrasse 129,
8600 Dübendorf, Switzerland

Aldo Steinfeld[1]
Department of Mechanical and Process Engineering,
ETH Zurich,
8092 Zurich, Switzerland;
and
Solar Technology Laboratory,
Paul Scherrer Institute,
5232 Villigen, Switzerland
e-mail: aldo.steinfeld@ethz.ch

Tomography-Based Heat and Mass Transfer Characterization of Reticulate Porous Ceramics for High-Temperature Processing

Reticulate porous ceramics employed in high-temperature processes are characterized for heat and mass transfer. The exact 3D digital geometry of their complex porous structure is obtained by computer tomography and used in direct pore-level simulations to numerically calculate their effective transport properties. Two-point correlation functions and mathematical morphology operations are applied for the geometrical characterization that includes the determination of porosity, specific surface area, representative elementary volume edge size, and mean pore size. Finite volume techniques are applied for conductive/convective heat transfer and flow characterization, which includes the determination of the thermal conductivity, interfacial heat transfer coefficient, permeability, Dupuit–Forchheimer coefficient, residence time, tortuosity, and diffusion tensor. Collision-based Monte Carlo method is applied for the radiative heat transfer characterization, which includes the determination of the extinction coefficient and scattering phase function. [DOI: 10.1115/1.4000226]

Keywords: reticulate, porous, ceramic, computer tomography, transport, radiation, conduction, convection, Monte Carlo, DPLS, solar energy, thermochemical cycle, hydrogen

1 Introduction

Reticulate porous ceramics (RPCs) exhibit favorable heat and mass transfer characteristics for high-temperature applications [1]. Examples are molten-metal and diesel-engine-exhaust filters [2,3], radiant burners [4], catalyst supports [5], and radiant absorbers in solar thermal and thermochemical reactors [6]. In the latter application, RPCs provide efficient absorption of concentrated solar radiation and large specific surface areas for heterogeneous chemical reactions [6–8]. The accurate knowledge of the RPCs' effective heat and mass transport properties is crucial for their optimal design and operation. Computer tomography (CT) enables the digital geometrical representation of their complex porous structure, which is needed for the direct pore-level numerical simulations (DPLSs).

Previous pertinent studies include the determination of the extinction coefficient, scattering coefficient, and scattering phase function of metal foams and RPCs for simplified geometries composed of pentagon dodecahedron or tetracaedecaedric [9] and spherical voided cubic unit cells [10]. The effective thermal conductivity was determined for simplified foam geometries composed of tetrakaidecahedron [11], hexagonal [12], and spherical or cubical voided cubic unit cells [13]. Permeability has been determined by simplifying the foam structure by parallel conduits [14] or by empirical correlations for fibrous beds [15,16]. The exact geometry of a porous magnetic gel sample, obtained by microCT, was used to compute the mean survival time, which was linked to the permeability by an empirical correlation [17]. More recently, CT-based methodology was applied to determine the effective transport properties of a Rh-coated SiC RPC used for the solar steam-reforming of CH_4 [18–21] and for a packed bed of semi-transparent, large $CaCO_3$ particles [22].

In the present study, CT-based DPLS is applied to determine porosity, specific surface area, representative elementary volume, pore size distribution, extinction coefficient, scattering phase function, effective conductivity, heat transfer coefficient, permeability, Dupuit–Forchheimer coefficient, tortuosity, residence time, and dispersion tensor for an uncoated, nonhollow SiSiC RPC. This material was recently used in a solar reactor for the thermal decomposition of H_2SO_4 as part of a water-splitting thermochemical cycle [23].

2 Morphological Characterization

2.1 Low-resolution CT. The RPC foam sample, made of SiSiC, is shown in Fig. 1. Its nominal pore diameter is $d_{\mathrm{nom}} = 1.27$ mm, corresponding to 20 pores per in. (ppi). The sample is exposed to an unfiltered polychromatic X-ray beam generated by electrons incident on a wolfram target. The generator is operated at an acceleration voltage of 60 keV and a current of 0.11 mA. A Hamamatsu flatpanel C7942 CA-02 protected by a 0.1 mm-thick aluminum filter is used to detect the transmitted X-rays. The sample is scanned at 900 angles (projections). Each projection consists of an average over six scans, each with an exposure time of 0.7 s. Low-resolution computer tomography (LRCT) is performed for voxel sizes of 30 μm and 15 μm and field of view of $2.3\times 2.3\times 1.2$ cm^3 and $1.2\times 1.2\times 0.6$ cm^3, respectively.

3D surface rendering of a sample subvolume, reconstructed

---

[1] Corresponding author.

Contributed by the Heat Transfer Division of ASME for publication in the JOURNAL OF HEAT TRANSFER. Manuscript received October 31, 2008; final manuscript received April 29, 2009; published online December 3, 2009. Assoc. Editor: Yogesh Jaluria.

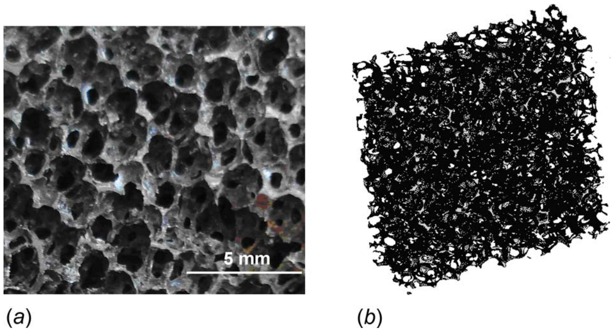

Fig. 1 Sample of RPC foam: (*a*) top view photograph and (*b*) 3D surface rendering of 15 μm voxel size tomography data

from the resulting tomography data, is depicted in Fig. 1(*b*). The histograms of the normalized absorption values, as shown in Fig. 2, have a bimodal character for both scan resolutions. The mode method is applied for phase segmentation [24,25]. The normalized phase threshold values $\alpha_t/\alpha_{\max}$ are 0.39 and 0.23 for scans with voxel sizes of 30 μm and 15 μm, respectively. These results are comparable to $\alpha_t/\alpha_{\max}=0.35$ and 0.20 for scans with voxel sizes of 30 μm and 15 μm, respectively, calculated using Otsu's method [24]. $\alpha_t/\alpha_{\max}$ varies by ± 0.04, as corroborated for three selected tomograms divided into 36 subelements and for voxel sizes of 15 μm and 30 μm, shown in Fig. 3.

2.2 High-resolution CT. Figure 4(*a*) shows a tomogram of a single RPC's strut obtained by high-resolution computer tomography (HRCT) of 0.37 μm voxel size and $0.76\times0.76\times0.62$ mm^3 field of view. The HRCT is performed on the TOMCAT beamline at the Swiss Light Source (SLS) of the Paul Scherrer Institute (Villigen, Switzerland) [26] for 14 keV photon energy, 400 μA beam current, 100 μm thick aluminum filter, 20× geometrical magnification, 0.8 s exposure time, and 1501 projections. A magnified fragment of the strut edge is shown in Fig. 4(*b*). The strut surface is irregularly shaped. Irregular spatial distribution of SiC and Si within the strut leads to internal heterogeneity but no pores are observed inside the strut.

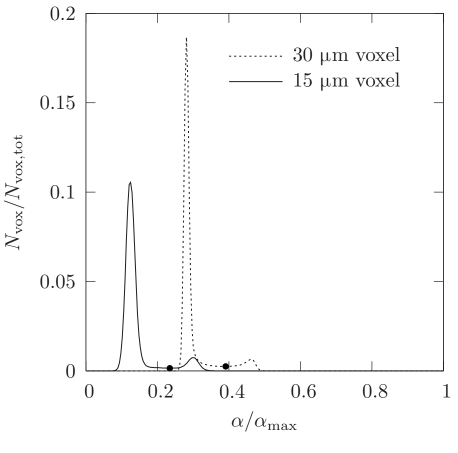

Fig. 2 Normalized histograms of the absorption values for the scans with 30 μm (dotted line) and 15 μm (solid line) voxel sizes. The points indicate the corresponding threshold values of $\alpha_t/\alpha_{\max}=0.39$ and 0.23.

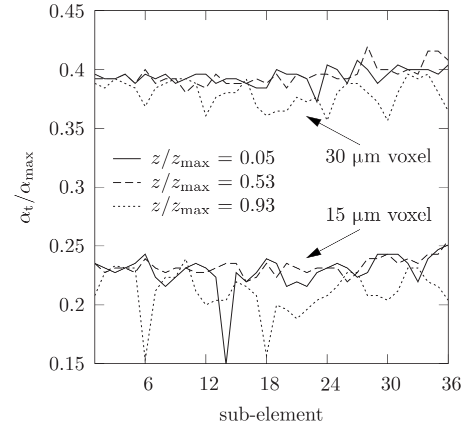

Fig. 3 Normalized threshold absorption values for 36 subelements of three selected tomograms for voxel sizes of 30 μm and 15 μm

2.3 Porosity and Specific Surface. The two-point correlation function

$$s_2(r)=\frac{\int_V\int_{4\pi}\psi(\mathbf{r})\psi(\mathbf{r}+r\hat{\mathbf{s}})\mathrm{d}\Omega\mathrm{d}V}{4\pi V} \tag{1}$$

with its properties $s_2(0)=\varepsilon$ and $(\mathrm{d}s/\mathrm{d}r)|_{r=0}=-(A_0/4)$ [27] is applied. $s_2(r)$ is computed using the Monte Carlo method. A random point is chosen within the fluid phase. A second random point is chosen at distance r. If the second point belongs to the fluid phase, the integrand in Eq. (1) is equal to 1. Otherwise, it is 0. The computation is performed for 10^8 random points and for r varying between 0 cm and 1 cm. The resulting porosity is $\varepsilon=0.91$. It compares well to the value obtained by weight measurement (0.90 ± 0.02) and it does not depend on the voxel size of the scan. In contrast, the specific surface area A_0 increases from 1367 m^{-1} to 1680 m^{-1} as the voxel size decreases from 30 μm to 15 μm because of the better resolution of surface irregularities for the smaller voxel size.

2.4 REV. The representative elementary volume (REV) is defined as the minimum volume of a porous material for which the continuum assumption is valid. It is determined based on porosity calculations for subsequent growing volumes until it asymptotically reaches a constant value within a band of $\pm\gamma$. The edge length of the cubic REV is defined by [18]

$$l_{\mathrm{REV},\gamma}=\min\{l\le l^* | \varepsilon-\gamma<\varepsilon(S_{l^*})<\varepsilon+\gamma\}, \quad \gamma<1 \tag{2}$$

where S_{l^*} is a sample subvolume of edge length l^*. For $\gamma=0.02$, $l_{\mathrm{REV},\gamma}=3.50$ mm and 3.39 mm for the scans with voxel sizes 30 μm and 15 μm, respectively, corresponding to $2.76d_{\mathrm{nom}}$ and $2.67d_{\mathrm{nom}}$, respectively. It is shown in the analysis that follows

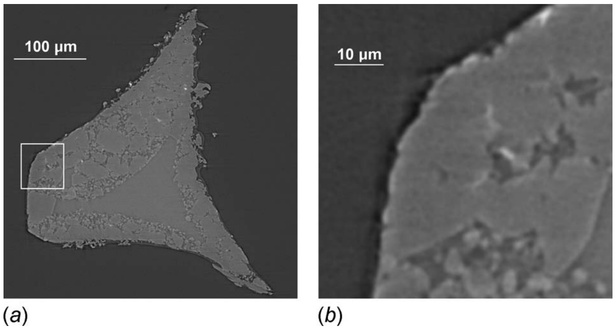

Fig. 4 (*a*) Tomogram of a single strut obtained by HRCT; (*b*) magnified fragment of the strut edge marked with the white frame in Fig. 4(*a*)

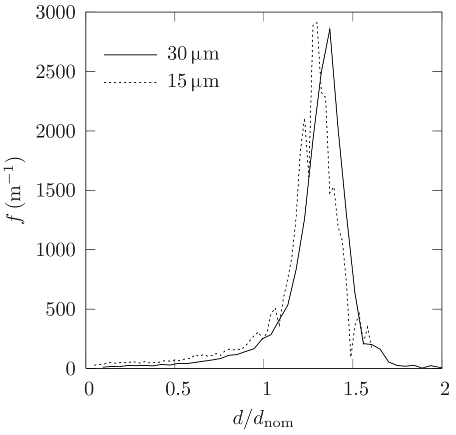

Fig. 5 Opening pore size distribution of the RPC foam for the 30 μm (solid curve) and 15 μm (dotted curve) voxel size tomography data

(Sec. 3.4) that at least $l_{\mathrm{REV}}=3.50d_{\mathrm{nom}}$ is required for computations of heat and mass transfer.

2.5 Pore Size Distribution. An opening operation, consisting of erosion, followed by dilation with structuring sphere of diameter d, is applied to compute the opening porosity $\varepsilon_{\mathrm{op}}$ as a function of the diameter d. $\varepsilon_{\mathrm{op}}$ is then used to determine the RPC's pore size distribution function f [18]

$$F(d) = \int_0^d f(d^*)\mathrm{d}d^* = 1 - \frac{\varepsilon_{\mathrm{op}}(d)}{\varepsilon_0} \tag{3}$$

where $\varepsilon_0=s_2(0)$. The resulting pore size distribution functions are shown in Fig. 5 for the 30 μm and 15 μm voxel size tomography data. Table 1 lists the median, mode, mean, and hydraulic ($d_{\mathrm{h}}=4\varepsilon/A_0$) diameters resulting from the distributions in Fig. 5.

Good qualitative and quantitative agreement of porosity, specific surface area, and pore size distribution is obtained for voxel sizes of 30 μm and 15 μm. Thus, the heat and mass transfer characteristics in Secs. 3 and 4 are computed by using the 30 μm resolution tomography data.

Table 1 Arithmetic mean, mode, median, and hydraulic diameter for the 30 μm and 15 μm voxel size tomography data

Voxel size (μm)	d_{am} (mm)	d_{mode} (mm)	d_{median} (mm)	d_{h} (mm)
30	1.64	1.74	1.69	2.76
15	1.55	1.65	1.62	2.24

3 Heat Transfer Characteristics

3.1 Radiative Properties. The complex refractive index of SiC is taken for the solid phase [28], which is assumed to be opaque in the visible and near infrared spectral region. The fluid phase is assumed to be radiatively nonparticipating. Hence, the governing equation of radiative transfer is [19,22,29,30]

$$\frac{\mathrm{d}I_\lambda(s,\hat{\mathbf{s}})}{\mathrm{d}s} + \beta_\lambda I_\lambda(s,\hat{\mathbf{s}}) = \kappa_\lambda I_{\lambda,\mathrm{b}}(s,\hat{\mathbf{s}}) + \frac{\sigma_{\mathrm{s},\lambda}}{4\pi}\int_{4\pi} I_\lambda(s,\hat{\mathbf{s}}_{\mathrm{in}})\Phi_\lambda(\hat{\mathbf{s}},\hat{\mathbf{s}}_{\mathrm{in}})\mathrm{d}\Omega_{\mathrm{in}} \tag{4}$$

where I_λ is spectral radiative intensity, κ_λ, $\sigma_{\mathrm{s},\lambda}$, and β_λ are the spectral absorption, scattering, and extinction coefficients, respectively, and Φ_λ is the spectral scattering phase function. The spectral subscript λ is omitted in the following text for brevity. The characteristic size parameter ($\pi d_{\mathrm{h}}/\lambda$) is much larger than 1; thus, geometric optics is valid. Collision-based Monte Carlo method is applied to compute the cumulative distribution functions of the radiation attenuation path s, and the distribution function of the cosine of incidence μ_{in} at the solid wall $G_{\mathrm{e}}(s)$ and $F_{\mu_{\mathrm{in}}}(\mu_{\mathrm{in}})$, respectively

$$G_{\mathrm{e}}(s) = \int_0^s \frac{1}{N_{\mathrm{r}}}\sum_{j=1}^{N_{\mathrm{r}}} \delta(s' - s_j')\mathrm{d}s' \tag{5}$$

$$F_{\mu_{\mathrm{in}}}(\mu_{\mathrm{in}}) = \frac{1}{N_{\mathrm{e}}}\sum_{j=1}^{N_{\mathrm{e}}} \delta(\mu_{\mathrm{in}} - \mu_{\mathrm{in},j}) \tag{6}$$

$G_{\mathrm{e}}(s)$ and $F_{\mu_{\mathrm{in}}}(\mu_{\mathrm{in}})$ are related to β and Φ by [19,22,29]

$$G_{\mathrm{e}}(s) \approx 1 - \exp(-\beta s) \tag{7}$$

$$\Phi(\mu_{\mathrm{s}}) = \frac{2\int_{\mu_{\mathrm{in}}=0}^{1}\int_{\varphi_{\mathrm{d}}=0}^{\pi}\int_{\mu_{\mathrm{r}}=0}^{1}\delta\left(\mu_{\mathrm{s}} - \sqrt{(1-\mu_{\mathrm{in}}^2)(1-\mu_{\mathrm{r}}^2)}\cos\varphi_{\mathrm{d}} - \mu_{\mathrm{in}}\mu_{\mathrm{r}}\right)\cdot\rho''(\mu_{\mathrm{in}},\mu_{\mathrm{r}},\varphi_{\mathrm{d}})F_{\mu_{\mathrm{in}}}\mu_{\mathrm{r}}d\mu_{\mathrm{r}}d\varphi_{\mathrm{d}}d\mu_{\mathrm{in}}}{\int_{\mu_{\mathrm{in}}=0}^{1}\int_{\varphi_{\mathrm{d}}=0}^{\pi}\int_{\mu_{\mathrm{r}}=0}^{1}\rho''(\mu_{\mathrm{in}},\mu_{\mathrm{r}},\varphi_{\mathrm{d}})F_{\mu_{\mathrm{in}}}\mu_{\mathrm{r}}d\mu_{\mathrm{r}}d\varphi_{\mathrm{d}}d\mu_{\mathrm{in}}} \tag{8}$$

where μ_{s} and μ_{r} denote the cosines of scattering and reflection angles. $G_{\mathrm{e}}(s)$ and $F_{\mu_{\mathrm{in}}}(\mu_{\mathrm{in}})$ are computed by following the histories of a large number ($N_{\mathrm{r}}=6\times10^6$) of stochastic rays launched at random locations within the fluid phase of the REV. N_{e} rays interact with the solid-fluid interface by either absorption or reflection. The path length s within REV is recorded for all N_{r} rays while the cosine of incidence μ_{in} is recorded for all N_{e} rays [19,22,29,30]. A sample of $18\times18\times12$ mm^3, corresponding to $600\times600\times400$ voxels, is investigated. The intersection point between a ray and the solid-fluid interface is found by following the ray in discrete steps until the normalized gray values are larger than $\alpha_{\mathrm{t}}/\alpha_{\mathrm{max}}$. Finally, the exact determination is achieved by applying the bisection method. Note that the interface is described by a continuous function and no numerical grid is required. The computations are performed with an in-house Fortran 95 code. $1-G_{\mathrm{e}}(s)$ is plotted in Fig. 6(a) as a function of the normalized path length for two values of the threshold $\alpha_{\mathrm{t}}/\alpha_{\mathrm{max}}$: 0.31 and 0.39. A least-square fit to Bouguer's law (Eq. (7)), also shown in Fig. 6(a), yields a constant extinction coefficient $\beta_{\mathrm{MC}}=628.4$ m^{-1} with root mean square (RMS) of 0.014 m^{-1} for $\alpha_{\mathrm{t}}/\alpha_{\mathrm{max}}=0.31$, and $\beta_{\mathrm{MC}}=430.8$ m^{-1} with RMS=0.014 m^{-1} for $\alpha_{\mathrm{t}}/\alpha_{\mathrm{max}}=0.39$. Separate computations along preferred directions showed slight anisotropy of β, as indicated in Table 2.

For assumed diffusely-reflecting surface of the solid phase, the scattering phase function is plotted in Fig. 6(b) as a function of the cosine of scattering angle. It is well approximated by (RMS =0.010)

$$\Phi = 0.5471\mu_{\mathrm{s}}^2 - 1.38838\mu_{\mathrm{s}} + 0.8176 \tag{9}$$

Also shown in Fig. 6(b) is the analytically determined scattering phase function for diffusely-reflecting large opaque spheres [31].

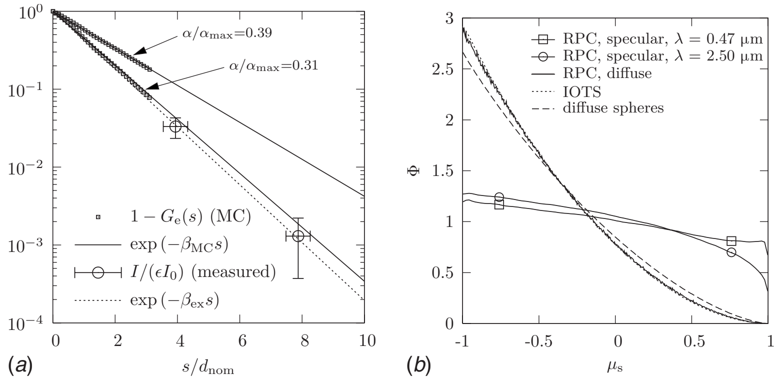

Fig. 6 (*a*) **Variation in computed and measured incident radiative intensities as a function of normalized path length in the sample; (*b*) scattering phase functions of the RPC foam, IOTS, and of large diffuse opaque spheres as a function of the cosine of scattering angle**

The RPC foam and identical overlapping transparent spheres (IOTS) [30] exhibit identical scattering behavior due to their morphological similarity. Compared with large diffuse opaque spheres, RPC exhibits enhanced scattering in backward direction and less in forward direction. For assumed specularly-reflecting surface, two exemplary scattering phase functions computed for $m_{\lambda=0.467\ \mu\text{m}}=2.707+1.46i$ and $m_{\lambda=2.50\ \mu\text{m}}=2.562+5.17i$ are shown in Fig. 6(*b*). Both exhibit nearly isotropic scattering behaviors with slightly increased backward scattering. Based on the irregular surface topography shown in Fig. 4, the solid phase is anticipated to show a dominant diffuse component in the reflection pattern.

The scattering albedo σ_s/β equals the surface reflectivity of the solid phase, assumed to be wavelength-independent and equal to 0.1 [32]. Hence, $\sigma_s=43.1\ \text{m}^{-1}$ and $62.8\ \text{m}^{-1}$ for $\alpha_t/\alpha_{\max}=0.31$ and 0.39, respectively.

The extinction coefficient is independently estimated based on experimental measurements by using the spectroscopy system shown in Fig. 7 [33]. The main hardware components of the setup are as follows: (1) a dual Xe-Arc/Cesiwid-Glowbar lamp as a source of radiation, (2) a double monochromator (Acton Research Spectra Pro Monochromator SP-2355 series) with monochromator exit slit (2′), ((3) and (5)) two imaging lens pairs (MgF_2, focal lengths $f=75$ mm and $f=150$ mm), (4) a sample holder, (6) a detector (Si/PC-HgCdTe sandwich with thermoelectric cooler), (7) an optical chopper to modulate the radiation leaving the monochromator, (8) a lock-in amplifier to measure the modulated signal, and (9) a PC data acquisition system. This setup enables measurements in the spectral range from 0.3 μm to 4 μm with a spectral resolution of ±1 nm and an angular resolution of 10 deg. The maximum acceptance angle for detection of an incoming ray measured with respect to the optical axis is less than 4 deg. Angular measurements are performed with two RPC foam samples of thicknesses 5 mm and 10 mm at radiation wavelengths of 0.3 μm, 0.6 μm, and 0.9 μm. The measured flux rapidly decreases with the increasing detection angle. At 10 deg, it is 10^3 smaller than that acquired in the forward direction. Since the reflectivity of the solid phase is comparable to that of SiC (0.1) [32] the contribution of the incoming scattering to the measured radiative fluxes is neglected. Thus, the extinction coefficient is estimated by assuming Bouguer's law-type dependency of the measured radiative fluxes on the sample thickness.

For all radiation wavelengths, the extinction coefficient is approximately constant and equal to $\beta_{ex}=673\pm30\ \text{m}^{-1}$. This value is larger than $\beta_{MC}=430.8\ \text{m}^{-1}$ determined numerically by MC for $\alpha_t/\alpha_{\max}=0.39$, but it is in good agreement with $\beta_{MC}=628.4\ \text{m}^{-1}$ computed for $\alpha_t/\alpha_{\max}=0.31$. Since $1/\sigma_s$ has the same order of magnitude as the measured sample thickness incoming scattering may affect the experimental results. In contrast, when comparing measured and calculated porosities, $(\varepsilon_{ex}-\varepsilon_{CT})/\varepsilon_{ex}=0.01$ and 0.06 for $\alpha_t/\alpha_{\max}=0.39$ and 0.31, respectively.

Table 2 Mean values and standard deviations of the extinction coefficient along three directions

	x-direction	*y*-direction	*z*-direction
β_{MC}, mean (m^{-1})	400.6	411.0	439.8
S_β (m^{-1})	35.8	37.5	28.4

3.2 Effective Thermal Conductivity. The governing steady-state heat conduction equations within the solid and fluid phases are

$$0=\nabla(k_s\nabla T_s) \tag{10}$$

$$0=\nabla(k_f\nabla T_f) \tag{11}$$

The boundary conditions are

$$T_s=T_f,\ \ \hat{\mathbf{n}}\cdot k_s\nabla T_s=\hat{\mathbf{n}}\cdot k_f\nabla T_f \quad \text{at solid-fluid interface} \tag{12}$$

$$\mathbf{q}''\cdot\hat{\mathbf{n}}=0 \quad \text{at the sample lateral walls} \tag{13}$$

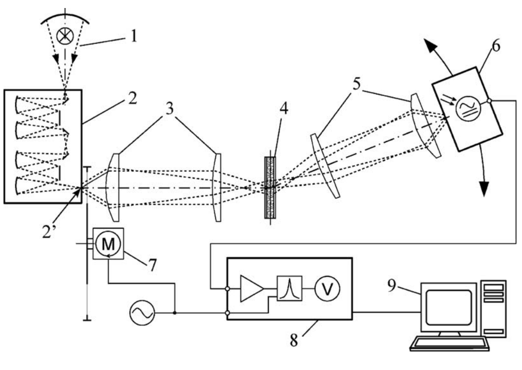

Fig. 7 Experimental spectroscopy setup: (1) dual Xe-Arc/Cesiwid-Glowbar lamp, (2) double monochromator, ((3) and (5)) collimating and focusing lens pairs, (4) sample mounted on a linear positioning stage, (6) detector, (7) optical chopper, (8) lock-in amplifier, (9) data acquisition system

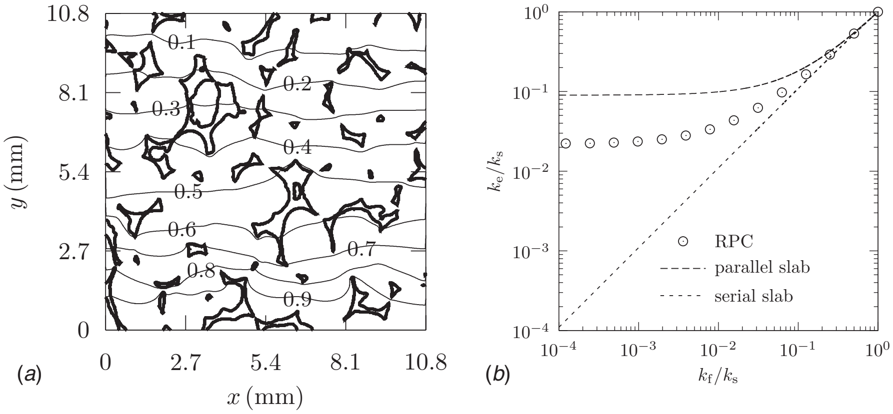

Fig. 8 **(*a*) Contour map of the normalized temperature distribution $(T - T_2)/(T_1 - T_2)$ along the axis perpendicular to the temperature boundary condition of the RPC foam (thick solid lines depict solid-fluid phase boundary) for $k_f/k_s = 1.0\times10^{-4}$; (*b*) the effective thermal conductivity of the RPC foam and of parallel and serial slabs at $\varepsilon = 0.91$**

$$T_s = T_f = T_1 \quad \text{at the sample inlet} \tag{14}$$

$$T_s = T_f = T_2 \quad \text{at the sample outlet} \tag{15}$$

The finite volume (FV) technique with successive over-relaxation (SOR) is applied to solve the Eqs. (10) and (11). The computations are performed with an in-house Fortran 95 code. A sample of $10.8\times10.8\times10.8$ mm^3, corresponding to $360\times360\times360$ voxels, is investigated. Grid convergence is obtained with mesh element size of 21.5 μm. The boundary conditions Eqs. (12)–(15) lead to a quasi-1D temperature profile. A contour map of the normalized temperature distribution along the axis perpendicular to the temperature boundary condition is shown in Fig. 8(*a*). The nonlinear temperature profile in the sample is used to determine the heat flux across the sample at any given cross-sectional plane perpendicular to the main heat flow direction. By applying the one-equation average model describing the conduction heat transfer in porous media [14,20], the heat flux can be linked to the effective conductivity by

$$k_e = l\frac{-\int_{A_s} k_s \nabla T_s \cdot \hat{\mathbf{n}} dA_s - \int_{A_f} k_f \nabla T_f \cdot \hat{\mathbf{n}} dA_f}{(T_1 - T_2)(A_s + A_f)} \tag{16}$$

The effective sample conductivity as a function of the solid and fluid conductivity is shown in Fig. 8(*b*). It is compared with the parallel and serial slab assumptions (at $\varepsilon = 0.91$), which indicate minimal and maximal possible conductivities.

The computed k_e/k_s was fitted to the linear combination of thermal conductivities of parallel and serial slabs [14]

$$\frac{k_e}{k_s} = e_1\frac{k_f/k_s}{\varepsilon(1 - k_f/k_s) + k_f/k_s} + e_2\left(\varepsilon\frac{k_f}{k_s} + 1 - \varepsilon\right) \tag{17}$$

resulting in $e_1 = 0.753$ and $e_2 = 0.267$. e_1 and e_2 depend strongly on the morphology. This can be seen when comparing k_e of the 20 ppi and the 10 ppi foams analyzed in Ref. [20], both having the same ε and a rather sharp pore size peak (peak width $\approx 0.5d_{\mathrm{nom}}$). The 20 ppi foam shows a larger A_0. For $k_f/k_s \approx 10^{-1}$ they differ by nearly 6% and at $k_f/k_s \approx 10^{-4}$ they differ by up to 40%. Obviously, the smaller k_f/k_s, the more important becomes the phase distribution. When using the RPC foam as solar absorber, larger k_e are preferred since they allow for faster heat transfer rate and a more uniform heating.

3.3 Interfacial Heat Transfer Coefficient.

The heat flux from the solid to the fluid phase is given by

$$q = h_{sf} A_{sf}(T_{\mathrm{interface}} - T_{\mathrm{mf}}) \tag{18}$$

The coupled continuity, momentum, and energy equations are solved within the fluid phase of a square duct containing a sample of the foam by using a computational fluid dynamics (CFD) code [34] to obtain the temperature distribution in the fluid phase and the heat fluxes through the solid-fluid interface.

The boundary conditions are

$$\overline{\mathbf{u}} = 0, \quad T = T_{sf} \quad \text{at the solid-fluid interface} \tag{19}$$

$$\overline{\mathbf{u}}\cdot\hat{\mathbf{n}} = 0, \quad \hat{\mathbf{n}}\cdot\nabla\overline{\mathbf{u}} = 0, \quad \mathbf{q}''\cdot\hat{\mathbf{n}} = 0 \quad \text{at the sample later walls} \tag{20}$$

$$\overline{\mathbf{u}}\cdot\hat{\mathbf{n}} = -u_0, \quad T = T_0 \quad \text{at the inlet} \tag{21}$$

$$p = p_{\mathrm{atm}} \quad \text{at the outlet} \tag{22}$$

h_{sf} is then determined as a function of Pr and Re by using

$$h_{sf} = \frac{\int_{A_{sf}} q'' dA_{sf}}{A_{sf}\cdot\Delta T_{\mathrm{lm}}} \tag{23}$$

A sample with dimensions of $11.4\times11.4\times3.78$ mm^3, corresponding to $380\times380\times126$ voxels, is investigated. Convergence was achieved for the termination residual RMS of the iterative solution below 10^{-4} and for the maximal mesh element length of 90 μm (corresponding to $0.07d_{\mathrm{nom}}$), resulting in 5.6×10^7 tetrahedral elements. The mesh is generated with an in-house mesh generator for unstructured body-fitted grids. The mesh generator covers the domain by tetrahedral elements and subsequently refines the elements at the phase boundary. Finally, a rounding, cutting, and smoothing process is made to achieve an accurate domain representation [21]. Two quad-core Intel Xeon 2.5 GHz processors and 32 Gbytes RAM are used to solve the equations in approximately 10 h.

Nu is shown in Fig. 9 as a function of Pr and Re. Assuming a correlation of the form $\mathrm{Nu} = a_0 + a_1\mathrm{Re}^{a_2}\,\mathrm{Pr}^{a_3}$, least-square fitting leads to (RMS = 0.817)

$$\mathrm{Nu} = 6.820 + 0.198\mathrm{Re}^{0.788}\,\mathrm{Pr}^{0.606} \tag{24}$$

These results compare well to those obtained experimentally for a 10 ppi foam [35].

3.4 Influence of l_{REV}.

Normalized porosity, extinction coefficient, and conductivity are plotted in Fig. 10 as a function of

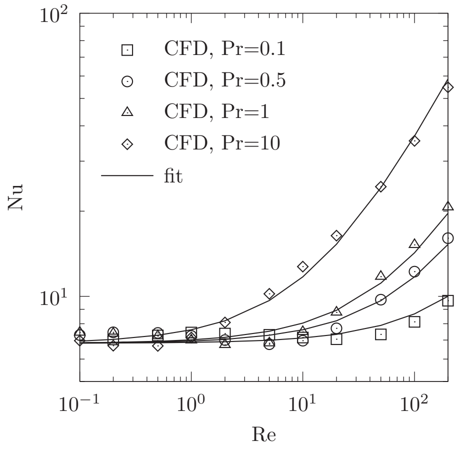

Fig. 9 Computed (points) and fitted (lines) Nu number as a function of Re and Pr numbers

l/d_{nom} varying between 0 and 6. All three parameters converge for approximately $l_{\mathrm{REV}}=3.5d_{\mathrm{nom}}$, with $\gamma=\pm 0.02$, ± 0.02, and ± 0.15, respectively.

4 Mass Transfer Characteristics

4.1 Permeability and Dupuit–Forchheimer Coefficient. Darcy's law [36] and its extensions [37,38] are applied for a fluid flow in an averaged isotropic porous medium

$$\nabla p = -\frac{\mu}{K}\overline{\mathbf{u}}_{\mathrm{D}} - F_{\mathrm{DF}}\rho\overline{\mathbf{u}}_{\mathrm{D}}|\overline{\mathbf{u}}_{\mathrm{D}}| \tag{25}$$

Nondimensionalization of Eq. (25) for the 1D case yields

$$\frac{\nabla p d^2}{\mu u_{\mathrm{D}}} = \Pi_{\mathrm{pg}} = -\frac{d^2}{K} - F_{\mathrm{DF}}d\,\mathrm{Re} = -c_0 - c_1\,\mathrm{Re} \tag{26}$$

The continuity and momentum equations are solved [34] within the fluid phase of a square duct containing a sample of the foam to obtain the velocity and pressure distributions for the following boundary conditions

$$\overline{\mathbf{u}} = 0 \quad \text{at the solid-fluid interface} \tag{27}$$

$$\overline{\mathbf{u}}\cdot\hat{\mathbf{n}} = 0, \quad \hat{\mathbf{n}}\cdot\nabla\overline{\mathbf{u}} = 0 \quad \text{at the sample lateral walls} \tag{28}$$

$$\overline{\mathbf{u}}\cdot\hat{\mathbf{n}} = -u_0 \quad \text{at the inlet} \tag{29}$$

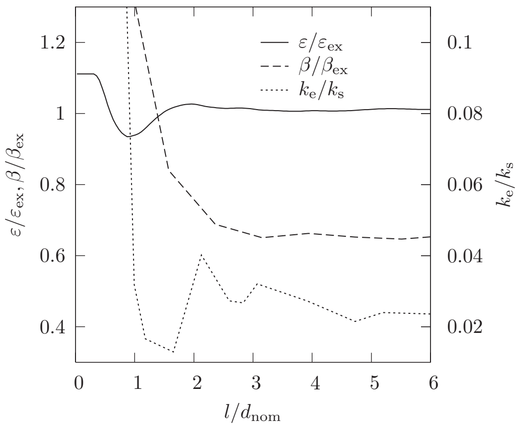

Fig. 10 Normalized porosity, extinction coefficient, and effective conductivity for cubic volumes with edge lengths *l*

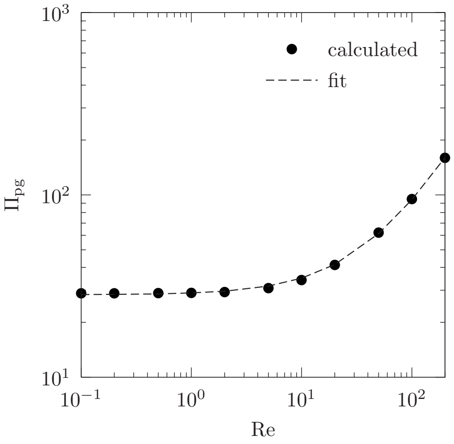

Fig. 11 Dimensionless pressure gradient as a function of Re number

$$p = p_{\mathrm{atm}} \quad \text{at the outlet} \tag{30}$$

A $11.4\times 11.4\times 3.78$ mm^3 sample, corresponding to $380\times 380\times 252$ voxels, is investigated. Convergence is achieved for the termination residual RMS of the iterative solution below 10^{-4} and for the maximal mesh element length of 180 μm (corresponding to $0.14d_{\mathrm{nom}}$), resulting in 5.6×10^7 tetrahedral elements. The dimensionless pressure gradient is plotted as a function of Re in Fig. 11. Least-square fitting (RMS=0.566) results in $c_0=28.334$ and $c_1=0.659$, which correspond to $K=5.69\times 10^{-8}$ m^2 and $F_{\mathrm{DF}}=519.0$ m^{-1}. Permeability values are compared with those obtained for the Hagen–Poisseuille model (4.59×10^{-8} m^2) [14], the Carman–Konzeny model (8.69×10^{-8} m^2) [14,15], the fibrous bed models (8.97×10^{-7} m^2) [15], and a model proposed by Macdonald et al. (5.34×10^{-8} m^2) [39]. The latter model yields $F_{\mathrm{DF}}=544.2$ m^{-1}. The nonlinear term in Eq. (25) comes into play for Re>1. Increased pore size leads to reduced pressure loss and consequently to a larger K and a smaller F_{DF}, as observed by comparing the SiSiC RPC to the Rh-coated SiC from Ref. [21].

4.2 Tortuosity and Residence Time Distributions. Tortuosity is defined as the ratio of the real length of the connected pore channels to the thickness of the porous sample in the main flow direction

$$\tau = \frac{l_{\mathrm{path}}}{l_{\mathrm{sample}}} \tag{31}$$

The residence time required for a particle to flow through the porous sample is defined as

$$t = \int_{l_{\mathrm{path}}} \frac{1}{u}\mathrm{d}l \tag{32}$$

The velocity distributions obtained in the Sec. 4.1 are now used to determine the tortuosity and residence time distributions. They are shown in Fig. 12 for Re=0.1, 1, 10, and 100. Mean tortuosity is 1.07. The peak of the tortuosity distribution shifts toward $\tau=1$ with increasing Re. Mean residence time is plotted in Fig. 13. All stream lines generated are able to pass through the sample, as no recirculation zones, dead ends, or flow reversals are observed. In most chemical applications, large τ, smaller Re, and consequently large t are preferred to allow for complete reaction conversion.

4.3 Dispersion Tensor. The governing equation coupling the convection and diffusion in the fluid phase is [40]

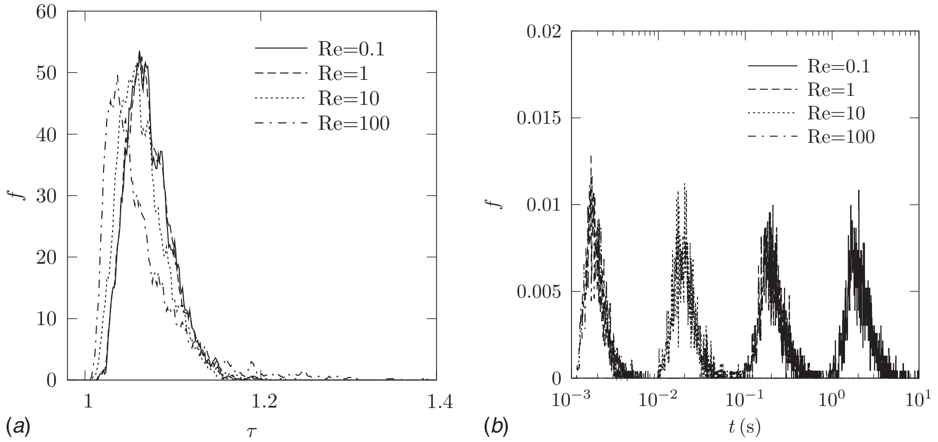

Fig. 12 (*a*) Tortuosity and (*b*) residence time distributions for four selected Re numbers of fluid flow through the RPC foam

$$\frac{\partial c}{\partial t} + \nabla(c\overline{\mathbf{u}}) - \nabla(\overline{\overline{\mathbf{D}}} \cdot \nabla c) = 0 \tag{33}$$

The dispersion tensor **D** in an isotropic medium can be decomposed in parallel and transverse components, D_{II} and $D_{\perp}$, respectively. For zero molecular diffusion

$$D_i = b_0 \, \mathrm{Re}^{b_1} \tag{34}$$

with b_0 and b_1 constants. The solution of Eq. (33) links **D** to the standard deviation of the normally distributed concentration c [41]

$$S_c = \sqrt{2D_i t} \tag{35}$$

D_x, D_y, and D_z are determined by following 2500 streamlines through the foam, registering their spatial displacement at a specific time instant (e.g., in z-direction: $\Delta z = z(t) - z(t_0)$), and subsequently fitting the registered distribution to a standard Gauss distribution. The normalized dispersion tensor components are shown in Fig. 14 as a function of Re. D_x and D_y are equal to the transverse component $D_{\perp}$; D_z is equal to the parallel component D_{II}. Fitting to Eq. (34) yields

$$\frac{D_{\perp}}{\nu} = \begin{cases} 6.560 \times 10^{-3}\,\mathrm{Re} & \mathrm{Re} \leq 5 \\ 4.896 \times 10^{-3}\,\mathrm{Re}^{1.104} & \mathrm{Re} > 5 \end{cases} \quad (\mathrm{RMS} = 6.0 \times 10^{-6}) \tag{36}$$

$$\frac{D_{\mathrm{II}}}{\nu} = \begin{cases} 6.297 \times 10^{-1}\,\mathrm{Re} & \mathrm{Re} \leq 5 \\ 7.045 \times 10^{-1}\,\mathrm{Re}^{0.942} & \mathrm{Re} > 5 \end{cases} \quad (\mathrm{RMS} = 4.2 \times 10^{-5}) \tag{37}$$

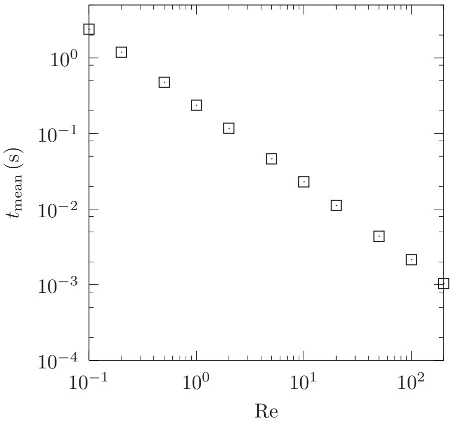

Fig. 13 Mean residence time as a function of Re number

5 Summary and Conclusions

We have numerically computed the effective heat and mass transport properties of a nonhollow RPC foam made of SiSiC, whose exact 3D geometry was determined by computer tomography. Computed porosity was 0.91 and compared well to experimentally measured value of 0.90 ± 0.02. Computed specific surface was 1367 m^{-1} and increased by 20% when increasing the scan resolution by a factor of 2 as smaller surface irregularities were resolved. Computed pore size distribution showed a sharp peak of approximately $0.5d_{\mathrm{nom}}$ and a mean diameter of $1.3d_{\mathrm{nom}}$. REV determined by porosity, extinction coefficient, and conductivity calculations on subsequently growing volumes was 87.8 mm^3. Radiative properties were determined from the extinction length and cosine of incidence distributions by applying the collision-based MC method. The computed extinction coefficient of 431 m^{-1} agreed quantitatively to the experimentally measured one estimated by measuring the transmitted radiative flux with a spectroscopy system. Computed scattering functions showed a large backward scattering peak for diffusely-reflecting surfaces and isotropic scattering behavior for specularly-reflecting surfaces. The scattering coefficient was a function of the surface reflectivity and determined to be 63 m^{-1}. The effective conductivity was calculated by solving the heat conduction equation within both phases by FV and fitted to a combination of parallel and serial slab models. For $k_{\mathrm{f}}/k_{\mathrm{s}} < 10^{-4}$, k_{e} remained constant and approximately $0.022k_{\mathrm{s}}$. The heat transfer coefficient was calculated by solving the continuity, momentum, and energy governing

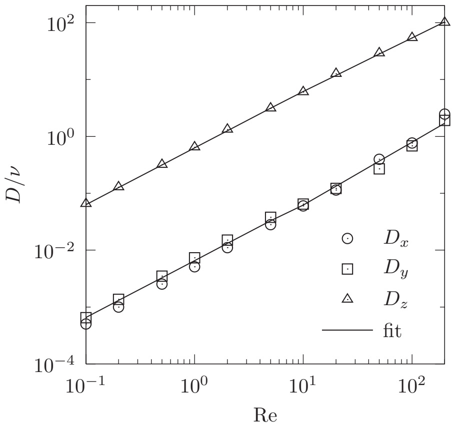

Fig. 14 Normalized dispersion tensor as a function of Re for the RPC foam

equations within the fluid phase by FV. A Re and Pr dependent Nu correlation of the form $\mathrm{Nu}=6.820+0.198\mathrm{Re}^{0.788}\,\mathrm{Pr}^{0.606}$ was fitted ($\mathrm{RMS}=0.817$). This correlation strongly depended on the morphology. Computed permeability and Dupuit–Forchheimer coefficient, determined based on the pressure and velocity distribution within the fluid, were $K=5.67\times10^{-8}$ m^2 and $F_{\mathrm{DF}}=519.0$ m^{-1} and compared well to the values found by applying different models available in the literature. Tortuosity distribution calculations resulted in a mean tortuosity of 1.07. Obviously, the mean residence time decreased with increasing Re. Neglecting molecular dispersion, a Re dependent function of the dispersion tensor was obtained by comparing the calculated spatial displacement distribution of streamlines within the foam to a Gaussian distribution.

The CT-based methodology is able to accurately account for the morphology of complex porous media, and, when coupled to Monte Carlo and CFD numerical techniques, provides pore-level solutions of the energy and fluid flow governing equations. The effective transport properties can be used in a continuum-scale heat and mass transfer model, which, in turn, may be used for the design and optimization of components for high-temperature applications. A follow-up study will determine the limits of applicability of combined conduction-convection-radiation computations utilizing the effective thermal properties.

Acknowledgment

This work has been financially supported by the Swiss National Science Foundation under Contract No. 200021-115888 and by the European Commission under Contract No. 212470 (Project HYCYCLES). We thank C. Suter for the technical support with the spectroscopy measurements and F. Marone for the technical support at SLS.

Nomenclature

a_0, a_1, a_2, a_3 = constants
b_0, b_1 = constants in Eq. (34)
A = surface (m^2)
A_0 = specific surface (m^{-1})
c = concentration (kg m^{-3})
c_0, c_1 = constants in Eq. (26)
$\mathbf{D}$ = dispersion tensor (m^2 s^{-1})
d = diameter, characteristic length scale (m)
d_{h} = hydraulic diameter (m)
d_{nom} = nominal diameter (m)
e_1, e_2 = constants in Eq. (17)
f = distribution function (m^{-1})
F = probability distribution function
F_{DF} = Dupuit–Forchheimer coefficient (m^{-1})
G = cumulative distribution function
h_{sf} = interfacial heat transfer coefficient (W m^{-2} K^{-1})
I = radiative intensity (W m^{-3} sr^{-1})
k = conductivity (W m^{-1} K^{-1})
k_{e} = effective conductivity (W m^{-1} K^{-1})
K = permeability (m^2)
l = length (m)
m = complex refractive index
$\hat{\mathbf{n}}$ = surface normal vector
N_{r} = number of rays
N_{e} = number of extincted rays
Nu = Nusselt number
p = pressure (N m^{-2})
Pr = Prandtl number
$\mathbf{q}''$ = heat flux vector (W m^{-2})
q = heat transfer rate (W)
r = distance between two points in the sample (m)
$\mathbf{r}$ = position vector for spatial coordinates in the sample (m)
Re = Reynolds number
s = path length (m)
$\hat{\mathbf{s}}$ = unit vector of path direction
s_2 = two-point correlation function
S = sample subvolume (m^3)
S_i = standard deviation of i ([i])
t = residence time (s)
T = temperature (K)
u = velocity (m s^{-1})
u_{D} = Darcean velocity (supervicial volume averaged velocity) (m s^{-1})
V = sample volume (m^3)
z = sample dimension in the z-direciton (m)

Greek

α = absorption values of tomographic scans (m^{-1})
β = extinction coefficient (m^{-1})
δ = Dirac delta function
γ = half bandwidth for REV determination
ε = porosity
κ = absorption coefficient (m^{-1})
λ = radiation wavelength (m)
μ = dynamic viscosity (kg m^{-1} s^{-1})
μ_{in} = cosine of incidence angle
μ_{r} = cosine of reflection angle
μ_{s} = cosine of scattering angle
ν = kinematic viscosity (m^2 s^{-1})
φ_{d} = difference azimutal angle, $\varphi_{\mathrm{d}}=\varphi_{\mathrm{in}}-\varphi_{\mathrm{r}}$ (rad)
ρ'' = bidirectional reflectivity (sr^{-1})
Π_{pg} = dimensionless pressure gradient
σ_{s} = scattering coefficient (m^{-1})
τ = tortuosity
Φ = scattering phase function
ψ = pore-scale indicator function (1=void phase; 0 =solid phase)
Ω = solid angle (sr)

Subscripts

am = arithmetic mean
atm = atmospheric
b = blackbody
ex = experimental
f = fluid
in = incident
lm = logarithmic mean
mf = mean fluid
op = opening
s = solid
sf = solid-fluid boundary
t = threshold
tot = total
0 = initial

References

[1] Nettleship, I., 1996, "Applications of Porous Ceramics," Adv. Ceram. Mater., **122**, pp. 305–324.
[2] Matthews, A. L., 1996, "Ceramic Filters for the Cast Metal Industry," Adv. Ceram. Mater., **122**, pp. 293–304.
[3] van Setten, B., Bremmer, J., Jelles, S., Makkee, M., and Moulijn, J., 1999, "Ceramic Foam as a Potential Molten Salt Oxidation Catalyst Support in the Removal of Soot From Diesel Exhaust Gas," Catal. Today, **53**, pp. 613–621.
[4] Barra, A., Diepvens, G., Ellzey, J., and Henneke, M., 2003, "Numerical Study of the Effects of Material Properties on Flame Stabilization in a Porous Burner," Combust. Flame, **134**, pp. 369–379.
[5] Dhamrat, R., and Ellzey, J., 2006, "Numerical and Experimental Study of the Conversion of Methan to Hydrogen in a Porous Media Reactor," Combust. Flame, **144**, pp. 698–709.
[6] Fend, T., Hoffschmidt, B., Pitz-Paal, R., Reutter, O., and Rietbrock, P., 2004,

"Porous Materials as Open Volumetric Solar Receivers: Experimental Determination of Thermophysical and Heat Transfer Properties," Energy, **29**, pp. 823–833.

[7] Buck, R., Muir, J. F., Hogan, R. E., and Skocypec, R. D., 1991, "Carbon Dioxide Reforming of Methane in a Solar Volumetric Receiver/Reactor: The CAESAR Project," Solar Energy Materials, **24**, pp. 449–463.

[8] Chavez, J. H., and Chaza, C., 1991, "Testing of Porous Ceramic Absorber for a Volumetric Air Receiver," Solar Energy Materials, **24**, pp. 172–181.

[9] Loretz, M., Coquard, R., Baillis, D., and Maire, D., 2008, "Metallic Foams: Radiative Properties/Comparison Between Different Models," J. Quant. Spectrosc. Radiat. Transf., **109**, pp. 16–27.

[10] Fu, X., Viskanta, R., and Gore, J. P., 1997, "A Model for the Volumetric Radiation Characteristics of Cellular Ceramics," Int. Commun. Heat Mass Transfer, **24**, pp. 1069–1082.

[11] Boomsma, K., and Poulikakos, D., 2001, "On the Effective Thermal Conductivity of Three-Dimensionally Structured Fluid-Saturated Metal Foam," Int. J. Heat Mass Transfer, **44**, pp. 827–836.

[12] Bhattacharya, A., Calmidi, V., and Mahajan, R., 2002, "Thermophysical Properties of High Porosity Metal Foams," Int. J. Heat Mass Transfer, **45**, pp. 1017–1031.

[13] Fu, X., Viskanta, R., and Gore, J. P., 1998, "Prediction of Effective Thermal Conductivity of Cellular Ceramics," Int. Commun. Heat Mass Transfer, **25**, pp. 151–160.

[14] Kaviany, M., 1995, *Principles of Heat Transfer in Porous Media*, Springer-Verlag, New York.

[15] Dullien, F., 1979, *Porous Media Fluid Transport and Pore Structure*, Academic, New York.

[16] Chen, C., 1955, "Filtration of Aerosols by Fibrous Media," Chem. Rev. (Washington, D.C.), **55**, pp. 595–623.

[17] Rintoul, M., Torquato, S., Yeong, C., Keane, D., Erramilli, S., Jun, Y., Dabbs, D., and Aksay, I., 1996, "Structure and Transport Properties of a Porous Magnetic Gel Via X-Ray Microtomography," Phys. Rev. E, **54**, pp. 2663–2669.

[18] Petrasch, J., Wyss, P., Stämpfli, R., and Steinfeld, A., 2008, "Tomography-Based Multiscale Analyses of the 3D Geometrical Morphology of Reticulated Porous Ceramics," J. Am. Ceram. Soc., **91**, pp. 2659–2665.

[19] Petrasch, J., Wyss, P., and Steinfeld, A., 2007, "Tomography-Based Monte Carlo Determination of Radiative Properties of Reticulate Porous Ceramics," J. Quant. Spectrosc. Radiat. Transf., **105**, pp. 180–197.

[20] Petrasch, J., Schrader, B., Wyss, P., and Steinfeld, A., 2008, "Tomography-Based Determination of the Effective Thermal Conductivity of Reticulate Porous Ceramics," ASME J. Heat Transfer, **130**, p. 032602.

[21] Petrasch, J., Meier, F., Friess, H., and Steinfeld, A., 2008, "Tomography Based Determination of Permeability, Dupuit–Forchheimer Coefficient, and Interfacial Heat Transfer Coefficient in Reticulate Porous Ceramics," Int. J. Heat Fluid Flow, **29**, pp. 315–326.

[22] Haussener, S., Lipiński, W., Petrasch, J., Wyss, P., and Steinfeld, A., 2009, "Tomographic Characterization of a Semitransparent-Particle Packed Bed and Determination of Its Thermal Radiative Properties," ASME J. Heat Transfer, **131**, p. 072701.

[23] Noglik, A., Roeb, M., Rzepczyk, T., Hinkley, J., Sattler, C., and Pitz-Paal, R., 2009, "Solar Thermochemical Generation of Hyrogen: Develpment of a Receiver Reactor of the Decomposition of Sulfuric Acid," J. Sol. Energy Eng., **131**, p. 011003.

[24] Gonzalez, R. C., and Woods, R. E., 2008, *Digital Image Processing*, 3rd ed., Prentice-Hall, Upper Saddle River, NJ.

[25] Weszka, Z., 1978, "A Survey of Threshold Selection Techniques," Comput. Graph. Image Process., **7**, pp. 259–265.

[26] Streun, A., Böge, A., Dehler, M., Gough, C., Joho, W., Korhonen, T., Lüdeke, A., Marchand, P., Muñoz, M., Pedrozzi, M., Rivkin, L., Schilcher, T., Schlott, V., Schulz, L., and Wrulich, A., 2001, "Commissioning of the Swiss Light Source," *Proceedings of the 2001 Particle Accelerator Conference*, P. Lucas and S. Webber, eds., IEEE, Piscataway, NJ, pp. 224–226.

[27] Berryman, J., and Blair, S., 1986, "Use of Digital Image Analysis to Estimate Fluid Permeability of Porous Material: Application of Two-Point Correlation Functions," J. Appl. Phys., **60**, pp. 1930–1938.

[28] Palik, E. D., 1998, *Handbook of Optical Constants of Solids II*, Elsevier, New York.

[29] Lipiński, W., Petrasch, J., and Haussener, S., 2009, "Application of the Spatial Averaging Theorem to Radiative Heat Transfer in Two-Phase Media," J. Quant. Spectrosc. Radiat. Transf., **111**, pp. 253–258.

[30] Tancrez, M., and Taine, J., 2004, "Direct Identification of Absorption and Scattering Coefficients and Phase Function of a Porous Medium by a Monte Carlo Technique," Int. J. Heat Mass Transfer, **47**, pp. 373–383.

[31] Modest, M., 2003, *Radiative Heat Transfer*, 2nd ed., Academic, San Diego, CA.

[32] Touloukian, Y., 1970, *Thermophysical Properties of Matter*, Plenum, New York.

[33] Coray, P., Lipiński, W., and Steinfeld, A., 2008, "Experimental and Numerical Determination of Thermal Radiative Properties of ZnO Particulate Media," ASME J. Heat Transfer, in press.

[34] Ansys Inc., 2006, ANSYS-CFX, www.ansys.com

[35] Buck, R., 2000, "Massenstrom-Instabilitäten bei volumetrischen Receiver-Reaktoren," Ph.D. thesis, Universität Stuttgart, Germany.

[36] Darcy, H., 1856, *Les Fontaines Publiques de la ville de Dijon*, Dalmont, Paris.

[37] Dupuit, J., 1863, *Etudes theoretiques et practiques sur le mouvement des eaux*, Dunond, Paris.

[38] Forchheimer, P., 1901, "Wasserbewegung durch den Boden," Z. Ver. Dtsch. Ing., **45**, pp. 1782–1788.

[39] Macdonald, I. F., El-Sayed, M. S., Mow, K., and Dullien, F. A. L., 1979, "Flow Through Porous Media—The Ergun Equation Revisited," Ind. Eng. Chem. Fundam., **18**, pp. 199–208.

[40] Hirsch, C., 2007, *Numerical Computation of Internal and External Flows*, 2nd ed., Elsevier, Amsterdam.

[41] Salles, J., Thovert, J.-F., Delannay, R., Prevors, L., Auriault, J.-L., and Adler, P. M., 1993, "Taylor Dispersion in Porous Media. Determination of the Dispersion Tensor," Phys. Fluids, **5**, pp. 2348–2376.

Infrared Radiative Properties of Thin Polyethylene Coating Pigmented With Titanium Dioxide Particles

Mehdi Baneshi[1]
School of Engineering,
Tohoku University,
6-6, Aoba, Aramaki-aza,
Aoba-ku, Sendai 980-8579, Japan
e-mail: mehdi.baneshi@pixy.ifs.tohoku.ac.jp

Shigenao Maruyama

Atsuki Komiya

Institute of Fluid Science,
Tohoku University,
2-1-1, Katahira,
Aoba-ku, Sendai 980-8577, Japan

The infrared (IR) radiative properties of TiO_2 pigment particles must be known to perform thermal analysis of a TiO_2 pigmented coating. Resins generally used in making pigmented coatings are absorbing at IR wavelengths, which means that the conventional Mie solution (MS) may not be adequate in this domain. There are two approaches to evaluating radiative properties in an absorbing medium: far field approximation (FFA) and near field approximation (NFA). In this study, after reviewing these two approaches, we evaluated the radiative properties of TiO_2 particles in polyethylene resin as an absorbing matrix in the wavelength range of 1.7–15 μm based on the MS, FFA, and NFA. We then calculated the effective scattering and absorption coefficients for different models. To investigate the effect of the particle size and volume concentration on the transmittance of IR wavelengths, we made a nongray radiative heat transfer in an anisotropic scattering monodisperse pigmented layer, with independent scattering using the radiation element method by the ray emission model. The results showed that all three approaches predicted similar results in the particle size domain and volume fraction range utilized in pigmented coatings. [DOI: 10.1115/1.4000235]

Keywords: far field approximation, near field approximation, pigmented coating, titanium dioxide

1 Introduction

The use of pigmented coatings is required for a wide variety of technological applications. These coatings are designed to reflect the visible (VIS) and/or near infrared (NIR) parts of sunlight and minimize heat transfer to the interior of a given structure, thus reducing the energy required for cooling. However, the transmission of long wavelength infrared (IR) rays with a wavelength of about 10 μm emitted from the body surface of a coated object can increase the efficiencies of air conditioning systems [1] and affect the thermal behavior of systems with pigmented coating. Thus, the IR radiative properties of pigmented coatings must be known, if researchers are to perform the necessary thermal analysis and investigate the effect of pigment particles on the performance of a pigmented layer.

Resins generally used as the matrix in making pigmented coatings are nonabsorbing in the VIS and NIR regions [1] but absorbing against IR wavelengths. This means that although predictions about the radiative properties of pigment particles based on the conventional Mie solution (MS), which ignores the continuous phase absorption index, are acceptable in the VIS and NIR regions, they may not be adequate in the IR region because of the absorbing characteristics of resins at IR wavelengths. The effect of absorption in the matrix can significantly influence the spectral behavior of the coating layer by changing not only the matrix properties but also the optical properties of the embedded particles.

To evaluate the radiative properties of a particle embedded in an absorbing medium, two approaches have been proposed in the literature: far field approximation (FFA) and near field approximation (NFA). FFA [2–6], developed by Mundy et al. [2] and Chylek [3], is based on the asymptotic form of the electromagnetic field in the radiation zone far from the scatterer. NFA [4–11] was proposed by Sudiarta and Chylek [7,8] and Lebedev and co-workers [9,10] and is based on the information of the electromagnetic field at the particle surface. Radiative transfer through absorbing media containing bubbles or particles is of interest to the developers of many practical engineering applications ranging from remote sensing of the ocean surface and fire fighting to materials processing and colloidal systems in liquids or in the atmosphere [6].

In this study we investigated the effect of the absorption of resins on the spectral behavior of a TiO_2 pigmented coating in the IR region. Polyethylene resin was used as the absorbing host medium in the wavelength range of about 1.7–15 μm. We developed computer programs to calculate the radiative properties of a TiO_2 particle, including the scattering, absorption, and extinction efficiencies, and asymmetry parameter, in an absorbing medium based on the MS, FFA, and NFA. First, the numerical codes were validated by comparing the results with available data in the literature for single scattering properties of bubbles and particles using different approaches. Then, databases of the radiative properties of a TiO_2 particle in polyethylene resin over a wide range of particle sizes (0.01–100 μm) in the wavelength range of 1.7–15 μm were constructed based on the MS, FFA, and NFA. To find the transmittance of IR wavelengths produced by emission from the substrate, we conducted a radiation analysis using the radiation element method by the ray emission model (REM^2) [12]. In the summary, we discuss the effects of using different approaches in evaluating radiative properties in addition to the size of pigment particles and the volume concentration of particles on IR behavior of a TiO_2 pigmented coating.

---

[1] Corresponding author.

Contributed by the Heat Transfer Division of ASME for publication in the JOURNAL OF HEAT TRANSFER. Manuscript received November 21, 2008; final manuscript revised April 9, 2009; published online December 4, 2009. Assoc. Editor: Yogesh Jaluria.

2 Radiative Properties of Particles in the Absorbing Medium

In the conventional Mie solution, the medium in which the particle is embedded is assumed to be a nonabsorbing material. However, when the medium is absorbing, the radiative properties cannot be correctly evaluated by simply modifying the refractive index of the host medium in the conventional Mie code. Two approaches have been used, as reported in the literature, to evaluate the radiative properties in an absorbing medium. Following is a brief summary and necessary formulation for these approaches.

2.1 The Far Field Approximation Model. Far field approximation is based on the asymptotic form of the electromagnetic field in the radiation zone. Mundy et al. [2] derived the following equations to calculate the scattering, absorption, and extinction efficiencies of a particle of size $d_p=2a$ and the complex index of refraction of $m'=n'-ik'$ embedded in an absorbing medium having $m=n-ik$:

$$Q_s = \frac{4k^2 e^{(-4\pi rk/\lambda)}}{(n^2+k^2)[1+(4\pi ak/\lambda-1)e^{(4\pi ak/\lambda)}]}\sum_{n=1}^{\infty}(2n+1)(|a_n|^2+|b_n|^2) \tag{1}$$

$$Q_e = \frac{4k^2 e^{(-4\pi rk/\lambda)}}{(n^2+k^2)[1+(4\pi ak/\lambda-1)e^{(4\pi ak/\lambda)}]}\mathrm{Re}\sum_{n=1}^{\infty}(2n+1)(a_n+b_n) \tag{2}$$

$$Q_a = Q_e - Q_s \tag{3}$$

where

$$a_n = \frac{m'\psi'_n(\alpha)\psi_n(\beta) - m\psi_n(\alpha)\psi'_n(\beta)}{m'\xi'_n(\alpha)\psi_n(\beta) - m\xi_n(\alpha)\psi'_n(\beta)} \tag{4}$$

$$b_n = \frac{m'\psi_n(\alpha)\psi'_n(\beta) - m\psi'_n(\alpha)\psi_n(\beta)}{m'\xi_n(\alpha)\psi'_n(\beta) - m\xi'_n(\alpha)\psi_n(\beta)} \tag{5}$$

Here, $\alpha=2\pi ma/\lambda$, $\beta=2\pi m'a/\lambda$, and ψ and ξ are Riccati–Bessel functions. In this model the host medium has not only attenuated the scattered waves in magnitude but also modulated the wave mode when the wave reaches the radiation zone. Thus for an observer in the radiation zone the particle's inherent optical properties are coupled with the absorption effect of the medium in a separable manner [6]. As Eqs. (1)–(5) show, because of the absorption in the host medium, the particle's efficiencies in this model depend on the radius of the conceptual integrating sphere ($r \gg a$) [10]. However as shown in Ref. [4], in evaluating the extinction and scattering coefficients that are due to the effect of the particle's scattering and absorption as viewed from the far field perspective rather than the absorption of the host medium, the particle's rescaled [4] or attenuated [2] efficiencies must be calculated by applying an exponential factor $\exp(\alpha(r-a))$ to Eqs. (1) and (2), as follows:

$$Q_s = \frac{4k^2 e^{-\eta}}{(n^2+k^2)[1+(\eta-1)e^{\eta}]}\sum_{n=1}^{\infty}(2n+1)(|a_n|^2+|b_n|^2) \tag{6}$$

$$Q_e = \frac{4k^2 e^{-\eta}}{(n^2+k^2)[1+(\eta-1)e^{\eta}]}\mathrm{Re}\sum_{n=1}^{\infty}(2n+1)(a_n+b_n) \tag{7}$$

where $\eta=2\pi ka/\lambda$. These efficiencies are independent of the radius of the integrating sphere. The extinction efficiency in Eq. (7) can be expressed as follows [2]:

$$Q_e = Q_s + (Q_a - Q_m) \tag{8}$$

where Q_m is the absorption efficiency when the scatterer contained the same substance as that of the surrounding medium. Depending upon the absorption properties of medium and particle, the extinction efficiency can be smaller than the scattering efficiency and even negative.

The scattering phase function can be derived by use of the far field approximation as follows [10]:

$$P(\cos\theta) = \frac{|S_1|^2+|S_2|^2}{\sum\limits_{n=1}^{\infty}(2n+1)(|a_n|^2+|b_n|^2)} \tag{9}$$

where

$$S_1 = \sum_{n=1}^{\infty}\frac{2n+1}{n(n+1)}[a_n\pi_n(\cos\theta)+b_n\tau_n(\cos\theta)] \tag{10}$$

$$S_2 = \sum_{n=1}^{\infty}\frac{2n+1}{n(n+1)}[a_n\tau_n(\cos\theta)+b_n\pi_n(\cos\theta)] \tag{11}$$

are amplitude functions. Then, the asymmetry parameter, which is an often-used parameter in radiative transfer calculation, can be evaluated as follows:

$$g = \tfrac{1}{2}\int_{-1}^{1}P(\cos\theta)\cos\theta d\cos\theta \tag{12}$$

2.2 The Near Field Approximation Model. In near field approximation the single scattering properties of the particle, including the absorption, scattering, and extinction efficiencies, are derived by using the electromagnetic fields on the surface of the particle [10]. These efficiencies are called inherent efficiency factors. Fu and Sun [11] derived the following equations to calculate the scattering, absorption, and extinction efficiencies:

$$Q_s^{\mathrm{NF}} = \frac{8\pi k^2}{\lambda n[1+(\eta-1)e^{\eta}]}\sum_{n=1}^{\infty}(2n+1)(B_n) \tag{13}$$

$$Q_a^{\mathrm{NF}} = \frac{8\pi k^2}{\lambda n[1+(\eta-1)e^{\eta}]}\sum_{n=1}^{\infty}(2n+1)(A_n) \tag{14}$$

$$Q_e^{\mathrm{NF}} = Q_s^{\mathrm{NF}} + Q_a^{\mathrm{NF}} \tag{15}$$

where

$$A_n = \frac{|c_n|^2\psi_n(\beta)\psi_n'^{*}(\beta) - |d_n|^2\psi'_n(\beta)\psi_n^{*}(\beta)}{2\pi m'/\lambda} \tag{16}$$

$$B_n = \frac{|a_n|^2\xi'_n(\alpha)\xi_n^{*}(\alpha) - |b_n|^2\xi_n(\alpha)\xi_n'^{*}(\alpha)}{2\pi m/\lambda} \tag{17}$$

Here, a_n and b_n are the same as in Eqs. (4) and (5) and c_n and d_n are derived as follows:

$$c_n = \frac{m'\xi_n(\alpha)\psi'_n(\alpha) - m'\xi'_n(\alpha)\psi_n(\alpha)}{m'\xi_n(\alpha)\psi'_n(\beta) - m\xi'_n(\alpha)\psi_n(\beta)} \tag{18}$$

$$d_n = \frac{m'\xi'_n(\alpha)\psi_n(\alpha) - m'\xi_n(\alpha)\psi'_n(\alpha)}{m'\xi'_n(\alpha)\psi_n(\beta) - m\xi_n(\alpha)\psi'_n(\beta)} \tag{19}$$

Particle efficiencies based on NFA are non-negative factors that depend only on the size of the particle and the optical properties of the particle and medium. This approach avoids difficulties in deriving the extinction efficiency when FFA is used. In the literature there is no established expression for the scattering phase function based on the NFA [5]. The scattering phase function and asymmetry parameter are similar to the FFA [5] given by Eqs. (9) and (12).

2.3 Validation of Computer Codes. In accordance with the theory discussed in Sec. 2, we developed three computer codes to

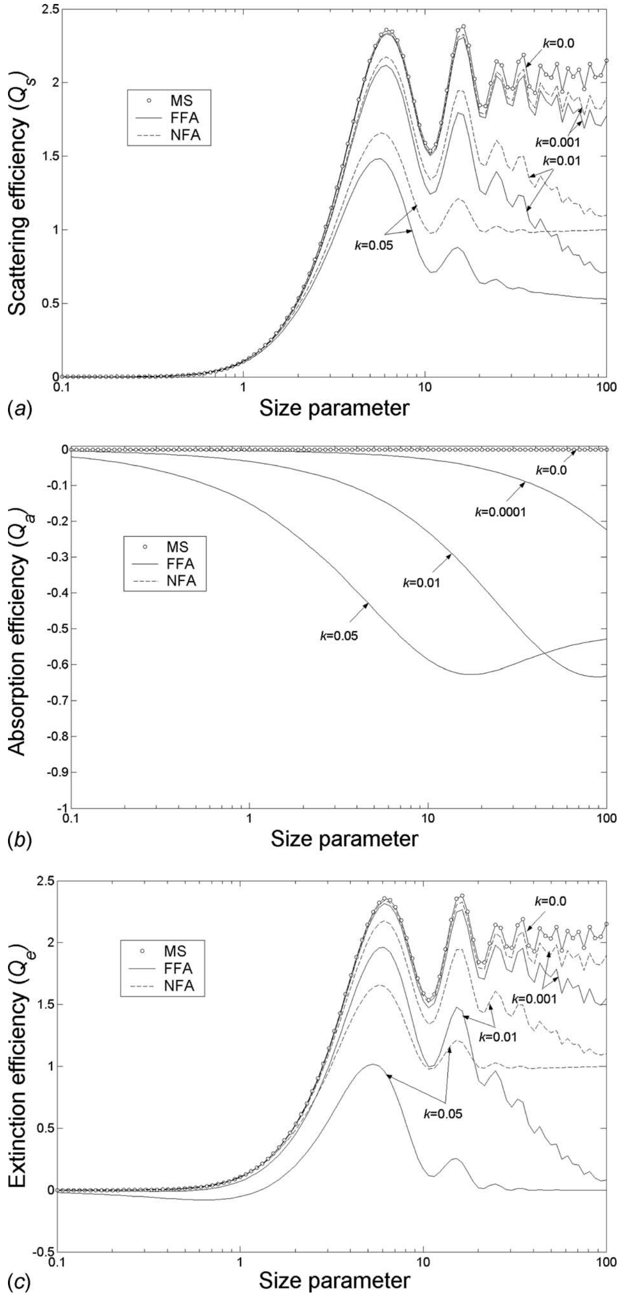

Fig. 1 Single scattering properties for a spherical bubble embedded in an absorbing medium with $m=1.34-ik$ where $k=0.0$, 0.001, 0.01, and 0.05

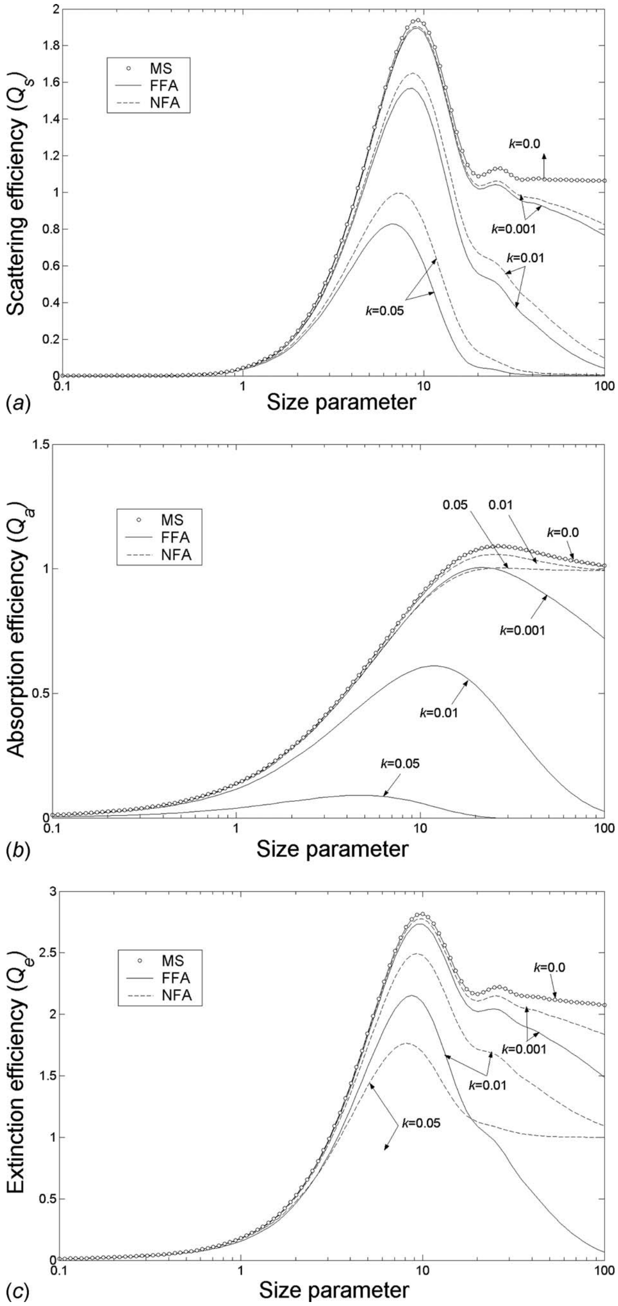

Fig. 2 Single scattering properties for a spherical particle ($m'=1.4-0.05i$) embedded in an absorbing medium with $m=1.2-ik$ where $k=0.0$, 0.001, 0.01, and 0.05

compute particle efficiencies based on the MS, FFA, and NFA, respectively. To validate our codes, we investigated two sets of refractive indices for the particle and medium as considered in Refs. [2,6,10]. In the first set, $m'=1-0i$ and $m=1.34-ik$, and in the second set $m'=1.4-0.05i$ and $m=1.2-ik$, where $k=0.0$, 0.001, 0.01, and 0.05. Figures 1 and 2 compare the single scattering properties based on different approaches for the two sets of refractive indices. The same results were obtained as those reported in the literature.

When the medium is nonabsorbing, both FFA and NFA show identical results with the MS. However, the difference between FFA and NFA increases as the absorptivity of the medium for both bubbles and particles increases. The values of Q_s and Q_e decrease as the absorptivity of the medium increases. Moreover, the scattering efficiency predicted by FFA is smaller than that for NFA with the same absorptivity of the medium. While the absorption efficiency evaluated by the MS and NFA is zero for a spherical bubble, the results of FFA show negative values for this parameter. This is related to the definition of absorption efficiency in FFA, as shown by Eq. (8). This causes the extinction efficiency obtained by FFA to become smaller than the scattering efficiency ($Q_e < Q_s$) for a spherical bubble or for a particle with smaller absorptivity than its host medium.

The asymptotic value of the scattering efficiency for a nonabsorbing particle is 2.0 for the MS, which is known as the diffraction paradox [13], 1.0 for NFA where diffraction can be neglected, and 0.5 for FFA [6]. Moreover, the absorption efficiency for a nonabsorbing particle converges to 0.0 for the MS and NFA and −0.5 for FFA [6]. Hence, the extinction efficiency for large size

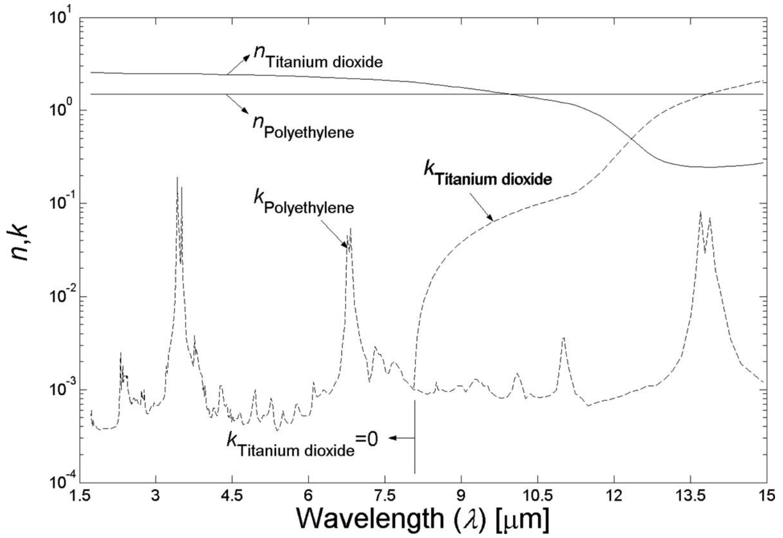

Fig. 3 Real (solid lines) and imaginary (dashed lines) parts of the complex index of refraction for TiO_2 and polyethylene

parameters converges to 2.0, 1.0, and 0.0 for the MS, NFA, and FFA, respectively.

For an absorbing particle, as shown in Fig. 2, the scattering efficiency converges to 1.0 for the MS due to diffraction and to 0.0 for FFA and NFA where there is no diffraction [6]. In addition, the asymptotic value of absorption efficiency is 1.0 for the MS and NFA and 0.0 for FFA [6], since in Eq. (8) both Q_m and $Q_{m'}$ are equal to 1.0 for large size parameters.

3 Radiative Properties of TiO_2 Particles in Polyethylene Resin

The radiative properties of a TiO_2 particle in polyethylene resin were computed for a wide range of particle sizes. The complex refractive index is quoted from a handbook [14] for both TiO_2 and polyethylene. The wavelength data, which are composed of 349 data points within the range of 1.7–15 μm, where the polyethylene behaves as the absorbing medium, are used. The diameter range is 0.01–100 μm and is composed of 1000 data points.

Real and imaginary parts of complex indices of refraction are shown in Fig. 3. TiO_2 is nonabsorbing in the range of 1.7–8.0 μm. However, its absorptivity increases sharply from 8.0 μm to 15.0 μm. The refractive index of polyethylene is constant and equal to 1.5. The absorptivity of polyethylene is strongly wavelength dependent and has some peaks at $\lambda=3.415$, 3.509, 6.08, 13.7, and 13.89 μm.

Figures 4 and 5 show the single scattering properties for a TiO_2 particle embedded in polyethylene host medium, including scattering, absorption, and extinction efficiencies, and the asymmetry parameter for two sets of wavelengths. For the first set, wavelengths were selected from the nonabsorbing part (1.7–8.0 μm) of TiO_2, while the wavelengths of the second set were chosen from the absorbing region (8.0–15 μm) of TiO_2.

Figure 4(*a*) compares the scattering efficiencies predicted by FFA and NFA at several wavelengths where TiO_2 is nonabsorbing. The information of Sec. 2.3 about nonabsorbing particles is validated again by these results. For example, at $\lambda=3.42$ μm, where polyethylene has its maximum absorptivity, the difference between the predicted efficiencies by FFA and NFA is the largest, and asymptotic values are reached for a smaller particle size. However, the absorptivity of TiO_2 rapidly increases from $\lambda=8$ μm, and the difference in the absorptivity of the particles and the host medium becomes very large, which significantly reduces the difference between predicted efficiencies by FFA and NFA, as seen in Fig. 5. Figure 5(*a*) shows the variation in scattering efficiency with the particle size at different wavelengths. At $\lambda=9.9$ μm, minimum scattering occurs independent of the size of the particle. This can be justified by the almost identical real part of complex refractive indices of TiO_2 and polyethylene at this wavelength. Since the absorptivity of TiO_2 is larger than that for polyethylene through the absorbing region of TiO_2, the absorption efficiency predicted by FFA is non-negative in this range of wavelengths, as is clear from Fig. 5(*b*), and hence $Q_e > Q_s$. The particle efficiencies tend to reach their asymptotic values at particle sizes larger than 100 μm.

The asymmetry parameter is shown in Figs. 4(*d*) and 5(*d*) for several wavelengths. These results show that the asymmetry parameter for TiO_2 is always positive and increases with increasing particle size. As explained in Sec. 2, there is no difference between the predicted value by FFA and NFA, since the scattering phase function is the same in both approximations.

4 Effective Scattering and Absorption Coefficients

After consideration of the different models used to evaluate the efficiencies of a single particle embedded in an absorbing medium, the question that arises is that among different approaches, which one can predict the radiative transfer through a heterogeneous medium? Several models to calculate the radiation characteristics such as scattering and absorption coefficients of an absorbing medium containing particles have been proposed.

As discussed in [11] M.F. Modest, Radiative heat transfer (2nd ed), Academic Press, San Diego (2003). Ref. [15], independent scattering is a good assumption for nearly all heat transfer application including paints and pigments and dependent scattering effects can be completely ignored when $f_v < 0.006$ or $c/\lambda > 0.5$, where c is the clearance. Several researches related to TiO_2 pigmented coatings [16,17] show that the independent scattering assumption gives reasonable results for volume fractions less than 0.1. In this work, to avoid the significant error in our results due to dependent scattering effects, the independent scattering approach is applied to low volume fractions up to 0.05. However, this assumption should be verified by comparison of theoretical predictions with experimental data as will be done in author's future works.

The general form of the scattering coefficient for particulate media containing monodisperse particles using the independent scattering approximation is as follows [15]:

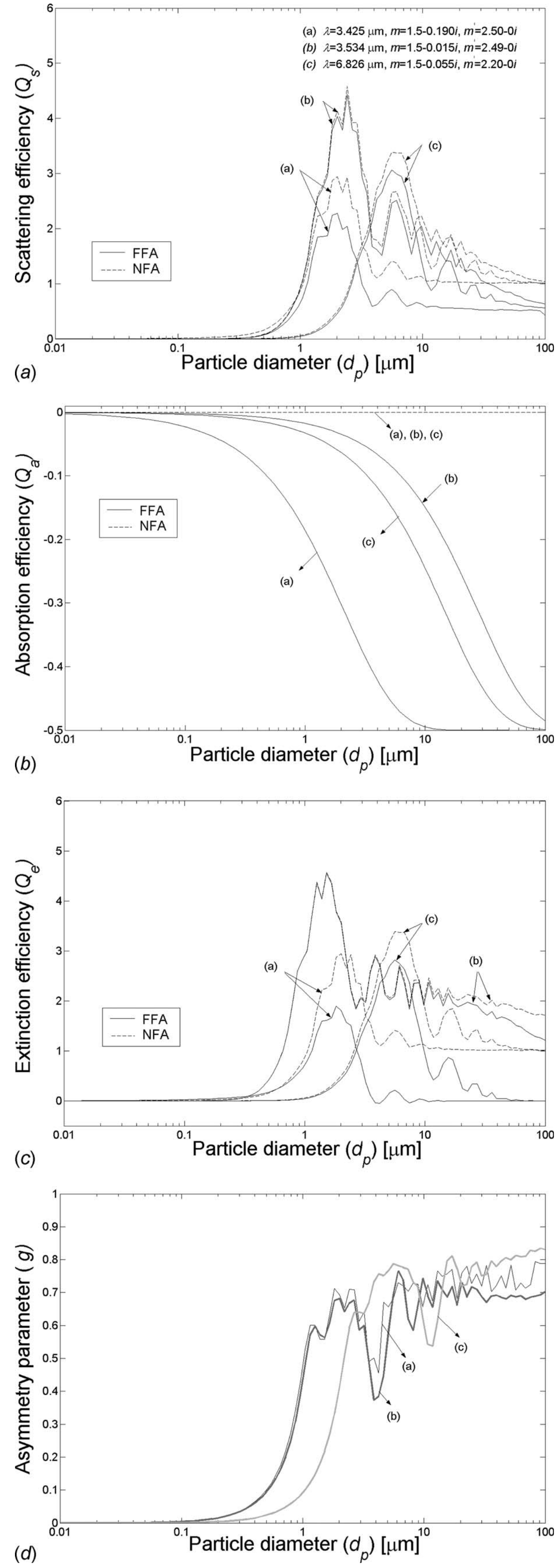

Fig. 4 Scattering, absorption, and extinction efficiencies, and asymmetry parameter as a function of the particle size for nonabsorbing TiO_2 particles in polyethylene resin at different wavelengths

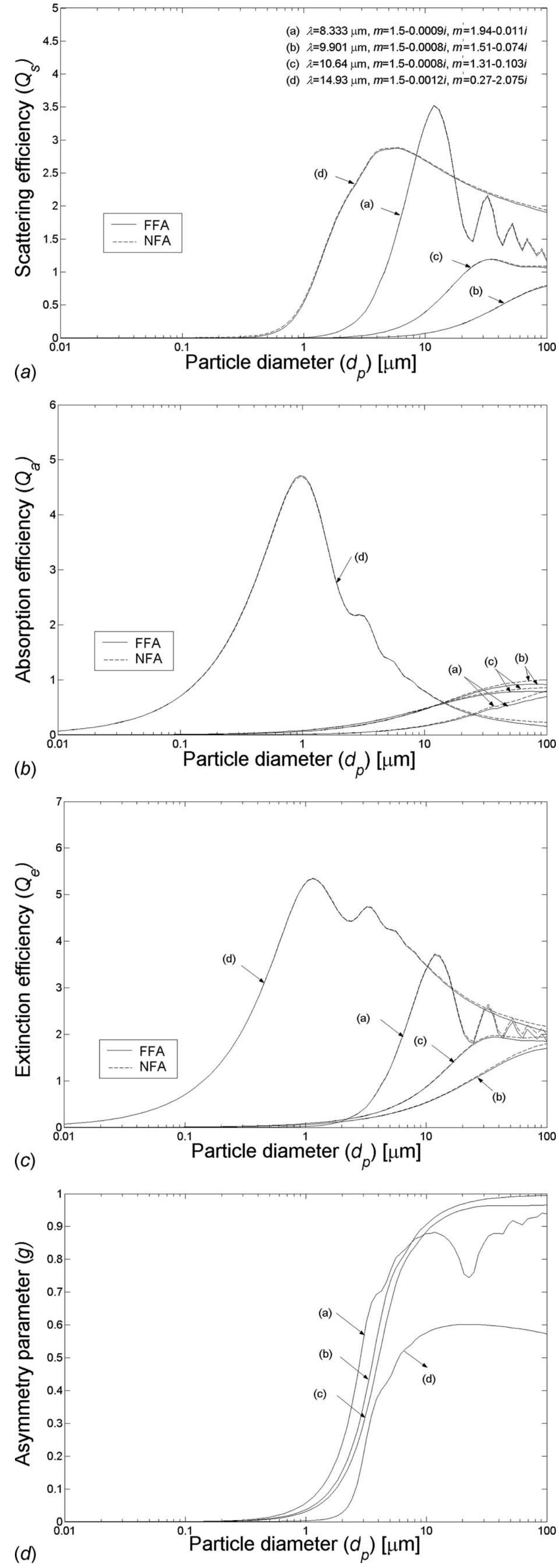

Fig. 5 Scattering, absorption, and extinction efficiencies, and asymmetry parameter as a function of the particle size for absorbing TiO_2 particles in polyethylene resin at different wavelengths

$$\sigma_{\mathrm{eff}} = \frac{3f_v}{4a} Q_s(a) \tag{20}$$

The scattering efficiency in Eq. (20) can be replaced by Q_s^M [5,15] for nonabsorbing media and Q_s^{FF} [4–6,18] and Q_s^{NF} [5] for absorbing media. The scattering efficiency based on considering the electromagnetic field at the particle's surface (NFA) cannot be used for modeling the effective scattering coefficient because predicting radiative transfer through heterogeneous media requires the efficiency factors of the particle in the far field, as discussed in Refs. [4,6].

The absorption coefficient based on the MS, NFA, and FFA approaches can be calculated using the independent scattering approximation as follows [6]:

$$k_{\mathrm{eff}}^M = \kappa - \frac{3f_v}{4a}[Q_{a,m}^M(a) - Q_{a,m'}^M(a)] \tag{21}$$

$$k_{\mathrm{eff}}^{\mathrm{NF}} = \kappa - \frac{3f_v}{4a}[Q_{a,m}^{\mathrm{NF}}(a) - Q_{a,m'}^{\mathrm{NF}}(a)] \tag{22}$$

$$k_{\mathrm{eff}}^{\mathrm{FF}} = \kappa + \frac{3f_v}{4a} Q_a^{\mathrm{FF}}(a) \tag{23}$$

where $\kappa = 4\pi k/\lambda$ is the absorption coefficient of the continuous phase. In the first two equations, $Q_{m'}$ is the absorption efficiency of the scatterer and Q_m is the absorption efficiency of the scatterer if it contains an identical substance as the surrounding medium. As discussed in Ref. [6], the absorption coefficient calculated based on the FFA approach was found to be negative for a large volume fraction, which is physically meaningless but the model proposed using NFA properties always show positive values and thus tends to give more physically acceptable results.

Based on Eqs. (20)–(23), we selected the following three sets of effective scattering and absorption coefficients needed to predict radiation transfer in a heterogeneous medium:

$$\begin{aligned}
&\text{model 1:} \quad \sigma_{\mathrm{eff}} = \sigma_{\mathrm{eff}}^{\mathrm{FF}}, \quad k_{\mathrm{eff}} = k_{\mathrm{eff}}^{\mathrm{FF}} \\
&\text{model 2:} \quad \sigma_{\mathrm{eff}} = \sigma_{\mathrm{eff}}^{\mathrm{FF}}, \quad k_{\mathrm{eff}} = k_{\mathrm{eff}}^{\mathrm{NF}} \\
&\text{model 3:} \quad \sigma_{\mathrm{eff}} = \sigma_{\mathrm{eff}}^{M}, \quad k_{\mathrm{eff}} = k_{\mathrm{eff}}^{M}
\end{aligned} \tag{24}$$

In models 1 and 2, as discussed before, the scattering coefficient is obtained using the scattering efficiency calculated based on the FFA approach. The difference between these two models is in the evaluation of absorption coefficient. The absorption coefficient is calculated based on FFA and NFA in models 1 and 2, respectively. To investigate the effect of neglecting the absorptivity of the host medium in obtaining the radiative properties of pigment particles, model 3 is used where both scattering and absorption coefficients are calculated based on the Mie solution.

5 Numerical Simulation and Analysis Model

5.1 Radiative Transfer Equation. We consider the participating medium in a plane parallel system. Neglecting the eventual wave interference effects, the spectral radiation intensity I_λ at $\mathbf{r}$ in the direction of $\hat{\mathbf{s}}$ can be expressed as follows [12]:

$$\frac{dI_\lambda(\mathbf{r},\hat{\mathbf{s}})}{ds} = \beta_\lambda \left[-I_\lambda(\mathbf{r},\hat{\mathbf{s}}) + (1-\omega_\lambda) I_{b\lambda}(\mathbf{r}) + \frac{\omega_\lambda}{4\pi}\int_{4\pi} I_\lambda(\mathbf{r},\hat{\mathbf{s}}')\Phi_\lambda(\hat{\mathbf{s}}' \to \hat{\mathbf{s}})\, d\Omega' \right] \tag{25}$$

where β_λ and ω_λ are the spectral extinction coefficient and single scattering albedo, respectively. Here, s is the path length in the direction $\hat{\mathbf{s}}$, and $\Phi(\hat{\mathbf{s}}' \to \hat{\mathbf{s}})$ is the phase function from $\hat{\mathbf{s}}'$ to $\hat{\mathbf{s}}$. One should note that the traditional radiative transfer equation can be applied when the optical thickness of the medium at distances comparable with the particle size is small. In this present study, this condition is satisfied except for large particles ($>0.5\ \mu$m) at the wavelength range of about 3 μm. Therefore, the results given at this wavelength range are not completely reliable and should be verified by experimental results. To solve this equation, Maruyama et al. [12] proposed the REM^2. They introduced the effective radiation area for both the surface and volume elements in the same manner. They also defined the extinction view factor $F_{i,j}^E$ as the fraction of energy radiated from radiation element i that is absorbed, isotropically scattered, or diffusely reflected by radiation element j. Once the extinction view factors have been obtained, the absorption view factors $F_{i,j}^A$ and diffuse scattering view factor $F_{i,j}^D$ can be written as

$$F_{i,j,\lambda}^A = \frac{\varepsilon_{j,\lambda}}{(1-\omega_{j,\lambda}^S)} F_{i,j,\lambda}^E, \quad F_{i,j,\lambda}^D = \frac{\omega_{j,\lambda}^D}{(1-\omega_{j,\lambda}^S)} F_{i,j,\lambda}^E \tag{26}$$

where $\varepsilon_{i,\lambda} = 1 - \omega_{i,\lambda}^D - \omega_{i,\lambda}^S$ is the emissivity, $\omega_{i,\lambda}^D$ is the diffuse reflectivity of the surface elements or the albedo of participating media elements, and $\omega_{i,\lambda}^S$ is the specular reflectivity of the surface elements. Once these coefficients are introduced, the radiative heat transfer under arbitrary thermal conditions can be determined for each participating radiation element and boundary surface. For a system consisting of N radiation elements, one can write the following equations:

$$Q_{J,i,\lambda} = Q_{T,i,\lambda} + \sum_{j=1}^{N} F_{j,i,\lambda}^D Q_{J,j,\lambda} \tag{27}$$

$$Q_{X,i,\lambda} = Q_{T,i,\lambda} - \sum_{j=1}^{N} F_{j,i,\lambda}^A Q_{J,j,\lambda} \tag{28}$$

where Q_T is emissive power and Q_J is the radiative energy emitted and isotropically scattered by the radiation element. The unknown $Q_{X,I,\lambda}$ can be obtained by solving Eqs. (27) and (28). The relationship between $q_{X,i}$ and $Q_{X,I,\lambda}$ is obtained by

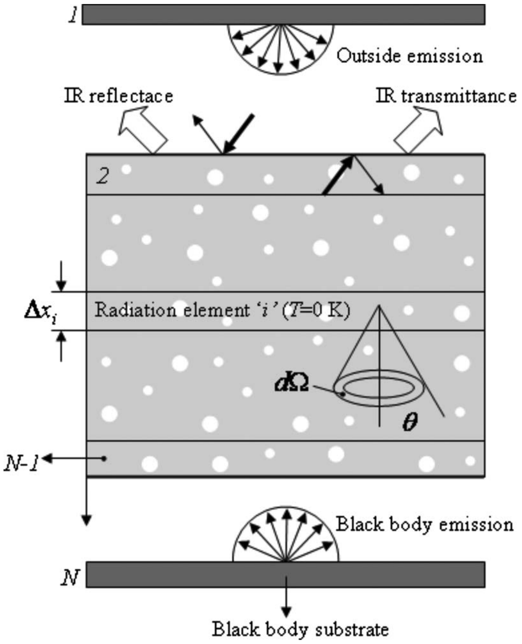

Fig. 6 Analysis model of a pigmented coating using the REM^2 with related boundary conditions

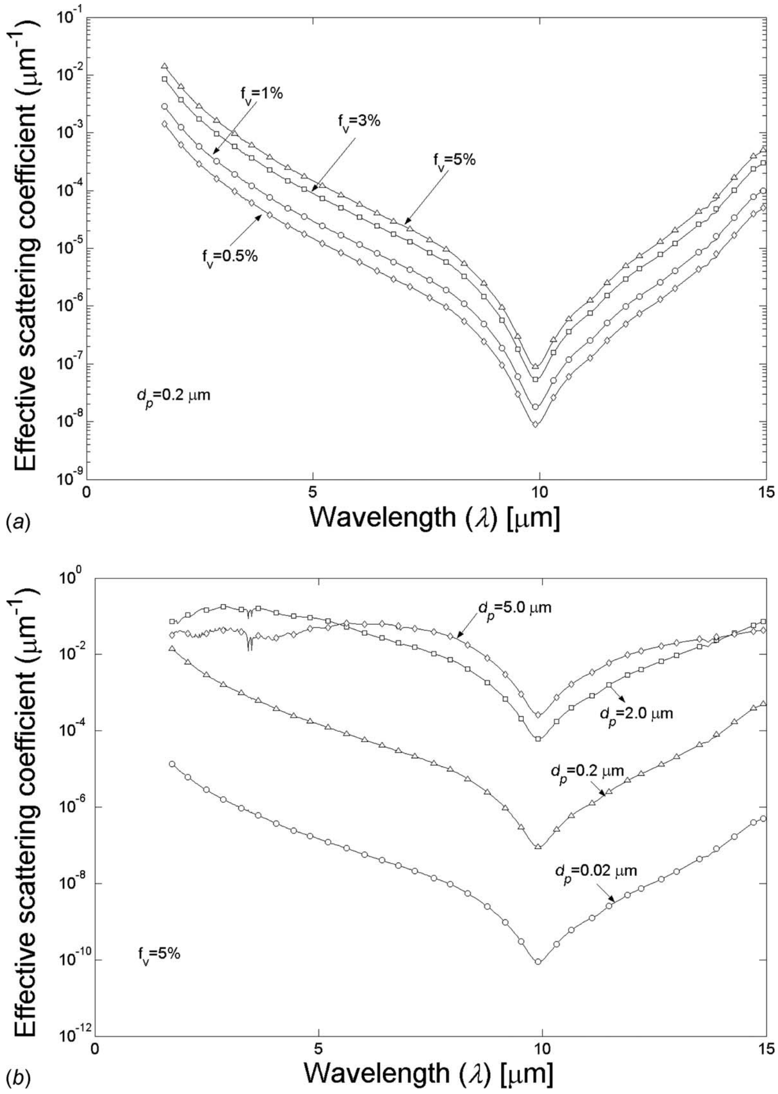

Fig. 7 Effective scattering coefficient of TiO_2 monodisperse particles in polyethylene predicted by FFA (solid lines) and the MS (symbols) when (*a*) *dp*=0.2 μm and *fv*=0.5%, 1.0%, 3%, and 5%, and (*b*) *fv*=5.0% and *dp* =0.02, 0.2, 2, and 5 μm

$$Q_{X,i} = \int_0^\infty Q_{X,i,\lambda} d\lambda \tag{29}$$

$$q_{X,i} = \frac{Q_{X,i}}{\Delta x_i} \tag{30}$$

The REM^2 is an extension of the zone method and is a generalized numerical method for analyzing radiation transfer in nongray and anisotropic participating media with specular and/or diffuse surfaces. The REM^2 can be easily applied to very complicated configurations [12] where the other methods like discrete ordinate method is frequently difficult to apply and the statistical methods like the Monte Carlo method may be extremely time-consuming and the results are subjected to statistical error [12]. The REM^2 has been used in several fields, e.g., in analyses of radiative heat transfer in clouds [19], solar collectors [20–23], fog layers [24], industrial equipment [25], polydisperse water particles [26], and pigmented coatings [1]. Although the approximation methods like two-flux [17,27], three-flux, and four-flux methods [28,29] are applicable to pigmented coating problems with collimated incident light; however, one of the important characteristics of the REM^2 is that both diffuse and collimated irradiations can be applied at the boundaries, enabling us to analyze coating problems illuminated by both collimated and diffuse light from the sun and with different boundary conditions at the substrate.

5.2 Analysis Model and Boundary Conditions. To model a pigmented coating system, we considered a one-dimensional parallel plane system. Figure 6 shows the analysis model and boundary conditions. A 50 μm thin film is divided into 100 elements. Elements 1 and N are taken as boundary elements. The S_{12} approximation of Fiveland is used for direction division [15]. The real part of the complex refractive indices of air (1) and of polyethylene resin (1.5) are assumed for the boundary element 1 and volume elements, respectively. Here, in element 1, specular reflection is produced by the difference between the refractive indices. The specular reflectivity is calculated with Fresnel's equation [15] using the value of the refractive indices mentioned above. The substrate is assumed to be a black body. The temperature of volume elements are assumed to be 0 K. In addition, the temperature of element 1 or element N is assumed to be 0 K for calculating the transmissivity of the substrate emission or reflectivity of the outside irradiation, respectively.

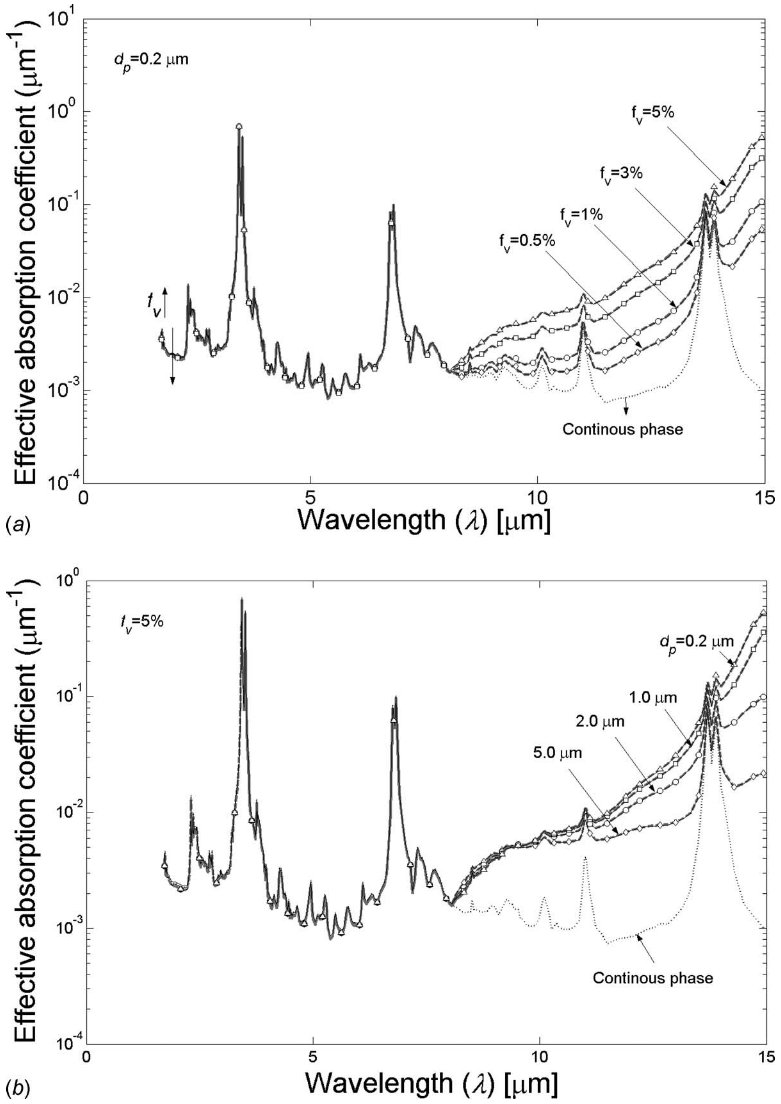

Fig. 8 Effective absorption coefficient of TiO_2 monodisperse particles in polyethylene predicted by the MS (symbols), NFA (dashed lines), and FFA (solid lines) when (*a*) $dp=0.2$ μm and $fv=0.5\%$,1%, 3%, and 5%, and (*b*) $fv=5.0\%$ and $dp=0.2$, 2, 1, and 5 μm

6 Results and Discussion

6.1 Spectral Changes of Effective Coefficients. Effective coefficients were evaluated using Eqs. (20)–(24). Figure 7(*a*) shows the effective scattering coefficient predicted by FFA and NFA for monodisperse TiO_2 particles 0.2 μm in diameter for different volume fractions. The results show that initially, increasing the wavelength causes the scattering coefficient to fall to its minimum value at $\lambda=9.9$ μm. Thereafter, the scattering coefficient increases with increasing wavelength. For a given wavelength the effective scattering coefficient increases with increasing volume fraction. Figure 7(*b*) shows the change in the effective scattering coefficient with wavelengths for particles of different sizes when $fv=5\%$. The results show that the maximum effective scattering coefficient occurs at $\lambda=3.0$ μm for 2.0 μm particles, as is clear from Fig. 7(*b*). There is no significant difference between the effective scattering coefficients predicted by FFA and the MS except for size particles about 10 μm.

Figure 8(*a*) compares the spectral effective absorption coefficient predicted by FFA with that predicted by NFA and the MS for different volume fractions when the particle size is 0.2 μm. In the wavelength range where TiO_2 is nonabsorbing (1.7–8.0 μm), absorption by the medium dominates the effective absorption coefficient and hence the absorption coefficient is close to the absorption coefficient of continuous phase. Increasing the volume fraction of particles decreases the absorption of the composite medium slowly in this wavelength domain. For the wavelengths larger than 8.0 μm where TiO_2 is strongly absorbing, using TiO_2 particles significantly increases the effective absorption coefficient even for small volume fractions. For example, the effective absorption coefficient of a composite medium increases from 0.001 μm^{-1} to 0.1 μm^{-1} at $\lambda=15.0$ μm when the volume fraction is 1%. The maximum absorption coefficient occurs at $\lambda=15.0$ μm, where TiO_2 has its largest absorptivity. The absorption efficiency is affected much more by the absorptivity of TiO_2 particles than by that of the polyethylene matrix. Thus, as seen in Fig. 8(*a*), the FFA, NFA, and MS approaches yield identical results for the effective absorption coefficient. Figure 8(*b*) shows the effective absorption coefficient based on different approaches for different sizes of particles when $fv=5\%$. As seen in this figure, there is no significant difference between the absorption coefficients of different particle sizes in the wavelength range of 1.7–8.0 μm. However, in the wavelength range of 8.0–

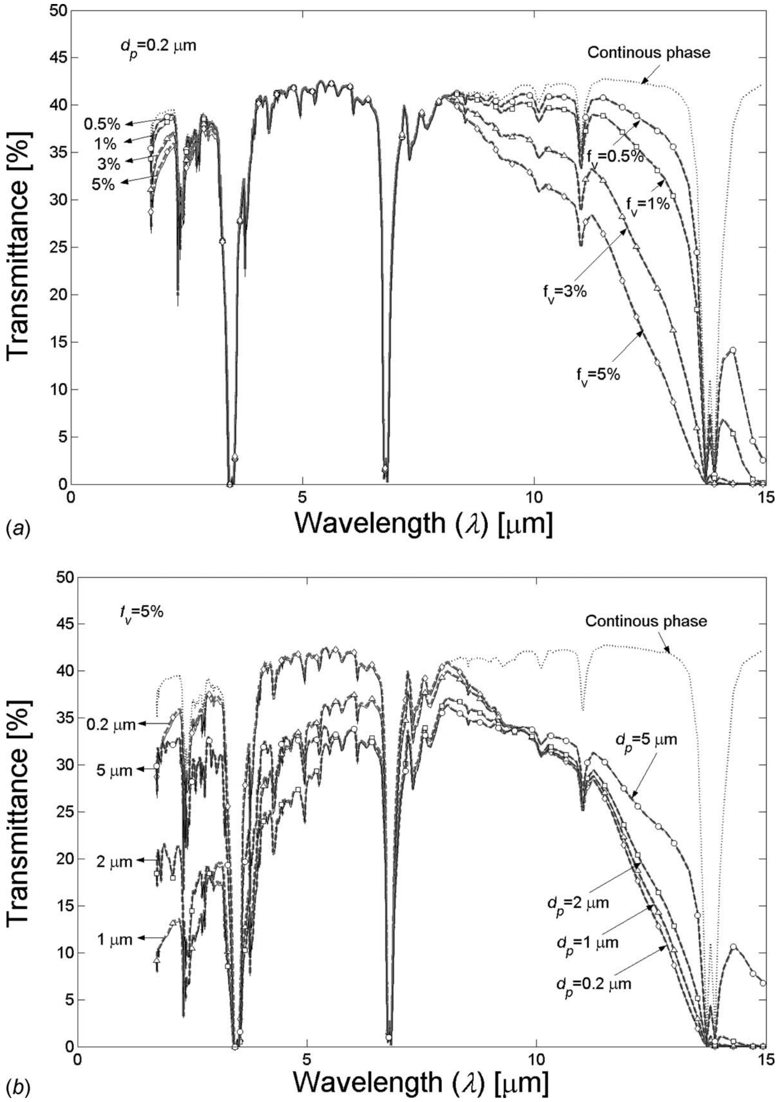

Fig. 9 Spectral hemispherical transmittance of TiO_2 monodisperse particles in polyethylene predicted by model 1 (solid lines), model 2 (dashed lines), and model 3 (symbols) when (*a*) $dp=0.2$ μm and $fv=0.5\%$, 1%, 3%, and 5%, and (*b*) $fv=5.0\%$ and $dp=0.2$, 1, 2, and 5 μm

15.0 μm, a large difference appears between different particle sizes. For a given wavelength in this range, the effective absorption coefficient decreases as the particle size increases. The FFA, NFA, and MS approaches predict similar results for effective scattering and absorption coefficients in the particle size domain and volume fraction range utilized in pigmented coatings.

6.2 Transmittance and Reflectance of IR Wavelengths. The main objective of this study was to investigate the effect of the particle size and volume concentration on spectral transmittance of the IR rays produced by emission from a black substrate and the reflectance at IR wavelengths, which may be due to diffuse solar irradiation or outside emission. Figure 9 shows the hemispherical spectral transmittance for monodisperse particles 0.2 μm in diameter with different volume fractions predicted by the models explained in Sec. 4. The spectral transmittance of the continuous phase is also shown. As is clear from this figure, using TiO_2 pigment particles decreases the transmittance in comparison with the transmittance of polyethylene matrix without any particles. The sudden decrease in transmittance is related to peaks in absorptivity of polyethylene, as seen in Fig. 1. In the wavelength range of 1.7–3.5 μm, transmittance decreases with increasing volume fraction. This can be explained by the increase in the scattering coefficient with increasing volume fraction and small value of asymmetry parameter for this particle size, which causes an increase in the backscattered rays absorbed by the black substrate and hence decreases the transmittance. For the wavelengths from 3.5 μm to 8.0 μm, increasing the volume fraction does not change the transmittance. Again, from $\lambda=8.0$ μm, the transmittance decreases with increasing volume fraction, due to the high absorptivity of TiO_2 particles in this region. As expected, all three models show identical results for transmittance.

Figure 9(*b*) shows the hemispherical transmittance for different particle sizes for $fv=5\%$. In the wavelength range of 1.7–8 μm, increasing the particle size decreases transmittance to its minimum for $dp=0.2$ μm. Thereafter, a further increase in the particle size increases the transmittance. This behavior can be justified by the change in the scattering coefficient with particle size, as seen in Fig. 7(*b*), and the renewed increase in backscattered rays, as explained above. From $\lambda=8.0$ μm, transmittance increases with an increasing particle size due to the decrease in the absorption coefficient, as shown in Fig. 8(*b*).

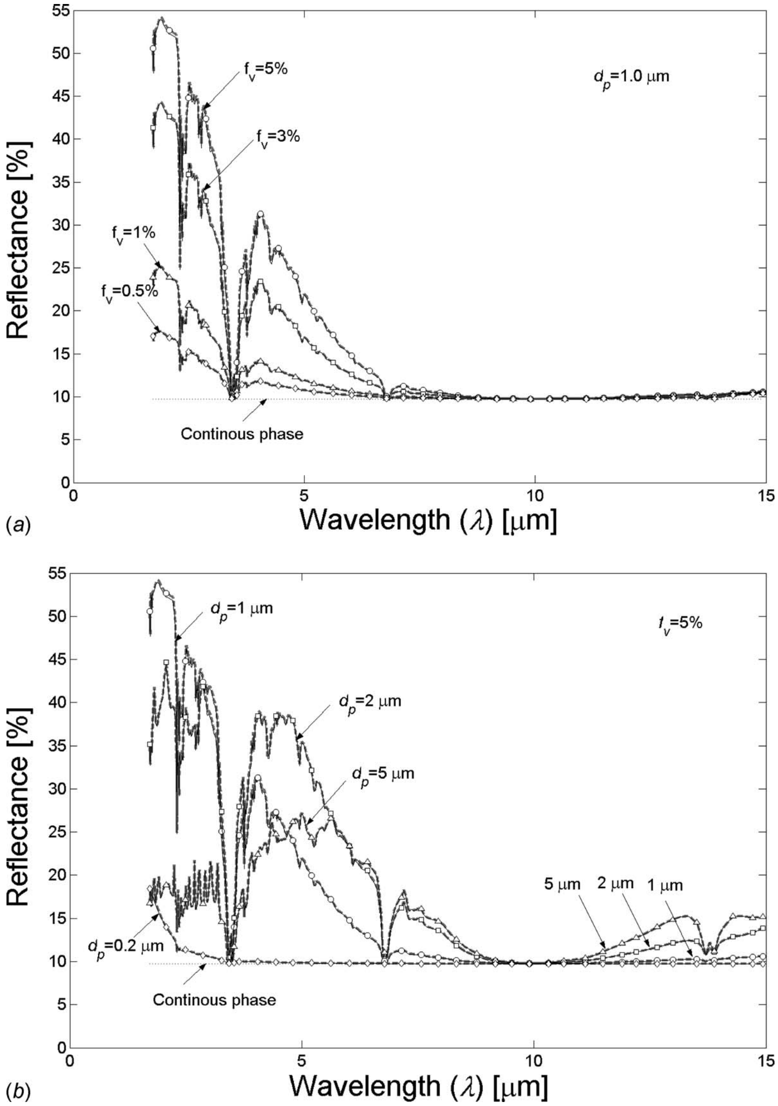

Fig. 10 Spectral hemispherical reflectance of TiO_2 monodisperse particles in polyethylene predicted by model 1 (solid lines), model 2 (dashed lines), and model 3 (symbols) when (*a*) *dp*=1 μm and *fv*=0.5%, 1%, 3%, and 5%, and (*b*) *fv*=5.0% and *dp*=0.2, 1, 2, and 5 μm

Figure 10(*a*) shows the hemispherical spectral reflectance for the polyethylene coating pigmented with 1.0 μm TiO_2 pigment particles with different volume fractions.

Figure 10(*a*) shows the hemispherical spectral reflectance for the polyethylene coating pigmented with 1.0 μm TiO_2 pigment particles with deferent volume fractions. The reflectivity of continuous phase is about 10% independent of wavelength, which can be calculated using Fresnel's equation [15] considering the diffuse incident radiation. By increasing the volume fraction of particles, the reflectivity increases due to increase in scattering coefficient. In the wavelength range of 1.7–8 μm, the change in absorption coefficient with volume fraction is very small, as seen in Fig. 8(*a*), but the increase in scattering coefficient by increasing the volume fraction is significant. Thus in this wavelength range, the variation in reflectance with volume fraction is much more noticeable than the wavelength range of 8–15 μm, as seen in Fig. 10(*a*). In the latter wavelength range, where the TiO_2 is strongly absorbing, with increasing the absorption coefficient, the reflectivity decreases to the limit value of the reflectivity of continuous matrix.

Figure 10(*b*) shows the hemispherical reflectance for different particle sizes for $fv=5\%$. The minimum value of reflectivity occurs at $\lambda=10$ μm where the scattering coefficient is minimum, as discussed in Sec. 6.1. In the wavelength range of 8–15 μm, as seen in Fig. 9(*b*), the absorption coefficient decreases when the size of particle increases. This causes the reflectivity to increase with increasing the size of particles in this wavelength range.

7 Conclusions

The single scattering efficiencies of a TiO_2 particle embedded in an absorbing medium over a wide range of particle sizes (0.01–100 μm) in the wavelength range of 1.7–15 μm were constructed based on the MS, FFA, and NFA. To find the transmittance of IR wavelengths produced by emission from a substrate, we conducted a radiation analysis using the radiation element method by the REM^2. The effective scattering coefficient was defined based on FFA and the MS, while three models based on three approaches were used to determine the effective absorption coefficient. The results based on different models for effective absorption and scattering coefficients as well as the hemispherical transmittance of the TiO_2 pigmented coating were compared for different particle sizes and volume concentrations. The following conclusions can be drawn.

(1) In the wavelength range of 1.7–8 μm, where TiO_2 is nonabsorbing, the particle efficiencies predicted by different approaches are significantly different at the wavelengths where polyethylene is strongly absorbing or when the particles are large. Since the matrix absorptivity is dominant in this region, the disagreement between different models does not affect the value of the effective absorption coefficient. Increasing the volume fraction of particles decreases the absorption coefficient slowly.

(2) For the wavelength from 8 μm to 15 μm, TiO_2 is strongly absorbing. Thus in this range of wavelengths the difference between different models significantly decreases, and hence all three models show identical results for the effective absorption coefficient. The effective absorption coefficient increases with an increasing volume fraction or a decreasing particle size.

(3) The effective scattering coefficients predicted by FFA and the MS are similar. The scattering coefficient increases with increasing volume fraction.

(4) The three approaches yield identical results for hemispherical transmittance in the particle size domain and volume fraction range utilized in pigmented coatings.

(5) Using TiO_2 pigment particles decreases the transmittance of IR rays in comparison with the continuous phase. The transmittance decreases with increasing particle volume fraction, especially for the wavelengths in the absorbing part of TiO_2 (8–15 μm). Increasing the particle size increases the transmittance of this wavelength range.

(6) Using TiO_2 pigment particles increases the reflectance of IR rays in comparison with the continuous phase. In the wavelength range of 1.7–8 μm the reflectivity is much higher than the wavelength range of 8–15 μm. In the absorbing part of TiO_2, the reflectivity increases with increasing the size of particles.

Nomenclature

a = radius of a particle
a_n, b_n, c_n, d_n = Mie coefficient
c = clearance
$d_p=2a$ = diameter of particles
f_v = volume fraction of particles
$F^A_{i,j}$ = absorption view factors
$F^D_{i,j}$ = diffuse scattering view factor
g = asymmetry parameter
Im = imaginary part
I = radiation intensity
k_{eff} = effective absorption coefficient
$m'=n'-ik'$ = complex refractive index of a particle
$m=n-ik$ = complex refractive index of a medium
N = number of radiation elements
P = scattering phase function
Q_s = scattering efficiency
Q_e = extinction efficiency
Q_a = absorption efficiency
Q_m = absorption efficiency of the scatterer contained the same substance as the medium
Q_T = heat transfer rate of the emissive power
Q_J = heat transfer rate of the diffuse radiosity
Q_X = net rate of heat generation
q_X = heat flux for the surface element or divergence of heat flux for the volume element
r = radius of the conceptual integrating sphere
$\mathbf{r}$ = position vector
s = path length through element
$\hat{\mathbf{s}}$, $\hat{\mathbf{s}}'$ = unit direction vector
S_1, S_2 = amplitude function
α = $2\pi ma/\lambda$
β = extinction coefficient or $\beta=2\pi m'a/\lambda$
ε = emissivity
η = $2\pi ka/\lambda$
κ = absorption coefficient of the continuous phase
λ = wavelength
σ_{eff} = effective scattering coefficient
$\Phi(\hat{\mathbf{s}}'\rightarrow\hat{\mathbf{s}})$ = phase function from $\hat{\mathbf{s}}'$ to $\hat{\mathbf{s}}$
ψ, ξ = Riccati–Bessel functions
ω = single scattering albedo
ω^D = diffuse reflectivity of the surface element or the albedo of the volume element
ω^S = specular reflectivity

Superscripts

FF = far field approximation
NF = near field approximation
M = Mie approximation

Subscripts

b = black body
i = element i
j = element j
n = index number
λ = spectral value

References

[1] Baneshi, M., Maruyama, S., and Komiya, A., 2009, "A New Approach to Optimizing Pigmented Coatings Considering Both Thermal and Aesthetic Effects," J. Quant. Spectrosc. Radiat. Transf., **110**, pp. 192–204.
[2] Mundy, W. C., Roux, J. A., and Smith, A. M., 1974, "Mie Scattering by Spheres in an Absorbing Medium," J. Opt. Soc. Am. A, **64**, pp. 1593–1597.
[3] Chylek, P., 1977, "Light Scattering by Small Particles in an Absorbing Medium," J. Opt. Soc. Am., **67**, pp. 561–563.
[4] Yang, P., Gao, B. C., Wiscombe, W. J., Mishchenko, M. I., Platnik, S. E., Huang, H.-L., Baum, B. A., Hu, Y. X., Winker, D. M., Tsay, S.-C., and Park, S. K., 2002, "Inherent and Apparent Scattering Properties of Coated or Uncoated Spheres Embedded in an Absorbing Host Medium," Appl. Opt., **41**, pp. 2740–2759.
[5] Randrianalisoa, J., Baillis, D., and Pilon, L., 2006, "Modeling Radiation Characteristics of Semitransparent Media Containing Bubbles or Particles," J. Opt. Soc. Am. A Opt. Image Sci. Vis., **23**, pp. 1645–1656.
[6] Yin, J., and Pilon, L., 2006, "Efficiency Factors and Radiation Characteristics of Spherical Scatterers in Absorbing Media," J. Opt. Soc. Am. A Opt. Image Sci. Vis., **23**, pp. 2784–2796.
[7] Sudiarta, I. W., and Chylek, P., 2001, "Mie-Scattering Formalism for Spherical Particle Embedded in an Absorbing Medium," J. Opt. Soc. Am. A Opt. Image Sci. Vis., **18**, pp. 1275–1278.
[8] Sudiarta, I. W., and Chylek, P., 2001, "Mie-Scattering Efficiency of a Large Spherical Particle Embedded in an Absorbing Medium," J. Quant. Spectrosc. Radiat. Transf., **70**, pp. 709–714.
[9] Lebedev, A. N., Gartz, M., Kreibig, U., and Stenzel, O., 1999, "Optical Extinction by Spherical Particles in an Absorbing Medium: Application to Composite Absorbing Films," Eur. Phys. J. D, **6**, pp. 365–373.
[10] Lebedev, N., and Stenzel, O., 1999, "Optical Extinction of an Assembly of Spherical Particles in an Absorbing Medium: Application to Silver Clusters in Absorbing Organic Materials," Eur. Phys. J. D, **7**, pp. 83–88.
[11] Fu, Q., and Sun, W., 2001, "Mie Theory for Light Scattering by a Spherical Particle in an Absorbing Medium," Appl. Opt., **40**, pp. 1354–1361.
[12] Maruyama, S., 2004, *Light Energy Engineering*, Yokendo, Tokyo.
[13] Bohren, C. F., and Huffman, D. R., 1983, *Absorption and Scattering of Light by Small Particles*, Wiley, New York.
[14] Palik, E. D., 1991, *Handbook of Optical Constants of Solids*, Academic, San Diego.
[15] Modest, M. F., 2003, *Radiative Heat Transfer*, 2nd ed., Academic, San Diego.
[16] Vargas, W. E., 2000, "Optimization of the Diffuse Reflectance of Pigmented Coatings Taking Into Account Multiple Scattering," J. Appl. Phys., **88**, pp. 4079–4084.
[17] Vargas, W. E., Amador, A., and Niklasson, G. A., 2006, "Diffuse reflectance of TiO_2 Pigmented Paints: Spectral Dependence of the Average Pathlength Parameter and the Forward Scattering Ratio," Opt. Commun., **261**, pp. 71–78.
[18] Dombrovsky, L. A., 2004, "The Propagation of Infrared Radiation in a Semitransparent Liquid Containing Gas Bubbles," High Temp., **42**, pp. 143–150.
[19] Sakurai, S., Maruyama, S., Sakai, S., and Nishikawa, T., 2005, "The Effect of Three-Dimensional Radiative Heat Transfer in Cloud Fields Using the Radiation Element Method," J. Quant. Spectrosc. Radiat. Transf., **93**, pp. 79–87.
[20] Khoukhi, M., Maruyama, S., and Sakai, S., 2007, "Non-Gray Calculation of

Plate Solar Collector With Low Iron Glazing Taking Into Account the Absorption and Emission With a Glass Cover," Desalination, **209**, pp. 156–162.
[21] Khoukhi, M., and Maruyama, S., 2006, "Theoretical Approach of a Flat-Plate Solar Collector Taking Into Account the Absorption and Emission Within Glass Cover Layer," Sol. Energy, **80**, pp. 787–794.
[22] Khoukhi, M., and Maruyama, S., 2005, "Theoretical Approach of a Flat Plate Solar Collector With Clear and Low-Iron Glass Covers Taking Into Account the Spectral Absorption and Emission Within Glass Covers Layer," Renewable Energy, **30**, pp. 1177–1194.
[23] Khoukhi, M., Maruyama, S., and Behnia, M., 2003, "Combined Non-Gray Radiative and Conductive Heat Transfer in Solar Collector Glass Cover," Sol. Energy, **75**, pp. 285–292.
[24] Maruyama, S., Mori, Y., and Sakai, S., 2004, "Nongray Radiative Heat Transfer Analysis in the Anisotropic Scattering Fog Layer Subjected to Solar Irradiation," J. Quant. Spectrosc. Radiat. Transf., **83**, pp. 361–375.
[25] Guo, Z., and Maruyama, S., 2001, "Prediction of Radiative Heat Transfer in Industrial Equipment Using the Radiation Element Method," ASME J. Pressure Vessel Technol., **123**, pp. 530–536.
[26] Maruyama, S., Nakai, H., Sakurai, A., and Komiya, A., 2008, "Evaluation Method for Radiative Heat Transfer in Polydisperse Water Droplets," J. Quant. Spectrosc. Radiat. Transf., **109**, pp. 1–15.
[27] Dombrovsky, L. A., Randrianalisoa, J. H., and Baillis, D., 2007, "Infrared Radiative Properties of Polymer Coatings Containing Hollow Microspheres," Int. J. Heat Mass Transfer, **50**, pp. 1516–1527.
[28] Levinson, R., Berdhal, P., and Akbari, H., 2005, "Solar Spectral Properties of Pigments—Part I: Model for Deriving Scattering and Absorption Coefficients From Transmittance and Reflectance Measurements," Sol. Energy Mater. Sol. Cells, **89**, pp. 319–349.
[29] Azan, V., Lecamp, L., Lebaudy, P., and Bunel, C., 2007, "Simulation of the Photopolymerization Gradient Inside a Pigmented Coating, Influence of TiO_2 Concentration on the Gradient," Prog. Org. Coat., **58**, pp. 70–75.

A Narrow Band-Based Multiscale Multigroup Full-Spectrum *k*-Distribution Method for Radiative Transfer in Nonhomogeneous Gas-Soot Mixtures

Gopalendu Pal

Michael F. Modest[1]
Fellow ASME
e-mail: mfmodest@psu.edu

Department of Mechanical and Nuclear Engineering,
Pennsylvania State University,
University Park, PA 16802

The full-spectrum k-distribution (FSK) approach has become a promising method for radiative heat transfer calculations in strongly nongray participating media, due to its ability to achieve high accuracy at a tiny fraction of the line-by-line (LBL) computational cost. However, inhomogeneities in temperature, total pressure, and component mole fractions severely challenge the accuracy of the FSK approach. The objective of this paper is to develop a narrow band-based hybrid FSK model that is accurate for radiation calculations in combustion systems containing both molecular gases and nongray particles such as soot with strong temperature and mole fraction inhomogeneities. This method combines the advantages of the multigroup FSK method for temperature inhomogeneities in a single species, and the modified multiscale FSK method for concentration inhomogeneities in gas-soot mixtures. In this new method, each species is considered as one scale; the absorption coefficients within each narrow band of every gas scale are divided into M exclusive spectral groups, depending on their temperature dependence. Accurate and compact narrow band multigroup databases are constructed for combustion gases such as CO_2 *and* H_2O*. Sample calculations are performed for a 1D medium and also for a 2D axisymmetric combustion flame. The narrow band-based hybrid method is observed to accurately predict heat transfer from extremely inhomogeneous gas-soot mixtures with/without wall emission, yielding close-to-LBL accuracy.* [DOI: 10.1115/1.4000236]

1 Introduction

Radiative heat transfer is a very important mode of heat transfer in high temperature combustion systems and atmospheric processes. Radiation calculations in participating media can be most accurately performed by the line-by-line (LBL) approach. However, LBL calculations require huge computer resources (both computational time and memory). For accurate and computationally efficient solutions of the radiative transfer equation (RTE), several models have been proposed, applying the concept of reordering the absorption coefficient across the entire spectrum. These include the spectral-line-based weighted-sum-of-gray-gases (SLW) model [1], the absorption distribution function (ADF) method [2], and the full-spectrum *k*-distribution (FSK) method [3]. Although the FSK scheme is exact for radiative calculations in homogeneous media, its application to strongly inhomogeneous emitting-absorbing mixtures, containing both molecular gases and nongray soot particles, challenges its accuracy.

Several advancements to the *k*-distribution method have been proposed to address the shortcomings of the basic FSK scheme. The advanced *k*-distribution methods with their advantages and shortcomings are summarized as follows.

- *Single scale FSK*. 8–10 RTEs. Advantages: Most CPU efficient; accurate for moderately inhomogeneous media. Disadvantages: Inaccurate for strongly inhomogeneous media; problems with mixing of species [3].
- *Narrow band-based single-scale FSK*. 8–10 RTEs. Advantages: Most CPU efficient; mixing of multiphase species; accurate for moderately inhomogeneous media. Disadvantages: Inaccurate for strongly inhomogeneous media [4].
- *Fictitious gas*. $(8-10)^N$ RTEs. Advantages: Accurate for mixing (gas only) temperature and species inhomogeneity. Disadvantages: Inaccurate for multiphase mixing; computationally expensive [2].
- *Multiscale FSK (MSFSK)*. $N\times(8-10)$ RTEs. Advantages: Accurate for mixing and species (gas only) inhomogeneity. Disadvantages: Inaccurate for strong temperature inhomogeneity and multiphase mixing [5].
- *Multigroup FSK (MGFSK)*. $M\times(8-10)$ RTEs. Advantages: Accurate for temperature inhomogeneity in a single gas. Disadvantages: No mixing of species; inaccurate for species inhomogeneity [6].
- *Narrow band-based MSFSK*. $N\times(8-10)$ RTEs. Advantages: Better accuracy for mixing of gases than MSFSK; potential for multiphase mixing. Disadvantages: Inaccurate for strong temperature inhomogeneity [7].
- *Multiscale multigroup FSK (MSMGFSK)*. $N\times M\times(8-10)$ RTEs. Advantages: Accurate for general inhomogeneity problems in gas mixtures. Disadvantages: Inaccurate for multiphase mixing [8].
- *Narrow band-based modified MSFSK*. $N\times(8-10)$ RTEs. Advantages: Accurate for multiphase mixing and species in-

---

[1] Corresponding author.

Contributed by the Heat Transfer Division of ASME for publication in the JOURNAL OF HEAT TRANSFER. Manuscript received November 26, 2008; final manuscript revised April 10, 2009; published online December 9, 2009. Assoc. Editor: Yogesh Jaluria.

homogeneity. Disadvantages: Inaccurate for strong temperature inhomogeneity [9].

Soot radiation constitutes an important part of radiation calculations in luminous flames. Because of the difficulties in soot modeling, soot radiation in combustion flames was commonly treated as gray [10]. Nongray soot with gas mixtures was investigated by Solovjov and Webb [11] using the SLW method, by Wang et al. [12] using the single-scale FSK method, and by Pal and Modest [9] using the narrow band-based modified MSFSK method. The modified MSFSK method has been found to produce high accuracy for isothermal multiphase mixtures with species concentration inhomogeneities. However, the modified MSFSK method fails in the presence of strong temperature inhomogeneities.

FSK calculations are very accurate and time efficient, provided that the required full-spectrum *k*-distributions are known, which are tedious to compile from spectroscopic databases. Wang and Modest [13] compiled a high accuracy, compact database of narrow band *k*-distributions for CO_2 and H_2O. Full-spectrum multigroup databases (with 32 groups for each species) were constructed by Zhang and Modest [6] for carbon dioxide and water vapor. It has been reported that close-to-LBL accuracy can be achieved by considering only four such groups. Recently, Pal and Modest [9] constructed a more accurate and compact full-spectrum multigroup database containing four groups for each species with spectral absorption coefficients for water vapor calculated from HITEMP 2000, and for carbon dioxide from CDSD-1000, which is considered more reliable [8]. The full-spectrum multigroup databases can be used for nonhomogeneous mixtures of gases only. Hence, narrow band multigroup databases are needed for the important combustion gases for accurate mixing of gases and nongray soot at the narrow band level.

In the present work, we have extended the previous (full-spectrum-based) hybrid MSMGFSK method to a narrow band-based hybrid MSMGFSK method, to allow incorporation of nongray soot into the gas mixture. In this method, soot is treated as a single-group scale, while the combustion gases, such as CO_2 and H_2O, can have a maximum of four scalable groups each. An accurate and compact narrow band multigroup database has been constructed by grouping the absorption coefficients within each narrow band of CO_2 and H_2O into four groups, with absorption coefficients of H_2O calculated from HITEMP 2000, and for CO_2 from CDSD-1000. Wall emission is treated within the soot scale as was done in the modified MSFSK method [9]. First, a brief mathematical discussion of the narrow band-based MSMGFSK method is presented here, followed by a discussion of the construction of the narrow band multigroup database. Sample calculations are performed for a 1D medium with step changes in species concentration and temperature with/without wall emission, and also for a 2D axisymmetric jet flame. For all cases, results are compared with FSK, MSFSK, and LBL calculations.

2 The Narrow Band-Based MSMGFSK Approach

A brief mathematical derivation of the narrow band-based MSMGFSK method is presented here. A participating medium containing molecular gases and nongray soot is considered. Scattering from the medium is assumed to be gray. The radiative transfer equation (RTE) for such a medium can be written as [14]

$$\frac{dI_\eta}{ds} = \kappa_\eta(\underline{\phi})I_{b\eta} - (\kappa_\eta(\underline{\phi}) + \sigma_s)I_\eta + \frac{\sigma_s}{4\pi}\int_{4\pi} I_\eta(\hat{s}')\Phi(\hat{s},\hat{s}')d\Omega' \tag{1}$$

which is subject to the boundary condition

$$\text{at } s=0: \quad I_\eta = \epsilon I_{b\eta w} + \frac{1-\epsilon}{\pi}\int_{2\pi} I_\eta|\hat{n}\cdot\hat{s}|d\Omega \tag{2}$$

Here, I_η is the spectral radiative intensity, κ_η is the absorption coefficient, $I_{b\eta}$ is the spectral blackbody intensity (or Planck function), σ_s is the gray scattering coefficient, Φ is the scattering phase function, and wavenumber η is the spectral variable. The vector $\underline{\phi}$ contains state variables that affect κ_η, which include temperature T, total pressure P, and gas mole fractions $\underline{x}$: $\underline{\phi} = (P,T,\underline{x})$. The boundary wall has been assumed to be gray and diffuse with ϵ being the emittance, $\hat{n}$ being the surface normal, $\hat{s}$ being the unit direction vector of incoming ray radiation, and Ω being the solid angle.

The mixture's spectral absorption coefficient κ_η is first separated into contributions from $N-1$ component gases and soot, and the radiative intensity I_η is also broken up accordingly

$$\kappa_\eta = \sum_{n=1}^{N} \kappa_{n\eta}, \quad I_\eta = \sum_{n=1}^{N} I_{n\eta} \tag{3}$$

The RTE in Eq. (1) is transformed into N component RTEs, one for each species or scale. For each scale, this leads to

$$\frac{dI_{n\eta}}{ds} = \kappa_{n\eta}(\underline{\phi})I_{b\eta} - (\kappa_\eta(\underline{\phi}) + \sigma_s)I_{n\eta} + \frac{\sigma_s}{4\pi}\int_{4\pi} I_{n\eta}(\hat{s}')\Phi(\hat{s},\hat{s}')d\Omega', \quad \text{for } n=1,\ldots,N \tag{4}$$

The intensity $I_{n\eta}$ is due to the emission by the *n*-th scale, but subject to absorption by all the scales. Now the spectral locations of the *n*-th gas absorption coefficients $\kappa_{n\eta}$, along with the *n*-th gas scale's radiative intensity $I_{n\eta}$, are sorted into M exclusive groups, that is

$$\kappa_{n\eta} = \sum_{m=1}^{M_n} \kappa_{nm\eta}, \quad I_{n\eta} = \sum_{m=1}^{M_n} I_{nm\eta} \quad \text{for } n=1,\ldots,N-1 \tag{5}$$

Considering the soot scale as a single-group scale, the RTE for the *m*-th group of the *n*-th gas scale is transformed into

$$\frac{dI_{nm\eta}}{ds} = \kappa_{nm\eta}(\underline{\phi})I_{b\eta} - (\kappa_\eta(\underline{\phi}) + \sigma_s)I_{nm\eta} + \frac{\sigma_s}{4\pi}\int_{4\pi} I_{nm\eta}(\hat{s}')\Phi(\hat{s},\hat{s}')d\Omega', \text{ for } n=1,\ldots,N-1; \quad m=1,\ldots,M_n(\text{gas scales}) \tag{6}$$

Note that the intensity $I_{nm\eta}$ is due to the emission by the *m*-th group of the *n*-th gas species (the *nm*-th group), but subject to absorption by all groups of the other gases, soot (single-group scale), and its own group. There is no overlap among groups of a single species and, therefore, there is no emission over wavenumbers where $\kappa_{nq\eta}(q \neq m)$ absorbs. Thus, in Eq. (6)

$$\kappa_\eta = \kappa_{nm\eta} + \sum_{\substack{l=1\\ l\neq n}}^{N} \sum_{q=1}^{M_l} \kappa_{lq\eta} \tag{7}$$

As was done in the modified MSFSK formulations [9], radiation from soot and from wall emission are combined into a single scale, due to their continuous nature. When wall emissions is added to the soot scale, Eq. (2) can be written as at $s=0$:

$$\begin{cases} I_{nm\eta} = \dfrac{1-\epsilon}{\pi}\displaystyle\int_{2\pi} I_{nm\eta}|\hat{n}\cdot\hat{s}|d\Omega & \text{for } n=1,\ldots,N-1; \\ & m=1,\ldots,M_n(\text{gas scales}) \\ I_{s\eta} = \epsilon I_{b\eta w} + \dfrac{1-\epsilon}{\pi}\displaystyle\int_{2\pi} I_{s\eta}|\hat{n}\cdot\hat{s}|d\Omega & \text{for } n=s=N(\text{soot scale}) \end{cases} \tag{8}$$

where the subscript s denotes the soot scale.

We now apply the FSK scheme [15] to each RTE. This process is demonstrated for the RTEs of each group of the gas scales. For the soot scale, i.e., the N-th scale ($n=s$), the same procedure needs to be followed for a scale with a single group, $M_s=1$. First, Eq. (6) is multiplied by Dirac's delta function $\delta(k_{nm}-\kappa_{nm\eta}(\underline{\phi}_0))$, followed by division with

$$f_{nm}(T_0,\underline{\phi}_0,k_{nm}) = \frac{1}{I_b(T_0)}\int_0^\infty I_{b\eta}(T_0)\,\delta(k_{nm}-\kappa_{nm\eta}(\underline{\phi}_0))d\eta \tag{9}$$

where $\underline{\phi}_0$ and T_0 refer to a reference state, and k_{nm} is the reordered absorption coefficient variable of the nm-th group of a gas scale. The resulting equation is then integrated over the entire spectrum, leading to

$$\begin{gathered}\frac{dI_{nmg}}{ds} = k_{nm}a_{nm}I_b - \lambda_{nm}I_{nmg} + \frac{\sigma_s}{4\pi}\int_{4\pi} I_{nmg}(\hat{s}')\Phi(\hat{s},\hat{s}')d\Omega' \\ \begin{array}{ll} \text{for } n=1,\ldots,N-1; & m=1,\ldots,M_n \\ \text{for } n=s; & m=1(nm=s) \end{array}\end{gathered} \tag{10}$$

where

$$I_{nmg} = \int_0^\infty I_{nm\eta}\delta(k_{nm}-\kappa_{nm\eta}(\underline{\phi}_0))d\eta \,/\, f_{nm}(T_0,\underline{\phi}_0,k_{nm}) \tag{11}$$

The cumulative k-distribution g is the nondimensional spectral variable of the reordered spectrum, and for the m-th group of the n-th scale [8]

$$g_{nm} = \int_0^{k_{nm}} f_{nm}(T_0,\underline{\phi}_0,k)dk \tag{12}$$

a_m is the stretching factor for the m-th group of the n-th scale [8], and is calculated from

$$a_{nm} = \frac{f_{nm}(T,\underline{\phi}_0,k_{nm})}{f_{nm}(T_0,\underline{\phi}_0,k_{nm})} \tag{13}$$

and, finally, λ_{nm} is the overlap parameter of the m-th group of the n-th scale [8] with all other scales, and can be written as

$$\begin{aligned}\lambda_{nm}I_{nmg} &= k_{nm}I_{nmg} \\ &\quad + \frac{\int_0^\infty\left(\sum_{l\neq n}\sum_{q=1}^{M_l}\kappa_{lq\eta}(\underline{\phi})\right)I_{nm\eta}\delta(k_{nm}-\kappa_{nm\eta}(\underline{\phi}_0))d\eta}{f_{nm}(T_0,\underline{\phi}_0,k_{nm})}\end{aligned} \tag{14}$$

Similarly, FSK reordering is performed on the boundary condition(s) with respect to $\kappa_{nm\eta}(\underline{\phi}_0)$ for each group of the gas scales, and $\kappa_{s\eta}(\underline{\phi}_0)$ for the soot scale, which results in

at $s=0$:

$$\begin{cases} I_{nmg} = \dfrac{1-\epsilon}{\pi}\displaystyle\int_{2\pi} I_{nmg}|\hat{n}\cdot\hat{s}|d\Omega & \text{for } n=1,\ldots,N-1; \\ & m=1,\ldots,M_n \\ I_{sg} = \epsilon a_w I_{bw} + \dfrac{1-\epsilon}{\pi}\displaystyle\int_{2\pi} I_{sg}|\hat{n}\cdot\hat{s}|d\Omega & \text{for } n=s=N \end{cases} \tag{15}$$

where a_w is the stretching factor for wall emission defined as

$$a_w = \frac{f_s(T_w,\underline{\phi}_0,k_s)}{f_s(T_0,\underline{\phi}_0,k_s)} \tag{16}$$

T_w is the wall temperature, which may be different from the medium temperature T.

Finally, the total radiative intensity is found by integrating each group over spectral space g, followed by summing over all groups and scales as

$$I = \sum_{n=1}^{N}\sum_{m=1}^{M_n} I_{nm} = \sum_{n=1}^{N}\sum_{m=1}^{M_n}\int_{g_{\min}}^{1} I_{nmg}dg_{nm} \tag{17}$$

The second term on the right hand side of Eq. (10) is due to the overlap of the absorption coefficient of the m-th group of the n-th scale $\kappa_{nm\eta}$ with those of all other scales, which occurs over a part of the spectrum. The overlap parameter is a function of the state variables, as well as of the k-g distributions. Here we follow the approximate approach for overlap parameter calculations, as was done in the modified MSFSK method for gas-soot mixtures, assuming that the intensity emanating from a homogeneous nonscattering layer bounded by black walls is predicted exactly [9].

In Eq. (10), the reordering is performed in terms of absorption coefficients $\kappa_{nm\eta}$, and the interaction between $\kappa_{nm\eta}$ and κ_η during the reordering process is lumped into the overlap parameter λ_{nm}. The reordering can also be performed in terms of κ_η, which, for a nonscattering homogeneous layer at temperature T, and bounded by a black wall at temperature T_w, leads to

$$\frac{dI^*_{nmg}}{ds} = \frac{k^*_{nm}I_b}{f(T,\underline{\phi},k)} - kI^*_{nmg}\begin{cases}\text{for } n=1,\ldots,N-1; & m=1,\ldots,M_n \\ \text{for } n=s; & m=1(nm=s)\end{cases} \tag{18}$$

where

$$f(T,\underline{\phi},k) = \frac{1}{I_b(T)}\int_0^\infty I_{b\eta}(T)\,\delta(k-\kappa_\eta(\underline{\phi}))d\eta \tag{19}$$

$$I^*_{nmg} = \int_0^\infty I_{nm\eta}\delta(k-\kappa_\eta(\underline{\phi}))d\eta/f(T,\underline{\phi},k) \tag{20}$$

$$k^*_{nm} = \frac{1}{I_b}\int_0^\infty I_{b\eta}(T)\kappa_{nm\eta}\delta(k-\kappa_\eta(\underline{\phi}))d\eta \tag{21}$$

Reordering the boundary condition(s) with respect to $\kappa_\eta(\underline{\phi})$ leads to at $s=0$:

$$\begin{cases} I^*_{nmg} = \dfrac{1-\epsilon}{\pi}\displaystyle\int_{2\pi} I^*_{nmg}|\hat{n}\cdot\hat{s}|d\Omega & \text{for } n=1,\ldots,N-1; \\ & m=1,\ldots,M_n \\ I^*_{sg} = \epsilon\dfrac{f(T_w,\underline{\phi},k)}{f(T,\underline{\phi},k)}I_{bw} + \dfrac{1-\epsilon}{\pi}\displaystyle\int_{2\pi} I^*_{sg}|\hat{n}\cdot\hat{s}|d\Omega & \text{for } n=s=N \end{cases} \tag{22}$$

The solutions to Eqs. (10), (15), (18), and (22) for a homogeneous layer at temperature T bounded by black walls can be obtained analytically, and the total exiting intensities from each group of the gas scales from a layer of thickness L are

$$\begin{aligned} I_{nm} &= \int_0^1 I_{nmg}dg \\ &= \int_0^\infty \frac{k_{nm}}{\lambda_{nm}} I_b[1-\exp(-\lambda_{nm}L)]f_{nm}(T,\underline{\phi},k_{nm})dk_{nm} \\ &\quad \text{for } n=1,\ldots,N-1; \quad m=1,\ldots,M_n \end{aligned} \tag{23}$$

and

$$\begin{aligned} I^*_{nm} = \int_0^1 I^*_{nmg}dg = \int_0^\infty \frac{k^*_{nm}}{k} I_b[1-\exp(-kL)]dk, \\ \text{for } n=1,\ldots,N-1; \quad m=1,\ldots,M_n \end{aligned} \tag{24}$$

respectively. Since wall emission is added to the soot scale, the total exiting intensity from the soot scale from a layer of thickness L is

$$\begin{aligned} I_s = \int_0^1 I_{sg}dg = \int_0^\infty a_w I_{bw}\exp(-\lambda_s L)f_s(T,\underline{\phi},k_s)dk_s \\ + \int_0^\infty \frac{k_s}{\lambda_s} I_b[1-\exp(-\lambda_s L)]f_s(T,\underline{\phi},k_s)dk_s = I_{s1}+I_{s2} \end{aligned} \tag{25}$$

where I_{s1} is shorthand for the first term (wall emission), and I_{s2} for the second term (medium emission), and

$$\begin{aligned} I^*_s = \int_0^1 I^*_{sg}dg = \int_0^\infty I_{bw}f(T_w,\underline{\phi},k)\exp(-kL)dk \\ + \int_0^\infty \frac{k^*}{k}I_b[1-\exp(-kL)]dk = I^*_{s1}+I^*_{s2} \end{aligned} \tag{26}$$

where, again, I^*_{s1} (wall emission) and I^*_{s2} (medium emission) abbreviates the first and second term, respectively.

The spectrally integrated intensity I_{nm} should be equal to I^*_{nm} (for each group of the gas scales), and I_s should be equal to I^*_s (for the soot scale). For the m-th group of the n-th gas scale, this requirement leads to

$$\lambda_{nm} = k \quad \text{and} \quad k_{nm}f_{nm}(T,\underline{\phi},k_{nm})dk_{nm} = k^*_{nm}(k)dk \tag{27}$$

Equation (27) provides the relationship between λ_{nm} and k_{nm} that is required to solve Eq. (10). One convenient way of determining λ_{nm} is using the relationship [5]

$$\int_0^{k_{nm}} k_{nm}f_{nm}(T,k_{nm})dk_{nm} = \int_0^{k=\lambda_{nm}} k^*_{nm}(k)dk \tag{28}$$

For the soot scale, we use the strategy that the overlap parameter λ_s is determined by equating medium emission I_{s2} and I^*_{s2}, as was done in the modified MSFSK formulation [9]. To equate the overall intensity for the soot scale, the wall emissions I_{s1} and I^*_{s1} must also be equal. The expression for I^*_{s1} is rearranged, employing the approximation for λ_s, as

$$I^*_{s1} = \int_0^\infty \frac{f(T_w,\underline{\phi},\lambda_s)}{k^*_s(T,\underline{\phi},\lambda_s)}k_s I_{bw}\exp(-\lambda_s L)f_s(T,\underline{\phi},k_s)dk_s \tag{29}$$

By comparison with the expression for I_{s1} in Eq. (24), it is clear that if

$$a_w(k_s) = \frac{f(T_w,\underline{\phi},\lambda_s)}{k^*_s(T,\underline{\phi},\lambda_s)}k_s, \quad \lambda_s = \lambda_s(k_s) \tag{30}$$

then I_{s1} is equal to I^*_{s1}.

3 Evaluation of Overlap Parameter

For efficient calculations, the overlap parameter needs to be available from a database of narrow band multigroup (NBMG) k-distributions for individual gas species. The advantages of using NBMG k-distributions are: (1) groups within each narrow band are scalable, and hence can be combined to obtain coarser k-g distributions; (2) the use of NBMG k-distributions of individual gas species allows the inclusion of nongray absorbing particles in the participating medium [4]; (3) mixing of k-g distributions is more accurate when performed at the narrow band level, as compared with the full-spectrum level; and (4) since the wavenumbers within a narrow band are grouped according to their temperature dependence, NBMG k-distributions can be used to construct full-spectrum multigroup k-g distributions, which are known to be more accurate for temperature inhomogeneities in multiphase mixtures.

For the m-th group of the n-th gas scale, substituting Eq. (21), the right hand side (RHS) of Eq. (28) may be rewritten in terms of a narrow band-based k^*_{nm}

$$\begin{aligned} \text{RHS} &= \sum_{i=1}^{N_{\text{nb}}} \frac{I_{\text{bi}}}{I_b}\int_0^{k=\lambda_{nm}} k^*_{nm,i}(k)dk \\ &= \int_0^{k=\lambda_{nm}} \sum_{i=1}^{N_{\text{nb}}} \frac{I_{\text{bi}}}{I_b}\frac{1}{\Delta\eta}\int_{\Delta\eta} \kappa_{nm\eta}\delta(k-\kappa_\eta)d\eta dk \end{aligned} \tag{31}$$

where $k^*_{nm,i}$ is the narrow band counterpart of k^*_{nm}, N_{nb} is the number of narrow bands comprising the entire spectrum, and the narrow band integrated Planck function I_{bi} is defined as

$$I_{\text{bi}} = \int_{\Delta\eta_i} I_{b\eta}d\eta \tag{32}$$

As always, in the narrow band-based k-distribution approach, we have assumed that $I_{b\eta}$ is constant over $\Delta\eta_i$ and can be approximated by $I_{\text{bi}}/\Delta\eta_i$.

In order to evaluate the integrals involving $k^*_{nm,i}$ in Eq. (31) in terms of NBMG k-distributions, we consider the quantity Q_{nm} as

$$Q_{nm} = \frac{1}{\Delta\eta}\int_{\Delta\eta} \kappa_{nm\eta}\exp(-\kappa_\eta L)d\eta \tag{33}$$

for the i-th narrow band. Physically, Q_{nm} is related to emission from the m-th group of the n-th scale for the given narrow band i, attenuated over path L by the entire gas mixture. Q_{nm} can be rewritten as

$$\begin{aligned} Q_{nm} &= \frac{1}{\Delta\eta}\int_{\Delta\eta} \kappa_{nm\eta}\int_0^\infty \exp(-kL)\delta(k-\kappa_\eta)dkd\eta \\ &= \int_0^\infty k^*_{nm,i}\exp(-kL)dk = \mathcal{L}(k^*_{nm,i}) \end{aligned} \tag{34}$$

i.e., Q_{nm} is the Laplace transform of $k^*_{nm,i}$.

Previously, in the modified MSFSK development [9], it was shown that, (1) on a narrow band basis, the spectral behavior of different species is essentially statistically uncorrelated, and (2) the soot absorption coefficient is approximately constant across each narrow band [4,7,9]. Since the wavenumbers within a narrow band are placed into exclusive spectral groups, the assumption of statistical uncorrelatedness in spectral behavior between a group (within a narrow band) of one gas species and the narrow band of another gas species still holds. With this assumption, Q_{nm} can be written as (after applying the k-distribution method [9])

$$Q_{nm} \approx \int_{g_{nm,i}=0}^{1} \prod_{l\neq s,n}^{N} \left(\int_{g_{l,i}=0}^{1} k_{nm,i} \exp\left(-\sum_{l\neq s,n} k_{l,i}L - k_{nm,i}L - \overline{k_{s,i}}L \right) dg_{l,i} \right) dg_{nm,i} \tag{35}$$

where $\overline{k}_{s,i}$ is the narrow band average value of the soot absorption coefficient.

Equating Eqs. (34) and (35), we have

$$\mathcal{L}(k^{*}_{nm,i}) \approx \int_{g_{nm,i}=0}^{1} \prod_{l\neq s,n}^{N} \left(\int_{g_{l,i}=0}^{1} k_{nm,i} \exp\left(-\sum_{l\neq s,n} k_{l,i}L - k_{nm,i}L - \overline{k_{s,i}}L \right) dg_{l,i} \right) dg_{nm,i} \tag{36}$$

Using the integral property of the Laplace transform and then taking the inverse, we obtain

$$\int_{0}^{k=\lambda_{nm}} k^{*}_{nm,i}(k)dk \approx \int_{g_{nm,i}=0}^{1} \prod_{l\neq s,n}^{N} \left(\int_{g_{l,i}=0}^{1} k_{nm,i} H\left(\lambda_{nm} - \sum_{l\neq s,n} k_{l,i} - k_{nm,i} - \overline{k_{s,i}} \right) dg_{l,i} \right) dg_{nm,i} \tag{37}$$

where H is the Heaviside step function.

The LHS of Eq. (28) is also readily expressed in terms of narrow band k-distributions for the m-th group of n-th gas scale as

$$\begin{aligned} \text{LHS} &= \int_{0}^{k_{nm}} k_{nm} \frac{1}{I_b} \int_{0}^{\infty} I_{b\eta}\delta(k_{nm} - \kappa_{nm\eta}) d\eta dk_{nm} \\ &= \sum_{i=1}^{N_{\text{nb}}} \frac{I_{\text{bi}}}{I_b} \int_{0}^{k_{nm}} k_{nm} \frac{1}{\Delta\eta_i} \int_{\Delta\eta_i} \delta(k_{nm} - \kappa_{nm\eta}) d\eta dk_{nm} \\ &= \sum_{i=1}^{N_{\text{nb}}} \frac{I_{\text{bi}}}{I_b} \int_{0}^{g_{nm,i}(k_{nm})} k_{nm,i} dg_{nm,i} \end{aligned} \tag{38}$$

Equating the LHS and RHS, we obtain a generic expression for the determination of the overlap parameter λ_{nm} of the m-th group of the n-th gas scale, based on NB k-distributions of individual gas species as

$$\begin{aligned} &\sum_{i=1}^{N_{\text{nb}}} \frac{I_{\text{bi}}}{I_b} \int_{0}^{g_{nm,i}(k_{nm})} k_{nm,i} dg_{nm,i} \\ &\quad = \sum_{i=1}^{N_{\text{nb}}} \frac{I_{\text{bi}}}{I_b} \int_{g_{nm,i}=0}^{1} \prod_{l\neq s,n}^{N} \left(\int_{g_{l,i}=0}^{1} k_{nm,i} H\left(\lambda_{nm} - \sum_{l\neq s,n} k_{l,i} - k_{nm,i} - \overline{k_{s,i}} \right) dg_{l,i} \right) dg_{nm,i}; \quad \text{for } \begin{array}{l} n = 1, \ldots, N-1, \\ m = 1, \ldots, M_n (\text{gas scales}) \end{array} \end{aligned} \tag{39}$$

The integrals in Eq. (39) can be evaluated efficiently, based on the NBMG database, as outlined by Wang and Modest [7]. The overlap parameter for soot, being treated as a single-group scale, can be obtained from the modified MSFSK formulation of Pal and Modest [9].

4 Evaluation of Modified Wall Stretching Factor

Incorporation of wall emission into the soot scale, Eq. (15), introduces the wall stretching factor a_w [9]. It was demonstrated by Pal and Modest [9] that MSFSK calculations using the modified a_w from Eq. (30) are more accurate, as compared with calculations using the direct a_w from Eq. (16), because only the modified a_w recovers the LBL results for homogeneous media with arbitrary boundary wall temperatures. For the calculation of the modified a_w in the present narrow band-based hybrid method, the same approach was considered as outlined in the modified MSFSK formulations [9].

5 NBMG Database Construction

Accurate and compact databases of NBMG k-distributions are constructed as part of this work. The spectral absorption coefficients for water vapor are calculated from HITEMP 2000, and for carbon dioxide from CDSD-1000. The resulting NBMG k-g distributions of the combustion gases are stored for various values of total pressure, local gas temperature, and species mole fraction, as described in Ref. [13], but now for four groups.

The wavenumbers within each narrow band of the gas species in 0.01 cm^{-1} intervals are placed into four exclusive spectral groups according to the temperature dependence of the absorption coefficients. Details of the grouping of wavenumbers can be obtained from Ref. [8]. Once all spectral locations are grouped, the narrow band k-g distributions are calculated for each group and each gas species. Details of the k-g distribution construction can be obtained from Ref. [13]. After the calculation of the initial k-distributions, data compaction is performed using a Gaussian quadrature scheme with fixed g-values, as outlined by Wang and Modest [13].

To obtain the k-distribution for an arbitrary state, interpolation is needed between precalculated states stored in the database. For a single gas species, the k-distribution is specified by total pressure (P), local gas temperature (T), and mole fraction (x). Hence, three-dimensional interpolation in (P,T,x) is required. In order to achieve acceptable accuracy with small computational cost, a 1D spline interpolation is used for T, and bilinear interpolation for P-$\underline{x}$ [13].

The newly constructed NBMG database is scalable, i.e., for faster computation, the groups can be combined to obtain coarser groups, both at the narrow band and full-spectrum level. The narrow band k-g distributions of the combined group n from finer groups m can be calculated [6,8] as

$$1 - g_{n,i}(k) = \sum_{m} (1 - g_{m,i}(k)) \tag{40}$$

where $g_{n,i}$ and $g_{m,i}$ are the cumulative k-distributions of the i-th narrow band for the same k-values of the combined groups and original groups, respectively [6].

6 Sample Calculations

6.1 1D Problem. Sample calculations were performed for a 1D medium, containing emitting-absorbing CO_2–H_2O–N_2 gas mixtures, as well as soot, confined between cold black walls. The mixture consists of two different homogeneous layers (denoted as left and right layers/column) adjacent to each other at a total pressure of 1 bar. The left layer has a fixed width of 50 cm. The width of the right layer was varied in the calculations. The radiative heat flux leaving from the right layer (i.e., radiative flux at the right wall) was calculated using the LBL method, the single-scale FSK method, the modified MSFSK method, and the present narrow band-based MSMGFSK method (using two and four groups).

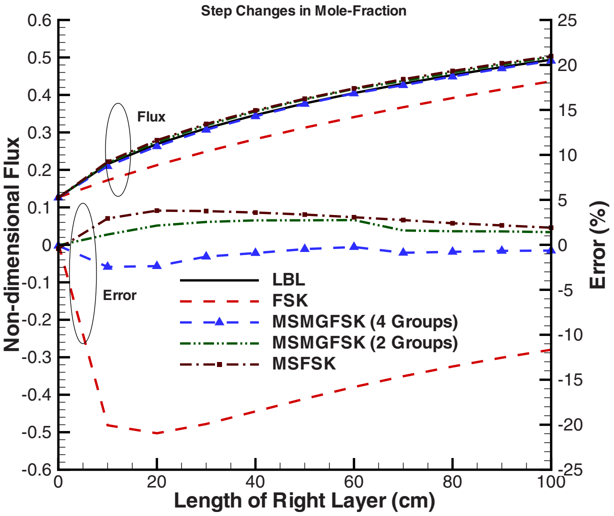

Fig. 1 Nondimensional heat flux leaving an inhomogeneous slab at a total pressure of 1 bar with step changes in mole fraction: The left layer contains 20% CO_2, 2% H_2O, and no soot, and the right layer contains 2% CO_2, 20% H_2O, and 0.1 ppm soot; both layers are at a constant temperature of 1000 K

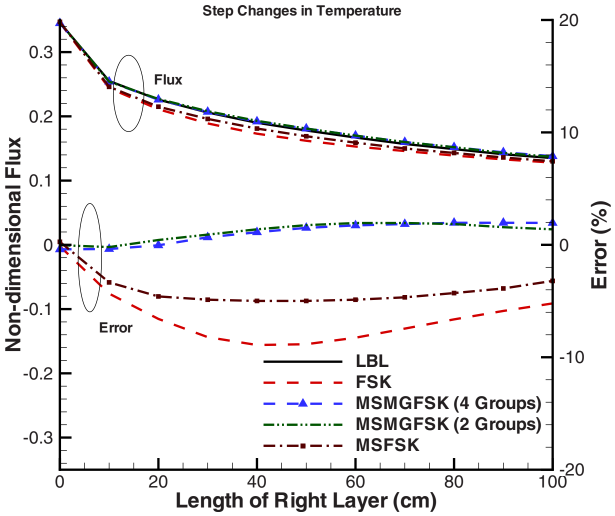

Fig. 2 Nondimensional heat flux leaving an inhomogeneous slab at a total pressure of 1 bar with step changes in temperature: left layer at 1500 K, and right layer at 500 K; both layers contain 20% CO_2, 20% H_2O, and 0.1 ppm soot

For all LBL calculations, absorption coefficients of CO_2 and H_2O were obtained from the CDSD-1000 and the HITEMP spectroscopic databases, respectively, and for the *k*-distribution based calculations, the *k*-*g* data for CO_2 and H_2O from the new narrow band multigroup databases. Soot absorption coefficients were evaluated, invoking the assumption of small particles (scattering from the agglomerated soot particles was ignored for all sample calculations) with the complex index of refraction given by Chang and Charalampopoulos [16].

Figure 1 shows the results for the case of a gas–soot mixture with mole fraction step changes in all three scales: CO_2, H_2O, and soot. The left layer contains 20% CO_2, 2% H_2O, and no soot, while the right layer contains 2% CO_2, 20% H_2O, and 0.1 ppm soot. Both layers are at a constant temperature of 1000 K. In this inhomogeneous problem, the error of the basic single-scale FSK method reaches more than 20%. In comparison to that, if the gas-soot mixture is broken up into several scales, one for each species, the modified MSFSK method produces considerably more accurate solutions, with a maximum error below 4%. The narrow band-based MSMGFSK calculations were performed using two or four groups for each gas scale, and soot was considered as a single-group scale. Both the two and four groups based MSMGFSK calculations result in slightly better accuracy (maximum error limited to less than 3%) compared with the modified MSFSK method.

Figure 2 shows the results for the case of a gas-soot mixture with step changes in temperature. Both layers contain 20% CO_2, 20% H_2O, and 0.1 ppm soot. The left layer is at 1500 K, while the right layer is at 500 K. In this case, the maximum error of the basic single-scale FSK method reaches 9%. The modified MSFSK method reduces the maximum error to below 5%. Both the two and four groups based MSMGFSK calculations still yield better accuracy (maximum error limited to 2% for both). It is observed that the accuracy of the two and four groups based calculations are close to each other, which apparently is due to the presence of compensating errors between grouping of absorption coefficients and mixing among different absorbing species.

Radiative transfer calculations were also performed for the case of a gas-soot mixture with mole fraction step changes in all the three scales (two gas species and soot) in addition to a step change in temperature, and results are shown in Fig. 3. The left hot layer contains 20% CO_2, 2% H_2O, and no soot; the right cold layer has 0.1 ppm of soot with the gas compositions reversed. It is observed here that the two and four group-based MSMGFSK method have a maximum error of only 5% for very high optical thickness, whereas the single-scale FSK method incurs a maximum error close to 60%. The modified MSFSK method incurs a maximum error of 40%, demonstrating its inability to handle strong temperature inhomogeneities in multiphase mixtures. In all cases, it is seen that the two group-based calculations result in excellent accuracy, and only 2*N* RTEs need to be solved (with *N* as the number of species/scales).

6.2 2D Problem. Next we consider a two-dimensional axisymmetric ethylene-air jet flame numerically studied by Mehta [17]. This flame simulates the jet flame experimentally studied by Kent and Honnery [18]. The burner of this Kent and Honnery flame (KH87) consists of a cylindrical nozzle of diameter $d_j = 3\,\text{mm}$. The Reynolds number varies from 7500 to 15,000. A three-dimensional wedge-like (wedge angle of 10 deg) grid system was employed to simulate the axisymmetric flame by applying periodic boundary conditions on the sides. The dimensions in the *x*- and *z*-directions are $30d_j$ and $250d_j$, respectively. The details of modeling the KH87 flame can be found elsewhere [17]. The converged results of that study were used as a frozen data field for radiation calculations. CO_2, H_2O, CO, and soot are the major products of combustion, and hence, are considered in radiation calculations in addition to ethylene (fuel). The concentrations of the major species and the temperature data are shown in Fig. 4. The pressure is uniform (equal to 1 bar). The local radiative heat source term is calculated using the LBL, the basic single-scale FSK, the modified MSFSK, and the two and four group narrow band-based MSMGFSK approaches, employing the P-1 method as the RTE solver. Relative errors are determined by comparison with LBL as

$$\text{error}(\%) = \frac{\nabla \cdot q_{\text{LBL}} - \nabla \cdot q_{\text{FSK/MSFSK/MSMGFSK}}}{\nabla \cdot q_{\text{LBL,max}}} \times 100 \qquad (41)$$

For 2D LBL calculations, the absorption coefficients of C_2H_4 and CO were obtained from the HITRAN-2004 [19] and HITEMP [20] spectroscopic databases, respectively. Narrow band single-group databases of *k*-*g* distributions were compiled for gas species such as C_2H_4 and CO, as outlined by Wang and Modest [13], and were used for 2D calculations. The total number of RTEs solved in each method for the 2D problem is: 1.5 million for LBL, 10 for single-scale FSK, 4 × 10 for modified MSFSK (CO_2 and H_2O as combined scale, each other species as one scale), and 7 × 10 and 11 × 10 for narrow band-based MSMGFSK (each species as one scale, CO_2 and H_2O scales having two and four groups each, respectively), where 10 is the number of quadrature points.

The local radiative heat source term calculated using the LBL method is shown in Fig. 5(*a*). Figure 5(*b*) shows that the single-scale FSK method generates large errors for gas-soot mixtures with varying ratios of concentrations (the maximum error in the present problem reaches as much as 35% near the inlet). In the multiscale approach, CO_2 and H_2O are combined into a single scale since they have approximately the same ratio of concentration throughout the combustion chamber, while C_2H_4, CO, and soot are treated as single-group individual scales. Mixing of CO_2 and H_2O is performed with their local concentrations using the narrow band-based *k*-distribution mixing rule [4]. The maximum error is now limited to 7% near the inlet (region of high errors), as seen in Fig. 5(*c*). Figure 5(*d*) shows the errors incurred in the two group narrow band-based MSMGFSK calculations. In this approach, the C_2H_4, CO, and soot are treated as single-group scales, while CO_2 and H_2O are treated as two separate scales, each having two spectral groups. The maximum error for this case is limited to 4%. The results from the four group-based MSMGFSK methods are approximately the same as the two group case and, hence, are not shown here. This is a substantial improvement, and the accuracy of the new narrow band-based MSMGFSK approach

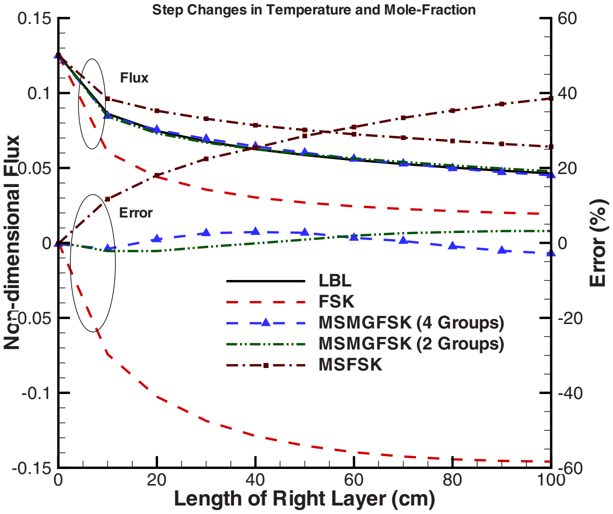

Fig. 3 Nondimensional heat flux leaving an inhomogeneous slab at a total pressure of 1 bar with step changes in temperature and mole fraction: The hot left layer contains 20% CO_2, 2% H_2O, and no soot at 1500 K, and the cold right layer contains 2% CO_2, 20% H_2O, and 0.1 ppm soot at 500 K

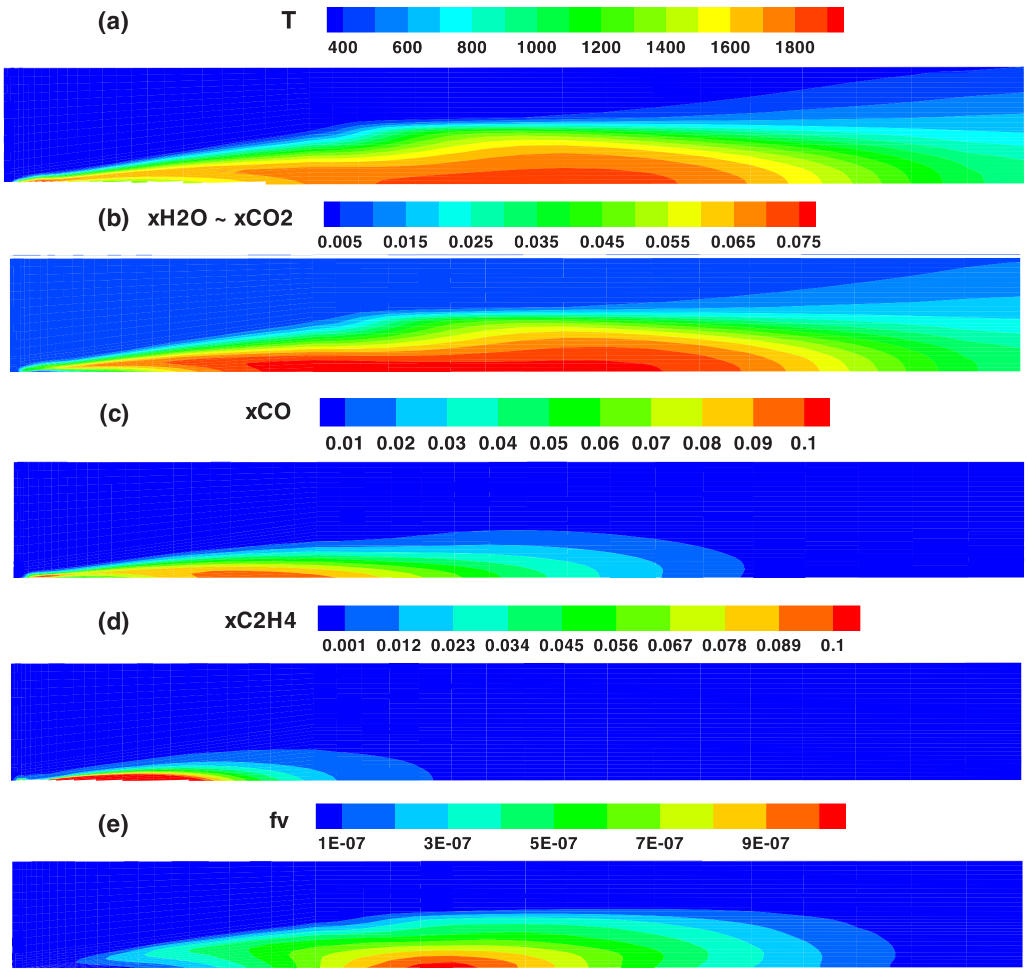

Fig. 4 Temperature and mole fraction distributions in numerically simulated KH87 flame, (*a*) temperature distribution, (*b*) mole fraction distribution of H_2O and approximately CO_2 (wherever there is little CO), (*c*) mole fraction distribution of CO, (*d*) mole fraction distribution of C_2H_4, and (*e*) distribution of soot volume fraction

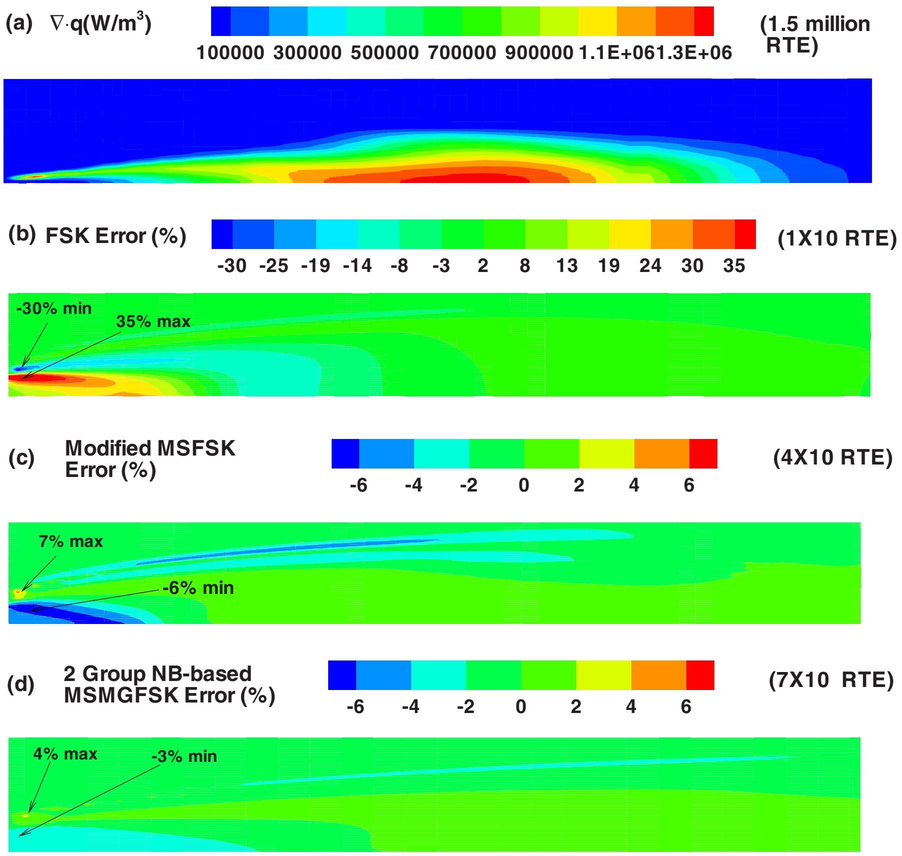

Fig. 5 (*a*) Local radiative heat source using LBL method and relative error (compared with LBL) for heat source calculations using (*b*) the single-scale FSK method, (*c*) the modified MSFSK method, and (*d*) the two group narrow band-based MSMGFSK method

for gas-soot mixtures is clearly demonstrated. CPU time for the LBL calculations is approximately 56 h on a 2.4 GHz AMD Opteron machine, while the single-scale FSK, the modified MSFSK, the two group-based MSMGFSK, and the four group-based MSMGFSK take only 7 s, 41 s, 78 s, and 110 s (i.e., typical times required for chemistry calculations in a combustion problem), respectively, for this calculation. This implies factors of 3×10^4, 5×10^3, 2.5×10^3, and 2×10^3 CPU time improvement, respectively, over LBL cost.

7 Conclusion

In this paper, a new narrow band-based multiscale multigroup full-spectrum *k*-distribution method has been developed for radiation calculations involving nongray gas-soot mixtures with gray wall emission. This spectral method is capable of producing close-to-LBL accuracy for radiation calculations in general combustion problems with multiphase mixtures, temperatures, and concentration inhomogeneities. Accurate and compact narrow band multigroup databases were constructed for the most important combustion gases: CO_2 and H_2O. Sample calculations were performed for both 1D media and for a 2D ethylene-air jet flame with gas-soot mixtures. The narrow band-based hybrid method is more accurate than the single-scale FSK method for all the cases, and more accurate than the modified MSFSK method for cases with temperature inhomogeneity. It is observed that the two group-based calculations produce similar accuracy as the four group-based calculations, both yielding close-to-LBL accuracy, but requiring less computational time. In realistic combustion problems, the narrow band-based multiscale multigroup method is able to provide very accurate results (an order of magnitude more accurate than the FSK, and with several orders of magnitude lesser computational cost than LBL).

References

[1] Denison, M. K., and Webb, B. W., 1993, "A Spectral Line Based Weighted-Sum-of-Gray-Gases Model for Arbitrary RTE Solvers," ASME J. Heat Transfer, **115**, pp. 1004–1012.

[2] Pierrot, L., Rivière, Ph., Soufiani, A., and Taine, J., 1999, "A Fictitious-Gas-Based Absorption Distribution Function Global Model for Radiative Transfer in Hot Gases," J. Quant. Spectrosc. Radiat. Transf., **62**, pp. 609–624.

[3] Modest, M. F., and Zhang, H., 2002, "The Full-Spectrum Correlated-*k* Distribution for Thermal Radiation From Molecular Gas-Particulate Mixtures," ASME J. Heat Transfer, **124**(1), pp. 30–38.

[4] Modest, M. F., and Riazzi, R. J., 2005, "Assembly of Full-Spectrum *k*-Distributions From a Narrow-Band Database; Effects of Mixing Gases, Gases and Nongray Absorbing Particles, and Mixtures With Nongray Scatterers in Nongray Enclosures," J. Quant. Spectrosc. Radiat. Transf., **90**(2), pp. 169–189.

[5] Zhang, H., and Modest, M. F., 2002, "A Multi-Scale Full-Spectrum Correlated-*k* Distribution for Radiative Heat Transfer in Inhomogeneous Gas Mixtures," J. Quant. Spectrosc. Radiat. Transf., **73**(2–5), pp. 349–360.

[6] Zhang, H., and Modest, M. F., 2003, "Scalable Multi-Group Full-Spectrum Correlated-*k* Distributions for Radiative Heat Transfer," ASME J. Heat Transfer, **125**(3), pp. 454–461.

[7] Wang, L., and Modest, M. F., 2005, "Narrow-Band Based Multi-Scale Full-Spectrum *k*-Distribution Method for Radiative Transfer in Inhomogeneous Gas Mixtures," ASME J. Heat Transfer, **127**, pp. 740–748.

[8] Pal, G., Modest, M. F., and Wang, L., 2008, "Hybrid Full-Spectrum Correlated *k*-Distribution Method for Radiative Transfer in Strongly Nonhomogeneous Gas Mixtures," ASME J. Heat Transfer, **130**, pp. 082701–082708.

[9] Pal, G. and Modest, M. F., 2009, "A Multi-Scale Full-Spectrum *k*-Distribution Method for Radiative Transfer in Nonhomogeneous Gas-Soot Mixture With Wall Emission," Comp. Therm. Sci., **1**(2), pp. 137–158.

[10] Wang, L., Haworth, D. C., Turns, S. R., and Modest, M. F., 2005, "Interactions Among Soot, Thermal Radiation, and NOx Emissions in Oxygen-Enriched Turbulent Nonpremixed Flames: A CFD Modeling Study," Combust. Flame, **141**(1–2), pp. 170–179.

[11] Solovjov, V., and Webb, B. W., 2001, "An Efficient Method of Modeling Radiative Transfer in Multicomponent Gas Mixtures With Soot," ASME J. Heat Transfer, **123**, pp. 450–457.

[12] Wang, L., Modest, M. F., Haworth, D. C., and Turns, S. R., 2005, "Modeling Nongray Soot and Gas-Phase Radiation in Luminous Turbulent Nonpremixed

Jet Flames," Combust. Theory Modell., **9**(3), pp. 479–498.

[13] Wang, A., and Modest, M. F., 2005, "High-Accuracy, Compact Database of Narrow-Band *k*-Distributions for Water Vapor and Carbon Dioxide," J. Quant. Spectrosc. Radiat. Transf., **93**, pp. 245–261.

[14] Modest, M. F., 2003, *Radiative Heat Transfer*, 2nd ed., Academic, New York.

[15] Modest, M. F., 2003, "Narrow-Band and Full-Spectrum *k*-Distributions for Radiative Heat Transfer—Correlated-*k* vs. Scaling Approximation," J. Quant. Spectrosc. Radiat. Transf., **76**(1), pp. 69–83.

[16] Chang, H., and Charalampopoulos, T. T., 1990, "Determination of the Wavelength Dependence of Refractive Indices of Flame Soot," Proc. R. Soc. London, **430**(1880), pp. 577–591.

[17] Mehta, R. S., 2008, "Detailed Modelling of Soot Formation and Turbulence-Radiation Interactions in Turbulent Jet Flames," Ph.D. thesis, Pennsylvania State University, University Park, PA.

[18] Kent, J. H., and Honnery, D., 1987, "Modeling Sooting Turbulent Jet Flames Using an Extended Flamelet Technique," Combust. Sci. Technol., **54**, pp. 383–397.

[19] Rothman, L. S., Jacquemart, D., Barbe, A., Chris Benner, D., Birk, M., Brown, L. R., Carleer, M. R., Chackerian, C., Jr., Chance, K., Coudert, L. H., Dana, V., Devi, V. M., Flaud, J.-M., Gamache, R. R., Goldman, A., Hartmann, J.-M., Jucks, K. W., Maki, A. G., Mandin, J.-Y., Massie, S. T., Orphal, J., Perrin, A., Rinsland, C. P., Smith, M. A. H., Tennyson, J., Tolchenov, R. N., Toth, R. A., Vander Auwera, J., Varanasi, P., and Wagner, G., 2005, "The HITRAN 2004 molecular spectroscopic database," J. Quant. Spectrosc. Radiat. Transf., **96**, pp. 139–204.

[20] Rothman, L. S., Wattson, R. B., Gamache, R., Schroeder, J. W., and McCann, A., and 1995, "HITRAN, HAWKS and HITEMP: High-Temperature Molecular Database," Proc. SPIE, **2471**, pp. 105–111.

Radiative Properties of Numerically Generated Fractal Soot Aggregates: The Importance of Configuration Averaging

Fengshan Liu

Gregory J. Smallwood

Institute for Chemical Process and Environmental Technology,
National Research Council,
Building M-9,
1200 Montreal Road,
Ottawa, ON, K1A 0R6, Canada

The radiative properties of numerically generated fractal soot aggregates were studied using the numerically accurate generalized multisphere Mie-solution method. The fractal aggregates investigated in this study contain 10–600 primary particles of 30 nm in diameter. These fractal aggregates were numerically generated using a combination of the particle-cluster and cluster-cluster aggregation algorithms with fractal parameters representing flame-generated soot. Ten different realizations were obtained for a given aggregate size measured by the number of primary particles. The wavelength considered is 532 nm, and the corresponding size parameter of primary particle is 0.177. Attention is paid to the effect of different realizations of a fractal aggregate with identical fractal dimension, prefactor, primary particle diameter, and the number of primary particles on its orientation-averaged radiative properties. Most properties of practical interest exhibit relatively small variation with aggregate realization. However, other scattering properties, especially the vertical-horizontal differential scattering cross section, are very sensitive to the variation in geometrical configuration of primary particles. Orientation-averaged radiative properties of a single aggregate realization are not always sufficient to represent the properties of random-oriented ensemble of fractal aggregates.

[DOI: 10.1115/1.4000245]

Keywords: fractal aggregates, soot, optical properties, configuration averaging

1 Introduction

The absorption and scattering properties of combustion-generated soot are required in many applications related to combustion and heat transfer. It is important to know the radiative properties of soot to quantify its contribution to thermal radiation transfer in flames, fires, and combustion systems. The radiative properties of soot are also essential in many optically based diagnostic techniques for quantitative measurements of soot properties, such as volume fraction and morphology (primary particle diameter and aggregate size). For example, the absorption cross section of soot aggregates is required to calculate the laser energy absorption rate and the thermal radiation intensity in laser-induced incandescence (LII) techniques when the effect of soot particle aggregation is taken into account [1,2] and the scattering properties of soot are required in multi-angle laser elastic scattering techniques for soot morphology measurements [3,4].

It has been established through thermophoretic sampling and subsequent transmission electron microscopy analysis that combustion-generated primary soot particle diameters fall in the range 10–60 nm for most combustion sources and, thus, can be reasonably assumed to be in the Rayleigh regime for the visible spectrum. It is also well known that soot forms aggregates containing nearly spherical primary particles [5,6]. Within any given aggregate, the sizes of the primary particle have a narrow distribution and can be approximately treated as identical in diameter [6]. Although there is a small degree of overlapping, bridging, or necking between two neighboring primary particles, it is reasonable to assume that primary particles are in point-contact [6]. This is an assumption commonly made in almost all theoretical and numerical studies of the optical properties of soot aggregates. Under these assumptions, the structure of soot aggregates can be described as mass fractal [5]. Due to such rather complex structure of soot aggregates, their optical properties cannot be adequately described by the Rayleigh approximation or the Mie-solution for the volume based equivalent sphere [7,8], since the rather open structure of soot aggregates cannot be represented by a compact sphere.

Various approximate methods have been developed and applied to calculate the radiative properties of fractal soot aggregates, such as the Rayleigh–Debye–Gans (RDG) theory [9], the discrete-dipole approximation [10], and the coupled electric and magnetic dipole (CEMD) method [11]. Although these methods are in general computationally efficient, especially the RDG theory, they can produce very inaccurate results under certain conditions. Two numerically accurate methods have been recently developed to predict the radiative properties of aggregates formed by nonoverlapping spherical particles: the cluster *T*-matrix method (CTM) [12,13] and the generalized multisphere Mie-solution (GMM) [14,15]. Executions of these numerically accurate methods require the position, diameter, and refractive index of each constituent sphere (primary particle). Although CTM has become the most popular method to study the radiative properties of various scatters [16–20], GMM has also been demonstrated to be a powerful tool to study the radiative properties of various particles [14,15,21,22]. In fact, CMT and GMM share a very similar theoretical framework, though differences exist [23]. However, GMM offers some advantages over CTM as discussed by Xu and Khlebtsov [23].

To represent the radiative properties of randomly oriented aggregates of a large population two kinds of averaging have been used [16]: one is the orientation averaging and the other is configuration or realization averaging. In the orientation averaging radiative properties are calculated for many different incident di-

---

Contributed by the Heat Transfer Division of ASME for publication in the JOURNAL OF HEAT TRANSFER. Manuscript received December 1, 2008; final manuscript received February 26, 2009; published online December 9, 2009. Assoc. Editor: Yogesh Jaluria.

rections for a single aggregate, and the results of all the orientations are averaged. In the latter, however, radiative properties are calculated for many different aggregates of identical morphological parameters at a fixed incident direction, and the results are averaged over all the configurations. A common assumption made in such practice is that orientation-averaged radiative properties of a single fractal aggregate can be used to represent those of an ensemble of random aggregates of identical morphological parameters (fractal dimension, prefactor, primary particle diameter, and number of primary particle) and optical properties (refractive index). Although this assumption seems reasonable based on the fact that the identical morphology parameters imply any fractal aggregate in this ensemble obey the same fractal scaling law and have the same radius of gyration, it is nevertheless questionable if one considers another fact that there are endless possibilities to generate a fractal aggregate of identical morphological parameters; i.e., the arrangement of individual constituent particles within the aggregate can still be random under the constraint that the fractal scaling law is satisfied.

This assumption has been recently investigated by Kolokolova et al. [17] and Liu and Mishchenko [19] using CTM. In the study of Kolokolova et al. [17], aggregates were numerically constructed using ballistic particle-cluster and cluster-cluster aggregation procedures [24,25]. Although it was not explicitly indicated in the study of Kolokolova et al. [17], these aggregates are indeed fractal, with a fractal dimension between 1.75 and 2.0 for cluster-cluster aggregation and about 2.45 for particle-cluster aggregation [25]. Moreover, Kolokolova et al. [17] did not mention the fractal dimensions for the aggregates they investigated. They investigated fractal aggregates containing 16 up to 128 primary particles and different primary particle size parameters in the range between 0.125 and 1.25. CTM calculations were conducted for only three different aggregate configurations for each set of morphological parameters. Their results showed that there are negligible variations in the absorption efficiency and the linear polarization with aggregate configuration; however, significant variations exist in the scattering efficiency, asymmetry factor, and scattering intensity, especially for smaller aggregates. In addition, that also found that the circular polarization is very sensitive to the arrangement of primary particles in an aggregate. For these reasons Kolokolova et al. [17] concluded that the orientation-averaged radiative properties of aggregates of the same structure and size often cannot represent those of an ensemble of such aggregates due to the influence of different arrangements of primary particles within the aggregate. They also recommended conducting both orientation and configuration averaging to obtain the correct results.

Liu and Mishchenko [19] studied the effect of aggregate realization (configuration) on orientation-averaged radiative properties of soot aggregates using the same solution method (CTM) as Kolokolova et al. [17], but a different method to numerically generate the fractal aggregates. In their study 20 different fractal aggregates containing 400 primary particles were generated using the algorithm described by Mackowski [26] along with morphological parameters typical of soot. Ensemble (realization) averaging of the orientation-averaged radiative properties was then carried out over the 20 realizations. The results of Liu and Mishchenko [19] showed that the standard deviations of scattering and absorption cross sections, the single-scattering albedo, and the asymmetry parameter are all within 3.5% of their corresponding mean. On the other hand, the relative differences in the scattering matrix elements are much larger but still within 15%. Based on these results, Liu and Mishchenko [19] concluded that the radiative properties obtained for one realization of a soot aggregate can be used to represent those of the entire ensemble of clusters having the same morphological parameters. Although Van-Hulle et al. [21] also investigated the effect of aggregate realization on the radiative properties of fractal soot aggregates, their results are not useful for examining the assumption mentioned above for the reason that the fractal aggregates they generated exhibit large variations in radius of gyration.

It is somewhat surprising to observe that Kolokolova et al. [17] and Liu and Mishchenko [19] reached opposite conclusions with regard to the importance of configuration or realization averaging to the radiative properties of a random-oriented ensemble of fractal aggregates. The present study is motivated by these contradictory findings. In this study, fractal soot aggregates containing 10–600 identical primary particles of 30 nm in diameter were numerically generated using a combined cluster-particle aggregation and cluster-cluster aggregation algorithm for specified fractal parameters (fractal dimension and prefactor). The resultant aggregates of different sizes have identical fractal parameters. Numerical calculations were conducted using GMM [14,15]. We attempt to conduct a similar study as that by Kolokolova et al. [17] and Liu and Mishchenko [19] to provide further numerical evidence to help answer the question if configuration averaging is necessary to predict the radiative properties of a random-oriented ensemble of aggregates.

2 Methodology

2.1 Numerical Generation of Fractal Aggregates. Soot, like many other fractal objects, is formed by the aggregation of small, nearly identical, and spherical primary particles into complex geometries. The fractal-like structure of soot aggregates obeys the following statistical scaling law [27]:

$$N = k_f \left(\frac{R_g}{a} \right)^{D_f} \tag{1}$$

where N is the number of primary particles within the aggregate, k_f and D_f are the prefactor and fractal dimension, respectively, a is the primary particle radius, and R_g is the radius of gyration defined as [28]

$$R_g{}^2 = \frac{1}{N} \sum_{i=1}^{N} (\mathbf{r}_i - \mathbf{r}^0)^2 + a^2 \tag{2}$$

$$\mathbf{r}^0 = \frac{1}{N} \sum_{i=1}^{N} \mathbf{r}_i \tag{3}$$

where vectors $\mathbf{r}_\mathrm{i}$ and $\mathbf{r}^0$ define the position of the center of the ith primary particle and the center of the aggregate, respectively. For the current study, fractal aggregates simulating flame-generated soot were numerically generated using the particle-cluster aggregation algorithm for small aggregates (up to $N=31$) and cluster-cluster aggregation algorithm for larger aggregates. The algorithms used in this study follow closely those described by Filippov et al. [28], and the details of our numerical implementation of these algorithms can be found in Ref. [22]. It is worth noting that the algorithms for the generation of numerical fractal aggregates in this study are also very similar to those used by Liu and Mishchenko [19]. As demonstrated by Filippov et al. [28], the density correlation functions of fractal aggregates generated by the cluster-cluster aggregation algorithm give the correct slope when plotted against the nondimensional distance on a log-log scale. The following morphological parameters were used in the generation of fractal aggregates: $k_f=2.3$, $D_f=1.78$, and $a=15$ nm, which are typical values for flame-generated soot. Fractal aggregates containing $N=10$, 20, 50, 100, 200, 400, and 600 primary particles were generated using this combined particle-cluster and cluster-cluster aggregation algorithm. For all the aggregate sizes except $N=200$, ten different realizations were generated. In the case of $N=200$, 30 different aggregates were constructed.

To demonstrate the variability in the arrangement of primary particles in aggregates of identical morphology, the first six aggre-

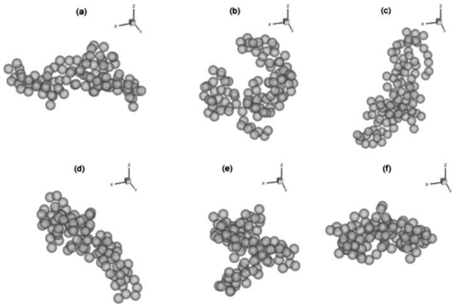

Fig. 1 The first six realizations for $N=100$

Table 1 Configuration-averaged absorption and total scattering cross sections and asymmetry parameter and their maximum relative deviations for orientation- and realization-averaged results, based on ten realizations unless otherwise noted

N	C_{abs} (nm^2)	Maximum ε in C_{abs} (%)	C_{sca} (nm^2)	Maximum ε in C_{sca} (%)	g	Maximum ε in g (%)
10	1,508.9	0.63	43.0	0.05	0.0481	3.69
20	3,046.5	1.31	154.2	1.04	0.0979	1.69
50	7,596.3	0.37	675.9	2.06	0.254	5.36
100	15,012.0	0.63	1,769.2	4.51	0.417	7.12
200	29,572.1	0.28	4,330.9	3.92	0.529	5.13
200[a]	29,559.0	0.60	4,312.8	4.36	0.533	6.54
200[b]	29,551.9	0.58	4,312.4	4.37	0.536	6.46
400	58,097.1	0.50	10,004.6	2.68	0.621	7.28
600	86,387.7	0.53	16,182.5	5.29	0.656	4.22

[a] Based on 20 realizations.
[b] Based on 30 realizations.

gate realizations for $N=100$ are displayed in Fig. 1. It is evident that the aggregates can have very different arrangements of individual primary particles. It is recognized that these aggregates are somewhat more compact than typical soot aggregates. This is because a somewhat large value of the prefactor $k_f=2.3$ is used.

2.2 Generalized Multisphere Mie-Solution. In this study GMM was used to calculate the orientation-averaged radiative properties of the numerically generated fractal aggregates. Similar to CTM, GMM is also numerically exact and much more efficient than the other numerical techniques based on an explicit solution of the Maxwell equations. GMM was developed by Xu [14,15] based on the framework of the Mie theory for a single sphere and the addition theorems for spherical vector wave functions. GMM provides a rigorous and complete solution to nonoverlapping multisphere light scattering problems and can be readily applied to fractal aggregates [21,22]. The key steps involved in the development of GMM include (a) expansion of the scattered, internal, and incident electromagnetic fields in terms of vector spherical functions; (b) formation of a linear equation system through the boundary condition at each primary particle in the aggregate; (c) transformation of the waves scattered by an individual primary particle into the incident waves of the other particles in the aggregate through the addition theorems for vector spherical functions; and (d) solution of the linear system of interactive coefficients. The absorption and scattering cross sections and the four scattering matrix coefficients are analytically given by Xu [14,15]. GMM rigorously accounts for the multiple scattering within the aggregate. However, GMM is still very computationally demanding and memory intensive for large aggregates containing several hundred primary particles, especially when the size parameter of the primary particle is relatively large.

3 Results and Discussion

Numerical calculations were conducted for 532 nm wavelength, which is of great interest in laser scattering and LII experiments. The corresponding primary particle size parameter is $x_p=\pi d_p/\lambda$, and is relatively small at 0.177. The refractive index of soot was assumed to be $m=1.6+0.6i$, which is again a typical value of soot in the visible spectrum. Orientation averaging was achieved numerically in the GMM calculations by dividing each Euler angle into 15 equal-intervals. Although the apparent number of orientations considered is 3375, the actual number of orientations to be calculated is doubled by selecting the feature of IDD=1 [29]. Such level of orientation averaging is considered sufficient based on previous studies [16]; i.e., further division of the three Euler angles would not affect the orientation-averaged results.

3.1 Absorption and Total Scattering Cross Sections and Asymmetry Parameter. The ensemble-averaged cross sections of absorption and total scattering and the asymmetry parameter were calculated using the following expressions [19]:

$$C_{abs}=\frac{1}{M}\sum_{i=1}^{M} C_{abs}{}^{i} \tag{4}$$

$$C_{sca}=\frac{1}{M}\sum_{i=1}^{M} C_{sca}{}^{i} \tag{5}$$

$$g=\frac{1}{MC_{sca}}\sum_{i=1}^{M} g^{i}C_{sca}{}^{i} \tag{6}$$

where subscripts abs and sca represent absorption and scattering, respectively, and superscript i denotes orientation-averaged quantities of the ith aggregate realization. The numerical results of the absorption and total scattering cross sections and the asymmetry parameter are summarized in Table 1. In this table, the relative deviation ε is defined as $|X^{i}-X_{mean}|/X_{mean}\times 100\%$ (X is either C_{abs}, C_{sca}, or g). It is evident that the absorption cross section varies negligibly with aggregate realization for all the aggregate sizes considered. Although the total scattering cross section and the asymmetry parameter exhibit larger variations with the aggregate realization than the absorption cross section, the relative deviations are still considered small as they remain less than 7.5%. Kolokolova et al. [17] reported that there are significant relative deviations in C_{sca} and g (about 15%) with aggregate realization for $N=16$ and $x_p=0.125$, which are comparable to the present conditions of $N=20$ and $x_p=0.177$. Unlike the results of Kolokolova et al. [17] for $N=16$ and $x_p=0.125$, however, our results of C_{sca} and g for $N=20$ and $x_p=0.177$ do not display large variations with aggregate realization. The relative deviations in C_{sca} and g for larger aggregates are similar but smaller to those reported by Kolokolova et al. [17]. The maximum relative deviations in C_{sca} and g are also comparable to the relative errors in C_{sca} and g of Liu and Mishchenko [19] measured by the ratio of standard deviation to mean.

The results for $N=200$ and different realizations indicate that 20 realizations seem sufficient to achieve converged results; however, 10 realizations can be considered as adequate. Nevertheless, the results shown in Table 1 suggest that the aggregate realization or configuration, i.e., the detailed arrangement of individual primary particles within the aggregate, has almost no influence on the orientation-averaged absorption cross section, and only small or modest impact on the total scattering cross section and the asymmetry parameter.

The present normalized averaged absorption and total scattering cross sections over both orientation and aggregate realization for a given aggregate size are compared with the results of RDG and

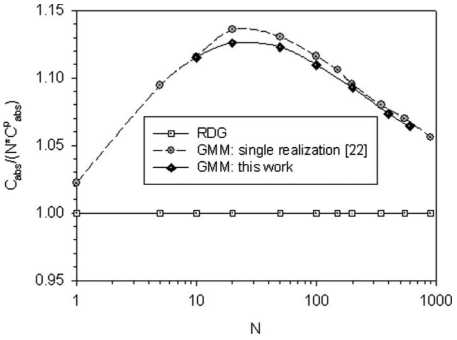

Fig. 2 Comparison of nondimensional aggregate absorption cross section

our previous GMM for a single aggregate realization using the same fractal parameters and soot refractive index [22] in Figs. 2 and 3, respectively. The superscript *p* indicates quantities of the primary particle in the Rayleigh limit. It is evident from these figures that the effect of realization averaging is quite small, consistent with the results displayed in Table 1. Nevertheless, realization averaging results in a smoother distribution of C_{abs}. The deviation of the RDG results from those of GMM or other more accurate solutions is well known, especially for the absorption cross section. These results indicate that it is adequate to perform GMM calculations for the absorption and total scattering cross sections and the asymmetry parameter of an ensemble of random-oriented fractal aggregates using just a single realization. In this regard, the present finding agrees with that made by Liu and Mishchenko [19]. This conclusion has significant implications in practice, since it means not only that previous results of the optical properties of fractal aggregates based on a single realization are valid but also huge computing efforts can be avoided in future studies.

3.2 Differential Scattering Cross Sections. The nondimensional differential scattering cross sections k^2C_{VV} for different realizations of $N=100$ and 400 are compared in Fig. 4; here $k=2\pi/\lambda$ is the wavenumber, the first subscript in C_{VV} refers to the incident polarization, and the second to the detected polarization. The following observations can be made from the results shown in this figure. First, the differential cross section C_{VV} in the near forward directions is almost independent of the aggregate realization. However, the angular range for such independence becomes narrower as the aggregates become larger. Second, the differential cross section C_{VV} displays a relatively large sensitivity to the aggregate realization at large scattering angles, i.e., in the backward directions. These results indicate the increasing importance of aggregate realization (arrangement of primary particles) as the scattering angle increases. A similar observation of such behavior of C_{VV} has been made previously by Farias et al. [30]. The results of horizontal-horizontal differential scattering cross section C_{HH} have a similar dependence on aggregate realization to C_{VV} and can be found in Ref. [22]. Therefore, the results of C_{HH} are not shown.

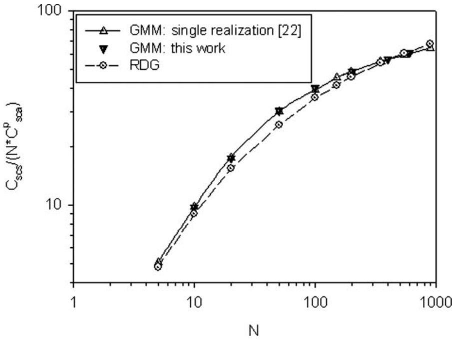

Fig. 3 Comparison of nondimensional aggregate total scattering cross section

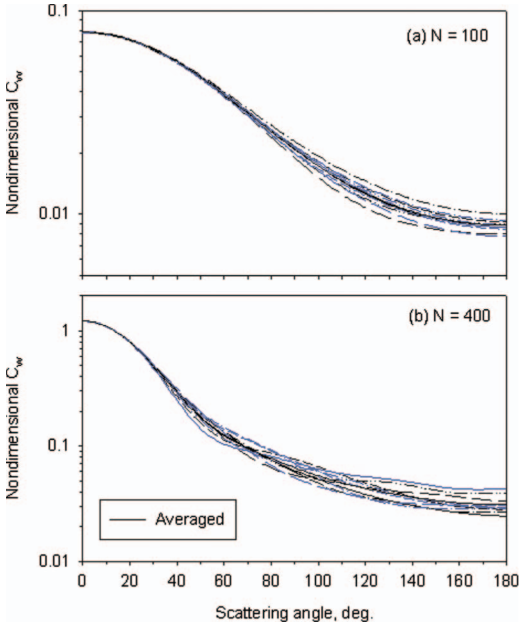

Fig. 4 Nondimensional vertical-vertical differential scattering cross sections for different aggregate realizations and *N*=100 and 400

The scattering phase function is related to the scattering cross sections as

$$\Phi(\theta) = \frac{4\pi}{C_{\text{sca}}} \frac{(C_{\text{VV}} + C_{\text{HH}})}{2} \tag{7}$$

The effects of aggregate realization on the scattering phase function for $N=100$ and 400 are shown in Fig. 5. In the calculation of the configuration-averaged phase function, the configuration-averaged total and differential scattering cross sections are used in Eq. (7). The scattering quickly becomes primarily in the forward direction as the aggregate size increases. The effect of aggregate realization is relatively small with deviations comparable to those for the total scattering cross section and the asymmetry parameter given in Table 1.

Although the results shown in Fig. 4 are a clear indication that the vertical-vertical differential scattering cross section is somewhat sensitive to the detailed arrangement of primary particles, C_{VV} is not the best quantity to demonstrate the importance of aggregate realization. This is because C_{VV} is dominated by single scattering [31], and a better way to reveal the importance of primary particle arrangement is to examine the quantities dominated by multiple scattering. Such quantities include the circular polarization [17] and depolarization [31,32]. It is well known that the presence of depolarization is an indication of multiple scattering. Here we examine depolarization quantified by the differential scattering cross section C_{VH} at the forward direction, i.e., at scattering angle $\theta=0$ deg. The results of orientation-averaged $C_{\text{VH}}(0\text{ deg})$ for different aggregate realizations and different *N* are summarized in Table 2. It is evident that $C_{\text{VH}}(0\text{ deg})$ is sensitive to aggregate realization and the relative variation can vary by more than a factor of 4. For this reason, our results support the conclusion reached by Kolokolova et al. [17] that it is important to perform configuration averaging to obtain correct complete radiative properties of random-oriented ensemble of fractal aggregates.

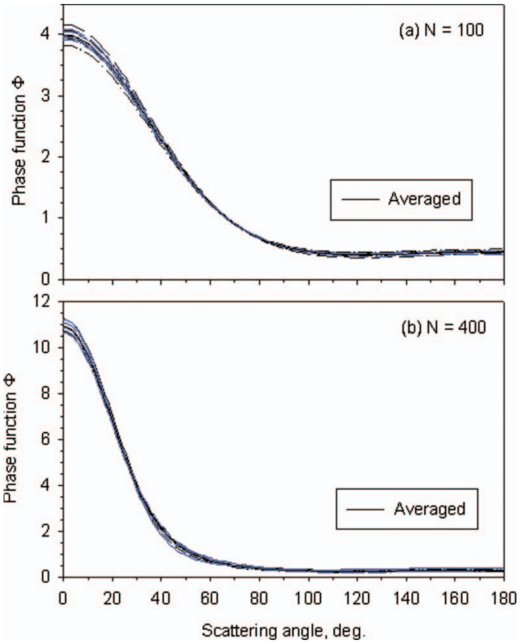

Fig. 5 Scattering phase functions for different aggregate realizations and $N=100$ and 400

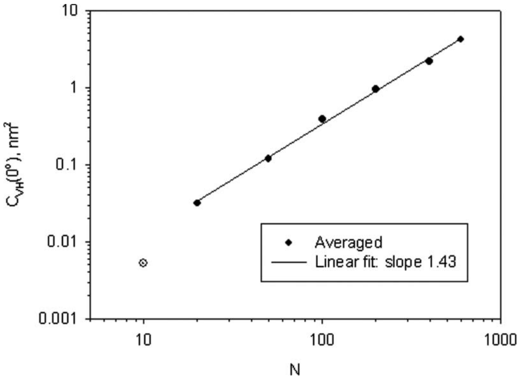

Fig. 6 Variation of configuration- and orientation-averaged $C_{VH}(0\ \text{deg})$ with aggregate size N

Chen et al. [33] showed that second-order light scattering (SOLS) (C_{VH} is a special case of SOLS) is sensitive to the structural anisotropy of a cluster, which is determined by the arrangement of primary particles. It is clear that the radiative properties of fractal aggregates that are dominated by multiple scattering and sensitive to the specific arrangement of primary particles require a certain tool to describe the subtle difference from one aggregate to the other among aggregates of identical morphology dictated by k_f, D_f, a, and N. Such subtle difference has been discussed by Seeley et al. [34] in terms of higher-order geometry of such fractal aggregates. The results shown in Table 2 clearly indicate that the orientation-averaged differential scattering cross section C_{VH} calculated from a particular aggregate realization cannot be used to represent that of a random-oriented ensemble of aggregates.

Because of the large variation of $C_{VH}(0\ \text{deg})$ from one realization to another, the adequacy of using only ten realizations for obtaining its configuration-averaged value is somewhat questionable. Nevertheless, variation of the configuration- and orientation-averaged $C_{VH}(0\ \text{deg})$ with aggregate size N is plotted in Fig. 6 in a log-log scale, since it is expected that C_{VH} is proportional to N^x [33]. Except for the point at the smallest aggregate size considered ($N=10$), there exists a very good linear fit with a slope of 1.43, which is close to the value of 1.5 obtained by Chen et al. [33] for bond-percolation clusters. The good linear fit implies that it is reasonable to use ten realizations for configuration averaging of $C_{VH}(0\ \text{deg})$. If the point at $N=10$ were included in the linear fit, a higher slope of 1.56 was obtained with a much worse fit quality.

4 Conclusion

The effect of configuration averaging on the radiative properties of soot fractal aggregates was investigated using the generalized multisphere Mie-solution method along with a combined particle-cluster and cluster-cluster aggregation algorithm for generating fractal aggregates of identical morphology. The present results show that the orientation-averaged absorption and total scattering cross sections and the asymmetry parameter exhibit relatively small variation from one realization to the other with a maximum relative deviation of less than about 7%, especially for the absorption cross section with a maximum relative deviation of about 1%. Such effects of aggregate realization are similar to some previous findings. Therefore, we can conclude that it is reasonable to conduct numerical calculations using just one aggregate realization to represent orientation-averaged absorption and total scattering cross sections, the asymmetry parameter, the scattering phase function, and the vertical-vertical and horizontal-horizontal differential scattering cross sections of an ensemble of random-oriented soot fractal aggregates. The present configuration- and orientation-averaged absorption and total scattering cross sections are in good agreement with our previous results obtained for a single aggregate realization.

The arrangement of primary particles in aggregates of identical morphological parameters has modest impact on the vertical-vertical differential scattering cross section at larger scattering angles. The quantities dominated by multiple scattering, such as the vertical-horizontal differential scattering cross section, display

Table 2 Orientation-averaged $C_{VH}(0\ \text{deg})$ (in nm^2) for different aggregate realizations and different aggregate sizes N

	$N=10$	$N=20$	$N=50$	$N=100$	$N=200$	$N=400$	$N=600$
1	3.70×10^{-3}	4.22×10^{-2}	0.181	0.425	0.782	3.968	8.083
2	7.57×10^{-3}	1.80×10^{-2}	0.145	0.656	1.659	4.287	6.219
3	3.66×10^{-3}	5.62×10^{-2}	0.104	0.159	0.793	1.323	3.624
4	3.30×10^{-3}	3.88×10^{-2}	0.139	0.518	1.818	1.613	6.266
5	3.51×10^{-3}	2.26×10^{-2}	0.146	0.290	0.584	0.398	1.473
6	5.91×10^{-3}	4.27×10^{-2}	0.0897	0.480	0.990	2.477	4.201
7	7.63×10^{-3}	2.97×10^{-2}	0.0543	0.0778	0.294	0.961	2.545
8	1.03×10^{-3}	1.37×10^{-2}	0.123	0.312	0.571	4.112	5.140
9	4.35×10^{-3}	3.81×10^{-2}	0.091	0.304	0.937	0.803	2.276
10	2.40×10^{-3}	1.13×10^{-2}	0.102	0.629	1.115	1.807	2.043
Averaged	5.23×10^{-3}	3.13×10^{-2}	0.118	0.385	0.954	2.175	4.187

a much higher sensitivity to aggregate realization. For this reason, it is concluded that a single aggregate realization cannot be used to represent the radiative properties of a random-oriented ensemble of aggregates as far as the vertical-horizontal differential scattering cross section is concerned. This finding is likely applicable to other quantities related to the asymmetric structure of fractal aggregates, but further investigation is required. The configuration- and orientation-averaged vertical-horizontal differential scattering cross sections of the soot aggregates investigated increase with the aggregate size as $N^{1.43}$.

Acknowledgment

We would like to thank Dr. Y.-L. Xu for making his GMM computer codes available. Financial support was provided in part by the Government of Canada's PERD Program through Project Nos. C23.006 and C11.003.

Nomenclature

a = radius of primary particle, nm
C = cross section area, nm^2
D_f = fractal dimension
g = asymmetry parameter
k = wavenumber
k_f = fractal prefactor
m = refractive index
N = number of primary particles in aggregate
$\mathbf{r}$ = center of primary particle
$\mathbf{r}^0$ = center of aggregate
R_g = radius of gyration, nm
x_p = size parameter of primary particle

Greek Symbols

λ = wavelength, nm
θ = scattering angle, deg
Φ = scattering phase function

Subscripts

abs = absorption
H = horizontally polarized
sca = total scattering
V = vertically polarized

References

[1] Snelling, D. R., Liu, F., Smallwood, G. J., and Gülder, Ö. L., 2004, "Determination of the Soot Absorption Function and Thermal Accommodation Coefficient Using Low-Fluence LII in a Laminar Coflow Ethylene Diffusion Flame," Combust. Flame, **136**, pp. 180–190.
[2] Liu, F., Yang, M., Hill, F. A., Snelling, G. J., and Smallwood, G. J., 2006, "Influence of Polydisperse Distributions of Both Primary Particle and Aggregate Size on Soot Temperature in Low-Fluence LII," Appl. Phys. B: Lasers Opt., **83**, pp. 383–395.
[3] Köylü, Ü. Ö., 1997, "Quantitative Analysis of In Situ Optical Diagnostics for Inferring Particle/Aggregate Parameters in Flames: Implications for Soot Surface Growth and Total Emissivity," Combust. Flame, **109**, pp. 488–500.
[4] Yang, B., and Köylü, Ü. Ö., 2005, "Soot Processes in a Strongly Radiating Turbulent Flame From Laser Scattering/Extinction Experiments," J. Quant. Spectr. Rad. Trans., **93**, pp. 289–299.
[5] Megaridis, C. M., and Dobbins, R. A., 1990, "Morphological Description of Flame-Generated Materials," Combust. Sci. Technol., **71**, pp. 95–109.
[6] Faeth, G. M., and Köylü, Ü. Ö., 1995, "Soot Morphology and Optical Properties in Nonpremixed Turbulent Flame Environments," Combust. Sci. Technol., **108**, pp. 207–229.
[7] Dalzell, W. H., Williams, G. C., and Hottel, H. C., 1970, "A Light-Scattering Method for Soot Concentration Measurements," Combust. Flame, **14**, pp. 161–170.
[8] Köylü, Ü. Ö., and Faeth, G. M., 1993, "Radiative Properties of Flame-Generated Soot," ASME J. Heat Transfer, **115**, pp. 409–417.
[9] Köylü, Ü. Ö., and Faeth, G. M., 1994, "Optical Properties of Overfire Soot in Buoyant Turbulent Diffusion Flames at Long Residence Time," ASME J. Heat Transfer, **116**, pp. 152–159.
[10] Draine, B. T., and Flatau, P. J., 1994, "Discrete-Dipole Approximation for Scattering Calculations," Opt. Soc. Am, **11**, pp. 1491–1499.
[11] Mulholland, G. W., Bohren, C. F., and Fuller, K. A., 1994, "Light Scattering by Agglomerates: Coupled Electric and Magnetic Dipole Method," Langmuir, **10**, pp. 2533–2546.
[12] Mishchenko, M. I., 1991, "Light Scattering by Randomly Oriented Axially Symmetric Particles," J. Opt. Soc. Am. A, **8**, pp. 871–882.
[13] Khlebtsov, N. G., 1992, "Orientational Averaging of Light-Scattering Observables in the T-Matrix Approach," Appl. Opt., **31**, pp. 5359–5365.
[14] Xu, Y.-L., 1995, "Electromagnetic Scattering by an Aggregate of Spheres," Appl. Opt., **34**, pp. 4573–4588.
[15] Xu, Y.-L., 1997, "Electromagnetic Scattering by an Aggregate of Spheres: Far Field," Appl. Opt., **36**, pp. 9496–9508.
[16] Riefler, N., di Stasio, S., and Wriedt, T., 2004, "Structural Analysis of Clusters Using Configurational and Orientational Averaging in Light Scattering Analysis," J. Quant. Spectr. Rad. Trans., **89**, pp. 323–342.
[17] Kolokolova, L., Kimura, H., Ziegler, K., and Mann, I., 2006, "Light-Scattering Properties of Random-Oriented Aggregates: Do They Represent the Properties of an Ensemble of Aggregates?," J. Quant. Spectr. Rad. Trans., **100**, pp. 199–206.
[18] Liu, L., and Mishchenko, M. I., 2005, "Effects of Aggregation on Scattering and Radiative Properties of Soot Aerosols," J. Geophys. Res., **110**, p. D11211.
[19] Liu, L., and Mishchenko, M. I., 2007, "Scattering and Radiative Properties of Complex Soot and Soot-Containing Aggregate Particles," J. Quant. Spectr. Rad. Trans., **106**, pp. 262–273.
[20] Mishchenko, M. I., Videen, G., Khlebtsov, G., Wriedt, T., and Zakharova, N. T., 2008, "Comprehensive T-Matrix Reference Database: A 2006-07 Update," J. Quant. Spectr. Rad. Trans., **109**, pp. 1447–1460.
[21] Van-Hulle, P., Weill, M.-E., Talbaut, M., and Coppalle, A., 2002, "Comparison of Numerical Studies Characterizing Optical Properties of Soot Aggregates for Improved EXSCA Measurements," Part. Part. Syst. Charact., **19**, pp. 47–57.
[22] Liu, F., and Snelling, D. R., 2008, "Evaluation of the Accuracy of the RDG Approximation for the Absorption and Scattering Properties of Fractal Aggregates of Flame-Generated Soot," Paper No. AIAA-2008-4362.
[23] Xu, Y.-L., and Khlebtsov, N. G., 2003, "Orientational-Averaged Radiative Properties of an Arbitrary Configuration of Scatters," J. Quant. Spectr. Rad. Trans., **79–80**, pp. 1121–1137.
[24] Meakin, P., 1983, "The Vold-Sutherland and Eden Models of Cluster Formation," J. Colloid Interface Sci., **96**, pp. 415–424.
[25] Meakin, P., 1984, "Effects of Cluster Trajectories on Cluster-Cluster Aggregation: A Comparison of Linear and Brownian Trajectories in Two- and Three-Dimensional Simulations," Phys. Rev. A, **29**, pp. 997–999.
[26] Mackowski, D. W., 2006, "A Simplified Model to Predict the Effects of Aggregation on the Absorption Properties of Soot Particles," J. Quant. Spectr. Rad. Trans., **100**, pp. 237–249.
[27] Forrest, S. R., and Witten, T. A., Jr., 1979, "Long-Range Correlations in Smoke-Particle Aggregates," J. Phys. A, **12**, pp. L109–L117.
[28] Filippov, A. V., Zurita, M., and Rosner, D. E., 2000, "Fractal-Like Aggregates: Relation Between Morphology and Physical Properties," J. Colloid Interface Sci., **229**, pp. 261–273.
[29] http://www.astro.ufl.edu/~xu/codes/gmm01f
[30] Farias, T. L., Carvalho, M. G., Köylü, Ü. Ö., and Faeth, G. M., 1995, "Computational Evaluation of Approximate Rayleigh-Debye-Gans/Fractal-Aggregate Theory for the Absorption and Scattering Properties of Soot," ASME J. Heat Transfer, **117**, pp. 152–159.
[31] Sorensen, C. M., 2001, "Light Scattering by Fractal Aggregates: A Review," Aerosol Sci. Technol., **35**, pp. 648–687.
[32] Lu, N., and Sorensen, C. M., 1994, "Depolarization Light Scattering From Fractal Soot Aggregates," Phys. Rev. E, **50**, pp. 3109–3115.
[33] Chen, Z.-Y., Weakliem, P., Gelbart, W. M., and Meakin, P., 1987, "Second-Order Light Scattering and Local Anisotropy of Diffusion-Limited Aggregates and Bond-Percolation Clusters," Phys. Rev. Lett., **58**, pp. 1996–1999.
[34] Seeley, G., Keyes, T., and Ohtsuki, T., 1988, "Higher-Order Fractal Geometry; Application to Multiple Light Scattering," Phys. Rev. Lett., **60**, pp. 290–293.

The Simplified-Fredholm Integral Equation Solver and Its Use in Thermal Radiation

K. G. Terry Hollands
Department of Mechanical and Mechatronics Engineering,
University of Waterloo,
Waterloo, ON, N2L 3G1, Canada

The application of a new Fredholm integral equation solver to problems in thermal radiation is explored. The new method provides a simplified version of Fredholm's own 1903 solution which, while being highly important from a theoretical point of view, had been considered too complex to provide a practical tool for solving integral equations. The method does not involve solving large arrays of simultaneous equations; rather, the simplified-Fredholm method provides an explicit solution. The solution consists of an infinite series with each term containing multiple integrals. It has been found, however, that the series can be safely truncated after about a dozen terms, and the multiple integrals can be resolved through repeated matrix multiplications, all of this leading to a practical methodology. Implicit in the method and highly useful in radiant analyses is the idea of the resolvent kernel, which permits generalized solutions to be obtained, independent of the forcing function. The method also adapts itself to a simple technique for establishing the possible error in any result. It is illustrated here on some enclosure problems that can be reduced to solving Fredholm's equation in a single variable.
[DOI: 10.1115/1.4000183]

Keywords: thermal radiation, integral equations, enclosures, exchange factors, cylindrical cavities, square cavities, kernel, coupled enclosures

Introduction

Integral equations arise naturally and often in thermal radiation problems, and methods for solving them are of paramount importance. The equations encountered are generally the second kind of Fredholm's type, and are in either one or two variables. The general statement of the relevant equation in one variable is

$$u(x) = f(x) + \int_a^b u(t)K(x,t)dt \tag{1}$$

where $u(x)$ is the unknown function and $f(x)$ (called here the forcing function) and $K(x,t)$ (called the kernel) are specified functions, while a and b are constants. Methods for solving this equation are given in mathematical textbooks on integral equations [1,2], while radiation texts [3–5] summarize some methods that have been used in radiation analysis. A popular method in radiant analysis, used, for example, by Daun and Hollands [6] and called here the "numerical method," replaces the unknown function and the variable by sets of nodal values. It uses numerical quadrature to approximate the integral and then ensures the equation holds at each nodal value; this leads to set of linear algebraic equations in the nodal values, which are solved. Other recent methods include, for example, the Trefftz method [7], the decomposition method [8] (for systems of equations), the hybrid Taylor method [9], the WPG method [10], and the Petrov–Galerkin method [11], but none of these is particularly suited to thermal radiation problems.

Recently a new method [12] has arisen in the mathematical literature, and it is the purpose of this paper to describe this method and to illustrate its use on some radiation problems. In contrast to other methods, the method gives an explicit expression for the solution (although numerical methods are still involved when it comes to evaluation). In addition, the method uses the idea of the "resolvent kernel," which gives it a theoretic and practical advantage for radiation situations, and also it lends itself to a technique for finding the possible error in any result. This paper is restricted to equations in one variable, and another showing its application to two-variable equations is planned for the future.

One prominent place where integral equations arise in radiant analysis is in the well-known enclosure problem, where a (normally transparent) gas or vacuum is enclosed by walls of specified temperature or heat flux distribution. Then the variable x in Eq. (1) represents the position on the enclosure wall, the unknown quantity, $u(x)$ is the outgoing radiant flux or radiosity, the specified function $f(x)$ relates directly to the specified temperature/heat flux distribution, and the kernel $K(x,t)$ relates to both the geometry of the enclosure and its surface properties. The well-known method of form factors and exchange factors is based on a rather crude approximation to the integral: the "lumped area approximation." Analyses that represent the integral rigorously are sometimes called "infinitesimal-area" analysis.

The new method described here drew directly on a 1903 analysis given by Fredholm [13]. Fredholm's analysis was ground breaking and fundamentally important in the theoretical context because it was the first to give the conditions under which a solution to the integral solution exists and when it is unique. But although it gave an explicit solution, that solution was never (except for a very few special cases) used in a practical way because of its highly complex nature. Subject to certain conditions on $K(x,t)$ and $f(x)$ to be given later, Fredholm showed that for any kernel there always exists a function $H(x,t)$, called the resolvent kernel, such that the solution to Eq. (1) is

$$u(x) = f(x) + \int_a^b H(x,t)f(t)dt \tag{2}$$

Fredholm's expression for the resolvent kernel, which is only dependent on $K(x,t)$, was considered intractable for practical use. The simplification offered by Hollands [12] to this expression reduced it to where it can be used for routine calculations, and the

---

Contributed by the Heat Transfer Division of ASME for publication in the JOURNAL OF HEAT TRANSFER. Manuscript received October 23, 2008; final manuscript received April 13, 2009; published online December 1, 2009. Assoc. Editor: Yogesh Jaluria.

corresponding method forms the basis for the present method. Here we describe the method, and then apply it to some well-known problems and variations thereof, demonstrating the resolvent kernel's ability to simplify problems. Next we explain the connection between the resolvent kernel and the exchange factor for infinitesimal analysis, and offer a calculation of such an exchange factor calculation.

It is useful to contrast the contribution of the present paper with the contribution of Ref. [12]. First, the present paper gives a much more compact description of the key equations, allowing the user to implement them without becoming familiar with their detailed derivation. Second, in applying the method to radiation problems (not considered in Ref. [12]), the present paper introduces the idea of the resolvent kernel to thermal radiation analysis and shows the important role it can play in coupled problems. Finally, it demonstrates that the concept of the exchange factor $\mathfrak{I}_{i-j}$ applies under infinitesimal-area analysis, by using the resolvent kernel. We now describe the method in its compact form.

The Simplified Solution

Before giving the simplified expression for the resolvent kernel, we first define iterated functions $K_n(x,t)$, $n=0,1,\ldots,\infty$, as follows: for $n=0$, we have

$$K_0(x,t) = K(x,t) \tag{3}$$

otherwise they are given recursively by

$$K_n(x,t) = \int_a^b K_{n-1}(x,t_1)K(t_1,t)dt_1 \tag{4}$$

With these items defined, the expression for the resolvent kernel is

$$H(x,t) = \frac{\displaystyle\sum_{n=0}^{\infty}\sum_{i=0}^{n} A_i K_{n-i}(x,t)}{\displaystyle\sum_{n=0}^{\infty} A_n} \tag{5}$$

Prior to giving the equation for the set of coefficients A_i, we first introduce a set of "counter matrices" denoted $\mathbf{M}(i)$, $i=1,\ldots,\infty$, all of whose entries are integers. Matrix $\mathbf{M}(1)$ has only one entry, namely, 1, and Table 1 gives $\mathbf{M}(i)$ for $i=2$ to 7 (the relevant value of i is shown at the lower left hand corner of the matrix). The symbol $R(i)$ will denote the number of rows in the ith matrix, and the symbol $S(i)_p$ will denote sum of the elements in the pth row of the ith matrix. Thus $R(5)=7$ and $S(5)_2=2$. With this in hand, A_i is given by

$$A_0 = 1 \quad \text{otherwise } A_i = \sum_{p=1}^{R(i)} (-1)^{S(i)_p} \prod_{j=1}^{i} \frac{J(j)^{M(i)_{p,j}}}{M(i)_{p,j}!} \tag{6}$$

in which $\mathbf{M}(i)_{p,j}$ is the jth column entry in the pth row of $\mathbf{M}(i)$, and the function $J(j)$ is defined by

$$J(j) = \frac{\displaystyle\int_a^b K_{j-1}(t,t)dt}{j}, \quad j = 1, \ldots, \infty \tag{7}$$

The two series in Eq. (6) (one in the numerator and one in the denominator) converge quickly, and it has been the experience of the author that for cases tested, they both can be safely truncated at $n=13$ for almost all cases of practical interest, and this is supported by the study by Hollands [12]. The choice of the maximum n, denoted $n_{\max}$, is guided by the error in the solution, a method for calculating this error being given later.

Table 1 Values of counter matrices $\mathbf{M}(i)$ for $i=2$ to 7

$$\begin{vmatrix} 0 & 1 \\ 2 & 0 \end{vmatrix} \qquad \begin{vmatrix} 0 & 0 & 1 \\ 1 & 1 & 0 \\ 3 & 0 & 0 \end{vmatrix} \qquad \begin{vmatrix} 0 & 0 & 0 & 1 \\ 0 & 2 & 0 & 0 \\ 1 & 0 & 1 & 0 \\ 2 & 1 & 0 & 0 \\ 4 & 0 & 0 & 0 \end{vmatrix}$$

$$\begin{vmatrix} 0 & 0 & 0 & 0 & 1 \\ 0 & 1 & 1 & 0 & 0 \\ 1 & 0 & 0 & 1 & 0 \\ 1 & 2 & 0 & 0 & 0 \\ 2 & 0 & 1 & 0 & 0 \\ 3 & 1 & 0 & 0 & 0 \\ 5 & 0 & 0 & 0 & 0 \end{vmatrix} \qquad \begin{vmatrix} 0 & 0 & 0 & 0 & 0 & 1 \\ 0 & 0 & 2 & 0 & 0 & 0 \\ 0 & 1 & 0 & 1 & 0 & 0 \\ 0 & 3 & 0 & 0 & 0 & 0 \\ 1 & 0 & 0 & 0 & 1 & 0 \\ 1 & 1 & 1 & 0 & 0 & 0 \\ 2 & 0 & 0 & 1 & 0 & 0 \\ 2 & 2 & 0 & 0 & 0 & 0 \\ 3 & 0 & 1 & 0 & 0 & 0 \\ 4 & 1 & 0 & 0 & 0 & 0 \\ 6 & 0 & 0 & 0 & 0 & 0 \end{vmatrix} \qquad \begin{vmatrix} 0 & 0 & 0 & 0 & 0 & 0 & 1 \\ 0 & 0 & 1 & 1 & 0 & 0 & 0 \\ 0 & 1 & 0 & 0 & 1 & 0 & 0 \\ 0 & 2 & 1 & 0 & 0 & 0 & 0 \\ 1 & 0 & 0 & 0 & 0 & 1 & 0 \\ 1 & 0 & 2 & 0 & 0 & 0 & 0 \\ 1 & 1 & 0 & 1 & 0 & 0 & 0 \\ 1 & 3 & 0 & 0 & 0 & 0 & 0 \\ 2 & 0 & 0 & 0 & 1 & 0 & 0 \\ 2 & 1 & 1 & 0 & 0 & 0 & 0 \\ 3 & 0 & 0 & 1 & 0 & 0 & 0 \\ 3 & 2 & 0 & 0 & 0 & 0 & 0 \\ 4 & 0 & 1 & 0 & 0 & 0 & 0 \\ 5 & 1 & 0 & 0 & 0 & 0 & 0 \\ 7 & 0 & 0 & 0 & 0 & 0 & 0 \end{vmatrix}$$

There remains the determination of the countermatrices, $\mathbf{M}(i)$ for $i=8$ to $n_{\max}$. Each row in the matrix corresponds to one solution for the set $z_1, z_2, z_3, \ldots, z_i$ to the linear equation

$$z_1 + 2z_2 + 3z_3 + \cdots iz_i = i \tag{8}$$

where only positive integer solutions are allowed. That is, $z_1, \ldots, z_i$ must all be positive integers or zero. The correspondence between these solutions and $\mathbf{M}(i)$ is such that if $z_1=m_1$, $z_2=m_2, \ldots, z_i=m_i$ is one solution to this equation, then the corresponding row is $(m_1, m_2, \ldots, m_i)$. Every possible such solutions and row must be included in $\mathbf{M}(i)$, but the order of the rows is irrelevant. For example, for $i=3$, there are three solutions: (0,0,1), (1,1,0), and (3,0,0), so the matrix is as given in Table 1. A simple algorithm can be readily constructed that will generate the counter matrix for any i: Here, one generates, in turn, each possible combination of values for the set of m_i and then tests each combination to see which ones satisfy Eq. (8) with z replaced by m; a matrix containing these satisfactory values, as rows, is then constructed.

The above equations are greatly simplified forms of the original equations given by Fredholm, which contained integrals of determinants of size that increased with n. No approximations were made in that simplification process. But the kernels that arise in radiant analysis will not be amenable to the repeated analytic integrations implicit in Eq. (4), and so their integrations will have to be done through some approximate quadrature scheme. Hollands [12] used an approximate scheme, which reduces them to matrix multiplications as follows. For convenience we will make $a=0$ and $b=1$; we can do this without loss in generality because x and t can always be scaled and the definitions of $K(x,t)$ and $f(x)$ altered accordingly. Let the interval (0,1) be divided into N equal-sized subintervals having centers at $\xi_1, \ldots, \xi_N$, respectively. Now define matrices $\mathbf{K}_n$ with $n=0,1,2\ldots,n_{\max}$ by

$$\mathbf{K}_n = \begin{vmatrix} K_n(\xi_1,\xi_1) & K_n(\xi_1,\xi_2) & \dots & K_n(\xi_1,\xi_n) \\ K_n(\xi_2,\xi_1) & K_n(\xi_2,\xi_2) & \dots & K_n(\xi_2,\xi_n) \\ : & : & : & : \\ K_n(\xi_N,\xi_1) & \dots & \dots & K_n(\xi_N,\xi_N) \end{vmatrix} \tag{9}$$

Note that $\mathbf{K}_0$ can be determined directly. It was then shown that the following approximation holds with increasing accuracy as N increases:

$$\mathbf{K}_n \cong \frac{\mathbf{K}_0^{n+1}}{N^n} \tag{10}$$

It follows from the same logic and to equivalent precision, that

$$J(m) \cong \frac{\mathrm{trace}(\mathbf{K}_{m-1})}{Nm} \tag{11}$$

(the trace of a matrix being the sum of the elements along the diagonal) and this result can be used directly in Eq. (6), to determine the full set of A_i. Consider now the matrix obtained by replacing $K_{n-i}(x,t)$ in Eq. (5) by $\mathbf{K}_{n-1}$; this will be a very good estimate for the matrix of H values. That is,

$$\mathbf{H} = \begin{vmatrix} H(\xi_1,\xi_1) & H(\xi_1,\xi_2) & \dots & H(\xi_1,\xi_n) \\ H(\xi_2,\xi_1) & H(\xi_2,\xi_2) & \dots & H(\xi_2,\xi_n) \\ : & : & : & : \\ H(\xi_N,\xi_1) & \dots & \dots & H(\xi_N,\xi_N) \end{vmatrix} \cong \frac{\sum_{n=0}^{n_{\max}} \sum_{i=0}^{n} A_i \mathbf{K}_{n-1}}{\sum_{n=0}^{n_{\max}} A_n} \tag{12}$$

Determining $\mathbf{H}$ from the expression on the right, the complete function $H(x,y)$ can then be closely estimated from the nodal values in $\mathbf{H}$ using (two-dimensional cubic spline) interpolation. This constitutes the crux of the method.

Of course, one is normally interested in the unknown function $u(x)$ as well. This can be found by either of the two methods. First, one can use any method of numerical integration to get $u(x)$ from Eq. (2). Second, one can use a discretized form of Eq. (2):

$$\mathbf{u} = \mathbf{f} + \mathbf{H} \cdot \mathbf{f} \tag{13}$$

in which vector $\mathbf{f}$ is (the transpose of) row vector $[f(\xi_1), f(\xi_2), f(\xi_3), \dots, f(\xi_N)]$, and vector $\mathbf{u}$ is (the transpose of) row vector $[u(\xi_1), u(\xi_2), u(\xi_3), \dots, u(\xi_N)]$, the function $u(x)$ then being obtained from the nodal values using interpolation. Hollands [12] used the latter method, but because of the importance of the resolvent kernel in radiation analysis, we will stress the former method here.

Illustrative Examples and Error Evaluation

We now choose to apply the method to the well-known problem of finding the temperature distribution on a hollow cylinder (diameter D, length L) open to an environment at 0 deg absolute at both ends and with uniform heat flux applied to its sides, a problem solved by three different methods by Usiskin and Siegel [14]. The governing integral equation is of the single-variable Fredholm type, like Eq. (1) with $u(x)$ being the radiosity $q_o(x)$, the kernel $K(x,t)$ being given by

$$K(x,t) = \frac{1}{2c}\left\{1 - |x-t|\frac{(x-t)^2 + 6c^2}{((x-t)^2 + 4c^2)^{3/2}}\right\}, \quad c = D/(2L) \tag{14}$$

the forcing function $f(x)$ being the applied heat flux $q_s(x)$ (which is a constant in this case), and the limits on the integral being 0 and 1, respectively. Once $q_o(x)$ has been determined by solving the integral equation, the temperature distribution $T(x)$ is to be determined by solving the equation

$$q_s(x) = \frac{\epsilon}{1-\epsilon}(\sigma T(x)^4 - q_o(x)) \tag{15}$$

for $T(x)$, ϵ being the emissivity of the cylinder's inside surface, and it is kept in mind that $q_s(x)$ is constant in the present case.

Table 2 Distribution of dedimensionalized radiosity along the inside surface of a hollow cylinder with open ends and under uniform heat flux

		q_o/q_s		
L/D	x/L	Present work	Prior work	Error (%)
1	0	2.06290	2.06	3×10^{-4}
	1/8	2.30580	2.31	
	1/4	2.48757	2.49	
	3/8	2.59967	2.60	
	1/2	2.63750		
4	0	4.956	4.95	8×10^{-3}
	1/8	8.633	8.61	
	1/4	11.212	11.2	
	3/8	12.709	12.6	
	1/2	13.201	13.2	

Table 2 gives the results obtained with $N=1000$ and $n=13$. The third column gives the dedimensionalized radiosity, q_o/q_s, for various values of the aspect ratio L/D, and for each aspect ratio, for five values of the relative distance x/L from either end. In the fourth column are shown the values obtained by Usiskin and Siegel [14] using the numerical method, which they considered the most precise of the three methods they tested. The results of the present work are shown to the proper number of significant figures, as established by an error analysis methodology described below. The final column gives the percent error (found to roughly independent of x/L) of the present results, as established in the same error analysis. Each table item took about 30 s to calculate on a contemporary PC programed in MATHCAD.

Hollands [12] methodology for error estimation started by calculating the residual, $\delta(x)$, defined by

$$\delta(x) = u_{n_{\max},N}(x) - f(x) - \int_0^1 u_{n_{\max},N}(t)K(x,t)dt \tag{16}$$

where $u_{n_{\max},N}(x)$ is the result obtained with specific values for $n_{\max}$ and N. The true solution, $u(x)$, has zero residual, so

$$0 = u(x) - f(x) - \int_0^1 u(t)K(x,t)dt \tag{17}$$

Subtracting Eq. (17) from Eq. (16) and letting the deviation of $u_{n_{\max},N}(x)$ from $u(x)$ (i.e., the error) be denoted by $\epsilon(x)$, we obtain

$$\epsilon(x) = \delta(x) + \int_0^1 \epsilon(t)K(x,t)dt \tag{18}$$

This is an integral equation having the same kernel as the original equation, but now $\delta(x)$ plays the role of $f(x)$ and $\epsilon(x)$ is the unknown function. It follows that

$$\epsilon(x) = \delta(x) + \int_0^1 \delta(t)H(x,t)dt \tag{19}$$

Now we have at hand an excellent estimate for the function $H(x,t)$, and we use it to calculate $\epsilon(x)$ from Eq. (19). This gives the error estimate. Hollands [12] tested this method on problems where the exact analytical solution was known; he did a direct comparison of the $\epsilon(x)$ obtained from Eq. (19) to the difference

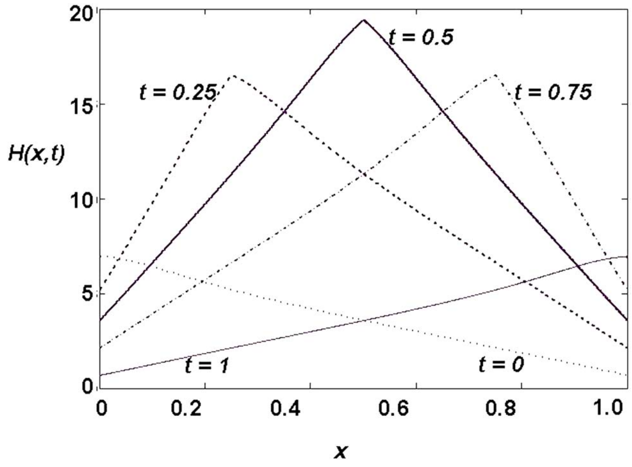

Fig. 1 Plot of resolvent kernel corresponding to a hollow cylinder open at both ends to an environment at 0 K and with a prescribed heat flux applied to its interior wall

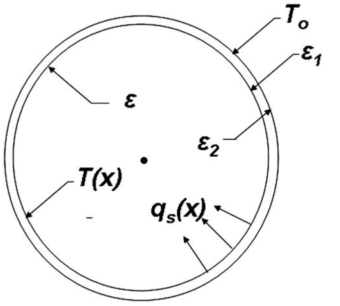

Fig. 2 Cross section of two concentric cylinders with a small gap between them, the outer one being at uniform temperature T_0 and the inner one open at both ends to an environment at 0 K

between $u_{n_{\max},N}(x)$ and the exact answer. He found excellent agreement between the two methods.

It should be noted that using modern computational tools (as opposed to those of Usiskin and Siegel [14]) similar accuracy can be obtained with the numerical method with about the same programming and computational effort. Thus if for the present problem, with the number of discrete values equal to N_d, one solves the above problem using the numerical method with, say, $N_d = 300$, 500, 700, and 900, and then one extrapolates (using Richardson extrapolation) to $N_d = \infty$, one obtains slightly better accuracy[1] than with the simplified-Fredholm method (SFM) with about the same execution and programming times. The advantage of the SFM, therefore, is not its ease or accuracy but in the availability of the resolvent kernel, as the problem to follow will demonstrate.

The resolvent kernel is plotted in Fig. 1 for the problem at hand. In general, the resolvent kernel provides a versatility that makes it very useful for solving more complicated problems. For example, suppose that the applied heat flux $q_s(x)$ at the cylinder walls had been variable rather than uniform. Then the radiosity $q_o(x)$ (and hence the temperature distribution from Eq. (15)) would be given directly by

$$q_o(x) = q_s(x) + \int_0^1 q_s(t)H(x,t)dt \tag{20}$$

which can be readily evaluated for any $q_s(x)$ once the resolvent kernel is at hand.

The resolvent kernel is also useful when there is an adjacent enclosure. Thus suppose (as shown in Fig. 2) that the walls of the cylinder are thin and there is a second cylinder that is concentric and of equal length to the first, but with slightly greater radius so that there is a small gap between the two cylinders, and let the temperature of the outer cylinder be fixed uniformly at T_0. The emissivities on either side of the gap are ε_1 and ε_2, respectively. A radiant analysis of the gap-enclosure gives

$$q_s(x) = \Im_{1-2}(\sigma T_0^4 - \sigma T(x)^4) \tag{21}$$

where $\Im_{1-2} = (1/\varepsilon_1 + 1/\varepsilon_2 - 1)^{-1}$. Equations (20), (21), and (15) give three simultaneous equations for the three unknowns $q_s(x)$, $T(x)$, and $q_o(x)$. When solved for $q_s(x)$, they yield the new integral equation

$$q_s(x) = \Im_t \sigma T_o^4 + \int_0^1 q_s(t)\hat{K}(x,t)dt \tag{22}$$

where $\Im_t = (1/\varepsilon + 1/\Im_{1-2})^{-1}$ and $\hat{K}(x,t) = -\Im_t H(x,t)$. Equation (22) can be solved for $q_s(x)$ using the techniques already described, and then $T(x)$ can be obtained from Eq. (21). Table 3 gives the results of such an analysis for $L/D = 4$, for several combinations of values for ε and $\Im_{1-2}$. The table gives the dimensionless fourth-power temperature θ, defined by

$$\theta(x) = (T_o^4 - T(x)^4)/T_o^4, \tag{23}$$

at the center and edge of the cylinder (i.e., at $x = 0$ and at $x = 0.5$, respectively).

Relation of Resolvent Kernel to Exchange Factor

Hottel [15] derived the following expression for the average heat flux $\overline{q_{s,k}}$ at the kth surface in a gray diffuse enclosure containing N surfaces, the N_T of which have specified uniform temperature and the remaining $N - N_T$ of which are uniformly adiabatic:

$$\overline{q_{s,k}} = \sum_{N_T} \Im_{k-i}(\sigma T_k^4 - \sigma T_i^4) \tag{24}$$

where, in the summation, i runs through the values of k relevant only to the N_T specified temperature surfaces and $\Im_{k-i}$, the exchange factor[2] from surface k to i, depends only on the enclosure geometry and on the emissivities of the temperature-specified surfaces.[3] The various matrix expressions derived by Hottel and others for $\Im_{k-i}$ are all based on a finite-area approximate analysis in which the radiosity is assumed to be uniform over each surface. We now demonstrate that $\Im_{k-i}$ exists under infinitesimal-area analysis and show its relation to the resolvent kernel, all for enclosures that can be reduced to single-variable problems. (The conditions under which the enclosure will lead to a single-variable integral equation are explained by Daun and Hollands [6], among others.)

For this class of enclosures, there will exist a single parameter t such that the enclosure surface can, for practical purposes, be represented parametrically by

---

[1] The accuracy of the numerical method is determined by the goodness of fit of the relation between N_d and the value of u computed at that N_d setting.

[2] Textbooks have attached various names to $\Im_{i,j}$: interchange factor [15], gray-body shape factor [16], total exchange factor [17] (this after division by $\varepsilon_i\varepsilon_j$), transfer factor [18], and exchange factor [4,5]. Several authors [19,20] elected not to give it a name. Thus the choice here of the term exchange factor is somewhat arbitrary.

[3] It should be noted that a simple extension to Eq. (24) applies when the adiabatic surfaces are of prescribed uniform heat flux instead. For simplicity, we do not consider that case here.

Table 3 Table of dimensionless fourth-power temperatures at center and edge of the hollow cylinder with open ends and cross section shown in Fig. 2

	$\theta(0)$	$\theta(0)$	$\theta(0)$	$\theta(0.5)$	$\theta(0.5)$	$\theta(0.5)$
$\Im_{1-2}$ →	0.25	0.5	0.75	0.25	0.5	0.75
ε ↓						
0.25	0.3820	0.2428	0.1784	0.1738	0.0908	0.0610
0.5	0.4856	0.3387	0.2617	0.1817	0.905	0.0587
0.75	0.5353	0.3926	0.3129	0.1830	0.880	0.0554

$$\mathbf{r} = \mathbf{r}(t), \quad 0 \leqslant t \leqslant 1 \tag{25}$$

where $\mathbf{r}$ is the position vector and $\mathbf{r}(t)$ is some vector function of t. As t runs from 0 to 1, the point at $\mathbf{r}(t)$ will visit and pass through representative points on every surface once. Similarly, as some other variable[4] χ runs from 0 to 1, the point at $\mathbf{r}(\chi)$ will visit and pass through representative points on every surface once. (It will be necessary to refer to two points and two variables.) Let surface k be defined by the interval $u_k \le t \le u_k'$ or $u_k \le \chi \le u_k'$. We will call this interval the kth nonadiabatic interval when the kth surface is temperature-specified, and the kth adiabatic interval when the kth surface is adiabatic. It follows that with χ on the kth nonadiabatic interval, the emitted flux will be $\varepsilon_k \sigma T_k^4(\chi)$ and with χ on the kth adiabatic interval the local heat flux q_s will be zero. So the governing integral equation is

$$q_o(\chi) = B(\chi) + \int_0^1 \beta(\chi)\frac{dF(\chi,t)}{dt} q_o(t)dt = B(\chi) + \int_0^1 K(\chi,t) q_o(t)dt \tag{26}$$

where $dF(\chi,t)$ is the infinitesimal point form factor from a point at χ to the area cut out when t runs from t to $t+dt$; $B(\chi)=\varepsilon_k \sigma T_k^4$ and $\beta(\chi)=1-\varepsilon_k$ for χ on the kth nonadiabatic interval, and $B(\chi)=0$ and $\beta(\chi)=1$ for χ on the kth adiabatic interval. Equation (26) has solution

$$q_o(\chi) = B(\chi) + \int_0^1 H(\chi,t)B(t)dt \tag{27}$$

where $H(\chi,t)$ is the resolvent kernel to kernel $K(\chi,t)$. Consider now the case where χ is on the kth nonadiabatic interval. The integral in the above equation can be split into a summation of integrals over each surface in turn, but when we are integrating over the adiabatic surfaces, $B(t)=0$, so there is no contribution and it is only necessary to sum over the non-adiabatic surfaces. Thus

$$q_o(\chi) = \varepsilon_k \sigma T_k^4 + \sum_{N_T} \int_{u_i}^{u_i'} H(\chi,t)\varepsilon_i \sigma T_i^4 dt, \quad u_k \leqslant \chi \leqslant u_k', \quad k = 1, \ldots, N_T \tag{28}$$

where, as before, in the summation, i runs through the values of k relevant only to the N_T specified temperature surfaces. Averaging this expression over the kth surface yields the average radiosity $\overline{q_{o,k}}$, at the kth nonadiabatic surface, and when this is substituted into the equation for the average heat flux $\overline{q_{s,k}}$ on the kth surface, namely, $\overline{q_{s,k}}=(\varepsilon_k/(1-\varepsilon_k))(\sigma T_k^4-\overline{q_{o,k}})$, there results an equation for $\overline{q_{s,k}}$. This equation can be simplified by noting that when all the temperatures are equal, we must have $\overline{q_{s,k}}=0$.

Following this, we find that it can be rearranged to an equation like Eq. (24), proving that Eq. (24) does indeed hold under infinitesimal-area analysis. Moreover, it is found that $\Im_{k-i}$ and $H(x,t)$ are related by

$$\Im_{k-i} = \frac{\varepsilon_k \varepsilon_i}{1-\varepsilon_k}\frac{1}{s_k}\int_{\chi=u_k}^{\chi=u_k'}\int_{t=u_i}^{t=u_j'} H(\chi,t)\frac{ds}{dx}dtd\chi \tag{29}$$

where ds is the elemental area cut out on the surface when χ goes from χ to $\chi+d\chi$ and s_k is the area of the kth surface.

To illustrate this relation, let us now apply these equations (29) to obtain the exchange factors in a problem whose geometry is axially invariant, like a very long duct. This is one of the two main geometries that lend themselves to single-variable analysis. Consider a very long duct whose cross section is a square, with opposing sides 1 and 3 each uniformly at a different temperatures, T_1 and T_3, the other pair of opposing surfaces being adiabatic, and all surfaces having an emissivity of 0.5. Let us locate the square in the X-Y plane with one vertex at the origin and one side along the X-axis. Then the parametric representation of the square is given by Eq. (25) with $\mathbf{r}(t)$ given by

$$\mathbf{r}(t) = (4t,0) \quad \text{for } A, \quad = (1,4t-1) \quad \text{for } B, \quad = (3-4t,1) \quad \text{for } C, \quad = (0,4-4t) \quad \text{for } D \tag{30}$$

where condition A is $0 \le t < 1/4$ (side 1), condition B is $1/4 \le t < 1/2$ (side 2), condition C is $1/2 \le t < 3/4$ (side 3), and condition D is $3/4 \le t < 1$ (side 4). According to Hollands [5], the kernel for axially invariant geometries is given by

$$K(\chi,t) = \frac{|(\mathbf{n}(\chi)\cdot(\mathbf{r}(\chi)-\mathbf{r}(t)))(\mathbf{n}(t)\cdot(\mathbf{r}(\chi)-\mathbf{r}(t)))\ |}{2|\mathbf{r}(\chi)-\mathbf{r}(t)|^3}\left|\frac{d\mathbf{r}(t)}{dt}\right|\beta(\chi) \tag{31}$$

where $\mathbf{n}(\chi)$ is the local inward normal at χ, which for the square is $\mathbf{n}(\chi)=(0,1)$ for A, $\mathbf{n}(\chi)=(-1,0)$ for B, $\mathbf{n}(\chi)=(-1,0)$ for C, and $\mathbf{n}(\chi)=(1,0)$ for D. Also, $\beta(\chi)=0.5$ for A and C, $\beta(\chi)=1$ for B and D, and $|d\mathbf{r}(t)/dt|$ is everywhere equal to 4. In applying Eq. (29), we note that $u_1=0$, $u_1'=1/4$, $u_2=1/2$, and $u_2'=3/4$. We also see that $ds=4dxW$ and $s_1=W$, where W, $\cong\infty$, is the length of the duct. Finding the resolvent kernel and evaluating the integral give the answer: $\Im_{1-3}=0.289$.

Once it is realized that Eq. (24) holds under infinitesimal analysis, the set of $\Im_{k-i}$ can also be determined using the numerical method, without evaluating the resolvent kernel, as will now be illustrated. In the above example, when we have put $\sigma T_1^4=1$ and $\sigma T_3^4=0$ in Eq. (24), we find that under these temperature conditions $\overline{q_{s,1}}=\Im_{1-3}$. Thus by determining the average heat flux $\overline{q_{s,1}}$ at surface 1 by the numerical method under the specified temperature conditions, $\Im_{1-3}$ can be determined once and for all from $\Im_{1-3}=\overline{q_{s,1}}$. This was done and yielded the same value (to three decimal places) as was determined from Eq. (29), namely, 0.289. (Of course, this value continues to hold, regardless of the temperature settings, as Eq. (29) makes clear.) In general, to determine $\Im_{i-j}$, one sets $\sigma T^4=1$ for all the temperature-specified surfaces except for surface j, σT_j^4 being set equal to 0; then one solves for

---

[4] We switch to χ as the second variable in our integral equation instead of x because x can also represent the coordinate in the X-Y plane.

$\overline{q}_{s,i}$ by the numerical method and equates this to $\Im_{i-j}$. One can repeat this for all possible values of i and j, yielding the full set of $\Im_{k-i}$.

Limitations

There are certain conditions under which Fredholm's solution does not apply, and this is true for the simplified version as well. For the solution method to apply, the kernel must be L_2 over $[a,b]\times[a,b]$ and the forcing function must be L_2 over $[a,b]$, by which it is meant that

$$\int_a^b \int_a^b K(x,t)^2 dx dt \quad \text{and} \int_a^b f(x)^2 dx \tag{32}$$

are both finite. One needs to test the kernel and the forcing function before proceeding. For radiant analysis, the forcing function is almost definitely L_2, but because the kernel can sometimes go to infinity over the range, one may find that the kernel is not L_2 for a specific enclosure. If $K(x,t)$ remains finite over the total range, it can, of course be concluded to be L_2, but if it does not remain finite it can still be L_2, and a test is necessary. All the enclosures tested by the author have been found to be L_2. The method used for the test has been to use the integrator routine in MATHCAD to calculate the integrals in Eq. (32), MATHCAD reports so if the integral is improper. It has also been found that if $K(t,t)=\infty$ for all t, the method fails. This would appear to prevent it from being used in the well-known integral equation that arises in a gray planar medium in radiative equilibrium, although there may be some ways around that problem.

Concluding Remarks

It appears that the simplified-Fredholm method for solving integral equations can play a useful role in radiant analysis. Not only does it give an explicit solution that is readily programmed but it also provides an expression for the resolvent kernel, a valuable tool both from a practical and a theoretic point of view. From a practical point of view, the resolution of the resolvent kernel permits one to more efficiently solve problems where a surface connects to another heat transfer mode or to an adjacent enclosure. From a theoretic point of view, the existence of the resolvent kernel can be used to demonstrate certain theoretic results, for example, the existence and interpretation of the exchange factor under infinitesimal-area analysis. Another important advantage of the method is that it allows the user to readily determine the possible error in any proffered solution to the subject integral equation.

The aforesaid advantages relate to problems in one variable. Remaining to be done is the extension of this work to problems in two variables. Although almost all of the enclosure problems solved in the literature were treatable by solving single-variable integral equations, two-variable integral equations arise much more commonly, and these are less often treated. Aiding in the extension will be the general-purpose methodology for obtaining the four-variable kernel, derived by Daun and Hollands [6] and further developed by Hollands [5]. The present paper has laid the foundations for the explication of an analogous two-variable integral equation solver and of its application to problems in radiant transfer. This is planned to be the topic of a future paper.

References

[1] Tricomi, F. G., 1967, *Integral Equations*, Interscience Publishers, Inc., New York.

[2] Prem, K., Kythe, P., and Puri, P., 2002, *Computational Methods for Integral Equations*, Birkhauser, Boston.

[3] Siegel, R., and Howell, J. R., 1992, *Thermal Radiation Heat Transfer*, 3rd ed., Hemisphere, Washington, DC, p. 288.

[4] Modest, M. F., 1993, *Radiative Heat Transfer*, McGraw-Hill, New York, p. 214.

[5] Hollands, K. G. T., 2004, *Thermal Radiation Fundamentals*, Begell House, Inc., New York, pp. 222–233.

[6] Daun, K. J., and Hollands, K. G. T., 2001, "Infinitesimal-area Radiative Analysis Using Parametric Surface Representation, Through NURBS," ASME J. Heat Transfer, **123**, pp. 249–256.

[7] Huang, R. P., and Shaw, R. P., 1995, "The Trefftz Method as an Integral Equation," Adv. Eng. Software, **24**, pp. 57–63.

[8] Babolian, E., Biazar, J., and Vahidi, A. R., 2004, "The Decomposition Method Applied to Systems of Fredholm Integral Equations of the Second Kind," Appl. Math. Comput., **148**, pp. 443–452.

[9] Maleknejed, K., and Mahmoudi, Y., 2004, "Numerical Solution of Linear Integral Equations by Using Hybrid Taylor and Block-Pulse Functions," Appl. Math. Comput., **149**, pp. 799–806.

[10] Maleknejed, K., and Karami, M., 2005, "Using the WPG Method for Solving Integral Equations of the Second Kind," Appl. Math. Comput., **166**, pp. 123–130.

[11] Maleknejad, K., and Karami, M., 2005, "Numerical Solution of Non-Linear Fredholm Integral Equations by Using Multiwavelets in Petrov-Galerkin Method," Appl. Math. Comput., **168**, pp. 102–110.

[12] Hollands, K. G. T., 2007, "A Simplification to Fredholm's Solution to the Fredholm Integral Equation of the Second Kind," Appl. Math. Comput., **189**, pp. 1078–1086.

[13] Fredholm, I., 1902, "Sur une Class d'Equations Fonctionnelles," Acta Math., **27**, pp. 365–390; collected in, 1961, *Collection of Modern Mathematical Classics*, R. A. Bellman, ed., Dover, New York, pp. 116–141.

[14] Usiskin, C. M., and Siegel, R., 1960, "Thermal Radiation From a Cylindrical Enclosure With Specified Wall Heat Flux," ASME J. Heat Transfer, **82**, pp. 369–374.

[15] Hottel, H. C., 1954, "Radiant-Heat Transmission," *Heat Transmission*, McGraw-Hill, New York, pp. 72–74.

[16] Kreith, F., 1961, *Principals of Heat Transfer*, International Textbook Company, Scranton, PA, p. 204.

[17] Duffie, J. A., and Beckman, W. A., 1991, *Solar Engineering of Thermal Processes*, 2nd ed., Wiley, New York, p. 157.

[18] Edwards, D. K., 1981, *Radiation Heat Transfer Notes*, Hemisphere, Washington, DC, p. 111.

[19] Sparrow, E. M., and Cess, R. D., 1970, *Radiation Heat Transfer*, rev. ed., Brooks/Coles, Belmont, CA, p. 92.

[20] Brewster, M. Q., 1992, *Thermal Radiative Transfer and Properties*, Wiley, New York, p. 95.

Finite-Volume Formulation and Solution of the P_3 Equations of Radiative Transfer on Unstructured Meshes

Mahesh Ravishankar

Sandip Mazumder[1]
e-mail: mazumder.2@osu.edu

Ankan Kumar

Department of Mechanical Engineering,
The Ohio State University,
Columbus, OH 43210

The method of spherical harmonics (or P_N) is a popular method for approximate solution of the radiative transfer equation (RTE) in participating media. A rigorous conservative finite-volume (FV) procedure is presented for discretization of the P_3 equations of radiative transfer in two-dimensional geometry—a set of four coupled, second-order partial differential equations. The FV procedure presented here is applicable to any arbitrary unstructured mesh topology. The resulting coupled set of discrete algebraic equations are solved implicitly using a coupled solver that involves decomposition of the computational domain into groups of geometrically contiguous cells using the binary spatial partitioning algorithm, followed by fully implicit coupled solution within each cell group using a preconditioned generalized minimum residual solver. The RTE solver is first verified by comparing predicted results with published Monte Carlo (MC) results for two benchmark problems. For completeness, results using the P_1 approximation are also presented. As expected, results agree well with MC results for large/intermediate optical thicknesses, and the discrepancy between MC and P_3 results increase as the optical thickness is decreased. The P_3 approximation is found to be more accurate than the P_1 approximation for optically thick cases. Finally, the new RTE solver is coupled to a reacting flow code and demonstrated for a laminar flame calculation using an unstructured mesh. It is found that the solution of the four P_3 equations requires 14.5% additional CPU time, while the solution of the single P_1 equation requires 9.3% additional CPU time over the case without radiation. [DOI: 10.1115/1.4000184]

Keywords: radiation, participating media, P_3, RTE solver, finite-volume, unstructured

1 Introduction

Radiation is the dominant mode of heat transfer in many high-temperature applications, such as combustion and rapid thermal chemical vapor deposition. With growing concerns over global warming, solar radiation transport through the atmosphere is rapidly becoming a subject of intense interest and research. Radiation is also a critical mode of energy transfer in modern laser-based manufacturing processes, and in biological applications—both for laser-induced remediation and cure of tissues, and for detection using optical tomography based techniques.

The problem of radiation transport entails solution of the radiative transfer equation (RTE) for the radiative intensity. The RTE is an integro-differential equation in seven independent variables—time, three space coordinates, two angular coordinates, and wave number. Therefore, it is difficult to solve exactly even for simple one-dimensional (1D) problems [1,2]. Hence, approximate solution methods are necessary to solve the RTE for more practical situations. A survey of the literature over the past four decades reveals that the four most popular methods to solve the RTE are as follows: (i) the spherical harmonics method and its variations [3–5], (ii) the discrete ordinates method and its variations, including its finite-volume variant (the so-called control angle discrete ordinates method) [6,7], (iii) the zonal method [8–10], and (iv) the Monte Carlo (MC) method [1,2].

Broadly, these four methods to solve the RTE can be categorized into two types, as follows: (1) photon-based methods, and (2) photon-free methods. The methods that belong to the former category are the discrete ordinates (S_N), zonal, and the MC methods, while the spherical harmonics (P_N) method is a photon-free method. In photon-based methods, photons are essentially tracked along a line of sight, and directional radiative intensities along various lines of sight are finally summed over solid angle 4π to obtain the net radiation intensity at any point. In the popular S_N method, the lines of sight are predetermined, resulting in a deterministic RTE solver. In the MC method, on the other hand, the lines of sight are stochastically determined. In the photon-free P_N method, integration over all lines of sight (or solid angles) is performed analytically using orthogonal basis functions: Legendre polynomials in spherical coordinates. The P_N method, as opposed to photon-based methods, is, thus, a spectral method. Each of these methods has its relative advantages and disadvantages.

To date, the S_N method has been arguably the most popular method for solving the RTE. In essence, the S_N method is a straightforward extension of the finite-difference method for spatial discretization, with additional discretization in the angular direction as well. The S_N method, however, suffers from a few well-known shortcomings. It produces inaccurate results in geometries with large aspect ratios, or geometries with sharp corners (e.g., a wedge) because of its inability to resolve acute solid angles using a finite number of predetermined directions. Inaccuracies resulting from this inability to properly resolve acute solid angles are often referred to in literature as “ray effects.” [11] The minimum number of partial differential equations (PDEs) that need to be solved in this method even for a gray gas is equal to the number of

---

[1] Corresponding author.

Contributed by the Heat Transfer Division of ASME for publication in the JOURNAL OF HEAT TRANSFER. Manuscript received October 23, 2008; final manuscript received March 3, 2009; published online December 1, 2009. Assoc. Editor: Yogesh Jaluria.

directions (NDIR). If, for example, the S_4 method is used, NDIR=12 in two-dimensional (2D) and NDIR=24 in three-dimensional (3D) geometries. The convergence of the S_N method deteriorates rapidly with increase in the optical thickness of the medium. This is because the boundary-to-boundary information (intensity) propagation is almost nonexistent in an optically thick medium. Numerically, this results in a poorly conditioned system of equations. In the presence of scattering, the S_N equations are strongly coupled. In such a scenario, segregated solution of the directional equations (i.e., one direction at a time) results in poor convergence [12]. While coupled solution of the S_N equations is conceivable [12], it is difficult both from algorithmic as well as memory standpoints.

The P_N method, as discussed above, is a spectral method in which no angular discretization is necessary, and thus, it does not suffer from any of the aforementioned problems encountered in the S_N method. In addition, the number of PDEs that ultimately need to be solved in the P_N method is substantially less compared with the S_N method. For example, the lowest order P_N method, namely, the P_1 method, results in a single Helmholtz equation with Robin-type boundary conditions [1]. Despite these advantages, the P_N method has its own set of shortcomings. The P_1 method is invalid for nonparticipating media. In other words, one cannot use this method in a scenario where the medium may be participating in some regions and nonparticipating in some others. The P_1 method is known to yield poor results in cases where emission from boundaries is dominant (i.e., cold medium bounded by hot walls) [1]. The convergence of the P_1 method is poor if the medium is optically thin—a scenario which renders the governing equations stiff [13]. Extension of the spherical harmonics method from P_1 to higher orders of accuracy (P_3, P_5, etc.) is quite cumbersome because the resulting partial differential equations have cross-derivatives, and because of the difficulty in implementing the boundary conditions [14,15].

The above discussion clearly points to the fact that both S_N and P_N methods are incapable of treating arbitrary optical thicknesses, especially when the extinction coefficient of the medium may vary by orders of magnitude within the computational domain. The accuracy of S_N method is particularly poor for optically thick situations, while P_N is invalid for transparent media. The MC method is capable of remedying most of the drawbacks with the S_N and P_N methods with relative ease. The MC method has long been known as the method of choice for obtaining benchmark solutions to the RTE. Unfortunately, the MC method can be prohibitively slow, especially in optically thick media and in complex 3D geometries. Even with modern computing technology and parallel architectures, the MC method is not deemed practical for engineering calculations. In recent years, in view of the shortcomings of both S_N and P_N methods, researchers have began to explore a new class of methods. In this new class of methods, strengths of the stochastic MC method are selectively combined with the computational efficiency of S_N and P_N deterministic approaches to yield more accurate results at reasonable computational costs. This class of methods is referred to as the hybrid approach. For example, the S_N method has been combined with MC to eliminate problems associated with "ray effects." Similarly, the P_1 method has been modified to yield the so-called modified differential approximation (MDA) [3,4] and improved differential approximation (IDA) [5] methods—both of which can better handle large variations in optical thickness of the medium. While the idea of hybrid methods has existed for quite some time, to the best of our knowledge, they have not been used often, and have not yet been demonstrated for practical engineering applications.

The P_1 method continues to be a popular method for solution of the RTE because it is easy to implement in a general-purpose computational fluid dynamics (CFD) code, and is, therefore, amenable for practical engineering calculations. However, as documented above and elsewhere [1], it often produces inaccurate results. Since the P_N method is a spectral method, it is conceivable that the gain in accuracy will be significant if one were to use the next higher order, namely, P_3. The P_3 method has witnessed limited use [14–19] on account of its complexity—both from a mathematical as well as a computational algorithm development standpoint. In recent years, Yang and Modest [14,15] generalized the P_N equations to make them amenable for solution using canned PDE solvers, such as FLEXPDE and PDE2D. Solution to the P_3 equations has been obtained for two different benchmark problems by Yang and Modest [14,15] using relatively coarse orthogonal meshes in 2D. Comparison of their P_1/P_3 results with MC results indicates that the accuracy of P_3 is superior to that of P_1, as expected, at least for optically thick situations. Other notable work in this area includes the work done by McClarren et al. [20], who solved the time-dependent one-dimensional P_3 equations using both finite-volume (FV) and finite-element techniques [20,21].

In order to make the P_3 method attractive for practical engineering calculations, it is necessary to develop a solution procedure that is compatible to the mesh topology and discretization procedures used in modern-day CFD codes. Most modern CFD codes use unstructured (or nonconformal) mesh topology and the finite-volume method. In such a framework, structured body-fitted meshes, which continue to be used in many codes within the government and academia, can be thought of simply as an unstructured mesh with skewed quadrilateral (in 2D) or hexahedral (in 3D) control volumes (or cells). In other words, an unstructured mesh formulation is all-encompassing, and can be used for any mesh topology. In this article, we present a conservative unstructured finite-volume formulation for solution of the P_3 equations of radiative transfer in two-dimensional geometry. The P_3 equations represent a set of four coupled, second-order elliptic PDEs. A new solver for coupled implicit solution of the four PDEs, after finite-volume discretization, is also developed and demonstrated. Finally, the new RTE solver is coupled to an unstructured CFD code, and demonstrated for a laminar flame calculation. While the method is demonstrated here only for 2D geometries, the finite-volume formulation presented here is also valid for 3D, and may be used as a starting point for future development in this area.

2 Mathematical Formulation and Solution

2.1 Governing Equations. In nondimensional optical coordinates, the RTE is written as [1]

$$\hat{\mathbf{s}}\cdot\nabla_\tau I(\underline{\tau},\hat{\mathbf{s}}) + I(\underline{\tau},\hat{\mathbf{s}}) = (1-\omega)I_b + \frac{\omega}{4\pi}\int_{4\pi} I(\underline{\tau},\hat{\mathbf{s}}')\Phi(\hat{\mathbf{s}},\hat{\mathbf{s}}')d\Omega' \tag{1}$$

where $I(\underline{\tau},\hat{\mathbf{s}})$ is the intensity at an optical position $\underline{\tau}$ and along a light of sight $\hat{\mathbf{s}}$, ω is the scattering albedo, I_b is the Planck function, and $\Phi(\hat{\mathbf{s}},\hat{\mathbf{s}}')$ is the scattering phase function. In the method of spherical harmonics, the intensity is expressed as an infinite series of orthogonal basis functions [14,15]

$$I(\underline{\tau},\hat{\mathbf{s}}) = \frac{1}{4\pi}\sum_n (2n+1)J_n(\underline{\tau},\hat{\mathbf{s}}) \tag{2}$$

where

$$J_n(\underline{\tau},\hat{\mathbf{s}}) = \frac{1}{2n+1}\sum_{m=-n}^{n} I_n^m(\underline{\tau})Y_n^m(\hat{\mathbf{s}}) \tag{3}$$

In Eq. (3), the function $J_n(\underline{\tau},\hat{\mathbf{s}})$ has been expressed as the sum of the product of two functions—a location-dependent coefficient function $I_n^m(\underline{\tau})$, and a spherical harmonic function $Y_n^m(\hat{\mathbf{s}})$. The spherical harmonic functions can be expressed in terms of Legendre polynomials [14,15]. Yang and Modest [14,15] recently formalized the P_N equations and boundary conditions of radiative transfer for 3D geometries. The result is a set of coupled, second-order, elliptic PDEs. In this section, rather than start from the general P_N equations, we start from the P_3 equations in 2D geometries, as presented by Yang and Modest [14,15]

$$\frac{\partial}{\partial x}\left[2\gamma_{8,3}\frac{1}{\beta}\frac{\partial I_2^{-2}}{\partial x}-\gamma_{1,1}\frac{1}{\beta}\frac{\partial I_2^0}{\partial y}+2\gamma_{7,-3}\frac{1}{\beta}\frac{\partial I_2^2}{\partial y}+\frac{5}{\alpha_1}\frac{1}{\beta}\frac{\partial I_0}{\partial y}\right] + \frac{\partial}{\partial y}\left[2\gamma_{8,3}\frac{1}{\beta}\frac{\partial I_2^{-2}}{\partial y}-\gamma_{1,1}\frac{1}{\beta}\frac{\partial I_2^0}{\partial x}-2\gamma_{7,-3}\frac{1}{\beta}\frac{\partial I_2^2}{\partial x}+\frac{5}{\alpha_1}\frac{1}{\beta}\frac{\partial I_0}{\partial x}\right] - 2\beta\alpha_2 I_2^{-2}=0 \tag{4a}$$

$$\frac{\partial}{\partial x}\left[\gamma_{6,1}\frac{1}{\beta}\frac{\partial I_2^0}{\partial x}-6\gamma_{1,1}\frac{1}{\beta}\frac{\partial I_2^2}{\partial x}-6\gamma_{1,1}\frac{1}{\beta}\frac{\partial I_2^{-2}}{\partial y}-\frac{5}{\alpha_1}\frac{1}{\beta}\frac{\partial I_0}{\partial x}\right] + \frac{\partial}{\partial y}\left[\gamma_{6,1}\frac{1}{\beta}\frac{\partial I_2^0}{\partial y}+6\gamma_{1,1}\frac{1}{\beta}\frac{\partial I_2^2}{\partial y}-6\gamma_{1,1}\frac{1}{\beta}\frac{\partial I_2^{-2}}{\partial x}-\frac{5}{\alpha_1}\frac{1}{\beta}\frac{\partial I_0}{\partial y}\right] - \beta\alpha_2 I_2^0=0 \tag{4b}$$

$$\frac{\partial}{\partial x}\left[2\gamma_{8,3}\frac{1}{\beta}\frac{\partial I_2^2}{\partial x}-\gamma_{1,1}\frac{1}{\beta}\frac{\partial I_2^0}{\partial x}-2\gamma_{7,-3}\frac{1}{\beta}\frac{\partial I_2^{-2}}{\partial y}+\frac{5}{\alpha_1}\frac{1}{\beta}\frac{\partial I_0}{\partial x}\right] + \frac{\partial}{\partial y}\left[2\gamma_{8,3}\frac{1}{\beta}\frac{\partial I_2^2}{\partial y}+\gamma_{1,1}\frac{1}{\beta}\frac{\partial I_2^0}{\partial y}+2\gamma_{7,-3}\frac{1}{\beta}\frac{\partial I_2^{-2}}{\partial x}-\frac{5}{\alpha_1}\frac{1}{\beta}\frac{\partial I_0}{\partial y}\right] - 2\beta\alpha_2 I_2^2=0 \tag{4c}$$

$$\frac{\partial}{\partial x}\left[\frac{5}{\alpha_1}\frac{1}{\beta}\frac{\partial I_0}{\partial x}-\frac{1}{\alpha_1}\frac{1}{\beta}\frac{\partial I_2^0}{\partial x}+\frac{6}{\alpha_1}\frac{1}{\beta}\frac{\partial I_2^2}{\partial x}+\frac{6}{\alpha_1}\frac{1}{\beta}\frac{\partial I_2^{-2}}{\partial y}\right] + \frac{\partial}{\partial y}\left[\frac{5}{\alpha_1}\frac{1}{\beta}\frac{\partial I_0}{\partial y}-\frac{1}{\alpha_1}\frac{1}{\beta}\frac{\partial I_2^0}{\partial y}-\frac{6}{\alpha_1}\frac{1}{\beta}\frac{\partial I_2^2}{\partial y}+\frac{6}{\alpha_1}\frac{1}{\beta}\frac{\partial I_2^{-2}}{\partial y}\right] - 5\beta\alpha_0(I_0-4\pi I_b)=0 \tag{4d}$$

where β is the extinction coefficient, and $\gamma_{i,j}$ are coefficients written as [14,15]

$$\gamma_{i,j}=\left(\frac{i}{\alpha_3}+\frac{j}{\alpha_1}\right) \tag{5}$$

where

$$\alpha_n=(2n+1)-\omega A_n \tag{6}$$

where A_n are the coefficients associated with expansion of the scattering phase function [15]. Equations (4*a*)–(4*d*) represent a set of four coupled, linear, second-order, elliptic PDEs for the four unknowns, namely, I_0, I_2^0, I_2^{-2}, and I_2^2. For nongray media, Eqs. (4*a*)–(4*d*) must be considered in a spectral sense.

Solution of Eqs. (4*a*)–(4*d*) requires four boundary conditions. Following Modest and Yang [15], who applied Marshak's procedure to derive the boundary conditions, the boundary conditions are written as [15]

$$I_0-\frac{3}{4}\sin 2\delta I_2^{-2}-\frac{1}{8}I_2^0-\frac{3}{4}\cos 2\delta I_2^2-\frac{12}{5\alpha_1}\frac{1}{\beta}\frac{\partial}{\partial \overline{x}}[\cos 2\delta I_2^{-2}-\sin 2\delta I_2^2]-\frac{2}{5\alpha_1}\frac{1}{\beta}\frac{\partial}{\partial \overline{z}}[5I_0-6\sin 2\delta I_2^{-2}-I_2^0-6\cos 2\delta I_2^2] = 4\pi I_S \tag{7a}$$

$$-\frac{3}{2}\cos 2\delta I_2^{-2}+\frac{3}{2}\sin 2\delta I_2^2+\frac{2}{5\alpha_1}\frac{1}{\beta}\frac{\partial}{\partial \overline{x}}[5I_0-I_2^0+6\sin 2\delta I_2^{-2}+6\cos 2\delta I_2^2]+\frac{12}{5\alpha_1}\frac{1}{\beta}\frac{\partial}{\partial \overline{z}}[\cos 2\delta I_2^{-2}-\sin 2\delta I_2^2]=0 \tag{7b}$$

$$I_0+3\sin 2\delta I_2^{-2}+\frac{1}{2}I_2^0+3\cos 2\delta I_2^2-\frac{48}{5\alpha_3}\frac{1}{\beta}\frac{\partial}{\partial \overline{x}}[\cos 2\delta I_2^{-2}-\sin 2\delta I_2^2]-\frac{24}{5\alpha_3}\frac{1}{\beta}\frac{\partial}{\partial \overline{z}}\left[3\sin 2\delta I_2^{-2}+\frac{1}{2}I_2^0+3\cos 2\delta I_2^2\right] = 4\pi I_S \tag{7c}$$

$$\frac{1}{2}\sin 2\delta I_2^{-2}-\frac{1}{4}I_2^0+\frac{1}{2}\cos 2\delta I_2^2-\frac{16}{5\alpha_3}\frac{1}{\beta}\frac{\partial}{\partial \overline{x}}[\cos 2\delta I_2^{-2}-\sin 2\delta I_2^2]-\frac{4}{5\alpha_3}\frac{1}{\beta}\frac{\partial}{\partial \overline{z}}[2\sin 2\delta I_2^{-2}-I_2^0+2\cos 2\delta I_2^2]=0 \tag{7d}$$

where I_S is the intensity at the surface, and is written as [15]

$$I_S=I_{bS}-\frac{4}{3}\left(\frac{1}{\varepsilon}-1\right)\overline{I_1^0} \tag{8}$$

where I_{bS} is the Planck function at the surface. The quantity $\overline{I_1^0}$ is one of the space-dependent coefficients of the intensity function written in the local (at the boundary surface) coordinate system, and can be expressed in terms of the dependent variables (namely, I_0, I_2^0, I_2^{-2}, and I_2^2) after tedious algebra using transformation relations from local $(\overline{x},\overline{y},\overline{z})$ to global (x,y,z) coordinate systems [15]. Following this transformation, Eqs. (7*a*) and (7*c*) can be written solely in terms of the four dependent variables. Similarly, the derivatives appearing in Eqs. (7*a*)–(7*d*) with respect to local space variables can be transformed to derivatives with respect to global space variables. In Eqs. (7*a*)–(7*d*), δ is an angle associated with the Euler angles of transformation from local to global coordinate systems, and can also be obtained using relations provided by Modest and Yang [15].

2.2 Finite-Volume Formulation and Block-Implicit Equations. In this subsection, the finite-volume formulation of the governing equations is presented. As a starting point, we introduce the following notations to make Eqs. (4*a*)–(4*d*) more general and compact

$$\phi_1=I_2^{-2},\quad \phi_2=I_2^0,\quad \phi_3=I_2^2,\quad \phi_4=I_0$$
$$\Gamma_1=\frac{2\gamma_{8,3}}{\beta},\quad \Gamma_2=\frac{\gamma_{1,1}}{\beta},\quad \Gamma_3=\frac{2\gamma_{7,-3}}{\beta},\quad \Gamma_4=\frac{5}{\beta\alpha_1},\quad \Gamma_5=\frac{2\alpha_2}{\beta} \tag{9}$$

Using these notations, Eq. (4*a*) may be written as

$$\frac{\partial}{\partial x}\left[\Gamma_1\frac{\partial\phi_1}{\partial x}-\Gamma_2\frac{\partial\phi_2}{\partial y}+\Gamma_3\frac{\partial\phi_3}{\partial y}+\Gamma_4\frac{\partial\phi_4}{\partial y}\right]+\frac{\partial}{\partial y}\left[\Gamma_1\frac{\partial\phi_1}{\partial y}-\Gamma_2\frac{\partial\phi_2}{\partial x}-\Gamma_3\frac{\partial\phi_3}{\partial x}+\Gamma_4\frac{\partial\phi_4}{\partial x}\right]-\Gamma_5\phi_1=0 \tag{10}$$

Rearranging, we get

$$\nabla\cdot\mathbf{U}_1-\nabla\cdot\mathbf{U}_2+\nabla\cdot\mathbf{U}_3+\nabla\cdot\mathbf{U}_4-\Gamma_5\phi_1=0 \tag{11}$$

where

$$\begin{aligned}\mathbf{U}_1&=\Gamma_1\nabla\phi_1\\ \mathbf{U}_2&=\Gamma_2\left[\frac{\partial\phi_2}{\partial y}\hat{i}+\frac{\partial\phi_2}{\partial x}\hat{j}\right]\\ \mathbf{U}_3&=\Gamma_3\left[\frac{\partial\phi_3}{\partial y}\hat{i}-\frac{\partial\phi_3}{\partial x}\hat{j}\right]\\ \mathbf{U}_4&=\Gamma_4\left[\frac{\partial\phi_4}{\partial y}\hat{i}+\frac{\partial\phi_4}{\partial x}\hat{j}\right]\end{aligned} \tag{12}$$

Equations (4*b*)–(4*d*) may also be written in a similar manner, and thus, the finite-volume procedure to be presented next is also applicable to Eqs. (4*b*)–(4*d*) without any major modifications. The

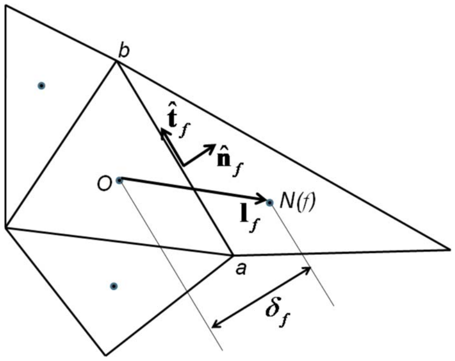

Fig. 1 Unstructured stencil showing the various geometrical entities and vectors used in the finite-volume formulation

four divergence terms in Eq. (11) can be categorized into two types of terms. The first term represents the divergence of a gradient operator, while the other three terms represent divergence of vectors that cannot be written as the gradient of a scalar. The treatment of these two types of terms is discussed next.

Finite-volume integration of the first term in Eq. (11) over a volume Ω_V and control surface area S, followed by application of the Gauss divergence theorem, results in

$$\int_{\Omega_V} \nabla \cdot \mathbf{U}_1 dV = \int_S \mathbf{U}_1 \cdot \hat{\mathbf{n}} dA = \sum_f (\mathbf{U}_{1,f} \cdot \hat{\mathbf{n}}_f) A_f = \sum_f (\Gamma_{1,f} \nabla \phi_{1,f} \cdot \hat{\mathbf{n}}_f) A_f \tag{13}$$

where the surface integral in Eq. (13) has been replaced by a summation over the discrete faces (f) of the control volume in question. $\Gamma_{1,f}$ is the value of Γ_1 at any face f, and can be computed using distance-weighted interpolation of the two cell center values straddling the face f. The area A_f and surface normal $\hat{\mathbf{n}}_f$ are known from the geometric description of the mesh. The objective of the finite-volume formulation is to ultimately derive a set of algebraic equations, linking the cell center values of the unknowns, namely, ϕ_1, ϕ_2, ϕ_3, and ϕ_4. In order to do so, the gradient at the cell face $\nabla\phi_{1,f}$ must be expressed in terms of the cell center values of ϕ_1. We start with the vector identity

$$\nabla \phi_{1,f} = (\nabla \phi_{1,f} \cdot \hat{\mathbf{n}}_f)\hat{\mathbf{n}}_f + (\hat{\mathbf{n}}_f \times \nabla \phi_{1,f}) \times \hat{\mathbf{n}}_f \tag{14}$$

For two-dimensional geometry, Eq. (14) can be written in simplified form as

$$\nabla \phi_{1,f} = (\nabla \phi_{1,f} \cdot \hat{\mathbf{n}}_f)\hat{\mathbf{n}}_f + (\nabla \phi_{1,f} \cdot \hat{\mathbf{t}}_f)\hat{\mathbf{t}}_f \tag{15}$$

where $\hat{\mathbf{t}}_f$ is the unit tangent of the face f (Fig. 1), and is also known from the geometric description of the mesh. Performing a dot product with the vector $\mathbf{l}_f$ (Fig. 1), we get

$$\nabla \phi_{1,f} \cdot \mathbf{l}_f = (\nabla \phi_{1,f} \cdot \hat{\mathbf{n}}_f)\hat{\mathbf{n}}_f \cdot \mathbf{l}_f + (\nabla \phi_{1,f} \cdot \hat{\mathbf{t}}_f)\hat{\mathbf{t}}_f \cdot \mathbf{l}_f \tag{16}$$

which upon further simplification, yields

$$\phi_{1,N(f)} - \phi_{1,O} = (\nabla \phi_{1,f} \cdot \hat{\mathbf{n}}_f)\delta_f + (\nabla \phi_{1,f} \cdot \hat{\mathbf{t}}_f)\hat{\mathbf{t}}_f \cdot \mathbf{l}_f \tag{17}$$

where $\phi_{1,N(f)}$ is the value of ϕ_1 at the center of the neighboring cell to face f, which is different from O, and δ_f is the distance in the direction of the surface normal between the two cells straddling the face f (Fig. 1). It is computed from the geometric description of the mesh, and is stored for each face. Equation (17) can be further rearranged as

$$(\nabla \phi_{1,f} \cdot \hat{\mathbf{n}}_f) = \frac{\phi_{1,N(f)} - \phi_{1,O}}{\delta_f} - \frac{(\nabla \phi_{1,f} \cdot \hat{\mathbf{t}}_f)\hat{\mathbf{t}}_f \cdot \mathbf{l}_f}{\delta_f} = \frac{\phi_{1,N(f)} - \phi_{1,O}}{\delta_f} - \frac{\Im_f}{\delta_f} \tag{18}$$

Essentially, in the above derivation, the flux normal to a cell face has been expressed in terms of the cell center values straddling the face, and a separate tangential flux term, which will, henceforth, be denoted by $\Im_f$, and is written as

$$\Im_f = \frac{(\phi_{1,b} - \phi_{1,a})}{|\overrightarrow{ab}|}\hat{\mathbf{t}}_f \cdot \mathbf{l}_f \tag{19}$$

where $\phi_{1,a}$ and $\phi_{1,b}$ are vertex values of ϕ_1 at vertices a and b (Fig. 1). If the vectors $\hat{\mathbf{n}}_f$ and $\mathbf{l}_f$ are aligned, this term vanishes since $\hat{\mathbf{t}}_f \cdot \mathbf{l}_f = 0$. Substitution of Eq. (18) into Eq. (13) yields

$$\int_{\Omega_V} \nabla \cdot \mathbf{U}_1 dV = \sum_f \Gamma_{1,f}(\nabla \phi_{1,f} \cdot \hat{\mathbf{n}}_f) A_f = \sum_f \Gamma_{1,f} A_f \left[\frac{\phi_{1,N(f)} - \phi_{1,O}}{\delta_f} - \frac{\Im_f}{\delta_f}\right] \tag{20}$$

In our scheme, the first term of the right hand side of Eq. (20) is treated implicitly, while the second term is treated explicitly, i.e., it is computed from previous iteration values. This computation of the second term requires determination of vertex values. While, in principle, the vertex values can be expressed in terms of the cell center values using interpolation functions, and the whole term can be treated implicitly, such a scheme becomes quite tedious, especially in 3D. Thus, the second term is treated explicitly.

Next, we consider the finite-volume integration of the second type of term, i.e., term that cannot be expressed as a divergence of a gradient. Finite-volume integration of the second term in Eq. (11) over a volume Ω_V and control surface area S, followed by application of the Gauss divergence theorem, results in

$$\int_{\Omega_V} \nabla \cdot \mathbf{U}_2 dV = \int_S \mathbf{U}_2 \cdot \hat{\mathbf{n}} dA = \sum_f (\mathbf{U}_{2,f} \cdot \hat{\mathbf{n}}_f) A_f \tag{21}$$

From Eq. (12), we get

$$\mathbf{U}_2 = \Gamma_2\left[\frac{\partial \phi_2}{\partial y}\hat{i} + \frac{\partial \phi_2}{\partial x}\hat{j}\right] = \Gamma_2[(\nabla \phi_2 \cdot \hat{j})\hat{i} + (\nabla \phi_2 \cdot \hat{i})\hat{j}] \tag{22}$$

Therefore,

$$\mathbf{U}_{2,f} \cdot \hat{\mathbf{n}}_f = \Gamma_{2,f}[(\nabla \phi_{2,f} \cdot \hat{j})n_x + (\nabla \phi_{2,f} \cdot \hat{i})n_y] \tag{23}$$

Using the same vector identity as before (Eq. (15)), we get

$$\nabla \phi_{2,f} \cdot \hat{i} = (\nabla \phi_{2,f} \cdot \hat{\mathbf{n}}_f)\hat{\mathbf{n}}_f \cdot \hat{i} + (\nabla \phi_{2,f} \cdot \hat{\mathbf{t}}_f)\hat{\mathbf{t}}_f \cdot \hat{i} \tag{24}$$

Substitution of Eq. (18) into Eq. (24) yields

$$\nabla \phi_{2,f} \cdot \hat{i} = \left[\frac{\phi_{2,N(f)} - \phi_{2,O}}{\delta_f} - \frac{(\nabla \phi_{2,f} \cdot \hat{\mathbf{t}}_f)\hat{\mathbf{t}}_f \cdot \mathbf{l}_f}{\delta_f}\right]\hat{\mathbf{n}}_f \cdot \hat{i} + (\nabla \phi_{2,f} \cdot \hat{\mathbf{t}}_f)\hat{\mathbf{t}}_f \cdot \hat{i} \tag{25}$$

Using $\hat{\mathbf{n}}_f \cdot \hat{i} = n_x$ and $\hat{\mathbf{t}}_f \cdot \hat{i} = t_x$, Eq. (25) may be simplified as

$$\nabla \phi_{2,f} \cdot \hat{i} = \left[\frac{\phi_{2,N(f)} - \phi_{2,O}}{\delta_f} n_x\right] + (\nabla \phi_{2,f} \cdot \hat{\mathbf{t}}_f)\left[t_x - \frac{(\hat{\mathbf{t}}_f \cdot \mathbf{l}_f)n_x}{\delta_f}\right] = \left[\frac{\phi_{2,N(f)} - \phi_{2,O}}{\delta_f} n_x\right] + \frac{\phi_{2,b} - \phi_{2,a}}{|\overrightarrow{ab}|}\left[t_x - \frac{(\hat{\mathbf{t}}_f \cdot \mathbf{l}_f)n_x}{\delta_f}\right] \tag{26}$$

Similarly,

$$\nabla\phi_{2,f}\cdot\hat{j} = \left[\frac{\phi_{2,N(f)}-\phi_{2,O}}{\delta_f}n_y\right] + \frac{\phi_{2,b}-\phi_{2,a}}{|\overrightarrow{ab}|}\left[t_y - \frac{(\hat{\mathbf{t}}_f\cdot\mathbf{l}_f)n_y}{\delta_f}\right] \tag{27}$$

Substitution of Eqs. (26) and (27) into Eq. (23), followed by substitution of the resulting equation into Eq. (21) yields

$$\begin{aligned}\int_{\Omega_V}\nabla\cdot\mathbf{U}_2 dV &= \sum_f(\mathbf{U}_{2,f}\cdot\hat{\mathbf{n}}_f)A_f = \sum_f\Gamma_{2,f}n_xA_f\left[\frac{\phi_{2,N(f)}-\phi_{2,O}}{\delta_f}\right.\\ &\quad\left.+\frac{\phi_{2,b}-\phi_{2,a}}{|\overrightarrow{ab}|}\left\{t_x-\frac{(\hat{\mathbf{t}}_f\cdot\mathbf{l}_f)n_x}{\delta_f}\right\}\right]\\ &\quad+\sum_f\Gamma_{2,f}n_yA_f\left[\frac{\phi_{2,N(f)}-\phi_{2,O}}{\delta_f}+\frac{\phi_{2,b}-\phi_{2,a}}{|\overrightarrow{ab}|}\right.\\ &\quad\left.\times\left\{t_y-\frac{(\hat{\mathbf{t}}_f\cdot\mathbf{l}_f)n_y}{\delta_f}\right\}\right]\end{aligned} \tag{28}$$

Equation (28) can be further simplified by using the relation $n_x^2+n_y^2=1$. The third and the fourth terms in Eq. (11), involving $\mathbf{U}_3$ and $\mathbf{U}_4$, can be treated in exactly the same manner as the second term involving $\mathbf{U}_2$, as just described. The fifth term in Eq. (11), upon finite-volume integration, yields

$$\int_{\Omega_V}\Gamma_5\phi_1 dV = \Gamma_{5,O}\phi_{1,O}\Omega_{V,O} \tag{29}$$

where $\Omega_{V,O}$ is the volume of the control volume with its centroid at O. The five terms in Eq. (11), after finite-volume integration, can be arranged to write a single algebraic equation for the cell center values of ϕ_1, namely, $\phi_{1,O}$, $\phi_{2,O}$, $\phi_{3,O}$, and $\phi_{4,O}$, and the cell center values of the neighboring cells. For cells adjacent to boundaries, the flux at the boundary face must be replaced by the appropriate boundary condition given by Eqs. (7*a*)–(7*d*). The treatment of such Robin-type boundary conditions in a finite-volume formulation is relatively straightforward, and is omitted here for the sake of brevity.

Thus far, only finite-volume integration of Eq. (4*a*) has been discussed. The same procedure can also be used to integrate Eqs. (4*b*)–(4*d*), resulting in three additional algebraic equations relating the cell center values of ϕ. Overall, these four sets of equations represent a total of $4\times N_C$ algebraic equations (i.e., for each cell there are four algebraic equations resulting from the finite-volume integration of Eqs. (4*a*)–(4*d*)). These equations actually have a block-implicit structure, as follows:

$$\begin{bmatrix}A_{1,1,O} & A_{1,2,O} & A_{1,3,O} & A_{1,4,O}\\ A_{2,1,O} & A_{2,2,O} & A_{2,3,O} & A_{2,4,O}\\ A_{3,1,O} & A_{3,2,O} & A_{3,3,O} & A_{3,4,O}\\ A_{4,1,O} & A_{4,2,O} & A_{4,3,O} & A_{4,4,O}\end{bmatrix}\begin{bmatrix}\phi_{1,O}\\ \phi_{2,O}\\ \phi_{3,O}\\ \phi_{4,O}\end{bmatrix} - \sum_{j=1}^{nb}\begin{bmatrix}A_{1,1,j} & A_{1,2,j} & A_{1,3,j} & A_{1,4,j}\\ A_{2,1,j} & A_{2,2,j} & A_{2,3,j} & A_{2,4,j}\\ A_{3,1,j} & A_{3,2,j} & A_{3,3,j} & A_{3,4,j}\\ A_{4,1,j} & A_{4,2,j} & A_{4,3,j} & A_{4,4,j}\end{bmatrix}\begin{bmatrix}\phi_{1,j}\\ \phi_{2,j}\\ \phi_{3,j}\\ \phi_{4,j}\end{bmatrix} = \begin{bmatrix}S_1\\ S_2\\ S_3\\ S_4\end{bmatrix} \tag{30}$$

where $A_{1,1,O}$, for example, denotes the coefficient premultiplying $\phi_{1,O}$ that arises out of finite-volume integration of Eq. (4*a*). Similarly, $A_{2,1,O}$ denotes the coefficient premultiplying $\phi_{1,O}$ that arises out of finite-volume integration of Eq. (4*b*). The second term denotes summation over all the neighboring cells, where *nb* is the total number of neighbors of node O. The right hand side denotes generic source terms that may arise due to the fact that the tangential flux terms are treated explicitly, as discussed earlier. There may also be additional sources due to the treatment of boundary conditions. Equation (30) addresses both variable-to-variable (i.e., ϕ_1 through ϕ_4), as well as node-to-node (spatial) coupling implicitly. When written for all nodes ($=N_C$) in the computational domain, i.e., $O\in 1,2,\ldots,N_C$, Eq. (30) represents a block matrix system of equations, where each element of the block matrix is a 4×4 matrix itself. These element matrices are shown explicitly in Eq. (30) for a representative node O.

2.3 Solution of Discrete Algebraic Equations. The discrete equations presented in Sec. 2.2 can be solved using several different techniques. One approach is to solve the system of equations directly using full lower-upper (LU) decomposition, followed by backward substitution, i.e., Gaussian elimination. Such a direct solution approach will provide the solution to the system of equations without any iteration since the governing equations are linear. Unfortunately, direct solution is prohibitive for two reasons, as follows: (1) the entire coefficient matrix of size $4N_C\times 4N_C$ need to be stored, and (2) the number of major floating point operations scales as $O(M^3)$ [22], where M is the total number of unknowns ($=4N_C$ in this case). For sufficiently large N_C, direct Gaussian elimination is prohibitive both from a memory as well as efficiency standpoint. The alternative is to adopt an iterative solution procedure. The simplest iterative procedure would entail sequential iterative solution of the discrete versions of Eqs. (4*a*) and (4*b*), i.e., first solve Eq. (4*a*) iteratively while holding ϕ_2, ϕ_3, and ϕ_4 constant, followed by solution Eq. (4*b*) while holding ϕ_1, ϕ_3, and ϕ_4 constant, and so on. During this study, it was found that this segregated method is inherently unstable because of the strong coupling between the four governing equations, and coupled (as opposed to segregated) solution of the governing equations is warranted.

The simplest coupled solution approach is to use the block-Gauss-Seidel (BGS) procedure [23]. In this procedure, the dependence of all spatial nodes around a given node is treated explicitly, and the whole computational domain is swept through point-by-point repeatedly until convergence is attained. In this case, at each point, a 4×4 matrix has to be inverted. Unfortunately, the BGS method becomes very slow as the mesh is refined because the spectral radius of convergence (largest eigenvalue of the iteration matrix) rapidly approaches unity as the mesh is refined [23]. Here, we use a new approach, which was originally developed for coupled implicit solution of the species conservation equations on an unstructured mesh [24,25]. This is described next.

The approach used here subdivides the computational domain into subdomains that are small enough such that for each of these subdomains a fully implicit solution of the governing equations is affordable from a memory standpoint. The rationale is that this approach will enable spatial as well as variable-to-variable implicit coupling, and the extent of spatial coupling is to be dictated by memory constraints. Thus, the performance of this approach is expected to be significantly better than a BGS solver.

The development of the coupled solver entails three major steps, as follows:

1. The computational domain is decomposed into smaller groups of cells that are geometrically contiguous—a process termed internal domain decomposition (IDD). This is a one-time preprocessing step. This step is performed using the binary spatial partitioning algorithm [26,27].
2. For each subdomain, an iterative solver based on Krylov subspace iterations (i.e., the restarted and preconditioned generalized minimum residual (GMRES) solver [28]) are employed to obtain the solution at all nodes within the subdomain and for all variables (ϕ_1 through ϕ_4) simultaneously. Other subdomains adjacent to the subdomain in question are treated explicitly, and ghost (or virtual) boundary conditions are applied at interfaces between subdomains to transfer information between subdomains.

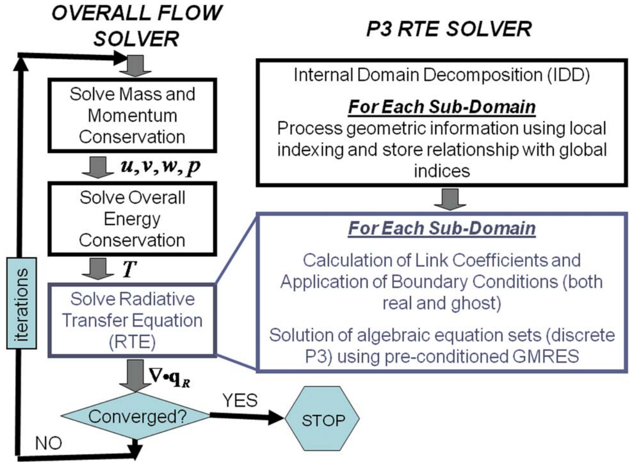

Fig. 2 Block-diagram representation of the coupled implicit solver (IDD+GMRES) for the P_3 equations and its relationship to the overall solution procedure

3. An overall (or outer) iteration is performed within which the preceding step is repeated until convergence. Iterations are necessary to resolve the explicit coupling between subdomains, and also to couple the RTE with the overall energy equation.

The overall algorithm for solution of the RTE, and how it is coupled to the overall energy conservation equation is depicted in Fig. 2. Further details pertaining to this solver, henceforth referred to as the IDD+GMRES solver, may be obtained from Kumar and Mazumder [24,25]. The factor that motivated the choice of GMRES over other iterative solvers is that it has extremely good convergence properties when preconditioned appropriately even for relatively large matrix sizes. In this solver, memory requirement can be limited by specifying the largest Krylov subspace size and the number of internal iterations can be limited by specifying the maximum number of GMRES iterations. In essence, the solver chosen is very flexible and appropriate for use in the current solution strategy.

3 Results and Discussion

In this section, the accuracy and efficiency of the P_3-based RTE solver is discussed. The standalone P_3-based RTE solver was first verified against MC results available from the literature for two benchmark problems. For comparison, a P_1-based RTE solver was also developed. The governing equation and boundary condition for the P_1 approximation are readily available [1], and are omitted here for the sake of brevity. Finally, both RTE solvers were coupled to an in-house unstructured reacting flow solver, and demonstrated for laminar flame calculations.

3.1 Verification of RTE Solvers. The two benchmark problems chosen for verification of the new RTE solvers are the same ones considered by Yang and Modest [14,15] because this enabled the use of the MC results presented by Yang and Modest [14,15].

The first problem considered is that of a gray participating gas confined within a square cavity, as shown in Fig. 3. The entire bottom wall is heated to a temperature T_h, while the other walls are maintained at 0 K. All walls are assumed to be black. The absorption coefficient of the gas is assumed to be zero, and only isotropic scattering is considered. Since the gas does not absorb or emit radiation, it is not necessary to couple the RTE to the overall energy equation in this case. The problem is one of radiative equilibrium, in which the radiation energy emitted by the hot wall is directionally redistributed by scattering. The dimension of the cavity h is kept fixed, while the scattering coefficient σ_s is varied to change the overall optical thickness of the medium, defined as $\tau_h = h\sigma_s$. Three different values of optical thickness are considered for the present study, namely, $\tau_h = 0.1$, 1, and 5.

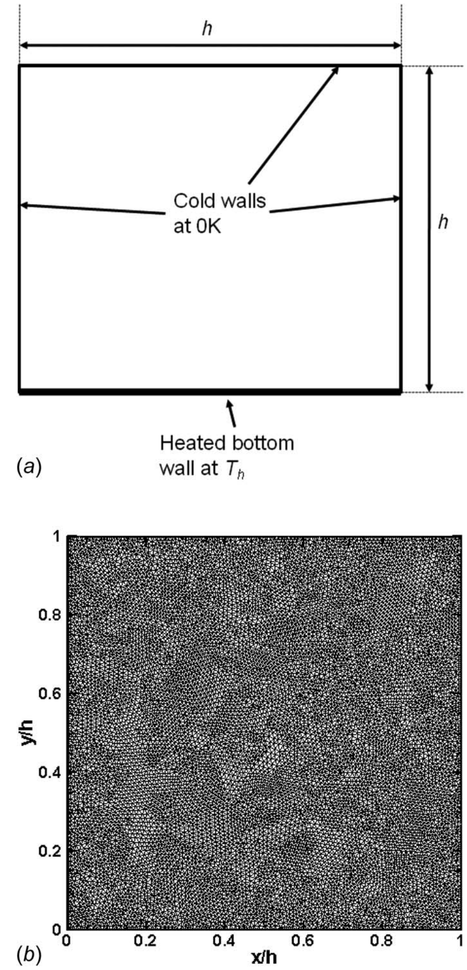

Fig. 3 (*a*) Geometry and boundary conditions for the first benchmark problem, and (*b*) computational mesh used for the verification study

Prior to comparison with MC results, grid independence studies were performed. Four different quadrilateral mesh sizes and four different triangular mesh sizes were considered. For these studies, the second verification problem, to be described shortly, was considered because this particular problem, with a partly heated bottom wall, has a discontinuity in temperature at the bottom wall, and therefore, requires high spatial resolution. The results of these studies are shown in Fig. 4. It is evident from Fig. 4 that grid-independent solution is obtained if the mesh size is increased beyond approximately 6000 cells for quadrilateral cells and beyond 9000 cells for triangular cells. Since the same mesh is used in both verification studies, the mesh that was determined to be appropriate for the second verification case was also deemed appropriate for the first verification case.

Figure 5 shows the nondimensional radiative heat fluxes (normalized by σT_h^4) predicted by the various methods for $\tau_h = 0.1$. These results were computed with 9492 triangular cells, and the computational mesh is shown in Fig. 3(*b*). Triangular mesh is chosen for these studies because they represent the worst-case scenario, both in terms of geometrical complexity in 2D and numerical convergence. While P_3 calculations have been performed in 2D using orthogonal meshes [14,15], to the best of our knowledge, no such calculations have been performed on unstructured meshes, and this is one of the key contributions of the current

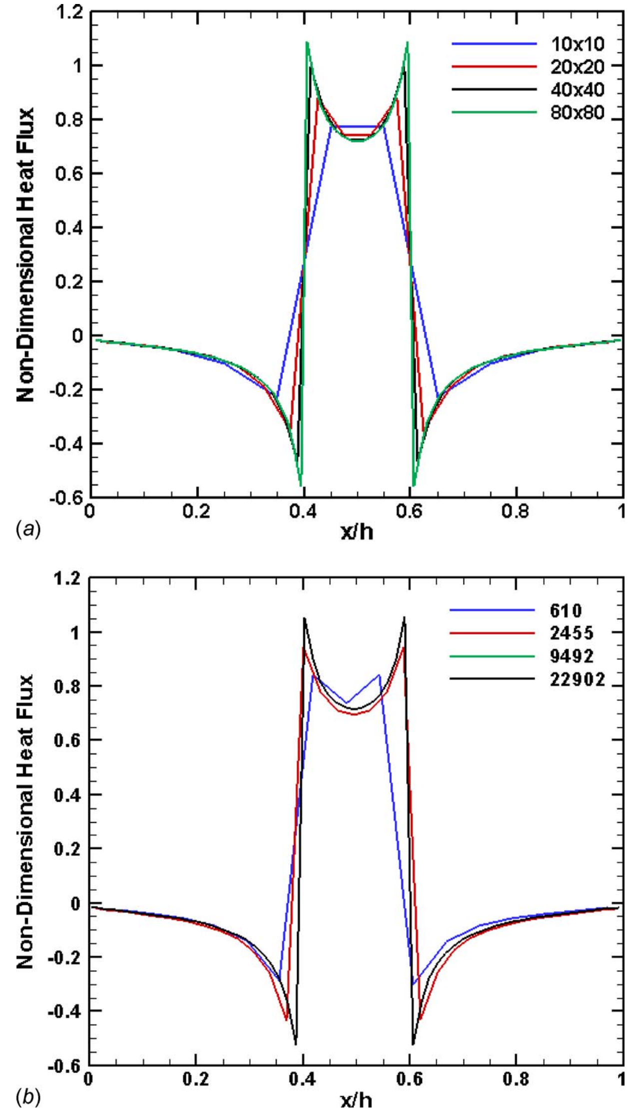

Fig. 4 Comparison of the nondimensional heat flux computed at the bottom (hot wall) using various mesh sizes and the P_3-based RTE solver: (*a*) various structured grids (quadrilateral cells), and (*b*) various unstructured grids (triangular cells)

article. It is worth noting that the calculations were conducted on the full cavity (rather than apply symmetry boundary conditions), and therefore, the mesh is not perfectly symmetric (see Fig. 3(*b*)) about the midplane. This was done so that we could use as large a mesh size as possible for efficiency studies to be presented in Sec. 3.2. Both P_1 and P_3 methods perform poorly for this optically thin case. In fact, both methods produce unphysical results, as evident from the fact that the nondimensional heat flux exceeds a value of unity. Similar unphysical results have also been reported by Modest and Yang [15], and are inherent to the P_N approximation for optically thin scenarios. Figure 6 shows the nondimensional radiative heat fluxes predicted by the various methods for $\tau_h=1$. In this case, the predictions by both P_1 and P_3 match the MC results better. Also, while the unphysical results are still present, they are confined to smaller regions, and the degree to which the nondimensional heat fluxes overshoot unity is significantly reduced. Figure 7 shows the nondimensional radiative heat fluxes predicted by the various methods for $\tau_h=5$. In this case, the match between results predicted by the P_N method and the MC method is quite good. In particular, the P_3 method is more accurate than the P_1 method for heat flux predictions at the bottom

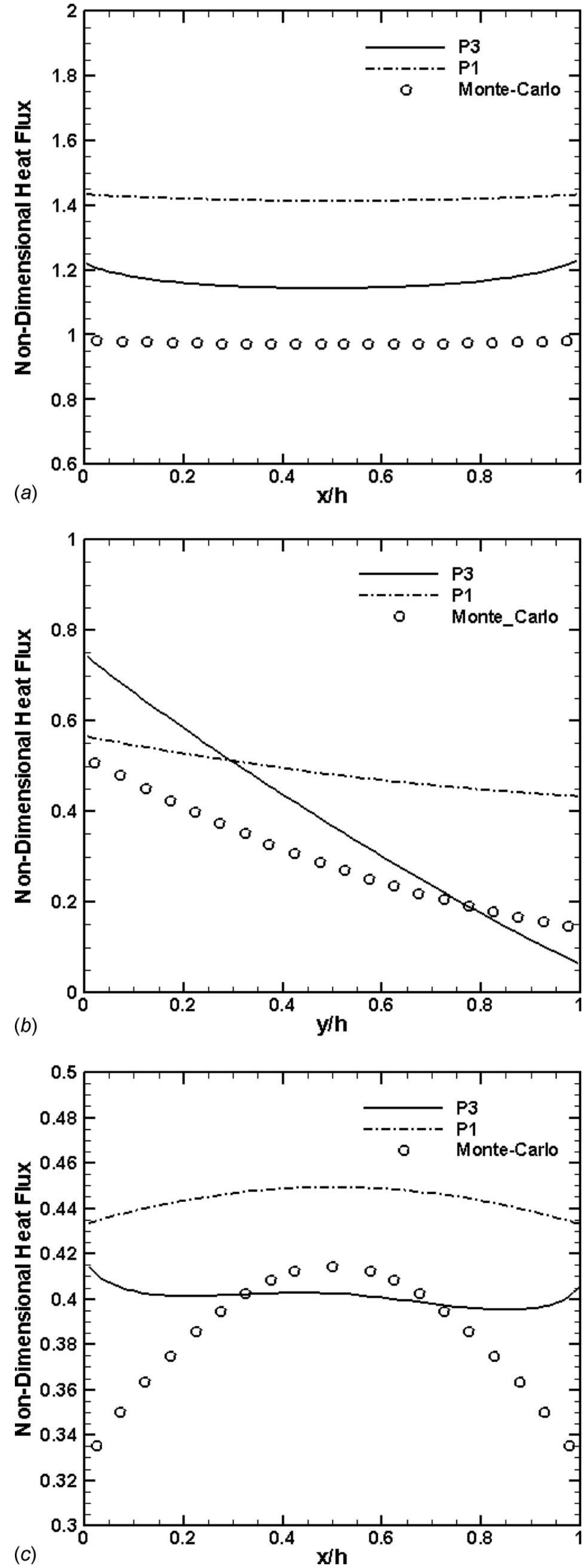

Fig. 5 Comparison of nondimensional heat fluxes predicted using the P_1 and P_3 methods with benchmark MC results [15] for $\tau_h=0.1$: (*a*) bottom, (*b*) right (side), and (*c*) top walls. The heat fluxes are normalized by σT_h^4.

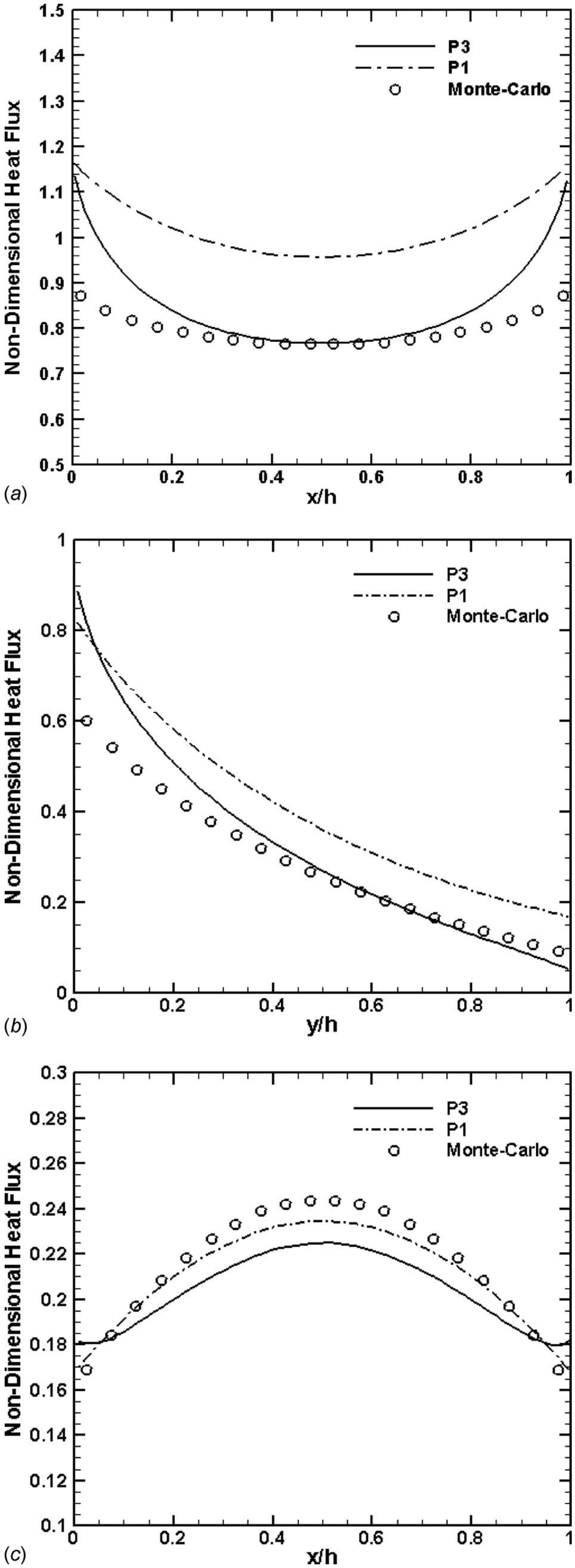

Fig. 6 Comparison of nondimensional heat fluxes predicted using the P_1 and P_3 methods with benchmark MC results [15] for τ_h=1: (*a*) bottom, (*b*) right (side), and (*c*) top walls. The heat fluxes are normalized by σT_h^4.

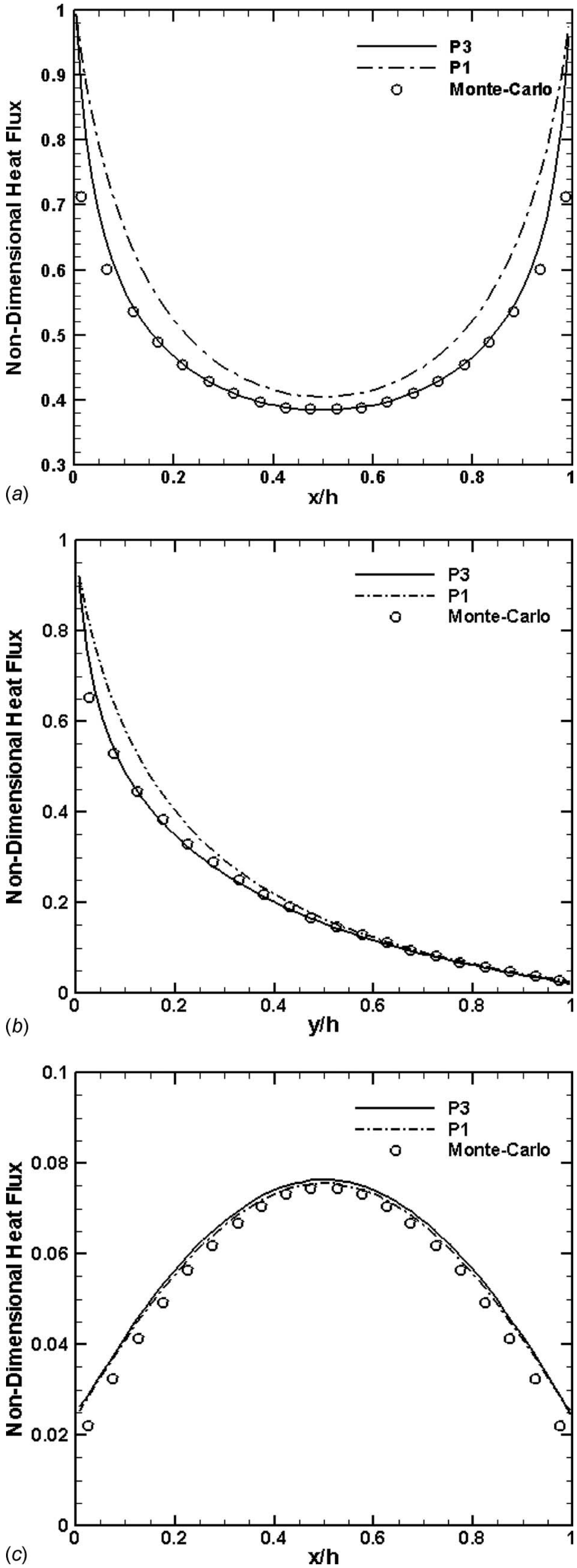

Fig. 7 Comparison of nondimensional heat fluxes predicted using the P_1 and P_3 methods with benchmark MC results [15] for τ_h=5: (*a*) bottom, (*b*) right (side), and (*c*) top walls. The heat fluxes are normalized by σT_h^4.

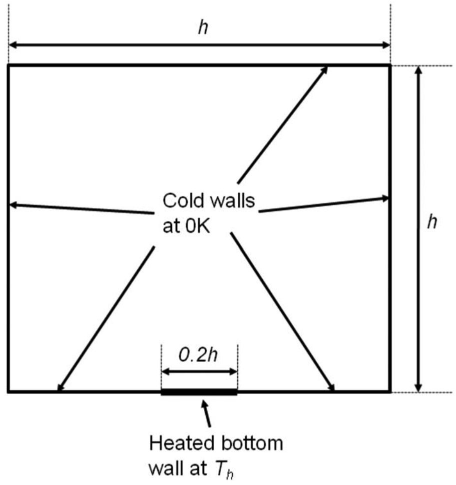

Fig. 8 Geometry and boundary conditions for the second benchmark problem

and right walls. At the top wall, it appears that the P_1 method slightly outperforms the P_3 method. However, the actual heat flux values are too small for this difference to be of much significance. No unphysical results are produced for the optically thick case with either of the two P_N methods.

The second verification study was performed on a case that is identical to the first case, except that only part of the bottom wall is heated, as shown in Fig. 8. The same computational mesh as the first case was used. The results are shown in Figs. 9–11 for the three different optical thickness values. Once again, it is observed that the predictions of both P_1 and P_3 do not match the "exact" MC results for $\tau_h=0.1$. In this case also, the nondimensional heat flux at the heated section of the bottom wall attains unphysical values above unity. Once again, though unphysical, these results are consistent with the results shown by Modest and Yang [15]. As the optical thickness is increased, the results start approaching MC results. For $\tau_h=5$, P_3 results are more accurate than P_1 results.

In the two problems just discussed, there is no emission or absorption by the medium. The energy emitted by the hot surface is simply scattered. Thus, both problems are that of radiative equilibrium, i.e., $\nabla \cdot q_R=0$, where q_R is the radiative heat flux. In a conservative finite-volume procedure, as used here, the radiative heat fluxes must balance when summed over all the boundary faces. In order to verify our formulation and code, the aforementioned flux balance test was conducted for both test cases. Table 1 shows the fluxes computed at each wall using the two P_N methods, as well as the overall imbalance in flux. In all cases, it is seen that the imbalance is approximately six orders of magnitude smaller than the flux at the hot surface. This is consistent with the fact that the convergence criterion used to generate these results was six orders of magnitude decrease in the residuals (l2 norm) of the P_N equations. These results indicate that even though for optically thin situations the P_N method produces unphysical results locally, the overall energy conservation (first law) is satisfied in all cases.

The P_3 equations arise out of mathematical manipulations of a physical conservation equation (the RTE). As such, they do not have a physical meaning. One of the key steps in the whole FV formulation presented here is to express the original equations proposed by Modest and Yang [15] in divergence form (Eq. (11)). Since the FV method solves the governing PDEs in weak form after integration, if the entire governing equation is in divergence form, as Eq. (11) is, the formulation is fully conservative, and will balance fluxes (not physical fluxes, but the sum of $\mathbf{U}_1$ through $\mathbf{U}_4$) even on the coarsest of meshes.

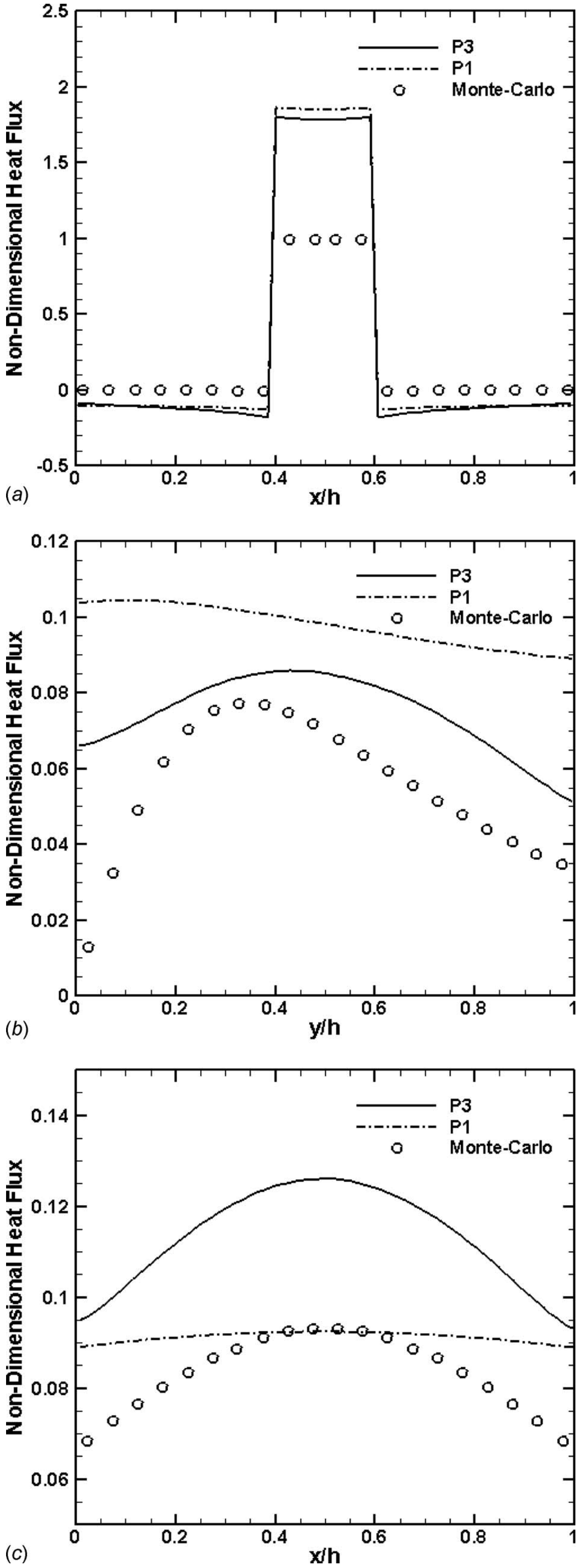

Fig. 9 Comparison of nondimensional heat fluxes predicted using the P_1 and P_3 methods with benchmark MC results [15] for $\tau_h=0.1$: (*a*) partly heated bottom, (*b*) right (side), and (*c*) top walls. The heat fluxes are normalized by σT_h^4.

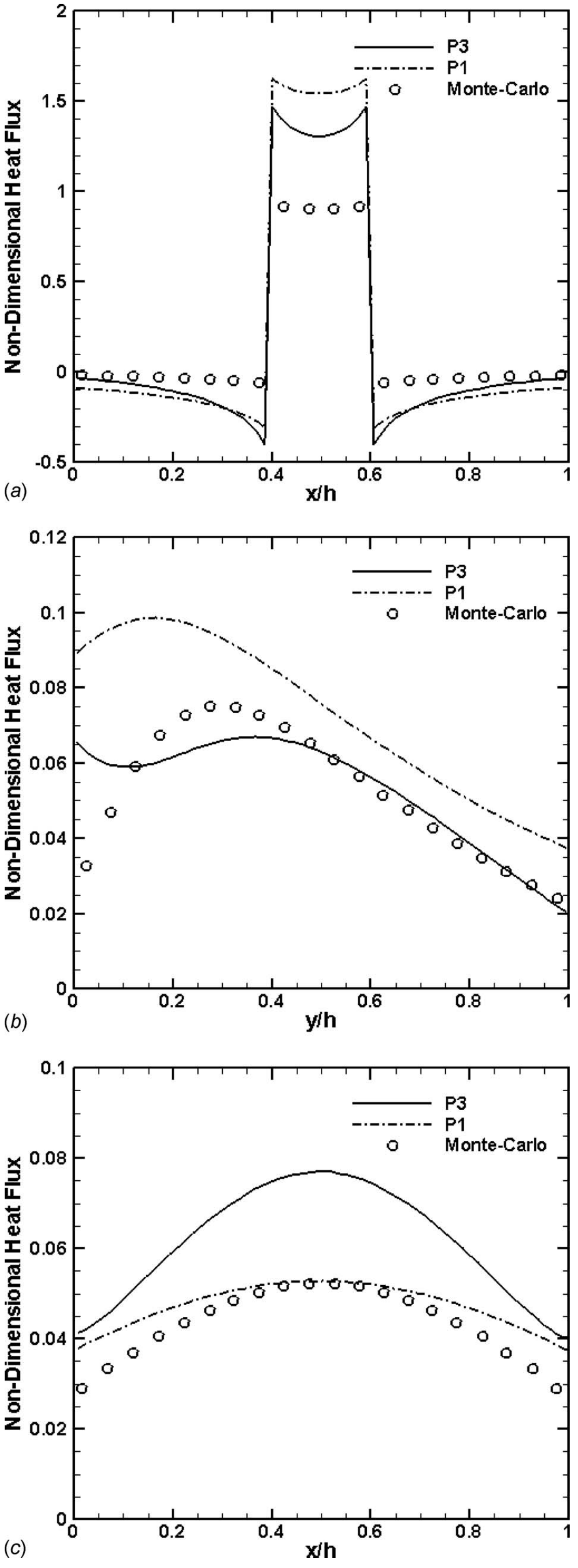

Fig. 10 Comparison of nondimensional heat fluxes predicted using the P_1 and P_3 methods with benchmark MC results [15] for $\tau_h=1$: (*a*) partly heated bottom, (*b*) right (side), and (*c*) top walls. The heat fluxes are normalized by σT_h^4.

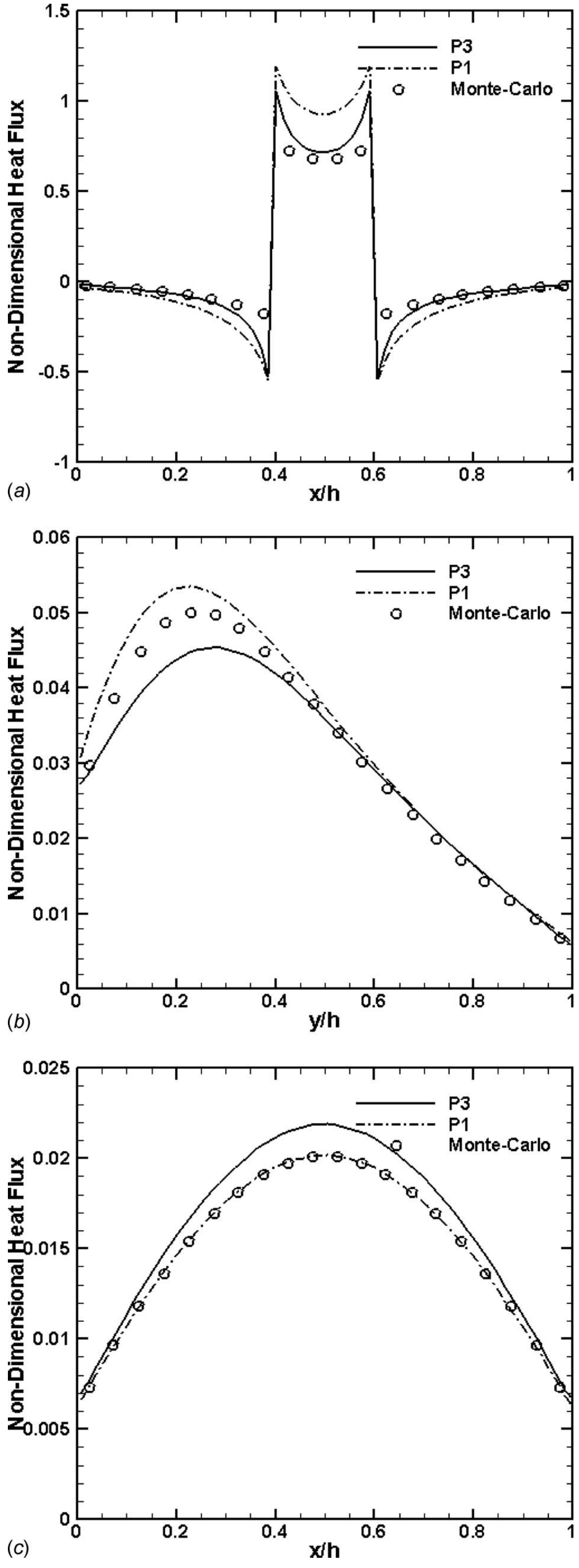

Fig. 11 Comparison of nondimensional heat fluxes predicted using the P_1 and P_3 methods with benchmark MC results [15] for $\tau_h=5$: (*a*) partly heated bottom, (*b*) right (side), and (*c*) top walls. The heat fluxes are normalized by σT_h^4.

Table 1 Radiative heat flux summary (nondimensional) for the two verification cases predicted using the two P_N methods

Case	Method	τ_h	Flux bottom wall	Flux left wall	Flux right wall	Flux top wall	Net imbalance
Full wall heated	P_3	5	0.492558	−0.217163	−0.217081	−0.058314	3.75×10^{-8}
		1	0.851047	−0.323475	−0.323126	−0.204446	3.20×10^{-8}
		0.1	1.164568	−0.384449	−0.379256	−0.400864	5.20×10^{-8}
	P_1	5	0.54314	−0.242844	−0.24281	−0.057485	4.72×10^{-8}
		1	1.019033	−0.403547	−0.40355	−0.211936	8.30×10^{-9}
		0.1	1.419656	−0.487861	−0.487864	−0.44393	2.50×10^{-7}
Part wall heated	P_3	5	0.077127	−0.030773	−0.030022	−0.016328	7.20×10^{-8}
		1	0.169036	−0.054103	−0.05308	−0.061854	1.50×10^{-7}
		0.1	0.263464	−0.075301	−0.074713	−0.11345	1.00×10^{-7}
	P_1	5	0.082922	−0.034302	−0.033442	−0.015178	1.03×10^{-7}
		1	0.194765	−0.07418	−0.073165	−0.04742	5.62×10^{-7}
		0.1	0.287098	−0.098049	−0.097813	−0.091236	2.86×10^{-8}

3.2 Performance of RTE Solver. The solution of the RTE using the P_3 method involves solution of a set of four coupled, second-order, elliptic PDEs. As mentioned earlier, it was found that these equations cannot be brought to convergence using a segregated solution approach, and a coupled solver was used in this study. One of the critical issues in the coupled solver, as described in Sec. 2.3, is how many cells should be included in each internal subdomain. The IDD+GMRES solver was tested for the first verification case with various numbers of cells in each subdomain. The overall computational domain consisted of 22,902 triangular cells. Table 2 shows the CPU time taken and the memory required for various subdomain sizes. All computations were performed on an Intel core 2 duo processor, with 2.3 GHz processor speed and 3.23 Gbytes of memory. The convergence criterion used is six orders of magnitude reduction in the l2 norm of all four P_3 equations. As expected, the convergence deteriorates with decrease in optical thickness. Also, as more cells are included in each subdomain, the convergence improves rapidly. For the best case, six orders of magnitude convergence is achieved in just 32 s for the optically thick case. This is also to be expected since more cells in each subdomain imply more implicitness. However, improved performance is achieved with a severe memory penalty. When all 22,902 cells are treated implicitly, the solver requires 152 Mbytes of memory, which is probably prohibitively large if extrapolated to complex 3D calculations. In other applications of this same solver [24,25], it was found that an optimum subdomain size exists from an efficiency perspective. In this case, however, an optimum was not apparent. Perhaps, the optimum, in this case, is beyond 22,902 cells, and may manifest itself if larger calculations with more cells are undertaken. However, since the mesh used in this case is already quite fine, further refinement was not pursued to investigate this matter further, and will be pursued once the formulation is extended to 3D geometries.

3.3 Coupling With Reacting Flow Solver. As a final step to demonstrate the new P_3-based RTE solver, it was coupled with an in-house 2D reacting flow solver [24,25]. Overall outer iterations were performed (Fig. 2) to couple all the conservation equations, and to address nonlinearities in the governing equations, which were all solved in appropriate linearized form.

The test problem considered is that of steady state homogeneous combustion of a methane-air mixture under laminar flow conditions, i.e., a laminar flame. A simple 2D diffusion flame configuration, as shown in Fig. 12(*a*), is considered. Based on the inlet conditions, the overall equivalence ratio is unity, and the Reynolds number based on the channel width is approximately 150. A two-step reaction mechanism [29] involving six gas-phase species (CH_4, CO_2, H_2O, N_2, O_2, and CO) was used for gas-phase chemistry calculations. The computational mesh comprised of 19,953 triangular cells, and part of the mesh is shown in Fig. 12(*b*). Convergence was deemed to have been attained when the l2 norm of all the governing equations decreased by six orders of magnitude. The extinction coefficient was assumed to be constant, and two different values were considered, as follows: 5 m^{-1} and 50 m^{-1} (resulting in optical thickness of 0.25 and 2.5, respectively, based on the channel width), while a constant value of 0.5 was assumed for the scattering albedo.

The temperature distributions predicted by the P_1 and P_3 methods are shown in Fig. 13 for the optically thick case since the P_N approximation is more accurate in optically thick situations, as found from the results of the preceding verification studies. It is clear that inclusion of radiation lowers the temperature of the

Table 2 CPU time taken, number of iterations required for six orders of magnitude convergence, and peak memory required by IDD+GMRES solver as a function of the subdomain size. All calculations were performed on an Intel core 2 duo processor with 2.3 GHz processor speed.

	$\tau_h=0.1$			$\tau_h=5$		
$N_{C,m}$	CPU time (s)	Iterations	Memory (Mbytes)	CPU time (s)	Iterations	Memory (Mbytes)
24,000	313.22	69	152	31.07	27	152
12,000	7154.43	7630	85	455.73	615	85
6000	12916.34	20548	51	608.64	1030	51
3000	19650.02	46065	34	882.15	1953	34
1600	34739.53	97454	26	1411.8	3725	26
800	-	-	-	2327.9	7267	21
400	-	-	-	3585.73	14,467	19
200	-	-	-	5346.59	28,368	19

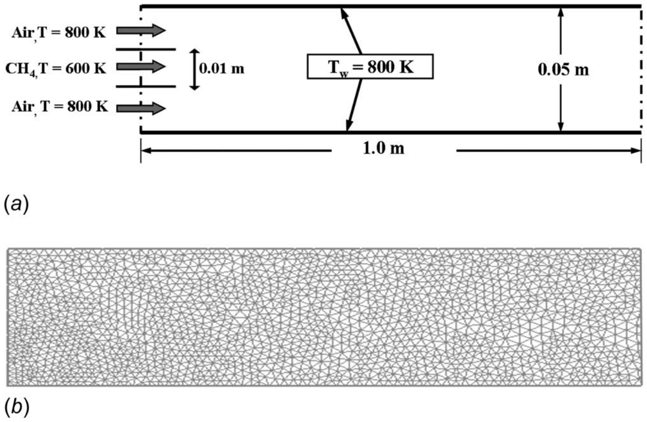

Fig. 12 (***a***) **Geometry and boundary conditions for the reaction flow test case** (**2D laminar methane-air flame**)**, and** (***b***) **computational mesh: only one-third of the channel is shown for clarity**

flame significantly, as expected. The temperature distributions predicted using both P_N methods are almost identical, although a close inspection reveals minor differences especially at the tip of the flame. Both methods resulted in smooth overall convergence, and the residuals for both optical thicknesses are shown in Fig. 14. It is worth noting that although the physical results are error-prone for the optically thin case, this case represents the worst-case scenario in terms of numerical convergence, and has, therefore, been considered in this study. The following discussion focuses on this optically thin case. For the P_1 approximation, the RTE converges ahead of the overall energy equation, and the overall convergence is held up by the energy equation. For the P_3 approximation, the convergence of the RTE (four P_3 equations) is slowest, and affects the overall convergence of the flow solver adversely. For the optically thick case (not shown), the P_N equations converged very rapidly compared with the other equations, as expected. From a memory standpoint, the P_1 solver required an additional 16% memory for the one additional PDE that needed to be solved: 77 Mbytes for overall solver with P_1 versus 67 Mbytes for solver without radiation. The memory requirement of the P_3 solver (IDD+GMRES solver) depends on the number of subdomains used. As discussed earlier, if no internal domain decomposition is performed, the performance is the best, but the memory requirement is too high. For the present computations, four subdomains were used. The rationale for this choice is that four subdomains resulted in an additional 40 Mbytes memory requirement for the four additional PDEs, which is roughly a linear scale-up from the memory required by the P_1 solver. Perhaps, because the most efficient setup (of using no internal domain decomposition) is not utilized in this case, the overall convergence of the flow solver is adversely affected by the slow convergence of the P_3 equations to some degree. One of the ways to improve the convergence is to use tighter tolerance criteria within the GMRES solver for the P_3 equations, and further research is underway to investigate this issue. The flow solver with P_3 requires slightly more number of outer iterations (2553 versus 2361) than the flow solver with P_1 for six orders of magnitude convergence (Fig. 14), and the overall CPU time consumed increases from an extra 9.3–14.5%. The total CPU time taken by the flow solver with P_1 is 11,242 s while the CPU time taken by the flow solver with P_3 is 12,746 s. The number of PDEs solved in the flow solver without radiation is 10, while the number of PDEs solved with P_3 radiation is 14. Thus, a 14.5% increase in the CPU time due to the extra four PDEs represents significantly better than linear scale-up, and is, therefore, deemed acceptable.

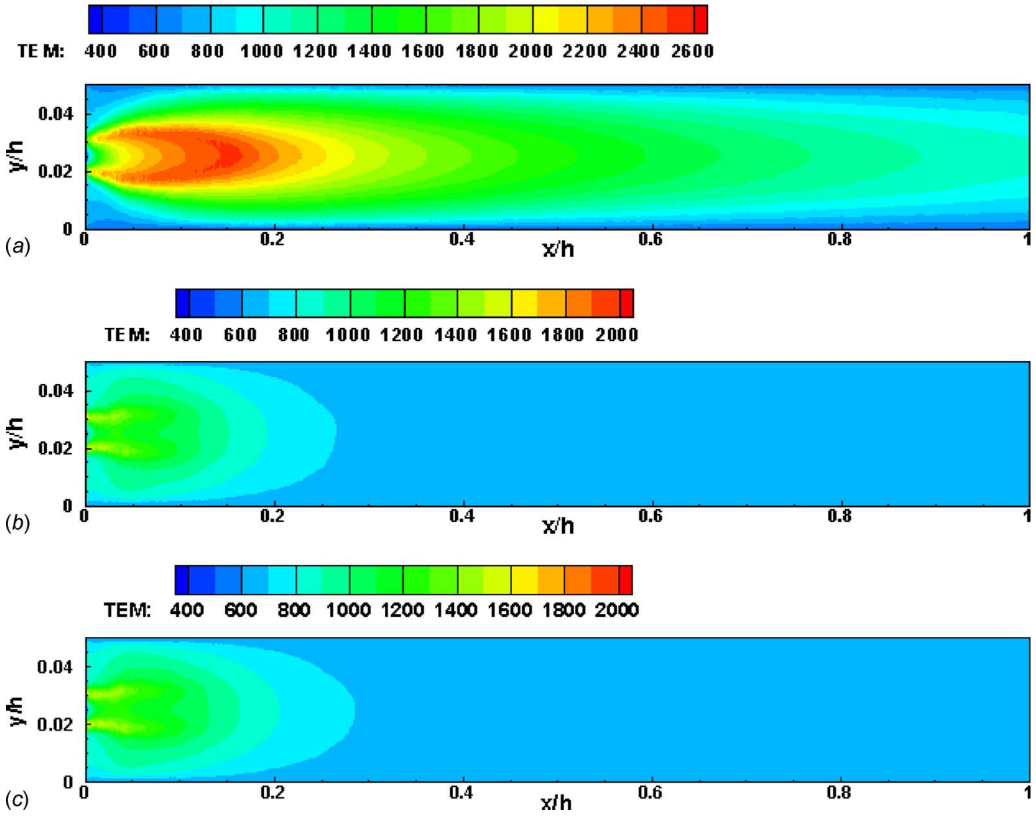

Fig. 13 Temperature distributions for a laminar methane-air diffusion flame: (***a***) **without including radiation,** (***b***) **including radiation calculated using P_1, and** (***c***) **including radiation calculated using P_3**

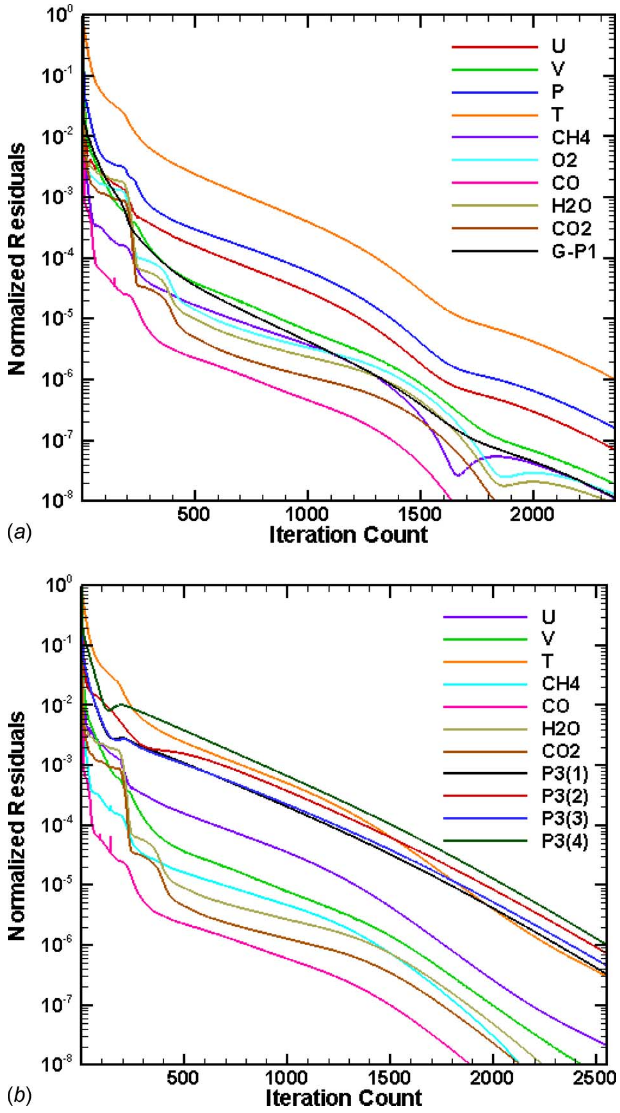

Fig. 14 Convergence of the overall flow solver using (*a*) P_1 and (*b*) P_3 approximations

4 Summary and Conclusions

A conservative finite-volume procedure has been presented for discretization of the P_3 equations of radiative transfer on an unstructured mesh. The resulting block-implicit equations have been solved using a new solver, referred to as the IDD+GMRES solver. The solver facilitates both variable-to-variable as well as spatial (cell-to-cell) coupling in an implicit manner. The solver is based on the decomposition of the computational domain into subdomains using the binary spatial partitioning algorithm, and subsequent solution of the block-implicit equations within each subdomain using an incomplete LU-preconditioned restarted GMRES solver.

The finite-volume procedure and the coupled solver were tested for two benchmark problems. The two benchmark problems were chosen such that they represent worst-case scenarios for the P_N method, namely, cold medium surrounded by hot walls [1]. It was found that for low to intermediate optical thicknesses, both P_1 and P_3 methods produce inaccurate results when compared with exact Monte Carlo results. In some cases, the results are also locally unphysical. For optically thick situations, both P_1 and P_3 produced reasonably accurate results. Overall, the P_3 method appears to be superior in accuracy over the P_1 method—a finding that is consistent with past findings [14,15], and one that warrants further research on higher-order P_N methods. It is worth emphasizing that the findings reported here are for worst-case scenarios for the P_N method, and by no means, discount either the P_1 or P_3 approximation as possible methods for solution of the RTE. For cases with cold walls and strongly emitting media, the accuracy of both P_1 and P_3 methods is expected to be substantially better [1].

Flux conservation property of the method was tested thoroughly, and it was found that the formulation and numerical procedure presented here conserves the radiative heat fluxes (overall energy) exactly, irrespective of the mesh or the optical thickness used. This is an important aspect of any numerical scheme for solution of the RTE since violation of the radiative flux conservation will also lead to violation of the overall energy conservation.

The performance of the new RTE solver was investigated by changing the maximum number of cells within each internal subdomain. The best performance was obtained when no partitioning was used and the RTE was solved using a full-field GMRES solver. Six orders of magnitude convergence was obtained on a 22,902-cell mesh in just 32 s. However, this required 152 Mbytes of memory. In order to keep memory requirements reasonable, it would be necessary to use more than one partition in large-scale computations, and further research is necessary to arrive at a compromise between memory and efficiency.

As a final step, the P_1/P_3-based RTE solver was coupled to a standalone flow and energy equation solver, and subsequently demonstrated for a 2D laminar flame case with six species, resulting in a total of ten PDEs for the flow, energy, and species conservation equations. The P_1 method (one additional PDE) was found to require approximately 9.3% additional CPU over the core flow solver, while the P_3 method (four additional PDEs) required an additional 14.5% CPU. The results presented here clearly demonstrate the feasibility of using the P_3 approximation for computation of reacting flows. Future work will focus on extension of the current procedure to three-dimensional geometry.

Acknowledgment

Financial support for this work was provided, in part, by the Ohio State University's graduate fellowship program, and in part by the Air Force Office of Scientific Research (Contract No. FA9550-08-C-0069). The authors also wish to thank Professor Michael F. Modest of the Pennsylvania State University for his support and technical guidance.

Nomenclature

A_f = area of face f (m^2)
$A_{i,j,k}$ = link coefficients
h = cavity width (m)
I = intensity (W m^{-2} sr^{-1})
I_S = intensity at surface (W m^{-2} sr^{-1})
I_b = Planck function (W m^{-2} sr^{-1})
I_n^m = position dependent coefficients in intensity expansion expression
$\overline{I_n^m}$ = position dependent coefficients expressed in local coordinates
$\hat{\mathbf{n}}$ = unit surface normal vector
N_C = total number of cells in computational domain
$N_{C,m}$ = maximum number of cells in subdomain
q_R = radiative heat flux (W m^{-2})
S = surface area of cell (m^2)
$\hat{\mathbf{s}}$ = direction vector
T = temperature (K)
$\underline{x}, \underline{y}, \underline{z}$ = global coordinates (m)
$\overline{x}, \overline{y}, \overline{z}$ = local coordinates (m)
Y_n^m = spherical harmonic functions

Greek

α_n = coefficients in P_3 equations (see Eq. (6))
β = extinction coefficient (m^{-1})
δ_f = distance between two cell centers straddling face f along normal (m)
ϕ_i = unknowns in general form of P_3 equation (see Eq. (9))
Φ = scattering phase function
$\gamma_{i,j}$ = coefficients in P_3 equations (see Eq. (4))
Γ_1 = coefficients in general for of P_3 equations (see Eq. (9))
$\underline{\tau}$ = optical coordinates (dimensionless)
τ_h = optical thickness based on cavity width (dimensionless)
ω = scattering albedo (dimensionless)
Ω = solid angle (sr)
Ω_V = volume of cell (m^3)
σ = Stefan–Boltzmann constant ($=5.67\times10^{-8}$ W m^{-2} K^{-4})
σ_S = scattering coefficient (m^{-1})

References

[1] Modest, M. F., 2003, *Radiative Heat Transfer*, 2nd ed., Academic, New York.
[2] Siegel, R., and Howell, J., 2001, *Thermal Radiation Heat Transfer*, 4th ed., Taylor and Francis, London.
[3] Olfe, D. B., 1967, "A Modification of the Differential Approximation for Radiative Transfer," AIAA J., **5**(4), pp. 638–643.
[4] Modest, M. F., 1989, "The Modified Differential Approximation for Radiative Transfer in General Three-Dimensional Media," J. Thermophys. Heat Transfer, **3**(3), pp. 283–288.
[5] Modest, M. F., 1990, "The Improved Differential Approximation for Radiative Heat Transfer in Multi-Dimensional Media," ASME J. Heat Transfer, **112**, pp. 819–821.
[6] Fiveland, W., and Jamaluddin, A., 1991, "Three-dimensional Spectral Radiative Heat Transfer Solutions by the Discrete Ordinates Method," J. Thermophys. Heat Transfer, **5**(3), pp. 335–339.
[7] Chai, J. C., Lee, H. S., and Patankar, S. V., 1994, "Finite-Volume Method for Radiative Heat Transfer," J. Thermophys. Heat Transfer, **8**, pp. 419–425.
[8] Yuen, W., and Takara, E., 1994, "Development of a General Zonal Method for Analysis of Radiative Transfer in Absorbing and Anisotropically Scattering Media," Numer. Heat Transfer, Part B, **25**, pp. 75–96.
[9] Shen, Z., Smith, T., and Hix, P., 1983, "Linearization of Thermal Radiation Terms for Improved Convergence by Use of the Zone Method," Numer. Heat Transfer, Part B, **6**, pp. 377–382.
[10] Smith, T., and Severin, S., 1985, "Development of the Finite Analytic With Radiation Method," ASME J. Heat Transfer, **107**, pp. 735–737.
[11] Chai, J. C., Lee, H. S., and Patankar, S. V., 1993, "Ray Effect and False Scattering in the Discrete Ordinates Method," Numer. Heat Transfer, Part B, **24**, pp. 373–389.
[12] Mathur, S. R., and Murthy, J. Y., 2001, "Acceleration of Anisotropic Scattering Computations Using Coupled Ordinates Method (COMET)," ASME J. Heat Transfer, **123**(3), pp. 607–612.
[13] Mazumder, S., 2005, "A New Numerical Procedure for Coupling Radiation in Participating Media With Other Modes of Heat Transfer," ASME J. Heat Transfer, **127**(9), pp. 1037–1045.
[14] Yang, J., and Modest, M. F., 2007, "Elliptic PDE Formulation of General, Three-Dimensional High-Order P_N-Approximations for Radiative Transfer," J. Quant. Spectrosc. Radiat. Transf., **104**(2), pp. 217–227.
[15] Modest, M. F., and Yang, J., 2008, "Elliptic PDE Formulation and Boundary Conditions of the Spherical Harmonics Method of Arbitrary Order for General Three-Dimensional Geometries," J. Quant. Spectrosc. Radiat. Transf., **109**, pp. 1641–1666.
[16] Bayazitoglu, Y., and Higenyi, J., 1979, "The Higher-Order Differential Equations of Radiative Transfer: P_3 Approximation," AIAA J., **17**, pp. 424–431.
[17] Ratzel, A. C., and Howell, J. R., 1983, "Two-Dimensional Radiation in Absorbing-Emitting-Scattering Media Using the P-N Approximation," ASME J. Heat Transfer, **105**, pp. 333–340.
[18] Menguc, M. P., and Viskanta, R., 1985, "Radiative Transfer in Three-Dimensional Rectangular Enclosures Containing Inhomogeneous, Anisotropically Scattering Media," J. Quant. Spectrosc. Radiat. Transf., **33**(6), pp. 533–549.
[19] Ou, S. C., and Liou, K. N., 1982, "Generalization of the spherical Harmonic Method to Radiative Transfer in Multi-Dimensional Space," J. Quant. Spectrosc. Radiat. Transf., **28**(4), pp. 271–288.
[20] McClarren, R. G., Evans, T. M., Lowrie, R. B., and Densmore, J. D., 2008, "Semi-Implicit Time Integration for P_N Thermal Radiative Transfer," J. Comput. Phys., **227**, pp. 7561–7586.
[21] McClarren, R. G., 2007, "Spherical Harmonics Methods for Thermal Radiation Transport," Ph.D. thesis, University of Michigan, Ann Arbor, MI.
[22] Cheney, W., and Kincaid, W., 1985, *Numerical Mathematics and Computing*, 2nd ed., Brooks-Cole, Belmont, MA.
[23] Ferziger, J., and Peric, M., 1999, *Computational Methods for Fluid Dynamics*, 2nd ed., Springer-Verlag, Berlin.
[24] Kumar, A., and Mazumder, S., "Coupled Solution of the Species Conservation Equations Using Unstructured Finite-Volume Method," Int. J. Numer. Methods Fluids, to be published.
[25] Kumar, A., and Mazumder, S., 2007, "A Low-Memory Block-Implicit Solver for Coupled Solution of the Species Conservation Equations on an Unstructured Mesh," *Proceedings of the International Mechanical Engineering Congress and Exposition IMECE2007*, Paper No. 2007-42517.
[26] Sung, K., and Shirley, P., 1992, "Ray Tracing With a BSP Tree," *Computer Graphics Gems III*, D. Kirk, ed., AP Professional, San Diego, CA, pp. 271–274.
[27] Karypis, G., and Kumar, V., 1998, "A Fast and High Quality Multilevel Scheme for Partitioning Irregular Graphs," SIAM J. Sci. Comput. (USA), **20**, pp. 359–392.
[28] Saad, Y., 2003, *Iterative Methods for Sparse Linear Systems*, 2nd ed., SIAM, Philadelphia, PA.
[29] Selle, L., Lartigue, G., Poinsot, T., Koch, R., Schildmacher, K. U., Krebs, W., Prade, B., Kaufmann, P., and Veynante, D., 2004, "Compressible Large Eddy Simulation of Turbulent Combustion in Complex Geometry on Unstructured Meshes," Combust. Flame, **137**, pp. 489–505.

An Efficient Sparse Finite Element Solver for the Radiative Transfer Equation

Gisela Widmer
Seminar for Applied Mathematics,
ETH Zürich,
Rämistrasse 101,
Zurich CH-8092, Switzerland
e-mail: gisela.widmer@math.ethz.ch

The stationary monochromatic radiative transfer equation is posed in five dimensions, with the intensity depending on both a position in a three-dimensional domain as well as a direction. For nonscattering radiative transfer, sparse finite elements [2007, "Sparse Finite Elements for Non-Scattering Radiative Transfer in Diffuse Regimes," ICHMT Fifth International Symposium of Radiative Transfer, Bodrum, Turkey; 2008, "Sparse Adaptive Finite Elements for Radiative Transfer," J. Comput. Phys., ***227****(12), pp. 6071–6105] have been shown to be an efficient discretization strategy if the intensity function is sufficiently smooth. Compared with the discrete ordinates method, they make it possible to significantly reduce the number of degrees of freedom N in the discretization with almost no loss of accuracy. However, using a direct solver to solve the resulting linear system requires $O(N^3)$ operations. In this paper, an efficient solver based on the conjugate gradient method with a subspace correction preconditioner is presented. Numerical experiments show that the linear system can be solved at computational costs that are nearly proportional to the number of degrees of freedom N in the discretization.*

[DOI: 10.1115/1.4000190]

Keywords: radiative transfer equation, least-squares finite elements, preconditioning, sparse grids

1 Introduction

It is widely known that radiation is an important mode of heat transfer in participating media at high temperatures. During the last decades, various methods have been developed to solve the radiative transfer equation (RTE) (e.g., see Refs. [1–5]). Very popular methods include the P_N-approximation, the finite volume method (FVM), finite element method (FEM) and, in particular, the discrete ordinates method (DOM). These methods are all based on a semidiscretization in solid angle with N_S degrees of freedom, which may correspond to spherical harmonics, discrete ordinates, or control volumes. Each of the resulting N_S equations is then discretized in physical space with N_D degrees of freedom, leading to $N_S \cdot N_D$ unknowns in total. As both N_S and N_D are the number of degrees of freedom arising from a two- or three-dimensional discretization, the computation of the radiative intensity becomes very costly when the meshes are refined.

In Refs. [6,7], an efficient discretization, the sparse tensor product approximation, was presented. Instead of using $N_S \cdot N_D$ degrees of freedom in the discretization, the number of unknowns is proportional to $N_D \log N_S + N_S \log N_D$. This can be achieved with almost no loss of accuracy if the radiation intensity is sufficiently smooth. For functions that do not satisfy the smoothness condition, adaptive sparse finite elements can improve the efficiency of the discretization [7]. In contrast to the discrete ordinates method, where the equation is discretized in the first step with respect to solid angle and in the second step with respect to physical space, a scaled least-squares approach similar to that in Ref. [3] is used, where basis and weight functions depend on both direction as well as position in physical space. Another key ingredient is the use of hierarchical basis functions. Instead of standard finite elements, products of hierarchical finite element basis functions span the finite element space.

In the papers [6,7] mentioned above, however, an essential aspect was missing, namely, the discussion of the computational costs that are required to compute for the intensity in the new discretization. Clearly, the significant reduction in the number of unknowns by itself reduces the computational costs compared with a standard discretization even if the full stiffness matrix of the finite element discretization was set up in the most straightforward way. However, if a standard direct solver is used, the computational costs are proportional to up to the third power of the number of unknowns in the discretization and as the matrix is very ill-conditioned, using iterative methods without preconditioning is also not a viable option.

This paper focuses on efficient algorithms that make it possible to solve the linear system, arising from the sparse tensor product approximation at computational costs that are almost proportional to the number of degrees of freedom in the discretization. With this method, the RTE can be solved with high accuracy at affordable computational costs.

Until now, this method has only been analyzed and tested for the monochromatic RTE in two dimensions without scattering for fully absorbing cold walls as boundary conditions

$$s \cdot \nabla_x I(x,s) + \kappa(x) I(x,s) = \kappa(x) I_b(x), \quad (x,s) \in D \times S^2 \tag{1}$$

$$I(x,s) = 0 \quad \text{for} \quad x \in \partial D, \quad s \cdot n(x) < 0 \tag{2}$$

Here, x is a position in a two-dimensional domain D, s is a direction in solid angle, $I(x,s)$ is the radiation intensity, $I_b(x)$ is the blackbody intensity, $\kappa(x)$ is the absorption coefficient, which is assumed to be uniformly bounded from below and above $(0 < \kappa_0 \le \kappa \le \kappa_1 < \infty)$, and $n(x)$ is the outer unit normal to D. As the RTE is simplified from a three-dimensional to a two-dimensional domain, the intensity is assumed to be constant with respect to the z-coordinate, i.e., $\partial I / \partial z = 0$.

The adaptation of the algorithms to three space dimensions is rather straightforward, while the analysis of the method for problems that take into account scattering effects is open. Both topics will be subjects for future research.

Contributed by the Heat Transfer Division of ASME for publication in the JOURNAL OF HEAT TRANSFER. Manuscript received October 30, 2008; final manuscript received April 30, 2009; published online December 2, 2009. Assoc. Editor: Yogesh Jaluria.

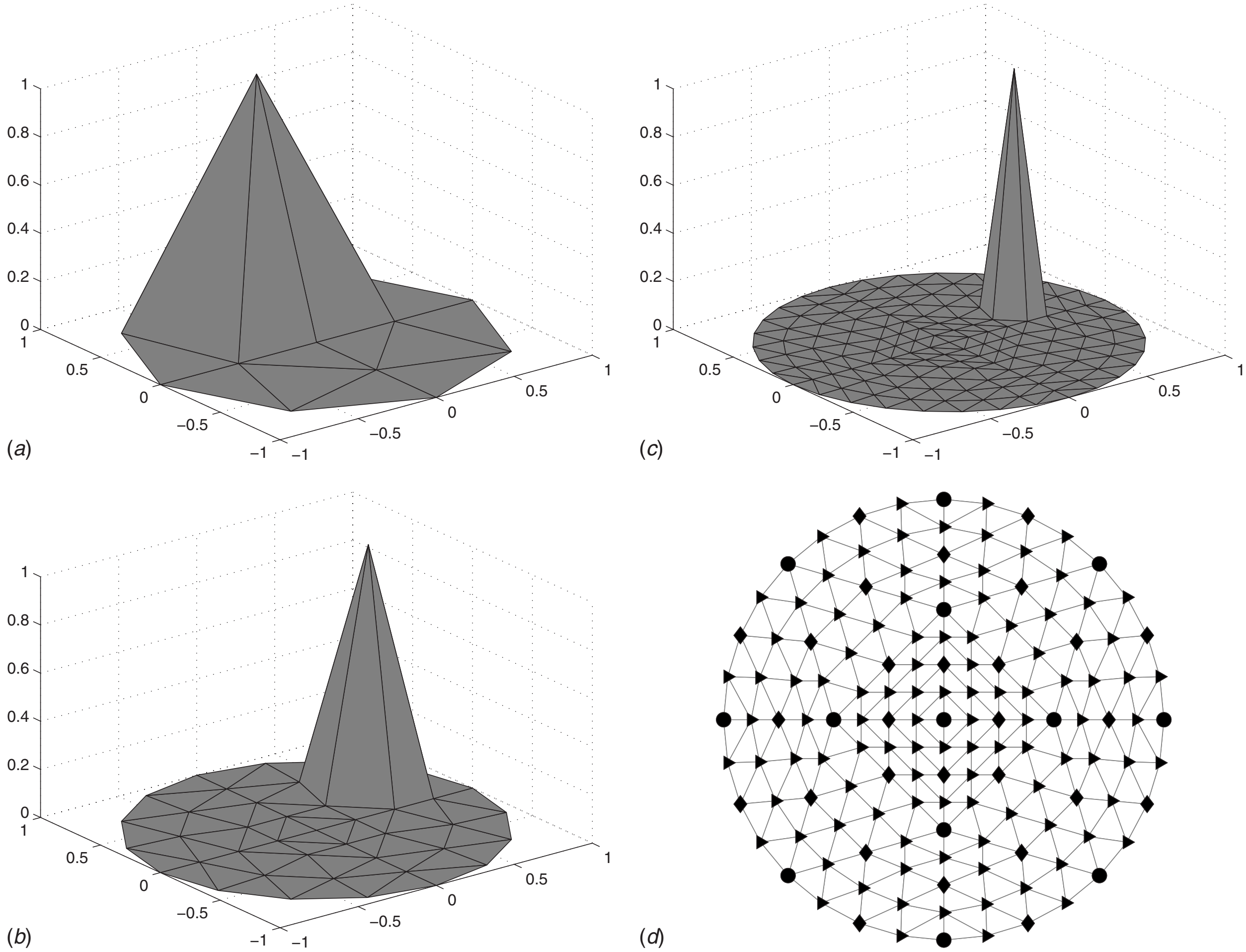

Fig. 1 (*a*)–(*c*) **Examples of hierarchical hat basis functions up to level 2. The hierarchical hat basis functions of level 0 correspond to the vertices of the coarsest mesh (marked with circles in (*d*)), while the basis functions of levels 1 and 2 correspond to the vertices marked with diamonds and triangles, respectively.**

This paper is structured as follows: Sec. 2 contains a summary of the sparse tensor product discretization as described in Ref. [6]. In Sec. 3 the conjugate gradient solver (CG) with the algorithms for efficient matrix-vector multiplication and preconditioning are presented, while numerical convergence results of the preconditioner are discussed in Sec. 4. Section 5 contains a summary of the results and conclusions.

2 Sparse Tensor Product Discretization

The sparse tensor product discretization is an adaptation of sparse grids [8,9] for the RTE. The discretization is based on two families of hierarchical basis sets. For the construction of these basis sets, the domains D and S^2 are equipped with hierarchies of dyadically refined meshes $\mathcal{T}_D^l$ and $\mathcal{T}_S^l, l=0,2,\ldots,L$, up to a given level L. Based on these meshes, hierarchical spaces of continuous, piecewise linear functions on $\mathcal{T}_D^L$ and discontinuous, piecewise constant functions on $\mathcal{T}_S^L$ are constructed. In physical space, the hierarchical basis of hat functions [10] is used, while in solid angle the space is constructed with $L^2(S^2)$-orthogonal Haar wavelets [7].

Let

$$\phi_i^{I_i}(x), \quad 0 \le i \le L, \quad I_i = 1, \ldots, N_D^i, \quad \text{and}$$

$$\psi_j^{J_j}(s), \quad 0 \le j \le L, \quad J_j = 1, \ldots, N_S^j$$

denote the set of basis functions in physical space and solid angle, respectively, up to level L. The indices i and j refer to the level of a basis function and the indices I_i and J_j are the level index on a given level i and j, respectively. N_D^i and N_S^j are the number of basis functions on level i in physical space and on level j in solid angle, respectively. Some examples of hierarchical hat basis functions $\phi_i^{I_i}(x)$ are shown in Fig. 1.

As both D and S^2 are two-dimensional domains

$$N_D^i = O(4^i) \quad \text{and} \quad N_S^j = O(4^j) \qquad (3)$$

A standard finite element discretization that uses all product basis functions $\phi_i^{I_i}(x)\psi_j^{J_j}(s)$ up to level L in physical space as well as solid angle would require $O(4^{2L})$ degrees of freedom. The idea of the sparse tensor product discretization now is to *reduce* the number of degrees of freedom to $O(L \cdot 4^L)$, which scales up to a logarithmic factor L like the number of degrees of freedom in one of the component spaces. The framework of sparse grids offers rules that allow to a priori select such a subspace without compromising accuracy for sufficiently smooth functions, namely, that the intensity function $I(x,s)$ is discretized with a linear combination of only those product functions of which the *sum of the levels* $i+j$ is smaller or equal to the maximum level L

$$I(x,s) = \sum_{i=0}^{L} \sum_{j=0}^{L-i} \sum_{I_i=1}^{N_D^i} \sum_{J_j=1}^{N_S^j} I_{i,j}^{I_i,J_j} \phi_i^{I_i}(x) \psi_j^{J_j}(s) \qquad (4)$$

This restriction to a *subset* of all product basis functions reduces the number of unknowns $I_{i,j}^{I_i,J_j}$ from $N_D \cdot N_S$ to a number $\mathcal{N}_L$ that is proportional to $N_D \log N_S + N_S \log N_D$.

Inserting the ansatz (Eq. (4)) into the weighted-residual (or weighted least-squares) variational formulation for (Eq. (1))

$$\underbrace{\int_D \int_{S^2} (s \cdot \nabla_x I(x,s) + \kappa(x) I(x,s)) W_{i,j}^{I_i,J_j}(x,s) ds dx}_{=:a(I,W_{i,j}^{I_i,J_j})}$$

$$\underbrace{= \int_D \int_{S^2} \kappa(x) I_b(x) W_{i,j}^{I_i,J_j}(x,s) ds dx}_{=:f(W_{i,j}^{I_i,J_j})} \tag{5}$$

with weighting functions

$$W_{i,j}^{I_i,J_j}(x,s) = \frac{1}{\kappa(x)}(s \cdot \nabla_x \phi_i^{I_i}(x) \psi_j^{J_j}(s) + \kappa(x) \phi_i^{I_i}(x) \psi_j^{J_j}(s)) \tag{6}$$

leads to a symmetric, positive definite linear system in the unknown coefficients (see Eq. (4))

$$I_{i,j}^{I_i,J_j}, \quad i = 0, \dots L, \quad j = 0, \dots, L - i,$$

$$I_i = 1, \dots, N_D^i, \quad J_j = 1, \dots, N_S^j$$

Using a level first ordering, these unknowns can be stored in the upper left part of a block matrix as displayed for $L=2$

$$\mathbf{I} = \begin{pmatrix} \mathcal{I}_{0,0} & \mathcal{I}_{0,1} & \mathcal{I}_{0,2} \\ \mathcal{I}_{1,0} & \mathcal{I}_{1,1} & 0 \\ \mathcal{I}_{2,0} & 0 & 0 \end{pmatrix} \quad \text{with } \mathcal{I}_{i,j} = \begin{pmatrix} I_{i,j}^{0,0} & \cdots & I_{i,j}^{0,N_S^j} \\ \vdots & \ddots & \vdots \\ I_{i,j}^{N_D^i,0} & \cdots & I_{i,j}^{N_D^i,N_S^j} \end{pmatrix} \tag{7}$$

3 Preconditioned CG-Algorithm

Due to the hierarchical basis functions, the full stiffness matrix from the discretization (Eqs. (4)–(6)) is ill-conditioned with at least $O(4^{2L})$ matrix entries. Using a standard direct linear solver would lead to computational costs proportional to up to $(\mathcal{N}_L)^3$. An alternative is the use of an iterative method. As the matrix is symmetric and positive definite, the CG-algorithm is the straightforward method of choice. To obtain an overall computational effort that scales like the number of unknowns $\mathcal{N}_L$ in the discretization, the number of CG-iterations has to be independent of the refinement level L and the number of operations in the matrix-vector multiplication has to be proportional to $\mathcal{N}_L$.

3.1 Matrix-Vector Multiplication. The matrix-vector multiplication can be carried out with optimal complexity, which means at computational costs proportional to the number of degrees of freedom $\mathcal{N}_L$ in the discretization, by taking advantage of the fact that the bilinear form of the variational formulation (Eq. (5)) separates in the sense that the integral over the product space can be written as a sum of products of integrals over S^2 and D.

$$a(\phi_i^{I_i} \cdot \psi_j^{J_j}, \phi_k^{I_k} \cdot \psi_l^{J_l}) = \sum_{m=1}^{9} b^m(\phi_i^{I_i}, \phi_k^{I_k}) \cdot c^m(\psi_j^{J_j}, \psi_l^{J_l}) \tag{8}$$

For every $m \in \{1, \dots, 9\}$ and $i,j,k,l \in \{1, \dots, L\}$ the matrices $\mathcal{B}_{ik}^m \in \mathbb{R}^{N_D^i \times N_D^k}$ and $\mathcal{C}_{jl}^m \in \mathbb{R}^{N_S^j \times N_S^l}$ are defined as the stiffness matrices from the bilinear forms $b^m(\phi_i^{I_i}, \phi_k^{I_k})$ and $c^m(\psi_j^{J_j}, \psi_k^{J_k})$ with matrix elements

$$\begin{aligned} (\mathcal{B}_{ik}^m)_{I_i,I_k} &= b^m(\phi_i^{I_i}, \phi_k^{I_k}), \quad I_i \leq N_D^i, \quad I_k \leq N_D^k, \\ (\mathcal{C}_{jl}^m)_{J_j,J_l} &= c^m(\psi_j^{J_j}, \psi_l^{J_l}), \quad J_j \leq N_S^j, \quad J_l \leq N_S^l \end{aligned} \tag{9}$$

The matrix-vector multiplication for the matrix from the discretization (Eqs. (4)–(6))

$$\widetilde{I}_{k,l}^{I_k,J_l} = \sum_{\substack{i+j \leq L \\ I_i \leq N_D^i, J_j \leq N_S^j}} \mathcal{A}_{i,j,k,l}^{I_i,J_j,I_k,I_l} I_{i,j}^{I_i,J_j}, \quad k + l \leq L, \quad I_k \leq N_D^k, \quad I_l \leq N_S^l \tag{10}$$

with

$$\mathcal{A}_{i,j,k,l}^{I_i,J_j,I_k,I_l} := a(\phi_i^{I_i} \cdot \psi_j^{J_j}, \phi_k^{I_k} \cdot \psi_l^{J_l}) \tag{11}$$

can then be written as a block matrix multiplication (shown for $L=2$)

$$\begin{pmatrix} \widetilde{\mathcal{I}}_{0,0} & \widetilde{\mathcal{I}}_{0,1} & \widetilde{\mathcal{I}}_{0,2} \\ \widetilde{\mathcal{I}}_{1,0} & \widetilde{\mathcal{I}}_{1,1} & 0 \\ \widetilde{\mathcal{I}}_{2,0} & 0 & 0 \end{pmatrix}$$

$$\leftarrow \sum_{m=1}^{9} \underbrace{\begin{pmatrix} \mathcal{B}_{0,0}^m & \mathcal{B}_{0,1}^m & \mathcal{B}_{0,2}^m \\ \mathcal{B}_{1,0}^m & \mathcal{B}_{1,1}^m & \mathcal{B}_{1,2}^m \\ \mathcal{B}_{2,0}^m & \mathcal{B}_{2,1}^m & \mathcal{B}_{2,2}^m \end{pmatrix}^T}_{=:(\mathcal{B}_2^m)^T} \underbrace{\begin{pmatrix} \mathcal{I}_{0,0} & \mathcal{I}_{0,1} & \mathcal{I}_{0,2} \\ \mathcal{I}_{1,0} & \mathcal{I}_{1,1} & 0 \\ \mathcal{I}_{2,0} & 0 & 0 \end{pmatrix}}_{=:\mathcal{I}_2} \underbrace{\begin{pmatrix} \mathcal{C}_{0,0}^m & \mathcal{C}_{0,1}^m & \mathcal{C}_{0,2}^m \\ \mathcal{C}_{1,0}^m & \mathcal{C}_{1,1}^m & \mathcal{C}_{1,2}^m \\ \mathcal{C}_{2,0}^m & \mathcal{C}_{2,1}^m & \mathcal{C}_{2,2}^m \end{pmatrix}}_{=:\mathcal{C}_2^m} \tag{12}$$

Here, "←" denotes the partial assignment, where only values that correspond to degrees of freedom in the sparse tensor product space are set.

A straightforward multiplication of the matrices on the right would require additional storage space in the lower right part of the block matrix, where the values in the intensity matrix $\mathcal{I}_L$ are zero for the intermediate state. As this would destroy the desired complexity, following the sparse grids multiplication strategy [11,12], the last matrix is split into an upper part and a lower part.

$$\begin{pmatrix} \mathcal{B}_{0,0}^m & \mathcal{B}_{0,1}^m & \mathcal{B}_{0,2}^m \\ \mathcal{B}_{1,0}^m & \mathcal{B}_{1,1}^m & \mathcal{B}_{1,2}^m \\ \mathcal{B}_{2,0}^m & \mathcal{B}_{2,1}^m & \mathcal{B}_{2,2}^m \end{pmatrix}^T \begin{pmatrix} \mathcal{I}_{0,0} & \mathcal{I}_{0,1} & \mathcal{I}_{0,2} \\ \mathcal{I}_{1,0} & \mathcal{I}_{1,1} & 0 \\ \mathcal{I}_{2,0} & 0 & 0 \end{pmatrix} \begin{pmatrix} \mathcal{C}_{0,0}^m & \mathcal{C}_{0,1}^m & \mathcal{C}_{0,2}^m \\ \mathcal{C}_{1,0}^m & \mathcal{C}_{1,1}^m & \mathcal{C}_{1,2}^m \\ \mathcal{C}_{2,0}^m & \mathcal{C}_{2,1}^m & \mathcal{C}_{2,2}^m \end{pmatrix} \tag{13}$$

$$= \begin{pmatrix} \mathcal{B}_{0,0}^m & \mathcal{B}_{0,1}^m & \mathcal{B}_{0,2}^m \\ \mathcal{B}_{1,0}^m & \mathcal{B}_{1,1}^m & \mathcal{B}_{1,2}^m \\ \mathcal{B}_{2,0}^m & \mathcal{B}_{2,1}^m & \mathcal{B}_{2,2}^m \end{pmatrix}^T \begin{pmatrix} \mathcal{I}_{0,0} & \mathcal{I}_{0,1} & \mathcal{I}_{0,2} \\ \mathcal{I}_{1,0} & \mathcal{I}_{1,1} & 0 \\ \mathcal{I}_{2,0} & 0 & 0 \end{pmatrix} \begin{pmatrix} \mathcal{C}_{0,0}^m & \mathcal{C}_{0,1}^m & \mathcal{C}_{0,2}^m \\ 0 & \mathcal{C}_{1,1}^m & \mathcal{C}_{1,2}^m \\ 0 & 0 & \mathcal{C}_{2,2}^m \end{pmatrix} \tag{14}$$

$$+ \begin{pmatrix} \mathcal{B}_{0,0}^m & \mathcal{B}_{0,1}^m & \mathcal{B}_{0,2}^m \\ \mathcal{B}_{1,0}^m & \mathcal{B}_{1,1}^m & \mathcal{B}_{1,2}^m \\ \mathcal{B}_{2,0}^m & \mathcal{B}_{2,1}^m & \mathcal{B}_{2,2}^m \end{pmatrix}^T \begin{pmatrix} \mathcal{I}_{0,0} & \mathcal{I}_{0,1} & \mathcal{I}_{0,2} \\ \mathcal{I}_{1,0} & \mathcal{I}_{1,1} & 0 \\ \mathcal{I}_{2,0} & 0 & 0 \end{pmatrix} \begin{pmatrix} 0 & 0 & 0 \\ \mathcal{C}_{1,0}^m & 0 & 0 \\ \mathcal{C}_{2,0}^m & \mathcal{C}_{2,1}^m & 0 \end{pmatrix} \tag{15}$$

The upper part (Eq. (14)) is evaluated first by partially multiplying the last two matrices

$$\begin{pmatrix} \hat{\mathcal{I}}_{0,0} & \hat{\mathcal{I}}_{0,1} & \hat{\mathcal{I}}_{0,2} \\ \hat{\mathcal{I}}_{1,0} & \hat{\mathcal{I}}_{1,1} & 0 \\ \widetilde{\mathcal{I}}_{2,0} & 0 & 0 \end{pmatrix} \leftarrow \begin{pmatrix} \mathcal{I}_{0,0} & \mathcal{I}_{0,1} & \mathcal{I}_{0,2} \\ \mathcal{I}_{1,0} & \mathcal{I}_{1,1} & 0 \\ \mathcal{I}_{2,0} & 0 & 0 \end{pmatrix} \begin{pmatrix} \mathcal{C}_{0,0}^m & \mathcal{C}_{0,1}^m & \mathcal{C}_{0,2}^m \\ 0 & \mathcal{C}_{1,1}^m & \mathcal{C}_{1,2}^m \\ 0 & 0 & \mathcal{C}_{2,2}^m \end{pmatrix} \tag{16}$$

before partially carrying out the first multiplication

$$\begin{pmatrix} \widetilde{\mathcal{I}}_{0,0} & \widetilde{\mathcal{I}}_{0,1} & \widetilde{\mathcal{I}}_{0,2} \\ \widetilde{\mathcal{I}}_{1,0} & \widetilde{\mathcal{I}}_{1,1} & 0 \\ \widetilde{\mathcal{I}}_{2,0} & 0 & 0 \end{pmatrix} \leftarrow \begin{pmatrix} \mathcal{B}^m_{0,0} & \mathcal{B}^m_{0,1} & \mathcal{B}^m_{0,2} \\ \mathcal{B}^m_{1,0} & \mathcal{B}^m_{1,1} & \mathcal{B}^m_{1,2} \\ \mathcal{B}^m_{2,0} & \mathcal{B}^m_{2,1} & \mathcal{B}^m_{2,2} \end{pmatrix}^T \begin{pmatrix} \hat{\mathcal{I}}_{0,0} & \hat{\mathcal{I}}_{0,1} & \hat{\mathcal{I}}_{0,2} \\ \hat{\mathcal{I}}_{1,0} & \hat{\mathcal{I}}_{1,1} & 0 \\ \widetilde{\mathcal{I}}_{2,0} & 0 & 0 \end{pmatrix} \tag{17}$$

For the lower part (Eq. (15)), the first two matrices are multiplied partially before evaluating the second matrix multiplication.

As hierarchical bases are used, the block matrices $\mathcal{B}^m_L$ and $\mathcal{C}^m_L$ of level L have $O(L \cdot 4^L)$ matrix entries and the partial matrix-vector multiplication requires $O(L^2 4^L) = O(L\mathcal{N}_L)$ operations. To obtain computational costs that are proportional to $\mathcal{N}_L$, basis transformations between hierarchical and standard basis functions are used

$$\phi_i^{I_i}(x) = \sum_{i'=0}^{N_D^0+\ldots+N_D^{l_D}} (\mathcal{R}^{i,l_D})_{I_i,i'} \varphi_{i'}^{l_D}(x),$$

$$\psi_j^{J_j}(s) = \sum_{j'=0}^{N_S^0+\ldots+N_S^{l_S}} (\mathcal{S}^{j,l_S})_{J_j,j'} \chi_{j'}^{l_S}(s) \tag{18}$$

Here, $\varphi_{i'}^{l_D}(x)$ $(i' \in \{1,\ldots,N_D^0+\ldots+N_D^{l_D}\})$ is the basis of standard finite element hat functions of level l_D on $\mathcal{T}_D^{l_D}$, $\chi_{j'}^{l_S}(s)$ $(j' \in \{1,\ldots,N_S^0+\ldots+N_S^{l_S}\})$ is the basis of piecewise constant functions of level l_S on $\mathcal{T}_S^{l_S}$, $\mathcal{R}^{i,l_D}$ is the matrix of basis transform from the standard basis of level l_D to the hierarchical basis on level i in physical space, and $\mathcal{S}^{j,l_S}$ is the matrix of basis transform from the standard basis of level l_S to the Haar basis on level j in solid angle. The submatrices $\mathcal{B}^m_{ik}$ and $\mathcal{C}^m_{jl}$ can then be written as

$$\mathcal{B}^m_{ik} = \mathcal{R}^{i,l_D}\mathbf{B}^{m,l_D}(\mathcal{R}^{k,l_D})^T, \quad i,k \le l_D, \quad \text{and}$$

$$\mathcal{C}^m_{jl} = \mathcal{S}^{j,l_S}\mathbf{C}^{m,l_S}(\mathcal{S}^{l,l_S})^T, \quad j,l \le l_S \tag{19}$$

where $\mathbf{B}^{m,l_D}$ and $\mathbf{C}^{m,l_S}$ are the standard finite element matrices with matrix entries

$$(\mathbf{B}^{m,l_D})_{i',k'} = b^m(\phi_{i'}^{l_D},\phi_{k'}^{l_D}), \quad (\mathbf{C}^{m,l_S})_{j',l'} = c^m(\chi_{j'}^{l_S},\chi_{l'}^{l_S}) \tag{20}$$

and the block matrices up to level l_D and l_S, respectively, can be written as

$$\mathcal{B}^m_{l_D} = \mathcal{R}^{l_D}\mathbf{B}^{m,l_D}(\mathcal{R}^{l_D})^T \quad \text{and} \quad \mathcal{C}^m_{l_S} = \mathcal{S}^{l_S}\mathbf{C}^{m,l_S}(\mathcal{S}^{l_S})^T \tag{21}$$

with

$$\mathcal{R}^{l_D} := \begin{pmatrix} \mathcal{R}^{0,l_D} \\ \vdots \\ \mathcal{R}^{l_D,l_D} \end{pmatrix} \quad \text{and} \quad \mathcal{S}^{l_S} := \begin{pmatrix} \mathcal{S}^{0,l_S} \\ \vdots \\ \mathcal{S}^{l_S,l_S} \end{pmatrix} \tag{22}$$

For fixed level j and index J_j in solid angle, with $\mathbf{I}_j^{J_j}$ denoting the corresponding column vector up to level $L-j$ of the coefficient matrix $\mathcal{I}_L$, the operation $\widetilde{\mathbf{I}}_j^{J_j} = (\mathcal{B}^m_{L-j})^T\mathbf{I}_j^{J_j}$ can be written as

$$\widetilde{\mathbf{I}}_j^{J_j} = (\mathcal{B}^m_{L-j})^T\mathbf{I}_j^{J_j} = \mathcal{R}^{l_{L-j}}(\mathbf{B}^{m,L-j})^T(\mathcal{R}^{l_{L-j}})^T\mathbf{I}_j^{J_j} \tag{23}$$

The matrix-vector multiplication $(\mathcal{R}^{l_{L-j}})^T\mathbf{I}_j^{J_j}$ (and analogously for $\mathcal{R}^{l_{L-j}}$) can be carried out at computational costs proportional to the length of the vector $\mathbf{I}_j^{J_j}$, using standard hierarchical reconstruction techniques [10]. As the finite element matrices with respect to standard basis are sparse, the matrix-vector multiplication (Eq. (23)) requires a computational effort proportional to the number of elements in $\mathbf{I}_j^{J_j}$ and the partial matrix-vector multiplication as in Eq. (17) requires $O(\mathcal{N}_L)$ operations. With analogous arguments for the solid angle matrices, it is easy to see that the partial matrix multiplication with respect to solid angle as in Eq. (16) can also be computed with the same complexity, which makes it possible to compute the matrix-vector multiplication for the linear system (Eq. (10)) with the optimal complexity of $O(\mathcal{N}_L)$ operations.

3.2 Preconditioning.

To be able to compute for the intensity at computational costs that are proportional to the number of degrees of freedom in the discretization $\mathcal{N}_L$, the number of iteration steps in the CG-solver must be independent of the refinement level. Without preconditioning, numerical experiments show that the number of iteration steps to solve the linear system grows rapidly when the discretization is refined (Figs. 5 and 6). Therefore, an efficient preconditioner is crucial to obtain the desired complexity of the solver.

A preconditioner for a linear system

$$\mathbf{A}x = b \tag{24}$$

with a symmetric positive definite operator $\mathbf{A}$ is a symmetric positive definite linear operator $\mathbf{M}$ that is used to transform Eq. (24) into an equivalent linear system

$$\mathbf{MA}x = \mathbf{M}b \tag{25}$$

For a preconditioner to be efficient it has to satisfy two criteria, as follows:

1. For any vector $\mathbf{y}$ the matrix-vector multiplication $\mathbf{My}$ has to be easy to compute, optimally at computational costs proportional to the dimension of $\mathbf{y}$.
2. $\mathbf{MA}$ should be close to the identity matrix in the sense that the condition number of $\mathbf{MA}$ is independent of the refinement level and close to 1 as this guarantees the number of CG-iterations to be small and bounded by a constant that is independent of the refinement level.

Numerical experiments show that using a multiplicative subspace preconditioner [13] is a successful strategy for the linear system from Eqs. (4)–(6). In a manner similar to sparse grid preconditioners for elliptic problems [14], the sparse tensor product space is divided into $(L+1)$ *overlapping* subspaces.

$$\hat{V}_L = \sum_{l_D+l_S=L} V_{l_D,l_S} \tag{26}$$

where the space V_{l_D,l_S} contains all product basis functions up to level l_D in physical space and up to level l_S in solid angle

$$V_{l_D,l_S} = \text{span}\{\phi_i^{I_i}(x)\psi_j^{J_j}(s); \quad i \le l_D, \quad j \le l_S, \quad I_i \le N_D^i, \quad J_j \le N_S^j\} \tag{27}$$

Or, in terms of coefficient matrices $\mathcal{I}_{i,j}$ from Eq. (7), V_{l_D,l_S} consists of the unknowns stored in the blocks $\mathcal{I}_{i,j}$ with $0 \le i \le l_D$ and $0 \le j \le l_S$ (see Fig. 2). However, as the RTE is a hyperbolic problem, some adaptations of the preconditioner are required.

The preconditioner is based on the following idea: If we discretized the RTE on any of these subspaces V_{l_D,l_S}, $l_D+l_S=L$, with standard finite elements, which means continuous, piecewise linear hat functions of level l_D in physical space and discontinuous, piecewise constant functions on the spherical triangles of level l_S in solid angle, we would obtain $N_S^0+\ldots+N_S^{l_S}$ transport equations, each corresponding to the direction of one spherical triangle. If a one-point quadrature rule was used for integrating over the solid angle, this discretization would be identical to a discrete ordinates method with $N_S^0+\ldots+N_S^{l_S}$ discrete ordinates, combined with a least-squares finite element discretization in physical space with $N_D^0+\ldots+N_D^{l_D}$ mesh vertices.

Thanks to the decoupling in solid angle, the RTE would be a simple transport equation for each triangle, which could be solved

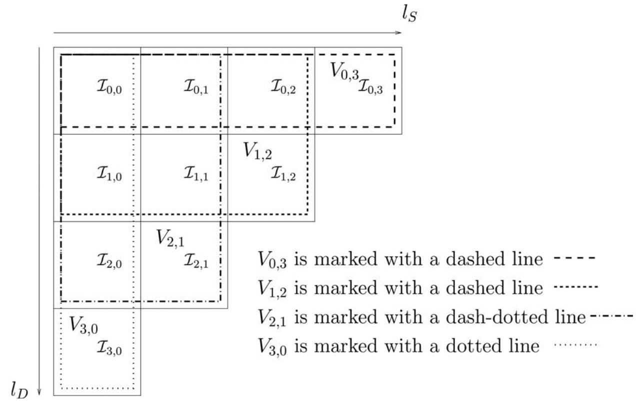

Fig. 2 The subspace V_{l_D,l_S} contains all degrees of freedom up to level l_D in physical space and up to level l_S in solid angle. The figure shows the subspaces V_{l_D,l_S} for $L=3$.

separately for each spherical triangle using an algebraic multigrid solver (AMG) [15]. As the relative complexity of the AMG algorithm is nearly independent of the number of degrees of freedom in the discretization, the computational costs for solving the RTE on such a subsystem with standard discretizations is nearly proportional to the number of degrees of freedom in the subspace.

When restricting the sparse tensor product discretization to one of these subspaces V_{l_D,l_S}, the solution in V_{l_D,l_S} is a good approximation for the solution of the sparse tensor product discretization, restricted to this subspace. This property can be used to subsequently solve a linear system on each of the subspaces and obtain a multiplicative subspace preconditioner **M** for the linear system from the sparse tensor product discretization that iteratively computes for *corrections* on the subspaces $V_{l_D,L-l_D}$ $(l_D=0,\dots,L)$, and adds them to the current approximation (Algorithms 1 and 2).

Algorithm 1 Subspace Correction Preconditioner $x \leftarrow \mathbf{M}y$

```
$x \leftarrow 0$
for $l_S=0$ to $L$ {Loop over levels in solid angle} do
    $l_D=L-l_D$ {Level in physical space}
    $r \leftarrow \mathbf{y}-\mathbf{A}x$
    $c_{l_D,l_S} \leftarrow$ Subspace solve$(l_D,l_S,r)$ {Subspace correction on $V_{l_D,l_S}$}
    $x \leftarrow x+c_{l_D,l_S}$
end for
for $l_D=0$ to $L${Loop over levels in physical space} do
    $l_S=L-l_D$ {Level in solid angle}
    $r \leftarrow \mathbf{y}-\mathbf{A}x$
    $c_{l_D,l_S} \leftarrow$ Subspace solve$(l_D,l_S,r)$ {Subspace correction on $V_{l_D,l_S}$, Algorithm 2}
    $x \leftarrow x+c_{l_D,l_S}$
end for
return $x$
```

Algorithm 2 Subspace solver $c_{l_D,l_S} \leftarrow$ Subspace solve(l_D,l_S,r)

```
$r_{l_D,l_S} \leftarrow r$ {Restriction of residual to levels $(l_D,l_S)$}
$\tilde{r} \leftarrow r_{l_D,l_S}(\mathcal{S}^{l_S})^{-T}$ {Transformation to standard representation in solid angle}
for $i=0$ to $\Sigma_{j=0}^{l_S}\mathcal{N}_i$ {Loop over triangles in solid angle} do
    $r_i^S \leftarrow (\mathcal{R}^{l_D})^{-1}\tilde{r}_i$ {Transformation to standard representation in physical space}
    $c_i^S \leftarrow (\Sigma_{m=1}^9(\mathbf{B}_{l_D}^m)^T(\mathbf{C}_{l_S}^m)_{i,i})^{-1}r_i^S$ {Solving the linear system using AMG}
    $\tilde{c}_i \leftarrow (\mathcal{R}^{l_D})^{-T}c_i^S$ {Transformation to hierarchical representation in physical space}
end for
$c_{l_D,l_S} \leftarrow \tilde{c}(\mathcal{S}^{l_S})^{-1}$ {Transformation to hierarchical representation in solid angle}
return $c_{l_D,l_S}$
```

In the sparse tensor product discretization the subspaces $V_{l_D,L-l_D}$ are discretized with hierarchical bases instead of standard bases as required for the AMG-solver. Therefore, after restricting the residual $r=b-\mathbf{A}x$ to the subspace $V_{l_D,L-l_D}$, it has to be transformed into standard bases with respect to space as well as solid angle. After solving the linear subsystem with respect to the standard bases, the correction has to be transformed back into hierarchical representation c_{l_D,l_S}. In terms of matrices, the linear system is transformed into a linear system with respect to the standard bases using basis transformation matrices (Eq. (22)) as follows:

$$\sum_{m=1}^{9}(\mathcal{B}_{l_D}^m)^T c_{l_D,l_S}\mathcal{C}_{l_S}^m = r_{l_D,l_S} \tag{28}$$

$$\mathcal{R}^{l_D}\sum_{m=1}^{9}((\mathbf{B}^{m,l_D})^T(\mathcal{R}^{l_D})^T c_{l_D,l_S}S^{l_S}\mathbf{C}^{m,l_S})(S^{l_S})^T = r_{l_D,l_S} \tag{29}$$

$$\sum_{m=1}^{9}((\mathbf{B}^{m,l_D})^T\underbrace{(\mathcal{R}^{l_D})^T c_{l_D,l_S}S^{l_S}}_{=:c_{l_D,l_S}^S}\mathbf{C}^{m,l_S}) = \underbrace{(\mathcal{R}^{l_D})^{-1}r_{l_D,l_S}(S^{l_S})^{-T}}_{r_{l_D,l_S}^S} \tag{30}$$

$$\sum_{m=1}^{9}((\mathbf{B}^{m,l_D})^T c_{l_D,l_S}^S\mathbf{C}^{m,l_S}) = r_{l_D,l_S}^S \tag{31}$$

Here, r_{l_D,l_S}^S and c_{l_D,l_S}^S denote the residual and the correction matrix with respect to the standard bases.

This transformation requires that the inverse of the operator $\mathcal{R}^{l_D}$ from the left and the inverse of $(\mathcal{S}^{l_S})^T$ from the right are applied to the residual matrix to obtain the residual in standard bases and, after the linear system has been solved in standard bases, analogous transformations have to be carried out to obtain the correction matrix in hierarchical representation.

As the hierarchical basis functions in solid angle are $L^2(S^2)$-orthogonal, the linear operator S^{l_S} satisfies

$$(\mathcal{S}^{l_S})^T\mathcal{S}^{l_S} = D \Rightarrow (\mathcal{S}^{l_S})^{-1} = (\mathcal{S}^{l_S})^T D \tag{32}$$

where D is a diagonal matrix with positive matrix entries. Therefore, the inverse operators $(\mathcal{S}^{l_S})^{-1}$ and $(\mathcal{S}^{l_S})^{-T}$ can be applied at computational costs proportional to the number of degrees of freedom in V_{l_D,l_S}.

In physical space, the operators $(\mathcal{R}^{l_D})^{-1}$ and $(\mathcal{R}^{l_D})^{-T}$ can be applied to the subspace coefficients by using the standard decomposition strategy [10] for the hierarchical basis at computational costs proportional to the number of degrees of freedom in V_{l_D,l_S}.

As the total sum of the degrees of freedom in the $L+1$ subspaces V_{l_D,l_S} is bounded by $2\mathcal{N}_L$

$$\sum_{l=0}^{L} V_{l,L-l} = \sum_{l=0}^{L}\mathcal{N}_l \le 2\mathcal{N}_L \tag{33}$$

the relative complexity of the preconditioner is nearly independent of the refinement level L.

4 Numerical Results and Discussion

If we assume that the corrections c_{l_D,l_S}^S can be computed at costs proportional to the number of elements in c_{l_D,l_S}^S, the computational effort in each CG-iteration step is proportional to the number of degrees of freedom $\mathcal{N}_L$ in the sparse tensor product discretization. The efficiency of the sparse tensor product solver therefore de-

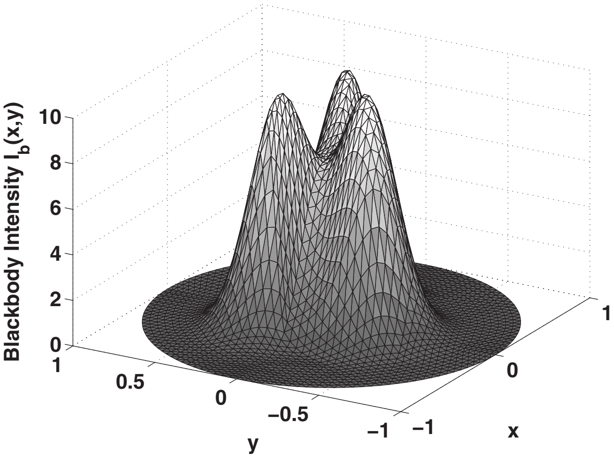

Fig. 3 The blackbody intensity $I_b(x)$ of example 2

pends on the quality of the preconditioner. An optimal preconditioner would reduce the number of iteration steps to a small number that is independent of the refinement level. In practice, however, a preconditioner where the number of iterations grows very slowly when the refinement level is increased is already very satisfactory.

The preconditioned CG-method for sparse finite elements is tested for the two-dimensional test problems on the unit circle presented in Ref. [6]. There, we assessed the approximation properties of the sparse tensor product approximation and showed that the sparse tensor product method allows to reduce the number of degrees of freedom from $N_D \cdot N_S$ to $O(N_S \log N_D + N_D \log N_S)$ with almost no loss of accuracy and that the method is clearly superior to pure refinement with respect to physical space.

In example 1, the absorption coefficient is equal to 5 and the blackbody intensity is given by

$$I_b(x) = \begin{cases} 10 \cdot (0.8 - |x|)/0.8, & |x| \leq 0.8 \\ 0, & |x| > 0.8 \end{cases} \tag{34}$$

In example 2, there are three emitting sources with maximum intensity 10 that decay exponentially (see Fig. 3). The absorption coefficient is equal to the blackbody intensity, which is increased by 0.5. In physical space, the coarsest mesh $\mathcal{T}_D^0$ is shown in Fig. 4, while the vertices of $\mathcal{T}_S^0$ are the corners of the octahedron.

The performance of the preconditioner is measured by comparing the number of CG-iteration steps with and without subspace correction preconditioner.

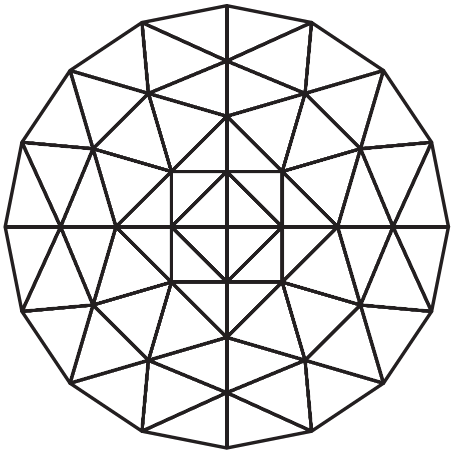

Fig. 4 The coarsest mesh $\mathcal{T}_D^0$ in physical space

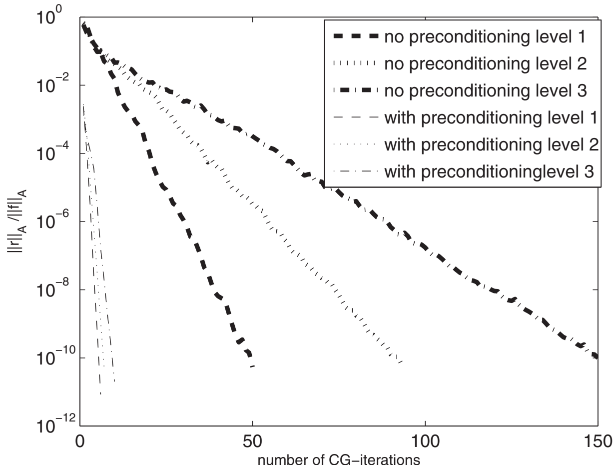

Fig. 5 Number of CG-iterations with and without preconditioning for example 1

Figure 5 shows the convergence of the CG-method to reduce the relative residual $\frac{\|r\|_A}{\|f\|_A}$ for example 1 with and without preconditioning. Here, $\|\cdot\|_A$ denotes the energy norm corresponding to the bilinear form in Eq. (5). Although the CG-method converges without preconditioning to the required tolerance of 10^{-10} for all levels, the number of iterations grows faster than linearly with respect to the refinement level. Applying the multiplicative subspace preconditioner significantly reduces the number of iterations to very small numbers of 5, 6, and 9 iterations on levels 1, 2, and 3. Although the number of iterations grows slowly when the space is refined, the increase is clearly sublinear with respect to the number of levels and the total number of iterations is very small.

The convergence of the CG-method in example 2, where the absorption coefficient is inhomogeneous, is shown in Fig. 6. The difference between the number of iterations with and without preconditioning is even more evident than for example 1. Without preconditioner, the convergence rate of the CG-method deteriorates drastically when the refinement level L is increased. The preconditioner reduces the number of iterations even more significantly than in example 1 to 7, 9, and 12 iterations.

5 Conclusions and Outlook

An efficient solver for computing the radiation intensity for the nonscattering RTE with the sparse tensor product discretization

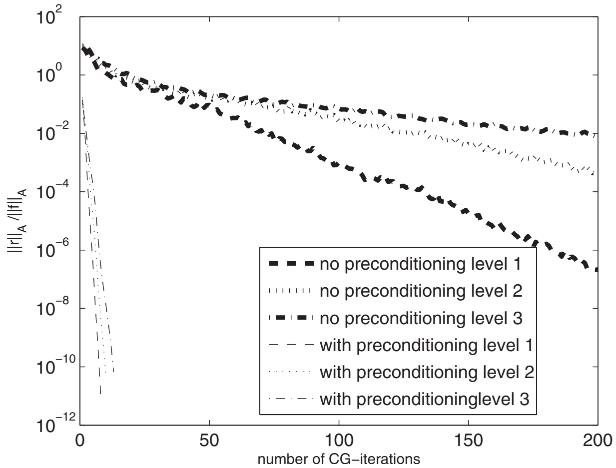

Fig. 6 Number of CG-iterations with and without preconditioning for example 2

has been presented. The algorithm uses the preconditioned CG-method with an efficient matrix-vector multiplication strategy and a multiplicative subspace preconditioner. The matrix-vector multiplication can be carried out at computational costs proportional to the number of degrees of freedom in the discretization $\mathcal{N}_L$. The number of operations to apply the preconditioner, which is based on an algebraic multigrid solver, is nearly proportional to $\mathcal{N}_L$. The preconditioner significantly reduces the number of CG-iterations to a number that grows very slowly when the discretization level L is increased. This makes it possible to solve the RTE with high accuracy at affordable computational costs.

As the variational formulation (Eq. (5)) can be easily adapted to the RTE with scattering [16], the sparse tensor product discretization will also be applicable to this case. However, as the scattering kernel couples different directions of the radiation intensity at a given position, performance and efficient implementation of an adapted subspace preconditioner are to date open and will be subject to future research.

References

[1] Howell, J. R., 1988, "Thermal Radiation in Participating Media: The Past, the Present and Possible Futures," ASME J. Heat Transfer, **110**, pp. 1220–1229.

[2] Modest, M. F., 2003, *Radiative Heat Transfer*, 2nd ed., Academic, Amsterdam.

[3] Ruan, L. M., An, W., Tan, H. P., and Qi, H., 2007, "Least-Squares Finite-Element Method of Multidimensional Radiative Heat Transfer in Absorbing and Scattering Media," Numer. Heat Transfer, **51**(7), pp. 657–677.

[4] An, W., Ruan, L. M., Tan, H. P., and Qi, H., 2006, "Least-Squares Finite Element Analysis for Transient Radiative Transfer in Absorbing and Scattering Media," ASME J. Heat Transfer, **128**(5), pp. 499–503.

[5] Viskanta, R., and Mengüc, M. P., 1987, "Radiating Heat Transfer in Combustion Systems," Prog. Energy Combust. Sci., **13**(2), pp. 97–160.

[6] Widmer, G., and Hiptmair, R., 2007, "Sparse Finite Elements for Non-Scattering Radiative Transfer in Diffuse Regimes," ICHMT Fifth International Symposium of Radiative Transfer, Bodrum, Turkey.

[7] Widmer, G., Hiptmair, R., and Schwab, C., 2008, "Sparse Adaptive Finite Elements for Radiative Transfer," J. Comput. Phys., **227**(12), pp. 6071–6105.

[8] Bungartz, H.-J., and Griebel, M., 2004, "Sparse Grids," Acta Numerica, **13**, pp. 147–169.

[9] Zenger, C., 1990, "Sparse Grids," *Parallel Algorithms for Partial Differential Equations: Proceedings of the Sixth GAMM-Seminar*, Vieweg-Verlag, Braunschweig, pp. 241–251.

[10] Cohen, A., 2003, *Numerical Analysis of Wavelet Methods*, Elsevier, Amsterdam.

[11] Bungartz, H.-J., 1997, "A Multigrid Algorithm for Higher Order Finite Elements on Sparse Grids," Electron. Trans. Numer. Anal., **6**, pp. 63–77.

[12] Gradinaru, V. C., 2002, "Whitney Elements on Sparse Grids," Ph.D. thesis, Eberhard-Karls University, Tübingen.

[13] Xu, J., 1992, "Iterative Methods by Space Decomposition and Subspace Correction," SIAM Rev., **34**(4), pp. 581–613.

[14] Achatz, S., 2003, "Adaptive finite Dünngitter-Elemente höherer Ordnung für elliptische partielle Differentialgleichungen mit variablen Koeffizienten," Ph.D. thesis, Technische Universität, München.

[15] De Sterck, H., Manteuffel, T. A., McCormick, S. F., and Olson, L., 2004, "Least-Squares Finite Element Methods and Algebraic Multigrid Solvers for Linear Hyperbolic PDEs," SIAM J. Sci. Comput., **26**(1), pp. 31–54.

[16] Austin, T. M., and Manteuffel, T. A., 2006, "A Least-Squares Finite Element Method for the Linear Boltzmann Equation With Anisotropic Scattering," SIAM (Soc. Ind. Appl. Math.) J. Numer. Anal., **44**(2), pp. 540–560.

R. Becker[1]
e-mail: becker@its.uni-karlsruhe.de

R. Koch

H.-J. Bauer

Institut für Thermische Strömungsmaschinen,
Universität Karlsruhe,
Kaiserstraße 12,
76128 Karlsruhe, Germany

M. F. Modest
Department of Mechanical and Nuclear
Engineering,
Pennsylvania State University,
University Park, PA 16802

A Finite Element Treatment of the Angular Dependency of the Even-Parity Equation of Radiative Transfer

The present article introduces a new method to solve the radiative transfer equation (RTE). First, a finite element discretization of the solid angle dependence is derived, wherein the coefficients of the finite element approximation are functions of the spatial coordinates. The angular basis functions are defined according to finite element principles on subdivisions of the octahedron. In a second step, these spatially dependent coefficients are discretized by spatial finite elements. This approach is very attractive, since it provides a concise derivation for approximations of the angular dependence with an arbitrary number of angular nodes. In addition, the usage of high-order angular basis functions is straightforward. In the current paper, the governing equations are first derived independently of the actual angular approximation. Then, the design principles for the angular mesh are discussed and the parameterization of the piecewise angular basis functions is derived. In the following, the method is applied to one-dimensional and two-dimensional test cases, which are commonly used for the validation of approximation methods of the RTE. The results reveal that the proposed method is a promising alternative to the well-established practices like the discrete ordinates method (DOM) and provides highly accurate approximations. A test case, which is known to exhibit the ray effect in the DOM, verifies the ability of the new method to avoid ray effects.

[DOI: 10.1115/1.4000233]

1 Introduction

During the last century numerous approximation methods for the calculation of radiation heat transfer were proposed. Acceptable numerical methods are accurate, easy to apply to complex geometries, and have the ability to deal with real radiation problems. Furthermore, the calculation methods should be computationally efficient in terms of memory usage and processing time. Extensive overviews of available methods are given by Viskanta and Mengüc [1], Mishra and Prasad [2] and recently by Viskanta [3].

Virtually all of the generally applicable methods are based on the solution of the radiative transfer equation (RTE), a first-order integrodifferential equation. These solution methods need to account for the spatial and the angular dependence of the radiative intensity. Regarding the angular dependence, the discrete ordinates method (DOM) [4] and the spherical harmonics (P_N) approximation [5] have attracted great attention.

In the DOM the governing equations are easy to derive, the extension to high- order angular approximations is straightforward, and it may be readily applied to complex geometries. Because of these advantages, the DOM has evolved as a standard solution method of the RTE. However, the DOM has several shortcomings, perhaps the most important one being the "ray effect" [6]: In cases with strongly confined radiation sources the integral quantities of radiation transport, e.g., the radiative heat flux, are over- and underestimated for distinct directions. The DOM solves the RTE for a set of discrete directions and the integral quantities are calculated by a weighted sum (quadrature) of the distinct solutions afterwards. This approach is the origin of the ray effect. The usage of higher order quadratures may mask it, but one must be aware that ray effects are inherent to the DOM and also to the derived methods like the finite volume method [7,8]. As a remedy for mitigating the ray effect the modified discrete ordinate method [9] was proposed. However, this method has significant restrictions regarding its general applicability.

In the P_N-approximation the angular dependence of the radiation intensity is expanded into a series of associated Legendre polynomials [10]. Mostly, the series is truncated to the P_1-approximation, seldom a P_3-approximation is used. The origin of this restriction is the serious deficiency of the P_N-approximations: The formulation of the boundary conditions is not straightforward and is tedious for general geometries and high-order approximations. Recently, Modest and Yang [11] published a concise derivation of the equations and the related boundary conditions for high-order P_N-approximations. This may stimulate the usage of P_3 and higher approximations in the future, but the mathematical formulation is still demanding.

These observations have led us to the development of an alternative treatment of the angular dependence in the RTE. Starting out from the second-order even-parity (EP) equation [12] of radiative transport, we derived a finite element discretization of the angular and the spatial domain. This approach enables a continuous representation of the angular dependence of the radiative intensity and hence eliminates ray effects rigorously. Since the mathematical formulation is independent in the selection of the basis functions used for the spatial and the angular finite elements, the extension of the method to high-order approximations is straightforward. This approach has evolved in the early days in the context of the neutron transport equation [13,14], but has received only little attention in the heat transfer community. The authors have adopted the method for solving the radiative heat transfer (RHT) equation as recently proposed by Becker et al. [15]. Comparable methods were lately published by Coelho [16], Pontaza and Reddy [17], Cui and Li [18], and Widmer and Hiptmair [19].

---

[1] Corresponding author.

Contributed by the Heat Transfer Division of ASME for publication in the JOURNAL OF HEAT TRANSFER. Manuscript received November 13, 2008; final manuscript received March 31, 2009; published online December 4, 2009. Assoc. Editor: Yogesh Jaluria.

2 Derivation of the Equations

2.1 Radiative Transfer Equation.

Considering an arbitrary volume V filled with a gray emitting-absorbing, isotropically scattering media, the balance of radiative intensity $I(\mathbf{r},\mathbf{s})$ along a direction $\mathbf{s}$ is given by the radiative transfer equation

$$\mathbf{s}\cdot\nabla I(\mathbf{r},\mathbf{s}) = \kappa I_b(\mathbf{r}) - \beta I(\mathbf{r},\mathbf{s}) + \frac{\sigma}{4\pi}\int_{4\pi} I(\mathbf{r},\mathbf{s}')d\Omega' \tag{1}$$

where α, β, and σ indicate the absorption, the extinction, and the scattering coefficient. I_b is the blackbody intensity, which is related to the temperature T of the medium by

$$I_b = \frac{E_b}{\pi} = \frac{\sigma}{\pi}T^4 \tag{2}$$

If the boundary A of the enclosure is assumed as black and nonreflecting, the intensity $I(\mathbf{r},\mathbf{s})$ at the boundary is

$$I(\mathbf{r}_{\text{wall}},\mathbf{s}) = I_b, \quad \mathbf{n}\cdot\mathbf{s} > 0 \tag{3}$$

for all outward directions $\mathbf{s}$. Equation (1) together with Eq. (3) constitutes a first-order initial value problem. Since this first-order equation is of the hyperbolic type, the stability and the accuracy of the numerical method may be critical and the numerical solution procedure requires provisions like the marching technique. In the current work the problem, as defined by Eqs. (1) and (3), is converted into an equivalent second-order boundary value problem of the parabolic type. This transformation is done by the EP formulation of radiative transfer, which was derived in context of the neutron transport equation [20] and was adopted to the RTE by Song and Park [12].

2.2 Even-Parity Formulation.

In the EP formulation the radiative intensity $I(\mathbf{r},\mathbf{s})$ is expressed as a sum of a directional, even-symmetric quantity $\Psi(\mathbf{r},\mathbf{s})$, and a directional, odd-symmetric quantity $\Lambda(\mathbf{r},\mathbf{s})$

$$I(\mathbf{r},\mathbf{s}) = \tfrac{1}{2}[\Psi(\mathbf{r},\mathbf{s}) + \Lambda(\mathbf{r},\mathbf{s})] \tag{4}$$

with

$$\Psi(\mathbf{r},\mathbf{s}) = I(\mathbf{r},\mathbf{s}) + I(\mathbf{r},-\mathbf{s}) \tag{5a}$$

$$\Lambda(\mathbf{r},\mathbf{s}) = I(\mathbf{r},\mathbf{s}) - I(\mathbf{r},-\mathbf{s}) \tag{5b}$$

By using the EP formulation the radiative transfer is fully defined by the calculation of $\Psi(\mathbf{r},\mathbf{s})$ and $\Lambda(\mathbf{r},\mathbf{s})$ in one arbitrary half of the solid angle. This can be easily shown by evaluating the radiative heat flux $q(\mathbf{r})$ and the incident radiation $G(\mathbf{r})$

$$\mathbf{q}(\mathbf{r}) = \int_{4\pi}\mathbf{s}I(\mathbf{r},\mathbf{s})d\Omega \tag{6a}$$

$$G(\mathbf{r}) = \int_{4\pi} I(\mathbf{r},\mathbf{s})d\Omega \tag{6b}$$

Substituting $I(\mathbf{r},\mathbf{s})$ as given by Eq. (4) into Eqs. (6*a*) and (6*b*) and using the symmetry properties of $\Psi(\mathbf{r},\mathbf{s})$ and $\Lambda(\mathbf{r},\mathbf{s})$, the integration in Eqs. (6*a*) and (6*b*) can be restricted to 1/2 of the solid angle

$$\mathbf{q}(\mathbf{r}) = \tfrac{1}{2}\int_{4\pi}\mathbf{s}[\Psi(\mathbf{r},\mathbf{s}) + \Lambda(\mathbf{r},\mathbf{s})]d\Omega = \int_{2\pi}\mathbf{s}\Lambda(\mathbf{r},\mathbf{s})d\Omega \tag{7a}$$

$$G(\mathbf{r}) = \tfrac{1}{2}\int_{4\pi}[\Psi(\mathbf{r},\mathbf{s}) + \Lambda(\mathbf{r},\mathbf{s})]d\Omega = \int_{2\pi}\Psi(\mathbf{r},\mathbf{s})d\Omega \tag{7b}$$

Formulating Eq. (1) for the two directions $\mathbf{s}$ and $-\mathbf{s}$, adding and subtracting the resulting equations and substituting Eqs. (5*a*) and (5*b*), a system of coupled differential equations in $\Psi(\mathbf{r},\mathbf{s})$ and $\Lambda(\mathbf{r},\mathbf{s})$ is obtained

$$\mathbf{s}\cdot\nabla\Lambda(\mathbf{r},\mathbf{s}) + \beta\Psi(\mathbf{r},\mathbf{s}) = 2\kappa I_b(\mathbf{r}) + \frac{\sigma}{2\pi}\int_{2\pi}\Psi(\mathbf{r},\mathbf{s}')d\Omega' \tag{8a}$$

$$\mathbf{s}\cdot\nabla\Psi(\mathbf{r},\mathbf{s}) + \beta\Lambda(\mathbf{r},\mathbf{s}) = 0 \tag{8b}$$

Solving Eq. (8*b*) for the odd quantity $\Lambda(\mathbf{r},\mathbf{s})$

$$\Lambda(\mathbf{r},\mathbf{s}) = -\frac{1}{\beta}\mathbf{s}\cdot\nabla\Psi(\mathbf{r},\mathbf{s}) \tag{9}$$

and inserting Eq. (9) in Eq. (8*a*), the following second-order differential equation

$$-\mathbf{s}\cdot\nabla\frac{1}{\beta}\mathbf{s}\cdot\nabla\Psi(\mathbf{r},\mathbf{s}) + \beta\Psi(\mathbf{r},\mathbf{s}) = 2\kappa I_b(\mathbf{r}) + \frac{\sigma}{2\pi}\int_{2\pi}\Psi(\mathbf{r},\mathbf{s}')d\Omega' \tag{10}$$

of radiative transfer is derived.

Contrary to the initial value problem, as defined in Sec. 2.1, the EP equation needs a boundary condition for the inward and the outward directions. These boundary conditions can be deduced from Eq. (3) by replacing the intensity $I(\mathbf{r},\mathbf{s})$ with Eq. (4) and using the symmetry properties of $\Psi(\mathbf{r},\mathbf{s})$ and $\Lambda(\mathbf{r},\mathbf{s})$. Following this path, the boundary condition

$$\Psi(\mathbf{r},\mathbf{s}) - \text{sign}(\mathbf{n}\cdot\mathbf{s})\frac{1}{\beta}\mathbf{s}\cdot\nabla\Psi(\mathbf{r},\mathbf{s}) = 2I_b(\mathbf{r}) \tag{11}$$

is obtained.

With Eqs. (10) and (11) the radiative transfer is transformed to a second-order differential equation of the parabolic type. The use of this second-order boundary value problem instead of the first-order initial value problem enables one to adopt the standard Galerkin approach, which provides unconditional stability, to solve the RTE.

2.3 Weak Solution.

A common procedure for the derivation of the governing equations of the Galerkin finite element method (FEM) is the application of the weighted residual method [21].

In this method the differential equation is multiplied by a weight function $W(\mathbf{r},\mathbf{s})$ and the integrated residual is set to zero. In the traditional approach this integration is restricted to the spatial domain, and the directional dependence is addressed by the DOM [22]. Here, the directional and the spatial dependence are approximated by means of the FEM. Therefore, the integration includes both, the angular and spatial, domains.

The weighted residual approach is written as

$$\int_{2\pi}\int_{V}\left[\mathbf{s}\cdot\nabla\frac{1}{\beta}\mathbf{s}\cdot\nabla\Psi(\mathbf{r},\mathbf{s}) - \beta\Psi(\mathbf{r},\mathbf{s}) + \frac{\sigma}{2\pi}\int_{2\pi}\Psi(\mathbf{r},\mathbf{s}')d\Omega' + 2\kappa I_b(\mathbf{r})\right]W(\mathbf{r},\mathbf{s})dVd\Omega = 0 \tag{12}$$

Using Green's theorem and integrating the second-order derivative by parts, leads to the so-called weak formulation of the EP equation

$$
\begin{aligned}
&\int_{2\pi}\int_{A}(\mathbf{n}\cdot\mathbf{s})\frac{1}{\beta}\mathbf{s}\cdot\nabla\Psi(\mathbf{r},\mathbf{s})W(\mathbf{r},\mathbf{s})dA d\Omega \\
&\quad -\int_{2\pi}\int_{V}\frac{1}{\beta}\mathbf{s}\cdot\nabla\Psi(\mathbf{r},\mathbf{s})\mathbf{s}\cdot\nabla W(\mathbf{r},\mathbf{s})dV d\Omega \\
&\quad -\int_{2\pi}\int_{V}\left[\beta\Psi(\mathbf{r},\mathbf{s})-\frac{\sigma}{2\pi}\int_{2\pi}\Psi(\mathbf{r},\mathbf{s}')d\Omega'\right]W(\mathbf{r},\mathbf{s})dV d\Omega \\
&\quad +\int_{2\pi}\int_{V}2\kappa I_b(\mathbf{r})W(\mathbf{r},\mathbf{s})dV d\Omega = 0 \qquad (13)
\end{aligned}
$$

where the integration over the boundary A is used to fulfill the boundary condition Eq. (11). The boundary condition is integrated in Eq. (13) by solving Eq. (11) for

$$
\frac{1}{\beta}\mathbf{s}\cdot\nabla\Psi(\mathbf{r},\mathbf{s}) = \mathrm{sign}(\mathbf{n}\cdot\mathbf{s})[\Psi(\mathbf{r},\mathbf{s})-2I_b(\mathbf{r})] \qquad (14)
$$

and replacing the integrand in the area term in Eq. (13). This leads to the integral equation

$$
\begin{aligned}
&\int_{2\pi}\int_{A}|\mathbf{n}\cdot\mathbf{s}|[\Psi(\mathbf{r},\mathbf{s})-2I_b(\mathbf{r})]W(\mathbf{r},\mathbf{s})dA d\Omega \\
&\quad -\int_{2\pi}\int_{V}\frac{1}{\beta}\mathbf{s}\cdot\nabla\Psi(\mathbf{r},\mathbf{s})\mathbf{s}\cdot\nabla W(\mathbf{r},\mathbf{s})dV d\Omega \\
&\quad -\int_{2\pi}\int_{V}\left[\beta\Psi(\mathbf{r},\mathbf{s})-\frac{\sigma}{2\pi}\int_{2\pi}\Psi(\mathbf{r},\mathbf{s}')d\Omega'\right]W(\mathbf{r},\mathbf{s})dV d\Omega \\
&\quad +\int_{2\pi}\int_{V}2\kappa I_b(\mathbf{r})W(\mathbf{r},\mathbf{s})dV d\Omega = 0 \qquad (15)
\end{aligned}
$$

which is the starting point for the following finite element discretization.

2.4 Finite Element Formulation. For the discretization of Eq. (15) and the derivation of the algebraic linear system by means of finite elements two formulations are suitable. On the one hand, the equations may be discretized by using elemental basis functions to approximate the solution and the weighting function as a series expansion locally. Afterwards the global system is constructed by superposition of the elemental contributions. This approach is often used, since it is the most convenient for implementing the finite element method in a computer code. On the other hand, the derivation of the algebraic system may be achieved by using globally defined basis functions. For the present purpose it is more advantageous to use the global approach, since it results in a formulation, which is much easier to compare with the DOM or the P_N-approximations. Later on, the separation of the globally defined functions into the elemental contributions will be examined in a brief manner.

By introducing the angular approximation, the EP quantity $\Psi(\mathbf{r},\mathbf{s})$ is written as

$$
\Psi(\mathbf{r},\mathbf{s}) = \sum_{n}^{M_\Omega}\Psi_n(\mathbf{r})\Phi_n(\mathbf{s}) \qquad (16)
$$

and the weight function $W(\mathbf{r},\mathbf{s})$ is

$$
W(\mathbf{r},\mathbf{s}) = \sum_{n}^{M_\Omega}W_n(\mathbf{r})\Phi_n(\mathbf{s}) \qquad (17)
$$

where the spatial dependence of $\Psi(\mathbf{r},\mathbf{s})$ and $W(\mathbf{r},\mathbf{s})$ is still unknown. Hence, the coefficients $\Psi_n(\mathbf{r})$ and $W_n(\mathbf{r})$ are just spatially dependent coefficients of the angular basis function $\Phi_n(\mathbf{s})$. The choice of suitable angular basis functions is limited by two restrictions: They must be linearly independent and they must also be square integrable over the angular domain. These requirements are fulfilled by every piecewise defined function of any order. Inserting the expansions (16) and (17) into the weighted residual Eq. (15), a system of M_Ω equations

$$
\begin{aligned}
&\sum_{n}^{M_\Omega}\int_{A}[\Psi_n(\mathbf{r})\overline{\Omega}_{nm}-2I_b(\mathbf{r})\overline{\omega_m}]W_m(\mathbf{r})dA \\
&\quad -\int_{V}\frac{1}{\beta}\nabla^T\Psi_n(\mathbf{r})\Omega^{11}_{nm}\nabla W_m(\mathbf{r})dV-\int_{V}\beta\Psi_n(\mathbf{r})\Omega^{00}_{nm}W_m(\mathbf{r})dV \\
&\quad +\int_{V}\left[\frac{\sigma}{2\pi}\Psi_n(\mathbf{r})\omega^{00}_n\omega^{00}_m+2I_b(\mathbf{r})\omega^{00}_m\right]W_m(\mathbf{r})dV = 0 \qquad (18)
\end{aligned}
$$

with the coefficients

$$
\Omega^{11}_{nm} = \int_{2\pi}\begin{pmatrix}\xi\xi & \xi\eta & \xi\mu \\ \eta\xi & \eta\eta & \eta\mu \\ \mu\xi & \mu\eta & \mu\mu\end{pmatrix}\Phi_n(\mathbf{s})\Phi_m(\mathbf{s})d\Omega \qquad (19a)
$$

$$
\Omega^{01}_{nm} = \int_{2\pi}\mathbf{s}\Phi_n(\mathbf{s})\Phi_m(\mathbf{s})d\Omega \qquad (19b)
$$

$$
\Omega^{00}_{nm} = \int_{2\pi}\Phi_n(\mathbf{s})\Phi_m(\mathbf{s})d\Omega \qquad (19c)
$$

$$
\omega^{00}_{m} = \int_{2\pi}\Phi_m(\mathbf{s})d\Omega \qquad (19d)
$$

$$
\overline{\Omega}_{nm} = \int_{2\pi}|\mathbf{n}\cdot\mathbf{s}|\Phi_n(\mathbf{s})\Phi_m(\mathbf{s})d\Omega \qquad (19e)
$$

$$
\overline{\omega_m} = \int_{2\pi}|\mathbf{n}\cdot\mathbf{s}|\Phi_m(\mathbf{s})d\Omega \qquad (19f)
$$

is obtained.

Equation (18) constitutes a linear system for the determination of the coefficients $\Psi_n(\mathbf{r})$ in the angular domain, where the spatial dependence is left to later analysis. Clearly, the choice of the basis functions determines the pattern of sparsity in the matrices. If, e.g., piecewise constant, nonoverlapping basis functions are used, all off-diagonal terms in the matrix are zero and a system of equations similar to the one derived by the DOM will be obtained [14]. On the other hand, if high-order polynomials defined in the whole angular domain are chosen, a system of equations comparable to the P_N-approximation will be derived. For the subsequent analysis, piecewise linear basis functions with compact support are applied for the angular approximation and, as a result, all off-diagonal terms marking adjacent nodes are nonzero.

The fully, spatially, and angularly, discretized algebraic equation for the RHT problem, as defined by Eq. (15), is derived by substituting a suitable approximation for the coefficients $\Psi_n(\mathbf{r})$ in Eq. (18). Again, the unknowns are expanded into a series of globally defined basis functions, here in the spatial domain $\hat{\Phi}_p(\mathbf{r})$. With

$$
\Psi_n(\mathbf{r}) = \sum_{p}^{M_r}\Psi_{np}\hat{\Phi}_p(\mathbf{r}) \qquad (20a)
$$

$$
W_n(\mathbf{r}) = \sum_{p}^{M_r}\hat{\Phi}_p(\mathbf{r}) \qquad (20b)
$$

the approximations of the EP quantity

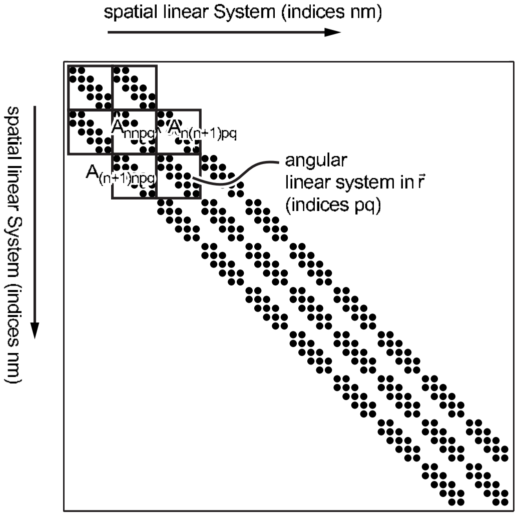

Fig. 1 Structure of the spatial and angular linear system

$$\Psi(\mathbf{r},\mathbf{s}) = \sum_{p}^{M_r}\sum_{n}^{M_\Omega} \Psi_{np}\hat{\Phi}_p(\mathbf{r})\Phi_n(\mathbf{s}) \tag{21}$$

and the weight function

$$W(\mathbf{r},\mathbf{s}) = \sum_{p}^{M_r}\sum_{n}^{M_\Omega} \hat{\Phi}_p(\mathbf{r})\Phi_n(\mathbf{s}) \tag{22}$$

are deduced as a product of basis functions for the direction **s** and position **r**. Substituting Eqs. (20*a*) and (20*b*) into Eq. (18), one equation of the resultant linear system in position and direction reads:

$$\sum_{p}^{M_r}\sum_{n}^{M_\Omega} A_{nmpq}\Psi_{mq} = b_{np} \tag{23}$$

with matrix elements

$$A_{nmpq} = \int_A \hat{\Phi}_p(\mathbf{r})\overline{\Omega}_{nm}\hat{\Phi}_q(\mathbf{r})dA - \int_V \frac{1}{\beta}\nabla^T\hat{\Phi}_p(\mathbf{r})\Omega^{11}_{nm}\nabla\hat{\Phi}_q(\mathbf{r})dV - \int_V \beta\hat{\Phi}_p(\mathbf{r})\Omega^{00}_{nm}\hat{\Phi}_q(\mathbf{r})dV + \int_V \frac{\sigma}{2\pi}\hat{\Phi}_p(\mathbf{r})\omega^{00}_n\omega^{00}_m\hat{\Phi}_q(\mathbf{r})dV \tag{24}$$

and source term

$$b_{np} = 2\int_A I_b(\mathbf{r})\overline{\omega_n}\hat{\Phi}_p(\mathbf{r})dA - 2\int_V I_b(\mathbf{r})\omega^{00}_n\hat{\Phi}_p(\mathbf{r})dV \tag{25}$$

Equation (23) defines the linear system

$$\mathbf{A}\Psi = \mathbf{b}$$

$$\Psi = (\Psi_{11},\Psi_{12},\ldots,\Psi_{1M_\Omega},\ldots,\Psi_{M_rM_\Omega}) \tag{26}$$

with an underlying block structure where the angular equations Eq. (18) are embedded in the system defined by the spatial approximation (Fig. 1).

With results calculated from the solution of Eq. (26), the incident radiation Eq. (7*b*) is calculated from

$$G(\mathbf{r}) = \sum_{p}^{M_r}\sum_{n}^{M_\Omega}\int_{2\pi}\Phi_n(\mathbf{s})d\Omega\Phi_p(\mathbf{r})\Psi_{np} = \sum_{p}^{M_r}\sum_{n}^{M_\Omega}\omega^{00}_n(\mathbf{s})\Phi_p(\mathbf{r})\Psi_{np} \tag{27}$$

and the heat flux Eq. (7*a*) is given by

$$\mathbf{q}(\mathbf{r}) = -\frac{1}{\beta}\sum_{p}^{M_r}\sum_{n}^{M_\Omega}\int_{2\pi}\mathbf{s}\otimes\mathbf{s}\Phi_n(\mathbf{s})d\Omega\,\nabla\Phi_p(\mathbf{r})\Psi_{np} = -\frac{1}{\beta}\sum_{p}^{M_r}\sum_{n}^{M_\Omega}\omega^{11}_n\nabla\Phi_p(\mathbf{r})\Psi_{np} \tag{28}$$

As stated earlier the most convenient way of implementing the finite element method in a computer code is by adding the global coefficients from the elemental contributions. In order to do this, the angular domain Ω and the spatial domain V are decomposed in nonoverlapping elements Ω^e and V^e in such a way that

$$V = \sum_e V^e \tag{29}$$

and

$$\Omega = \sum_e \Omega^e \tag{30}$$

With these subdivisions the global angular and spatial basis functions are split into the elemental parts

$$\hat{\Phi}_p(\mathbf{r}) = \sum_e \hat{\Phi}^e_p(\mathbf{r}) \tag{31a}$$

$$\Phi_n(\mathbf{s}) = \sum_e \Phi^e_n(\mathbf{s}) \tag{31b}$$

and hence the coefficients can be calculated by restricting the integrations to the elements V^e and Ω^e. Afterwards, the elemental coefficients are added according to the continuity requirements as defined by Eqs. (31*a*) and (31*b*).

2.5 Angular Discretization and Definition of the Basis Functions. Up to this point, no assumptions about the nature of the basis functions other than those at the beginning of Sec. 2.4 were made. As stated earlier, piecewise angular functions are used in the subsequent calculations. Consequently, the definition of the basis functions requires two steps: First, the elemental decomposition of the solid angle, and second, the definition of the elemental basis functions on those elements.

To perform the angular decomposition, meshes based on octahedrons were used, even if simpler schemes, e.g., the classical longitudinal/latitudinal subdivisions, are available. The reason for this choice is the symmetry under rotations of $\pi/2$ and the nearly equally sized angular elements of the octahedral meshes. According to the principles for the construction of quadratures for use with the DOM, these attributes are believed to be crucial for the accuracy of numerical results [23].

The angular meshes are constructed in the following way. Starting out from an octahedron inscribed in the unit sphere with the vertices placed on the coordinate axes, the edges of the basic planar triangles are subdivided into N equal parts by $N-1$ new nodes. Afterwards the nodes are connected by lines parallel to the edges of the basic triangles leading to a finer triangular grid. On each intersection of the connecting lines, additional nodes are placed. An example of this triangulation of order $N=2$ is presented in Fig. 2. The spherical grid is built afterwards by projecting the triangulation onto the unit sphere (Fig. 2). Following this procedure, grids with

$$M_\Omega = 6, 18, 38, \ldots, (4N^2+2) \tag{32}$$

nodes and $8, 32, 72, \ldots, 8N^2$ elements are obtained.

It should be emphasized that the procedure described here sub-

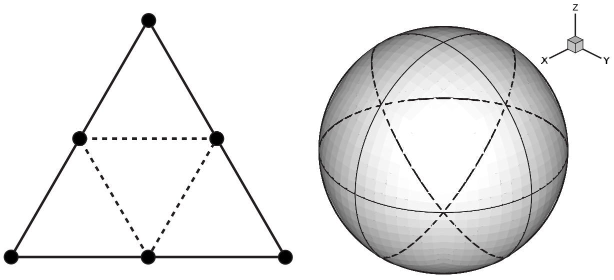

Fig. 2 Triangulation of the order $N=2$ and the derived octahedral angular finite element mesh

divides the whole solid angle, even though the application of the EP formulation requires only the partitioning of one arbitrary half of the solid angle. This reduction to the half angle is readily obtained by splitting the mesh at, e.g., the equatorial plane.

The basis functions in solid angle are defined by the parameterization of planar triangles, since the definition of general functions on spherical triangles is not achievable. If the vertices of a planar triangle are denoted by $\mathbf{r}_1$, $\mathbf{r}_2$, and $\mathbf{r}_3$, each point $\mathbf{r}$ in the planar triangle may be described by the barycentric coordinate system as

$$\mathbf{r} = \begin{pmatrix} x_1 & x_2 & x_3 \\ y_1 & y_2 & y_3 \\ z_1 & z_2 & z_3 \end{pmatrix} \begin{pmatrix} \gamma_1 \\ \gamma_2 \\ \gamma_3 \end{pmatrix} = A\gamma \quad \text{with} \quad \sum_{i=1}^{3} \gamma_i = 1 \tag{33}$$

A point $\mathbf{r}$ on the planar triangle is assigned to a point $\mathbf{s}$ on the spherical triangle by

$$\mathbf{s} = \frac{\mathbf{r}}{|\mathbf{r}|} \tag{34}$$

By inverting Eq. (33) and inserting Eq. (34), $\mathbf{s}$ is represented by a unique parameterization γ_i

$$\gamma = A^{-1}\mathbf{r} = A^{-1}|\mathbf{r}|\mathbf{s} \tag{35}$$

where the distance $|\mathbf{r}|$ of the point on the planar triangle to the origin is unknown. Noting that the planar triangle is part of the plane with the normal form

$$(\mathbf{r} - \mathbf{r}_i) \cdot \mathbf{n} = 0 \rightarrow \mathbf{r} \cdot \mathbf{n} = D = \mathbf{r}_i \cdot \mathbf{n}, \quad i = \{1,2,3\} \tag{36}$$

where $\mathbf{r}_i$ is one of the vertices of the planar triangle and the normal vector is given by

$$\mathbf{n} = (\mathbf{r}_1 - \mathbf{r}_2) \times (\mathbf{r}_1 - \mathbf{r}_3) \tag{37}$$

the norm $|\mathbf{r}|$ is expressed by the points in the spherical triangle by inserting Eq. (34) in Eq. (36)

$$|\mathbf{r}| = \frac{D}{\mathbf{n} \cdot \mathbf{s}} \tag{38}$$

Using this result, Eq. (35) is a function

$$\gamma = \gamma(\mathbf{s}) = A^{-1}\frac{D}{\mathbf{n} \cdot \mathbf{s}}\mathbf{s} \tag{39}$$

of the points on the spherical triangle or the direction $\mathbf{s}$. By using Eq. (39) each basis function

$$\hat{\Phi}^e(\mathbf{r}) = f(\gamma) \tag{40}$$

defined on the planar triangle may be used as basis function

$$\Phi^e(\mathbf{s}) = f(\gamma(\mathbf{s})) \tag{41}$$

of the direction $\mathbf{s}$.

By noting that the restriction

$$\sum_{i=1}^{3} \gamma_i = 1 \tag{42}$$

in Eq. (33) requires $\gamma_3 = 1 - \gamma_1 - \gamma_2$, it is obvious that the inverse of Eq. (33) directly defines the commonly used linear basis function on the planar triangle and, hence, Eq. (39) defines the equivalent linear function on the spherical triangle.

3 Results and Discussion

Based on the theoretical and analytical considerations described previously, computer codes have been developed that are able to simulate one-dimensional, two-dimensional, and three-dimensional RHT problems. While the one-dimensional code is implemented using the MATLAB [24] environment, the multidimensional codes are implemented in the C programming language. For the results to be discussed subsequently, linear basis functions in the spatial domain and linear basis functions in the angular domain were used as defined by Eq. (39). The angular discretizations were obtained from different stages of refinement of the octahedron and are labeled as "SAFE M_Ω," where M_Ω is the number of nodes of the mesh in the total solid angle as given by Eq. (32) and SAFE is an acronym for solid angle finite element. The coefficients of the angular linear system Eq. (18) were calculated by numerical integration, where each spherical triangle is subdivided in a number of smaller triangles and a Newton–Cotes quadrature is employed in the subtriangles. A criterion for the accuracy of the integration was the total sum of the distinct coefficients, which must conform to the analytical values of the well-known angular moments [23]. Solutions of the linear system of equations were calculated by the stabilized conjugate gradient method from van der Vorst [25]. To compare the proposed method to well-established methods, computer codes based on the same spatial finite element code using the EP-DOM [26] together with the level symmetric hybrid (LSH)-quadratures [27], and the P_1-approximation [28] with Marshak's boundary conditions were developed.

In order to assess the performance of the method, benchmarks were computed and compared with the exact solution. These benchmarks are commonly used to analyze the performance of a computational solution technique for the RTE [16,22]. In all cases the incident radiation, Eq. (27), and the radiative heat flux, Eq. (28), were calculated. For the assessment of the accuracy the errors are quantified by the root mean square (rms) defined as

$$\text{rms}(y) = \sqrt{\frac{1}{N}\sum_{i}^{N} (y(z_i) - y^{\text{exact}}(z_i))^2} \tag{43}$$

In the following, test cases with highly simplified geometries were investigated, for which analytical solutions are available. The application of the method to more realistic three-dimensional geometries has been reported recently [15].

3.1 Test Case A: Emitting and Absorbing Plane-Parallel Medium. An emitting and absorbing plane-parallel medium with prescribed temperature bounded by black, cold walls was investigated as a first test case. This problem is attractive since the analytical solution is easily calculated to arbitrary precision, and it allows to obtain a first impression of the fundamental quality of the approximation method.

In Figs. 3 and 4 the net heat flux q and the incident radiation G are plotted as calculated by the finite element method for optical thicknesses $\kappa L = 0.1$, 1.0, and 10.0. In each case, the temperature of the medium was equivalent to $I_b = 1/\pi$. Because of the symmetry of the problem, the figures show only 1/2 of the solution domain. The analytical solutions are calculated from the equations given in the textbook by Modest [28].

While the finite element method predicts the net radiative heat flux with good accuracy for all stages of refinement of the angular mesh and optical thicknesses κL, the predicted incident radiation

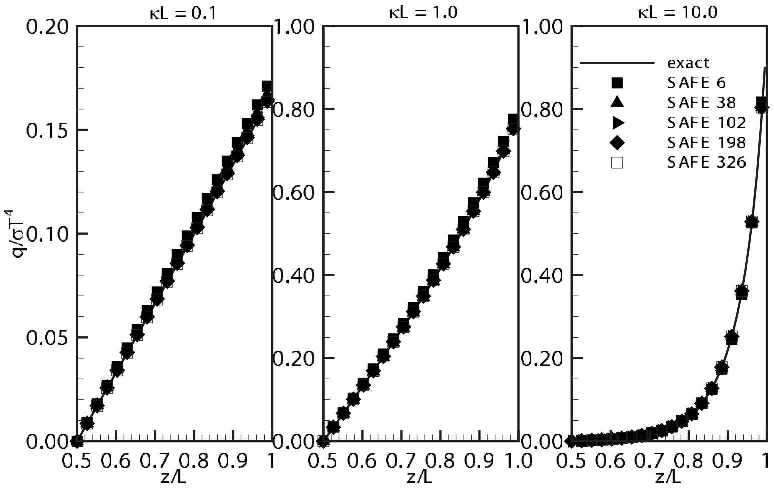

Fig. 3 Test case A: Radiative heat flux *q* in an emitting-absorbing plane-parallel medium

in the optically thin case differs significantly from the analytical results for coarser angular grids. A detailed insight in the prediction quality of the SAFE in dependence of the angular and spatial mesh is given by Figs. 5 and 6. The reason for the error trends as displayed by these figures is easily understood by the inspection of Fig. 7.

Independent of the optical thickness the intensity in directions parallel to the walls is $I(z,0)=I_b$. In the optically thick case approximately the same intensity is obtained independent of the direction for locations far enough from the walls. Approaching the cold walls, the intensity in either the upper or the lower hemisphere will drop rapidly to zero. From this observation the values for Ψ in the EP equation may be deduced. With Eq. (4) and the symmetry properties of Ψ, the value $\Psi(z)=2/\pi$ can be derived for all directions in the symmetry plane $z=L/2$. Using again Eq. (4), the direction independent value $\Psi(z,\mu)=1/\pi$, for $\mu\neq 0$, can be derived for positions in the vicinity of the walls. A directional dependence of Ψ can only be observed at positions between the symmetry plane and the wall. There, Ψ decreases smoothly from $2/\pi$ to $1/\pi$ for directions perpendicular to the wall, while $\Psi(z,\mu)$ for directions nearly parallel to the wall displays a steep gradient in the close vicinity to the boundary. Summarizing these considerations, it can be concluded that in the optically thick case a moderate number of angular nodes is sufficient, but a small spatial element size is necessary. This conclusion is confirmed by the rms values calculated from the predicted net heat fluxes and incident radiation as depicted in Figs. 5 and 6. It is obvious that the lowest-order angular discretization does not yield a satisfactory accuracy and the rms rapidly converges toward a limit when refining the spatial grid. As expected, the refinement of the spatial grid has a strong major influence on the accuracy of the solution, provided the angular discretization is fine enough.

The opposed characteristics can be found for the optically thin case. In the symmetry plane the intensity normal to the walls is $I(z,\pm 1)\approx(\kappa L I_b)/2$. It increases for $\mu\rightarrow 0$ exponentially toward the limit $I(z,0)=I_b$. When approaching the upper wall, the intensity $I(z,0)$ remains constant and $I(L,1)$ is twice the value in the symmetry plane. According to Eq. (4) and the symmetry properties of Ψ, this implies that $\Psi(z,\mu)$ is nearly independent of the position inside the medium and decreases only for directions near $\mu=0$ approximately to the half. Therefore, the spatial element size plays a less significant role. These assumptions are confirmed by the results of the finite element calculations presented in Fig. 4. Clearly, the finite element approximation is not capable of predicting the incident radiation with an error less than 40% in the case of a coarse angular mesh. Only with the refinement of the angular grid satisfactory predictions can be obtained. This is verified by the results plotted in Figs. 5 and 6. Obviously, an improvement of

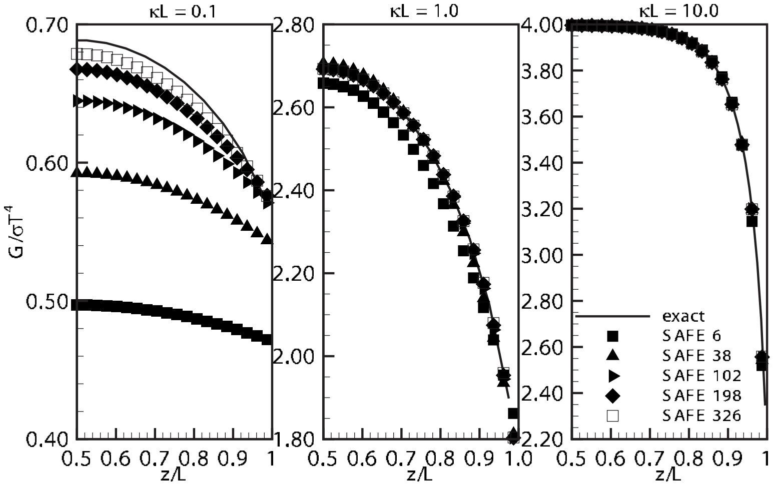

Fig. 4 Test case A: Incident radiation *G* in an emitting and absorbing parallel medium

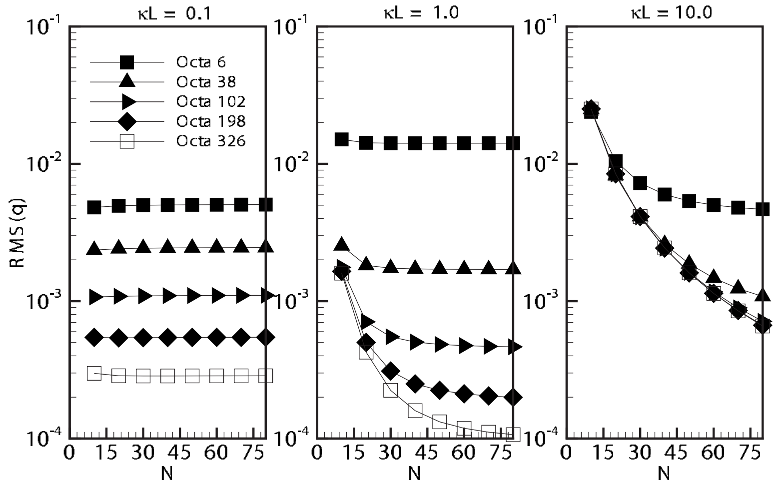

Fig. 5 Test case A: rms values of net heat flux predictions

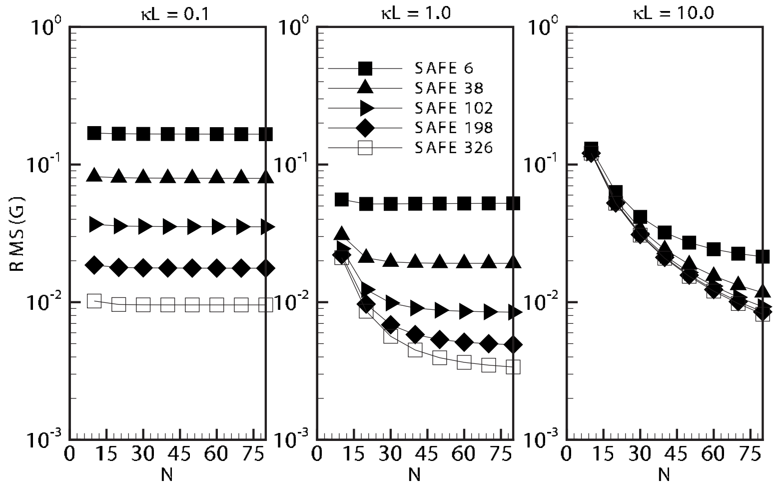

Fig. 6 Test case A: rms values of incident radiation predictions

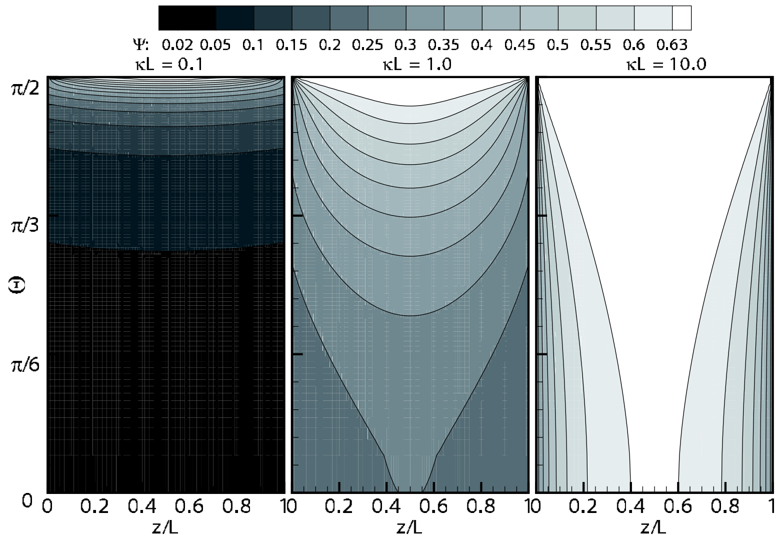

Fig. 7 Contour plots of the exact solution of the even-parity equation

Table 1 rms of the net heat flux and the incident radiation in case of the emitting-absorbing one-dimensional media. The CPU times for the solution of the linear systems is also given.

	κ	SAFE 6	SAFE 38	SAFE 102	SAFE 198	S_4	S_6	S_8	S_{10}	P_1
rms(q)	0.1	0.00502	0.00244	0.00110	0.00054	0.00538	0.00349	0.00280	0.00235	0.00838
	1.0	0.01412	0.00172	0.00050	0.00025	0.00468	0.00741	0.00577	0.00427	0.07325
	10.0	0.00598	0.00260	0.00243	0.00244	0.00724	0.00206	0.00173	0.00175	0.02532
rms(G)	0.1	0.16658	0.07959	0.03544	0.01772	0.17956	0.11548	0.09233	0.07746	0.28245
	1.0	0.05192	0.01929	0.00906	0.00581	0.04322	0.03972	0.03185	0.02544	0.23916
	10.0	0.03208	0.02420	0.02184	0.02115	0.03780	0.02808	0.02573	0.02451	0.05922
CPU time (s)	0.1	0.05300	0.53264	5.01022	5.88745	0.05244	0.08104	0.10606	0.13590	0.01463
	1.0	0.08041	0.34273	0.78240	1.73669	0.04869	0.08678	0.10012	0.16603	0.01506
	10.0	0.02777	0.06405	0.13680	0.24494	0.04613	0.06248	0.08591	0.11616	0.01794

the quality of the prediction is only possible with refinement of the angular mesh and an influence of the spatial grid size is not observed.

3.1.1 Comparison to the DOM and the P_1-Approximation. For comparison of the finite element method with the well-established DOM and P_1-approximation the same test case was calculated using these methods. The rms values obtained from these approximations are tabulated in Table 1, together with the results obtained from the SAFE method. Comparison of the rms reveals that the SAFE outperforms the DOM for all angular discretizations. In the optically thin case, $\kappa L=0.1$, and the optical intermediate case, $\kappa L=1.0$, the SAFE 38 with 38 angular nodes predicts the heat flux and the incident radiation with comparable accuracy to the DOM with the S_{10} quadrature (120 nodes). A very different behavior is found in the optically thick case. Here, the two coarsest angular grids predict the radiative heat flux with an accuracy comparable to the S_4 and S_6 DOM. If angular meshes with more nodes are used, the rms reaches a limiting value (see Fig. 5) and the results obtained with the DOM simulations are of higher quality than those calculated by the finite element method. The rms values of the incident radiation as calculated by the finite element method are always lower than the rms values calculated by the DOM.

The effect of the optical thickness on the accuracy of the SAFE, the DOM, and the P_1 was investigated from the calculations as presented in Fig. 8. In this figure the rms is plotted versus the optical thickness for two spatial discretizations. It can be seen that the SAFE ensures better results than the two other angular discretization methods provided the spatial grid is fine enough. If not, the prediction error increases linearly with increasing optical thickness. The same behavior is found for the DOM, but with the DOM the increase in the error starts at larger optical thicknesses as compared with the finite element method.

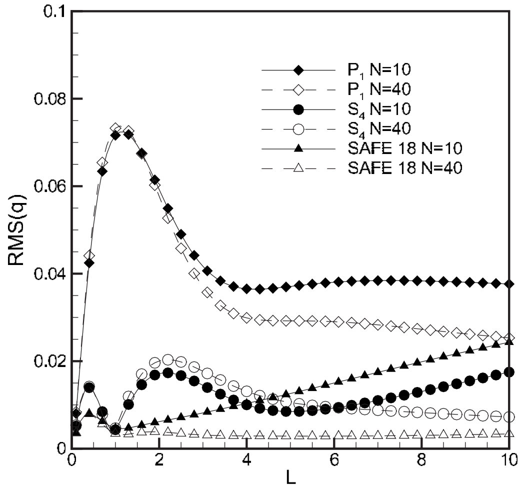

Fig. 8 Test case A: Comparison of the rms(q) calculated with the finite element method, the DOM, and the P_1-approximation

A second criterion besides accuracy is computational time needed by a solution method. Table 4 tabulates the CPU time required for the solution of the linear systems resulting from the DOM, the P_1, and the SAFE. For absorbing and emitting media the SAFE needs, in general, more CPU time in optically thin cases than in optically thick cases. This is not surprising since the FEM for parabolic second-order equations gives rise to coefficient matrices with a condition number inversely proportional to the square of the effective mesh width. Furthermore, the typical convergence rates of conjugate gradient methods are proportional to the root of the condition number [21]. Summarizing this, convergence rates directly proportional to the inverse of the optical thickness can be expected. Compared with the DOM, the SAFE method needs notably larger computational resources in the thinner media. Here the low convergence rate combined with the larger number of unknowns strongly increases runtime. In the optically thick case, the CPU times of the DOM and the SAFE are of comparable order. However, it should be remembered that in all cases the SAFE provides better accuracy than the DOM at a given number of angular nodes; hence, runtime increase may be less significant.

3.2 Test Case B: Isotropically Scattering, Nonabsorbing Plane-Parallel Medium.

In this test case the RHT in a nonabsorbing, isotropically scattering medium was considered. The wall at $z=0$ was held at a temperature equivalent to the blackbody intensity $I_b=1/\pi$ and the wall at $z=L$ was assumed black and cold. The test case was calculated for three optical thicknesses, $\sigma L=0.2$, 1.0, and 2.0. Since the medium is gray, this problem is physically equivalent to radiative equilibrium where the divergence of the radiative heat flux is zero. Highly accurate solutions for this test case are available from the studies of Heaslet and Warming [29,30].

Again, the test cases were calculated with multiple subdivisions of the octahedron. The predicted net heat fluxes and incident radiation are tabulated in Table 2 and depicted in Fig. 9, respectively. Because of the symmetry of the problem, Fig. 9 shows only 1/2 of the domain. As in the absorbing and emitting case, the usage of coarser angular grids results in a large error for the optically thin case. In all other cases the predictions of the incident radiation are good. The results in Table 2 indicate that even the angular approximation SAFE 6 with six angular nodes predicts the net heat flux within a deviation of 0.9–0.4% from the expected values depending on the optical thickness. The results of all other angular discretizations are much closer to the analytical results. Again, the rms of the net heat flux and incident radiation were calculated for the predictions obtained from different angular discretizations and for different refinements of the spatial grid. These rms values are plotted in Fig. 10 for the net heat flux and in Fig. 11 for the incident radiation. Similar to the absorbing-emitting,

Table 2 Predictions for the heat flux from the finite element method, the DOM, and the P_1-approximation

σ	Exact	SAFE 6	SAFE 38	SAFE 102	SAFE 198	S_4	S_6	S_8	S_{10}	P_1
0.2	0.8491	0.8567	0.8502	0.8494	0.8493	0.8406	0.8446	0.8459	0.8467	0.8696
1.0	0.5532	0.5567	0.5540	0.5536	0.5534	0.5416	0.5513	0.5526	0.5529	0.5714
2.0	0.3900	0.3917	0.3904	0.3901	0.3901	0.3836	0.3893	0.3897	0.3898	0.4000

optically thin medium, the error in the case of $\sigma=0.2$ is only a function of the angular mesh size and not of the spatial mesh. A different result is obtained in the optically intermediate and thick cases. Comparing Figs. 10 and 11 it is obvious that the error in the prediction of the incident radiation is more dependent on the spatial mesh than in the prediction of the net heat flux. Starting out from a coarse angular and a coarse spatial mesh, only the refinement of both, the spatial and the angular, grids together improves the accuracy of the calculation of G. However, for all angular discretizations the rms rapidly approaches a limiting value, and further spatial refinement does not enhance the solution quality; though, an anomaly arises for the finest angular grid. First, the refinement of the spatial grid decreases the rms, then a minimum value of the rms is reached and with further refinement, the error increases slightly above the rms values of the next coarser angular grid. The reason for this behavior may be found in the interaction of the errors caused by the spatial and the angular discretizations. The two sources of error seem to balance each other for coarse grids, but with the refinement of the angular and spatial discretizations the compensation effect is reduced.

For comparison of the finite element method with the DOM and the P_1-approximation the heat fluxes computed with these methods are also listed in Table 2. Additionally, the rms values for the predictions obtained by the DOM and the P_1 are tabulated in Table 3. Again, the SAFE method guarantees superior accuracy compared with both other methods. In the optically thin case, the octahedral mesh with 38 angular nodes is capable to achieve better accuracy than the DOM S_{10} with 120 directions. For $\sigma=1.0$ and $\sigma=2.0$ the gap between the methods is smaller, but usage of the SAFE method still ensures a lower rms.

The CPU times needed in this test case are tabulated in Table 4. As observed in the emitting and absorbing medium, the computational time needed by the SAFE decreases with increasing optical

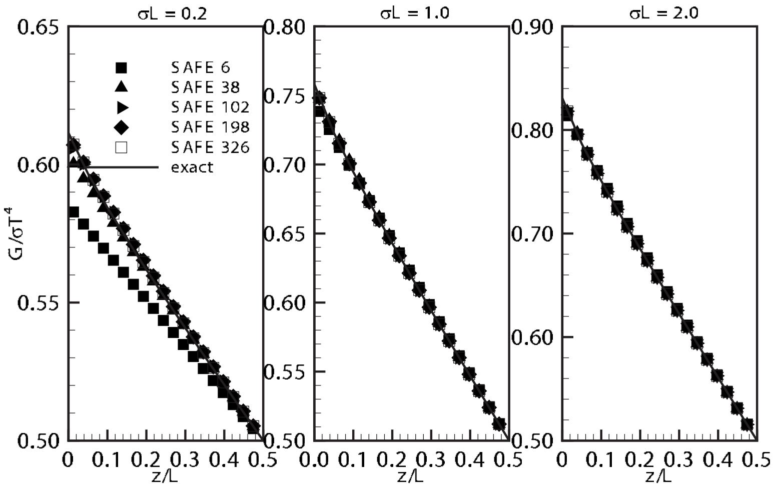

Fig. 9 Test case B: Incident radiation *G*

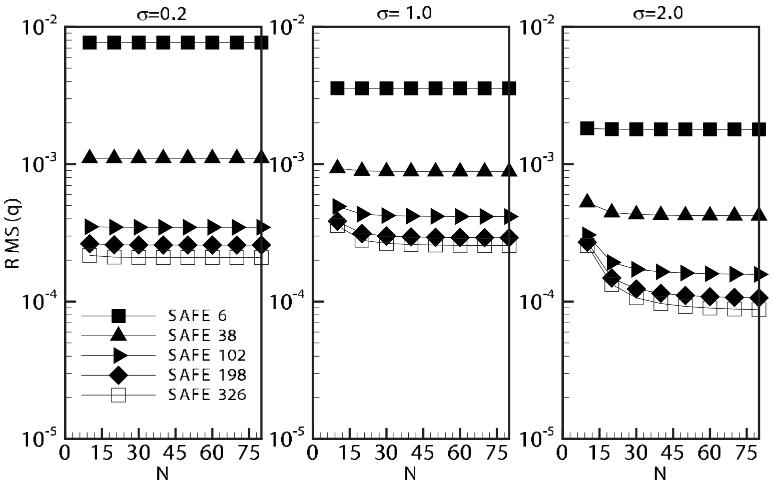

Fig. 10 Test case B: rms values of the net heat flux

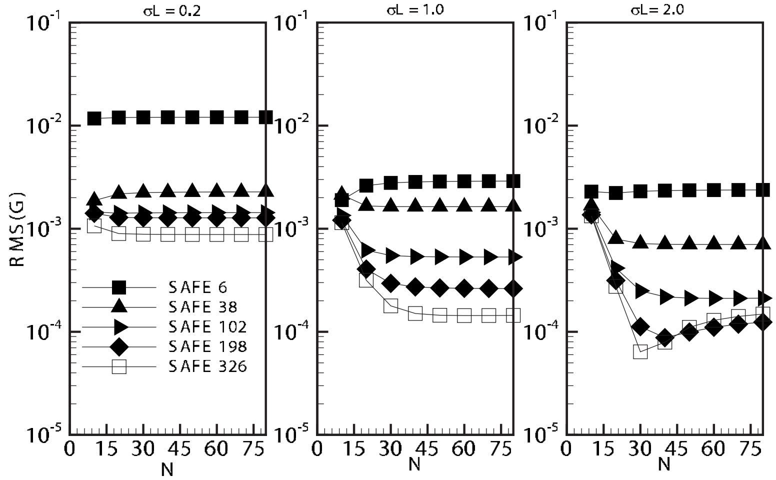

Fig. 11 Test case B: rms values of the incident radiation

thickness. However, compared with the absorbing and emitting media the runtime is increased for angular meshes with a large number of nodes, which is a consequence of the increased number of floating point operations per solver iteration due to the fully occupied angular system in the presence of scattering. In contrast, the runtime of the DOM increases with increasing optical thickness, which is a well-known effect of the outer iteration used in the DOM implementation to update the radiative source term in the RTE [22]. This results in a substantially larger computational effort in the optically intermediate and thick cases compared with the SAFE method.

3.3 Test Case C: Emitting and Absorbing Two-Dimensional Medium. In this section the SAFE method, the EP-DOM, and the P_1-approximation were applied to a two-dimensional, rectangular enclosure with cold, black walls and filled with an absorbing and emitting medium. The medium was maintained at an emissive power of unity everywhere, i.e., the medium is isothermal. The “exact” solution was calculated by a modified exchange factor method. For the approximate methods, the enclosure was discretized with a grid of 20×20 bilinear elements. Calculations were performed for optical thicknesses κL

Table 3 rms of the net heat flux and the incident radiation in case of the isotropically scattering one-dimensional media. The CPU times for the solution of the linear systems are also given.

	σ	SAFE 6	SAFE 38	SAFE 102	SAFE 198	S_4	S_6	S_8	S_{10}	P_1
rms(q)	0.2	0.00768	0.00110	0.00035	0.00026	0.00847	0.00445	0.00318	0.00244	0.02047
	1.0	0.00357	0.00089	0.00042	0.00030	0.01160	0.00192	0.00065	0.00034	0.01823
	2.0	0.00179	0.00043	0.00016	0.00011	0.00646	0.00070	0.00029	0.00024	0.01000
rms(G)	0.2	0.01205	0.00226	0.00143	0.00128	0.00348	0.00185	0.00258	0.00290	0.02338
	1.0	0.00284	0.00164	0.00054	0.00027	0.00814	0.00387	0.00233	0.00161	0.01742
	2.0	0.00234	0.00071	0.00022	0.00009	0.00532	0.00139	0.00104	0.00081	0.00924
CPU time (s)	0.2	0.07417	0.40852	1.61102	5.41748	0.48638	0.79392	1.06637	1.32141	0.02629
	1.0	0.07076	0.23242	0.70655	1.89832	1.34552	1.99621	2.64747	3.33634	0.02545
	2.0	0.06998	0.17427	0.49531	1.26530	2.47727	3.48432	4.73401	5.79145	0.02327

Table 4 rms of the net heat flux and the incident radiation in case of an emitting-absorbing and an isotropically scattering two-dimensional medium. The CPU times for the solution of the linear systems are also given.

Test case C	βL	SAFE 18	SAFE 38	SAFE 66	SAFE 102	S_4	S_6	S_8	P_1
rms(q)	0.1	0.00963	0.00499	0.00664	0.00686	0.01088	0.00965	0.00805	0.02158
	1.0	0.03819	0.01858	0.01922	0.02433	0.05286	0.02238	0.02756	0.12401
	10.0	0.09804	0.11488	0.12252	0.12594	0.10186	0.10607	0.10899	0.08331
rms(G)	0.1	0.08116	0.03071	0.02834	0.04319	0.01644	0.02457	0.03724	0.26145
	1.0	0.17569	0.06889	0.02429	0.02030	0.13579	0.03982	0.09387	0.67349
	10.0	0.03412	0.02728	0.02453	0.02449	0.06440	0.03444	0.02012	0.12955
CPU times (s)	0.1	2.297	5.713	11.280	17.136	1.150	2.457	4.500	0.041
	1.0	0.740	1.939	3.533	5.704	0.885	1.751	3.025	0.038
	10.0	0.523	1.017	2.439	3.709	0.619	1.289	2.145	0.037
Test case D									
rms(q)	1.0	0.07181	0.03732	0.02665	0.02234	0.14479	0.06472	0.04343	0.01377
rms(G)	1.0	0.18534	0.12030	0.11223	0.10978	0.25752	0.09945	0.11552	0.28216
CPU times (s)	1.0	0.593	2.476	7.115	18.264	4.874	9.091	17.073	0.041

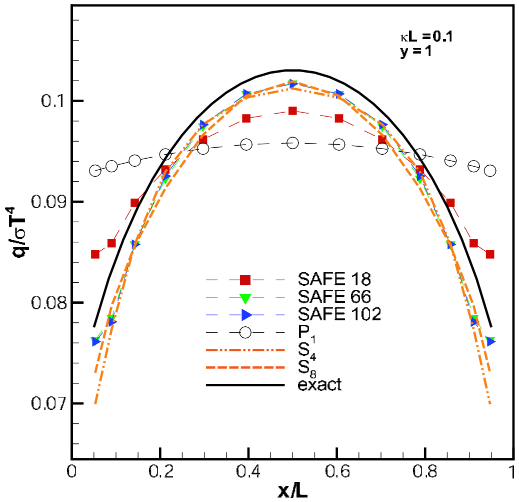

Fig. 12 Test case C: Radiative heat flux profiles at the walls of an emitting and absorbing two-dimensional medium

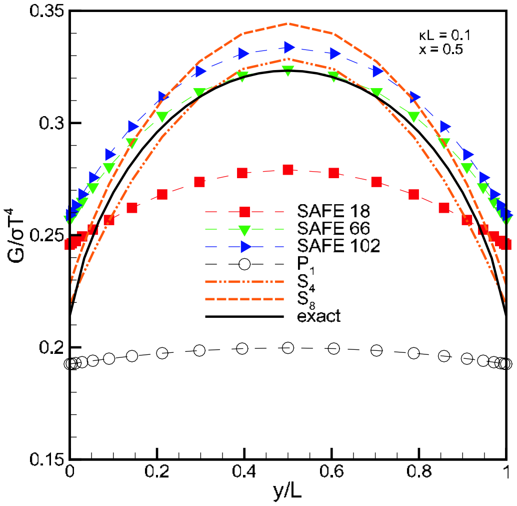

Fig. 14 Test case C: Incident radiative intensity in the centerline of an emitting and absorbing two-dimensional medium

$=0.1$, $\kappa L=1.0$, and $\kappa L=10.0$.

Figures 12 and 13 show the radiative heat fluxes at the top of the two-dimensional enclosure for an optical thickness $\kappa L=0.1$ and $\kappa L=1.0$, respectively. The incident radiation at the centerline $y=0.5$ is presented in Figs. 14 and 15. In both cases the finite element solutions are able to predict the expected heat flux q and incident radiation G with satisfactory accuracy. As in the one-dimensional case the incident radiation calculated from SAFE with coarse angular grids differs considerably from the exact values in the optically thin medium. The reason for this deviation may be directly understood from the discussion for the one-dimensional case. As pointed out there, the intensity in optically thin media is strongly dependent on direction. Hence, increased coupling between different directions in a low-order approximation has a negative influence on the accuracy. This fact is clearly confirmed by comparison of the results of the SAFE with the results obtained from the P_1-approximation and the DOM, as depicted in Fig. 14. While the SAFE 18 and the P_1 cannot reproduce the profile of the incident radiation, the S_4 DOM represents the expected distribution fairly well. Furthermore, the gradient of the incident radiation nearby the walls is greatly underpredicted by the SAFE and the P_1. This could be due to the Marshak boundary conditions used by both of these methods. In contrast, the DOM, which uses Marshak-like boundary conditions, calculates the incident radiation in the vicinity of the walls much better. Consequently, a comparative study of the boundary conditions applied to the angular finite element method is desired for the future.

The rms values calculated according to Eq. (43) are tabulated in Table 4. Again, the SAFE predicts the heat flux with better accuracy as compared with the two other angular approximation methods considered here. In the case of incident radiation the approximations obtained from the DOM are less error-prone than the results from the angular FEM for optically thin media, as can be expected from the discussion above. In the optically intermediate case, e.g., $\kappa L=1.0$, the coarser angular meshes SAFE 18 and SAFE 38 perform less well than the S_4 and the S_6 approximations with comparable numbers of angular directions. Nearly always the much simpler P_1-approximation is outperformed by the two other angular approximation methods.

Table 4 lists the CPU times needed for the calculations by the FEM, the DOM, and the P_1. Just as observed for the one-dimensional test cases, the runtime decreases with increasing optical thickness for all methods. Particularly in the optically thin case the CPU usage of the SAFE rises rapidly with the increasing

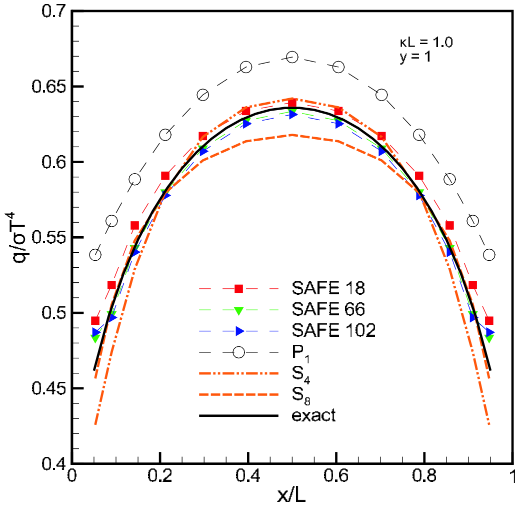

Fig. 13 Test case C: Radiative heat flux profiles at the walls of an emitting and absorbing two-dimensional medium

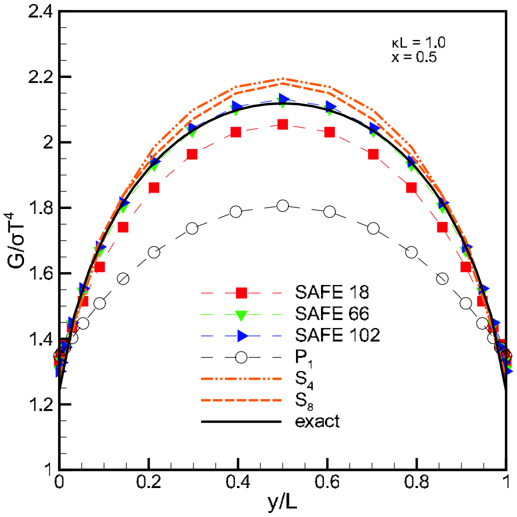

Fig. 15 Test case C: Incident radiative intensity in the centerline of an emitting and absorbing two-dimensional medium

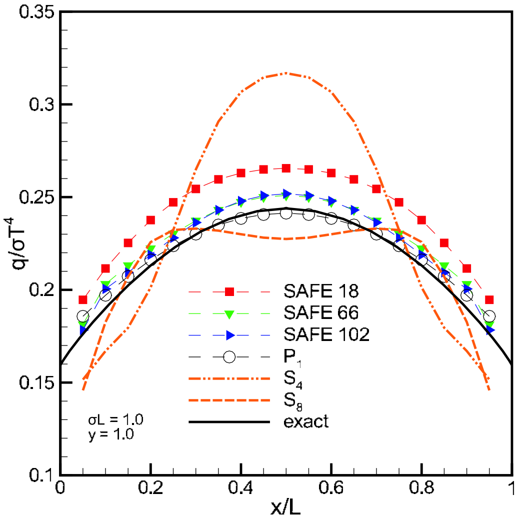

Fig. 16 Test case D: Radiative heat flux at the top of a purely isotropically scattering two-dimensional medium

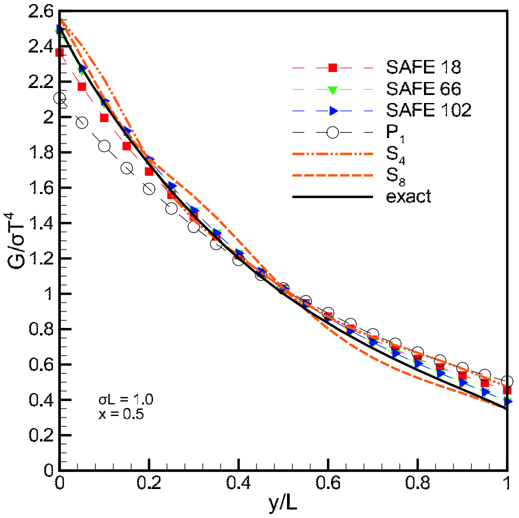

Fig. 17 Test case D: Incident radiative intensity in the center of a purely isotropically scattering two-dimensional medium

number of angular nodes and exceeds the runtime of the DOM. In thicker media the runtime of the SAFE is of the same order as compared with the DOM.

3.4 Test Case D: Purely Isotropically Scattering Two-Dimensional Medium. In this test case the radiative transfer in an isotropically scattering, nonabsorbing two-dimensional medium was considered. The medium was exposed to diffuse irradiation $I=\sigma T^4/\pi$ incident at $y=0$. Since this problem is known to emphasize ray effects [9], it is routinely studied as a benchmark for the DOM. Highly accurate approximations of the radiative heat flux and the source terms for this test case were tabulated by Crosbie and Schenker [31].

Figure 16 shows the net heat flux at the top wall for several SAFE solutions together with the DOM approximations, the P_1, and the results from Crosbie and Schenker [31]. It is clearly visible that the DOM is prone to ray effects in this setup. Hence, the S_4 DOM solution deviates up to 30% from expected values and cannot capture the expected heat flux profile. Using an S_8 quadrature with 80 directions minimizes the ray effect, but does not eliminate it. In contrast, both methods using continuous functions for the approximation of the angular dependence, SAFE and P_1, do not suffer from ray effects. Even the lowest-order SAFE, the SAFE 18 with 18 directions, is capable of predicting the heat flux without any ray effect within a deviation of 7%. By increasing the number of angular nodes the predictions obtained from the finite element approximation approach the exact values. However, the SAFE 102 method does not predict the heat flux closer to the exact values than the SAFE 66 approximation, an effect that has been observed in the one-dimensional case as well. From the results obtained there, it can be concluded that further improvement of the prediction is only available from the refinement of the angular and the spatial grids together.

The incident radiation G on the centerline of the enclosure is depicted in Fig. 17. Again, the DOM is affected by the ray effect, independent of the angular quadrature used. As observed in the predictions of the radiative heat flux no ray effect occurs in the angular finite element method and the P_1-approximation. However, the finite element method calculates the incident radiation with a smaller error nearby the walls than the P_1.

4 Conclusion

In the present paper a new and promising solution technique is presented for the radiative heat transfer equation. Starting out from the even-parity formulation, a finite element discretization is applied to the angular and the spatial domains. The mathematical formulation of the angular discretization is general in the sense that nearly arbitrary angular basis functions may be used. In the present work, the angular dependence was treated by a series expansion of piecewise linear basis functions defined on subdivisions of an octahedron. This approach enables a sound derivation of angular approximations with high order. For the assessment of the solution capabilities the convergence characteristics of the spatial and the angular refinement were inspected in one-dimensional test cases. These tests revealed the high accuracy of the present method compared with the commonly used discrete ordinate method and the P_1-approximation. The application of the proposed method to two-dimensional test cases demonstrated the advantageous attributes in higher dimensional calculations as well. Unfavorable may be the somewhat larger runtime of the new method, particularly in optically thin media. Most notably is the ability of the new method to avoid ray effects efficiently, as was demonstrated in a two-dimensional medium exposed to diffuse radiation.

Even though the method was presented and formulated here only for gray media, the incorporation of typical spectral models is straightforward.

Acknowledgment

Thanks are due to Prof. Sigmar Wittig, who initiated the research on radiative transfer in the institute and to the state of Baden-Württemberg, which supported the research through the TECFLAM cooperation. During his research visit at the Universität Karlsruhe, M.F.M. was financially supported by the research award of the Alexander von Humboldt Stiftung, Germany.

Nomenclature

A_{nmpq} = matrix element of a linear system
b_{np} = element of a source vector
E_b = blackbody emissive power (W m^{-2})
E_n = exponential integral of order n
f = arbitrary function
G = incident radiation (W m^{-2})
I = radiative intensity (W m^{-2} sr^{-1})
I_b = blackbody radiative intensity (W m^{-2} sr^{-1})
L = length (m)
m = index
M_Ω = number of angular basis functions
M_r = number of spatial basis functions

n = index
N = number of samples
$\mathbf{n}$ = unit surface normal
p = index
q = index
$\mathbf{q}, q$ = radiative heat flux (W m^{-2})
$\mathbf{r}$ = position vector (m)
$\mathbf{r}_i$ = position vector of node i (m)
$\mathbf{s}$ = unit vector into a direction
T = temperature (K)
V = volume (m^3)
W = weight function
z = Cartesian coordinate (m)

Greek

β = extinction coefficient (m^{-1})
γ_i = barycentric coordinate
κ = absorption coefficient (m^{-1})
η = direction cosine
Ψ = even-order intensity (W m^{-2} sr^{-1})
μ = direction cosine
ξ = direction cosine
σ = scattering coefficient (m^{-1})
σ = Stefan–Boltzmann constant 5.670×10^{-8} W m^{-2} K^{-4}
Φ_n = nth angular basis function
$\hat{\Phi}_n$ = nth spatial basis function
Λ = odd-order intensity (W m^{-2} sr^{-1})
$\underline{\omega_n^{ij}}$ = coefficient (angular linear system) (sr)
ω_n = coefficient (angular linear system) (sr)
Ω = solid angle (sr)
$\underline{\Omega}_{nm}^{ij}$ = coefficient (angular linear system) (sr)
Ω_{nm} = coefficient (angular linear system) (sr)

References

[1] Viskanta, R., and Mengüç, M. P., 1987, “Radiation Heat Transfer in Combustion Systems,” Prog. Energy Combust. Sci., **13**(2), pp. 97–160.
[2] Mishra, S. C., and Prasad, M., 1998, “Radiative Heat Transfer in Participating Media—A Review,” Sadhana: Proc., Indian Acad. Sci., **23**(2), pp. 213–232.
[3] Viskanta, R., 2008, “Computation of Radiative Transfer in Combustion Systems,” Int. J. Numer. Methods Heat Fluid Flow, **18**(3/4), pp. 415–442.
[4] Chandrasekhar, S., 1960, *Radiative Transfer*, Dover, New York.
[5] Davison, B., 1958, *Neutron Transport Theory*, Clarendon, Oxford.
[6] Lathrop, K. D., 1968, “Ray Effects in Discrete Ordinates Equations,” Nucl. Sci. Eng., **32**, pp. 357–369.
[7] Raithby, G. D., and Chui, E. H., 1990, “A Finite-Volume Method for Predicting a Radiant Heat Transfer in Enclosures With Participating Media,” ASME J. Heat Transfer, **112**, pp. 415–423.
[8] Chai, J. C., Lee, H. S., and Patankar, S. V., 1994, “Finite Volume Method for Radiation Heat Transfer,” J. Thermophys. Heat Transfer, **8**(3), pp. 419–425.
[9] Ramankutty, M. A., and Crosbie, A. L., 1997, “Modified Discrete Ordinates Solution of Radiative Transfer in Two-Dimensional Rectangular Enclosures,” J. Quant. Spectrosc. Radiat. Transf., **57**(1), pp. 107–140.
[10] Gradstejn, I. S., and Ryzik, I. M., 2007, *Table of Integrals, Series, and Products*, 7th ed., Academic, New York.
[11] Modest, M., and Yang, J., 2008, “Elliptic PDE Formulation and Boundary Conditions of the Spherical Harmonics Method of Arbitrary Order for General Three-Dimensional Geometries,” J. Quant. Spectrosc. Radiat. Transf., **109**(9), pp. 1641–1666.
[12] Song, T.-H., and Park, C. W., 1992, “Formulation and Application of the Second-Order Discrete Ordinate Method,” *Transport Phenomena and Science*, B.-X. Wang, ed., Higher Education, Beijing, pp. 833–841.
[13] Ohnishi, T., 1972, “Finite-Element Solution Techniques for Neutron-Transport Equations,” *Proceedings of the Conference on Numerical Reactor Calculations*, Int. Atomic Energy Agency, pp. 629–638.
[14] Briggs, L. L., Miller, W. F., and Lewis, E. E., 1975, “Ray-Effect Mitigation in Discrete Ordinate-Like Angular Finite Element Approximations in Neutron-Transport,” Nucl. Sci. Eng., **57**, pp. 205–217.
[15] Becker, R., Koch, R., and Bauer, H.-J., 2007, “Solution of the Radiative Transfer Equation by a Finite Element Discretization of the Solid Angle,” *Proceedings of the Fifth International Symposium on Radiative Transfer*, ICHMT.
[16] Coelho, P., 2005, “Fundamentals of a New Method for the Solution of the Radiative Transfer Equation,” Int. J. Therm. Sci., **44**, pp. 809–821.
[17] Pontaza, J., and Reddy, J., 2005, “Least-Squares Finite Element Formulations for One-Dimensional Radiative Transfer,” J. Quant. Spectrosc. Radiat. Transf., **95**, pp. 387–406.
[18] Cui, X., and Li, B. Q., 2005, “A Mixed-Mesh and New Angular Space Discretization Scheme of Discontinuous Finite Element Method for Three-Dimensional Radiative Transfer in Participating Media,” ASME J. Heat Transfer, **127**, pp. 1236–1244.
[19] Widmer, G., and Hiptmair, R., 2007, “Sparse Finite Elements for Non-Scattering Radiative Transfer in Diffuse Regimes,” *Proceedings of the Fifth International Symposium on Radiative Transfer*, ICHMT.
[20] Lewis, E. E., and Miller, W. F., 1984, *Computational Methods of Neutron Transport*, Wiley Interscience, New York.
[21] Eriksson, K., Estep, D., Hansho, P., and Johnson, C., 1996, *Computational Differential Equations*, Cambridge University Press, Cambridge, England.
[22] Fiveland, W. A., and Jessee, J. P., 1994, “Finite-Element Formulation of the Discrete-Ordinate Method for Multidimensional Geometries,” J. Thermophys. Heat Transfer, **8**(3), pp. 426–433.
[23] Koch, R., and Becker, R., 2004, “Evaluation of Quadrature Schemes for the Discrete Ordinate Method,” J. Quant. Spectrosc. Radiat. Transf., **84**(4), pp. 423–435.
[24] MathWorks Inc., 2006, “MATLAB—The Language of Technical Computing.”
[25] van der Vorst, H. A., 1992, “Bi-CGSTAB: A Fast and Smoothly Converging Variant of Bi-CG for the Solution of Nonsymmetric Linear Systems,” SIAM (Soc. Ind. Appl. Math.) J. Sci. Stat. Comput., **13**, pp. 631–644.
[26] Koch, R., Krebs, W., Wittig, S., and Viskanta, R., 1995, “A Parabolic Formulation of the Discrete Ordinates Method for the Treatment Of Complex Geometries,” *Proceedings of the First International Symposium on Radiative Transfer*, M. P. Mengüç, ed., ICHMT, Begell House, Redding, CT, pp. 43–61.
[27] Fiveland, W. A., 1991, “The Selection of Discrete Ordinate Quadrature Sets for Anisotropic Scattering,” *Fundamentals of Radiation Heat Transfer*, W. A. Fiveland, A. L. Crosbie, A. M. Smith, and T. F. Smith, eds., ASME, New York, **HTD-160**, pp. 89–96.
[28] Modest, M. F., 2003, *Radiative Heat Transfer*, 2nd ed., Academic, New York.
[29] Heaslet, M. A., and Warming, R. F., 1965, “Radiative Transport and Wall Temperature Slip in an Absorbing Planar Medium,” Int. J. Heat Mass Transfer, **8**, pp. 979–994.
[30] Heaslet, M. A., and Warming, R. F., 1967, “Radiative Transfer in an Absorbing Planar Medium II—Predictions of Radiative Source Functions,” Int. J. Heat Mass Transfer, **10**, pp. 1413–1427.
[31] Crosbie, A. L., and Schenker, R. G., 1984, “Radiative Transfer in a Two-Dimensional Rectangular Medium Exposed to Diffuse Radiation,” J. Quant. Spectrosc. Radiat. Transf., **31**(4), pp. 339–372.

Radiative Transfer in Dispersed Media: Comparison Between Homogeneous Phase and Multiphase Approaches

Jaona Randrianalisoa
e-mail: jaona.randrianalisoa@insa-lyon.fr

Dominique Baillis

CETHIL UMR5008,
CNRS, INSA-Lyon,
Université Lyon 1,
F-69621 Villeurbanne, France

The radiative transfer in dispersed media in the geometric optic regime is investigated through two continuum-based approaches. The first one is the traditional treatment of dispersed media as continuous and homogeneous systems, referred here as the homogeneous phase approach (HPA). The second approach is based on a separate treatment of the radiative transfer in the continuous and dispersed phases, referred here as the multiphase approach (MPA). The effective radiative properties involved in the framework of the HPA are determined using the recent ray-tracing (RT) method, enabled to overcome the modeling difficulties such as the dependent scattering effects and the misunderstanding of the effective absorption coefficient. The two modeling approaches are compared with the direct Monte Carlo simulation. It is shown that (i) the HPA combined with effective radiative properties, such as those from the RT method, is satisfactory in analyzing the radiative transfer in dispersed media constituting of transparent, semitransparent, or opaque particles. Therefore, the use of more complex continuum models such as the dependence included discrete ordinate method (Singh, B. P., and Kaviany, M., 1992, "Modelling Radiative Heat Transfer in Packed Beds," Int. J. Heat Mass Transfer, ***35****, pp. 1397–1405) is not imperative anymore. (ii) The MPA, though a possible candidate to handle nonequilibrium problems, is suitable if the particle (geometric) backscattering is weak or absent. It is the case, for example, for dispersed media constituted of opaque particles or air bubbles. However, caution should be taken with the MPA when dealing with the radiative transfer in dispersed media constituted of nonopaque particles having refractive indexes greater than that of the continuous host medium.*

[DOI: 10.1115/1.4000237]

Keywords: radiative transfer, dispersed media, opaque particles, semitransparent particles, ray-tracing, Monte Carlo, transmittances, reflectances

1 Introduction

The radiative transfer plays a crucial role in many engineering applications involving continuous solid or fluid media embedding dispersed particles, usually referred to as "dispersed media." Examples of these applications are the solar-thermochemical energy conversion, material processing, microstructure diagnostic via light scattering, fire suppression by water sprays, thermal insulations, thermal barrier coating, etc. [1–6].

The exact solution of the radiation propagation in dispersed media should be determined from first principles that consists of solving the Maxwell equations for the electromagnetic field. However, such approach is only suitable for a small number of scatterers, because of the limits imposed by modern computers. The alternative approach frequently used consists to consider the dispersed system as a continuous one and to treat the radiative problem in the framework of the radiative transfer theory consisting to solve the radiative transfer equation (RTE). The RTE has been derived from the equations of multiple scattering of waves [7–12], although it was originally established from the energy balance of corpuscles in an elementary volume [13–17]. The RTE has, as main parameters, propagation constants called "radiative properties." The applicability conditions of the RTE are now defined as we can find in the series of papers and textbook by Mischenko et al. [12] One of these criteria is the far-field approximation (FFA), which imposes that (i) the scatterers must be located far from each other; and (ii) the distance between the scatterers and the observation point must be much greater than the radiation wavelength [18]. For random dispersed media having low concentration (or volume fraction) of scatterers, the FFA is generally fulfilled and the RTE is suitable. Moreover, the interferences between scattered waves occur in a random way, and the radiation interaction with particles can be viewed as point scattering. Therefore, the exact solution of the radiative transfer problem is expected because the radiative properties can be also determined, for example, from the interaction of a plane electromagnetic wave with an isolated particle known as "independent scattering theory." [19–21] For dispersed media having significant scatterer concentration leading to closely spaced particles, the radiative transfer problem becomes more complex. Generally speaking, the RTE cannot be used due particularly to the failure of the FFA. Other approaches such as the full wave Monte Carlo [22] and the T-matrix [23] or different techniques based on the multiple scattering of waves (such as Foldy's [7], Twersky's [24], and quasicrystalline approximations [25]) can be adopted. These methods have been shown to be straightforward for scatterers with size smaller than or comparable to the radiation wavelength. However, they are not convenient when the particles are very large compared to the wavelength due to excessive computation time and memory consumption.

Since exact solution of the radiative transfer problem in such systems cannot be obtained, at least in the near future, coarse approximations are necessary. (i) The most common assumption

---

Contributed by the Heat Transfer Division of ASME for publication in the JOURNAL OF HEAT TRANSFER. Manuscript received December 3, 2008; final manuscript received June 15, 2009; published online December 9, 2009. Assoc. Editor: Yogesh Jaluria.

consists of treating the dispersed medium as continuous and homogeneous, and using the standard RTE with "effective radiative properties" [26–33], which differs from the radiative properties of dilute media [19–21]. This approximate method is referred to in this study as "homogeneous phase approach" (HPA). In thermal engineering problems, the thermal equilibrium between the continuous and dispersed phases is often assumed through the HPA. To deal with multitemperature phases, additional terms should be introduced in the RTE [34,35]. (ii) Other less-frequented technique is called "multiphase approach" (MPA) consists of assigning to both continuous and dispersed phases their own transport equation (but coupled to each other) and their own effective radiative properties [36]. Thus, through the MPA, each phase can have its own temperature field. To our knowledge, the capability of the MPA to model the radiative transfer in dispersed materials is not sufficiently studied yet.

This study deals with the radiative transfer in dispersed media constituted of closely spaced large particles. For practical reasons, we adopted the approximate HPA and MPA. Therefore, the knowledge of effective radiative properties is crucial. In contrast to dispersed media constituted of very spaced particles where the radiative properties can be correctly obtained, the effective radiative properties of densely packed scatterers are quite complex due to two phenomena. The first one is known as "dependent scattering," which includes the "interference effects" (i.e., the radiation incoming on each particle undergoes an interference with the radiation scattered by neighboring particles) and the "multiple scattering effects" (i.e., the radiation scattered by a particle is incident on another particle to be scattered again) [31]. The second phenomenon, known as the "nonpoint scattering" is purely geometric effects due especially to the proximity of particles compared to their size [33]. To overcome such theoretical difficulties, the most straightforward models of effective radiative properties, in the large particle limit, are based on the geometric optic approximations (GOAs) by neglecting the interference of waves and the diffraction patterns as detailed later [37,38]. The radiation is then treated as a "*straight-ray*." In this framework, most prediction models of effective radiative properties are focused only on densely packed particles embedded in transparent media [30–33]. For closely spaced particles in semitransparent host media, few prediction models exist. One can note that based on the ray-tracing technique recently developed by the current authors [39].

The main objective of this study is to identify what approach better models the radiative transfer in densely packed large particles in semitransparent media. In this aim, the HPA and the MPA are analyzed and compared. Due to the lack of experimental data, these two approaches are compared with the direct Monte Carlo (MC) simulation usually considered as a method of reference. At first, the general hypothesis, common to both approaches, are discussed. Then, the homogeneous phase approach is recapitulated. In particular, the prediction of effective radiative properties is discussed. The multiphase approach is presented. Its physical basis and the different effective radiative properties are briefly described. Finally, the radiative transfer in dispersed media is investigated in term of transmittances and reflectances through one-dimensional (1D) samples exposed to a collimated radiation.

2 General Hypothesis

Let us denote λ as the radiation wavelength, d as the particle size, c as the interparticle (particle surface-to-surface) distance, and n_1 and n_0 as the refractive indexes of the dispersed phase (particles in this study) and the continuous phase (the medium surrounding the particles). The current approaches use the GOA of electromagnetic waves; thus, it neglects the wave effects such as interferences and diffraction. Therefore, the radiation is treated as a superposition of pencils of rays propagating according to a straight line. In order for this assumption to be valid, we only focused our attention to the following cases:

- The size of particles d is much greater than the wavelength (known as the limit of large particles). The practical criterion is $x=\pi d/\lambda \gg 1$, where x is the size parameter. The phase change of the radiation passing through the particle along the diameter is large (known as the limit of hard particles), i.e., $x|n_1/n_0-1| \gg 1$. Therefore, the propagation of the radiation within the particle can be modeled using the geometric optic laws of reflection and refraction.
- The interparticle distance c is much greater than the wavelength, i.e. $c \gg \lambda$, and the particles are randomly dispersed in space, therefore there are not any interference effects. Such criterion is fulfilled when dealing with media of dispersed large particles encountered in engineering problems.
- Only the half of the total scattering, i.e., that due to reflection and refraction, is considered. The other half, i.e., the scattering due to diffraction, is neglected. In fact, the diffraction by large scatterers is expected to be close to the direction of incidence. Thus, the diffraction can be treated as unscattered radiation.

In addition to the above assumptions, we also considered that

- The thermal conductivity of particles is not too high so that the radiation absorbed at one face of a particle does not emit from the other face.
- The effective radiative properties are independent of the azimuth angle. Thus, the radiative transfer in presence of azimuthal symmetry is assumed.

3 Homogeneous Phase Approach (HPA)

Let us consider a 1D problem in the steady-state regime. By omitting the term from emission, the conventional RTE in the presence of the azimuthal symmetry can be written as follows [40]:

$$\mu \frac{\partial I(z,\mu)}{\partial z} = -(\alpha_e+\sigma_e)I(z,\mu) + \frac{\sigma_e}{2}\int_{-1}^{1} I(z,\mu')\Phi_e(\Theta)d\mu' \qquad (1)$$

where I is the radiation intensity at the abscise z in the direction of cosine μ, with respect to the z axis. The effective radiative properties are the absorption coefficient α_e, the scattering coefficient σ_e, and the phase function Φ_e. Θ refers to the angle between the direction of the intensity $I(z,\mu')$ and the direction of the intensity $I(z,\mu)$. Note that the intensities and the propagation constants that appeared in Eq. (1) are wavelength-dependent, but this dependence is not shown for convenience.

Let us consider spherical and monodispersed particles of radius denoted by a, randomly positioned in a semitransparent matrix. According to the independent scattering based model, the effective absorption coefficient is given by [41–45]:

$$\alpha_e = \alpha_0 + 0.75 f_v \frac{Q_a}{a} \qquad (2)$$

where $\alpha_0=4\pi\kappa_0/\lambda$ is the absorption coefficient of the continuous phase (in which κ_0 is its absorption index) and the last term in the right hand side of Eq. (2) is the absorption coefficient of particles. f_v refers to the particle volume fraction.

The effective scattering coefficients σ_e and effective phase function Φ_e are given by the famous independent scattering theory [19–21]:

$$\sigma_e = 0.75 f_v \frac{Q_s}{a} \qquad (3)$$

$$\Phi_e(\Theta) = \phi(\Theta) \qquad (4)$$

ϕ, Q_a, and Q_s are, respectively, the famous single phase function, absorption, and scattering efficiency factors of a particle of radius a and complex refraction index "n_1-$j\kappa_1$" placed in a medium of complex refraction index "n_0-$j\kappa_0$" [2,41,43]. Note that the sign of the absorption efficiency factor Q_a depends on the relative complex refractive index of the particle substance, i.e., $(n_1\text{-}j\kappa_1)/(n_0\text{-}j\kappa_0)$.

The model based on Eqs. (2)–(4) is useful but questionable when the volume fractions of the dispersed and the continuous phases are comparable. Firstly, the limits of applicability of the effective absorption coefficient (Eq. (2)) are not well known. Secondly, this model does not take into account the dependent scattering effects when particles are closely spaced. Remember that for dispersed media constituted of large particles, the two following purely geometric phenomena may prevail: (i) the "nonpoint scattering effect" [33] causing an increase in the scattering cross section in a representative elementary volume; and (ii) the "radiation transportation effect" due to the transportation of radiation beams across substantial distances (through the particles) compared to the interparticle distance [31]. The later effect occurs only when the particles are transparent or semitransparent.

Attempts to account for the nonpoint scattering and/or the radiation transportation effects have been carried out essentially for packed-beds with transparent air as continuous phases [28,30–33]. For example, the radiation transportation effect has been accounted for by using an unusual phase function, i.e., depending not only on the scattering angle but also on the exit point of the scattering and the number of internal reflections. The transport equation using this modified phase function is known as dependence included discrete ordinate method (DIDOM) [31], which differs from the usual RTE. The nonpoint scattering has been taken into account by scaling the absorption and scattering coefficients with a scaling-factor dependent on the particle volume fraction [30–33].

For dispersed media constituted of semitransparent continuous phase, the use of this scaling technique is not known. Moreover, the use of a complex phase function to account for the radiation transportation phenomenon is far from practice. An alternative approach in determining the effective radiative properties of such media is currently based on the ray-tracing (RT) technique [39]. This method enables to retrieve the effective radiative properties, especially the effective absorption coefficient, thus to overcome the doubt related to the Eq. (2) when the continuous phase is semitransparent. Also, it can account for both nonpoint scattering and radiation transportation effects. In the following, a short description of this prediction method is given. For more details concerning its derivation, the readers are recommended to the original paper [39].

The RT method uses the geometric optic point of view of the radiation. The main assumptions associated with this theory are listed in Sec. 2. For simplicity, let us consider the two-dimensional configuration showed in Fig. 1; even if in practice, this method is performed on a three-dimensional (3D) geometry. Moreover, the particles are assumed spherical of radius a (or diameter d). In Fig. 1, gray spheres refer to particles, while the space between them designates the continuous phase. The histories of N_{RAY} radiation bundles propagating inside this dispersed medium are traced as follows. For a given radiation bundle, the RT process consists of:

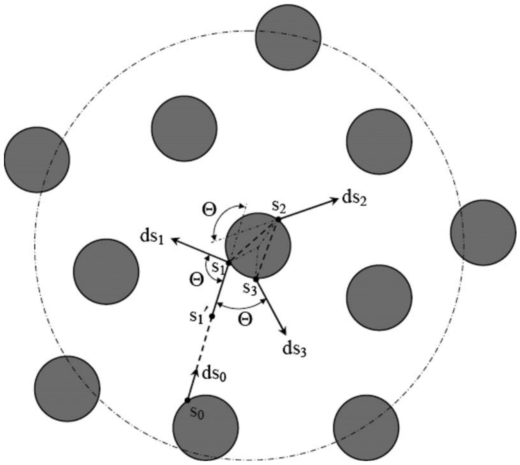

Fig. 1 Illustration of the ray-tracing algorithm on a 2D dispersed medium

- (S1): Select, in a random way, the initial location of the ray on a particle surface (e.g., the point s_0 in Fig. 1) and the initial direction, oriented toward the surrounding medium (e.g., the vector ds_0 in Fig. 1). Note that the particle, from which the ray path starts, is randomly chosen among the existing particles.
- (S2): Track the ray path through the sample until it undergoes extinction. The type of the extinction event (i.e., scattering or absorption) is chosen by considering the most probable one through a classical Monte Carlo test [15–17]. The ray bundle may be absorbed in a particle (e.g., at the position s_1 in Fig. 1) or in the host medium (e.g., at the position s_1' in Fig. 1).

Therefore, the absorption distance is given by the traveled path between the initial position s_0 and the absorption location s_1 or s_1'. The scattering event is considered when the ray is reflected at a particle surface (e.g., at the position s_1 in Fig. 1) or it crosses a particle after undergoing one or several internal transversals (e.g., at the position s_2 or s_3 in Fig. 1 by representing only the two first interior transversals). Note that generally, the surface reflection and the two or three first internal reflections contain more than 99% of the scattered energy. When the ray is reflected at the particle surface (e.g., at s_1) or exits from the same side as it first enters the particle (e.g., at s_3), the scattering distance is just the distance from the initial position s_0 to the location at which the ray interacts with the external particle surface, i.e., s_1. Now, when the ray crosses the particle from one side (e.g., at s_1) to the opposite side (e.g., at s_2), the scattering distance is given by the distance $s_1 - s_0$ plus a transportation distance, denoted by d_{tr}. For spherical particles with smooth surfaces, it was shown that d_{tr} depends only on the particle size d and the ratio of the refractive indices of the particles and the continuous phase, defined by $\eta = n_1/n_0$, according to the Eq. (5) [39]:

$$d_{\mathrm{tr}}/d = \begin{cases} 1.02 - \exp\left[-\left(\dfrac{C_1}{\eta} - C_2\right)\right] & \text{for } 0.5 \le \eta < 1 \text{ and } 1 < \eta \le 8 \\ 1 & \text{elsewhere} \end{cases} \tag{5}$$

for $0.5 \leq \eta < 1$, $C_1 = 3.20$ and $C_2 = 1.47$, while for $1 < \eta \leq 8$, $C_1 = 2.89$ and $C_2 = 0.72$.

The result of the Eq. (5) reaches a minimal value when the contrast of refractive indices is small (i.e., η tends to 1); it increases as long as η moves away from 1; and finally, it converges to the asymptotic value of about 1 for $\eta > 8$ and $\eta < 0.5$. In fact, when $\eta > 8$ or $\eta < 0.5$, most of the rays striking a particle far from its center undergo a surface reflection because the local reflectivity approaches 1. Only the incident rays that are approximately normal to the particle surface are probable to be refracted inside the particle; they travel a distance of about d before crossing this particle. For η approaching 1, the reflectivity approaching zero, thus most of the rays interacting with the particle cross it without being reflected. In addition, the ray directions are not much altered and as result, the calculated average distance traveled by these rays inside the particle tends to approach the theoretical value of the mean distance of scattering inside a particle, $2d/3$ [33,36].

The extinction distance (either the scattering or absorption distance) is stored. When a scattering event occurs, the angle Θ, between the initial direction of the ray (i.e., ds_0) and the direction of the ray after scattering (i.e., ds_1, ds_2, or ds_{S3} in Fig. 1) is also stored. The track of the path of the radiation bundle is stopped after the extinction event.

The steps (S1) and (S2) are carried out for N_{RAY} different radiation bundles. Through this algorithm, the three following counters, namely, dist, N_{SCA}, and $W(\Theta)$, are produced. (i) dist refers to the sum of extinction distances traveled by the N_{RAY} radiation bundles; (ii) N_{SCA} refers to the number of occurrence of scattering events; $N_{\mathrm{ABS}} = N_{\mathrm{RAY}} - N_{\mathrm{SCA}}$ corresponds then to the number of occurrence of absorption events; and (iii) $W(\Theta)$ refers to the number of scattering events where a ray bundle is scattered into the angular interval Θ and $\Theta + d\Theta$ from the incidence direction. $d\Theta$ is the elementary angle.

The effective absorption and scattering coefficients are, respectively, deduced from the calculation of the absorption mean-free-path, denoted by $\mathrm{mfp}_{\mathrm{ABS}}$, and the scattering mean-free-path, denoted by $\mathrm{mfp}_{\mathrm{SCA}}$. In fact, the absorption (or scattering) mean-free-path can be given by the ratio between the total extinction distances dist and the number of absorption (or scattering) events. We then obtain [39]

$$\alpha_e^{-1} = \mathrm{mfp}_{\mathrm{ABS}} = \frac{\mathrm{dist}}{N_{\mathrm{ABS}}} \tag{6}$$

$$\sigma_e^{-1} = \mathrm{mfp}_{\mathrm{SCA}} = \frac{\mathrm{dist}}{N_{\mathrm{SCA}}} \tag{7}$$

The effective phase function can be calculated from the knowledge of the number of scattering events occurring in each scattering angle interval $\Theta + d\Theta$ according to

$$\Phi_e(\Theta) = \frac{W(\Theta)}{\dfrac{1}{4\pi}\displaystyle\int_0^{4\pi} W(\Theta)\,d\Omega} \tag{8}$$

The integration in Eq. (8) is performed over 4π steradians (i.e., over all directions) with $d\Omega = \sin\Theta\, d\Theta\, d\varphi$ as unit solid angle, where φ is the azimuthal angle defined in the interval $0-2\pi$. This scattering phase function is also normalized as follows:

$$\frac{1}{4\pi}\int_0^{4\pi} \Phi_e(\Theta)\,d\Omega = 1 \tag{9}$$

It can be noted that for suspensions of opaque particles in a nonabsorbing host medium, the effective extinction coefficient given by the sum of Eqs. (6) and (7) converges approximately to the well-known scaled effective extinction coefficient of packed-bed media of opaque large particles, denoted here by β_{SC} [31,33]:

$$\beta_{SC} = \frac{0.75 f_v}{a} S_R \quad \text{with} \quad S_R = \frac{1}{1 - f_v} \approx 1 + 1.84 f_v - 3.15 f_v^2 + 7.20 f_v^3 \tag{10}$$

where S_{R} is the famous scaling factor for opaque large particles. In addition, the use of d_{tr} in the calculation of the scattering distance enables to account for the ray transportation effects, particularly important when the radiation can be transmitted through the particles.

In the following, typical evolutions of effective radiative properties of dispersed media constituted of semitransparent continuous phase and monodispersed large spheres are explored using both independent scattering model (Eqs. (2)–(4)) and the ray-tracing method (Eqs. (6)–(8)). The case of specular particles is analyzed. The particle arrangements in the matrix are generated using a 3D computer algorithm described in the literature [32]. Two different dispersed media are considered, (i) The suspension of totally reflecting particles in a semitransparent host medium and (ii) the suspension of semitransparent particles in a semitransparent host medium. The effective absorption and scattering coefficients as functions of the particle volume fraction corresponding to these two types of media are, respectively, shown in Figs. 2(*a*) and 2(*b*). The radiation wavelength λ and the size parameter x are taken to be equal to $\lambda = \pi$ μm and $x = 100$, respectively. A relative refractive index of $n_1/n_0 = 1.5$ is considered for the dispersed media of semitransparent particles. In these figures, the dimensionless radiative properties defined by the product of effective radiative properties and the particle diameter d are plotted. We can note that

- With the typical values of the absorption index of the continuous medium, the current RT method shows that the effective absorption coefficient of suspension of totally reflecting particles is approximately equal to that of host medium. In fact, for totally reflecting particles in an absorbing medium, no radiation beam penetrates the particles. As a consequence, the mean-free-path in-between of absorption in the homogeneous medium is identical to that in the host medium. The independent scattering model is in disagreement with this observation because it gives an effective absorption coefficient, which decreases when the particle concentration increases since Q_a in Eq. (2) is negative for nonabsorbing particles in an absorbing host medium [45]. For dispersed medium of semitransparent particles, although both prediction models tend to converge at low particle concentrations, the independent scattering model gives smaller effective absorption coefficient than the RT method. The difference between them increases as the particle volume fraction increases.
- The effective scattering coefficients increase with the particle volume fraction due to the increase in the number of scattering centers. The effective scattering coefficient is greater for dispersed media of totally reflecting particles than those of semitransparent particles. In fact, the nonpoint scattering tends to increase scattering coefficient while the transportation of rays tends to decrease it. That is why the higher the particle reflectivity is, the lower the ray transportation effect, thus, the higher the scattering coefficient. For dispersed media of opaque particles, the agreement between the RT model and the theoretical result from Eq. (10) (plotted in the same figures) is satisfactory. This shows that the current RT method captures appropriately the nonpoint scattering phenomenon. For dispersed media of semitransparent particles, the results from the independent scattering model are relatively lower than those from the RT method, although both predictions tend to converge at low particle volume fractions. The agreement between the RT and the independent scattering models for the transparent particle cases ($\kappa_1 = 0.0$) is a pure coincidence. Finally, it can also be

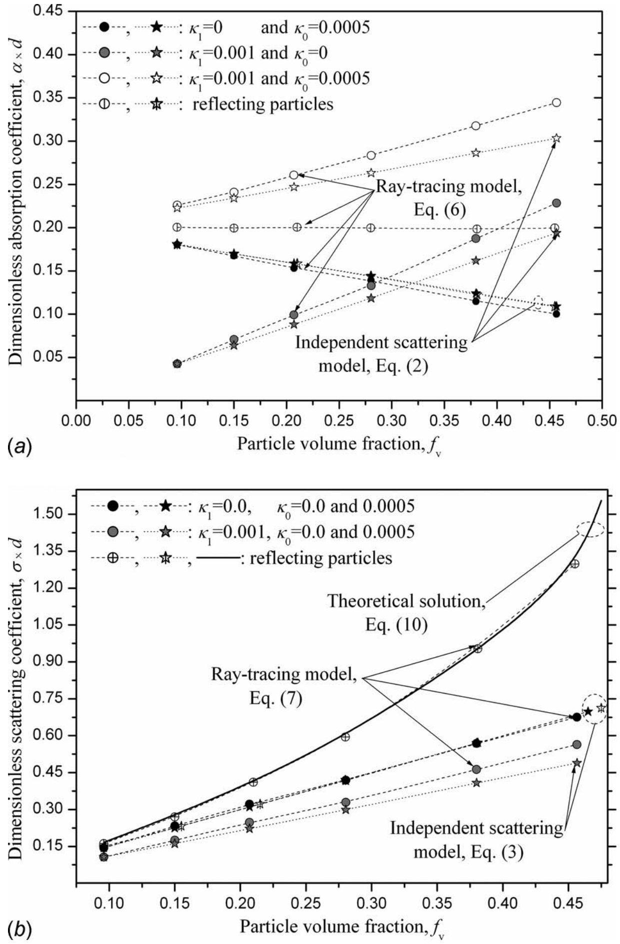

Fig. 2 (*a*) Effective absorption coefficients of dispersed media of large spheres with relative refractive index $n_1/n_0=1.5$ at the wavelength $\lambda=\pi$ μm. Circle symbols with dash lines: the ray-tracing prediction and star symbols with dot lines: the independent scattering model. (*b*) Effective scattering coefficients of dispersed media of large spheres with relative refractive index $n_1/n_0=1.5$ at the wavelength $\lambda=\pi$ μm. Circle symbols with dash lines: the ray-tracing prediction, star symbols with dot lines: the independent scattering model, and solid line: theoretical solution from Eq. (10).

noted that for a host medium absorption index κ_0 less than 0.0005, the effective scattering coefficient is not influenced by the host medium absorption. In Fig. 2(*b*), the results for $\kappa_0=0$ and $\kappa_0=0.0005$ are overlapped.

In Figs. 3(*a*) and 3(*b*) are, respectively, shown the effective phase functions of dispersed media of transparent particles with a relative refractive indices of $n_1/n_0=1.5$ and $n_1/n_0=2/3$. The contributions of surface reflections, denoted by ϕ_0; the first interior transversal, denoted by ϕ_1; and the second interior transversal, denoted by ϕ_2 are also highlighted. It can be noted that the behavior of effective phase functions Φ_e of these two types of dispersed media differs essentially in the backward scattering directions (i.e., $90 \text{ deg} < \Theta \leq 180$ deg). This difference is essentially due to the opposite contribution of the second interior transversal in these two cases. Indeed, the second interior transversal occurs in the backward scattering directions and produces one of the famous rainbow peaks when $n_1/n_0 > 1$ [46], while it produces a peak in the forward scattering directions (i.e. $0 \text{ deg} < \Theta \leq 90$ deg) when $n_1/n_0 < 1$. Note that for beds of opaque (totally reflecting or not) particles, the effective phase function Φ_e is only characterized by the surface reflection ϕ_0.

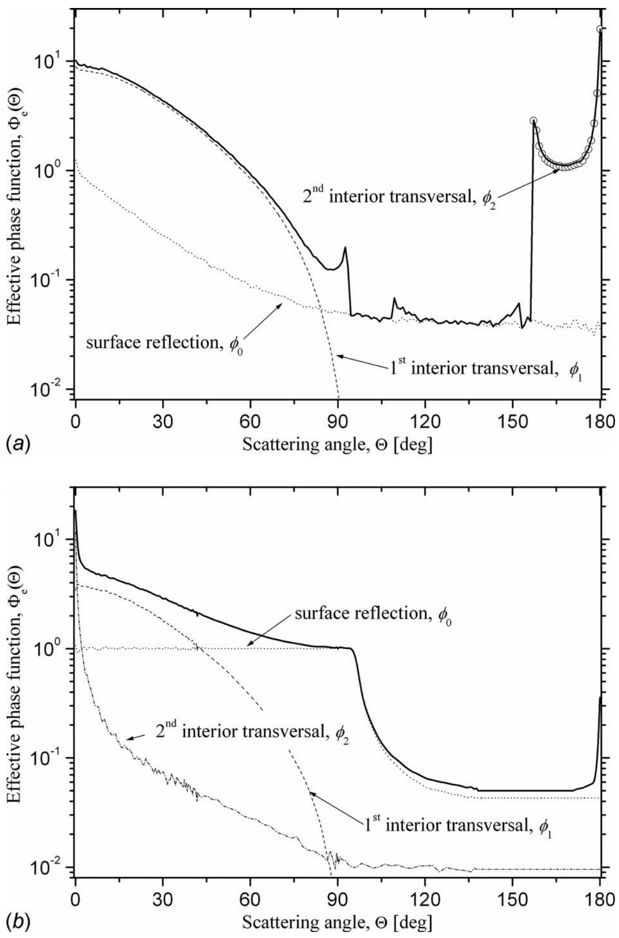

Fig. 3 (*a*) Effective phase function of dispersed media of transparent particles with relative refractive index $n_1/n_0=1.5$. (*b*) Effective phase function of dispersed media of transparent particles with relative refractive index $n_1/n_0=2/3$.

4 Multiphase Approach

Let consider a thin slab of a heterogeneous medium constituted of a continuous phase (matrix) and a dispersed phase (particles) illustrated in Fig. 4(*a*). As before, *c* is the nearest distance between the particles and *d* is the typical size of particles. The characteristic sizes *c* and *d* are assumed much greater than the dominant wavelength λ, so that the geometric optic treatment of the radia-

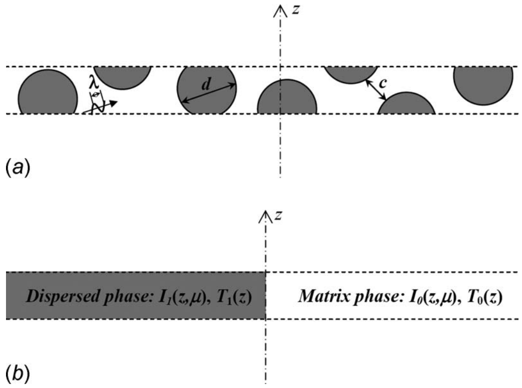

Fig. 4 (*a*) Schematization of a thin slab of a heterogeneous medium and (*b*) modeling of a thin slab of heterogeneous according to the MPA

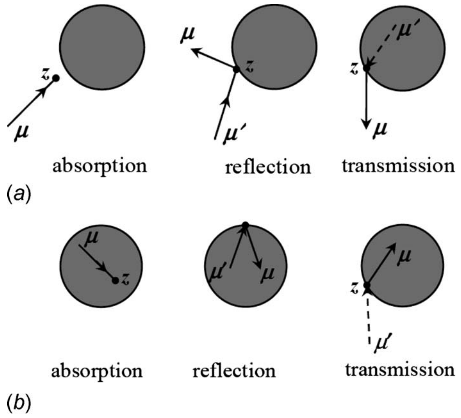

Fig. 5 (*a*) Radiation extinction in the matrix substance at the abscise *z*. Absorption (left); scattering by reflection (center); and scattering by transmission (right). (*b*) Radiation extinction in the particle substance at the abscise *z*. Absorption (left); scattering by reflection (center); and scattering by transmission (right).

tion is applicable. The main idea behind the multiphase approach is (i) to assume that each phase (the matrix or the particles) is a homogeneous and continuous medium and (ii) the radiative transfer in each phase is modeled by a local transport equation, coupled to each other. The solutions of these transport equations can enable to retrieve the intensity and temperature fields in each phase. Figure 4(*b*) schematizes the treatment of the radiation transfer in the heterogeneous medium according to the MPA. It can be noted that with this model, the thermal equilibrium between the continuous and dispersed phases is not imposed. Remember that such treatment is frequently encountered in computations of heat transfer in porous media.

The different mechanisms of radiation extinctions in the matrix and particle substance are schematized in Figs. 5(*a*) and 5(*b*), respectively. When the radiation intensity I_i propagates in the substance i (i=matrix or particle), it may be absorbed (see left figure) or scattered (see center and right figures) by a phase boundary. During the scattering, if the interface between the phases is totally reflecting, the intensity I_i is entirely reflected back to the phase i (see center figure), or else an amount of it is transmitted to the neighboring phase (see right figure). Assuming that the particles are randomly dispersed in the matrix, the extinction of the radiation in the substance i (matrix or particle) can be characterized by an absorption coefficient α_i, a scattering coefficient σ_i, and phase function Φ_i. Moreover, the energy reinforcement from the neighboring phase j can be also characterized by a scattering coefficient σ_{ji} and a phase function Φ_{ji}. Such radiation transfer is similar as the usual radiation transfer in a single phase homogeneous medium except the presence of the energy exchange between phases. Therefore, the transport equation in each phase can be derived in a similar manner as for the usual RTE (see Refs. [15–17]) by taking into account, in more, the energy exchange between phases. The resulting transport equations, called here as multiphase radiative transport equation (MRTE), take the following form [36].

- In the matrix substance,

$$\mu\frac{\partial I_0(z,\mu)}{\partial z} = -(\alpha_0+\sigma_0)I_0(z,\mu) + \frac{\sigma_0}{2}\int_{-1}^{1} I_0(z,\mu')\Phi_0(\Theta)d\mu' + I_{10}(z,\mu) \qquad (11)$$

- In the particle substance,

$$\mu\frac{\partial I_1(z,\mu)}{\partial z} = -(\alpha_1+\sigma_1)I_1(z,\mu) + \frac{\sigma_1}{2}\int_{-1}^{1} I_1(z,\mu')\Phi_1(\Theta)d\mu' + I_{01}(z,\mu) \qquad (12)$$

Note that these equations have similar forms as the usual RTE except for the presence of exchange terms I_{10} and I_{01}. Let us consider the radiation propagation in the substance i (i=matrix or particles). By integrating the intensity coming from all directions of the neighboring phase j, the intensity reinforcement from the substance j to the substance i can be give by [36]

$$I_{ji}(z,\mu) = \frac{\sigma_{ji}}{2}\int_{-1}^{1} I_j(z,\mu')\Phi_{ji}(\Theta)d\mu' \quad \text{for } i=0, \quad j=1 \text{ and } i=1, \quad j=0 \qquad (13)$$

The radiative properties that occurred in Eqs. (11)–(13) can be determined by analyzing the propagations of the radiation in the matrix phase and in the particle phase. When the microstructure of the dispersed medium and their optical properties are known, the calculation of these radiative properties is not challenging. They can be determined either by an analytical analysis [36] or by the RT approaches [32,39,47,48]. For the dispersed media constituting of a continuous host medium (referred hereafter to phase 0) and monodispersed optically large spherical particles (referred hereafter to phase 1), the derivation of their radiative properties has been well detailed in Ref. [36], and in the following, the final results are only recapitulated.

- The absorption coefficients are just those of the constituting materials because each phase is continuous and homogeneous:

$$\alpha_i = \frac{4\pi\kappa_i}{\lambda} \quad \text{for } i=0 \text{ and } 1 \qquad (14)$$

- The scattering coefficients and phase functions due to reflections at matrix/particle interfaces are

$$\sigma_0 = \frac{0.75 f_v}{a}S_R\rho_0, \quad \sigma_1 = \frac{0.75}{a}\rho_1, \quad \text{and}$$

$$\Phi_i(\Theta) = \frac{\rho_i'(\Theta)}{\rho_i} \quad \text{for } i=0 \text{ and } 1 \qquad (15)$$

  where $S_R=1/(1\text{-}f_v)$ is the scaling factor accounting for the nonpoint scattering effect. ρ_i' and ρ_i are, respectively, the usual directional and hemispherical reflectivities at the matrix/particle interface for a radiation propagating in the substance i [15–17,46].
- The scattering coefficient for a radiation in the substance i to be scattered in the substance j are similar to the scattering coefficient due to reflections in the substance i, except that the interface transmittivity $1-\rho_\mathrm{i}$ is used instead of the reflectivity ρ_i:

$$\sigma_{01} = 0.75\frac{f_v}{a}S_R(1-\rho_0) \quad \text{and} \quad \sigma_{10} = \frac{0.75}{a}(1-\rho_1) \qquad (16)$$

- The phase functions corresponding to transmissions from one phase to the other can be obtained by analyzing the refraction of rays at interfaces using the reflection and refraction laws. It can be shown that they are identical for spherical particles [36]:

$$\Phi_{01}(\Theta) = \Phi_{10}(\Theta) = 2\frac{1-\rho_0'}{1-\rho_0}\frac{d\cos^2\delta}{d\cos(\delta-\delta')} \qquad (17)$$

  δ refers to the reflection angle between the outward normal to the particle surface and the ray direction, while δ' refers

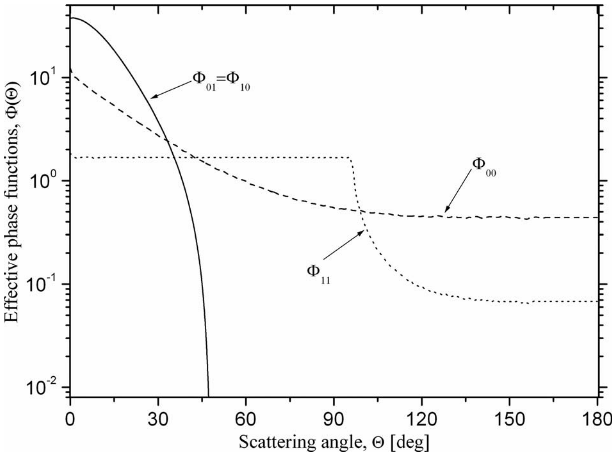

Fig. 6 MPA effective phase functions of dispersed media of transparent particles with relative refractive index $n_1/n_0=1.5$

to the refraction angle connected to δ through the Snell's law, i.e., $n_0 \sin \delta = n_1 \sin \delta'$, for a radiation propagating in the matrix phase. Moreover, δ and δ' are connected to the scattering angle Θ by the relation $\delta=\Theta+\delta'$ [46].

Hereafter, the evolution of phase functions is only shown since these radiative properties have been the subject of previous investigation [36]. Figure 6 reports the phase functions for dispersed media constituted of transparent particles with a refractive index ratio $n_1/n_0=1.5$. For a refractive index ratio equal to $n_1/n_0=2/3$, similar phase functions as reported in this figure can be observed if the curves ϕ_0 and ϕ_1 are interchanged. Compared to the effective phase function in the HPA (see Fig. 3(*a*)), we can note, in Fig. 6, the absence of the rainbow peaks at the scattering angles beyond 150 deg. These rainbow peaks correspond to the rays scattered after undergoing internal reflections inside a particle. They are accounted for in the HPA phase function but not in the MPA phase functions. The influence of these features of the phase function on the radiative transfer is not known and is investigated in this study. Note that, in this work, the radiative properties involved in the MPA are calculated from Eqs. (14)–(17).

5 Results and Discussion

The radiative transfer through two-phase dispersed media constituted of semitransparent host medium and spherical (smooth) particles is analyzed using the HPA and MPA. In this aim, we considered as configuration 1D slabs exposed, in one side, to collimated unpolarized radiation of wavelength λ. The environment surrounding the sample is transparent with a refraction index equal to 1. Different sample thicknesses and different couples of optical properties of the dispersed and continuous phases are considered. The famous discrete ordinate method (DOM) is used to solve the transport equations in both approaches [15–17]. For simplicity, smooth or transparent boundary conditions (BC) are considered depending on the host medium refractive index. Consequently, no particle crosses the sample boundaries. In the HPA, details concerning the transparent BC (when $n_0=1$) and smooth BC (when $n_0>1$) for 1D parallel slabs can be found, respectively, in standard textbooks [15–17] and in Ref. [40]. In the MPA, since no particle crosses the boundaries, the external incident radiation penetrates first in the matrix phase; therefore, the transparent or smooth BC are still suitable as boundary conditions to the transport equation (12). The radiations penetrating the dispersed phase come only from scattering from the matrix. In this way, the radiation intensity at the abscise z and direction μ of the dispersed medium, $I(z,\mu)$, is just the sum of the intensities in the two phases.

Due to lack of experimental data, we compare our calculations with the results from the direct Monte Carlo (MC) simulation. In this work, we implemented the algorithm previously described in Ref. [49] to generate the current MC data. To enable comparison of the current results with future experimental data such as those from Fourier transform infrared (FTIR) spectrometric devices [40], we focused our analysis on results of (i) directional transmittances and reflectances defined by T_D:

$$T_D(\mu)=\begin{cases}\dfrac{I(L,\mu)}{q(0,\mu_0)} & for\ \ 0<\mu\le 1\\[2ex] \dfrac{I(0,\mu)}{q(0,\mu_0)} & for\ \ -1\le\mu<0\end{cases} \tag{18}$$

and (ii) hemispherical transmittance, denoted by T_H, and hemispherical reflectance, denoted by R_H:

$$T_H=2\pi\int_0^1 T_D(\mu)\mu d\mu \quad \text{and} \quad R_H=2\pi\int_{-1}^0 T_D(\mu)\mu d\mu \tag{19}$$

In Eq. (18), $I(z,\mu)$ is the intensity at abscise z and in the direction μ. $z=0$ refers to the boundary at which the external collimated flux $q(0,\mu_0)$ arrives, while $z=L$ indicates the opposite boundary. L refers to the sample thickness. $\mu_0>0$ is the direction cosine of the incident beam measured from the inward normal to the boundary at $z=0$. $\mu>0$ and $\mu<0$ indicate the directional regions of transmittances and reflectances, respectively.

In the following, three types of samples are analyzed. (1) Suspension of particles of $n_1=1.5$ in a host medium of $n_0=1$, (2) suspension of opaque particles in a host medium of $n_0=1$, and finally (3) semitransparent matrix of $n_0=1.5$ containing air bubbles of $n_1=1$. In all cases, the incident external radiation is taken normal to the sample boundaries, i.e., $\mu_0=1$; and two values of the matrix absorption index ($\kappa_0=0$ and 0.0005) are considered. Higher values of matrix absorption index are not taken to avoid completely opaque samples.

The first analysis is focused on the evolution of directional transmittances and reflectances T_D as a function of the scattering angles θ issued from a Gaussian quadrature of 20 orders (i.e., 20 transmittance directions in the range of $0<\mu\le 1$ and 20 reflectance directions in the range of $-1\le\mu<0$). Note that θ is not identical to the scattering angle Θ. Indeed, θ measures the angle between the direction of the intensity leaving the sample μ and the direction of the incident external beam μ_0. For the three types of dispersed media, a reduced thickness, defined by L/d, of 10 and a fixed particle volume fraction of about 0.278 are considered, where d is the particle size. We report in Fig. 7(*a*), the results of samples of transparent particles ($n_1=1.5$, $\kappa_1=0$); in Fig. 7(*b*), the results of samples of opaque particles considering uniform reflectivities $\rho_0=1$; and in Fig. 7(*c*), the results of semitransparent matrixes ($n_0=1.5$) containing air bubbles ($n_1=1$, $\kappa_1=0$). Qualitatively, the results from samples containing opaque particles and air bubbles are similar, while those from samples containing semitransparent particles are slightly different especially on the reflectances. This difference can be explained as follows. Opaque particles and air bubbles do not present significant backscattering and as a result, the reflectance is rather smooth, transparent particles of $n_1=1.5$ in a host medium of $n_0=1.0$ backscatter strongly radiation and create the famous rainbows. As consequence, the rays backscattered by particles propagate in the opposite direction of the incident external radiation and cause an increase in reflectance beyond the angle 150 deg.

- The results from the HPA are generally in good agreement with the MC simulation. For samples of transparent particles, the HPA reproduces satisfactorily the increase in reflectances from $\theta=150$ deg (see Fig. 7(*a*)). This tends to show that in the geometric optic regime, the RT technique as described in this paper is appropriate to predict the effective

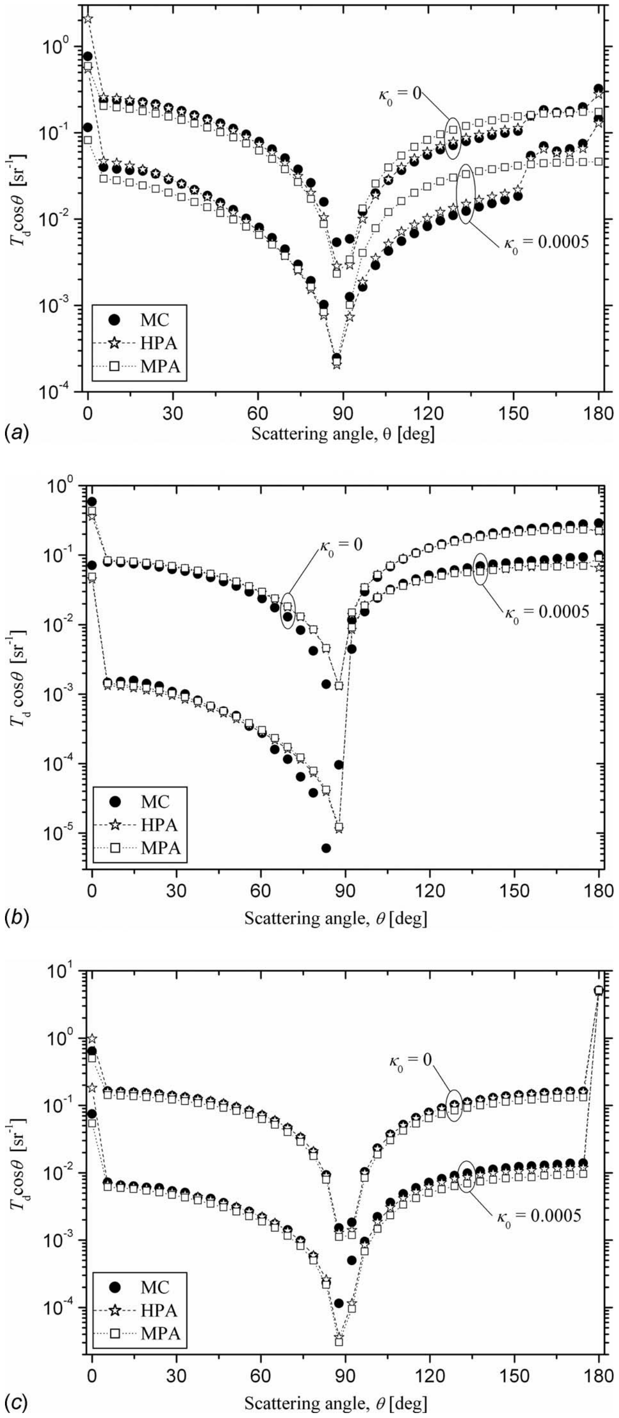

Fig. 7 (*a*) Directional transmittances and reflectances through slabs of suspension of nonabsorbing particles with $n_1=1.5$ in a semitransparent host medium with $n_0=1$. (*b*) Directional transmittances and reflectances through slabs of totally reflecting particles in a semitransparent host medium with $n_0=1$. (*c*) Directional transmittances and reflectances through slabs of semitransparent matrixes with $n_0=1.5$ embedding nonabsorbing air bubbles with $n_1=1$.

radiative properties of dispersed media. Moreover, the HPA enables to model radiative transfer in dispersed media even in the presence of high concentration of the dispersed phase and semitransparent host medium.

- The MPA predicts also well the MC results for samples of opaque particles (see Fig. 7(*b*)) or air bubbles (see Fig. 7(*c*)). Note that for the samples containing opaque particles, the MPA results are overlapped with those of HPA. In fact, when particles are opaque, (i) the radiative transfer in the particle phase is negligible, hence, the transport equations in the MPA reduce to a single RTE in the matrix phase and (ii) the radiative properties in the matrix phase are due only to the absorption and reflection mechanisms, hence, they become identical to the effective radiative properties from the HPA. For samples containing transparent particles, the MPA gives unsatisfactory agreement (see Fig. 7(*a*)). This discrepancy can be explained by the fact that the MPA phase functions do not account for the (geometric) backscattering peaks inherent to transparent particles considered here. The MPA tends to average the reflectance. As proof, when the particles do not present backscattering (e.g., for the samples of air bubbles or opaque particles), the MPA seems appropriate.
- The disparities between both prediction approaches and the MC simulation on transmittances in the directions parallel to the sample surface can be explained partially by the uncertainties of the MC method. In these directions, the magnitude of transmittances is too small and the accuracy of MC simulation is poor. Increasing the number of radiation samples used in MC method may improve it; however, the gain in accuracy is not worth the cost of the computation.
- The HPA and MPA fail to predict the transmittance in the direction of the incident external beam (i.e., $\mu=\mu_0=1$). We do not well understand the reasons of this discrepancy. However, we have verified that it has no consequence on heat transfer calculations. In fact, this problem is only noticeable for particle volume fractions greater than 0.15. In these cases, it could not induce much error on the flux calculation because the magnitude of the intensity in this direction is very small compared to the magnitude of the total scattered intensities. Moreover, this discrepancy is insignificant for media with particle volume fractions less than 0.15 since in these cases, the transmittance in the direction $\mu=\mu_0=1$ contains mainly the external unscattered radiation. It is also interesting to note that this problem occurs only when the external radiation source is a collimated beam because we have not found noticeable discrepancy with diffuse incident radiation whatever the particle volume fraction.

The second analysis is focused on the results of hemispherical transmittances T_H and reflectances R_H as functions of the sample thickness. To study the influence of the absorptivity of each constituting phase, different couples of optical constants of the continuous medium and particles are considered. As in the above analysis, only the results for the particle volume fraction of about 0.278 is shown, even if the subsequent conclusions have been generally observed for samples having particle volume fractions in the range 0.10 to 0.45. The radiative transfer in dispersed media with particle volume fraction below 0.10 falls in the independent scattering regime as we have shown in Figs. 2(*a*) and 2(*b*); hence, previous radiative transfer models are suitable [2,6,45].

- The hemispherical transmittances and reflectances through samples of suspension of opaque particles (with uniform reflectivity $\rho_0=0.9$) are depicted in Figs. 8(*a*) and 8(*b*), respectively. It can be noted that the MPA and HPA predict correctly the hemispherical transmittances. The maximal deviation, less than 15%, occurs for thick samples. Concerning reflectances, however, a gap occurs between the results from both predictions and the MC data. A discrepancy also exists in the results of directional reflectance (Fig. 7(*b*)) but it is directionally less noticeable. Moreover, we have observed that the higher the particle reflectivity ρ_0, the greater this gap width. This discrepancy is especially due to the difficulties of the continuum-based approaches (such as the HPA and MPA) to model properly the radiation transfer near the

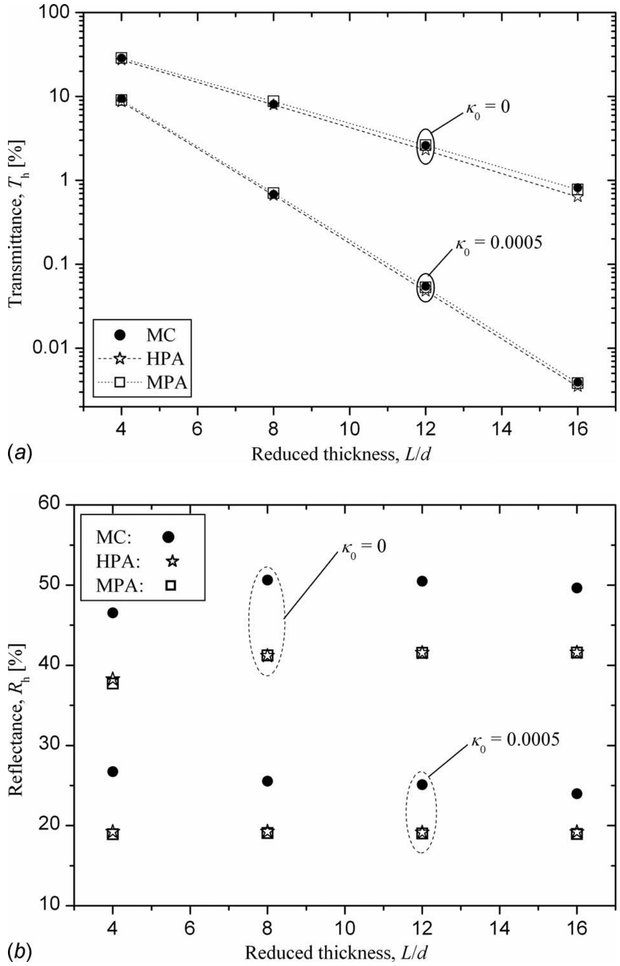

Fig. 8 (*a*) **Hemispherical transmittances through samples of opaque particles of uniform reflectivities $\rho_0=0.9$ in a host medium with $n_0=1.0$.** (*b*) **Hemispherical reflectances through samples of opaque particles of uniform reflectivities $\rho_0=0.9$ in a host medium with $n_0=1.0$.**

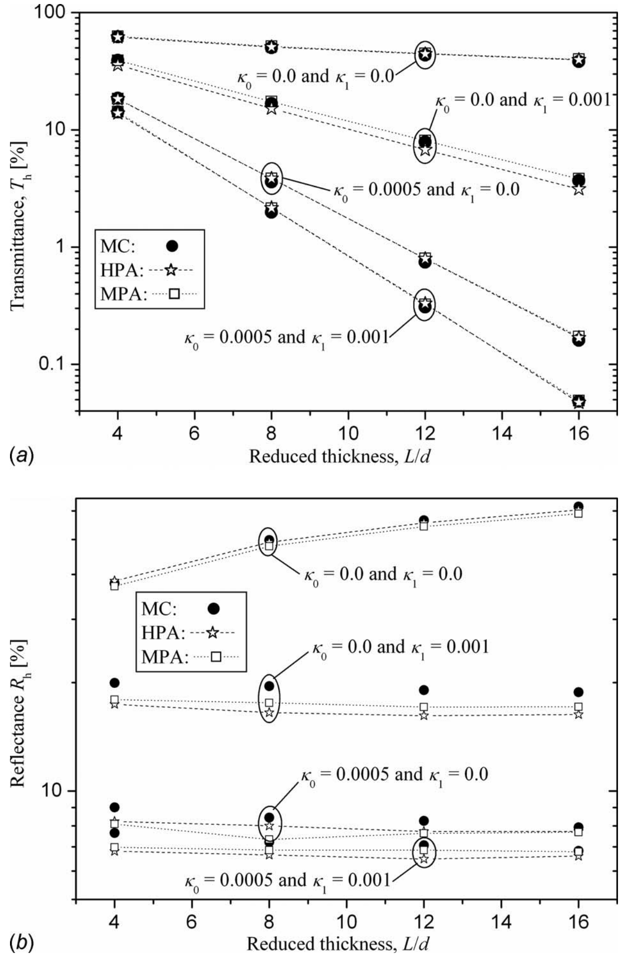

Fig. 9 (*a*) **Hemispherical transmittances through samples of semitransparent matrix with $n_0=1.5$ embedding air bubbles with $n_1=1.0$.** (*b*) **Hemispherical reflectances through samples of semitransparent matrix with $n_0=1.5$ embedding air bubbles with $n_1=1.0$.**

sample boundaries at which the continuum treatment is questionable. Indeed, some amount of incident energy is reflected back to the outside medium by particles near the surface of the sample. Such situation is well modeled in the direct MC simulation but not in the HPA and MPA, where the radiative properties (that are bulk properties) are not yet applicable. Note that a similar gap between continuum approaches and MC method was also observed in the past studies [31,36]. An attempt to improve the current predictions may be performed by using partially scattering BC at the boundary $z=0$ instead of the current transparent BC. However, this issue is out of the objective of the current study.

- Figures 9(*a*) and 9(*b*) show the results of samples of semitransparent matrix containing air bubbles. We can see that both approaches are suitable (with a maximal deviation less than 10%, for thick samples) to model radiative transfer, especially the transmittance and reflectance, in such media. Moreover, the gaps on reflectances observed on samples containing opaque particles are not observed any more. In fact, the amount of reflected energy from the bubbles near the sample surface is insignificant compared to the energy backscattered from the medium volume.
- The transmittances and reflectances through samples of transparent and semitransparent particles are reported in Figs. 10(*a*) and 10(*b*). While the current HPA provides satisfactory predictions (with a maximal error smaller than 5%), the MPA generally overpredicts the reflectances, and the transmittances for samples of semitransparent particles while it underpredicts the transmittances of transparent particles. The source of the discrepancy of the MPA, as discussed previously, is due to the failure of the effective phase function models, which do not capture the (geometric) backscattering of these types of particles.
- Through the comparison of the current approaches with MC data, the radiative transfer in dispersed media (of large dispersed phase) in presence of semitransparent host medium can be now properly predicted. In general, we have observed that the higher the host medium (κ_0) and the particle absorption index (κ_1) are, the lower the transmittances and reflectances.

6 Conclusion

The modeling of radiative transfer in dispersed media is a formidable task. In literature, few studies are reported in this area. Moreover, doubts exist on the radiation transfer modeling when using the radiative properties derived from the Independent scattering theory, especially, when the volume fraction of the dispersed phase is high. In this study, we suggested the use of two approaches such as the HPA and the MPA. To determine which of them (including the corresponding radiative properties) is appropriate and to define their limits in analyzing the radiation transfer

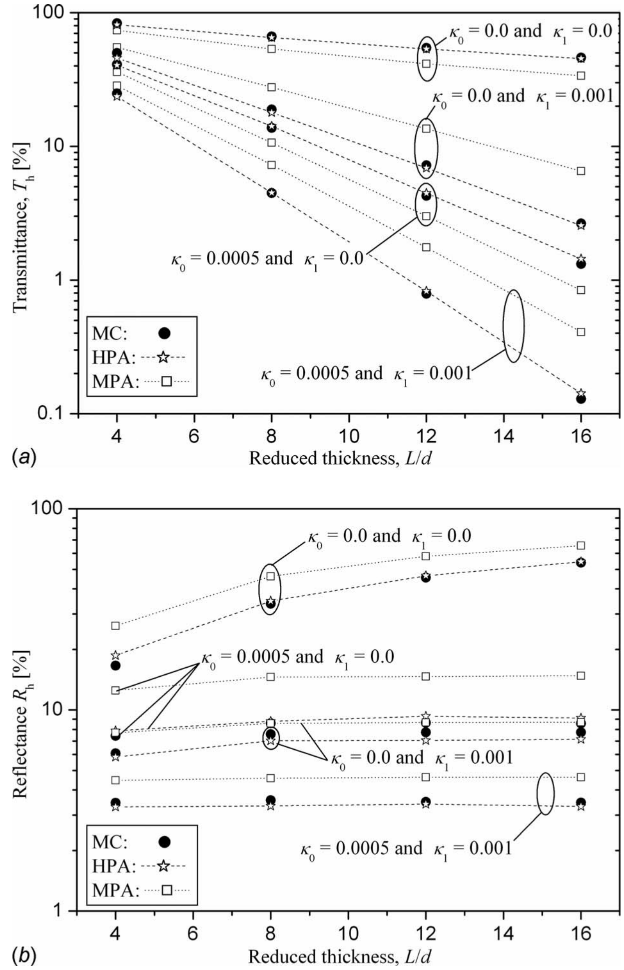

Fig. 10 (*a*) **Hemispherical transmittances through samples of semitransparent particles with n_1=1.5 in suspension in a host medium with n_0=1.0. (*b*) Hemispherical reflectances through samples of semitransparent particles with n_1=1.5 in suspension in a host medium with n_0=1.0.**

in dispersed materials, these two approaches are compared with the direct Monte Carlo simulation. The main conclusions obtained from this study are recalled.

- Using the effective radiative properties derived from the RT technique, the HPA is shown to be suitable for analyzing the radiative transfer, especially to calculate the transmittances and reflectances, through dispersed media. It tends to confirm the capability of the RT model to capture the geometric scattering phenomena. In addition, the radiative transfer problems in presence of a semitransparent host medium can be now correctly predicted.
- For dispersed media having large particle volume fractions (e.g., greater than 0.10), caution should be made when using the effective radiative properties from the independent scattering model. In fact, beyond this volume fraction value, the deviation between the radiative properties from the independent scattering model and those from the ray-tracing method becomes significant.
- The phase functions of the MPA do not capture all features of the (geometric) backscattering from transparent or semitransparent particles. As a consequence, the radiative transfer solution in dispersed media based on this approach is shown unsatisfactory. In absence of strong particle backscattering (e.g., for samples of opaque particles or air bubbles in a matrix), the predictions from the MPA are correct.
- For dispersed media of highly reflecting particles, it has been noted that a gap occurs between the reflectances from predictions and those from MC simulation due to the difficulties to model properly the boundary conditions.

Finally, it is important to note that the radiation emission mechanism is not taken into account in the current HPA and MPA models. Therefore, the above conclusions should be considered only for the radiative transfer problems unaffected by the emitted radiations.

Nomenclature

a = particle radius, m
c = interparticle distance, m
C_1, C_2 = constants in Eq. (5)
d = particle diameter, m
dist = extinction distance, m
ds_0, ds_1, ds_2, ds_3 = direction vectors in the ray-tracing method
d_{tr} = radiation-transport distance, m
$d\Omega$ = unit solid angle, sr
f_v = dispersed phase volume fraction
I = radiation intensity, W m^{-2} sr^{-1}
L = sample thickness, m
mfp = mean-free-path, m
n = real part of the complex refractive index
N = ray number
$q(z,\mu)$ = collimated radiation flux at the abscise z propagating in the direction of cosine μ with respect to the z axis, W m^{-2}
Q = particle efficiency factors
R = hemispherical reflectance
s_0, s_1, s_1', s_2, s_3 = position vectors in the ray-tracing method, m
S_R = scaling factor of nonpoint scattering in Eqs. (10), (15), and (16)
T = hemispherical transmittance, directional transmittance or reflectance, sr^{-1}
x = particle size parameter
$W(\Theta)$ = number of occurrence of scattering events in the angular interval Θ and $\Theta+\mathrm{d}\Theta$
z = abscise of the intensity measured from the illuminated boundary, m

Greek Symbols

α = effective absorption coefficient, m^{-1}
β = effective extinction coefficient, m^{-1}
δ, δ' = angles in Eq. (17), rad
ϕ = phase function of a single particle
ϕ_0 = contribution of surface reflections to the phase function
ϕ_1 = contribution of the first interior transversal to the phase function
ϕ_2 = contribution of the second interior transversal to the phase function
Φ = effective phase function of a dispersed medium
η = ratio of the refractive indexes of the particles and the host medium
φ = azimuthal angle, rad
κ = imaginary part of the complex refractive index or absorption index
λ = wavelength, m
μ, μ' = cosine of the angles θ and θ', respectively
θ = transmittance or reflectance angle, rad
Θ = scattering angle during the interaction of the radiation and the scatterer, rad

ρ, ρ' = hemispherical and directional reflectivities, respectively
σ = effective scattering coefficient, m^{-1}

Subscripts

a = refers to the absorption efficiency factor
ABS = refers to the absorption mean-free-path or the total number of radiation bundles undergoing absorption events in the Ray-tracing method
D = refers to directional transmittance or reflectance
e = refers to effective radiative properties
H = refers to hemispherical transmittance or reflectance
i = refers to parameters characterizing the radiative transfer in the ith phase
ji = refers to radiative properties characterizing the radiative transfer from the jth phase to the ith phase
RAY = refers to the total ray number used in the Ray-tracing method
s = refers to the scattering efficiency factor
SC = refers to the effective extinction coefficient after a nonpoint scattering correction
SCA = refers to the scattering mean-free-path or the total number of radiation bundles undergoing scattering events in the Ray-tracing method
0 = refers to the continuous phase surrounding the scatterers
1 = refers to the dispersed phase

References

[1] Muller, R., Lipinski, W., and Steinfeld, A., 2008, "Transient Heat Transfer in a Directly-Irradiated Solar Chemical Reactor for the Thermal Dissociation of ZnO," Appl. Therm. Eng., **28**, pp. 524–531.
[2] Randrianalisoa, J., Baillis, D., and Pilon, L., 2006, "Modeling Radiation Characteristics of Semitransparent Media Containing Bubbles or Particles," J. Opt. Soc. Am. A Opt. Image Sci. Vis, **23**, pp. 1645–1656.
[3] Jones, A. R., 1999, "Light Scattering for Particle Characterisation," Prog. Energy Combust. Sci., **25**, pp. 1–53.
[4] Gusarov, A. V., and Kruth, J.-P., 2005, "Modelling of Radiation Transfer in Metallic Powders at Laser Treatment," Int. J. Heat Mass Transfer, **48**, pp. 3423–3434.
[5] Parent, G., Boulet, P., Gauthier, S., Blaise, J., and Collin, A., 2006, "Experimental Investigation of Radiation Transmission Through a Water Spray," J. Quant. Spectrosc. Radiat. Transf., **97**, pp. 126–141.
[6] Dombrovsky, L., Randrianalisoa, J., and Baillis, D., 2007, "Infrared Radiative Properties of Polymer Coatings Containing Hollow Microspheres," Int. J. Heat Mass Transfer, **50**, pp. 1516–1527.
[7] Foldy, L. L., 1945, "The Multiple Scattering of Waves. I. General Theory of Isotropic Scattering by Randomly Distributed Scatterers," Phys. Rev., **67**, pp. 107–119.
[8] Goldberg, M. L., and Watson, K. M., 1964, *Collision Theory*, Wiley, New York.
[9] Ishimaru, A., 1978, *Wave Propagation and Scattering in Random Media*, Academic, New York.
[10] Apresyan, L. A., and Kravtsov, Y. A., 1983, *Radiative Transfer Theory*, Nauka, Moscow.
[11] Papanicolaou, G. C., and Burridge, R., 1975, "Transport Equations for the Stokes Parameters From Maxwell Equations in a Random Media," J. Math. Phys., **16**, pp. 2074–2082.
[12] Mishchenko, M. I., Travis, L. D., and Lacis, A. A., 2006, *Multiple Scattering of Light by Particles: Radiative Transfer and Coherent Backscattering*, Cambridge University Press, Cambridge.
[13] Chandrasekhar, S., 1950, *Radiative Transfer*, Oxford University Press, Oxford.
[14] Lenoble, J., 1985, *Radiative Transfer in Scattering and Absorbing Atmospheres: Standard Computational Procedures*, Deepak, Hampton.
[15] Brewster, M. Q., 1992, *Thermal Radiative Transfer and Properties*, Wiley, New York.
[16] Modest, M. F., 2003, *Radiative Heat Transfer*, Academic, New York.
[17] Siegel, R., and Howell, J. R., 2002, *Thermal Radiation Heat Transfer*, Taylor & Francis, New York.
[18] Mishchenko, M. I., 2006, "Far-Field Approximation in Electromagnetic Scattering," J. Quant. Spectrosc. Radiat. Transf., **100**, pp. 268–276.
[19] Kerker, M., 1966, *The Scattering of Light and Other Electromagnetic Radiation*, Academic, New York.
[20] Van de Hulst, H. C., 1981, *Light Scattering by Small Particles*, Dover, New York.
[21] Bohren, C. F., and Huffman, D. R., 1983, *Absorption and Scattering of Light by Small Particles*, Wiley, New York.
[22] Durant, S., Calvo-Perez, O., Vukadinovic, N., and Greffet, J. J., 2007, "Light scattering by a Random Distribution of Particles Embedded in Absorbing Media: Full-Wave Monte Carlo Solutions of the Extinction Coefficient," J. Opt. Soc. Am. A Opt. Image Sci. Vis, **24**, pp. 2953–2962.
[23] Waterman, P. C., and Truell, R., 1961, "Multiple Scattering of Waves," J. Math. Phys., **2**, pp. 512–537.
[24] Twersky, V., 1962, "On Scattering of Waves by Random Distributions. I. Free-Space Scatterer Formalism," J. Math. Phys., **3**, pp. 700–715.
[25] Lax, M., 1952, "Multiple Scattering of Waves. II. The Effective Field in Dense Systems," Phys. Rev., **85**, pp. 621–629.
[26] Cartigny, J. D., Yamada, Y., and Tien, C. L., 1986, "Radiative Transfer With Dependent Scattering by Particles: Part I—Theoretical Investigation," ASME J. Heat Transfer, **108**, pp. 608–613.
[27] Yamada, Y., Cartigny, J. D., and Tien, C. L., 1986, "Radiative Transfer With Dependent Scattering by Particles: Part II—Experimental Investigation," ASME J. Heat Transfer, **108**, pp. 614–618.
[28] Drolen, B. L., and Tien, C. L., 1987, "Independent and Dependent Scattering in Packed-Sphere Systems," J. Thermophys. Heat Transfer, **1**, pp. 63–68.
[29] Kumar, S., and Tien, C. L., 1990, "Dependent Absorption and Extinction of Radiation by Small Particles," ASME J. Heat Transfer, **112**, pp. 178–185.
[30] Kamiuto, K., 1990, "Correlated Radiative Transfer in Packed-Sphere Systems," J. Quant. Spectrosc. Radiat. Transf., **43**, pp. 39–43.
[31] Singh, B. P., and Kaviany, M., 1992, "Modelling Radiative Heat Transfer in Packed Beds," Int. J. Heat Mass Transfer, **35**, pp. 1397–1405.
[32] Coquard, C., and Baillis, D., 2004, "Radiative Characteristics of Opaque Spherical Particle Beds: A New Method of Prediction," J. Thermophys. Heat Transfer, **18**(2), pp. 178–186.
[33] Brewster, M. Q., 2004, "Volume Scattering of Radiation in Packed Beds of Large, Opaque Spheres," ASME J. Heat Transfer, **126**, pp. 1048–1050.
[34] Dombrovsky, L., 2000, "Thermal Radiation From Nonisothermal Spherical Particles of a Semitransparent Material," Int. J. Heat Mass Transfer, **43**, pp. 1661–1672.
[35] Dombrovsky, L., 2007, "Large-Cell Model of Radiation Heat Transfer in Multiphase Flows Typical for Fuel-Coolant Interaction," Int. J. Heat Mass Transfer, **50**, pp. 3401–3410.
[36] Gusarov, A. V., 2008, "Homogenization of Radiation Transfer in Two-Phase Media With Irregular Phase Boundaries," Phys. Rev. B, **77**, p. 144201.
[37] Kokhanovsky, A. A., 1999, *Optics of Light Scattering Media, Problems and Solutions*, Wiley, Chichester.
[38] Welford, W. T., 1962, *Geometrical Optics: Optical Instrumentation*, North-Holland, Amsterdam.
[39] Randrianalisoa, J., and Baillis, D., "Radiative Properties of Densely Packed Spheres in Semitransparent Media: A New Geometric Optics Approach," J. Quant. Spectrosc. Radiat. Transf., submitted.
[40] Randrianalisoa, J., Baillis, D., and Pilon, L., 2006, "Improved Inverse Method for Radiative Characteristics of Closed-Cell Absorbing Porous Media," J. Thermophys. Heat Transfer, **20**(4), pp. 871–883.
[41] Lebedev, N., Gartz, M., Kreibig, U., and Stenzel, O., 1999, "Optical Extinction by Spherical Particles in an Absorbing Medium: Application to Composite Absorbing Films," Eur. Phys. J. D, **6**, pp. 365–373.
[42] Pilon, L., and Viskanta, R., 2002, "Apparent Radiation Characteristics of Semitransparent Media Containing Gas Bubbles," Proceedings of the 12th International Heat Transfer Conference, Elsevier, France, pp. 645–650.
[43] Yang, P., Gao, B.-C., Wiscombe, W. J., Mishchenko, M. I., Platnick, S. E., Huang, H.-L., Baum, B. A., Hu, Y. X., Winker, D. M., Tsay, S.-C., and Park, S. K., 2002, "Inherent and Apparent Scattering Properties of Coated or Uncoated Spheres Embedded in an Absorbing Host Medium," Appl. Opt., **41**, pp. 2740–2759.
[44] Dombrovsky, L., 1996, *Radiation Heat Transfer in Disperse Systems*, Begell House, New York.
[45] Dombrovsky, L., 2004, "The Propagation of Infrared Radiation in a Semitransparent Liquid Containing Gas Bubbles," High Temp., **42**(1), pp. 133–139.
[46] Hottel, H. C., and Sarofim, A. F., 1967, *Radiative Transfer*, McGraw-Hill, New York.
[47] Tancrez, M., and Taine, J., 2004, "Direct Identification of Absorption and Scattering Coefficients and Phase Function of a Porous Medium by a Monte Carlo Technique," Int. J. Heat Mass Transfer, **47**, pp. 373–383.
[48] Zeghondy, B., Estelle, Y., and Taine, J., 2006, "Determination of the Anisotropic Radiative Properties of a Porous Material by Radiative Distribution Function Identification (RDFI)," Int. J. Heat Mass Transfer, **49**, pp. 2810–2819.
[49] Yang, Y. S., Howell, J. R., and Klein, D. E., 1983, "Radiative Heat Transfer Through a Randomly Packed Bed of Spheres by the Monte Carlo Method," ASME J. Heat Transfer, **105**, pp. 325–332.

Takashi Ozawa
Postdoctoral Fellow
Aerospace Research and Development
Directorate,
Japanese Aerospace Exploration Agency,
Chofu, Tokyo 182–8522 Japan
e-mail: takashi@chofu.jaxa.jp

Michael F. Modest
Distinguished Professor
Fellow ASME
Shaffer and George Professor of Engineering,
Science and Engineering Building, Rm. 392
University of California,
Merced, CA 95343
e-mail: MModest@eng.ucmerced.edu

Deborah A. Levin
Professor
Department of Aerospace Engineering,
Pennsylvania State University,
University Park, PA 16802
e-mail: dalevin@engr.psu.edu

Spectral Module for Photon Monte Carlo Calculations in Hypersonic Nonequilibrium Radiation

In this paper, efficient spectral modules and random number databases are developed for atomic and diatomic species for use in photon Monte Carlo (PMC) modeling of hypersonic nonequilibrium flow radiation. To model nonequilibrium flow conditions, the quasisteady state assumption was used to generate electronic state populations of atomic and diatomic gas species in the databases. For atomic species (N and O), both bound-bound transitions and continuum radiation were included and were separately databased as a function of electron temperature and number density as well as the ratio of atomic ion to neutral number density. For the radiating diatomic species of N_2^+*,* N_2*,* O_2*, and NO databases were generated for each electronic molecular electronic system. In each molecular electronic system, the rovibrational transition lines were separately databased for each electronic upper state population forming the electronic system. The spectral module for the PMC method was optimized toward computational efficiency for emission calculations, wavelength selections of photon bundles and absorption coefficient calculations in the ray tracing scheme.* [DOI: 10.1115/1.4000242]

Keywords: Monte Carlo, nonequilibrium, radiation, QSS, hypersonic

1 Introduction

In recent years, there has been great interest in modeling of high-speed reentry vehicles, such as Stardust [1–3] and the upcoming Crew Exploration Vehicle [4]. In these hypersonic reentry flows, radiation effects significantly influence the prediction of the heat shield design and efficiency [5]. For Stardust reentry flows, the ratio of radiative heat flux to convective heat flux was investigated in Ref. [6], and was found to be sufficiently high for altitudes lower than 80 km (e.g., 20% at 68.9 km) that coupling between flow field and radiation calculations is required. For hypersonic reentry flows, the ions and electrons inside the shock layer lead to complicated reactions among charged and neutral particles, which affect nonequilibrium atomic and molecular energy distributions and radiation behavior. Olynick et al. [2] applied a continuum Navier–Stokes flow solver loosely coupled to radiation and material thermal ablation models to predict the Stardust reentry flows at altitudes of 43–80 km and demonstrated the importance of coupling between flow field and radiation calculations. In their work, a simplistic quasi-1D tangent slab (TS) radiative transfer equation (RTE) solver was used assuming equilibrium conditions, and the radiation calculations cannot be expected to be accurate in highly nonequilibrium conditions.

To calculate radiation in nonequilibrium flows accurately, the nonequilibrium air radiation (NEQAIR) [7] code has been developed. In the NEQAIR code, the quasisteady state (QSS) assumption is used to determine the excited state populations of nonequilibrium gas species and, therefore, is considered the best line-by-line (LBL) solver for nonequilibrium flows. However, the NEQAIR LBL code, which includes a 1D tangent slab radiative transport solver, is so expensive that the code is not suitable for radiation calculations for 2D or 3D flow fields. Thus, in the work of Sohn et al. [8], a NEQAIR-based efficient databasing scheme of emission and absorption coefficients was developed. In this database, the QSS assumption is used to generate the electronic state populations of atomic and diatomic gas species. Emission and absorption coefficients for any given flow condition and wavelength range are accurately calculated using the database and its associated interpolation schemes as compared with NEQAIR results. In Ref. [9], the new database was used together with a 1D tangent slab RTE solver and the atomic radiation field was predicted for a Stardust computational fluid dynamics (CFD) simulation. The 1D RTE solver was integrated and loosely coupled with a hypersonic CFD solver. Coupling was shown to reduce the total heat load on the vehicle by about 3.5% at peak heating conditions and decreases the shock stand-off distance by 10%.

Although the NEQAIR-based database provides a means for accurate radiation calculations in nonequilibrium conditions, the 1D tangent slab radiative transport solver is not sufficiently accurate to simulate radiation for 2D or 3D flow fields. In addition, high-resolution LBL calculations require hundreds of thousands RTE solutions and become too expensive for 2D or 3D flow fields. For such cases, the photon Monte Carlo (PMC) method is accurate and can be more efficient for strongly nongray radiation fields and has been employed for such cases [10,11]. A general discussion of the Monte Carlo method for radiative transfer can be found in standard textbooks [12]. In this method radiative transfer is modeled by allowing each cell to emit its emission energy in the form of photon bundles (rays) into random directions. In Ref. [11], direct simulation Monte Carlo (DSMC) was used to study the impact of radiation on the flow, loosely coupled with the particle-based photon Monte Carlo (p-PMC) method of Wang and Modest [10] for a Stardust reentry flow field. In the p-PMC method employed in Ref. [11], emission and absorption coefficients for atomic N and O were calculated by our new NEQAIR-based line-by-line database [8]. However, it was found that tightly coupled computations between DSMC and the p-PMC are too expensive in the presence of millions of DSMC particles. Instead, a finite volume (FV) PMC method is presently being developed and close coupling between a FV-PMC and a CFD solver appears

---

Contributed by the Heat Transfer Division of ASME for publication in the JOURNAL OF HEAT TRANSFER. Manuscript received December 19, 2008; final manuscript received April 24, 2009; published online December 9, 2009. Assoc. Editor: Yogesh Jaluria.

more realistic. In order to couple a CFD solver with PMC radiation calculations, the time-consumption for flow field and radiation is approximately 3% and 97%, respectively. Even in such case, the PMC simulation will consume very substantial CPU time, making an efficient implementation crucial.

To carry out strongly nongray hypersonic PMC simulations with emission and absorption coefficients from many species, each depending on a large number of flow field variables, the computational efficiency of selecting wavelengths for photon bundles (rays) and of the computation of absorption coefficients at given wavelengths for each cell or each particle is crucial. In this work, we have developed new spectral modules and an emission random number database (ERND) for the PMC method to improve its computational efficiency and to solve its storage size issues. The newly developed spectral modules and random number databases can be used for both p-PMC and FV-PMC methods. Since monatomic and diatomic gases behave in a very different manner, radiatively speaking, separate databases have been constructed for the important monatomic (N, O) and diatomic (N_2^+, N_2, O_2, NO) radiating species.

2 Modeling of Spectral Module

The RTE for nonequilibrium hypersonic flow fields in the absence of scattering [13] may be written as

$$\frac{dI_{\lambda,\mathrm{tot}}}{ds} = \hat{s} \cdot \nabla I_{\lambda,\mathrm{tot}} = \varepsilon_{\lambda,\mathrm{tot}} - \kappa_{\lambda,\mathrm{tot}} I_{\lambda,\mathrm{tot}} \tag{1}$$

where $I_{\lambda,\mathrm{tot}}$ is the spectral radiative intensity of all species, $\varepsilon_{\lambda,\mathrm{tot}}$ is the (nonequilibrium) emission coefficient of all species, and $\kappa_{\lambda,\mathrm{tot}}$ is the absorption coefficient of all species. The total emission from a given cell of volume V_{cl} is

$$E_{\mathrm{emis,cl}} = \int_{V_{\mathrm{cl}}} \int_0^\infty \int_{4\pi} \varepsilon_{\lambda,\mathrm{tot}} d\Omega d\lambda dV_{\mathrm{cl}} = 4\pi \times Q_{\mathrm{emis,tot}} \times V_{\mathrm{cl}} \tag{2}$$

where $Q_{\mathrm{emis,tot}}$ is the total integrated emission energy per unit volume per steradian and is equal to the summation of $Q_{\mathrm{emis},i}$ of all species in the cell. To calculate the total emission energy, the following cell-based variables are required:

1. four temperatures $(T_{\mathrm{tr}}, T_{\mathrm{rot}}, T_{\mathrm{vib}}, T_e)$ (K)
2. radiating species (N, O, N_2^+, N_2, O_2, NO) number densities (cm^{-3})
3. N^+ and O^+ ion number densities (cm^{-3})
4. electron number density n_e (cm^{-3})

In general, to simulate nonequilibrium hypersonic flows, four temperatures can be calculated separately in DSMC [1], while in CFD codes, only two or three temperature models are used [9], and T_e can be assumed to be the same as T_{vib}. In the PMC method, the RTE is solved by tracing statistical photon bundles. This implies that the total energy carried by all emitted photon bundles must be equal to $E_{\mathrm{emis,cl}}$ as given by Eq. (2). So-called random number relations must be developed to obtain statistically meaningful locations, directions, and wavelengths of emitted bundles as explained in detail by Modest [12]. While locations and directions of photon emission are straightforward, emission wavelengths for a nonequilibrium gas mixture require special attention and are a focus of the present paper. In a hypersonic plasma, there are multiple radiating species, each with multiple dependencies. First, the emitting species for a given ray is selected, based on the ratio of emitting energies for each species. A random number R'_λ, uniformly distributed from 0 to 1, is compared with the ratio of emission energies. If

$$\frac{\sum_{i \le i_{\mathrm{sp}}-1} Q_{\mathrm{emis},i}}{Q_{\mathrm{emis,tot}}} < R'_\lambda < \frac{\sum_{i \le i_{\mathrm{sp}}} Q_{\mathrm{emis},i}}{Q_{\mathrm{emis,tot}}} \tag{3}$$

the index of the emitting species for the ray is i_{sp}. The random number for the wavelength selection is then adjusted

$$0 \le R_\lambda = \frac{R'_\lambda \times Q_{\mathrm{emis,tot}} - \sum_{i \le i_{\mathrm{sp}}-1} Q_{\mathrm{emis},i}}{Q_{\mathrm{emis},i_{\mathrm{sp}}}} \le 1 \tag{4}$$

Following Modest [12]

$$R_\lambda = \frac{Q_{\mathrm{emis},\lambda}}{Q_{\mathrm{emis}}} = \frac{\int_{\lambda_{\min}}^{\lambda} \varepsilon_\lambda d\lambda}{\int_{\lambda_{\min}}^{\lambda_{\max}} \varepsilon_\lambda d\lambda} \tag{5}$$

where λ is the corresponding wavelength of photon bundle emission from the i_{sp} species. A bisection method is used to select wavelengths of photon bundles.

2.1 Construction of Atomic Database. Emission random number databases (ERND) have been developed for conditions that occur in nonequilibrium flows, based on our NEQAIR-based emission and absorption coefficient database. Details on that database can be found in the work of Sohn et al. [8]. Briefly, in the atomic database, the excitation population is calculated using the QSS model as a function of electron temperature T_e, electron number density n_e, and the ratio of ion to neutral number density n^+/n_a. In the ERND, the atomic lines for N and O are databased and accumulated emission and absorption coefficient line strengths are precalculated as a function of T_e, n_e, and n^+/n_a. N and N^+, and O and O^+, respectively, are treated as single species since they have common bound-bound (bb) lines. The translational temperature is needed to determine the Doppler broadening line shape for each atomic line. Although the Doppler line shape is used as a default setting, the broadening line shape can be switched from the Doppler to the Voigt shape.

In addition to bb transitions, there are two other transition mechanisms, which lead to changes in electronic energy levels by emission and absorption of a photon, namely, transitions from a bound state to an ionized state, called bound-free (bf) transition or vice versa and transitions between two different continuum states, called free-free (ff) transitions. Bound-free radiation occurs when the upper state is ionized and the wavelength of the transition is determined by the free electron energy. For most hypersonic reentry flows the contribution from ff transitions is negligibly small. While the contribution of ff transitions are included as an option, in the default setting of the module ff transitions are not considered. In the ERND, bb transitions are separated from bf and ff transitions.

For bb transitions, the centerline wavelength λ_k (Å) and the accumulated normalized emission coefficients are stored for each line k, which is defined as

$$Q^*_{a,\mathrm{emis},k}(T_e, n_e, n^+/n_a) = \sum_{i \le k} \varepsilon^*_{a,i}(T_e, n_e, n^+/n_a) \tag{6}$$

i.e., the accumulated strength of all lines with $\lambda_i < \lambda_k$. The superscript $*$ denotes a normalized quantity (i.e., divided by n_a). $\varepsilon^*_{a,i}$ is the normalized emission coefficient in units of W/sr for an atomic line i and is obtained from

$$\varepsilon^*_{a,i}(T_e, n_e, n^+/n_a) = \varepsilon^{c,*}_{a,i} \times \frac{n_U}{n_a} \tag{7}$$

where $\varepsilon^{c,*}_{a,i}$ is the atomic normalized emission line strength of a bound-bound transition, which is a constant. The electronic state population, n_U, is calculated as

$$n_U = \left[F(T_e, n_e, i_U) \frac{n^+}{n_a} + G(T_e, n_e, i_U) \right] \times n_a \tag{8}$$

where i_U is an upper state electronic level between 1 and 22. $\varepsilon^{c,*}_{a,i}$, i_U, and F and G are acquired from our NEQAIR-based database, which contains $\varepsilon^{c,*}_{a,i}$ and i_U for each bb line and the F and G functions are databased for each electronic level from one to 22 for a given set of T_e and n_e values.

For N and O, 170 and 86 atomic lines are included in the databases, respectively, and are sorted in order of increasing wavelength. Based on investigations of hypersonic reentry flow fields [1,9], the important range of the electron temperature T_e has been identified as 1000–28000 K; similarly for electron number densities n_e, as 1×10^{13}–4×10^{16} cm^{-3}. For each electronic state i_U the functions F and G have been databased for equidistant values of $T_e^{0.1}$ (70 points) and $[\log(n_e)]^{0.1}$ (50 points), which was found to provide best accuracy with a minimum number of data points.

For bb transitions, the partially integrated emission is calculated as

$$\begin{aligned} Q^*_{a,\text{emis},\lambda} &= \int_{\lambda_{\min}}^{\lambda} \varepsilon^*_{a,\lambda}(T_e,n_e,n^+/n_a,T_{\text{tr}})d\lambda = \sum_{i\le k_1}\varepsilon^*_{a,i}(T_e,n_e,n^+/n_a) \\ &\quad + \sum_{k_1<i\le k_2}\int_{\lambda-b_{\text{hw,max}}}^{\lambda}\varepsilon^*_{a,\lambda,i}(T_e,n_e,n^+/n_a,T_{\text{tr}})d\lambda \\ &= Q^*_{a,\text{emis},k_1}(T_e,n_e,n^+/n_a) + \sum_{k_1<i\le k_2}\varepsilon^*_{a,i}\int_{\lambda-b_{\text{hw,max}}}^{\lambda}\phi_i(\lambda)d\lambda \end{aligned} \tag{9}$$

where $\phi(\lambda)$ is the line broadening function. In Eq. (9), first the line indices, k_1 and k_2, are selected as follows: k_1 is the maximum integer with $\lambda_{k1}<\lambda-b_{\text{hw,max}}$, where $b_{\text{hw,max}}$ is a maximum half width of line broadening that needs to be considered (set to a constant value of 0.4 Å) and k_2 is the maximum integer with $\lambda_{k2}<\lambda+b_{\text{hw,max}}$. In other words, k_1+1 is the first line (in order of increasing λ), whose ϕ_λ is not yet totally integrated, while k_2 is the last line, which is affected at all be the integration. To determine k_1 and k_2, the number of accumulated lines from $\lambda_{\min}$ to a given wavelength is stored for 800–13,200 Å with a resolution of 0.1 Å. The arrays contain k_1 and k_2 as a function of λ, where $k_{1,\text{db}}(\lambda)$ is the number of lines for which $\lambda_i<\lambda-b_{\text{hw,max}}$ and $k_{2,\text{db}}(\lambda)$ is the number of lines for which $\lambda_i<\lambda+b_{\text{hw,max}}$.

As seen from Eqs. (7) and (8), $\varepsilon^*_{a,i}$ is proportional to n^+/n_a, and thus, the accumulated normalized emission of lines can be expressed as

$$Q^*_{a,\text{emis},k} = A_k \times \frac{n^+}{n_a} + B_k \tag{10}$$

In the ERND, A_k and B_k are stored for each atomic line at all different electron temperature and number density data points.

For bf and ff transitions, partially integrated normalized emission as a function of λ, is stored for each T_e, n_e, and n^+/n_a condition. For bf and ff transitions, the considered wavelength range is $\lambda=500-6000$ Å with a resolution of $\Delta\lambda=10$ Å.

The size of the ERND, including the accumulated emission lines for bb lines, the integrated emission for bf and ff transitions and k_1 and k_2 information, is approximately 31 MB and 26 MB for N and O, respectively. In Fig. 1, the line index database k_1 and k_2-k_1 for N are shown. If k_2 is not the same as k_1 at a wavelength, integrated line broadening is applied to the last term in Eq. (9). As seen from Fig. 1, the maximum of k_2-k_1 is three and, thus, partial line broadening must be applied to at most three atomic lines. For most of the lines, we do not have to consider any overlapping of lines.

2.2 Implementation of Atomic Spectral Module. In the spectral module species indices of 1 and 2 are assigned for N and O, respectively. To utilize the atomic spectral module, one calls subroutines that read λ_i, $\varepsilon^{c,*}_{a,i}$, $F(T_e,n_e,i_U)$, and $G(n_e,T_e,i_U)$ from the database for each species [8]. The integrated emission energy of each species per unit volume, $Q_{\text{emis},i}$, is interpolated for atomic species following Eq. (9), with $Q_{\text{emis}}=n_a\times Q^*_{\text{emis}}$. For atomic species, T_e, n_a, n_a^+, and n_e must be known to calculate the integrated emission energy. Next, a bisection method is used to select a wavelength following Eq. (5). To this purpose a two-stage process is applied, a coarse preselection, followed by a correction. For both bb and continuum transitions, a spline interpolation scheme is used to determine the normalized emission coefficient at a given T_e and n_e. For a given n^+/n_a, the linear dependence is applied. To reduce the CPU time for spline interpolation calculations, we use linear interpolation for the preselection of wavelength.

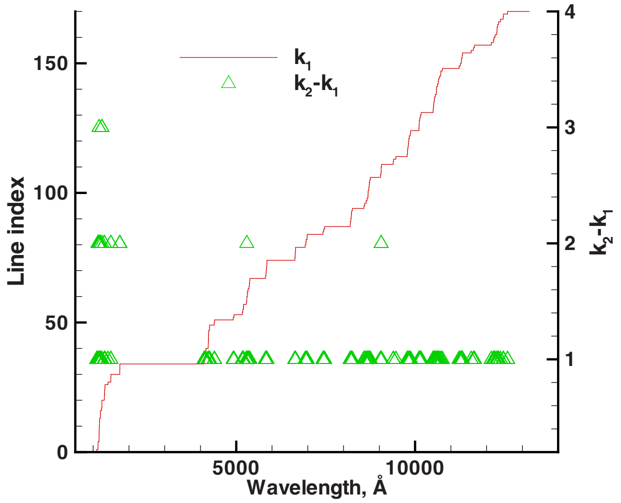

Fig. 1 Line index database of k_1 and k_2 as a function of wavelength for N

The bisection method is used to find the resulting line (e.g., between 1 and 170 for N). In the preselection, we only consider accumulated bb line strengths and continuum contributions that are calculated using linear interpolation for T_e and n_e and n^+/n_a. Line broadening is not applied in the preselection calculations. First the line index k is identified where k with $Q^*_{a,\text{emis},k}/Q^*_{a,\text{emis}}<R_\lambda$. The accumulated atomic line strength $Q^*_{a,\text{emis},k}$ from $i=1$ to k is read from the ERND and $\varepsilon^*_{a,i}$ is calculated as

$$\varepsilon^*_{a,i} = Q^*_{a,\text{emis},i} - Q^*_{a,\text{emis},i-1} \tag{11}$$

For continuum radiation, linear interpolation is used in terms of wavelength. The contributions of bb and bf transitions are summed up at a given wavelength.

Once k has been identified, the limiting line numbers k_1 and k_2 for use in Eq. (9) are found with the aid of the pretabulated accumulated lines versus wavelength array. A more accurate wavelength is then found by the bisection method from a rearranged Eq. (9)

$$(R_\lambda Q^*_{a,\text{emis}} - Q^*_{a,\text{emis},k1}) = \sum_{k_1<i\le k_2}\varepsilon^*_{a,i}\overline{\phi_i}(\lambda) \tag{12}$$

where the $\overline{\phi_i}(\lambda)$ come from pretabulated array of partially integrated line broadening functions. In the case of Doppler broadening this array is a function of $|\lambda-\lambda_i|/b_D$ only. For Voigt broadening, it is a two-parameter dependence, also including the ratio of Lorentz-to-Doppler broadening widths. The bisection method is applied until a λ accurate to 10^{-3} Å is found after which linear interpolation is applied.

Since the emitted ray's energy may be absorbed by any species, the absorption coefficient of all species must be known at the emission wavelength. To this purpose, the range of line numbers $k_{\text{ab},1}<i\le k_{\text{ab},2}$ that can contribute to the absorption coefficient is

Table 1 Random number databases for six radiating species

Species	i_{sp}	Number of bands	Transitions
N	1	1	170 bb transitions
O	2	1	86 bb transitions
N_2^+	3	2	$N_2^+(1-)$, N_2^+ (Meinel)
N_2	4	5	$N_2(1+)$, $N_2(2+)$, N_2 (Birge–Hopfield 2), N_2 (Birge–Hopfield), N_2 (Carrol–Yoshino)
O_2	5	1	O_2 (Schumann–Runge)
NO	6	18	NO(β), NO(γ), NO(Δ), NO(ε), NO(β'), NO(γ'), NO(C-A), NO(D-A), NO(B$'$-B), NO(E-C), NO(F-C(3)), NO(H-C), NO(H$'$-C), NO(E-D(5)), NO(F-D(3)), NO(H-D), NO(H$'$-D), NO(IR)

determined for all species, using the k_1- and k_2-arrays employed in Eq. (9).

The absorption coefficient, $\kappa_\lambda(T_e, n_e, n^+/n_a, T_{\mathrm{tr}})$, is then calculated from the database [8] on the fly during ray tracing. The absorption coefficient of the ith bb line κ_i can be expressed as

$$\kappa_i = \kappa_{a,i}^{c,*} n_U \left(\frac{n_L}{n_U} - 1 \right)$$

$$= \kappa_{a,i}^{c,*} n_a \left[(F(i_L) - F(i_U)) \frac{n^+}{n_a} + G(i_L) - G(i_U) \right] \tag{13}$$

For calculations, $\kappa_{a,i}^{c,*}$, F, and G are obtained from databases (see Ref. [8]). In each cell, the F and G functions are interpolated in terms of electron temperature and number density. Using the interpolated F and G functions, absorption cross sections for lines between $k_{\mathrm{ab},1}$ and $k_{\mathrm{ab},2}$ are calculated. The half-widths for line broadening for lines between $k_{\mathrm{ab},1}+1$ and $k_{\mathrm{ab},2}$ are calculated, and line broadening is applied to the selected atomic lines. The bb absorption coefficient at a given wavelength is calculated as the summation of $\kappa_{i,\lambda}$ from $k_{\mathrm{ab},1}+1$ to $k_{\mathrm{ab},2}$. The bf and ff absorption coefficients at a given wavelength are calculated separately from the database [8] and are added.

2.3 Construction of Database for Molecules. For molecular radiation, N_2^+, N_2, O_2, and NO are considered in this work. A species index is assigned for each species as follows: three for N_2^+, four for N_2, five for O_2, and six for NO. In the molecular species database the excitation population is again calculated using the QSS model as a function of temperatures T_{tr}, T_{rot}, T_{vib}, T_e, n_e, and the appropriate heavy species' number densities n_h. First, the electronic systems for each electronic transition are separated, leading to two electronic systems for N_2^+, five for N_2, one for O_2, and 18 for NO based on the NEQAIR code for a total of 26 electronic systems as summarized in Table 1. For each molecular electronic system, an expression of normalized emission line strengths for rovibrational transitions can be found in Ref. [8] and the emission coefficients can be calculated as

$$\varepsilon_{\lambda,i} = \varepsilon_{m,i}^{c,*} n_U \phi_{i,\lambda} \tag{14}$$

In the database of Sohn et al. [8], $\varepsilon_m^{c,*}$, a constant, is stored for each rovibrational line for each molecular electronic system.

The rovibrational normalized line strength, $\varepsilon_{m,i}^{\mathrm{RV}}(T_{\mathrm{rot}}, T_{\mathrm{vib}})$ is defined as $\varepsilon_{m,i}/n_U^e(2J_U+1)$ and is given by

$$\varepsilon_{m,i}^{\mathrm{RV}} = \frac{\varepsilon_{m,i}^{c,*}}{(Q_{\mathrm{RV}})_U} \times \exp\left[-\frac{hc}{k_B} \left(\frac{G(V_U)}{T_{\mathrm{vib}}} + \frac{F(J_U)}{T_{\mathrm{rot}}} \right) \right] \tag{15}$$

with λ_i, $\varepsilon_{m,i}^{c,*}$, $-hcG(V_U)/k_B$, and $-hcF(J_U)/k_B$ databased [8], while the rovibrational partition function $(Q_{\mathrm{RV}})_U$ is calculated on the fly. The emission line strength for line i can simply be expressed as

$$\varepsilon_{m,i} = n_U^{e,d}(T_{\mathrm{tr}}, T_{\mathrm{rot}}, T_{\mathrm{vib}}, T_e, n_e, n_h) \times \varepsilon_{m,i}^{\mathrm{RV}}(T_{\mathrm{rot}}, T_{\mathrm{vib}}) \tag{16}$$

where $n_U^{e,d}$ is defined as $n_U^e \times (2J_U+1)$ and is calculated by the QSS method as a function of T_{tr}, T_{rot}, T_{vib}, T_e, n_e, and n_h.

Similar to the atomic species in Eq. (9), the partially integrated emission for each electronic system is calculated from

$$\begin{aligned} Q_{\mathrm{emis},\lambda}(i_{\mathrm{band}}) &= \int_{\lambda_{\min}}^{\lambda} \varepsilon_\lambda(T_e, n_e, n_a, n_a^+, T_{\mathrm{rot}}, T_{\mathrm{vib}}, T_{\mathrm{tr}}) d\lambda \\ &= n_U^{e,d}(T_e, n_e, n_a, n_a^+) \left[\sum_{i \le k_1} \varepsilon_{m,i}^{\mathrm{RV}}(T_{\mathrm{rot}}, T_{\mathrm{vib}}) \right. \\ &\quad \left. + \sum_{k_1 < i \le k_2} \int_{\lambda - b_{\mathrm{hw,max}}}^{\lambda} \varepsilon_{\lambda,i}^{\mathrm{RV}}\ (T_{\mathrm{rot}}, T_{\mathrm{vib}}, T_{\mathrm{tr}})) d\lambda \right] \\ &= n_U^{e,d}(T_e, n_e, n_a, n_a^+) \left[Q_{m,\mathrm{emis},k_1}^{\mathrm{RV}}(T_{\mathrm{rot}}, T_{\mathrm{vib}}) \right. \\ &\quad \left. + \sum_{k_1 < i \le k_2} \varepsilon_{\lambda,i}^{\mathrm{RV}} \int_{\lambda - b_{\mathrm{hw,max}}}^{\lambda} \phi_i(\lambda) d\lambda \right] \end{aligned} \tag{17}$$

In this work, the accumulated emission line strength $Q_{m,\mathrm{emis},k}^{\mathrm{RV}}(T_{\mathrm{rot}}, T_{\mathrm{vib}})$ is databased for each rotational and vibrational temperature in the ERND. The modified upper electronic state population $n_U^{e,d}$ is calculated on the fly for each flow condition. The overall emission at a given wavelength for each species is the summation over all molecular electronic systems. The ERND is prepared separately for each molecular electronic system. For molecular radiation there are too many rovibrational lines to save all line information for all rotational and vibrational conditions. Similar to what was shown in Fig. 1, Fig. 2 shows the line index of k_1 and k_2 as a function of wavelength for the $N_2^+(1-)$ transition molecular electronic system. For this system, the total number of lines is 122,606 and the maximum of $k_2 - k_1$ is 112 as shown in the figure. Therefore, for most of the lines, we do have to consider overlapping of lines for molecules. Instead of storing the line-by-line information, $Q_{m,\mathrm{emis},j_{\mathrm{db}}}^{\mathrm{RV}}$ is stored with a resolution of $\Delta\lambda_{j_{\mathrm{db}}}$ for each rotational and vibrational temperature and the total number of lines for $\lambda_i < \lambda_{\max}$ for each molecular electronic system is also stored. $Q_{m,\mathrm{emis},j_{\mathrm{db}}}^{\mathrm{RV}}$ is the accumulated $\varepsilon_{m,i}^{\mathrm{RV}}$ in units of W/sr between $\lambda_{\min}$ and $\lambda_{j_{\mathrm{db}}}$, where $\lambda_{j_{\mathrm{db}}}$ is the j_{db}-th wavelength in the database (equally spaced with resolution $\Delta\lambda_{\mathrm{db}}$). Between the data points, the emission line strength of individual lines $\varepsilon_{m,i}^{\mathrm{RV}}$ is computed in the main PMC calculations whenever necessary. In this manner the values of k_1 and k_2 similar to the atomic case are determined. For each rotational and vibrational condition, the partition function Q_{RV}, is calculated.

As for T_e, described in the atomic database, rotational and vibrational temperatures are taken to range between 1000 and

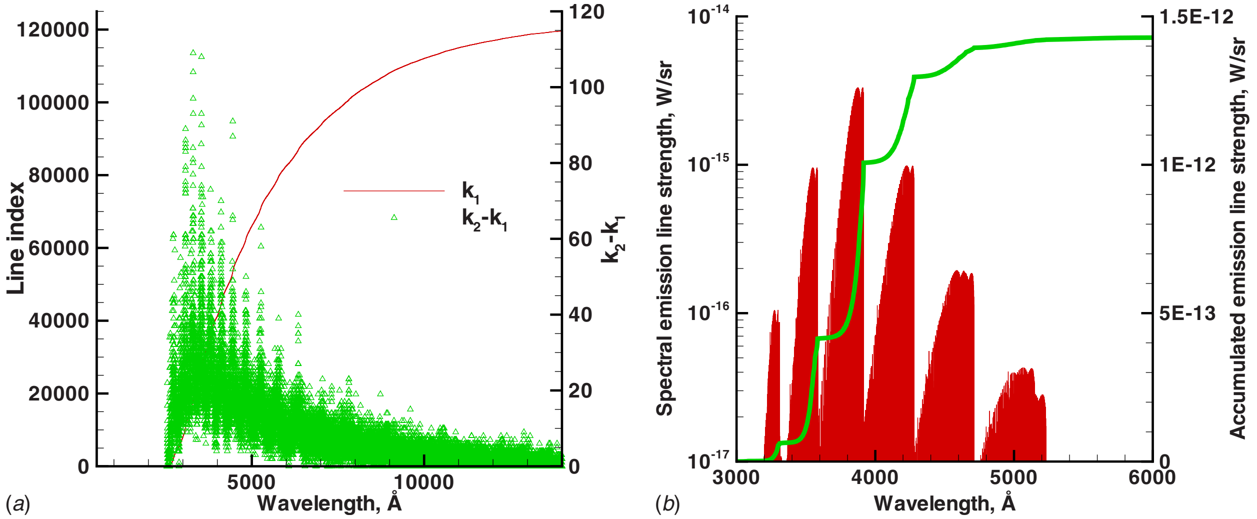

Fig. 2 Line index database of k_1 and k_2 as a function of wavelength (left) and spectral normalized emission lines and accumulated lines at temperatures of 5000 K (right) for $N_2^+(1-)$ transition molecular electronic system

28,000 K. The values have been databased for equidistant values of $T_{\text{rot}}^{0.1}$ (35 points) and $T_{\text{vib}}^{0.1}$ (35 points). For all electronic systems, a minimum wavelength λ_{min}, a maximum wavelength λ_{max}, and the wavelength resolution $\Delta\lambda_{\text{db}}$ are specified. At the default setting, λ_{min} and λ_{max} are 500 Å and 20,000 Å, respectively, and $\Delta\lambda_{\text{db}}$ is set to 2 Å. λ_{min} and λ_{max} can be different for each molecular electronic system but $\Delta\lambda_{\text{db}}$ is assumed to be the same constant value for all species. The information for k_1 and k_2 at a given wavelength $\lambda_{j_{\text{db}}}$, is also databased for each molecular electronic system. At the default setting, the ERND size is approximately 63 MB for each molecular electronic system. Figure 2 also shows the spectral normalized emission lines, $\varepsilon_{m,i}^{\text{RV}}$ and accumulated emission lines $Q_{m,\text{emis},j_{\text{db}}}$ for the $N_2^+(1-)$ transition molecular electronic system at temperatures equal to 5000 K. This shows an example of the ERND, indicating that for this electronic system strong lines are located between 3850 Å and 3900 Å.

2.4 Implementation of Molecular Spectral Module.

To utilize the molecular spectral module, one needs to specify the molecular transition electronic systems to be considered. One sets the number of molecular species, and the number of electronic band systems. At the default setting, the numbers are set to four and 26, respectively, (the ones listed in Table 1). Each molecular electronic system to be included in the molecular radiation calculations is set individually as done in NEQAIR. The molecular line information λ_i, $\varepsilon_{m,i}^{c,*}$, $-hcG(V_U)/k_B$, $-hcF(J_U)/k_B$, $-hcG(V_L)/k_B$, and $-hcF(J_L)/k_B$ is read from our database [8] to calculate emission and absorption rovibrational line strengths.

In the main PMC calculations, one calculates electronic state populations and partition functions for each cell and each molecular species prior to ray tracing. The QSS calculations are performed by solving the four electronic states for the cell conditions on the fly. Electronic state populations $n^{e,d}$ $(T_{\text{tr}}, T_{\text{rot}}, T_{\text{vib}}, T_e, n_e, n_h)$ and partition functions $(Q_{\text{RV}})_U$ are calculated. These calculations need to be performed for all cells for both emission and absorption.

To calculate the integrated normalized emission energy per unit volume, $Q_{m,\text{emis}}^{\text{RV}}$, which is integrated from a minimum to a maximum wavelength in Eq. (17), one first obtains $Q^{\text{RV}}_{m,\text{emis},j_{\text{db,max}}}$ from the ERND and interpolates the data in terms of rotational and vibrational temperatures. The upper state level i_U, is read from our NEQAIR-based database and $Q_{m,\text{emis}}$ is multiplied by the upper state population $n_U^{e,d}$. The total integrated emission energy for the species per unit volume is calculated as the summation of $Q_{m,\text{emis}}$ over the electronic systems. The total emission energy of a cell is calculated from Eq. (2), and the number of photon bundles to be emitted from the cell is decided on. Similar to the atomic spectral module, based on the ratio of $Q_{\text{emis},i}$ for a species to $Q_{\text{emis,tot}}$ we determine, which species is emitting a photon bundle, by comparison with a random number, which is then scaled for the wavelength selection by Eq. (4).

For molecules, $Q_{m,\text{emis},j_{\text{db}}}$ in W/cm^3/sr is calculated as

$$Q_{m,\text{emis},j_{\text{db}}}(i_{\text{sp}}) = \sum_{\text{bands}} n_U^{e,d} Q^{\text{RV}}_{m,\text{emis},j_{\text{db}}} \tag{18}$$

The emission wavelength is found in a two-stage process very similar to the atomic species case. First limiting line numbers k_1 and k_2 are found, in this case from $Q^{\text{RV}}_{m,\text{emis},j}$, but in $\Delta\lambda_{\text{db}}$ increments rather than for each individual line. Consequently, for the many lines of diatomic species, k_1 and k_2 may overshoot somewhat on the safe side. After k_1 and k_2 have been identified, the actual emission wavelength is found by bisection of the remainder, identical to the atomic species as indicated in Eq. (12).

Once a wavelength is selected, the absorption coefficient $\kappa_\lambda(T_{\text{tr}}, T_{\text{rot}}, T_{\text{vib}}, T_e, n_e, n_h)$, is calculated similar to the atomic species: the half width for line broadening at a given wavelength is calculated and $k_{\text{ab},1}$ and $k_{\text{ab},2}$ are read from the line index databases. Line broadening is then applied to lines between $k_{\text{ab},1}+1$ and $k_{\text{ab},2}$. The effective volumetric absorption coefficient line strength for a rovibrational transition line is given by

$$\kappa_{i,v} = \varepsilon_{m,i} \times \frac{\lambda_i^5}{2hc^2} \times \left(\frac{n_L}{n_U} - 1\right) \tag{19}$$

where

$$\frac{n_L}{n_U} = \frac{n_L^{e,d}}{n_U^{e,d}} \frac{(Q_{\text{RV}})_U}{(Q_{\text{RV}})_L} \exp\left[-\frac{hc}{k_B}\left(\frac{G(V_U)-G(V_L)}{T_{\text{vib}}} + \frac{F(J_U)-F(J_L)}{T_{\text{rot}}}\right)\right] \tag{20}$$

For rovibrational transition lines with a center wavelength of $|\lambda - \lambda_i| < 3 \times b_{\text{hw},\lambda}$, the line broadening is applied, and the absorption coefficient for the species is summed over the molecular electronic systems.

3 Results and Discussion

To demonstrate the validity and efficiency of the spectral module using the ERND, three test cases have been carried out and are presented in this section. The first case investigates the computa-

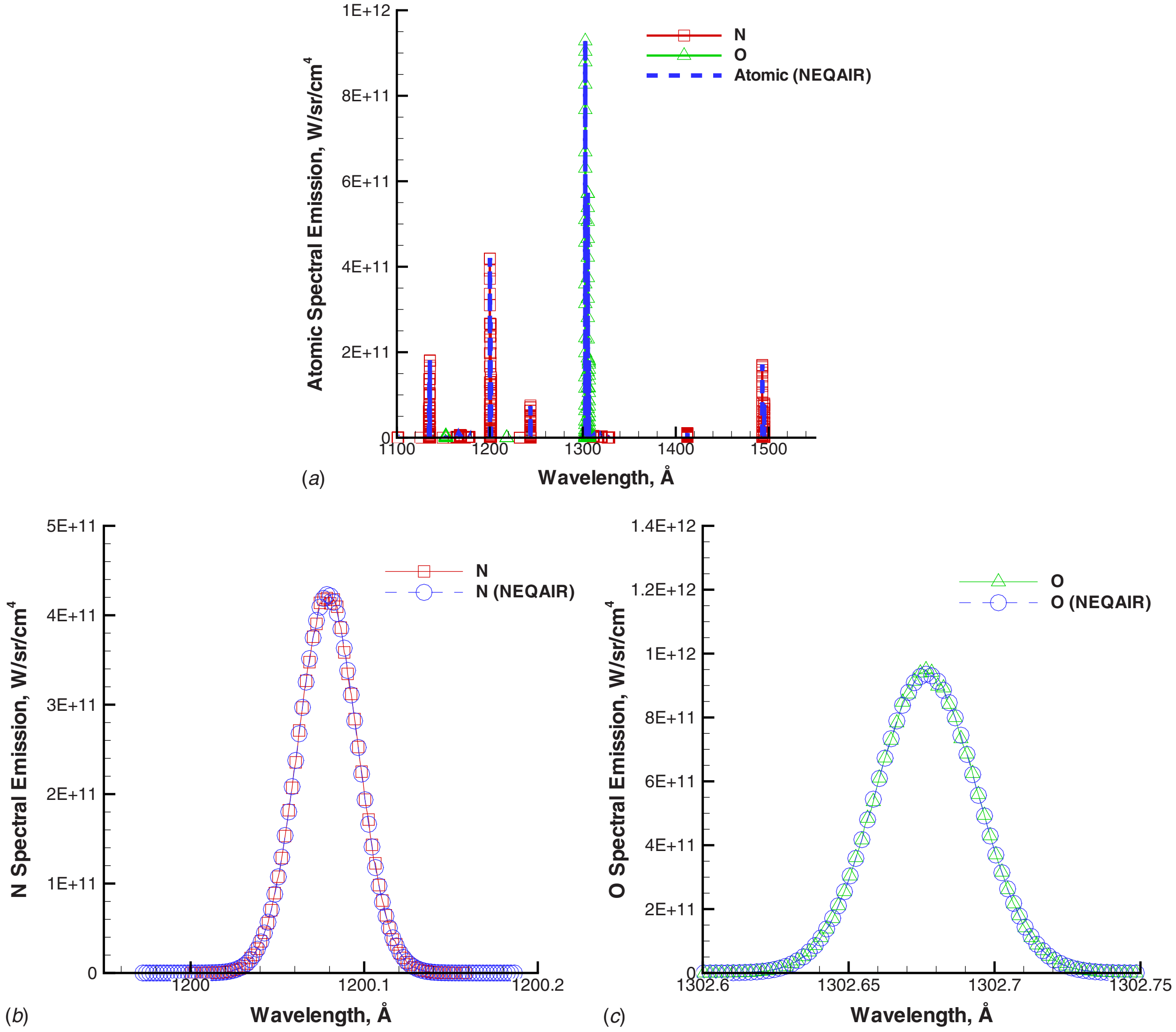

Fig. 3 Comparison of spectral emission of atomic species between spectral module and NEQAIR results

tional efficiency for wavelength selection in the PMC ray tracing scheme for both atomic and molecular spectral modules as well as the accuracy of the sampled spectral emission distributions. One arbitrary cell condition is used for emission calculations and both atomic and molecular spectral emission obtained using the spectral module are compared with NEQAIR spectral results. The second case investigates the computational efficiency to carry out a full FV-PMC calculation using a total number of 10,000 cells. Necessary steps for the FV-PMC method were considered and the CPU time was measured for each step. Finally, the FV-PMC method was used to simulate atomic radiation for a one-dimensional disk with the Stardust stagnation line flow field at 68.9 km. The flow field was obtained with a DSMC simulation and the radiative source $\nabla \cdot q$ was compared with NEQAIR tangent slab results. For these demonstrations, dual 2.4 GHz AMD Opteron Processors were used.

3.1 Accuracy and Spectral Emission Investigation. One arbitrary cell condition was used to examine the accuracy and wavelength selection efficiency of spectral modules using the ERND. Emission energies of four species (N, O, N_2^+, and N_2) were considered. Two transitions for N_2^+, $N_2^+(1-)$ and N_2^+ (Meinel), and two major transitions for N_2, $N_2(1+)$ and $N_2(2+)$, were considered, respectively. In order to have the emission energy of each species to be of the same order, the cell condition was selected as follows. Temperatures $(T_{\mathrm{tr}}, T_{\mathrm{rot}}, T_{\mathrm{vib}}, T_e)$ are 31,113 K, 18,027 K, 12,280 K, 14,888 K, respectively. Number densities of radiating species (N, O, N_2^+, N_2, N^+, and O^+) and electrons were 1.34×10^{16}, 1.01×10^{17}, 2.27×10^{16}, 1.75×10^{19}, 1.59×10^{14}, 1.24×10^{14}, 5.02×10^{14}, respectively. Using this cell condition, emission energies per unit volume $Q_{\mathrm{emis}}(i_{\mathrm{sp}})$ were calculated using the spectral module and ERND and for N, O, N_2^+, and N_2, are 790.9 $\mathrm{W/cm^3/sr}$, 779.3 $\mathrm{W/cm^3/sr}$, 522.1 $\mathrm{W/cm^3/sr}$, and 498.9 $\mathrm{W/cm^3/sr}$, respectively. 5×10^6 samples were taken using this cell condition, and the number of photon bundles for each emitting species were 1,523,992, 1,502,284, 1,002,381, 895,369, respectively. The ratio of number of samples for each species agree well with the ratio of emission energies.

Considering only atomic N and O radiation, the CPU time is approximately 220 s for 5×10^6 wavelength selections. On the other hand, for the two diatomic species N_2^+ and N_2 only, the CPU time is approximately 1600 s. For diatomic species, one needs to calculate several electronic systems for each species and, in addition, in each molecular electronic system there are many rovibrational transition lines, making them computationally more expensive than atomic species.

In Fig. 3, spectral emission of atomic species using the spectral module with the ERND is compared with NEQAIR. The photon bundle energy per sample is calculated as $Q_{\mathrm{emis,tot}}/\Delta\lambda/N_{\mathrm{sample}}$.

Table 2 Computational time

Step	Species	Cells	Samples	CPU time (s)
1	N, O	10,000		6
2	N_2^+, N_2	10,000		38
3	N, O, N_2^+, N_2	10,000		1
4	Selected	10,000	10	6
5	Selected	10,000	10	8

This energy is added to a wavelength column (equally spaced in $\Delta\lambda = 0.005$ Å increments), if the spectral module selects a wavelength within the column for the sample. Most selected samples were wavelengths within bb transition lines and good agreement is shown between the spectral module and the NEQAIR results. With 10×10^6 samples, the difference between the spectral module result and NEQAIR is less than 1% in the top figure. With 1×10^6 samples, the difference is approximately 5%. Detailed comparisons of spectral emission between the spectral module and NEQAIR for the strongest lines at 1200.079 Å for N and 1302.677 Å for O are also shown in the figure. Good agreement is found between the two results and line broadening (here Doppler) is well represented by the spectral module. At any selected wavelength, spectral absorption coefficients also agreed well with those of NEQAIR. Accuracy investigation was performed for the spectral emission of N_2^+ between 3000 Å and 5000 Å using the spectral module with ERND with a resolution of 0.1 Å. Since there are so many lines for molecules, more samples are required to reproduce spectral emission. For N_2^+ spectral emission, the difference between the spectral module and NEQAIR is less than 5% with 10×10^6 samples and 2% with 50×10^6 samples.

3.2 Computational Efficiency Investigation. In this subsection, the computational efficiency of FV-PMC calculations is investigated. Considering the FV-PMC method for an actual flow simulation, the total number of cells was set to 10,000. Temperatures and number densities in each cell were randomly chosen. Necessary steps for the FV-PMC method were considered and the CPU time was measured for each step. Four species (N, O, N_2^+, and N_2) were considered, and the ERNDs for these species were created. In this case, for N_2^+, two ERNDs were created for the two molecular electronic systems, $N_2^+(1-)$ and N_2^+ (Meinel). For N_2, two major electronic systems, $N_2(1+)$ and $N_2(2+)$, were selected from among five molecular electronic systems, and ERNDs were created for them. In order to employ the FV-PMC method for atomic and molecular radiation, the necessary steps are as follows:

1. F_i and G_i function interpolations
2. $n^{e,d}$ and Q_{RV} evaluations for molecules
3. total emission evaluation for four species in each cell
4. wavelength selection for ten photon bundles in each cell
5. ten absorption coefficients for each photon bundle

For each procedure, computational time was calculated and compared in Table 2. Step 1 is required to determine absorption coefficients of atomic species, and a spline interpolation scheme is used for electron temperature and linear interpolation for electron number density. In step 2 one needs to calculate the electronic excited states for each cell solving the 4×4 matrix in the QSS assumption. Also, for the partition function calculations for each electronic level, the Q_{RV} is calculated as the summation over all vibrational and rotational levels. This can be improved if Q_{RV} is databased as a functions of T_{rot} and T_{vib}. In step 4, one needs to select a wavelength for each photon bundle and the total number of photon bundles is 100,000. In step 5, the total number of absorption coefficient calculations is 1×10^6. Note that this number depends on the optical thickness of the flow and how far the photon bundle travels over cells. As one can see, the computational times for steps 3–5 are small. However, step 2 is more expensive compared with other procedures but efficient enough to allow inclusion of molecular radiation in tight coupling between the FV-PMC method and a flow field solver. During the development of the present spectral modules this test was used to identify inefficiencies in each individual schemes. The present results are for the optimized schemes described in this paper. All in all, the spectral module is so efficient that the FV-PMC method for both atomic and molecular radiation can be tightly coupled with a flow field solver.

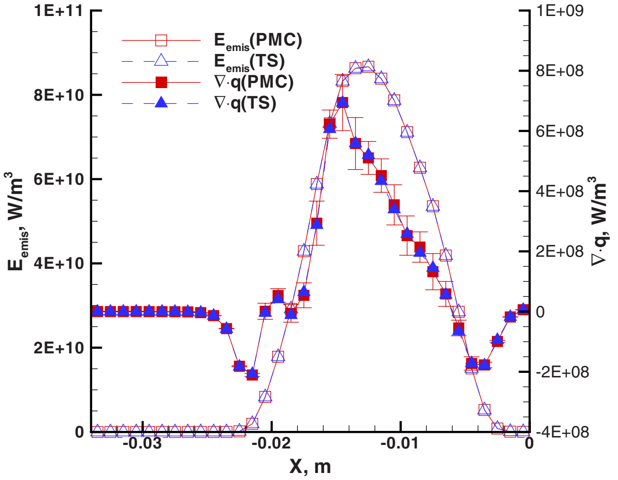

Fig. 4 Comparison of emission and $\nabla\cdot q$ of N and O gas mixture along the stagnation line between the PMC and TS (NEQAIR)

3.3 Full Flow Field Monte Carlo Simulation. A full demonstration of our spectral module was performed using the Stardust reentry flow field at 68.9 km, as calculated by a DSMC simulation [11]. The Stardust stagnation line flow field at 68.9 km mapped to a one-dimensional disk (34×5 cells) was used in the calculation to allow comparison with NEQAIR, which is limited to 1D (tangent slab) solutions and only atomic radiation was considered in the comparison [14]. Figure 4 shows combined N and O contributions to local volumetric emission $4\pi Q_{emis}$ and the local radiative source

$$\nabla \cdot q = 4\pi Q_{emis} - \int_0^\infty \int_{4\pi} \kappa_\lambda I_\lambda d\Omega d\lambda \qquad (21)$$

It is seen that agreement is excellent, well within one standard variation in the PMC results. For the PMC method, the standard variation in $\nabla \cdot q$ is set to 0.1 and the total number of photon bundles is approximately 250×10^6. Because this case is optically very thick and almost 1D, PMC calculations are more expensive than those for NEQAIR.

4 Conclusions

New efficient spectral modules and ERNDs have been developed for both atomic and diatomic species to allow for PMC calculations of hypersonic nonequilibrium flow radiation. The QSS assumption was used to generate electronic state populations of atomic and diatomic gas species. By using the QSS assumption, the spectral module can produce accurate spectral emission coefficients for nonequilibrium flows and can select wavelengths for photon bundles efficiently. For atomic N and O, bb transitions and continuum radiation were databased separately. For the bb contribution, all accumulated bb line strengths were databased as a function of electron temperature and number density as well as the ratio of ion to neutral number density. For continuum radiation, partially integrated emission was databased with a constant resolution wavelength. For the diatomic species N_2^+, N_2, O_2, and NO, ERNDs were generated for each electronic molecular electronic system. In each molecular electronic system, the accumulated rovibrational transition lines were divided by the electronic upper state population for the electronic system, and the normalized lines were stored with a resolution of 2 Å as a function of rotational and vibrational temperatures. To improve the computational efficiency, a bisection scheme in terms of line indices was implemented for preselection of the wavelength range and another bisection in terms of wavelength was performed after the preselection. The developed spectral module optimizes computational efficiency for emission calculations, wavelength selections of photon bundles, and absorption coefficient calculations in the ray tracing schemes used in the PMC method.

Acknowledgment

The research performed at the Pennsylvania State University was supported by NASA through Grant No. NNX07AC47A.

Nomenclature

b_{hw} = half width of the Doppler broadening, Å
c = speed of light, 2.9979×10^{10} cm/s
e = electron charge, 4.8030×10^{10} statcoul
E = energy, W
F = rotational energy quantum level for a molecule, cm^{-1}
F_i = assembled collisional and radiative coefficient of electronic state i, dimensionless
G = vibrational energy quantum level for a molecule, cm^{-1}
G_i = assembled collisional and radiative coefficient of electronic state i, dimensionless
h = Planck's constant, 6.6262×10^{-34} J s
i_{sp} = species index
I_λ = spectral intensity, $\mathrm{W/cm^2/sr/Å}$
J = rotational quantum number, dimensionless
k = line index
k_B = Boltzmann's constant, 1.3806×10^{-23} J/K
n = number density, cm^{-3}
$n_U^{e,d}$ = modified upper electronic state population of molecule, $n_U^{e,d} = n_U^e \times (2J_U + 1)$
Q_{emis} = integrated emission coefficient, $\mathrm{W/cm^3/sr}$
$Q_{\mathrm{emis},\lambda}$ = partially integrated emission coefficient, $\mathrm{W/cm^3/sr}$
Q_{RV} = rovibrational partition function, dimensionless
R = uniform random number between 0 and 1
T = temperature, K
V_{cl} = volume of a cell, cm^3
ε_λ = emission coefficient, $\mathrm{W/cm^3/sr/Å}$
ε_i = emission line strength at the centerline, $\mathrm{W/cm^3/sr}$
κ_λ = absorption coefficient, cm^{-1}
κ_i = absorption coefficient line strength, dimensionless
λ = wavelength, Å
$\phi(\lambda)$ = line broadening function, $\mathrm{Å}^{-1}$
$+$ = ion
RV = rotational and vibrational temperature dependence (divided by $n_U^{e,d}$)
$*$ = normalized quantity

References

[1] Ozawa, T., Zhong, J., and Levin, D. A., 2008, "Development of Kinetic-Based Energy Exchange Models for Non-Continuum, Ionized Hypersonic Flows," Phys. Fluids, **20**(4), p. 046102.
[2] Olynick, D., Chen, Y.-K., and Tauber, M. E., 1999, "Aerothermodynamics of the Stardust Sample Return Capsule," J. Spacecr. Rockets, **36**(3), pp. 442–462.
[3] Park, C., 2007, "Calculation of Stagnation-Point Heating Rates Associated With Stardust Vehicle," J. Spacecr. Rockets, **44**(1), pp. 24–32.
[4] Johnson, E. J., Starkey, R. P., and Lewis, M. J., 2006, "Aerodynamic Stability of Reentry Heat Shield Shapes for a Crew Exploration Vehicle," J. Spacecr. Rockets, **43**(4), pp. 721–730.
[5] Zhong, J., Ozawa, T., and Levin, D. A., 2008, "Modeling of Stardust Reentry Ablation Flows in the Near-Continuum Flight Regime," AIAA J., **46**(10), pp. 2568–2581.
[6] Ozawa, T., Zhong, J., Levin, D. A., Boger, D. A., and Wright, M., 2007, "Modeling of the Stardust Reentry Flows With Ionization in DSMC," AIAA Paper No. 2007-0611.
[7] Park, C., 1985, "Nonequilibrium Air Radiation (NEQAIR) Program: Users Manual," Ames Research Center, NASA.
[8] Sohn, I., Bansal, A., Levin, D. A., and Modest, M., 2008, "Advanced Radiation Calculations of Hypersonic Reentry Flows Using Efficient Databasing Schemes," Seattle, WA, AIAA Paper No. 2008-4091.
[9] Feldick, A. M., Modest, M., and Levin, D. A., 2008, "Closely Coupled Flowfield-Radiation Interactions for Flowfields Created During Hypersonic Reentry," 40th Thermophysics Conference, Seattle, WA, Jun. 23–26, AIAA Paper No. 2008-4104.
[10] Wang, A., and Modest, M. F., 2006, "Photon Monte Carlo Simulation for Radiative Transfer in Gaseous Media Represented by Discrete Particle Fields," ASME J. Heat Transfer, **128**(10), pp. 1041–1049.
[11] Ozawa, T., Wang, A., Modest, M., and Levin, D. A., 2008, "Development of a Coupled DSMC-Particle Photon Monte Carlo Method for Simulating Atomic Radiation in Hypersonic Reentry Flows," Seattle, WA, AIAA Paper No. 2008-3916.
[12] Modest, M. F., 2003, *Radiative Heat Transfer*, 2nd ed., Academic, New York.
[13] Park, C., 1990, *Nonequilibrium Hypersonic Aerothermodynamics*, Wiley, New York.
[14] Sohn, I., Ozawa, T., Levin, D. A., and Modest, M., 2009, "DSMC Hypersonic Reentry Flow Simulations With Photon Monte Carlo Radiation," Orlando, FL, AIAA Paper No. 2009-1566.

A Numerical Simulation of Combined Radiation and Natural Convection in a Differential Heated Cubic Cavity

P. Kumar
e-mail: dpradeep@iitk.ac.in

V. Eswaran[1]
e-mail: eswar@iitk.ac.in

Department of Mechanical Engineering,
Indian Institute of Technology Kanpur,
Kanpur 208 016, India

This article presents a numerical simulation of combined radiation and natural convection in a three-dimensional differentially heated rectangular cavity with two opposite side walls kept at a temperature ratio $T_h/T_c=2.0$ and $T_c=500$ K, with others walls insulated. A non-Boussinesq variable density approach is used to incorporate density changes due to temperature variation. The Navier–Stokes (NSE), temperature, as well as the radiative transfer (RTE) equations are solved numerically by a finite volume method, with constant thermophysical fluid properties (except density) for Rayleigh number $Ra=10^5$ and Prandtl number $Pr=0.71$. The convective, radiative, and total heat transfer on the isothermal and adiabatic walls is studied along with the flow phenomena. The results reveal an extraordinarily complex flow field, wherein, along with the main flow, many secondary flow regions and singular points exist at the different planes and are affected by the optical properties of the fluid. The heat transfer decreases with increase in optical thickness and the pure convection Nusselt number is approached as the optical thickness $\tau>100$, but with substantially different velocity field. The wall emissivity has a strong influence on the heat transfer but the scattering albedo does not.
[DOI: 10.1115/1.4000180]

Keywords: multimode heat transfer, radiative heat transfer, transparent and participating medium, three-dimensional natural convection, variable density formulation

1 Introduction

A large volume of research on natural convection exists today due to its importance in a wide range of applications in the cooling of electronic devices, energy storage systems, solar collectors, fire-related phenomenon, nuclear reactor safety, etc. The natural convection in an enclosure is a classical case study of the interaction of heat transfer and flow phenomena. Generally, heat transfer by radiation is neglected while studying this problem. Nevertheless, in high temperature engineering applications, thermal radiation contributes as much as any other modes to the overall heat transfer. However, there is paucity of literature combining natural convection and thermal radiation.

The radiation problem is usually treated in either of two ways: only as surface-to-surface radiation, or by including the emission, absorption, and/or scattering of radiation in a participating medium between the surfaces. For the later approach, the solution of an integro-differential radiative transfer equation (RTE) is required. In this work we include the effect of the participating medium. Very few studies have considered the coupling of convection and radiation. We briefly review below the work on combined natural convection and radiation in participating media.

The two-dimensional differentially heated cavity [1–3] is one of the classic benchmark problems of natural convection. The flow structure and heat transfer in a three-dimensional cavity, which is heated at two opposite vertical walls has also been studied numerically for the pure convection case and provides useful insight of the three-dimensional aspect of buoyancy driven flow [4–7].

Tan and Howell [8] solved the combined radiation and natural convection for a 2D differential heated cavity problem with a radiatively participating medium. The product-integral method and stream-vorticity formulation were used to solve the RTE and the flow field for three Rayleigh numbers 10^3, 10^4, and 10^5 for radiation-conduction parameter values ranging from 0 to ∞. Yücel et al. [9] carried out a study of combined natural convection and radiation for a radiatively participating medium for a vertical ($\theta=90$ deg) and an inclined ($\theta=60$ deg) differential heated 2D cavity of equal sides for a Rayleigh number of 5×10^6 and Plank number of 0.02. It was shown that there is significant change in the flow pattern due to the change in the orientation of the square cavity. Krishnaprakas et al. [10] showed that isotropic scattering of radiative energy had little effect on heat flux in natural convection. Fusegi and Farouk [11] did a numerical and experimental study on natural convection with gas radiation in a square cavity. Colomer et al. [12] studied natural convection with radiation for participating and nonparticipating media in a three-dimensional differential heated cavity. Recently, Borjini et al. [13] also studied the effect of radiation in a three-dimensional natural cavity problem with a velocity-vorticity formulation. Although, some work has been done on the natural convection with radiation in a similar three-dimensional geometry, these papers [13,12] assume only a small temperature difference and that the Boussinesq approximation is valid. In the present work, a non-Boussinesq variable density formulation is used to simulate three-dimensional natural convection with radiation for a large temperature difference ($T_c=500$ K, $T_h=1000$ K), where the Boussinesq approximation is unlikely to be valid. This study, therefore, despite its idealized nature, is closer to real world applications, where radiation heat transfer usually occurs over large temperature differences.

Mixed convection with radiation is important in some applications (i.e., energy storage devices, crop dryers, crude oil storage tanks, heat exchangers, etc.), and attempts have been made to

---

[1] Corresponding author.

Contributed by Heat Transfer Division of ASME for publication in the JOURNAL OF HEAT TRANSFER. Manuscript received September 30, 2008; final manuscript received August 15, 2009; published online November 30, 2009. Assoc. Editor: Yogesh Jaluria.

study it. Mahapatra et al. [14] used the stream-vorticity formulation for the flow field and the discrete ordinates method for the RTE to study the interaction of radiation and mixed convection in a two-sided lid-driven differentially heated square cavity. It was observed that buoyancy-aiding movement of the lid increases both the flow and heat transfer rate, whereas radiation is more sensitive to the buoyancy-opposing movement of the lid. Yan and Li [15,16] studied the effect of radiation on the mixed convection both in an inclined and a vertical square duct, using the vorticity-velocity method to solve the three-dimensional Navier–Stokes equation. They found that radiation reduces the buoyancy effect, whereas the local friction factor and Nusselt number are enhanced by buoyancy-assisting flow. Chiu et al. [17] studied the effect of radiation on mixed convection in a horizontal rectangular duct for a range of values of the aspect ratio for the duct, conduction-radiation parameter, optical length, scattering albedo, and wall emissivity.

Numerous methods have been proposed to solve the RTE numerically. Among the most popular are the spherical harmonics (P_N), Monte Carlo, Zonal, discrete ordinates (DOM, S_N) and finite volume (FVM) methods.

The FVM for the RTE was first proposed by Raithby and Chui [18]. They used a higher order exponential scheme for an absorbing-emitting and scattering medium. Later, this method has been used [19] for nonorthogonal two-dimensional geometries. Chai et al. [20,21] presented a FVM formulation and its implementation for orthogonal and nonorthogonal two-dimensional and orthogonal three-dimensional geometries. Chai et al. [22] investigated the numerical stability of different numerical schemes for the discrete ordinates method.

In the present work, numerical simulations of combined radiation and natural convection in a three-dimensional differential heated natural cavity at Rayleigh number 10^5 and Prandtl number $\mathrm{Pr}=0.71$ are performed using a FVM scheme [23–27] for both the flow equations and the RTE. The purpose of this study is to investigate the effect of radiation on three-dimensional natural convection. The effect of optical length, scattering albedo, and wall emissivity has been studied, keeping thermophysical properties (except density) of the fluid constant.

This work is briefly summarized as follows: Sec. 2 presents the problem definition, the general assumptions made in the study, the governing equations, the FVM method for the RTE, boundary conditions, solution algorithms, code verification, and grid independent tests. Section 3 presents the effect of radiation parameters on the heat and flow phenomenon in the three-dimensional natural convection.

2 Problem Specification

Figure 1 shows the geometry of the problem. The walls are of unit length. The front, back, top, and bottom (see Fig. 1) walls are insulated and the remaining two walls are isothermal, having a temperature ratio $T_h/T_c=2$ (hot to cold) with $T_c=500$ K. The origin of the coordinate system is shown as the vertex at the common corner of the hot, back, and bottom walls. The gravity force acts in the negative y-direction. The density is allowed to change according to the ideal gas law. The cavity is filled with a Newtonian fluid of $\mathrm{Pr}=0.71$. The study has been carried out for single Rayleigh number ($\mathrm{Ra}=10^5$) and conduction radiation parameter of 0.1 corresponding to an extinction coefficient value of $\beta=1.0$.

2.1 Analysis. These assumptions are made as follows:

1. The flow is laminar, Newtonian, and incompressible.
2. The thermophysical properties, except density, of the fluid are constant.
3. A non-Boussinesq variable density formulation is used to incorporate change in density due to temperature difference.
4. Viscous dissipation is neglected.
5. The medium is gray for radiative heat transfer.

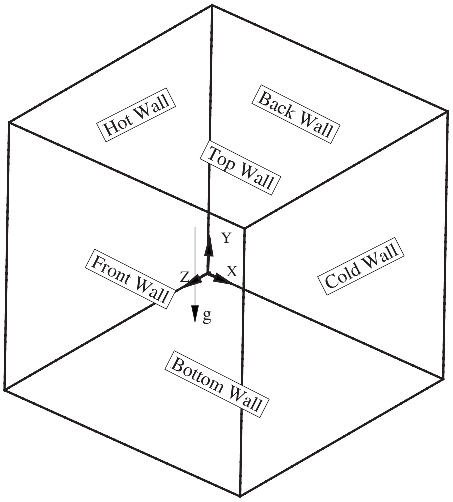

Fig. 1 The geometry of the three-dimensional natural cavity problem

6. The medium absorbs, emits, and/or scatters the radiation energy.
7. The refractive index of the medium and walls are constant and equal to one.

Based on the above assumptions, the basic equations of the flow and temperature, in Cartesian coordinates, are given by

$$\frac{\partial \rho u_i}{\partial x_i} = -\frac{\partial \rho}{\partial t} \tag{1}$$

$$\frac{\partial \rho u_i}{\partial t} + \frac{\partial \rho u_i u_j}{\partial x_j} = -\frac{\partial p}{\partial x_i} + \mu \frac{\partial^2 u_i}{\partial x_j \, \partial x_j} + \rho f_i \tag{2}$$

$$\frac{\partial \rho C_p T}{\partial t} + \frac{\partial \rho C_p u_j T}{\partial x_j} = k \frac{\partial^2 T}{\partial x_j \, \partial x_j} - \frac{\partial q_{R,j}}{\partial x_j} \tag{3}$$

where f_i is the body force. The continuity (Eq. (1)) emphasizes the fact that we must enforce continuity at each time step by equating the divergence of mass flux to the time rate of change in density, which is independently determined here by the temperature ideal gas law

$$\rho = \frac{p}{RT}$$

where R is the gas constant. In the calculations that follow we assume that the density at the mean temperature (=750 K) of the cavity is $1(\mathrm{kg/m^3})$. The last term in Eq. (3) is the divergence of the radiative flux, which can be calculated as

$$\nabla \cdot q_R = \kappa(4\pi I_b - G) \tag{4}$$

where κ is the absorption coefficient, I_b is the black body intensity, and G is the irradiation, evaluated by integrating the radiative intensity (I) over all directions, i.e.

$$G = \int_{4\pi} I d\Omega$$

The radiative intensity itself is calculated by solving the RTE

$$\xi_i \frac{\partial I}{\partial x_i} + \beta I = \kappa I_b + \frac{\sigma_s}{4\pi} \int_{4\pi} I(\xi_i) \Phi(\xi_i, \xi_i') d\Omega' \tag{5}$$

where ξ_i ($i=1,2,3$) are the direction cosines, σ_s is the scattering coefficient, β ($=\kappa+\sigma_s$) is the extinction coefficient, and $\Phi(\xi_i,\xi_i')$

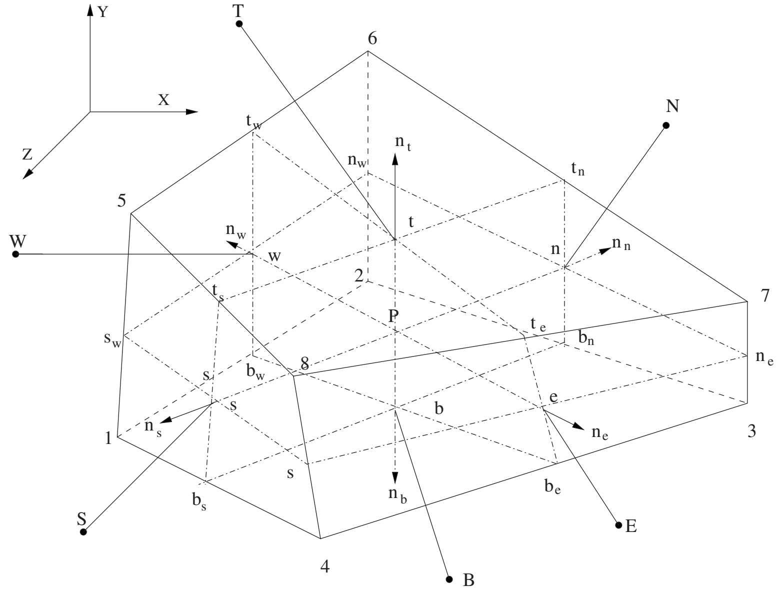

Fig. 2 Hexahedral cell

is the scattering phase function prescribing the probability of radiative intensity scatter from the direction prescribed by ξ_i' to the direction ξ_i. If linear anisotropic scattering is assumed, then the phase function is of the form

$$\Phi = 1.0 + a_0 \xi_i \xi_i' \quad (6)$$

where a_0 is called the asymmetric factor, with values -1, 0, and 1 of a_0 corresponding to backward, isotropic, and forward scattering, respectively.

2.2 Finite Volume Approximation of the RTE. The FVM is used to solve both the Navier-Stokes equation (NSE) and the RTE on a structured nonorthogonal hexahedral grid (Fig. 2). The detailed solution methodology of the NSE for variable density formulation and RTE are given in Refs. [26,27], respectively. The FVM formulation is obtained by (double) integrating the RTE [27] with respect to the control volume and control angle (see Figs. 2 and 3). The parametrization of the control volume faces and volumes are as in references [24,25].

The discretized FVM form of Eq. (5) for the cell P is

$$\sum_{f=\text{all faces}} I_f^m \Delta A_f D_f^m + \beta I_P^m = \kappa_P I_{bP}^m \Delta V_P \Delta\Omega^m + \frac{\sigma_{sP}}{4\pi}\sum_{m'} I_P^{m'} \Phi(m;m') \Delta\Omega^{m'} \Delta V_P \Delta\Omega^m \quad (7)$$

where the subscript P indicates the cell centroid value, subscript f indicates the value at the cell face ($f=e,w,n,s,t,b$), and superscript m indicates the discretized direction (i.e., the center of the control angle $\Delta\Omega^m$ in Fig. 3) of the intensity I^m. The directional weight is

$$D_f^m \equiv \int_{\Delta\Omega^m} (\hat{n}_f \cdot \hat{s}^m) d\Omega$$

where $\hat{n}_f$ is the outward surface normal to the face f between the cell P and its neighbors, $\hat{s}^m$ is the direction of the radiation, and $d\Omega$ is the discrete solid angle attributed to direction m.

With a step [27] interpolation scheme to represent face values in terms of centered values, Eq. (7) can be reduced to the standard form

$$a_P I_P^m = a_E I_E^m + a_W I_W^m + a_N I_N^m + a_S I_S^m + a_T I_T^m + a_B I_B^m + S_P^m \quad (8)$$

which can be solved by an iterative technique.

Due to limitations of space, we will not discuss the solution technique of NSE, as the discretization scheme and numerical solution technique used here for the variable density formulation is given in Ref. [26].

2.3 Nondimensional Variables and Boundary Conditions. The following are the nondimensional variables and parameters used in this study:

$$T_h^* = \frac{T_h}{T_c}, \quad \beta = \kappa + \sigma_s, \quad \tau = \beta L, \quad \omega = \frac{\sigma_s}{\beta}$$

$$\text{Pr} = \frac{\nu}{\alpha}, \quad \text{Ra} = \frac{g\beta_T L^3 (T_H - T_{\text{ref}})}{\alpha\nu}, \quad N = \frac{k\beta}{\sigma T_c^3}$$

where β_T is the volumetric thermal expansion coefficient $\beta_T \equiv -1/\rho(\partial\rho/\partial T)_P = 1/T$ for an ideal gas.

The boundary conditions for momentum and energy equations are as follows:

$$u_i = 0 \text{ at all walls}$$

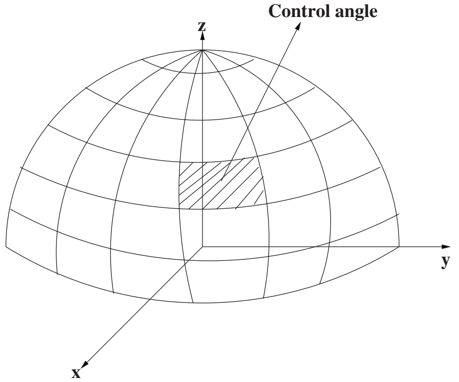

Fig. 3 Angular discretization

$$\frac{\partial p}{\partial n} = 0 \ \text{ at all walls}$$

$$T^* = 2 \ \text{ at the hot wall}$$

$$T^* = 1 \ \text{ at the cold wall}$$

$$q_r + q_c = 0 \ \text{ at the insulated (front, back, top, and bottom) walls (see Fig. 1)}$$

The RTE (Eq. (5)) is subjected to the following boundary condition at diffusely emitting and reflecting isothermal walls

$$I(r_w,\hat{s}) = \epsilon_w I_b(r_w) + \frac{1-\epsilon_w}{\pi}\int_{\hat{n}\cdot\hat{s}>0} I(r_w,\hat{s})|\hat{n}\cdot\hat{s}|d\Omega \quad \text{for } \hat{n}\cdot\hat{s} < 0 \tag{9}$$

where $\hat{n}$ is the outward normal at the boundary.

The total wall heat flux is calculated as

$$q_{tw} = q_{Cw} + q_{Rw}$$

where q_{Cw} and q_{Rw} are the convective and radiative heat fluxes at the wall, calculated as

$$q_{Cw} = -k\frac{\partial T}{\partial n}$$

and

$$q_{Rw} = \int_{4\pi} I(\hat{n}\cdot s)|_w d\Omega$$

The total Nusselt number at the wall is calculated from the convective and radiative Nusselt numbers as

$$\mathrm{Nu}_t = \mathrm{Nu}_C + \mathrm{Nu}_R$$

where

$$\mathrm{Nu}_C = \frac{q_{Cw}L}{k(T_h - T_c)}$$

and

$$\mathrm{Nu}_R = \frac{q_{Rw}L}{k(T_h - T_c)}$$

respectively. The average Nusselt Number $\overline{\mathrm{Nu}}$ at the wall is the area-averaged value of Nu.

2.4 Solution Algorithm. The individual solution algorithm for the NSE and RTE are given in Refs. [26,27], respectively. The strategy of the NSE and RTE solution is a false-transient technique and is briefly stated as follows:

1. Initialize the velocity, temperature, and intensity field.
2. Solve the RTE from the current temperature field until convergence.
3. Compute the divergence radiative source term using Eq. (4).
4. Solve the coupled velocity and temperature field, for one time step, with the above radiative source term.
5. Update the temperature field.
6. Repeat 2 to 5 for successive time-steps till the residuals for velocity and temperature fields reach steady state.

2.5 Code Verification. The computer code being used to study the present problem is verification in two steps. First, the numerical code being used to solve the Navier–Stokes and temperature equations is verification against results of Fusegi et al. [6] for the three-dimensional cubic cavity shown in Fig. 1 for purely convection buoyancy-driven flow (without thermal radiation). The nondimensional temperatures (nondimensionalized by $(T_h + T_c)/2$) at the hot and cold walls are 1.05 and 0.95, respectively. Table 1 shows the plane average Nusselt number from the present calculation against the values of Fusegi et al. for various Rayleigh numbers. Fusegi et al. used the Boussinesq approximation for the buoyancy while a non-Boussinesq method is used here. Nevertheless, the values of Nusselt numbers are within 1–2% of each other.

Table 1 Comparison of plane average Nusselt number $\overline{\mathrm{Nu}_t}$ for pure convection case with the values of Fusegi et al. [6]

	$\overline{\mathrm{Nu}_t}$ (Pure convection)		
Ra	Fusegi et al.	Present	% difference
10^3	1.085	1.0713	1.26
10^4	2.10	2.07	1.42
10^5	4.361	4.45	2.04
10^6	8.770	8.96	2.17

Next, for the verification of the RTE code, the three-dimensional furnace case proposed by Mengüç and Viskanta [28] is used. The problem comprises a 3D rectangular enclosure of size $4\times 2\times 2$ in the x-, y-, and z-directions, respectively, filled with an absorbing emitting gas of absorbing coefficient 0.5 m^{-1}. There is a volumetric heat generation of 5 $\mathrm{kW/m^3}$. The end-wall conditions are as follows:

$$x = 0, \quad \epsilon = 0.85, \quad T_w = 1200 \ \mathrm{K}$$

$$x = 4, \quad \epsilon = 0.70, \quad T_w = 400 \ \mathrm{K}$$

while the other walls are at 900 K with an emissivity of 0.7. The domain is discretized into $25\times 25\times 25$ spatial grids point and 6×8 spherical control angles. The domain temperature is calculated as

$$T^4 = \frac{1}{4\sigma}\left(\frac{q_{\text{gen}}}{\kappa} + G\right) \tag{10}$$

where G is the irradiation, defined as $G \equiv \int_{4\pi} I d\Omega$, and σ is the Stefan–Boltzmann constant. Figure 4 shows the present results for temperature with Chai et al. [20] at three different lines at $x = 0.4$, 2, and 3.6 and at $y = 1$. The comparison is good.

2.6 Grid Independent Test. To check whether the grid resolution used is adequate, a grid independent is carried out for the chosen problem ($T_h/T_c = 2.0$, $T_c = 500$ K, $\mathrm{Ra} = 10^5$, $\mathrm{Pr} = 0.71$, $N = 0.1$) at three spatial grid sizes, i.e., $41\times 41\times 41$, $61\times 61\times 61$, and $81\times 81\times 81$. The angular resolution is 6×8. The calculated Nusselt numbers at the hot wall for the optical thickness of 1.0 for the three grid sizes are 63.078, 62.56, and 62.085, respectively. The percentage of difference between the first and

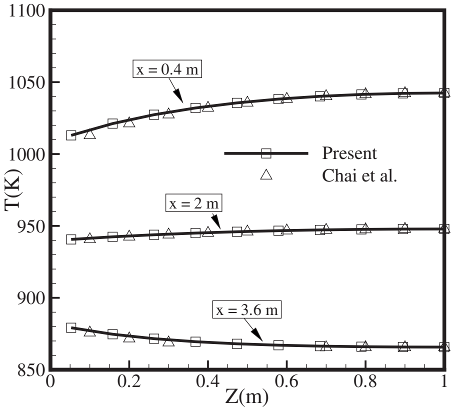

Fig. 4 Temperature distribution at $y=1$ m

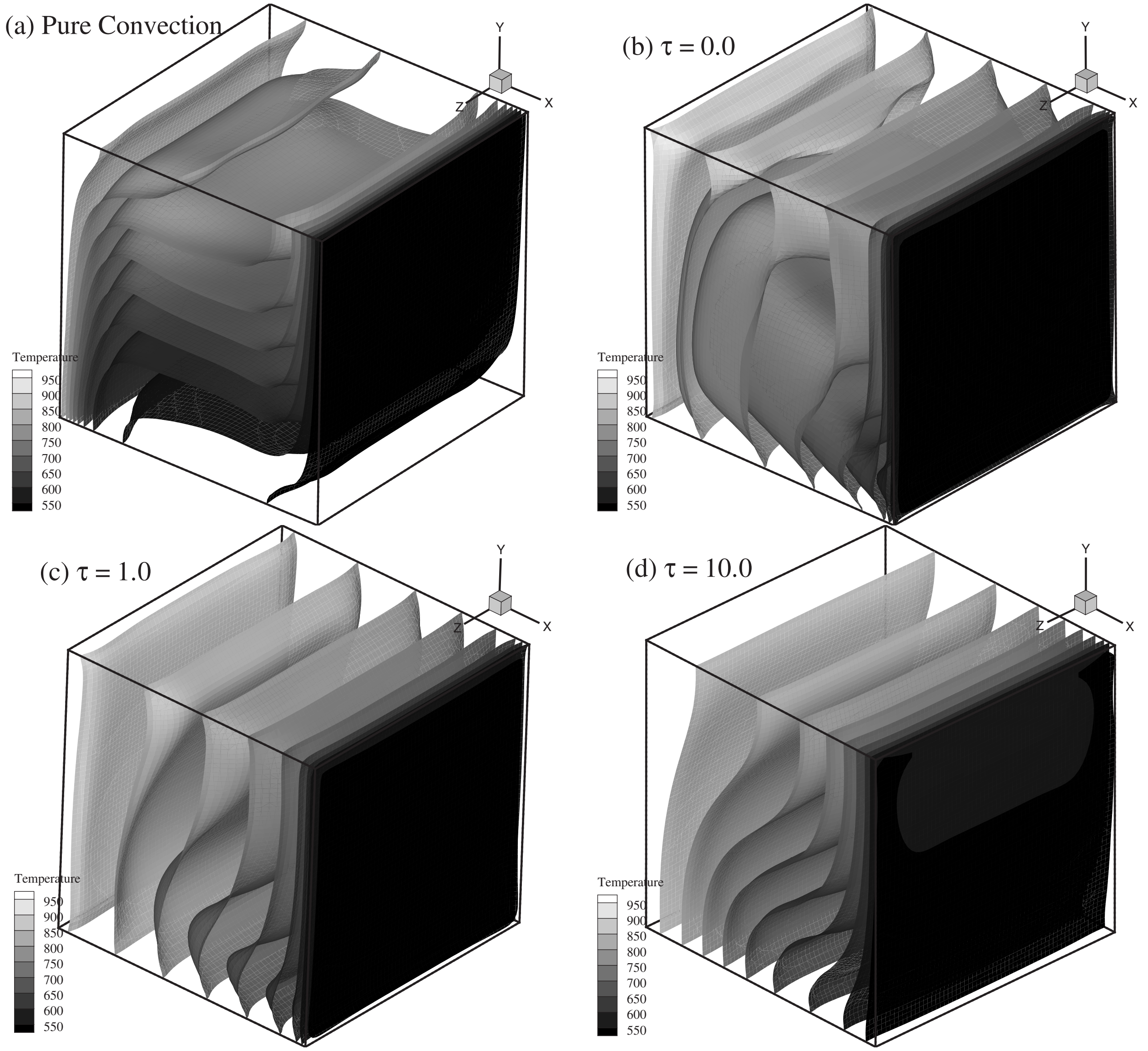

Fig. 5 Distribution of isosurfaces of temperature for (*a*) pure convection, (*b*) $\tau=0.0$ (transparent medium), (*c*) $\tau=1.0$, and (*d*) $\tau=10.0$

second grid values is 0.83% and between the second and third grid values is 0.76%.

The independent test of angular resolution is done with three angular discretizations, i.e., 4×6, 6×8, and 8×10, on the same problem with spatial resolution of $40\times 40\times 40$. The calculated Nusselt numbers for these three angular resolutions are 59.12, 63.078, and 63.84, respectively. The percentage of difference between the first and second values is 6.27% and between the second and third values is 1.19%. Using these results, a spatial grid size of $61\times 61\times 61$ and angular resolution of 6×8 was chosen as optimum for the present problem.

3 Results and Discussion

The main objective of the present study is to determine the effect of radiative heat transfer on the three-dimensional natural convection in a cubical cavity for Rayleigh number $\mathrm{Ra}=10^5$, Prandtl number $\mathrm{Pr}=0.71$, and conduction-radiation parameter $N=0.1$ (corresponding to extinction coefficient $\beta=1.0$). First, we will discuss the effect of optical thickness, scattering albedo, and wall emissivity on the three-dimensional heat transfer characteristics and, in Sec. 3.2, the effect of optical thickness on the flow characteristics.

3.1 Heat Transfer Characteristics. We now consider the effect of the radiative heat transfer characteristics on the three-dimensional natural convection. When studying the effect of optical thickness, the scattering albedo and wall emissivity are fixed at 0 and 1.0, respectively; likewise optical thickness and wall emissivity are kept at 1.0 and 1.0 when studying the effect of scattering albedo, and we use values of 1.0 and 0.0 for optical thickness and scattering albedo, respectively, when studying the effect of wall emissivity.

3.2 Effect of Optical Thickness. The problem is computed for various values of optical thickness $\tau=0.0$, 1.0, and 10.0 as well as for the pure convection case. It should be noted that the $\tau=0$ is distinct from the pure convection case, as the former allows surface-to-surface radiative transfer even if the medium is radiatively nonparticipative.

The isosurfaces of temperature are depicted in Fig. 5 for various values of optical thicknesses and for pure convection. A quasitwo-dimensional horizontally stratified structure is visible in the case of pure convection. However, with the inclusion of radiative heat transfer more complex three-dimensional isosurfaces of temperature are seen. The isothermal surfaces are more closely

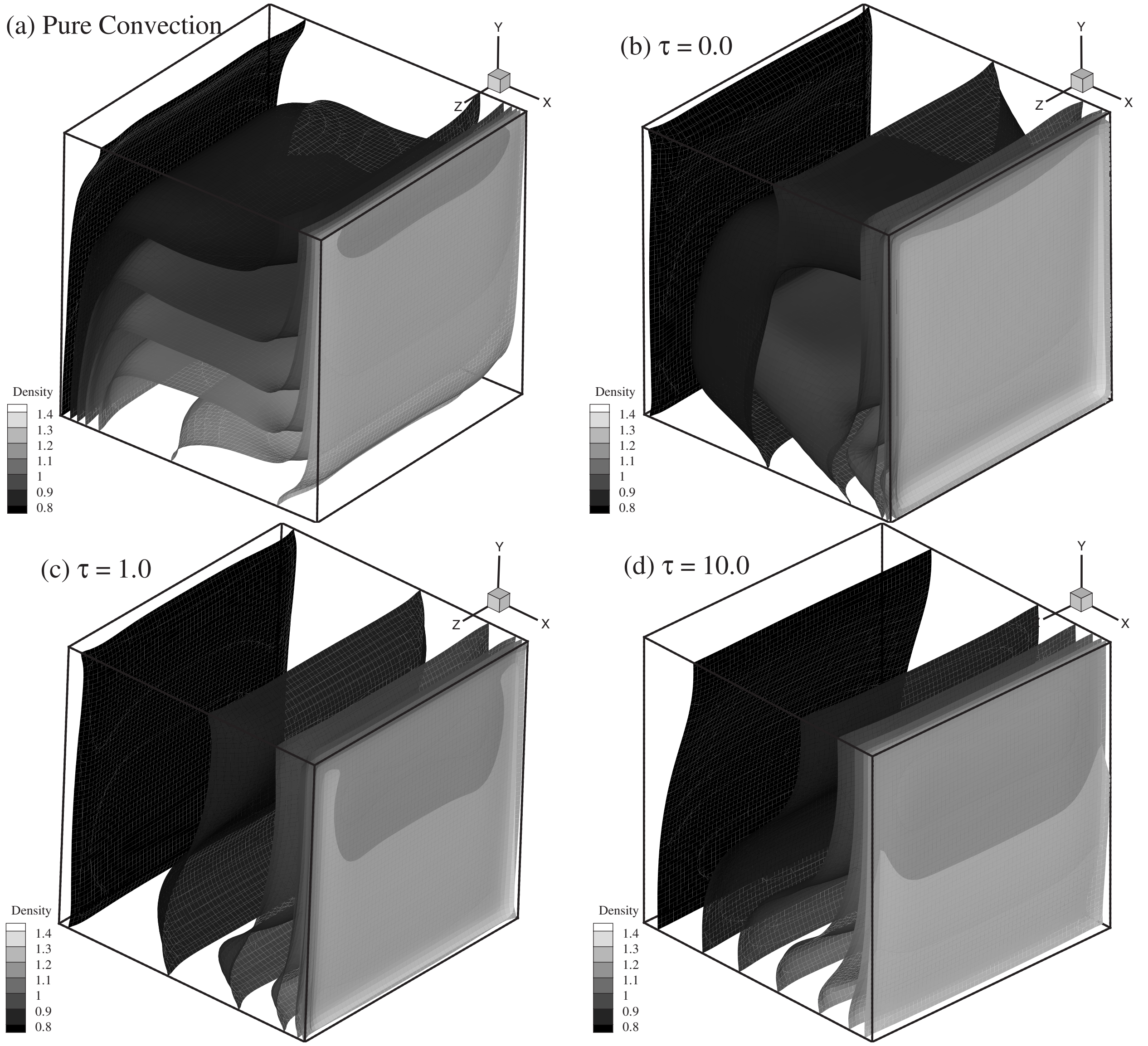

Fig. 6 Distribution of isosurfaces of density for (*a*) pure convection, (*b*) $\tau=0.0$ (transparent medium), (*c*) $\tau=1.0$, and (*d*) $\tau=10.0$

spaced near the cold wall, indicating an increase in the bulk mean temperature. A curved bathtublike isothermal plane, which is more prominently curved at the bottom is formed a distance away from the hot wall for the radiative transparent medium ($\tau=0.0$). This isothermal surface shape can be explained by the fact that convective heat flux is higher at the insulated bottom wall than the top wall; so curvature of the isotherms are higher at the bottom than the top wall. Recall that at the insulated boundaries, while the *total* heat transfer is zero, the convective and radiative transfers can be nonzero, but equal and opposite to each other. The bottom wall is convectively cooled, while the top wall is convectively heated, so the sign of the curvature of the isothermal surfaces changes from negative to positive from the bottom to top wall. The same effect also holds at the front and back insulated walls. The curvature of the isothermal surfaces decreases with the increase in optical thickness as the medium absorbs more of the radiative energy and less radiative flux reaches the wall. A quantitative analysis of the pattern is done below.

Figure 6 shows the variation in density inside the cavity for the assumed ideal gas. The isoplanes of density follow the isotherms, as the effect of difference in pressure are negligible as compared with the effect of temperature variation.

The distributions of local convective and radiative Nusselt numbers at the cold wall is shown in Fig. 7 for the transparent medium $\tau=0.0$ as well as for the participative medium with $\tau=10.0$. It is interesting to note that the radiative Nusselt number for the transparent medium shows close to fourfold symmetry while the convective Nusselt numbers of both cases and the radiative Nusselt number of the $\tau=10.0$ case show twofold symmetry. The former is influenced primarily by the temperatures and insulated conditions at the four adjoining walls, while the latter are influenced most strongly by the fluid temperature profile inside the cube. A relatively high convective Nusselt number is seen, which decreases from top to bottom. The radiative Nusselt number for the $\tau=10.0$ case decreases from top to bottom on the cold plate for the participative medium. The convective Nusselt number increases marginally, whereas the radiative Nusselt number decreases very significantly, with the increase in the optical thickness of the medium.

The vertically line-averaged convective and radiative Nusselt numbers along the *z*-direction at the cold wall is shown in Fig. 8. The convective Nusselt number is seen to increase with increase in the optical thickness of the medium up to $\tau=10$, but for τ

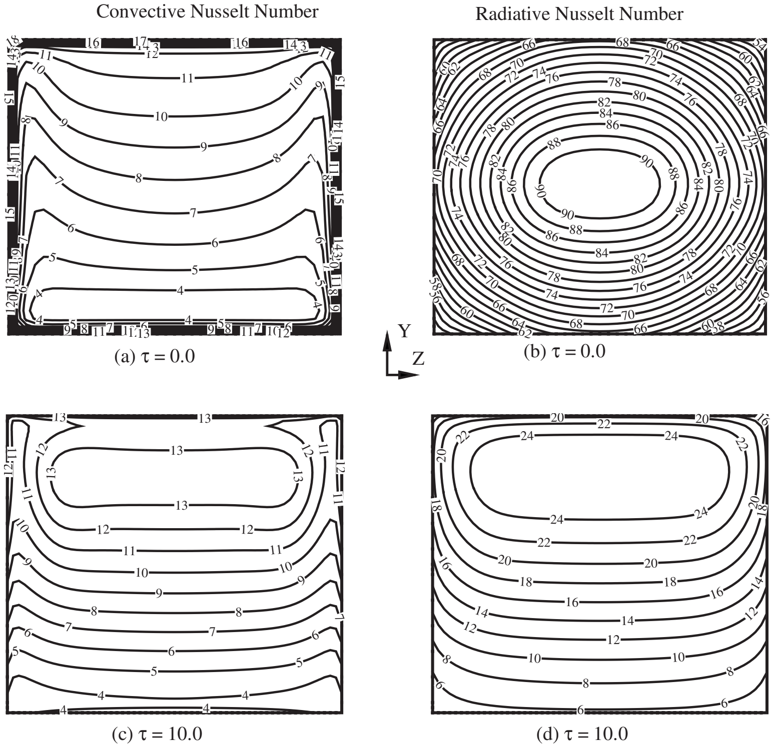

(a) τ = 0.0

(b) τ = 0.0

(c) τ = 10.0

(d) τ = 10.0

Fig. 7 Effect of optical thickness on the local convective and radiative Nusselt numbers on the cold wall

=100 (not shown here) it was found to have decreased. A nearly one-and-half-fold increase is seen in the convective Nusselt number from pure convection to a radiative transparent medium, but hardly any increase in the convective Nusselt number is seen from optical thickness from $\tau=1.0$ to $\tau=10$, However, the radiative Nusselt number decreases consistently with increases in the optical length in the range studied.

The contours of the total Nusselt number at the cold wall are shown in Fig. 9 for various values of optical thicknesses. The heat transfer is highest at the top of the cold wall in the case of pure convection, while the highest heat transfer is observed at the center of the wall for the transparent medium, and the region of highest heat transfer moves up the wall as optical thickness of the medium increases, even while the maximum flux itself decreases.

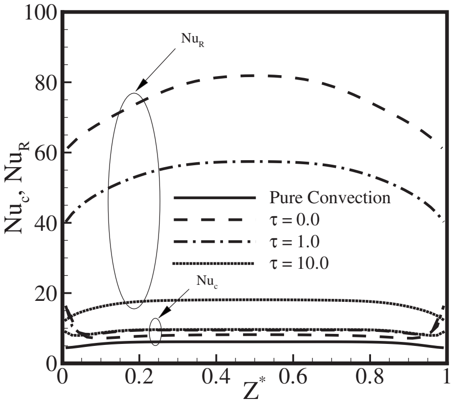

Fig. 8 The vertical line-averaged convective and radiative Nusselt numbers at the cold wall for various values of optical thickness

A very high Nusselt number is observed for the radiative transparent medium, which decreases with increasing optical thickness.

Figure 10 depicts the vertically line-averaged total Nusselt number along in the *z*-direction at the cold wall. The total Nusselt number decreases with increase in optical thickness. A many-fold increase in the total Nusselt number is observed from the pure convection to the transparent medium case, which is reduced to a factor of around two at $\tau=100.0$. A slight increase in the total Nusselt near the end-wall is seen, which diminishes with the optical length.

The top, bottom, front, and back walls are insulated and have no net heat transfer. It will be informative to know, however, the individual convective and radiative heat flux at these walls. The local convective and radiative Nusselt numbers and the vertical line-averaged convective and radiative Nusselt numbers on the bottom and top walls are shown in Figs. 11–14, respectively. The figures indicate that the bottom wall is heated by radiation and cooled by convection, whereas the reverse is true for the top wall. The contours of the convective and radiative Nusselt numbers are identical but opposite in sign, as the total Nusselt number is zero, indicating the correct implementation of the adiabatic boundary condition. The magnitude of these fluxes decreases with increasing optical thickness. The convective as well as radiative Nusselt numbers are close to zero over most of the top wall for optical thickness $\tau=10.0$. All these suggest that, at that optical thickness, the heat transfer by radiation becomes an essentially local phenomenon.

3.3 Effect of Optical Properties on the Heat Transfer.

The effect of optical thickness, scattering albedo, and wall emissivity on the plane average Nusselt number is shown in Tables 2–4, respectively. The average total Nusselt numbers at the hot and cold walls are equal (and opposite), while it is zero at the insulated walls. So the values are shown for only the cold wall. It is to be noted that the emissivity of only the isothermal walls are varied, while the adiabatic walls are kept black and that isotropic

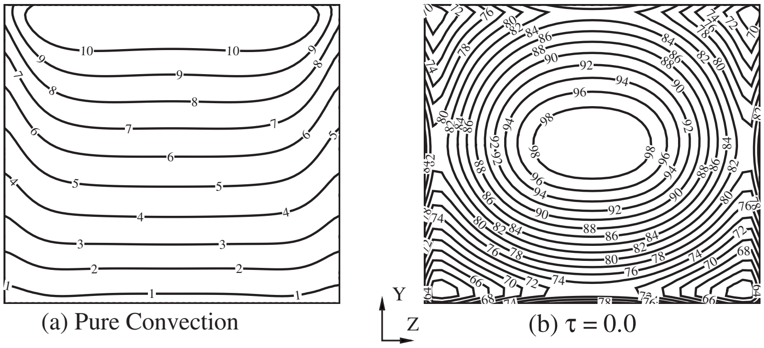

(a) Pure Convection (b) τ = 0.0

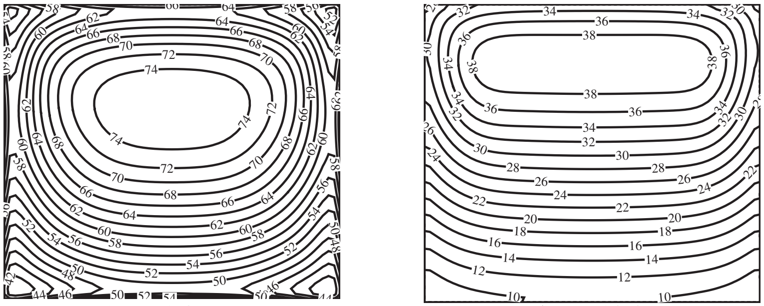

(c) τ = 1.0 (d) τ = 10.0

Fig. 9 Effect of optical thickness on the total Nusselt number at the cold wall

scattering is assumed. A drastic increase in the Nusselt number is observed from the pure convection case to the radiative transparent medium. The average Nusselt number decreases with increase in optical length as expected. A reduction of 83% in the total average Nusselt number is seen from $\tau=0-100$ to $\tau=100.0$. However, hardly any change is found with increase in scattering albedo, while the average Nusselt number increases with the increase in wall emissivity.

3.4 Flow Characteristics. It is well established that the three-dimensional flow in an enclosure is characterized by a large number of different eddies [29]—the principal eddy (PE), downstream secondary eddy (DSE), upstream secondary eddy (USE), upper upstream eddy (UUE), and end-wall vortices (EWV) to name a few—at different locations and orientations in the cavity. Two reasons are given for the creation of these eddies: The first invokes the interactions of the rotating fluid with the stationary end walls, whereby inertia forces induce the secondary flow; the second, the temperature gradient normal to the vertical walls causing buoyancy-induced velocity variation in the flow.

The terminology used in describing the flow topology in the 3D cavity follows that of Sheu and Tsai [30]. Figure 15 shows the projection of streamlines on the yz-plane along with nondimensionalized u (nondimensional scale is $(\nu\sqrt{\mathrm{Gr}}/L)$) velocity contours at different X-locations for pure convection. The projection of streamlines are symmetric about $Z^*=0.5$, so only half the plane in the z-direction is shown. As we observed, these planes have quite different characteristics. The streamlines near to the wall ($X^*=0.01$) show no singular point and the viscous effect is prominent and the value of u velocity is also quite small. Both the concavity and convexity of the flow is displayed, in contrast to the concavity of the flow at the plane $X^*=0.9$ mentioned by Borjini et al. [13]. The flow in this plane is basically one-dimensional, showing the character of boundary layer flow. As we move further into the core, the complexity of the flow increases. The plane $X^*=0.25$ is characterized by two (only one is shown) spiral inward rotating end-wall vortices (foci) both near the end of the top wall and a line of attachment and a node of separation. The streamlines originate from the line of attachment and converge to the node of separation located near the top wall. The u velocity is quite strong. The value of incoming velocity (positive velocity) is higher than the outgoing velocity (negative velocity) through this plane. It is interesting that the incoming hotter fluid occupies less area than the outgoing colder fluid. Next, the plane $X^*=0.35$ shows only two (one is shown, the other is systematically located in the other half plane) outward spiraling vortices at the bottom. The end-wall vortices appear in the plane $X^*=0.25$, do not stretch until this plane, and remain local phenomenon near about this plane only. The same is true for end-wall vortices in plane $X^*=0.35$. Still the hotter fluid moves with higher velocity than colder fluid and inward and outward moving fluids in this plane cover almost the same area. The middle plane $X^*=0.5$ has only one singular point, i.e., a node of separation. At this point the u velocity is also zero. So, the center of cavity is the stagnation point. The area covered by incoming and outgoing fluids is the same, but the hotter fluid

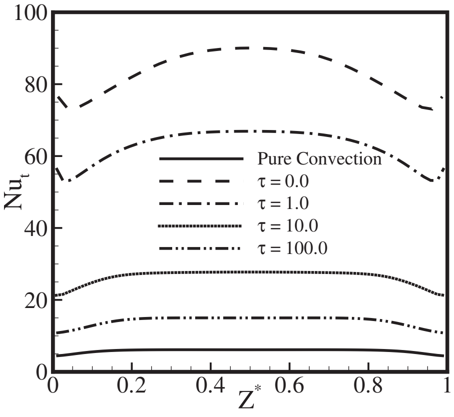

Fig. 10 The vertically line-averaged total Nusselt number at the cold wall for various values of optical thickness

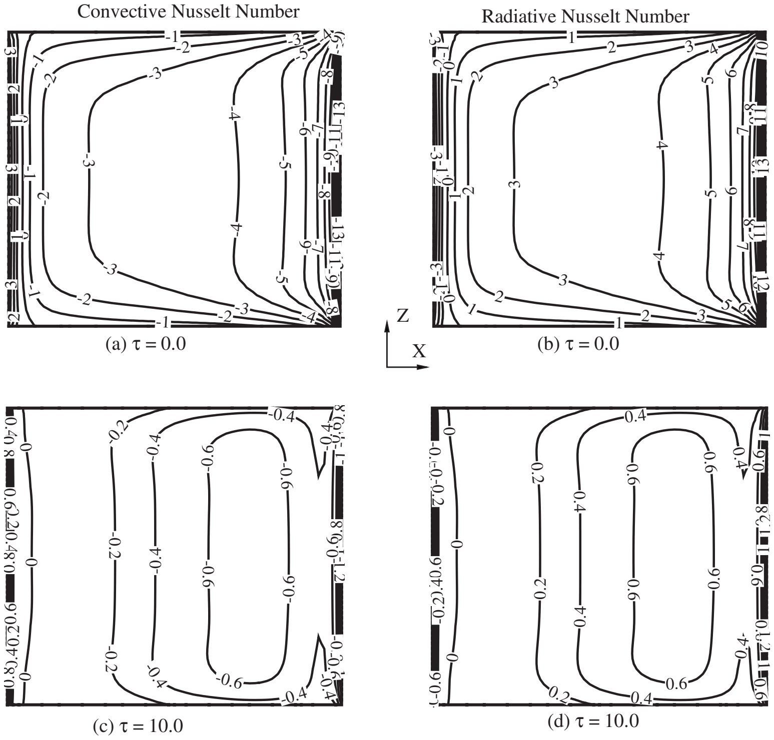

(a) τ = 0.0 (b) τ = 0.0

(c) τ = 10.0 (d) τ = 10.0

Fig. 11 Effect of optical thickness on the local convective and radiative Nusselt numbers on the bottom wall

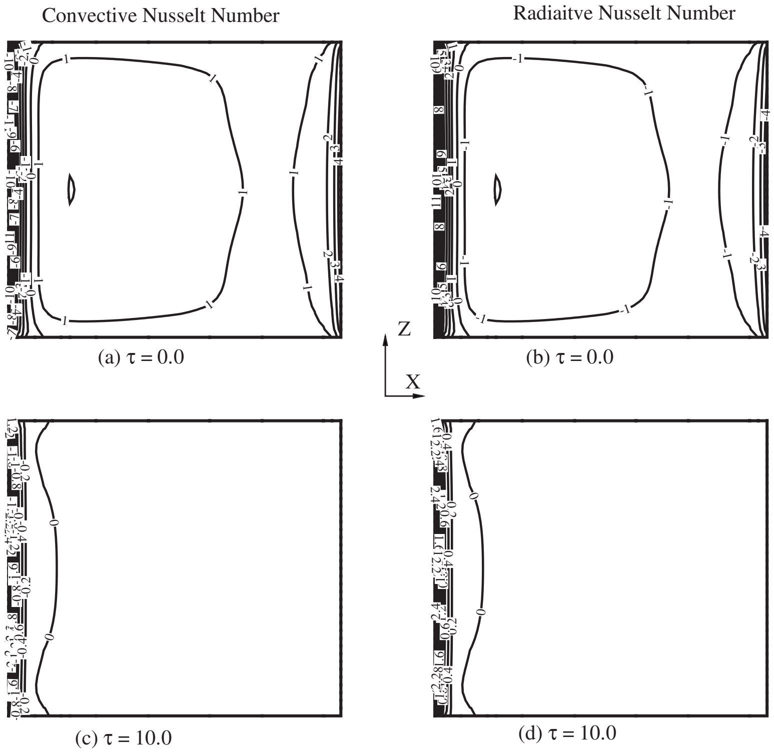

(a) τ = 0.0 (b) τ = 0.0

(c) τ = 10.0 (d) τ = 10.0

Fig. 12 Effect of optical thickness on the local convective and radiative Nusselt numbers on the top wall

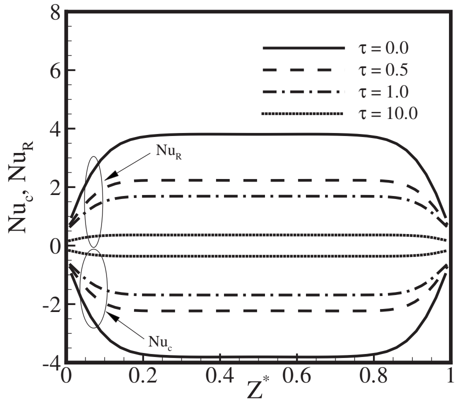

Fig. 13 Effect of optical thickness on the line-averaged convective and radiative Nusselt numbers on the bottom wall

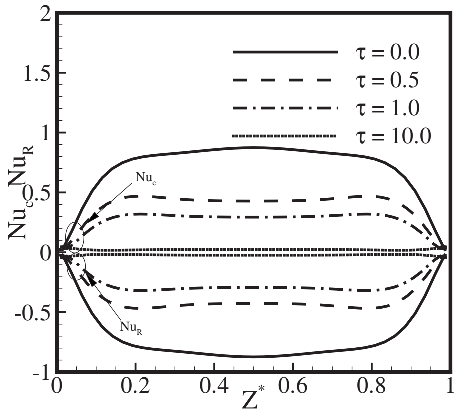

Fig. 14 Effect of optical thickness on the line-averaged convective and radiative Nusselt numbers on the top wall

Table 2 Variation in the average total Nusselt number with optical length

	$\overline{\mathrm{Nu}_t}$ $(\omega=0.0,\ \epsilon_w=1.0)$
Pure convection	5.84
$\tau=0$	83.25
$\tau=0.5$	71.28
$\tau=1.0$	62.56
$\tau=10.0$	26.35
$\tau=100.0$	14.08

Table 3 Variation in the average total Nusselt number with scattering albedo

ω	$\overline{\mathrm{Nu}_t}$ $(\tau=1.0,\ \epsilon_w=1.0)$
0	62.56
0.5	62.80
1.0	62.73

Table 4 Variation in the average total Nusselt number with wall emissivity of the isothermal walls (emissivity of the insulated walls is 1.0)

ϵ_w	$\overline{\mathrm{Nu}_t}$ $(\tau=1.0,\ \omega=0.0)$
0	11.19
0.5	37.88
1.0	62.56

moves with higher velocity. As we go further toward the cold wall, the magnitude of both velocities (inward and outward) becomes equal, but the area covered by the incoming fluid increases. In the plane near the cold wall, i.e., $X^*=0.75$, a line of separation and a node of attachment is seen, mirroring its counterpart plane near to hot wall, i.e., $X^*=0.25$, but this plane does not have any focal singular point.

The streamline projection of constant Z-planes are shown in Figs. 16 at $Z^*=0.065$, $Z^*=0.5$, and $Z^*=0.99$. The near wall plane $Z^*=0.99$ shows two spiral points of detachment and are joined by a line of detachment. The focal point near the cold wall moves down and the focal point near the hot wall moves up as we move away from the wall. The line of detachment disappears ($Z^*=0.065$) and the focal points become clockwise moving vortices. The w velocity is negative at the corners of the cavity and velocity but very small (almost zero) on the rest of the plane $Z^*=0.065$. The middle plane $Z^*=0.5$ has zero w velocity due to symmetry.

The plane $Y^*=0.5$ (see Fig. 17) for the transparent medium also has distinct features compared with pure convection. This plane only has two spiral points of detachment symmetrically placed about the middle of the z-axis near the cold wall. The ascending hot fluid covers almost 80% of the area near the bottom and accelerates until middle of the height and then decelerates. The fluid not only near the hot wall but also at the front and back walls rises. Near the bottom, the rising fluid covers the whole length of the front and back walls.

The biggest change in the streamline structures is seen in the Z-plane (see Fig. 18). The plane near the wall ($Z^*=0.99$) shows a spiral node of detachment located near the cold wall, which becomes a spiral node of attachment, still located near the cold wall in the plane $Z^*=0.15$, and remains a spiral node of attachment in the plane $Z^*=0.5$ but is relocated near the hot wall of the cavity. Unlike the pure convection case, the w velocity is negative at the bottom corner at the hot wall and the upper corner of the top wall in the plane $Z^*=0.15$. The w velocity is again zero in the middle plane due to symmetry.

The plane $Z^*=0.99$ near the wall shows a spiral point of detachment located approximately at the middle of the plane, changing to a spiral point of attachment at the plane $Z^*=0.5$ centered at nearly the same location as at plane $Z^*=0.15$ (see Fig. 19). The corner of the cavity is occupied by negative w velocity fluid and contours of the positive w velocity are almost circular around the center of the plane $Z^*=0.15$. The positive w velocity fluid accelerates from the wall to one-fourth of the z length, then decelerates and becomes zero at the middle of the cavity.

It may be noted that there is no substantial increase in the u and v velocities due to the inclusion of radiation for optical thickness $\tau<10$, but substantial increases are seen in w velocity.

4 Concluding Remarks

The combined radiation and natural convection in a three-dimensional cubical cavity differentially heated at two vertical opposite walls is studied numerically for constant (except density) thermophysical properties by solving the continuity, Navier–Stokes, radiation transfer, and temperature equations by a finite volume method for $\mathrm{Ra}=10^5$, $\mathrm{Pr}=0.71$, $T_h/T_c=2$, $T_c=500$ K, and optical thicknesses $\tau=0-100$. A non-Boussinesq variable density formulation is used to model buoyancy. The heat transfer and flow characteristics are examined at the different planes. The following conclusions are drawn from the study:

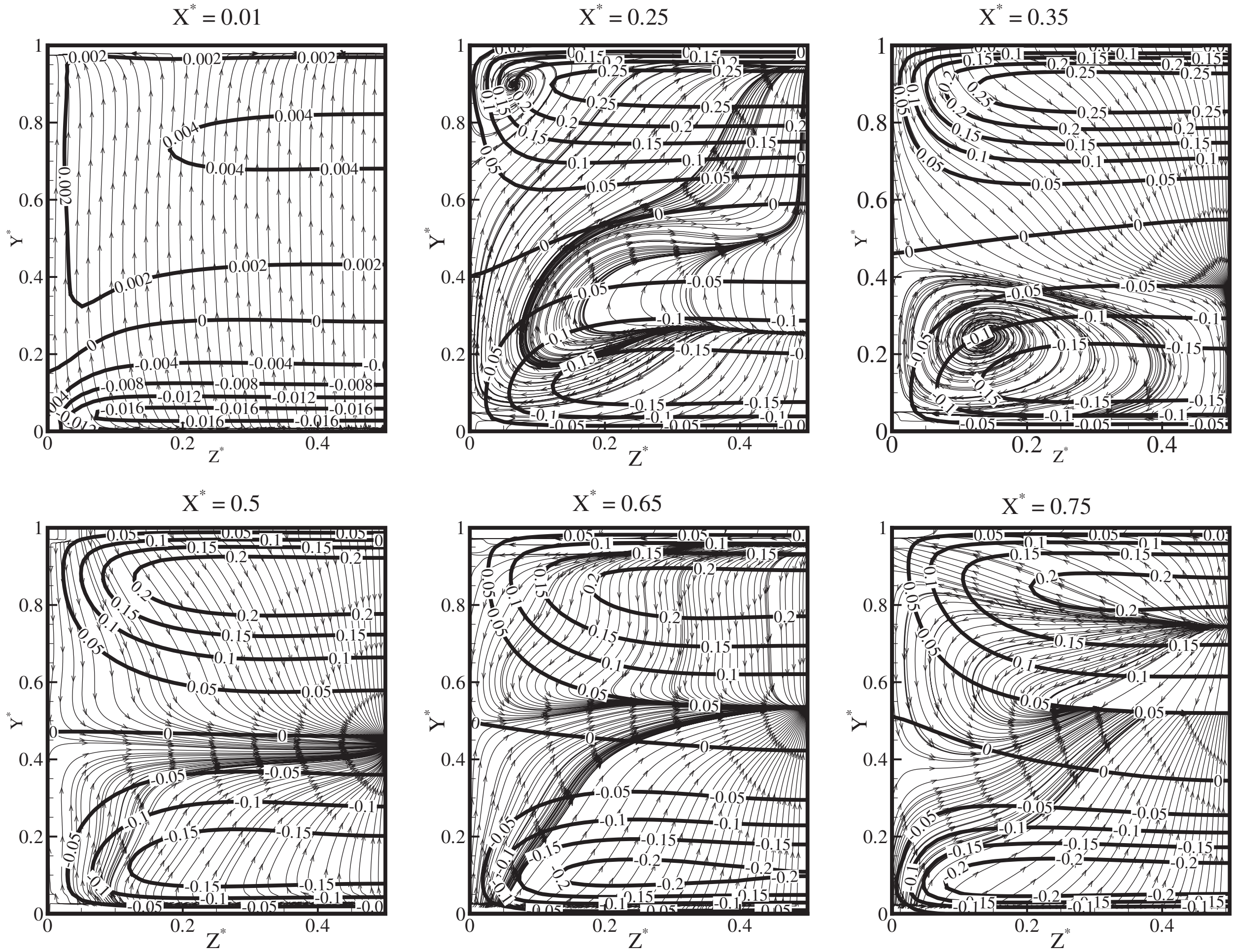

Fig. 15 Projection of streamlines and contours of nondimensionalized normal velocity on the *X*-plane for the pure convection for Ra=10^5 and Pr=0.71: (*a*) X^*=0.01, (*b*) X^*=0.25, (*c*) X^*=0.35, (*d*) X^*=0.50, (*e*) X^*=0.65, and (*f*) X^*=0.75

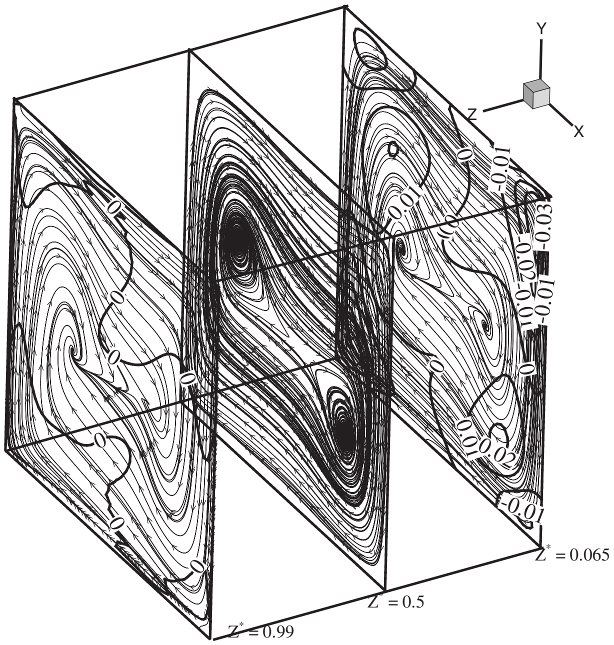

Fig. 16 Projection of streamlines and contours of nondimensionalized normal velocity on the *Z*-plane for the pure convection for Ra=10^5 and Pr=0.71

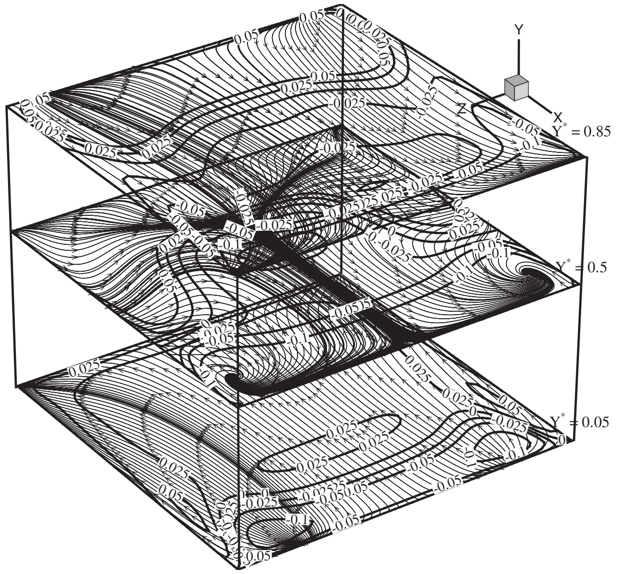

Fig. 17 Projection of streamlines and contours of nondimensionalized normal velocity on the *Y*-plane for the transparent medium for Ra=10^5 and Pr=0.71

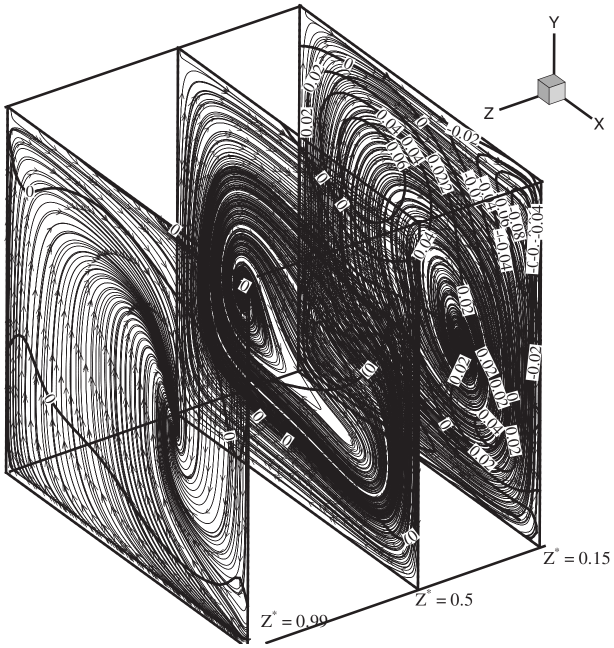

Fig. 18 Projection of streamlines and contours of nondimensionalized normal velocity on the *Z*-plane for the transparent medium for Ra=10^5 and Pr=0.71

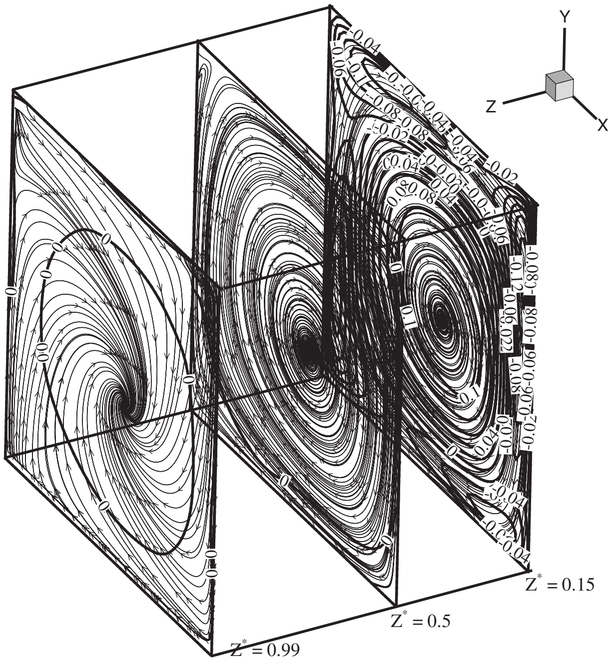

Fig. 19 Projection of streamlines and contours of nondimensionalized normal velocity on the *Z*-plane for the radiative medium of optical thickness τ=10.0 for Ra=10^5 and Pr=0.71

1. The temperature contours are quasitwo-dimensional for the pure convection case; however complex three-dimensional isotherm structures predominate when heat transfer by radiation is also considered for a radiatively transparent medium (τ=0).
2. Isosurface plots of temperature reveal that with further increase in optical thickness of the medium, a quasitwo-dimensional temperature field is recovered. However, *w* velocity increases tremendously. This means the temperature field is two-dimensional but the velocity field is three-dimensional.
3. The heat transfer is dominated by the radiation, which is highest for the radiatively transparent medium, decreasing progressively for higher optical thicknesses.
4. The radiative as well as total Nusselt number on all walls decrease with the optical thickness, while the convective Nusselt number increases then decreases with optical thickness. At very high τ (>100) the pure convection limit is again approached by the overall Nusselt number, but the velocity field is substantially different.
5. The scattering albedo has hardly any effect on the overall heat transfer, whereas heat transfer increases significantly with the wall emissivity of the isothermal walls.
6. The flow field is very complex even for the pure convection problem. However, as the radiation is included, the flow becomes more organized and smooth with increasing optical thickness.

Nomenclature

a_0 = asymmetric factor
k = thermal conductivity
$\hat{n}$ = unit normal vector
p = pressure
$\mathbf{s}$ = directional vector
q = heat flux
t = time
u_i = velocity
x_i = Cartesian coordinates $(x_1=x,\ x_2=y,\ x_3=z)$
C_p = specific energy
D_f^m = directional weight
G = irradiation
L = length
I = radiative intensity
N = conduction-radiation parameter $(k\beta/\sigma T_c^3)$
Nu = Nusselt number $((q_{Cw}+q_{Rw})L/k(T_h-T_c))$
Ra = Rayleigh number $(g\beta_T L^3(T_H-T_{\mathrm{ref}})/\alpha\nu)$
Gr = Grashof number $(g\beta_T L^3(T_H-T_{\mathrm{ref}})/\nu^2)$
T = temperature
T^* = T/T_c
u = $(u_1 L/\nu\sqrt{\mathrm{Gr}})$
v = $(u_2 L/\nu\sqrt{\mathrm{Gr}})$
V = volume

Greek Symbols

ρ = density
ν = kinematic viscosity
ξ_i = direction cosines
α = weight ratio
β = extinction coefficient
κ = absorption coefficient
σ_s = scattering coefficient
θ, ϕ = polar and azimuthal angles, respectively
ϵ = emissivity
Φ = phase function
Ω = solid angle
τ = optical thickness

Subscripts

b = black body
f = face center
t = total
w = wall
L = length
R = radiation
C = convection
P = cell center

$E, W, N, \ldots$ = east, west, north…

Superscripts

$*$ = nondimensional form
m = direction indices

References

[1] De Vahl Davis, G., and Jones, I. P., 1983, "Natural Convection in a Square Cavity: A Comparison Exercise," Int. J. Numer. Methods Fluids, **3**, pp. 227–248.

[2] Markatos, N. C., and Perikleous, K. A., 1984, "Laminar and Turbulent Natural Convection in an Enclosed Cavity," Int. J. Heat Mass Transfer, **27**, pp. 755–772.

[3] Demirdžić, I., Lilek, Ž., and Perić, M., 1992, "Fluid Flow and Heat Transfer Test Problems for Non-Orthogonal Grids: Bench-mark Solutions," Int. J. Numer. Methods Fluids, **15**, pp. 329–354.

[4] Mallinson, G. D., and De Vahl Davis, G., 1977, "Three Dimensional Natural Convection in a Box: A Numerical Study," J. Fluid Mech., **83**, pp. 1–31.

[5] Fusegi, T., Hyun, J. M., and Kuwahara, K., 1991, "A Numerical Study of 3D Natural Convection in a Cube: Effect of the Horizontal Thermal Boundary Conditions," Fluid Dyn. Res., **8**, pp. 221–230.

[6] Fusegi, T., Hyun, J. M., Kuwahara, K., and Farouk, B., 1991, "A Numerical Study of Three-Dimensional Natural Convection in a Differentially Heated Cubical Enclosure," Int. J. Heat Mass Transfer, **34**, pp. 1543–1557.

[7] Fusegi, T., and Hyun, J. M., 1994, "Laminar and Transitional Natural Convection in an Enclosure With Complex and Realistic Conditions," Int. J. Heat Fluid Flow, **15**, pp. 258–268.

[8] Tan, Z., and Howell, J. R., 1991, "Combined Radiation and Natural Convection in a Two-Dimensional Participating Square Medium," Int. J. Heat Mass Transfer, **34**, pp. 785–793.

[9] Yücel, A., Acharya, S., and Williams, M. L., 1989, "Natural Convection and Radiation in a Square Enclosure," Numer. Heat Transfer, **15**, pp. 261–278.

[10] Krishnaprakas, C. K., Narayana, K. B., and Dutta, P., 1999, "Interaction of Radiation With Natural Convection," J. Thermophys. Heat Transfer, **13**, pp. 387–390.

[11] Fusegi, T., and Farouk, B., 1990, "A Computational and Experimental Study of Natural Convection and Surface/Gas Radiation Interactions in a Square Cavity," ASME J. Heat Transfer, **112**, pp. 802–804.

[12] Colomer, G., Costa, M., Cònsul, R., and Oliva, A., 2004, "Three-Dimensional Numerical Simulation of Convection and Radiation in a Differentially Heated Cavity Using the Discrete Ordinates Method," Int. J. Heat Mass Transfer, **47**, pp. 257–269.

[13] Borjini, M. N., Aissia, H. B., Halouani, K., and Zeghmati, B., 2008, "Effect of Radiation on the Three-Dimensional Buoyancy Flow in Cubic Enclosure Heated From Side," Int. J. Heat Fluid Flow, **29**, pp. 107–118.

[14] Mahapatra, S. K., Nanda, P., and Sarkar, A., 2006, "Interaction of Mixed Convection in Two-Sided Lid Driven Differentially Heated Square Enclosure With Radiation in Presence of Participating Medium," Heat Mass Transfer, **42**, pp. 739–757.

[15] Yan, W.-M., and Li, H.-Y., 1999, "Radiation Effects on Laminar Mixed Convection in an Inclined Square Duct,"ASME J. Heat Transfer, **121**, pp. 194–200.

[16] Yan, W.-M., and Li, H.-Y., 2001, "Radiation Effects on Laminar Mixed Convection in a Vertical Square Duct," Int. J. Heat Mass Transfer, **44**, pp. 1401–1410.

[17] Chiu, H.-C., Jang, J.-H., and Yan, W.-M., 2007, "Mixed Convection Heat Transfer in Horizontal Rectangular Ducts With Radiation Effects," Int. J. Heat Mass Transfer, **50**, pp. 2874–2882.

[18] Raithby, G. D., and Chui, E. H., 1990, "A Finite-Volume Method for Predicting a Radiant Heat Transfer in Enclosures With Participating Media," ASME J. Heat Transfer, **112**, pp. 415–423.

[19] Chui, E. H., and Raithby, G. D., 1993, "Computation of Radiant Heat Transfer on a Nonorthogonal Mesh Using the Finite-Volume Method," Numer. Heat Transfer, Part B, **23**, pp. 269–288.

[20] Chai, J. C., Lee, H. S., and Patankar, S. V., 1994, "Finite Volume Method for Radiation Heat Transfer," J. Thermophys. Heat Transfer, **8**, pp. 419–425.

[21] Chai, J. C., Parthasarathy, G., Lee, H. S., and Patankar, S. V., 1995, "Finite Volume Radiative Heat Transfer Procedure for Irregular Geometries," J. Thermophys. Heat Transfer, **9**, pp. 410–415.

[22] Chai, J. C., Patankar, S. V., and Lee, H. S., 1994, "Evaluation of Spatial Differencing Practices for the Discrete-Ordinates Method," J. Thermophys. Heat Transfer, **8**, pp. 140–144.

[23] Ferziger, J. H., and Peric, M., 1998, *Computational Methods for Fluid Dynamics*, Springer-Verlag, Berlin, Heidelberg.

[24] Eswaran, V., and Prakash, S., 1998, "A Finite Volume Method for Navier–Stokes Equation," *Proceedings of the Third Asian Computational Fluid Dynamics Conference*, Vol. 1, pp. 127–136.

[25] Sharma, A., and Eswaran, V., 2003, "A Finite Volume Method," *Computational Fluid Flow and Heat Transfer*, Narosa Publishing House, New Delhi, pp. 445–482.

[26] Rahul, S., Eswaran, V., and Sunder, P. S., 2007, "An Algorithm for Variable Density Flow," *Proceedings of ASME-JSME Thermal Engineering Summer Heat Transfer Conference*, Vancouver, BC, Canada.

[27] Kumar, P., and Eswaran, V., 2007, "A Hybrid Scheme for Spatial Differencing in the Finite Volume Method for Radiative Heat Transfer in Complex Geometries," The Fifth International Symposium on Radiative Transfer, Bodrum, Turkey.

[28] Mengüç, M. P., and Viskanta, R., 1985, "Radiative Transfer in Three-Dimensional Rectangular Enclosure," J. Quant. Spectrosc. Radiat. Transf., **33**, pp. 533–549.

[29] Shankar, P. N., and Deshpande, M. D., 2000, "Fluid Mechanics in the Driven Cavity," Annu. Rev. Fluid Mech., **32**, pp. 93–136.

[30] Sheu, T. W. H., and Tsai, S. F., 2002, "Flow Topology in a Steady Three-Dimensional Lid Driven Cavity," Comput. Fluids, **31**, pp. 911–934.

An Extension of the Large-Cell Radiation Model for the Case of Semitransparent Nonisothermal Particles

Leonid A. Dombrovsky
Joint Institute for High Temperatures of the Russian Academy of Sciences,
NCHMT,
Krasnokazarmennaya 17A,
Moscow 111116, Russia
e-mail: dombr@online.ru

The recently developed model for thermal radiation in multiphase flows typical of melt-coolant interactions is generalized to account for transient temperature profile in large semitransparent particles of solidifying melt. A modification of the large-cell radiation model (LCRM) is based on the approximate solution for coupled radiation and conduction in optically thick spherical particles of a refractive material. The simplicity of the suggested approximation enables one to implement the modified model in a multiphase computational fluid dynamics code. The LCRM extension makes possible the use of this approach not only for the core melt in nuclear fuel-coolant interactions but also for other melt substances, which are widely used in the laboratory experiments. The numerical data demonstrate an effect of absorption coefficient of the particle substance on the rate of particle cooling and solidification. [DOI: 10.1115/1.4000181]

Keywords: thermal radiation, multiphase flow, melt-coolant interaction, combined heat transfer, semitransparent particle, solidification

1 Introduction

The present state of the art in modeling of thermal radiation transfer in disperse systems is characterized by numerous methods ranging from simple approaches based on diffusionlike models to detailed mathematical procedures for a discrete or continuous description of the process. One can find a comprehensive analysis of these models in the book by Modest [1]. The detailed mathematics for radiative transfer is usually too complicated to be employed in engineering solutions. Fortunately, some specific simplifications appear to be very effective in solving the radiation heat transfer problems in a host medium containing numerous particles, bubbles, or fibers [2]. As an example, one can remember also the problem of thermal radiation in combustion considered in the recent book by Viskanta [3].

One can expect that a set of engineering models elaborated for various applied problems is complete, and it is sufficient to choose simply one of the known approaches to solve one or another heat transfer problem. But there are some examples that demonstrate that engineers should be ready to develop a modified or new approach adopted to specific physical conditions of the real problem.

In the present paper, we consider a model for thermal radiation in the so-called fuel-coolant interaction (FCI), which takes place in hypothetical severe accident of light-water nuclear reactors. This process is usually treated as a penetration of the core melt of temperature about 3000 K into the water pool. The melt jets are first fragmented to numerous droplets by a hydrodynamic interaction with ambient water. After this premixing stage, the thermal interaction of melt droplets with water is considered as a major process. The physical picture of this interaction is very complex, and its analysis is beyond the scope of the paper. In all cases, the role of thermal radiation coming from droplets of high temperature melt (usually close to the eutectic composition: $70\%UO_2+30\%ZrO_2$) is of great importance. It was first discussed about 10 years ago by Dinh et al. [4], Fletcher [5], and Dombrovsky [6,7]. After a more recent analysis, there is no doubt in the predominant role of thermal radiation at least at the initial stage of the melt-coolant interaction [8,9].

To suggest an adequate model of radiation heat transfer in water containing hot corium particles and steam bubbles, one should take into account the specific optical properties of water in the visible and near-infrared spectral ranges. It is well-known that water is semitransparent in the short-wave range of $\lambda<\lambda_* \approx 1.2\ \mu\text{m}$ and practically opaque at $\lambda>\lambda_*$ [10]. In the range of water semitransparency, there is a radiative transfer between corium particles, and one can use the traditional radiative transfer theory to calculate the volume distribution of the radiation power. In the opacity range, the radiative transfer problem degenerates because of strong absorption at distances comparable with both particle sizes and distances between the particles. One can assume that radiation emitted by corium particles in this spectral range is totally absorbed in ambient water.

The complete spectral solution to the radiation heat transfer problem in a multiphase flow typical of fuel-coolant interaction is too complicated even in the case when the P_1 approximation is employed. The main computational difficulty is related to the wide range of optical thicknesses of the medium at different wavelengths. One should consider not only the visible radiation when the optical thickness of the medium is determined by numerous particles but also a part of the infrared range characterized by the large absorption coefficient of water.

An appropriate radiation model for the problem discussed should be adequate to the present-day multiphase flow modeling with the usual size of computational cells about several centimeters and constant characteristics of the medium in single cells. The presence of numerous particles and bubbles in the host medium increases considerably the optical thickness of these cells even in the spectral range of water semitransparency. It makes reasonable an assumption of negligible radiation heat transfer between the cells. The latter is a basis of the large-cell radiation model (LCRM) [11].

In the original version of LCRM, only the case of totally opaque particles was considered. Most likely, it is a good ap-

---

Contributed by the Heat Transfer Division of ASME for publication in the JOURNAL OF HEAT TRANSFER. Manuscript received October 20, 2008; final manuscript received March 23, 2009; published online November 30, 2009. Assoc. Editor: Yogesh Jaluria.

proach for the corium particles of real size from 1 mm to 5 mm in diameter [12]. This version of the LCRM has been already implemented in the code VAPEX-P for multiphase flow calculations in FCIs [9]. A comparison with the calculations using the P_1 approximation indicated that LCRM is sufficiently accurate for the realistic range of the problem parameters. At the same time, the assumption of opacity of the molten and solid particles of arbitrary size is expected to be incorrect for other melts, which are used in some laboratory studies of FCIs. Moreover, the limited experimental data for uranium dioxide in the near-infrared do not exclude that thin layers of liquid or solid corium of thickness about 50–100 μm are semitransparent, and the thermal radiation has a contribution to heat transfer in solidifying corium particles. Therefore, one should consider a modification of the LCRM to take into account the semitransparency of radiating particles. It is an objective of the present paper.

It can be done on the basis of the known studies on thermal radiation from single semitransparent particles [8,13–15]. The problem is not simple because one should take into account several factors, which affect thermal radiation from the particle. Note that the semitransparency of an isothermal particle decreases the particle emissivity. In the case of a semitransparent particle with a relatively high internal temperature, one can expect that the thermal radiation flux is greater than the value determined on the basis of the hypothesis of surface emission of the radiation. The latter effect appears to be more pronounced due to the predominant role of the central core of relative radius $r_* = a/n_\lambda$ (a is the particle radius and n_λ is the spectral index of refraction) in thermal radiation of refractive particles [13] (see also Refs. [16–18]).

There are several alternative ways for modeling of thermal radiation from nonisothermal semitransparent particles. In the case of particles, which are large in comparison with the radiation wavelength, there is no need in the rigorous Mie theory to take into account the wave effects [19,20]. It was shown in papers [13,18] that one can use the geometrical optics approximation and the radiative transfer equation when the diffraction parameter, $x = 2\pi a/\lambda$, is greater than 20. Following Refs. [8,13–15], we use an additional simplification of the mathematical formulation of the problem. It is based on a differential approximation called the MDP$_0$ (the modified DP$_0$, see Refs. [18,21] for the details). This approach appears to be fairly accurate in the engineering calculations.

2 The General Concept of the Large-Cell Radiation Model

In this section, the main attention will be paid to the conventional wavelength range of $\lambda_1 < \lambda < \lambda_*$, where water can be treated as a semitransparent host medium. It is assumed that water contains polydisperse corium particles and steam bubbles. For simplicity, we do not consider the so-called "steam cells" with steam as a host medium and suspended corium particles and water droplets. This specific case is not so important for FCIs. It was discussed in the recent paper by Dombrovsky et al. [9].

It is well-known that the integration of the radiative transfer equation (RTE) over all values of the solid angle yields the following important equation of spectral energy balance [1]:

$$\nabla \boldsymbol{q}_\lambda = p_\lambda(\boldsymbol{r}) - \alpha_\lambda(\boldsymbol{r}) I_\lambda^0(\boldsymbol{r}) \tag{1}$$

where $\boldsymbol{q}_\lambda$ is the spectral radiative flux, α_λ is the spectral absorption coefficient, I_λ^0 is the quantity proportional to the local radiation energy density I_λ^0/c_0

$$\boldsymbol{q}_\lambda(\boldsymbol{r}) = \int_{(4\pi)} I_\lambda(\boldsymbol{r},\boldsymbol{\Omega})\boldsymbol{\Omega}\, d\boldsymbol{\Omega}, \quad I_\lambda^0(\boldsymbol{r}) = \int_{(4\pi)} I_\lambda(\boldsymbol{r},\boldsymbol{\Omega})\, d\boldsymbol{\Omega} \tag{2}$$

where $I_\lambda(\boldsymbol{r},\boldsymbol{\Omega})$ is the spectral radiation intensity at point $\boldsymbol{r}$ in direction $\boldsymbol{\Omega}$, and c_0 is the velocity of light. For brevity, the name "spectral radiation energy density" is often used for the quantity I_λ^0. The function $p_\lambda(\boldsymbol{r})$ in Eq. (1) is the spectral radiation power generated in a unit volume of the medium in the vicinity of the point $\boldsymbol{r}$. In the simplest case of the so-called one-temperature medium, the function p_λ is directly proportional to the Planck function

$$p_\lambda(\boldsymbol{r}) = 4\pi n_{w,\lambda}^2 \alpha_\lambda(\boldsymbol{r}) B_\lambda[T(\boldsymbol{r})] \tag{3}$$

But it is not the case for the problem under consideration because we consider a multicomponent medium characterized by different temperatures of water and particles of different size in every small volume of the medium.

As it was mentioned in the Introduction, the LCRM is applied to single computational cells with constant physical parameters, and it is assumed that there is no radiative transfer between the neighboring cells. It does not mean that one should consider radiative transfer inside the cell. It is sufficient to find the radiation power emitted and/or absorbed by each component of the multiphase medium. The resulting sources or sinks of heat are then taken into consideration in the energy equations for hot polydisperse particles and cold water. In the range of water semitransparency, the local radiative balance in every cell yields the following relation for radiation energy density instead of Eq. (1):

$$I_\lambda^0 = p_\lambda/\alpha_\lambda \tag{4}$$

It means that the divergence of the spectral radiation flux is assumed to be zero in the cell. In the case of a one-temperature medium, Eq. (4) is equivalent to the equilibrium condition of $I_\lambda^0 = B_\lambda(T)$. But the problem considered is not so simple due to the presence of several components of different temperatures in every small volume of the medium. It means that the absorption coefficient and the emitted radiation power can be expressed as follows:

$$\alpha_\lambda = (1 - f_v^s)\alpha_{\lambda,w} + \sum_i \alpha_{\lambda,i}, \quad p_\lambda = \sum_i p_{\lambda,i} \tag{5}$$

where $\alpha_{\lambda,w}$ is the spectral absorption coefficient of water, $f_{v,s}$ is the volume fraction of steam bubbles (the void fraction), $\alpha_{\lambda,i}$ is the spectral absorption coefficient of the ith size fraction of hot particles, and $p_{\lambda,i}$ is the spectral radiation power emitted by the particles of this fraction. In the original version of the LCRM, it was assumed that every size fraction of polydisperse particles has a definite temperature T_i, which can be treated as a surface temperature of opaque particles. In this case, one can write

$$p_{\lambda,i} = 4\pi n_{w,\lambda}^2 \alpha_{\lambda,i} B_\lambda(T_i) \tag{6}$$

and the resulting radiation energy density is

$$I_\lambda^0 = \frac{4\pi n_{w,\lambda}^2}{\alpha_\lambda} \sum_i \alpha_{\lambda,i} B_\lambda(T_i) \tag{7}$$

For homogeneous spherical particles of radius a_i, the spectral absorption coefficient is expressed as follows [2]:

$$\alpha_{\lambda,i} = 0.75 \frac{f_{v,i}}{a_i} Q_{a,i} \tag{8}$$

where $Q_{a,i}$ is the absorption efficiency factor, and $f_{\lambda,i}$ is the volume fraction of particles having radius a_i.

The resulting radiation power for every component of the multiphase medium in the range of water semitransparency is as follows:

$$P_w^{(1)} = -\sum_{i=1}^{N} P_i^{(1)}, \quad P_i^{(1)} = \int_{\lambda_1}^{\lambda_*} \alpha_{\lambda,i}[4\pi n_{w,\lambda}^2 B_\lambda(T_i) - I_\lambda^0]\, d\lambda \tag{9}$$

In the range of water opacity, $\lambda_* < \lambda < \lambda_2$, we have

$$P_w^{(2)} = -\sum_{i=1}^{N} P_i^{(2)}, \quad P_i^{(2)} = 4\pi\int_{\lambda_1}^{\lambda_*} \alpha_{\lambda,i} n_{w,\lambda}^2 B_\lambda(T_i)d\lambda \tag{10}$$

The positive value of P_i corresponds to the case when the power emitted by the ith component of the medium is greater than the radiation power absorbed by this component. It goes without saying that the integral radiation power over the spectrum is given by

$$P_w = P_w^{(1)} + P_w^{(2)}, \quad P_i = P_i^{(1)} + P_i^{(2)}, \quad i = 1, \ldots, N \tag{11}$$

It is important that the radiation power absorbed in water is less than the total thermal radiation emitted by all corium particles:

$$-P_w < P_c, \quad P_c = 4\pi\sum_i \int_{\lambda_1}^{\lambda_2} \alpha_{\lambda,i} n_{w,\lambda}^2 B_\lambda(T_i)d\lambda \tag{12}$$

It is a result of the radiative transfer between the corium particles of different temperatures in the range of water semitransparency.

It is clear that the LCRM has some physical advantages when compared with the opaque medium model (OMM) [9]. First of all, the heat transfer by radiation between the particles of different temperatures is taken into account. It is also important that one can separate the radiation power absorbed in the water volume from the power absorbed just on steam-water interface near the hot particle.

In this paper, we consider a general case when thermal radiation from a single nonisothermal particle of radius a_i is characterized by spectral radiation flux $q_{\lambda,i}^{(p)}$ (per unit surface of the particle), and there is no simple analytical relation between $q_{\lambda,i}^{(p)}$ and temperature profile in the particle. In this case, one should use the following equations instead of Eqs. (6)–(10) and (12):

$$p_{\lambda,i} = 0.75\frac{f_{v,i}}{a_i}q_{\lambda,i}^{(p)}, \quad I_\lambda^0 = \frac{1}{\alpha_\lambda}\sum_i p_{\lambda,i}, \quad P_c = \sum_i \int_{\lambda_1}^{\lambda_2} p_{\lambda,i}d\lambda \tag{13}$$

$$P_w^{(1)} = -\sum_i P_i^{(1)}, \quad P_i^{(1)} = \int_{\lambda_1}^{\lambda_*} (p_{\lambda,i} - \alpha_{\lambda,i}I_\lambda^0)d\lambda,$$

$$P_w^{(2)} = -\sum_i P_i^{(2)}, \quad P_i^{(2)} = \int_{\lambda_1}^{\lambda_*} p_{\lambda,i}d\lambda \tag{14}$$

One can see that the major problem in the application of the LCRM to semitransparent particles is the determination of spectral radiation flux from single nonisothermal particles. This radiation flux can be found on the basis of a separate combined heat transfer problem for a spherical particle. It is sufficient to assume that a contribution of the external radiation to the temperature field formation in the particle. This assumption is based on the computational results for the radiation heat transfer between the corium particles [9].

3 Combined Heat Transfer by Thermal Radiation and Conduction in Optically Thick Solidifying Particles

The transient thermal state of a solidifying semitransparent particle can be determined by solving a combined radiative-conductive heat transfer problem in the particle. Strictly speaking, the general problem statement should take into account a complex behavior of the solidifying melt. Even in the case of a pure substance or eutectic chemical composition of the melt, the internal radiative cooling of a semitransparent particle may lead to the existence of a two-phase zone or "mushy zone" in the particle. This effect was originally discussed by Chan et al. [22] (see also the book by Modest [1]). The other physical cause of the mushy zone formation is a noneutectic composition of the melt when the temperatures of liquidus and solidus corresponding to the beginning and completion of equilibrium solidification do not coincide with each other. One can expect that the radiative transfer in a solidifying particle is complicated by the radiation scattering by small solid particles in the mushy zone [23,24]. An analysis of the possible formation of the mushy zone and its effect on the process are not a specific subject of this paper. Therefore, we consider the case of optically thick particles and small temperature difference between the liquidus and solidus [25]. It is assumed that these conditions enable us to neglect specific radiation effects in a narrow mushy zone.

The one-dimensional mathematical formulation of the problem for a single semitransparent spherical particle is based on the following transient energy equation accompanied by the boundary and initial conditions [8]:

$$\rho[c + Lf(T)]\frac{\partial T}{\partial t} = \frac{1}{r^2}\frac{\partial}{\partial r}\left(r^2 k\frac{\partial T}{\partial r}\right) - W(t,r) \tag{15}$$

$$t = 0, \quad T = T_{\text{liq}} \tag{16}$$

$$r = 0, \quad \frac{\partial T}{\partial r} = 0, \quad r = a, \quad -k\frac{\partial T}{\partial r} = h(T - T_e) \tag{17}$$

where

$$f(T) = \frac{\Theta(T - T_{\text{sol}}) - \Theta(T - T_{\text{liq}})}{T_{\text{liq}} - T_{\text{sol}}} \tag{18}$$

and Θ is the Heaviside unit step function. The last term in Eq. (15) is a volumetric heat loss rate due to the thermal radiation.

As was mentioned above, the problem of thermal radiation emitted by a semitransparent spherical particle can be formulated on the basis of the MDP_0 approximation. The corresponding boundary-value problem is as follows [13,21]:

$$-\frac{1}{r^2}\frac{d}{dr}\left(r^2 D_\lambda \frac{dI_{p,\lambda}^0}{dr}\right) + \alpha_{p,\lambda}(1 - \mu_*)I_{p,\lambda}^0 = 4\alpha_{p,\lambda}(1 - \mu_*)n_\lambda^2 \pi B_\lambda(T) \tag{19}$$

$$r = 0, \quad \frac{dI_{p,\lambda}^0}{dr} = 0, \quad r = a, \quad -D_\lambda\frac{dI_{p,\lambda}^0}{dr} = \frac{I_{p,\lambda}^0}{n_\lambda(n_\lambda^2 + 1)} \tag{20}$$

where the variable radiation diffusion coefficient is

$$D_\lambda = \frac{1 + \mu_*}{4\alpha_{p,\lambda}}(1 - \mu_*^2), \quad \mu_* = \sqrt{1 - \frac{r_*^2}{r^2}\Theta(r - r_*)} \tag{21}$$

The spectral radiation flux from the particle and the spectral radiation power inside the particle are calculated as follows:

$$q_\lambda^{(p)} = \frac{I_{p,\lambda}^0(a)}{n_\lambda(n_\lambda^2 + 1)}, \quad w_\lambda(r) = \alpha_{p,\lambda}(1 - \mu_*)[4\pi n_\lambda^2 B_\lambda(T) - I_{p,\lambda}^0(r)] \tag{22}$$

The subscript p is used in Eqs. (19)–(22) to remember that the marked quantities are referred to a single particle and its material. The independent variable t is omitted in these equations because it can be considered as a parameter in the steady-state radiative transfer formulation. The integral radiation flux from the particle and the volumetric heat loss rate due to thermal radiation are expressed as

$$Q^{(p)} = \int_{\lambda_1}^{\lambda_2} q_\lambda^{(p)}d\lambda, \quad W = \int_{\lambda_1}^{\lambda_2} w_\lambda(r)d\lambda \tag{23}$$

The data for optical properties of metal oxides near the melting temperature are very limited. Molten alumina is used in some experiments as a simulant material instead of corium [26]. The analysis of experimental data for infrared radiative properties of alumina showed that this material can be considered as a gray substance near the melting point [8]. Note that alumina is one of the most transparent materials used instead of the real corium in

Table 1 Physical parameters used in the calculations

ρ, kg/m^3	8000
c, kJ/kg K	0.6
k, W/m K	3
L, kJ/kg	400
T_{liq}, K	2840
T_{sol}, K	2820
ε_c	0.85
n	2.3

model experiments. There is no data for near-infrared properties of the oxide composition $Bi_2O_3-WO_3$, and some others used in laboratory experiments by Kudinov et al. [27]. It is natural to employ the gray model for these compositions too. To the best of the author's knowledge, there is no data for infrared properties of corium, i.e., binary composition of uranium dioxide and zirconium dioxide. Experimental data by Bober et al. [28,29] for pure UO_2 were obtained in the visible range $0.45 \leq \lambda \leq 0.75$ μm, where this substance is opaque. The value of index of absorption $\kappa_\lambda = 0.8$ corresponds to the absorption coefficient $\alpha_{p,\lambda} = 4\pi\kappa_\lambda/\lambda \sim 10^7$ m^{-1}, which is four orders of magnitude greater than the absorption coefficient of alumina. It is known that the absorption coefficient of uranium dioxide strongly decreases by transfer from the visible to the near-infrared spectral range [30,31]. But this coefficient remains much greater than that for alumina. Anderson [30] recommended using the Rosseland average value $\alpha_p = 5 \times 10^3$ m^{-1} for UO_2 melt. It may be the minimal estimate for the absorption coefficient of UO_2. The recent study of the spectral absorption of UO_2 in the temperature range from room temperature up to 1173 K by Ruello et al. [31] confirms the high absorption in the visible and near-infrared spectral ranges. It was also shown that the boundary of the strong optical absorption band moves to the infrared range when the sample is heated.

Having in mind the above information on optical properties of uranium dioxide, we employ the gray model and consider only the case of highly absorbing material of solidifying melt droplets with the absorption coefficient $\alpha_p \geq 10^4$ m^{-1}. The values of other physical parameters of corium used in calculations are given in Table 1 (see Refs. [32–34] for more details). The values of T_{sol} and T_{liq} from Table 1 correspond to 20% of ZrO_2 in the corium [25]. In the gray approximation, Eqs. (19)–(23) can be written as follows:

$$-\frac{1}{r^2}\frac{d}{dr}\left(r^2 D\frac{dI_p^0}{dr}\right)+\alpha_p(1-\mu_*)I_p^0=4\alpha_p(1-\mu_*)n^2\sigma T^4,$$

$$D=\frac{1+\mu_*}{4\alpha_p}(1-\mu_*^2) \tag{24}$$

$$r=0, \quad \frac{dI_p^0}{dr}=0, \quad r=a, \quad -D\frac{dI_p^0}{dr}=\frac{I_p^0}{n(n^2+1)} \tag{25}$$

$$Q^{(p)}=\frac{I_p^0(a)}{n(n^2+1)}, \quad W(r)=\alpha_p(1-\mu_*)[4n^2\sigma T^4-I_p^0(r)] \tag{26}$$

Note that the solution for problems (24)–(26) is insufficient even in the case of a gray particle substance because (according to the LCRM) we should determine the spectral radiation flux $q_\lambda^{(1)}$ in the range of water semitransparency.

The combined heat transfer problem formulated by Eqs. (15)–(18) and (24)–(26) is a typical problem of the radiative-conductive interaction. Problems of this kind have been investigated in some details starting from the classic study by Viskanta and Grosh [35]. The comprehensive review of combined conduction-radiation heat transfer investigations in the period before 1998 has been given by Siegel [36,37]. Information on more recent studies can be found in the book by Modest [1]. In our case, the interaction of the two modes of heat transfer is determined by three additional dimensionless parameters: the index of refraction n, the optical thickness of the particle $\tau_p = \alpha_p a$, and the conduction-to-radiation parameter

$$N=\frac{k}{4\sigma T_*^3/\alpha_p} \tag{27}$$

which characterizes the relative part of conductive and radiative heat transfer in an optically dense medium when $N \gg 1$. In further calculations, we use the value of T_{liq} as a characteristic temperature T_* in Eq. (27). It is known that the problem degenerates in the limit of highly absorbing medium when the effect of radiation on temperature field can be estimated by introducing the effective total conductivity

$$k_t=k+k_{\text{rad}}, \quad k_{\text{rad}}=\frac{16}{3}\frac{\sigma T^3}{\alpha_p} \tag{28}$$

where T is the current local temperature. Equation (28) can be written in the form

$$k_t=k\left[1+\frac{4}{3N}\left(\frac{T}{T_{\text{liq}}}\right)^3\right] \tag{29}$$

In our case, parameter N is equal to 5.77 even at $\alpha_p = 10^4$ m^{-1}. It means that the effect of thermal radiation on the temperature profile is expected to be like the effect of a small increase in thermal conductivity. As for effect of the semitransparency on radiation flux from optically thick particle, it is characterized by the difference between the surface temperature T_s and the temperature $T_\delta > T_s$ at distance from the surface $\delta = a \cdot (\tau_\delta/\tau_p)$, where $\tau_\delta \sim 1$. In the case of predominant radiative cooling, the relative increase in radiation flux is estimated as follows:

$$\frac{\Delta Q^{(p)}}{Q^{(p)}}\approx\frac{1}{2N} \tag{30}$$

Let us consider some numerical results obtained at parameters from Table 1 and convective heat transfer coefficient $h = 300$ W m^{-2} K^{-1}. This average value of heat transfer coefficient for the conditions of film boiling on the particle surface has been used in the calculations of Dombrovsky and co-worker [8,38,39]. Note that this was recently confirmed by the numerical simulation of film boiling on a sphere by Yuan et al. [40]. The temperature profiles shown in Fig. 1 indicate a considerable effect of the particle semitransparency, especially in the central region of the particle. This effect should be taken into account even in the case of absorption coefficient $\alpha_p = 4 \times 10^4$ m^{-1}. It is explained by specific temperature profiles characterized by a significant temperature difference in a solid crust on the particle surface. This surface layer is not optically thick at the initial stage of solidification. As a result, the time of particle solidification depends on the absorption coefficient of the particle material even in the case of optically thick particle: the variation in absorption coefficient from $\alpha_p = 8 \times 10^4$ m^{-1} to 10^4 m^{-1} leads to about a 20% decrease in the solidification time (see Fig. 2). Note that the conventional position of solidification front $\overline{r}_f = r_f/a$ shown in Fig. 2 is treated as a current position of the isotherm $T_f = (T_{\text{sol}} + T_{\text{liq}})/2$. The calculated values of the time of solidification, t_{sol}, are in a good agreement with the theoretical predictions based on Eq. (29) for the effective thermal conductivity

$$t_{\text{sol}}=\frac{t_{\text{sol}}^0}{1+4/(3N)} \tag{31}$$

where t_{sol}^0 is the solidification time for the totally opaque particle.

The integral radiation flux from the particle is not so sensitive to the variation in absorption coefficient (see Fig. 3), and one can neglect the effect of semitransparency at $\alpha_p > 2 \times 10^4$ m^{-1}. This result is also predicted by approximate Eq. (30).

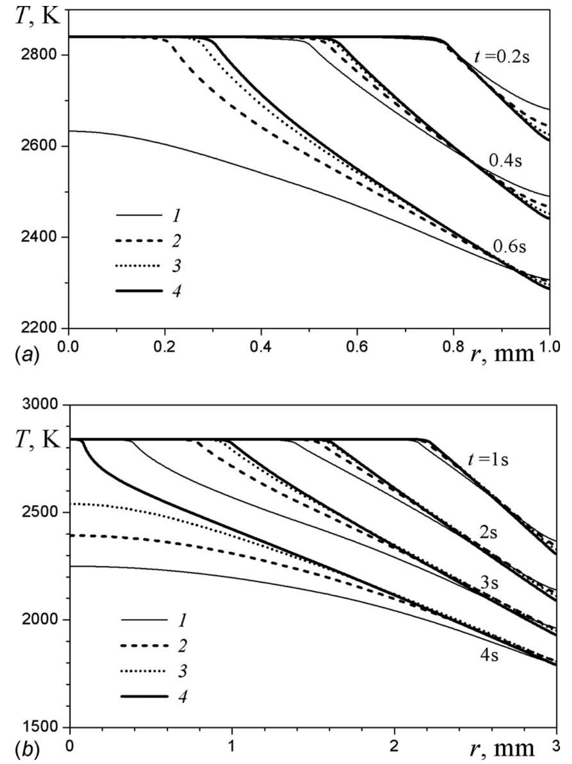

Fig. 1 Transient temperature profiles in solidifying particles of radius $a=1$ mm (*a*) and 3 mm (*b*) at various absorption coefficients of the particle substance: 1—$\alpha=10^4$ m^{-1}, 2—2×10^4 m^{-1}, 3—4×10^4 m^{-1}, and 4—8×10^4 m^{-1}

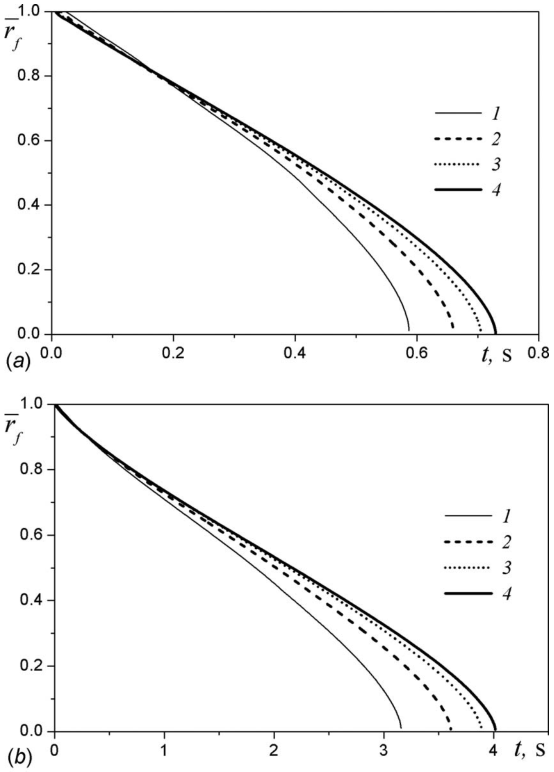

Fig. 2 The relative position of solidification front in particles of radius $a=1$ mm (*a*) and 3 mm (*b*) at various absorption coefficients of the particle substance: 1—$\alpha=10^4$ m^{-1}, 2—2×10^4 m^{-1}, 3—4×10^4 m^{-1}, and 4—8×10^4 m^{-1}

4 Approximate Solution for Cooling and Solidification of Single Particles

The computational model for the transient thermal state of solidifying corium particles and time variation of the integral radiation flux from single particles should be radically simplified to be implemented into the multiphase computational fluid dynamics (CFD) codes for FCI calculations. For the limiting case of totally opaque particles, it was done by Dombrovsky and co-workers [8,9] on the basis of the linear approximation of temperature profile in solid crust layer

$$T(r,t) = T_{\rm liq} - [T_{\rm liq} - T_s(t)]\frac{r-r_f}{a-r_f}\Theta(r-r_f), \quad t \le t_{cs} \tag{32}$$

and the parabolic temperature profile in the particle just after solidification [41]

$$T(r,t) = T_c(t) - [T_c(t) - T_s(t)](r/a)^2, \quad t > t_{cs} \tag{33}$$

The same idea can be used to derive ordinary differential equations for functions $T_s(t)$ and $r_f(t)$ in the case of optically thick particles at a finite value of the absorption coefficient $\alpha_p > 10^4$ m^{-1}. Two additional assumptions are made to derive the modified equations: (1) the effect of radiation on temperature profile in the particle can be described by the constant effective thermal conductivity

$$k_t = k\left(1 + \frac{4}{3N}\right), \quad N = \frac{k\alpha_p}{4\sigma T_{\rm liq}^3} \tag{34}$$

and (2) the integral radiation flux from the particle can be estimated as

$$Q^{(p)} = \tilde{\varepsilon}_c\sigma(T_s^4 - T_e^4), \quad \tilde{\varepsilon}_c = \varepsilon_c(1 + 0.5/N) \tag{35}$$

where ε_c is the hemispherical emissivity of bulk corium. After the transformations similar to those of Dombrovsky and Dinh [8], we

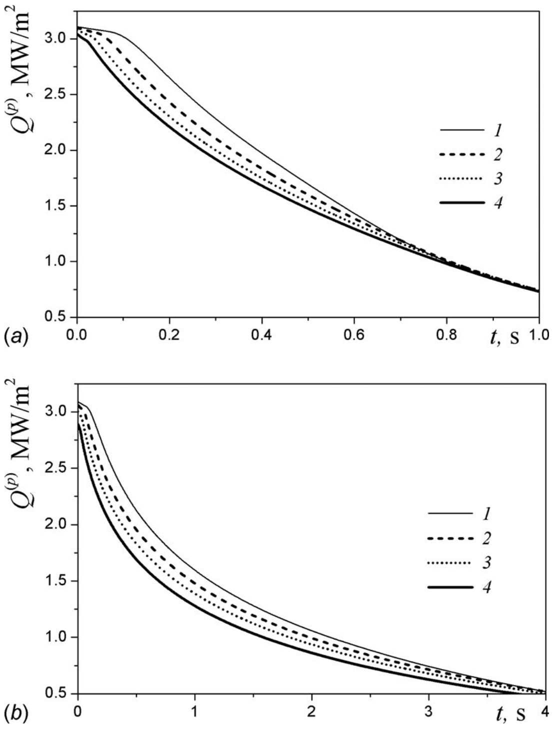

Fig. 3 Time variation of integral radiation flux from solidifying particles of radius $a=1$ mm (*a*) and 3 mm (*b*) at various absorption coefficients of the particle substance: 1—$\alpha=10^4$ m^{-1}, 2—2×10^4 m^{-1}, 3—4×10^4 m^{-1}, and 4—8×10^4 m^{-1}

obtain the Cauchy problem for coupled ordinary differential equations

$$\left[(T_{\text{liq}}-T_s)\frac{1+2\overline{r_f}+3\overline{r_f}^2}{4}+3L\overline{r_f}^2/c\right]\frac{d\overline{r_f}}{dt}+\frac{3-\overline{r_f}-\overline{r_f}^2-\overline{r_f}^3}{4}\frac{dT_s}{dt}=-\frac{3q_t}{\rho ca} \tag{36a}$$

$$\frac{dT_s}{dt}=\frac{q_t}{k_t/a+h_t(1-\overline{r_f})}\frac{d\overline{r_f}}{dt},\quad q_t=h(T_s-T_e)+Q^{(p)},\quad h_t=h+4\tilde{\varepsilon}_c\sigma T_s^3 \tag{36b}$$

$$\overline{r_f}(0)=1,\quad T_s(0)=T_{\text{liq}} \tag{36c}$$

Note that we use here a simplified term for thermal radiation on the particle surface. The complete formulation taking into account a contribution of other particles from the same computational cell (according to the LCRM) can be found in Ref. [9]. Equation (36) should be used before the complete solidification of the particle, i.e., from $t=0$ to $t=t_{cs}$, which is defined by equation $\overline{r_f}(t_{cs})=0$. After solidification, one can consider the simple problem

$$\frac{dT_s}{dt}=-\frac{3}{\rho ca}\frac{q_t}{1+0.2(a/k_t)h_t} \tag{37}$$

At initial time moment, one can assume T_s to be equal to $T_s(t_{cs})$ taken from the solution of problem (36). Note that there is no rigorous matching condition at $t=t_{cs}$ because it is impossible to satisfy all the physical conditions in this approximation: the conservation of energy and the absence of jumps in heat flux and surface temperature. Fortunately, it is not so important because the temperature difference in solid particle is much less than that during the particle solidification.

Equations (36) and (37) are similar to those for the opaque particle. The only difference is in coefficients k_t and $\tilde{\varepsilon}_c$ instead of k and ε_c. It makes the extension of the previously developed model very simple, and there is no need in additional computational resources to use the modified approximation in the multiphase code VAPEX-P [9] or in other CFD codes of the same level. As was discussed above, the corrected approximation is applicable to optically thick particles. But it is not a limiting condition for the millimeter-size corium particles and, most likely, for the particles of stimulant oxide compositions.

Some results of the calculations using the approximate model (36) are presented in Fig. 4. A comparison with the exact numerical solution indicates that the effect of the particle semitransparency is well described by this approximate model.

The approximate differential model (36) has two advantages over the simplest model of isothermal particles. The first obvious advantage is that calculations of heat transfer between corium and water are more accurate; however, it is also important that we obtain quantitative information on the solidification dynamics of solidification of corium particles. The crust layer on the surface of solidifying particles should be taken into account in the estimates of possible further fragmentation of the melt particles. The latter is especially important for predicting the melt explosivity at specific conditions of FCI. Obviously, the break-up models cannot be based only on the value of volume averaged temperature of the particle. A role of the crust layer in the stability of solidifying corium droplets by action of pressure drop in a steam blanket and then due to the tensile thermal stresses in the growing crust layer has been analyzed recently by Dombrovsky [38,42]. These papers were concerned with the totally opaque corium particles when the simplified version of problem (36) for the limiting case of $N\to\infty$ can be employed. It goes without saying that the results reported in Refs. [38,42] can be easily generalized for the case of optically thick but not totally opaque particles.

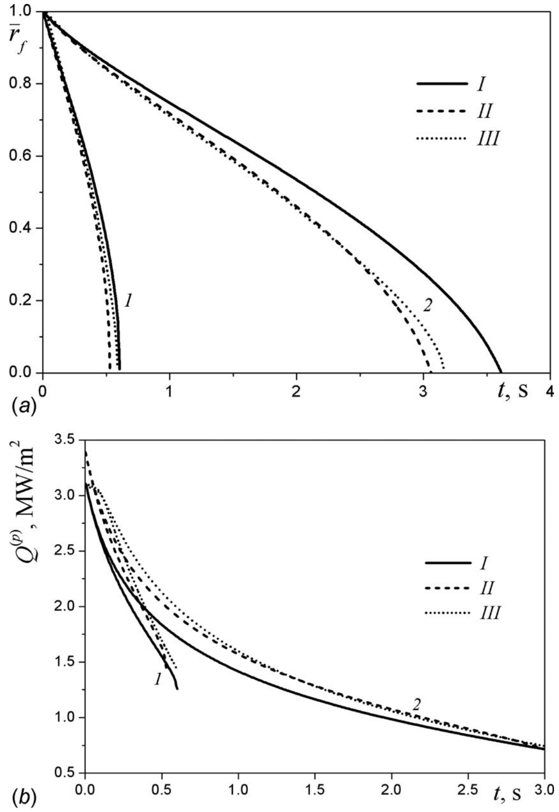

Fig. 4 The relative position of solidification front and the integral radiation flux for particles of radius $a=1$ mm (1) and 3 mm (2) at various absorption coefficient of the particle substance: I—$\alpha\to\infty$ (opaque substance), II, and III—$\alpha=10^4$ m^{-1} (II—calculations by using the approximate model (36), III—exact numerical solution)

5 Conclusions

The recently developed large-cell radiation model for thermal radiation in multiphase flows typical for melt-coolant interactions is generalized to account for transient temperature profile in large semitransparent particles of solidifying melt. The LCRM predicts the radiation heat transfer between corium particles of different temperatures and gives an estimate of the radiation power absorbed in water far from the steam/water interface. The latter is important to determine the radiation power, which does not directly contribute to steam production.

The proposed modification of LCRM is based on approximate solution for coupled radiative and conductive heat transfer in optically thick spherical particles of a refractive material during the solidification of these particles in water pool. The model includes the determination of the transient position of the solidification front in single particles. The predicted thickness of the solid crust on the particle surface can be used to improve the current models for corium particle fragmentation at the final stage of the FCI premixing process.

The simplicity of the suggested approximation enables one to implement the modified model in a multiphase CFD code. The LCRM extension makes possible the use of this approach not only for core melt in nuclear fuel-coolant interactions but also for other melt substances, which are widely used in the laboratory experiments. The numerical data demonstrate an effect of the absorption coefficient of the particle substance on the rate of particle cooling and solidification.

Acknowledgment

I am happy to submit this paper for the special issue of ASME Journal of Heat Transfer because my first publication in this journal was kindly considered by Professor Michael F. Modest as an Associate Editor.

The author is also grateful to the Russian Foundation for Basic Research (Grant No. 07-08-00015) for the financial support of this work.

Nomenclature

a = particle radius
B_λ = Planck's function
c = heat capacity
c_0 = velocity of light
D = radiation diffusion coefficient
f = function introduced by Eq. (18)
f_v = volume fraction
h = heat transfer coefficient
I^0 = radiation energy density
k = thermal conductivity
L = latent heat of melting
n = index of refraction
N = conduction-to-radiation parameter
p_λ, P = radiation power in multiphase medium
q_λ, Q = radiative flux
Q_a = efficiency factor of absorption
r = radial coordinate
t = current time
T = temperature
w_λ, W = radiation power in the particle
x = diffraction parameter

Greek Symbols

α = absorption coefficient
δ = thickness of the radiating layer
κ = index of absorption
λ = radiation wavelength
μ_* = coefficient determined by Eq. (21)
ε = hemispherical emissivity
ρ = density
σ = Stefan–Boltzmann constant
τ = optical thickness

Subscripts and Superscripts

c = corium
cs = complete solidification
e = external
f = front of solidification
i = particle fraction number
liq = liquidus
p = particle
rad = radiative
s = surface, steam
sal = solidus, solidification
t = total
w = water
λ = spectral
(1) = semitransparency range
(2) = opacity range
$*$ = characteristic value

References

[1] Modest, M. F., 2003, *Radiative Heat Transfer*, 2nd ed., Academic, New York.
[2] Dombrovsky, L. A., 1996, *Radiation Heat Transfer in Disperse Systems*, Begell House, New York.
[3] Viskanta, R., 2005, *Radiative Transfer in Combustion Systems: Fundamentals and Applications*, Begell House, New York, Chap. 7.
[4] Dinh, T. N., Dinh, A. T., Nourgaliev, R. R., and Sehgal, B. R., 1999, "Investigation of Film Boiling Thermal Hydraulics Under FCI Conditions: Results of Analyses and Numerical Study," Nucl. Eng. Des., **189**(1–3), pp. 251–272.
[5] Fletcher, D. F., 1999, "Radiation Absorption During Premixing," Nucl. Eng. Des., **189**(1–3), pp. 435–440.
[6] Dombrovsky, L. A., 1999, "Radiation Heat Transfer From a Spherical Particle Via Vapor Shell to the Surrounding Liquid," High Temp., **37**(6), pp. 912–919.
[7] Dombrovsky, L. A., 2000, "Radiation Heat Transfer From a Hot Particle to Ambient Water Through the Vapor Layer," Int. J. Heat Mass Transfer, **43**(13), pp. 2405–2414.
[8] Dombrovsky, L. A., and Dinh, T. N., 2008, "The Effect of Thermal Radiation on the Solidification Dynamics of Metal Oxide Melt Droplets," Nucl. Eng. Des., **238**(6), pp. 1421–1429.
[9] Dombrovsky, L. A., Davydov, M. V., and Kudinov, P., 2009, "Thermal Radiation Modeling in Numerical Simulation of Melt-Coolant Interaction," Comput. Thermal Scien., **1**(1), pp. 1–35.
[10] Hale, G. M., and Querry, M. P., 1973, "Optical Constants of Water in the 200 nm to 200 μm Wavelength Region," Appl. Opt., **12**(3), pp. 555–563.
[11] Dombrovsky, L. A., 2007, "Large-Cell Model of Radiation Heat Transfer in Multiphase Flows Typical for Fuel-Coolant Interaction," Int. J. Heat Mass Transfer, **50**(17–18), pp. 3401–3410.
[12] Magallon, D., 2006, "Characteristics of Corium Debris Bed Generated in Large-Scale Fuel-Coolant Interaction Experiments," Nucl. Eng. Des., **236**(19–21), pp. 1998–2009.
[13] Dombrovsky, L. A., 2000, "Thermal Radiation From Nonisothermal Spherical Particles of a Semitransparent Material," Int. J. Heat Mass Transfer, **43**(9), pp. 1661–1672.
[14] Dombrovsky, L. A., 2002, "A Modified Differential Approximation for Thermal Radiation of Semitransparent Nonisothermal Particles: Application to Optical Diagnostics of Plasma Spraying," J. Quant. Spectrosc. Radiat. Transf., **73**(2–5), pp. 433–441.
[15] Dombrovsky, L. A., 2007, "Thermal Radiation of Nonisothermal Particles in Combined Heat Transfer Problems," *Proceedings of the Fifth International Symposium on Radiative Transfer*, M. P. Mengüç and N. Selçuk, eds., Begell House, New York.
[16] Mackowski, D. W., Altenkirch, R. A., and Mengüç, M. P., 1990, "Internal Absorption Cross Sections in a Stratified Sphere," Appl. Opt., **29**(10), pp. 1551–1559.
[17] Lai, H. M., Leung, P. T., Poon, K. L., and Young, K., 1991, "Characterization of the Internal Energy Density in Mie Scattering," J. Opt. Soc. Am. A, **8**(10), pp. 1553–1558.
[18] Dombrovsky, L. A., 1999, "Thermal Radiation of a Spherical Particle of Semitransparent Material," High Temp., **37**(2), pp. 260–269.
[19] Bohren, C. F., and Huffman, D. R., 1983, *Absorption and Scattering of Light by Small Particles*, Wiley, New York.
[20] Prishivalko, A. P., 1983, *Optical and Thermal Fields in Light Scattering Particles*, Nauka i Tekhnika, Minsk, Belarus (in Russian).
[21] Dombrovsky, L. A., 2004, "Absorption of Thermal Radiation in Large Semi-Transparent Particles at Arbitrary Illumination of the Polydisperse System," Int. J. Heat Mass Transfer, **47**(25), pp. 5511–5522.
[22] Chan, S. H., Cho, D. H., and Kocamustafaogullari, G., 1983, "Melting and Solidification With Internal Radiative Transfer—A Generalized Phase Change Model," Int. J. Heat Mass Transfer, **26**(4), pp. 621–633.
[23] Oruma, F. O., Özişik, M. N., and Boles, M. A., 1985, "Effects of Anisotropic Scattering on Melting and Solidification of a Semi-Infinite, Semi-Transparent Medium," Int. J. Heat Mass Transfer, **28**(2), pp. 441–449.
[24] Rubtsov, N. A., and Savvinova, N. A., 2003, "Effect of Radiation Scattering on the Dynamics of the Transitional Zone During Solidification of Semitransparent Material," J. Appl. Mech. Tech. Phys., **44**(5), pp. 676–680.
[25] Min, B. T., Song, J. H., Park, Y. S., and Kim, J. G., 2006, "A Physical and Chemical Analysis of Fast Quenched Particles of UO_2 and ZrO_2 Mixture," J. Nucl. Mater., **358**(2–3), pp. 243–254.
[26] Huhtiniemi, I., Magallon, D., and Hohmann, H., 1999, "Results of Recent KROTOS FCI Tests: Alumina Versus Corium Melts," Nucl. Eng. Des., **189**(1–3), pp. 379–389.
[27] Kudinov, P., Karbojian, A., Ma, W., and Dinh, T.-N., 2008, "An Experimental Study on Debris Formation With Corium Simulant Materials," *Proceedings of the International Congress on Advances in Nuclear Power Plants (ICAPP'08)*, Anaheim, CA, Jun. 8–12, Paper No. 8390.
[28] Bober, M., Singer, J., and Wagner, K., 1981, "Determination of the Optical Constants of Liquid UO_2 From Reflectivity Measurements ," *Proceedings of the Eighth Symposium on Thermophysical Properties*, Gaithersburg, MD, Vol. II, pp. 234–244.
[29] Bober, M., Singer, J., and Wagner, K., 1984, "Bestimmung der Optischen Konstanten von Geschmolzenen Kernbrennstoffen," J. Nucl. Mater., **124**, pp. 120–128.
[30] Anderson, E. E., 1976, "Radiative Heat Transfer in Molten UO_2 Based on the Rosseland Diffusion Method," Nucl. Technol., **30**, pp. 65–70.
[31] Ruello, P., Becker, K. D., Ulrich, K., Desgranges, L., Petot, C., and Petot-Ervas, G., 2004, "Thermal Variation of the Optical Absorption of UO_2: Determination of the Small Polaron Self-Energy," J. Nucl. Mater., **328**, pp. 46–54.
[32] Okkonen, T., and Sehgal, B. R., 1996, "Influence of Melt Freezing Characteristics on Steam Explosion Energetic," *Proceedings of the ASME/JSME Fourth International Conference on Nuclear Engineering (ICONE-4)*, Vol. 1, pp. 923–934.
[33] Fink, J. K., 2000, "Thermophysical Properties of Uranium Dioxide (Review)," J. Nucl. Mater., **279**, pp. 1–18.
[34] Journeau, C., Piluso, P., and Frolov, K. N., 2004, "Corium Physical Properties for Severe Accident R&D," *Proceedings of the ICAPP'04*, Pittsburg, PA, pp.

1062–1071, Paper No. 4140.

[35] Viskanta, R., and Grosh, R. J., 1962, "Heat Transfer by Simultaneous Conduction and Radiation in an Absorbing Medium," ASME J. Heat Transfer, **84**(1), pp. 63–72.

[36] Siegel, R., 1998, "Transient Thermal Effects of Radiant Energy in Translucent Materials," ASME J. Heat Transfer, **120**(1), pp. 4–23.

[37] Siegel, R., 1998, "Transient Effects of Radiative Transfer in Semitransparent Materials," Int. J. Eng. Sci., **36**(12–14), pp. 1701–1739.

[38] Dombrovsky, L. A., 2009, "Approximate Model for Break-Up of Solidifying Melt Particles Due to Thermal Stresses in Surface Crust Layer," Int. J. Heat Mass Transfer, **52**(3–4), pp. 582–587.

[39] Dombrovsky, L. A., 2009, "A Model for Solid Bubbles Formation in Melt-Coolant Interaction," Int. J. Heat Mass Transfer, **52**(5–6), pp. 1085–1093.

[40] Yuan, M. H., Yang, Y. H., Li, T. S., and Hu, Z. H., 2008, "Numerical Simulation of Film Boiling on a Sphere With a Volume of Fluid Interface Tracking Method," Int. J. Heat Mass Transfer, **51**(7–8), pp. 1646–1657.

[41] Dombrovsky, L. A., and Sazhin, S. S., 2003, "A Parabolic Temperature Profile Model for Heating of Droplets," ASME J. Heat Transfer, **125**(3), pp. 535–537.

[42] Dombrovsky, L. A., 2007, "An Estimate of Stability of Large Solidifying Droplets in Fuel–Coolant Interaction," Int. J. Heat Mass Transfer, **50**(19–20), pp. 3832–3836.

Effect on Radiant Heat Transfer at the Surface of a Pool Fire Interacting With a Water Mist

J. P. Garo[1]
e-mail: garo@lcd.ensma.fr

J. P. Vantelon

Laboratoire de Combustion et de Détonique,
University of Poitiers,
ENSMA,
1 Avenue Clément Ader Téléport 2—BP 40109,
86961 Futuroscope Chasseneuil Cédex, France

D. Lemonnier
Laboratoire d'Etudes Thermiques,
University of Poitiers,
ENSMA,
1 Avenue Clément Ader Téléport 2—BP 40109,
86961 Futuroscope Chasseneuil Cédex, France

It is well established that the use of water mist can be an attractive alternative to gaseous suppression agents to extinguish fires for specific scenarios. Among the main mechanisms, which act together to extinguish fires when using a water mist: heat extraction, oxygen displacement, and radiant heat attenuation, the last one has received the less attention, especially regarding the energy balance at the fuel surface and, therefore, the rate of generation of flammable vapors. The objective of this work is to analyze, on the one hand, the perturbing influence of a mist addition as an opposed flow to a small-scale liquid (heptane) pool fire structure, especially at its base, the more interesting zone regarding the mechanisms of flame stabilization and extinction and, on the other hand, the effect on the surface radiant heat feedback. Experiments conducted give an order of magnitude estimate in essential agreement with a radiation computation, based on the mappings, previously obtained, of the two major parameters: temperature and extinction coefficient, that determine the thermal radiation of the flame. The important information is the confirmation that radiation attenuation cannot be identified as a predominant mechanism of extinguishment. [DOI: 10.1115/1.4000185]

Keywords: pool fire, fire suppression, water mist, radiation

1 Introduction

Since the withdrawal of halon for environmental reasons, the use of water mist is widely considered to be an efficient alternative to extinguish or limit the spread of fires.

The dominant extinguishing actions of water mist are those of water, heat extraction, and oxygen displacement, but the very fine droplet size (typically less than 400 μm) provides a considerable benefit in evaporation and heat absorption rapidity. As a corollary to this increasing efficiency, fine droplets may be used without causing serious collateral damages.

If the two above-mentioned main mechanisms, which act together to extinguish fires when using water mist are described for a long time (see for instance, Braidech et al. [1] and Rasbash et al. [2] in 1960s, but more particularly, the excellent overview by Mawhinney et al. [3]), a third mechanism is not as well understood: the expected attenuation of the radiant heat from the flame (change of radiant heat through scattering and absorption of thermal energy). Although this attenuation has never been referenced as a determining mechanism of extinguishment, all efforts in water mist suppression modeling needs to explore its implication.

The blocking radiant heat effect of water mist presents, in fact, a twofold interest: reduce the radiant heat flux to targets in the surroundings (important benefit, both in compartment and open fires) and, reduce the vaporization or pyrolysis rate at the fuel surface.

The possibility of using water mist as a barrier or curtain against radiation damage was widely investigated in the past decades (Refs. [4–13] for instance). The proposed models consider the medium as a two phase semitransparent medium constituted by polydisperse water droplets and possibly participating gases such as water vapor and carbon dioxide. In contrast, the characterization of radiant heat attenuation between flame and fuel surface is much more complex, and has received, until now, much less attention. It appears that there has been no systematic study of this. In addition, to quote Mawhinney et al. [3]: "One question that arises is to what extent is the measured reduction in radiant heat due to the cooling and reduced size of the flame, and to what extent is it due to attenuation of the radiant heat through scattering and absorption of thermal energy." It is theoretically expected that radiant heat from the flame to the fuel could be absorbed by droplets and water vapor inrushing the flame, but this is particularly difficult to quantify [14–16]. In fact, the resulting effect is difficult to predict, and more experiments are needed to assess the relative importance of radiant heat change in the energy balance at the fuel surface.

The work is to ensure a better understanding of the effect of a water mist entering a flame, regarding the energy balance at the fuel surface and, therefore, the rate of generation of flammable vapors.

The thermal radiation from any combustion system is mainly controlled by the temperature and extinction coefficient distributed throughout the flame. The distribution of these two major properties, temperature and extinction of light, due primarily to the presence of soot particles and water droplets, is provided. This is used to infer the establishment, the structure, and the stabilization of the flame during water mist addition, but it is also more especially used to provide a database to calculate the flame radiation, and to compare the results to radiant heat flux measurements at the surface.

For convenience, the study is conducted with a horizontal liquid fuel surface (pool fire) of medium scale. This has both practical and fundamental interest because, on the one hand, an experiment of this type can be conducted in the laboratory while conserving the major characteristics of an actual fire and, on the other hand, pool fire is one of the most basic forms of fuel combustion, and is often present in accidental fires involving liquid fuels.

2 Experiment

For purposes of designing a laboratory experimental system, facilitating analysis of radiation heat feedback to the fuel during extended experimental times, the idea was to insure conditions, such that neither gas-phase cooling nor vapor dilution were sufficient to suppress the flame and the fire as it continues to burn in spite of the mist addition.

---

[1] Corresponding author.

Contributed by the Heat Transfer Division of ASME for publication in the JOURNAL OF HEAT TRANSFER. Manuscript received October 28, 2008; final manuscript received April 9, 2009; published online December 1, 2009. Assoc. Editor: Yogesh Jaluria.

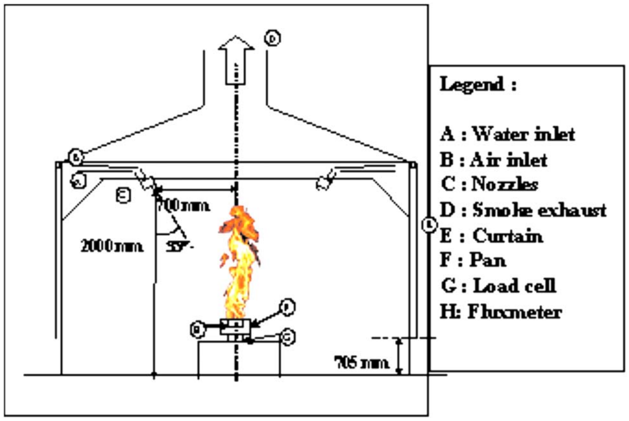

Fig. 1 Experimental device

The pool burning tests were conducted in a rectangular chamber (8 cm^3) vented by natural convection; the section diameter of the exhaust duct is 40 cm.

Experiments are performed with heptane (floating on water) pool fires of moderate scale. Heptane was chosen because it has the advantage of a fixed boiling point (98°C) below that of water, and as a consequence, it does not experience boil over, avoiding any serious splashing effect of water droplets striking the surface, which may disturb the measurements. On the other hand, due to its low flash point temperature (−4°C) and high vapor pressure, it is difficult to reduce the vapor/air mixture to below its lean flammability limit.

Heptane is contained in a circular stainless steel pan, 10 cm deep, with a diameter of 23 cm. The pan is placed on a load cell to measure the fuel mass loss as a function of time. The load cell has a response time of 60 ms, and the uncertainty of measurements is within 5%. Before each test, water was first poured on the pan until it reached the radiometer window. The radiometer was horizontally oriented, and it was submerged. Fuel is added so that the pan is filled to 1 mm below the pan lip. During the combustion, the location of the top of the radiometer (window)/water interface remained fixed. Therefore, since the height of the burning fuel surface decreases as combustion progresses, the freeboard length increases during the experiment. Each test was repeated three times.

2.1 Water Mist Characteristics and Application. It is well established that for the success in extinguishing fires, water mist characteristics require droplets to be distributed with enough energy to penetrate the flame, mixed turbulently, and, as much as possible, mixed uniformly in all zones of the flame. This implies that the mist must be delivered as an opposed cloud with high momentum, properly oriented, in order to push the water vapor formed against the fuel surface. Therefore, great attention must be paid to the location and orientation of application of the nozzles, to their type, to droplets size distribution and mist momentum, and to the mass of water added.

Thus, the water mist system consists of three nozzles located symmetrically with respect to the flame axis (120 deg), and directed toward the fuel surface center. The distance between the nozzles and the liquid surface is 129 cm, and their radial position is 70 cm (Fig. 1).

The nozzles are twin fluid (water/air) pressure assisted atomizers permitting the control of the droplet size, flow density, and momentum of the mist. The applied air pressure and water flow are chosen, as explained above, in such a way that complete extinguishment is not be achieved, giving enough time for experimental purpose. It is noteworthy that the difficulty to reduce the heptane vapor/air mixture above the surface below to lean flammability limit makes it easy.

In the described experiments, each nozzle works at a normal operating air/pressure of 1 bar and a water mass flow rate of 3.5 g s^{-1}. In such condition, the mean drop size (maximum of the unimodal distribution characterized by particle Doppler analyzer) is 30 μm.

2.2 Temperature. The temperature measurements were performed with an array of chromel-alumel thermocouples, type K of 120 μm wire diameter. The first thermocouple was placed 1 cm above the top of the support, and the others were located 1 cm apart from each other. The array was mounted on a two-dimensional traverse mechanism, which allowed a positioning in both horizontal and vertical directions to within 0.5 mm. The output signals are fed to a high-gain DC amplifier and then to a data acquisition system. The digitized signals are sampled and stored at a rate of 500 Hz. Notice that measurements were made only during short periods not exceeding 30 s, immediately following the insertion of the thermocouples in the flame, to avoid, as much as possible, the effect of soot deposition. The measured temperatures were time averaged; the variations in the mean did not exceed 5%. Each test was repeated three times. As seen above, for a water mist to be efficient, the droplets must be capable of penetrating the flame. The proposed design generates sufficient momentum, at the three points of discharge, to overcome the upward momentum of the plume, and it is well-suited for the analysis of the interaction between the water mist and flame.

2.3 Extinction Coefficient. Local monochromatic extinction coefficients were measured with a laser light attenuation method. A laser beam was directed to a specified localization in the flame through a stainless steel tube, 1 cm in diameter, and the attenuated intensity light passing through a second stainless steel tube of the same diameter, was received by an appropriate detector, which had a narrow band pass filter in front of it, centered at the wavelength of the emitting beam. The distance between the laser beam and the detector was about 2 m. Comparison of the light intensity through a fixed path length (2 cm) between the two tubes and the intensity of the emitting beam permitted the deduction of the local value of the monochromatic extinction coefficient $k_{e,\lambda}$ (m^{-1}) by using Beer's law at the wavelength of the light used in the experiments. The laser probe positioning was also controlled with the aforementioned two-directional system.

The data were also time averaged, and the uncertainty associated with each value could be high (up to 15%), a problem that is inherent in the experimental technique. The mesh size for the measurements was 1 cm for both axial and radial directions. No measurements were performed for distances closer than 3 cm to the liquid surface because of the dimensions of the laser probe system. Each test was repeated three times.

2.4 Radiant Heat Flux. Radiant heat flux at the fuel surface was measured by means of a water cooled Gardon-gauge-type radiometer (MEDTHERM: a cylinder stainless steel pan, 1 in. deep, with a diameter of 1 in.) working in the range 0–2 W cm^{-2}, and equipped with a window (with a diameter of 6 mm). The radiometer was water cooled and was purged. The water cooling tubes are 1/8 in. in diameter of stainless steel.

The addition of a window eliminates the convective heat flux from the sensor, but restricts the spectral content of the radiation to that within the range of its spectral transmittance.

The window used was in calcium fluoride, which offers a useful range of spectral transmittance between 0.3 μm and 11.5 μm. This spectral range was very convenient to take into consideration the contribution of water droplets or vapor within the flame that can interact with radiation until about 10 μm, and, a fortiori, from luminous flames that have almost all their contribution below about 5–6 μm (the spectral range from the luminous flame without water mist addition is between 0.5 μm and 5 μm).

The attachment of a window also requires a window mount that reduces the field of view from 180 deg to 150 deg. The radiation

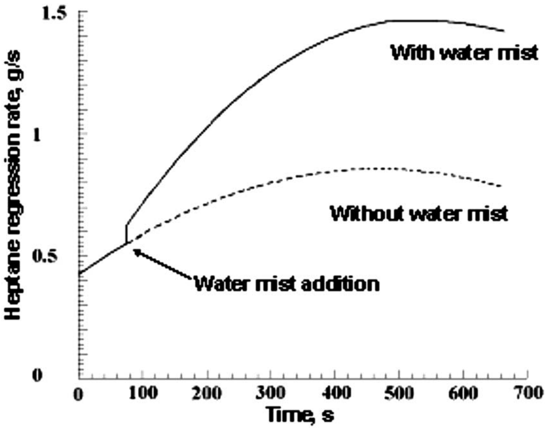

Fig. 2 Evolution of the mass burning rate as a function of time

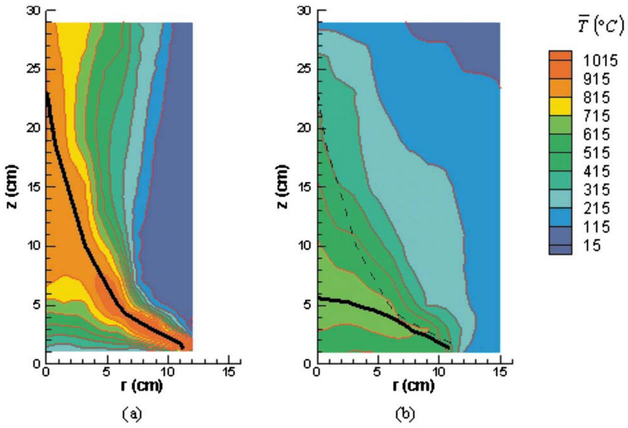

Fig. 3 Field of temperature at the base of the heptane pool fire (the line of temperature maximum is also indicated for reference) (***a***) before mist addition, and (***b***) during mist addition

form factor is then slightly reduced, but the calibration takes this into consideration. The uncertainty in flux measurements was 3%. The radiometer was located along the pan axis at a fixed position, and the radiant heat flux at the surface was determined when the regressing surface of the fuel reaches this position. This position is fixed at 12 mm from the initial fuel surface in the water. In such position, there was no limitation of view by the edge of the pan, and the time for the fuel surface to reach the sensor was long enough to insure the flame establishment and stabilization. In this configuration, the millivolt response of the Gardon-type heat flux gauge represents only the incident radiative heat flux. The radiant heat flux at the surface was obtained by extrapolating the measured heat flux evolution across the fuel. The measurements were done at a steady state condition defined when the mass burning rate seems constant, and when the mass burning rate was maximum (between 450 s and 55O s). Each test was repeated three times, but we must be well aware that the deduced radiant heat fluxes at the fuel surface were only approximate (uncertainty associated with the method).

3 Results

A large number of studies were performed on the characteristics of buoyant diffusion flames established at the surface of laboratory-scale liquid pool fires (see for example Refs. [17,18]). Recall that the fire plume is customarily divided into three regions. At the flame base is the "persistent" zone, which is characterized by a luminous annular flame that surrounds a central zone rich in vapor fuel, which appears, at least statistically, to have a constant shape and structure (in fact, the flame fluctuates back and forth across a mean position). This zone has chemical reactions and air entrainment taking place. It is followed by the "intermittent" zone that has a turbulent character giving rise periodically to rising rolling structures. The last region is the "plume" zone that is not reacting, and where the velocity and temperature decrease progressively with height. Of these zones, the persistent zone is the most interesting regarding flame establishment, stabilization, and extinction. The temperature and extinction coefficient were measured when the mass burning rate was maximum (between 450 s and 55O s) at discrete locations along a radial vertical plane at the base of the heptane pool fire, without and with water mist addition. Because the flame characteristics in this zone are statistically axisymmetric, the measurements are also considered to be axisymmetric and consequently, representative of those in any radial vertical plane.

3.1 Without Water Mist Addition

3.1.1 Mass Burning Rate. The broken line in Fig. 2 shows the evolution of the mass burning rate as a function of time, without water mist addition. It can be observed that the rate increases first, reaches a maximum ($0.89\ \mathrm{g\ s^{-1}}$), and then decreases slightly, showing a dependence of freeboard height. As the freeboard increases when the burning fuel surface regresses, the heat loss to the freeboard of the pan increases and becomes more and more significant.

3.1.2 Temperature. The measured isotherm field is presented in Fig. 3(*a*). The maximum temperature location, which represents the presence of the reactivity maximum, is also indicated in the figure. It is seen that the maximum is displaced from the edge of the pan to the flame axis, surrounding a central zone, rich in vapor fuel. At the flame axis, the maximum is located around 25 cm, which corresponds approximately to one pool diameter, a value that has been generally observed previously in other free fires of same diameters. The overall temperature distribution is characteristic of that encountered in diffusion flames, with a narrow band of maximum temperature and relatively large temperature gradients at both sides (see for example Ref. [17]). At the lower leading edge, there is a region of high temperature with large gradients in the normal and radial directions. The convective mixing is due to the strong radial component of the air velocity induced by the plume in this region. In fact, this has an important role in anchoring the diffusion flame and in its stabilization and extinction. The middle region is where the temperature distribution indicates the presence of a well-defined diffusion character, at least statistically. The maximums of temperature are relatively low, which suggests the existence of fluctuations since the temperatures recorded are averaged temperatures.

The region closer to the pool centerline is characterized by low temperature gradients and a wider maximum temperature band with a lower maximum value. This is the indication that it is in this region that the strong intermittency of the fire is established. In summary, it is possible to say that the base of the fire is characterized by a fluctuating laminar diffusion flame that is transformed into a turbulent one in the upper region.

As the measurements are not instantaneous, they will provide averaged values where the measured properties are influenced by the flame fluctuation or intermittency. Because the physical parameters controlling the radiation heat transfer interact in a highly nonlinear fashion, radiation calculation based upon time mean values of temperature are known to be subject to serious errors.

3.1.3 Extinction Coefficient. Measurements of extinction coefficients were performed in the visible range of the spectrum with a helium /neon laser emitting at 633 nm, wavelength at which the extinction is due primarily to the presence of soot. Due to their small size (60–80 nm), the soot particles are mainly absorbing particles (scattering is negligible), and the actual coefficients are

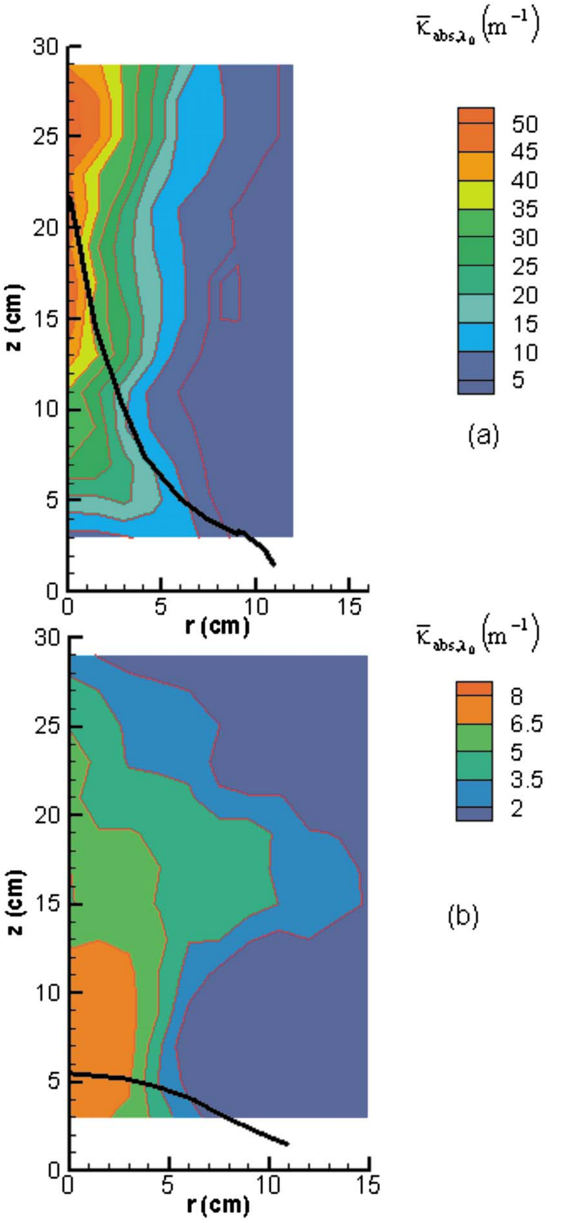

Fig. 4 Field of monochromatic (λ=633 nm) absorption coefficient due to soot at the base of the heptane pool fire (the line of temperature maximum is also indicated for reference) (*a*) before mist addition, and (*b*) during mist addition

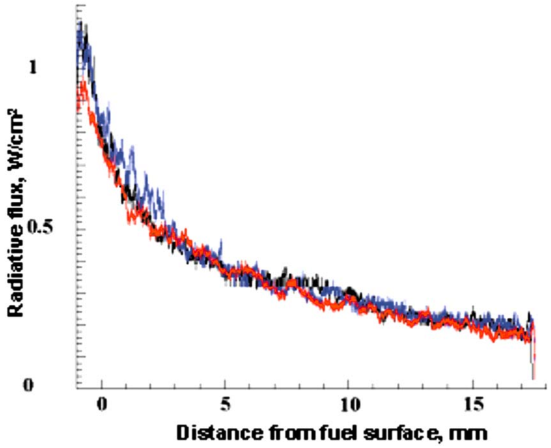

Fig. 5 Evolution of the radiant heat flux in depth as a function of the distance from the fuel surface (for three tests conducted in similar conditions without mist addition)

absorption coefficients $k_{a,\lambda}$ rather than extinction coefficients. Thence, the contour of the lines can also be viewed as lines of equal soot concentration (Fig. 4(*a*)).

The measurements show a region of elevated soot concentration along the axis, at both sides of the maximum temperature. In the region near the axis and under the maximum temperature line, the existence of stagnant and recirculating gas would result in the accumulation of fuel vapor, pyrolysis products, and soot.

But, at the base of the flame, near the lower leading edge, the level of temperature is too high for soot to remain unburnt, which explains the low values obtained here. Soot concentration also peaks near the pool surface centerline, as generally observed. Indeed, the formation of soot is initiated near the liquid, and the pyrolysis of the vaporized fuel takes place and is enhanced but it is progressively counterbalanced upper by a more efficient oxidation. Above the temperature maximum, the presence of elevated soot concentration at the centerline indicates the presence of unburnt fuel, and corresponds to the continuation of the combustion reaction in the intermittent zone of the flame.

3.1.4 Radiant Flux Measurements. The radiant heat flux is recorded as a function of time. Knowing the initial fuel level position (measured accurately), the location of the radiometer, and the instantaneous burning rate, it is easy to deduce the evolution of the radiant heat flux in depth as a function of the distance from the sensitive surface of the radiometer.

Figure 5 shows this evolution for three tests conducted in similar conditions without water mist addition. A very satisfying reproducibility is seen. From these measurements, the radiant heat flux at the fuel surface (the distance from the fuel surface is 0) at the center of the pool can be estimated to be in the range 0.79–0.85 W cm^{-2}. But it is well-known that the rate of burning is not constant across any horizontal fuel surface and is more rapid toward the center.

In a previous work, Richard et al. [19], performing measurements for different radial positions with a pan with a diameter of 23 cm (0, 1/3, and 2/3 of the radius), showed that the mean radiant heat flux received by the heptane surface can be estimated as 90% from the maximum radiant heat flux measured at the center (without and with water mist addition).

Thus, from the present results, a mean radiant heat flux value at the surface $\overline{\dot{q}''_{r,s}}=0.74$ W cm^{-2} can be deduced. This value is slightly higher than the value 0.52 W cm^{-2} reported by Richard et al. [19], with a mass burning rate $\dot{m}''=1.59.10^{-2}$ kg/m^{-2} s^{-1}. The discrepancy must be attributed to the difference of experimental method. In the previous work, the authors used the same type of radiometer, but located at different depths in the fuel; the level of the fuel surface being kept constant by means of a gravity liquid-feeding system. Therefore, the radiant heat flux at the surface was obtained by extrapolating the measured heat flux evolution across the fuel. Even if the measurements were done at steady state conditions, defined when the mass burning rate becomes constant, the method required a test for each location, in depth of the radiometer, and this repetition multiplied the uncertainties of measurement. This previous method was obviously less accurate than the present one. This can also be attributed to the less accurate previous method of measurement, as mentioned above, but also to the use of a radiometer equipped with a sapphire window, which offered a spectral transmittance limited to 5 μm

Table 1 Energy balance at the heptane surface without and with mist addition

	Without water mist addition (a)	With water mist addition (b)
$\dot{m}''(\mathrm{kg/m^{-2}\ s^{-1}})$	1.99×10^{-2}	3.54×10^{-2}
$\overline{\dot{q}''_{r,s}}(\mathrm{W\ m^{-2}})$	7.4×10^{3} (60%)	3.5×10^{3} (16%)
$\overline{\dot{q}''_{\mathrm{cv},s}}(\mathrm{W\ m^{-2}})$	5.02×10^{3} (40%)	18.9×10^{3} (84%)

$$\dot{m}'' = \frac{\dot{q}''_{r,s} + \dot{q}''_{\mathrm{cv},s}}{\Delta H_v + C_{Pl}(T_s - T_l)} \tag{1}$$

Knowing the instantaneous mass burning rate $\dot{m}''$, the latent heat of heptane vaporization, the specific heat at constant pressure, the boiling point of the fuel, and the initial temperature of the fuel ($\Delta h_v = 4.7.10^5$ J kg^{-1}, $C_{Pl} = 1.85.10^3$ J/kg^{-1} K^{-1}, $T_s = 98$°C), it is possible to consider the energy balance at the surface (relation (1)). The results of the calculations are given in Table 1. It is seen that the radiant heat feedback to the surface falls far short of that necessary to generate the flow of combustible vapors. Near the pool centerline, the existence of stagnant and recirculation gas zone results in the accumulation of fuel vapor, pyrolysis products, and soot in this region. This attenuates the radiation reaching the surface, and the difference between the estimated radiant heat flux and the heat flux required to produce the flow of vapors is supplied by convection. For the results (Table 1), the radiant component of the total heat flux is 60%, and the convective component is 40%. Notice that the relative magnitude of the effects is similar than in the work by Richard et al. [19]: 59%/41%. The predominance of the radiant component is in agreement with that generally observed for the burning of heptane pools of this size.

3.2 With Water Mist Addition. When water mist is added, with the adopted conditions of application, the flame structure changes completely. The interaction between mist and flame can be divided into three phases.

During the first phase, the behavior of the flame does not really differ from those before mist application. The flame only seems to be pushed against the fuel surface and its volume is significantly reduced, especially at the top. During the second phase, the flame suddenly seems to "explode" with random lateral projections of more or less large pockets of warm unburnt fuel and products (see Fig. 6). This is the result of penetration of droplets in all regions of the flame and of their rapid evaporation and expansion, which causes gas displacement in the vicinity. During this phase of lateral expansion, the flame appears to be concentrated around the inside edge of the pan with clearances from a part or even the whole of the liquid surface. The flame looks like an annular flame concentrated and anchored around the inside edge of the pan. It is noteworthy that it is during this phase expansion, with full clearance of the surface, that the extinction could be obtained. This requires that the mist be applied with enough momentum so as to overcome the anchoring effect, and to avoid flashback. A third phase corresponds to a flashback, the flame recovering a behavior characteristic of the one observed during the first phase. Afterwards, a new cycle can take place. An analysis of simultaneous video recording shows that, on the whole, the time between two "puffs" is approximately 4–5 s, and that the puff time is about 0.5 s.


The first phase The second phase The third phase

Fig. 6 Photograph of the flame during the vaporization-expansion phase

Although less relevant to the present work because of the lack of detailed measurement of flame structure, the work of Rasbash et al. [2] 40 years ago reported that during the application of mist, hydrocarbon flames were unstable, with size and shape varying continuously, and that there were frequent clearances of the surface, sometimes followed by extinction. This behavior suggests that extinction is rather achieved by a rapid and total clearance of the surface, resulting from water evaporation and expansion, than from the reduction of the rate of evolution of combustible vapor from the liquid. Moreover, vapor fuel is probably pushed against the surface by the high momentum and expansion effect of the mist, with subsequent increase in concentration. The remark is especially true for liquids with low flash points such as heptane: flashback may occur easily, and any hot object near the fuel surface such as the pan edge can cause reignition.

The measurements, being not instantaneous, give averaged values when the measured properties are influenced by flame fluctuation or disruption resulting from droplets vaporization.

3.2.1 Mass Burning Rate. The solid line in Fig. 2 shows likewise the evolution of the mass burning rate as a function of time, but with water mist addition. The general trend is the same but, once the water mist is activated, the burning rate deeply increases. Afterwards, the maximum reaches 1.46 g s^{-1}. The sudden increase observed at the onset of water mist addition is the result of an apparent change of weight caused by the high momentum of the mist directed toward the fuel surface. Notice that the presented curve is a corrected curve for water recuperated at the bottom of the pan (some droplets reaching the fuel surface fall on the bottom). The mean mass rate of recuperation, determined from the total mass recuperated, divided by the overall combustion duration, was 0.12 g s^{-1}.

It appears clearly that with the adopted conditions of application, the water mist significantly intensifies the pool fire (with a small amount of water, the heat transfer increases [20]). The visual evidence corroborated by measurements is that the turbulence generated in the flame acts to increase the burning rate of the fuel. A similar increase in water mist is often observed when using underdesigned systems (unable to lead to complete extinction).

3.2.2 Temperature. It is clear evidence that the tridimensional and transient aspects are dominant, and that it is difficult to characterize how the mist and fire plume are likely to interact. Despite the periodic cycle eruptive vaporization flashback and a much less ordered structure than the unperturbed heptane pool fire, the flame can be considered as statistically axisymmetric over a sustained period of mist addition, and the measurements are also considered to be axisymmetric. The measured isotherm field is presented in Fig. 3(*b*). By comparison with measurements without mist addition, an overall decrease in the temperature level can be observed (about 700°C instead of 1000°C for the maximum). Moreover, the line of temperature maximum is very significantly displaced toward the surface (about 5 cm instead of 25 cm). The general isotherm pattern is not representative of a fire plume but rather of an opposed flow system, except that the outwards direction at the base turns inward in the upper region, owing to the orientation and the force of mist application. The general decrease in temperature is due primarily to the very efficient cooling effect of the mist, but it reflects also the existence of strong disturbances. The flame is characterized, on average, by low temperature gradients and a wider maximum temperature band with a lower maximum value. Colder and hotter gases periodically reach the thermocouples, and this much more randomly occur than without mist addition. In fact, the fluctuations are no longer the result of the periodic flapping of the flame, due to the inward entrainment of fresh air.

3.2.3 Extinction Coefficient. The disturbances are generated by the expansion and break up of the flame in pockets of hot gases or large turbulent structures. Unlike the unperturbed flame for which the structure is determined by buoyancy, which is the predominant driving force, the strong radial convective component induced by the expansion effect of mist evaporation dominates the behavior. With water mist, in addition to soot particles, water droplets contribute to some extent to changes not only in the radiant heat through absorption but also through scattering. For soot particles, we have seen that scattering can be ignored due to their small size, but for water droplets, whose dimension is much larger, scattering becomes rapidly comparable to absorption or being predominant. Droplets may scatter in a nearly isotropic manner or forward, in such a way that the bulk of the scattered radiation is contained in a narrow solid angle around the incident direction.

Considerations based on the Mie theory show that for a monodispersed spherical droplets cloud and in absence of multiple scattering, the monochromatic extinction coefficient $k_{e\lambda}$ is the sum, over individual droplets, of the extinction cross section $C_{e\lambda}$

$$k_{el} = NC_{e\lambda} \tag{2}$$

where N is the droplets concentration.

In terms of extinction, absorption, and scattering efficiencies, $Q_{e\lambda}$, $Q_{a\lambda}$, and $Q_{s\lambda}$, the apparent monochromatic extinction coefficient $k_{e\lambda}$ can be written as

$$k_{e\lambda} = sNQ_{e\lambda} = sN(Q_{a\lambda} + Q_{s\lambda}) \tag{3}$$

where

$$Q_{e\lambda} = Q_{a\lambda} + Q_{s\lambda} = \frac{2}{\alpha^2}\sum_{n=1}^{\infty} (2n+1)\{\mathrm{Re}(a_n + b_n)\}$$

with $\alpha = \pi d/\lambda$ (d is the diameter of the particle), and a_n and b_n can be calculated from Ricatti–Bessel functions.

Let us consider a detector of surface S centered on an incident beam axis at a given distance from a droplet. The radius of the detector and its location determine the collected scattered power in the forward direction. Relation (3) becomes

$$k_{e\lambda} = sN(Q_{a\lambda} + Q_{s\lambda}(1 - R_\lambda)) \tag{4}$$

where s is the droplet cross section, and $R_\lambda = \int\int_s I_s(\theta\phi)dS/I_oC_s$ is the normalized collected scattered power for the detector used, dependent on the droplet diameter and on the wavelength, $(I_s(\theta,\phi)$ is the scattered intensity distribution, with θ and ϕ as the common angles of a spherical coordinate system intrinsic to the incident beam, and I_oC_s is the total scattered power with C_s the scattering cross section).

Relation (4) can also be simply written in terms of absorption and scattering coefficients $k_{a\lambda}$ and $k_{s\lambda}$ as

$$k_{e\lambda} = k_{a\lambda} + k_{s\lambda}(1 - R_\lambda) \tag{5}$$

For experiments performed in a medium containing both soot particles and water droplets, the apparent extinction coefficient is then written as follows:

$$k_{e\lambda} = k_{as} + k_{ad} + k_{sd}(1 - R) \tag{6}$$

where the second subscripts s and d pertain to soot and water droplet, respectively (subscript λ is omitted to simplify the writing). Due to their small size (60–80 nm), the soot particles are mainly absorbing particles (scattering is negligible), and the actual coefficients are absorption coefficients. The extinction coefficient can be expressed as

$$k_{e\lambda} = k_{as} + k_{sd}[(1 - R) + k_{ad}/k_{sd}] \tag{7}$$

The ratio between absorption and scattering coefficients, which is equal to the ratio of the corresponding absorption or scattering efficiencies, can be used as

$$\frac{k_{ad}}{k_{sd}} = \frac{NsQ_{ad}}{NsQ_{sd}} = \frac{Q_{ad}}{Q_{sd}} \quad \text{or} \quad \frac{k_{as}}{k_{ss}} = \frac{Q_{as}}{Q_{ss}} \tag{8}$$

Relation (8) can also be written as

$$k_{e\lambda} = k_{as} + k_{sd}[(1 - R) + Q_{ad}/Q_{sd}] \tag{9}$$

where the absorption and scattering efficiencies Q_{ad} and Q_{sd} can be calculated from the Mie theory since they are independent of particle concentration and medium depth, provided that the assumption of single scattering holds.

Calculations have been performed considering, as stated earlier, a monodispersed water droplet suspension with a diameter of 30 μm, and, likewise, a monodispersed soot particle suspension with a diameter of 70 nm. In a first approach, the residence time of the droplets in the flame is considered as large compared with their vaporization time. The optical properties used are, for soot particles, those proposed by Chang and Charalampopoulos [21], and for water droplets, those proposed by Hale and Querry [22].

For experiments performed, as previously described, at a wavelength of 633 nm, the calculation gives

$$Q_{ad} = 0.734 \times 10^{-5}, \quad Q_{sd} = 2.06, \quad \text{and} \quad R = 0.162$$

and it appears that relation (9) is reduced to

$$k_e = k_{as} + 0.838 \cdot k_{sd} \quad (\lambda = 633 \text{ nm}) \tag{10}$$

The concentrations of soot and water droplets, being unknown, is clear evidence that this relation is not sufficient to determine the respective contribution of soot and droplets to the detector signal. Thus, it was necessary to perform measurements at another wavelength. In order to minimize the forward scattering of water droplets, the wavelength was chosen in the infrared range: a helium/neon laser emitting at 3390 nm (notice that there is no contribution of gaseous combustion products at this wavelength).

The calculation gives

$$Q_{ad} = 0.922, \quad Q_{sd} = 1.369, \quad \text{and} \quad R = 0.44 \times 10^{-2}$$

and relation (10) becomes

$$k_e = k_{as} + 1.670 \cdot k_{sd} \quad (\lambda = 3390 \text{ nm}) \tag{11}$$

In addition, a relation between the measurements at the two wavelengths is needed. The ratio between absorption or scattering coefficients, which is equal to the ratio of the corresponding absorption or scattering efficiencies, can be used as

$$\frac{k_{as_{\lambda_1}}}{k_{as_{\lambda_2}}} = \frac{Q_{as_{\lambda_1}}}{Q_{as_{\lambda_2}}} \quad \text{or} \quad \frac{k_{sd_{\lambda_1}}}{k_{sd_{\lambda_2}}} = \frac{Q_{sd_{\lambda_1}}}{Q_{sd_{\lambda_2}}} \tag{12}$$

and

$$(k_{as})_{\lambda_1} = \frac{k_{e,\lambda_1} - \dfrac{R_{\lambda_1}}{R_{\lambda_2}}\dfrac{(Q_{sd,\lambda_1})}{(Q_{sd,\lambda_2})}k_{e,\lambda_2}}{1 - \dfrac{R_{\lambda_1}}{R_{\lambda_2}}\dfrac{(Q_{sd,\lambda_1})}{(Q_{sd,\lambda_2})}\dfrac{(Q_{as,\lambda_1})}{(Q_{as,\lambda_2})}} \tag{13}$$

For example, the ratio between the soot absorption coefficients at the two wavelengths, which is equal to the ratio of the corresponding absorption efficiencies, can be used as

$$k_{as}(633 \text{ nm}) = k_{as}(3390 \text{ nm})Q_{as}(633 \text{ nm})/Q_{as}(3390 \text{ nm})$$

$$\text{with} \quad Q_{as}(633 \text{ nm}) = 0.347 \quad \text{and} \quad Q_{as}(3390 \text{ nm}) = 0.074 \tag{14}$$

Finally, combining relations (10)–(14) permits the determination of the fields of soot absorption coefficient and water droplet scat-

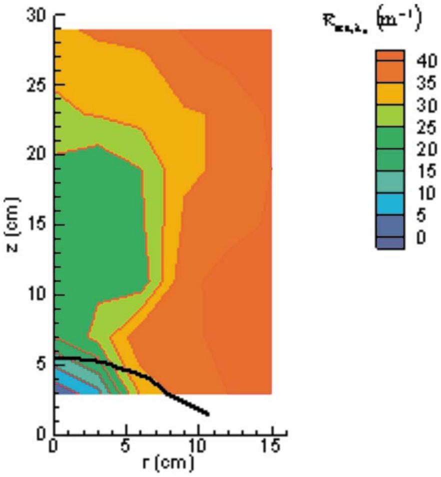

Fig. 7 Field of monochromatic ($\lambda=633$ nm) scattering coefficient due to water droplets at the base of the heptane pool fire

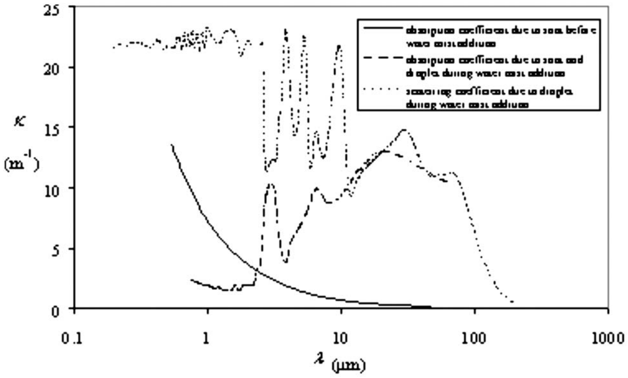

Fig. 8 Evolution of: (*a*) absorption coefficient without mist addition (due to soot particles), (*b*) total absorption coefficient with mist addition (due to soot particles and droplets), and (*c*) scattering coefficient with mist addition (due to droplets) as a function of wavelength at a discrete location in the flame ($r=0,75$ cm, $z=9$ cm)

tering coefficient, which are representative of the corresponding concentrations.

The field of monochromatic soot absorption coefficient ($\lambda=633$ nm) with water mist addition is presented in Fig. 4(*b*). It is seen that the values are, on the whole, much lower than without mist addition. The region of more elevated soot concentration is always near the pool axis. However, near the pool centerline, there is no more stagnant and recirculating region with accumulation of fuel vapor and pyrolysis products and, therefore, soot concentration is lower. The results suggest that mist addition should have an important role in the combustion process: mixing and chemical effects. Water addition disturbs the flow, the temperature, and the fuel concentration fields; this greatly affects both chemical and physical phenomena. The expansion effect, due to water vaporization, tends to increase buoyancy, and the combustion efficiency is increased. But, in addition, the strong entrainment and penetration of O_2 over most of the regions, and the probable presence of OH radicals, also lead to a decrease in the yield of soot.

Figure 7 shows the field of monochromatic droplet scattering coefficient ($\lambda=633$ nm). It reveals a surrounding zone of high concentration in the upper region of the flame. This is logical since the injection of a finely divided water mist into a flame results in rapid drop evaporation. Droplets can be present in noticeable quantity only in the upper region, at the periphery. Next, they evolve as they move into the flame; water vapor created is pushed in the inner regions of the flame, onto the fuel surface. A region of very low concentration is located along the pan axis, under the level of temperature maximum (about 5 cm above the surface). This is likely due to the difficulty for the droplets to counter the force of buoyancy.

Moreover, due to the high level of temperature, the vaporization is very intense. Between these two zones is a transient zone where the droplets concentration decreases progressively. It is worth noting that these general characteristics are in qualitative agreement with temperature measurements and particularly with the intense fluctuating character of the temperature at the liquid gas interface.

3.2.4 Radiant Flux Measurements. When water mist is activated, the flame structure changes completely. As explained above, a much less ordered structure than that exhibited by the unperturbated pool fire is observed. The periodic cycle, eruptive vaporization flashback, results in more fluctuating recordings. Nevertheless, the measurements are perfectly exploitable. A mean radiant heat flux incident upon the surface $\overline{\dot{q}''_{r,s}}=0.35$ W cm^{-2} is deduced. This is indicative of a significant reduction of the radiant component to the burning rate. Furthermore, as seen above, the burning rate is also significantly increased. From the energy balance, it is deduced that the convective flux is also intensified, leading to a relative contribution radiation/convection of 16%/84% (see Table 1). This value is slightly higher than the value 0.1 W cm^{-2}, reported by Richard et al. [19], with a mass burning rate $\dot{m}''=2.82\times10^{-2}$ kg/m^{-2} s^{-1}. The discrepancy must be attributed to the difference of experimental method. In the previous work, the authors used the same type of radiometer, but located at different depths in the fuel; the level of the fuel surface being kept constant by means of a gravity liquid-feeding system. Therefore, the radiant heat flux at the surface was obtained by extrapolating the measured heat flux evolution across the fuel. Even if the measurements were done at steady state conditions, defined when the mass burning rate becomes constant, the method required a test for each location in depth of the radiometer, and this repetition multiplied the uncertainties of measurement. This previous method was obviously less accurate than the present one. This can also be attributed to the less accurate previous method of measurement, as mentioned above, but also to the use of a radiometer equipped with a sapphire window, which offered a spectral transmittance limited to 5 μm.

Contrary to what is generally expected, there is no radiant heat attenuation between the flame and fuel surface, except for a substantial increase. In the same time, the addition of entrained air in the mist leads to invigorate the convective mixing so that the resulting burning rate is increased. In other terms, the extinguishment of the flame is not obtained by a reduction in the evolution of flammable vapors.

In fact, the addition of droplets complicates the radiant transfer. It produces a temperature decrease and a variation in properties and emission within the flame. The resulting radiant heat change at the fuel surface is understandable by considering the evolution of the absorption coefficient due to soot without mist addition, the evolution of the overall absorption coefficient due to soot and droplets, and the scattering coefficient due to droplets during mist addition, as a function of wavelength, at a discrete location in the flame (Fig. 8), combining relations (8)–(14) permits the determination of the fields of soot absorption coefficient and water droplet scattering coefficient, which are representative of the corresponding concentrations. It is seen that during mist addition, under about 1–2 μm, the scattering effect of droplets is predominant, and that above, in the infrared region, absorption is not negligible any longer. The radiant contribution of the flame (soot particles) to the surface is low. The increase in the radiant heat flux can be due to the droplets, whose contribution is extended over the entire spectrum, but more likely to the water vapor.

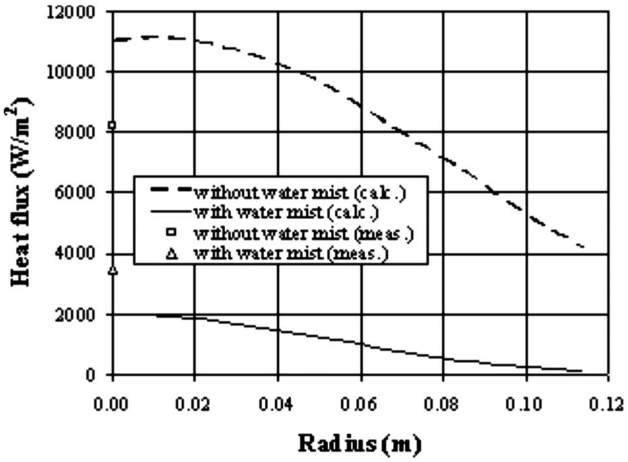

Fig. 9 Measured and calculated radiant heat flux at the heptane surface as a function of radial position

3.3 Comparison With Computation. An estimation of the radiant flux falling to the fuel surface can be attempted. Notice that the heat radiated by gaseous products is considered as negligible, and that water vapor, certainly present in appreciable quantities, is, for the moment, disregarded in default of reliable measurement procedure.

Considerable progress is being made toward developing reliable methods for calculating flame radiation with a proper degree of accuracy. The common techniques generally rely on various degrees of approximation. Among them, the discrete ordinates technique approximates integrals over direction by a numerical quadrature, and it is then assumed that the radiant intensity is constant within each solid angle around each discrete direction. The details of this well-known method can be found in Refs. [23,24], for instance. The method is implemented in cylindrical coordinates and is based on a constant weight quadrature with a discretization of polar angles into 1000 directions. Such conditions of discretization appeared necessary because, in the present medium, the well-known ray effect affects the SN classical quadrature (on the flame, there are many localized hot zones and sharp temperature gradients). This is particularly true with the unperturbated flame. In contrast, when water mist is added, scattering mitigates the ray effect, and practically no difference is observed by using an S8 quadrature or the finer discretization of polar angles.

The chosen quadrature technique is associated to a gray per band model: ten bands covering near and midinfrared regions. Notice that an increase in the number of bands does not affect significantly the results. The computational domain is a cylinder with a radius of 12 cm, extended to 15 cm when water mist is added, in order to take into consideration the flame expansion effect, and a height of 30 cm (the base of the flame that has chemical reaction and air entrainment taking place is the main contributing zone regarding flame radiation to the pool surface). The lower and upper temperature boundary conditions are, respectively, the temperature of vaporization of heptane and the ambient temperature, and the boundaries are assumed to be black. The phase function is approximated by a linear Dirac delta phase function, well-suited in the case of predominant forward scattering conditions such as encountered here.

The results obtained without and with water mist addition are presented in Fig. 9. The trend is consistent with the experimental observation that the incident radiant flux is not constant across the surface of the pool, and greater near the center. Without mist addition, the maximum radiant flux at the center is 1.1 W cm^{-2}, and a mean value integrated (till 2/3 of the radius) is 0.85 W cm^{-2}. We can see that calculations predict greater values than measurements. In addition to the uncertainties inherent to measurements or calculations, the mean reason of this discrepancy could be the fact that a thin layer of heptane remains at the surface of the sensor, and may absorb some radiation when it emerges from the regressing liquid. But, however that may be, the order of magnitude estimate is in essential agreement. With water mist addition, the maximum calculated value at the center is 0.2 W cm^{-2} instead 0.35 W cm^{-2}. That time, the pattern is reversed.

The main reason of this underestimation is certainly the fact that the contribution of water vapor is not accounted for when, from the observed characteristics of the flame structure, there is evidence of the existence, in the centerline region near the liquid surface, of a zone of elevated water vapor concentration at elevated temperature, able to radiate significantly.

But the important reduction in the radiant heat flux falling to the fuel surface is due to absorption by unvaporated droplets, which reradiate weakly. Only soot particles emit at the lower temperature level, and their concentration is much lower than before mist addition. In both cases, without or with mist addition, care must be taken in the computation of the grid point's location and the mesh sizes sources of uncertainties. A very low staggering, for example, may induce a variation of 10% or 15% in the computed flux (inherent to the presence of sharp gradients as previously mentioned). In addition, the minimum mesh size of measurements being 1 cm, the interpolation may generate significant uncertainties.

Finally, it is also important to mention that the measurements that are not being instantaneous provide averaged values where the measured properties are influenced by the flame fluctuation and disturbance, while, actual values are not. Then, care must be taken when reaching quantitative conclusions that are based on the comparison of measured averaged values on the fluctuating fields with values from a steady state modeling.

4 Concluding Remarks

The benefit of radiation attenuation by water mist in surroundings of a fire is evident and now well analyzed. In contrast, the role of fine droplets entering the flame on the amount of heat radiated to the fuel surface, particularly with liquid pool fires, is less evident and difficult to quantify. The fuel surface energy balance governing the burning rate indicated that the relative magnitude of the radiation/convection effects was decreased by water mist addition, but that this decrease was due to the significant intensification of the burning rate.

The behavior of the flame, especially at its base (the most interesting zone regarding flame establishment, stabilization, and extinction), changes totally. The flame becomes very unstable with a continuous variation in shape and size. Periodically, it seems to explode with sudden short, more or less, partial clearances from the surface, followed by a flashback. Sometimes a full clearance may be followed by suppression. The detailed mapping obtained of the temperature and extinction properties due to soot and water droplets show a substantial decrease in the flame temperature and soot concentration, and permit the determination of the pattern of water droplets entering into the flame. Water droplets entering into the flame, especially water vapor, do not shield the surface from radiation.

Therefore, it is suggested that suppression of the flame is rather achieved by decreasing enough temperature and vapor/air concentration throughout the flame, due to water vaporization and expansion effect (cooling and dilution effect), than from a reduction of the rate of evolution of flammable vapors from the liquid surface.

The experiments are complemented with modeling using the discrete ordinates method, which helps to backup the experimental observations. The calculations provide incident radiant flux distribution that is in satisfying agreement for the free fire, but is significantly underestimated with water mist addition. It is expected that this discrepancy is due to the fact that calculations left water vapor out of consideration.

As regards with the intensification of the fire under water mist addition, the main reason is that the induced turbulence acts to increase the burning rate of the fuel.

However, if the results bring improved information about the controlling mechanisms of pool fire extinguishment, it is important to realize that the measurements, being not instantaneous, provide only averaged values (which must be only viewed as an order of magnitude), and do not permit the analysis of the short period of droplets vaporization, which is the so-called puff phase leading to the clearance of the fuel. Also, the measurements are the ones responsible of flame suppression, when it occurs. A worthwhile project would be to investigate the conditions (flame temperature, incident flux, and burning rate) that define extinguishment at the end of this very brief phase (≈ 0.5 s). Unfortunately, except for temperature measurements, such investigations are still out of range.

Acknowledgment

The authors express their thanks to Total Elf Co. for its interest and help in this study.

Nomenclature

$C_{e\lambda}$ = extinction cross section (m^2)
$k_{e,\lambda}$ = monochromatic extinction coefficient (m^{-1})
$k_{a\lambda}$ = absorption coefficient (m^{-1})
$k_{s\lambda}$ = scattering coefficient (m^{-1})
$\dot{m}''$ = mass burning rate $\mathrm{kg/m^{-2}\ s^{-1}}$
N = droplets concentration (m^{-3})
$Q_{e\lambda}$ = extinction efficiency
$Q_{a\lambda}$ = absorption efficiency
$Q_{s\lambda}$ = scattering efficiency
$\overline{\dot{q}''}_{\mathrm{cv},s}$ = convective heat flux ($\mathrm{W\ cm^{-2}}$)
$\overline{\dot{q}''}_{r,s}$ = radiant heat flux ($\mathrm{W\ cm^{-2}}$)
R_{λ} = normalized collected scattered power for the detector
s = droplet cross section (m^2)
S = surface of detector (m^2)
T = temperature (K)
Dh_v = latent heat of vaporization ($\mathrm{J\ kg^{-1}}$)

Subscripts

a = absorption
cv = convection
d = water droplet
e = extinction
l = liquid
r = radiant
s = scattering
s = soot
S = surface
v = vaporization
λ = monochromatic

References

[1] Braidech, M. M., Neale, J. A., Matson, A. F., and Dufour, R. E., 1955, *The Mechanism of Extinguishment of Fire by Finely Divided Water*, Underwriters Laboratories Inc. for the National Board of Fire Underwriters, New York, pp. 73–85.

[2] Rasbash, D. J., Rogowski, Z. W., and Stark, G. W. V., 1960, “Mechanism of Extinction of Liquid Fires With Water Sprays,” Combust. Flame, **4**(3), pp. 223–234.

[3] Mawhinney, J. R., Dlugogorski, B. Z., and Kim, A. K., 1994, “A Closer Look at the Fire Extinguishing Properties of Water Mist,” *Proceedings of the Fourth International Fire Safety Science Conference*, Ottawa, Canada, July 13–17, pp. 47–60.

[4] Stephenson, S., and Conrad, M. J., 1986, “Attenuation of Radiant Heat on LNG/LPG Carriers With Freestanding Water Curtains,” *Proceedings of the Gastech 86 LNG/LPG Conference*, Hamburg, Germany, pp. 157–168.

[5] Ravigururajan, T. S., and Beltran, M. R., 1989, “A Model for Attenuation of Fire Radiation Through Water Droplets,” Fire Saf. J., **15**, pp. 171–181.

[6] Coppalle, A., Nedelka, D., and Bauer, B., 1993, “Fire Protection: Water Curtains,” Fire Saf. J., **20**, pp. 241–255.

[7] Dembele, S., Delmas, A., and Sacadura, J. F., 1997, “A Method for Modeling the Mitigation of Hazardous Fire Thermal Radiation by Water Spray Curtains,” ASME J. Heat Transfer, **119**, pp. 746–753.

[8] Keramida, E. P., Karayannis, A. N., Boudouvis, A. G., and Markatos, N. C., 2000, “Numerical Modeling of Radiant Heat Attenuation Through Water Mist,” Combust. Sci. Technol., **159**, pp. 351–371.

[9] Dembele, S., Wen, J. X., and Sacadura, J. F., 2000, “Analysis of the Two-Flux Model for Predicting Water Spray Transmittance in Fire Protection Application,” ASME J. Heat Transfer, **122**, pp. 183–188.

[10] Dembele, S., Wen, J. X., and Sacadura, J. F., 2001, “Experimental Study of Water Sprays for the Attenuation on Fire Thermal Radiation,” ASME J. Heat Transfer, **123**, pp. 534–543.

[11] Boulet, P., Collin, A., and Parent, G., 2006, “Heat Transfer Through a Water Spray Curtain Under the Effect of a Strong Radiative Source,” Fire Saf. J., **41**, pp. 15–30.

[12] Parent, G., Boulet, P., Gauthier, S., Blaise, J., and Collin, A., 2006, “Experimental Investigation of Radiation Transmission Through a Water Spray,” J. Quant. Spectrosc. Radiat. Transf., **97**, pp. 126–141.

[13] Hostikka, S., and McGrattan, K., 2006, “Numerical Modeling of Radiative Heat Transfer in Water Sprays,” Fire Saf. J., **41**, pp. 76–86.

[14] Jones, A., and Thomas, G. O., 1993, “The Action of Water Sprays in Fires and Explosions,” Trans. Inst. Chem. Eng., Part B, **71**, pp. 41–49.

[15] Consalvi, J.L., Porterie, B., and Loraud, J.C., 2003, “On the Use of Gray Assumption for Modeling Thermal Radiation Through Water Sprays,” Numer. Heat Transfer, Part A, **44**, pp. 505–519.

[16] Yang, W., Parker, T., Ladouceur, H. D., and Kee, R. J., 2004, “The Interaction of Thermal Radiation and Water Mist in Fire Suppression,” Fire Saf. J., **39**, pp. 41–66.

[17] Bouhafid, A., Vantelon, J. P., Joulain, P., and Fernandez-Pello, A. C., 1988, “On the Flame Structure at the Base of a Pool Fire,” Proc. Combust. Inst., **22**, pp. 1291–1298.

[18] Venkatesh, S., Ito, A., Saito, K., and Wichman, I. S., 1996, “Flame Base Structure of Small-Scale Pool Fire,” Proc. Combust. Inst., **26**, pp. 1437–1443.

[19] Richard, J., Garo, J. P., Souil, J. M., Vantelon, J. P., and Lemonier, D., 2002, “Addition of a Water Mist on a Small-Scale Liquid Pool Fire: Effect on Radiant Heat Transfer at the Surface,” Proc. Combust. Inst., **29**, pp. 377–384.

[20] Sozbir, N. Y., Chang, W., and Yao, S. C., 2003, “Heat Transfer of Impacting Water Mist on High Temperature Metal Surfaces,” ASME J. Heat Transfer, **125**, pp. 70–74.

[21] Chang, H., and Charalampopoulos, T. T., 1990, “Determination of the Wavelength Dependence of Refractive Indices of Flame Soot,” Proc. R. Soc. London, **430**, pp. 577–587.

[22] Hale, G. M., and Querry, M. R., 1973, “Optical Constants of Water in the 200 nm to 200 μm Wavelength Region,” Appl. Opt., **12**(3), pp. 555–563.

[23] Fiveland W.A., 1982, “A Discrete Ordinates Method for Predicting Radiative Heat Transfer in Axisymmetric Enclosures,” ASME Paper No. 82-HTD-20.

[24] Fiveland, W. A., 1984, “Discrete Ordinates Solutions of the Radiation Transport Equations for Rectangular Enclosures,” ASME J. Heat Transfer, **106**, pp. 699–706.

Fixed Grid Simulation of Radiation-Conduction Dominated Solidification Process

Piotr Łapka
e-mail: plapka@itc.pw.edu.pl

Piotr Furmański
e-mail: pfurm@itc.pw.edu.pl

Institute of Heat Engineering,
Warsaw University of Technology,
Nowowiejska Street 21/25, Warsaw 00-665,
Poland

In this paper conduction-radiation controlled solidification process of semitransparent materials was numerically analyzed. New approach in this kind of simulations, which is based on the fixed grid front tracking method combined with the immersed boundary technique, was adopted and examined. The presented method enables accurate dealing with solidification processes of semitransparent materials which have different optical and thermophysical properties of solid and liquid phases as well as with absorption, emission, and reflection of the thermal radiation at the solid-liquid interface without applying moving mesh methods. The proposed numerical approach was examined by solving several simplified thermal radiation problems with complex fixed and moving boundaries both in two-dimensional and axisymmetric spaces. For some of them the accuracy of obtained results was proved by comparing with reference works, other showed capabilities of the proposed method. For simplified solidification processes of semitransparent materials three configurations of optical properties, i.e., semitransparent solid phase and opaque liquid phase, opaque solid phase and semitransparent liquid phase, and semitransparent both phases were considered. The interface between solid and liquid phases was treated to be opaque, absorbing, emitting, and reflecting diffusely the thermal radiation. Results of the numerical simulations show that the presented numerical approach works well in this kind of problems and is promising for simulation of real solidification processes of semitransparent materials. [DOI: 10.1115/1.4000188]

Keywords: semitransparent material, solidification, thermal radiation, conduction-radiation heat transfer

1 Introduction

The phase-change process of semitransparent materials is found in several devices and manufacturing processes, as well as in the nature. The most well known are glass and optical fibers manufacturing. Some translucent fluoride of alkali metals, e.g., lithium fluoride (LF), potassium fluoride (KF), or eutectic mixture of lithium, magnesium, and potassium fluorides ($\mathrm{LiF-MgF_2-KF}$) are used as phase-change materials (PCMs) in high temperature thermal energy-storage systems, which are elements of solar dynamic space power systems [1]. For the sake of mass performance, semitransparent PCMs are very useful for the space application because thermal radiation increases overall heat transfer about 2.5–6 times [1] in comparison to opaque PCMs. So fins or extend surfaces assisting in transporting energy between working fluid and PCM are redundant. Semitransparent single oxide crystals such as yttrium aluminum garnet (YAG), gadolinium gallium garnet (GGG), and lithium niobate (LN), which are widely used in electronic, opto-electronic, and acousto-opto-electronic devices are commonly produced by Czochralski and Bridgman methods. During production of these single crystals, heat transfer mainly controlled by the thermal radiation exerts strong influence on crystals quality [2]. It means that formation of both structural defects and nonhomogeneities in crystals is affected by the solid-liquid interface shape and temperature distribution in the furnace. Melting of ice by solar radiation and solidification of water in the presence of sunlight are examples of phase-change processes of translucent materials found in nature. From the ecological or the global warming point of view these processes are very important.

Abovementioned technical applications of phase-change processes of semitransparent materials occur at high temperatures, which sometimes reach almost 2000 K. Therefore, experiments or observations are extremely difficult to carry out and highly expensive. This is the reason why numerical simulation becomes essential for development of these manufacturing processes.

Due to the complex interactions of heat conduction, radiation, and fluid flow, thermal modeling of phase-change phenomena of semitransparent materials is a challenging task. The heat transfer process with phase change becomes additionally complicated by nonlinear influence of the thermal radiation on temperature field. Radiation in semitransparent materials is a volumetric phenomenon, i.e., emission, absorption, and scattering of the thermal radiation is found in the whole volume so that semitransparent materials behave differently than opaque ones. Additionally, the thermal radiation is expected to affect dynamics of melting and solidification, and its neglecting in the analysis may lead to serious errors in predicting the solid-liquid interface shape, location and temperature distributions in the domain.

Effects of the thermal radiation upon melting and solidification of semitransparent materials have been studied since the 1970s. In one of the first papers, Abrams and Viskanta [3] analyzed one-dimensional transient melting and solidification in translucent medium. The conclusion of their work was that the radiation could significantly affect the dynamics of the phase-change process of semitransparent materials and the stability of the planar interface. Chan et al. [4] were the firsts who proposed a one-dimensional model of internal melting or solidification of semitransparent pure materials, which accounts for an isothermal two-phase region, i.e., the mushy zone between liquid and solid zones. Analytical results of their work showed that internal radiative heating or cooling enforces internal melting or solidification and leads to a wide two-phase zone. This model was validated by meteorological observations. Small cavities partially filled with water were observed

---

Contributed by the Heat Transfer Division of ASME for publication in the Journal of Heat Transfer. Manuscript received October 30, 2008; final manuscript received May 25, 2009; published online December 2, 2009. Assoc. Editor: Yogesh Jaluria.

during the melting process of ice exposed to the sunlight [5,6]. The study [4] of Chan et al. was further developed by several other researchers [7,8]. Lately, Łapka and Furmański [9] extended the earlier work in Ref. [4] and analyzed the two-dimensional solidification of semitransparent pure materials, and binary or eutectic alloys. Nonequilibrium planar solidification model for emitting, absorbing, and isotropically scattering medium subjected to radiative and convective cooling was introduced by Yao et al. [10]. They found that internal radiative heat transfer enhances removal of the latent heat and leads to higher interface velocity and large melt undercooling, but the planar interface can still be stable if the system is strongly cooled by the thermal radiation [11].

The simulation of a canister with semitransparent PCM used as element of high temperature thermal energy-storage system was performed by Sokolov et al. [12]. It was found that radiation reduces thermal resistance of the canister and results in decreasing of the canister's wall temperature. In the next paper, Yimer [13] numerically determined transient temperature distribution, solid-liquid interface location, and energy-storage capacity of a canister filled with semitransparent PCM. Both works adopted the enthalpy method for numerically solving solidification phenomenon. In the case of numerical simulations of semitransparent oxide single crystal growth processes, Brandon and Derby [14] were the pioneers. They analyzed the vertical Bridgman growth process, including for the first time internal radiative heat transfer through a crystal. Their results demonstrate sensitivity of the solid-liquid interface shape, location, and temperature distribution to changes in optical properties of the crystal. The first global analysis of heat transfer in the Czochralski growth process of semitransparent crystals was carried out by Tsukada et al. [2]. They analyzed the influence of different optical properties on the solid-liquid interface shape, flow patterns, and temperature distribution in the furnace. Until now there are also several studies, which consider different aspects of the growth process of semitransparent single oxide crystal, for example, simulation of face formation as well as coupled heat flow and segregation in the Bridgman growth of oxide crystals [15,16], investigation of the effect of internal radiative heat transfer in a crystal and melt on interface inversion in the Czochralski growth of oxide crystals [17], simulation of specular reflection at crystal side in the Czochralski furnace [18], simulation of 3D melt flow in the Czochralski system [19,20], and simulation of vertical Bridgman growth of thermally anisotropic optical materials [21].

In the quoted works, simulations of the solidification process of semitransparent materials are based on the enthalpy method (simulation of PCM's canister) or on the complex moving mesh methods (simulation of crystal growth process). The enthalpy method assumes averaged properties in the grid elements that capture the solid-liquid interface, therefore in this method accurate modeling of different optical properties of solid and liquid phases, and taking into account the emission, absorption, reflection, and refraction of the radiation at the solid-liquid interface is difficult. Furthermore, the moving mesh methods are complicated and time consuming because in every iteration the interface between solid and liquid phase is varying and the mesh is adjusted to its new position. Additionally, interpolation or extrapolation of all field variables is needed here. The idea underlying the current work is to study and present capability of the fixed grid front tracking method [22] combined with the immersed boundary technique [23,24] for solving the simplified conduction-radiation controlled planar solidification process of semitransparent materials with different optical properties in solid and liquid phases, and with the absorption, emission, and reflection of the thermal radiation at the solid-liquid interface. The fixed grid front tracking method is widely applied to examine solidification processes in opaque materials including opaque binary alloys with kinetic effects but until now was not applied in simulating the solidification process of semitransparent materials with different radiative properties of solid and liquid phases. The immersed boundary technique is also well known in heat transfer and computational fluid dynamics but until now was not used to simulate conjugated conductive-radiative heat transfer with moving boundaries. The current work demonstrates that both these methods can be combined together, enabling accurate simulation of the thermal radiation in solid and liquid phases with participating, moving, and highly curved solid-liquid interface between them. The main objective of the paper was the presentation of this new numerical approach but not the physical modeling. Therefore, the convection in the melt, which plays the important role in real solidification processes, was neglected. In Secs. 2 and 3, mathematical formulation and details of implementation of our numerical approach are presented. Furthermore, several simplified thermal radiation problems with complex fixed and moving boundaries both in two-dimensional and axisymmetric spaces, with different configuration of optical properties of the solid and liquid phases, were solved and discussed to show accuracy, capability, and future development of the presented numerical approach.

2 Mathematical Formulation

The present study was limited to two-dimensional and axisymmetric geometries. Only the conductive and the volumetric radiative heat transfer modes were considered at current stage of work. It was assumed that external walls of the computational domain might be opaque, emitting, and reflecting diffusively the thermal radiation and simultaneously subjected to the external convective cooling by the surroundings, or they may be adiabatic. The medium inside the domain was treated as gray, emitting, absorbing, and anisotropically scattering the thermal radiation. Thermophysical and optical properties of the medium were assumed constant and fixed for a particular phase. For the simulations with moving boundaries the computational domain was initially filled with superheated, solidifying pure liquid phase at temperature T_{init}. The solidification process started when temperature of the external walls was decreased below the melting temperature of the medium T_m. Additionally, it was assumed that solidification occurred at fixed temperature equal to the melting point of the pure material. The solid-liquid interface was treated to be opaque, absorbing, emitting and reflecting diffusively the thermal radiation.

Considering the assumptions listed above, the transient energy equation (EE) for particular phase including the heat conduction and the internal thermal radiation can be written as follows:

$$\rho_z c_{p,z}\frac{\partial T}{\partial t} = \nabla k_z \nabla T - \nabla \cdot \dot{\mathbf{q}}_{r,z} \tag{1}$$

where $z=s$ for the solid phase and $z=l$ for the liquid phase. The last term at the right hand side of Eq. (1), i.e., divergence of the radiative heat flux vector, contributes to influence of the thermal radiation on temperature field. The convective and adiabatic boundary conditions for external walls were given in the form:

$$-k_z\frac{\partial T}{\partial n_w} = h(T_w - T_\infty) \quad \text{and} \quad -k_z\frac{\partial T}{\partial n_w} = 0 \tag{2}$$

The radiative heat transfer in absorbing, emitting, and isotropically scattering gray media along the line-of-sight s is described by the radiative transfer equation (RTE):

$$\frac{dI}{ds} = -K_{e,z}I + \frac{n_z^2\sigma K_{a,z}T^4}{\pi} + \frac{K_{s,z}}{4\pi}\int_{4\pi} I\Phi_z(\mathbf{s}' \to \mathbf{s})d\Omega' \tag{3}$$

Terms present on the right hand side of Eq. (3) contribute to attenuation of the radiation intensity by the absorption and out-scattering of the medium, augmentation of the radiation intensity by the self emission of the medium, and augmentation of the intensity by the in-scattering from other directions, respectively. The radiation direction vector **s** can be expressed as follows:

$$\mathbf{s} = [\sin\,\theta \cos\,\phi, \quad \sin\,\theta \sin\,\phi, \quad \cos\,\theta] \tag{4}$$

The polar angle θ is measured from the z-axis in the x-z Cartesian plane: $\theta \in (\mathbf{0}, \pi)$, whereas the azimuthal angle ϕ is measured form the x-axis in the x-y Cartesian plane: $\phi \in (\mathbf{0}, 2\pi)$.

The divergence of radiative heat flux vector, which appears in the EE, Eq. (1), can be calculated, for a gray medium, from the following expression:

$$\nabla \cdot \dot{\mathbf{q}}_{r,z} = K_{a,z}\left(4n_z^2\sigma T^4 - \int_{4\pi} I d\Omega\right) \tag{5}$$

The scattering phase function in Eq. (3) was represented by the Legendre polynomial expansion:

$$\Phi_z(\mathbf{s}' \to \mathbf{s}) = \sum_{n=1}^{N} C_n P_n(\mathbf{s} \cdot \mathbf{s}') \tag{6}$$

where C_n is the nth expansion coefficient, and P_n is the nth order Legendre polynomial. For isotropic scattering, the phase function is equal to $\Phi_z = 1$. For backward or forward scattering the values of C_n can be taken after Kim and Lee [25].

Assuming that walls of the domain and the solid-liquid interface were opaque, absorbing, emitting, and reflecting diffusively, the internal radiative boundary and interface conditions for the RTE, Eq. (3), for all outgoing directions ($\mathbf{s} \cdot \mathbf{n}_w > 0$) took the following form:

$$I_{w/i} = \frac{n_z^2 \sigma \varepsilon_{w/i} T_{w/i}^4}{\pi} + \frac{1 - \varepsilon_{w/i}}{\pi} \int_{\mathbf{s}\cdot\mathbf{n}_{w/i}<0} I |\mathbf{s} \cdot \mathbf{n}_{w/i}| d\Omega \tag{7}$$

The wall and the solid-liquid interface radiative heat fluxes were calculated from the formula:

$$q_{rw/i} = \int I |\mathbf{s} \cdot \mathbf{n}_{w/i}| d\Omega \tag{8}$$

with following conditions: $\mathbf{s} \cdot \mathbf{n}_{w/i} < 0$ for incident radiative flux (in) and $\mathbf{s} \cdot \mathbf{n}_{w/i} > 0$ for emitted radiative flux (out).

The local solid-liquid interface velocity was determined from the energy balance at the solid-liquid interface (Stefan condition), including incident radiative heat fluxes at the interface from the solid phase ($q_{ri,s,\text{in}}$) and liquid phase ($q_{ri,l,\text{in}}$), as well as emitted radiative heat fluxes at the interface into solid phase ($q_{ri,s,\text{out}}$) and liquid phase ($q_{ri,l,\text{out}}$):

$$V_i = \frac{k_s \left.\dfrac{\partial T}{\partial n}\right|_s - k_l \left.\dfrac{\partial T}{\partial n}\right|_l - q_{ri,s,\text{in}} - q_{ri,l,\text{in}} + q_{ri,s,\text{out}} + q_{ri,l,\text{out}}}{\rho_l(L_f + (c_l - c_s)(T_i - T_m))} \tag{9}$$

In the above equation, incident and emitted fluxes at the solid-liquid interface were calculated using Eq. (8) and the nearest nodal intensity values.

Equations (1)–(9) were subsequently made nondimensional using the following dimensionless quantities: specific heat $c^* = c_l/c_s$, thermal conductivity $k^* = k_l/k_s$, refraction index $n^* = n_z/n_{\text{ref}}$, radiation intensity $i = I/(4n_{\text{ref}}^2 \sigma T_m^4)$, absorption coefficient $K_a^* = K_{a,z}/K_{a,\text{ref}}$, extinction coefficient $K_e^* = K_{e,z}/K_{e,\text{ref}}$, scattering coefficient $K_s^* = K_{s,z}/K_{s,\text{ref}}$, heat flux $q^* = q/(4n_{\text{ref}}^2 \sigma T_m^4)$, temperature $T^* = T/T_m$, velocity $V^* = V c_s \rho_s L_x / k_s$, coordinates $x^* = x/L_x$ and $y^* = y/L_x$ (Cartesian 2D), $r^* = r/L_r$ and $z^* = z/L_r$ (axisymmetric), dimensions $L_{x^*} = L_x/L_x = 1.0$ and $L_{y^*} = L_y/L_x$ or $L_{r^*} = L_r/L_r = 1.0$ and $L_{z^*} = L_z/L_r$, density $\rho^* = \rho_l/\rho_s$, optical thickness $\tau = K_{e,\text{ref}} L_x$, albedo $\omega = K_{s,\text{ref}}/K_{e,\text{ref}}$, Fourier number $\text{Fo} = k_s t/(c_s \rho_s L_x^2)$, conduction-radiation parameter $N_r = k_s/(4n_{\text{ref}}^2 \sigma T_m^3 L_x)$, Nusselt number $\text{Nu} = hL_x/k_s$, and Stefan number $\text{Ste} = c_s T_m / L_f$. Optical dimensionless parameters used in the presented study depend on the configuration between optical properties of the solid and liquid phases, i.e., when solid phase was semitransparent and liquid phase was opaque the RTE was solved only in solid phase, the liquid phase was blocked off and it was assumed that $z = s$, ref $= s$. Similarly for other cases, when solid phase was opaque and liquid phase was semitransparent: $z = l$, ref $= l$ and when both phases were semitransparent: $z = s$, ref $= l$.

The final form of nondimensional governing equation and respective boundary or solid-liquid interface conditions can be written as follows:

- Dimensionless EE with the radiation source term in solid and liquid phase, respectively,

$$\frac{\partial T^*}{\partial \text{Fo}} = \nabla^{*2} T^* - \frac{1-\omega}{N_r} n^* K_a^* \tau \left(T^{*4} - \int_{4\pi} i d\Omega\right) \tag{10}$$

$$\rho^* c^* \frac{\partial T^*}{\partial \text{Fo}} = \nabla^* k^* \nabla^* T^* - \frac{1-\omega}{N_r} n^* K_a^* \tau \left(T^{*4} - \int_{4\pi} i d\Omega\right) \tag{11}$$

with boundary conditions:

$$\begin{gathered} -\frac{\partial T^*}{\partial n_w^*} = \text{Nu}(T_w^* - T_\infty^*) \quad \text{or} \quad -\frac{\partial T^*}{\partial n_w^*} = 0 \quad \text{and} \\ -k^* \frac{\partial T^*}{\partial n_w^*} = \text{Nu}(T_w^* - T_\infty^*) \quad \text{or} \quad -k^* \frac{\partial T^*}{\partial n_w^*} = 0 \end{gathered} \tag{12}$$

- Dimensionless RTE in solid or liquid phase:

$$\frac{1}{\tau}\frac{di}{ds^*} = -K_e^* i + \frac{(1-\omega) n^* K_a^*}{4\pi} T^{*4} + \frac{\omega K_s^*}{4\pi} \int_{4\pi} i \Phi(\mathbf{s}' \to \mathbf{s}) d\Omega' \tag{13}$$

with boundary or solid-liquid interface conditions:

$$i_{w/i} = \frac{n^* \varepsilon_{w/i} T_{w/i}^{*4}}{4\pi} + \frac{1 - \varepsilon_{w/i}}{\pi} \int_{\mathbf{s}\cdot\mathbf{n}_{w/i}<0} i |\mathbf{s}^* \cdot \mathbf{n}_{w/i}^*| d\Omega \tag{14}$$

- Dimensionless local interface velocity:

$$V_i^* = \frac{\left.\dfrac{\partial T^*}{\partial n^*}\right|_s - k^* \left.\dfrac{\partial T^*}{\partial n^*}\right|_l + \dfrac{1}{N_r}(-q_{ri,s,\text{in}}^* - q_{ri,l,\text{in}}^* + q_{ri,s,\text{out}}^* + q_{ri,l,\text{out}}^*)}{\rho^*(1/\text{Ste} + (c^* - 1)(T_i^* - 1))} \tag{15}$$

3 Numerical Solution

3.1 Discretization of Governing Equations. The nondimensional EE, Eqs. (10) and (11) as well as RTE, Eq. (13), were discretized using the finite volume method (FVM) [26]. The computational domain was uniformly divided into a nonoverlapping rectangular grid with a size dx in the x- or r-axis direction and dy in the y- or z-axis direction. Each term of the nondimensional EE was integrated over an interval of a dimensionless time dFo and over a control volume dV. The divergence of radiative heat flux vector, Eq. (5), in dimensionless form was subsequently expanded in the Taylor series close to the central node P. Highly nonlinear implicit system of equations for temperature was then obtained:

$$
\begin{aligned}
a(T_P^{*n+1} - T_P^{*n})dV &= \sum_j^N b\mathbf{n}_j \cdot \mathrm{grad}_j T^{*n+1} dA_j d\mathrm{Fo} \\
&- \frac{1-\omega}{\mathrm{N_r}} n^* K_a^* \tau \left(4(T_P^{*n})^3 T_P^{*n+1} - 3(T_P^{*n})^4 - \sum_m^M i_P^m d\Omega^m \right) dV d\mathrm{Fo}
\end{aligned}
\quad \text{(for 2D case)} \qquad (16)
$$

where $a=1$, $b=1$ are for solid phase and $a=\rho^* c^*$, $b=k^*$ are for liquid phase. The subscript P denotes nodal value, the superscript n denotes time level, while $\mathbf{n}_j$ stands for the outward normal vector of control volume j-th face. Moreover, the symbol N denotes total number of control volume faces, while dA_j is the face area of the control volume.

The dimensionless RTE was solved by the FVM for the radiative heat transfer [27]. The method was based on integration of the RTE over a control volume dV and over a control solid angle $d\Omega^m$. The same uniform, rectangular spatial grid as for the EE was used. Additionally, in the FVM for the thermal radiation it is necessary to divide the whole solid angle into control solid angles. Therefore the whole azimuthal angle 2π and the whole polar angle π were divided uniformly into a nonoverlapping angular grid with spacing $d\phi$ and $d\theta$, respectively, and the total number of control angles (discrete directions) was M. The final form of the discrete RTE in discrete direction m looks as follows:

$$
\begin{aligned}
\frac{1}{\tau}\sum_j^N i_j^m dA_j D_j^m &= \left(-K_e^* + \frac{\omega K_s^*}{4\pi} \Phi^{mm} d\Omega^m \right) i_P^m d\Omega^m dV + \\
&+ \frac{(1-\omega) n^* K_a^*}{4\pi} (T_P^{*n})^4 d\Omega^m dV + \frac{\omega K_s^*}{4\pi} \sum_{l=0, l\neq m}^M i_P^l \Phi^{lm} d\Omega^l d\Omega^m dV
\end{aligned}
\quad \text{(for 2D case).} \qquad (17)
$$

Geometrical weigh, control angle, and average phase function were calculated from the following formulas:

$$
D_j^m = \int_{d\Omega^m} \mathbf{n}_j \cdot \mathbf{s}^m d\Omega^m \qquad (18)
$$

$$
d\Omega^m = \int_{\theta^-}^{\theta^+} \int_{\phi^-}^{\phi^+} \sin\, \theta d\theta d\phi \qquad (19)
$$

$$
\Phi^{lm} = \frac{\int_{d\Omega^m}\int_{d\Omega^l} \Phi(\mathbf{s}' \to \mathbf{s}) d\Omega^m d\Omega^l}{d\Omega^m d\Omega^l} \qquad (20)
$$

with $\theta^+ = \theta^m + d\theta/2$, $\theta^- = \theta^m - d\theta/2$, $\phi^+ = \phi^m + d\phi/2$, $\phi^- = \phi^m - d\phi/2$, where for isotropic scattering $\Phi^{lm} = 1$. Discrete form of RHT for the axisymmetric geometry was derived from 3D formulation by applying special mapping procedure as explained in Ref. [28]. In such implementation, the angular redistribution terms, which are found in RTE for cylindrical coordinates, were avoided.

The step scheme, in which a downstream face intensity is set equal to upstream nodal value, was used to relate the control volume face intensity to the nodal intensity [29]. Typical relationship for this scheme is as follows:

$$
i_j^m D_j^m = i_P^m D_{j,\mathrm{out}}^m + i_J^m D_{j,\mathrm{in}}^m \qquad (21)
$$

where index J denotes nodal value of neighbor control volume and

$$
\begin{aligned}
D_{j,\mathrm{out}}^m &= \max(D_j^m, 0) \quad \text{for} \quad \mathbf{n}_j \cdot \mathbf{s}^m > 0 \quad \text{and} \\
D_{j,\mathrm{in}}^m &= -\max(-D_j^m, 0) \quad \text{for} \quad \mathbf{n}_j \cdot \mathbf{s}^m < 0
\end{aligned}
\qquad (22)
$$

The discrete form of the boundary or interface condition for RHT was expressed as:

$$
i_{w/i} = \frac{n^* \varepsilon_{w/i} T_{w/i}^{*4}}{4\pi} + \frac{1-\varepsilon_{w/i}}{\pi} \sum_{\mathbf{s}^m \cdot \mathbf{n}_{w/i} < 0} i_{w/i}^m |D_{w/i}^m| \quad \text{for} \quad \mathbf{n}_{w/i} \cdot \mathbf{s}^m > 0 \qquad (23)
$$

where $D_{i/w}^m$ is calculated with conditions: $\mathbf{s} \cdot \mathbf{n}_{w/i} < 0$ for incident radiation flux.

The wall or the solid-liquid interface radiative heat fluxes can be estimated from the formula:

$$
q_{rw/i} = \sum_m^M i^m D_{w/i}^m \qquad (24)
$$

where $D_{i/w}^m$ is calculated with conditions: $\mathbf{s} \cdot \mathbf{n}_{w/i} < 0$ for incident radiation flux or $\mathbf{s} \cdot \mathbf{n}_{w/i} > 0$ for emitted radiative flux, and intensities i^m at the wall or solid-liquid interface are found following Eq. (29).

3.2 Front Tracking Method. Solidification problem was solved by the front tracking method [22]. In this method the nondimensional governing equations, Eqs. (10), (11), and (13), were solved implicitly on a fixed mesh and the interface was tracked explicitly. The solid-liquid interface was identified by an ordered set of massless marker points. A line connecting marker points represents the solid-liquid interface. If the distance between two marker points was larger than the assumed value the new marker point was placed between them. On the other hand, if the distance between two marker points was smaller than the assumed value one of them was replaced or removed. Initially marker points were distributed uniformly over boundaries subjected to the external cooling. Marker points always advanced in a direction perpendicular to the solid-liquid interface at a growth velocity calculated form Eq. (15) and they had the temperature T_i^*. New positions of marker points were determined from their old positions, time interval, and velocities:

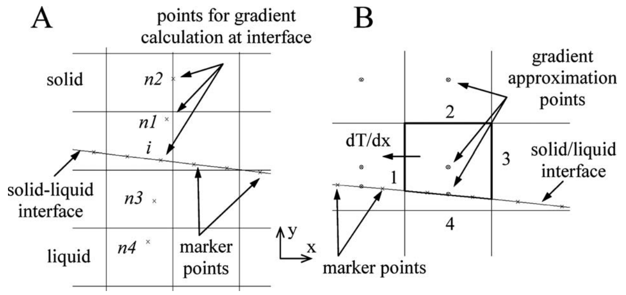

Fig. 1 Scheme for interpolation: (*a*) normal temperature gradients at interface and (*b*) gradients at faces of trapezoidal cells

$$x_i^{*\text{new}} = x_i^{*\text{old}} + d\text{Fo} \cdot V_i^* \tag{25}$$

The marker velocity was calculated as described by Udaykumar et al. [22], with modification accounting for radiative heat transfer. Temperature normal gradients into solid and liquid phase, which appear in Eq. (15), were obtained by using the linear interpolation along the normal to the interface at point *i*, as shown in Fig. 1(*a*). This approach was simple and convenient. Four points, two in the solid phase (n_1 and n_2) and two in the liquid phase (n_3 and n_4), which lie at the line normal to the interface at point *i*, were selected. The spacing between points *i*, n_1, n_2, and *i*, n_3, n_4 (Fig. 1(*a*)) was fixed and equal to Δ. Then temperature values at these four points (n_1–n_4) were obtained by the bilinear interpolation based on four nearest nodal values of temperatures. The gradient pointing into solid phase was then calculated from the expression:

$$\left.\frac{\partial T^*}{\partial n^*}\right|_s = \frac{4T^*_{n1} - T^*_{n2} - 3T^*_i}{2\Delta} \tag{26}$$

Similar expression was applied for the gradient pointing into liquid phase. Next, by using Eq. (24), the incident ($q_{ri,s,\text{in}}, q_{ri,l,\text{in}}$) and emitted ($q_{ri,s,\text{out}}, q_{ri,l,\text{out}}$) radiative heat fluxes at the marker point *i* were calculated. To find these incident fluxes, nodal intensity values of the control volume, at which boundary marker point *i* lies, were used. Finally, the marker velocity was obtained from Eq. (15).

3.3 Immersed Boundary Technique for Energy Equation. Calculations were performed on the fixed Cartesian grid. For the case when the rectangular mesh was cut by the solid-liquid interface the immersed boundary technique was applied [23]. This technique enables handling different optical and thermophysical properties of solid and liquid phases and phenomena that occur at the solid-liquid interface. This is different than in the case of the enthalpy method, which assumes average properties at control volumes that contain the solid-liquid interface, and therefore, is not suitable for dealing with opaque, absorbing, emitting, and reflecting diffusively interface. In the immersed boundary technique these phenomena can be incorporated into calculations with ease. Also, the refraction of radiation at the solid-liquid interface can be included. At first, cells cut by the interface were selected and intersection points were found. Then the phase, in which cell center lied, was identified. By using special procedure new control volumes, which were in general trapezoidal in shape, were formed on both sides of the solid-liquid interface as shown in Fig. 1(*b*). Subsequently the finite volume discretization was applied to those irregular cells. Heat fluxes at face nos. 1 and 3 (see Fig. 1(*b*)) were calculated using the two-dimensional interpolation function that was linear in the *x*- or *r*-axis direction and quadratic in the *y*- or *z*-axis direction:

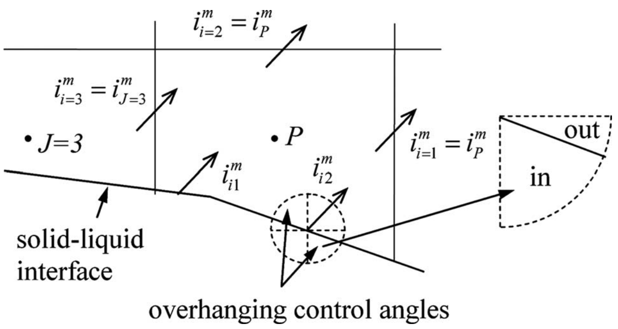

Fig. 2 Sketch of control volume, which adjoins the solid-liquid interface, and a view of the overhanging control angles. Face intensities ($i^m_{i=1,2,3}$) were interpolated following step scheme Eq. (21), whereas the interface intensities ($i^m_{i=1,2}$) following Eq. (29).

$$T = c_1xy^2 + c_2y^2 + c_3xy + c_4y + c_5x + c_6 \quad (\text{for 2D case}) \tag{27}$$

The *x*- or *r*-component of temperature gradient was then directly determined by differentiation of Eq. (27):

$$\frac{\partial T}{\partial x} = c_1y^2 + c_3y + c_5 \quad (\text{for 2D case}) \tag{28}$$

Similar expressions were obtained for gradients in the *y*- or *z*-axis directions but the interpolation function was quadratic in the *x*- or *r*-axis directions, while linear in the *y*- or *z*-axis directions. The temperature gradient at face no. 4 was calculated by using the linear interpolation along the normal to the interface—Eq. (26), while for the face no. 2 the standard finite volume approximation was adopted. Then Eqs. (26) and (28) for gradients at trapezoidal control volume faces were incorporated into the global system of equations for temperature, Eq. (16), substituting in the implicit manner for expression $\mathbf{n}_j \cdot \text{grad}_j T^{*n+1}$ at respective faces.

3.4 Immersed Boundary Technique for RTE. In the case of the immersed boundary technique for the RTE, additional terms, which accounted for the emission and reflection of the thermal radiation at the solid-liquid interface, were added to the left hand side of discrete RTE, Eq. (17), for the reshaped trapezoidal control volumes (Fig. 2) following Byun et al. [24]. These terms were expressed in the form: $i^m D^m dA_i$. For the control volumes adjacent to the solid-liquid interface, the discrete angular direction does not coincide with control volume faces and control angles overhanging these faces as shown in Fig. 2. The solution for this problem is to use the exact treatment, which keeps conservation of radiant energy. In this approach the overlapped control angle is divided into two parts associated with incoming and outgoing intensities (Fig. 2), and then the step scheme is applied [29] as follows:

$$i^m D^m = i^m_P D^m_P + i^m_i D^m_i \tag{29}$$

where D^m_P is associated with incoming part of the overhanging control angle (Fig. 2, in) and D^m_i is associated with outgoing part of the overhanging control angle (Fig. 2, out).

In the present paper it was assumed that the thermal radiation may propagate either in one phase: solid or liquid, or in both phases. For the case when the thermal radiation was present only in one phase, the other one was blocked off [24]. The solid-liquid interface was assumed to be opaque, absorbing, emitting, and reflecting diffusively, kept at fixed temperature equal to the melting temperature. But the presented numerical approach can also be implemented when the solid-liquid interface is semitransparent and is treated as the Fresnel interface. Then this numerical procedure should incorporate Snell's law at the solid-liquid interface and should be developed to conserve radiant energy transferred from one angular direction to another as a results of reflection and

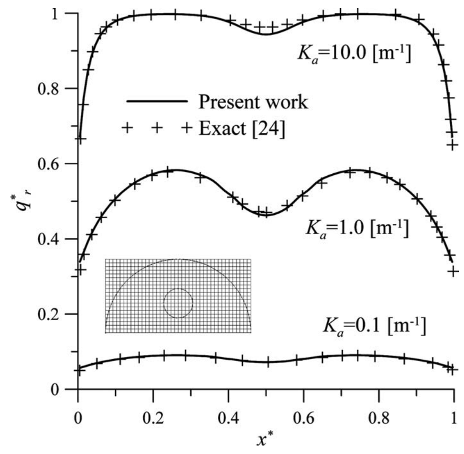

Fig. 3 Comparison of dimensionless radiative heat fluxes distribution at the bottom wall of the two-dimensional semicircular enclosure with an internal circle

refraction of the thermal radiation at the solid-liquid interface, in similar manner as was done by Murthy and Mathur [30] for the fixed interface.

4 Verification of the Numerical Model

Results obtained from the presented numerical model were compared with results of other studies. For the sake of brevity only a few examples for the thermal radiation were presented. Details about numerical calculations setup were omitted but they can be found in the references. The results only for solidification of opaque pure materials, pure radiation and combined radiation-conduction problems were checked because the literature lacks results of conduction-radiation controlled solidification. First, the results for solidification of opaque pure materials were compared with Swaminathan and Voller [31] and the commercial code FLUENT. Then numerical results for pure radiation problem for two-dimensional and axisymmetric geometry were compared with the results presented by Byun et al. [24] and by Salah et al. [32], respectively. In Fig. 3 dimensionless radiative heat fluxes at the bottom wall of the two-dimensional semicircular enclosure with empty internal circle for different values of the absorption coefficients are presented against the exact results [24]. Comparison of the results of Salah et al. [32] for the axisymmetric nozzle-shaped enclosure with current work is shown in Fig. 4. Finally, the results for two-dimensional transient combined conduction-radiation problem without solidification were matched with the results of Mishra et al. [33], Fig. 5, for an absorbing, emitting, and isotropically scattering medium with the albedo $\omega=0.5$. All results are found to be in good agreement. It is worth noting that values of the Fourier number in Fig. 5 correspond to nondimensional time ζ, introduced by Mishra et al. [33] as follows: $\zeta=\mathrm{Fo}\tau$.

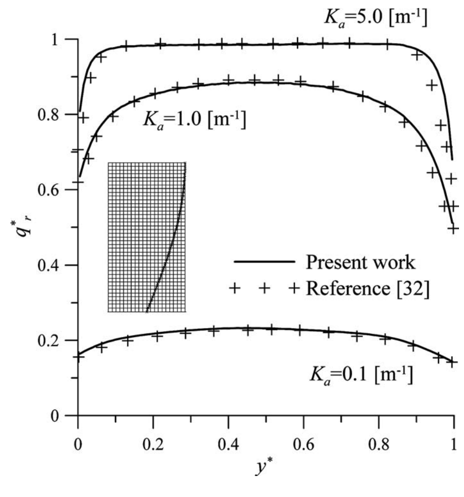

Fig. 4 Comparison of dimensionless radiative heat fluxes distribution at the right wall of the axisymmetric nozzle-shaped enclosure

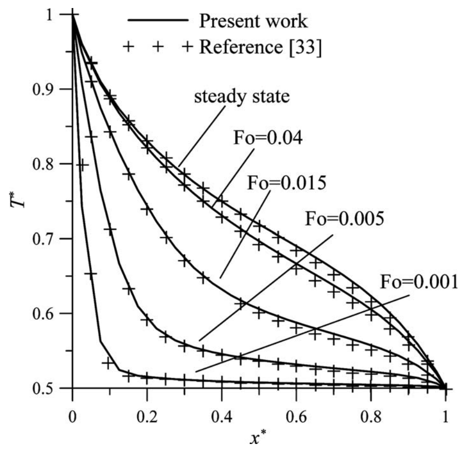

Fig. 5 Comparison of transient dimensionless temperature distribution along the centerline for two-dimensional conduction-radiation heat transfer for an absorbing, emitting, and isotropically scattering medium with $\omega=0.5$

5 Simulation Results and Discussion

The proposed fixed grid front tracking model with the immersed boundary technique was subsequently applied to solve radiation-conduction dominated solidification process of semitransparent materials for two-dimensional and axisymmetric geometry, to show capabilities and potential application area of the presented method. Influence of the conduction-radiation parameter N_r and the optical thickness of the layer τ on temperature fields and on the solid-liquid interface locations were also examined in order to find an impact of the thermal radiation on phase-change process. Calculations were performed assuming following configurations of the optical properties: (a) semitransparent solid phase and opaque liquid phase, (b) opaque solid phase and semitransparent liquid phase, and (c) semitransparent both solid and liquid phases.

5.1 Two-Dimensional Cartesian Simulation. The two-dimensional rectangular enclosure with the width and the height equal to $2L_{x^*}$ and L_{y^*}, as shown in Fig. 6(*a*), was first investigated. It was assumed that the bottom boundary was opaque, emitting, and reflecting diffusively, and subjected to the external convective cooling by the surroundings. The other walls were treated as adiabatic. Most of thermophysical and optical properties of the medium were taken according to Lan and Tu [15] (properties of the YAG crystals). The dimensionless quantities were fixed at the following constant values: $c^*=1.0$, $k^*=0.5$, $n^*=1.0$, $T^*_{\text{init}}=1.1$, $L_{x^*}=1.0$, $L_{y^*}=2.0$, $K^*_e=1.0$, $K^*_s=1.0$, $\mathrm{Fo}=0.3$, $\mathrm{Nu}=10^6$, $\mathrm{Ste}=3.46$, $\varepsilon_w=1.0$, $\varepsilon_i=0.3$, and $\rho^*=1.0$. The scattering phase function was assumed isotropic. To make the problem two-dimensional, the ambient temperature was assumed to vary according to the relation: $T^*_\infty=0.85-0.1\cos(\pi x^*)$. The properties, which changed during the calculation, were made equal to $N_r=1.0,\mathbf{0.1},0.01$, $\tau=10.0,\mathbf{1.0},0.01$ (the bold values were taken as the default ones). The spatial domain and the solid angle were discretized as $N_x\times N_y=20\times 40$ and $N_\phi\times N_\theta=8\times 4$, respectively. Due to symmetry of the thermal problem half of the medium in the cavity was considered. At the symmetry plane appropriate symmetry boundary conditions for EE and RTE [30] were applied, i.e.,

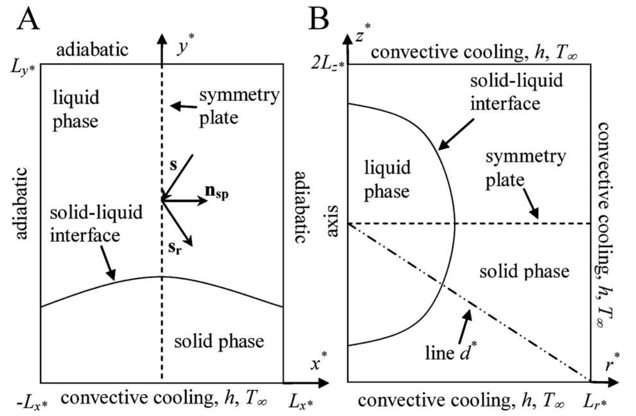

Fig. 6 Schematic sketches of computational domains: (*a*) two-dimensional and (*b*) axisymmetric

$$\frac{\partial T^*}{\partial n^*_{\mathrm{sp}}} = 0 \quad \text{and} \quad i(\mathbf{s_r}) = i(\mathbf{s}) \tag{30}$$

where $\mathbf{s_r}=\mathbf{s}-\mathbf{2}(\mathbf{s}\cdot\mathbf{n_{sp}})\mathbf{n_{sp}}$ is the symmetric direction of $\mathbf{s}$, with respect to the boundary. Temperature distributions at $x^*=0.5$ and locations of the solid-liquid interface in cavity are shown at the accompanying figures.

In Fig. 7(*a*)–7(*c*) distributions of dimensionless temperature and solid-liquid interface locations are shown as a function of the conduction-radiation parameter N_r. As N_r increases, the heat conduction becomes dominant. Semitransparent solid or liquid phase are then less radiatively cooled and eventually for N_r above unity solidification proceeds as for an opaque material. Decreasing N_r favors internal radiative cooling and limits the share of conductive heat transfer in the total heat flux. For semitransparent solid (Figs. 7(*a*) and 7(*c*)) temperature distribution becomes concave as heat becomes more directly transmitted to the wall by the thermal radiation. More heat is removed from the vicinity of the solid-liquid interface and therefore the rate of solidification is increased. For semitransparent liquid phase (Figs. 7(*b*) and 7(*c*)) the internal radiation decreases temperature in bulk liquid, more heat is transferred by the thermal radiation to the solid-liquid interface, and therefore, the rate of solidification is lower than for semitransparent solid phase.

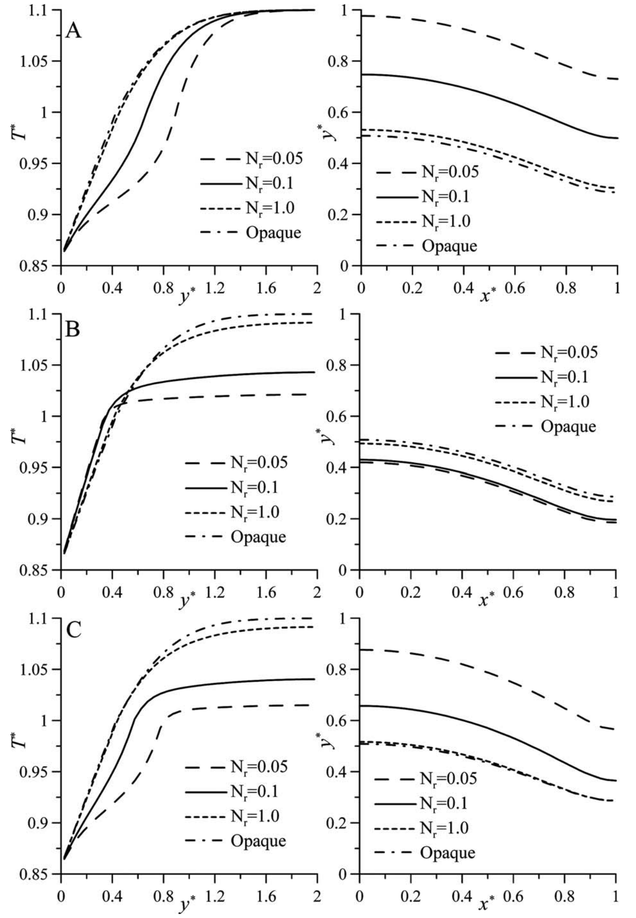

Fig. 7 Temperature distributions along $x^*=0.5$ (left) and front locations (right) for varying N_r ((*a*) semitransparent solid phase, opaque liquid phase; (*b*) opaque solid phase, semitransparent liquid phase; and (c) semitransparent both phases)

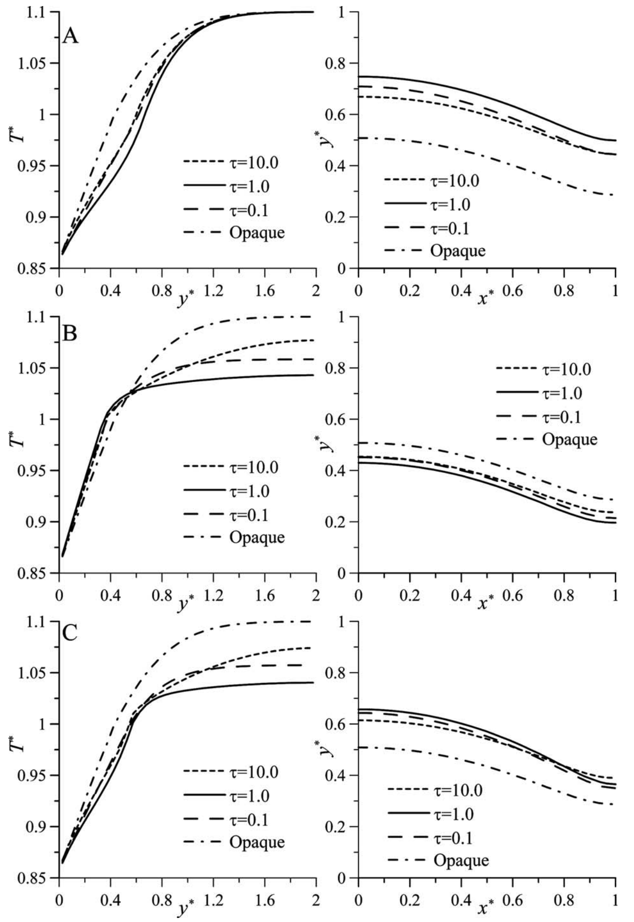

Fig. 8 Temperature distributions along $x^*=0.5$ (left) and front locations (right) for varying τ ((*a*) semitransparent solid phase, opaque liquid phase; (*b*) opaque solid phase, semitransparent liquid phase; and (*c*) semitransparent both phases)

The optical thickness of the layer τ exerts the strongest effect on temperature distribution and solidification rate when it is close to unity—Fig. 8. Increasing in τ above unity reduces radiative cooling, because the distance between successive absorption and scattering of the radiation decreased as τ increases and the medium becomes optically thicker. Decreasing τ below unity also contributes in reducing radiative cooling, because of the medium becomes more transparent as τ falls. More comments on influence of N_r and τ on the solidification process can be found in Refs. [9,10,14,17].

5.2 Axisymmetric Simulation. The axisymmetric rectangular domain with the width and the height equal to L_{r^*} and $2L_{z^*}$, as

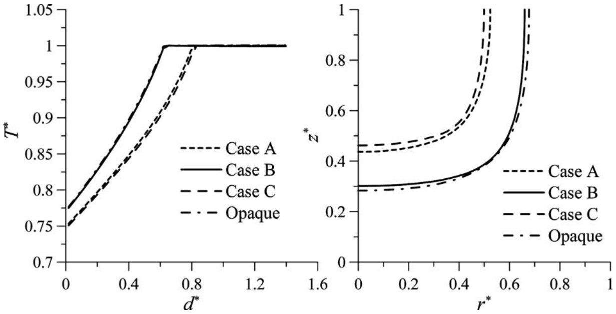

Fig. 9 Temperature distributions along line d^* (left) and front locations (right) for different optical configurations (case A: semitransparent solid phase, opaque liquid phase; case B: opaque solid phase, semitransparent liquid phase; and case C: semitransparent both phases)

shown in Fig. 6(*b*), was also investigated. This geometry mimics a metal canister used in the high temperature thermal energy-storage system for the space applications. The void that normally exists in such a canister due to different densities in solid and liquid phases, was neglected in the current work, because it was assumed that densities of solid and liquid phase had the same value. For the space applications, the convection in the liquid phase can be also neglected as in the considered example. Right, top, and bottom boundaries of the domain were subjected to external convective cooling by the surroundings, left wall was the axis of symmetry. Moreover, only a half of the medium in the cavity was considered due symmetry of the thermal problem. Most of thermophysical and optical properties of the medium were taken according to Yimer [13] (properties of fluoride salt with eutectic weight composition of LiF—41.27%, MgF_2—48.76%, and KF—8.95%). The dimensionless quantities were fixed at the following constant values: $c^*=1.0$, $k^*=1.0$, $n^*=1.0$, $\rho^*=1.0$, $T^*_{\text{init}}=1.1$, $T^*_\infty=0.6$, $L_{r^*}=1.0$, $L_{z^*}=2.0$, $K^*_a=1.0$, $K^*_e=1.0$, $K^*_s=1.0$, $\text{Fo}=0.5583$, $\text{Nu}=1.1$, $\text{Ste}=1.69$, $\varepsilon_w=0.8$, $\varepsilon_i=0.6$, and $\omega=0.0$. The scattering phase function was assumed isotropic. The properties, which varied during the calculation, were made equal to: $N_r=0.1, \mathbf{0.2}, 0.42$, $\tau=0.03, \mathbf{0.3}, 3.0, 30.0$ (the bold values were taken as the default ones). The spatial domain and the solid angle were discretized as $N_r \times N_z=40\times 40$ and $N_\phi \times N_\theta=8\times 4$, respectively.

In Fig. 9 distributions of dimensionless temperature along line d^* (Fig. 6(*b*)) and position of the solid-liquid interface are plotted for different optical configuration (cases A, B, C, and opaque material). The internal radiation in liquid phase contributes to decreasing liquid temperature at the initial state of the process and to a little increase in solidification rate, whereas internal radiation in solid phase increases heat transfer from the solid-liquid interface to the cooled boundaries and therefore strongly accelerates solidification. For cases A and C, the solid-liquid interface propagates further than for case A and opaque material. The thermal radiation effect is the most pronounced for the case C, and therefore, only results obtained for this case are further presented.

The influence of the conduction-radiation parameter N_r for case C (semitransparent both solid and liquid phases) is shown in the Fig. 10. The conclusion is the same as for Fig. 7—the share of the radiation in the total heat transfer increases as N_r falls and then radiative cooling through semitransparent solid is enhanced. Therefore more material is solidified as can be observed in Fig. 10.

The influence the optical thickness of the layer τ is shown in Fig. 11. The most pronounced radiative cooling is for τ close to 1.0 (the same value as for 2D Cartesian simulation, Fig. 8). Above $\tau=1.0$ the material becomes optically thicker whereas below $\tau=1.0$ more transparent, and therefore less radiatively cooled.

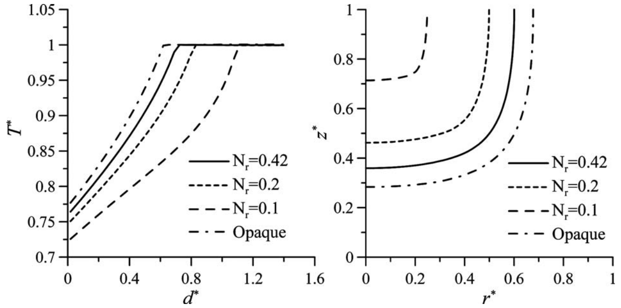

Fig. 10 Temperature distributions along line d^* (left) and front locations (right) for varying N_r for case C: semitransparent both phases

6 Conclusions

In this work the front tracking method together with the immersed boundary technique was applied to solve solidification process of semitransparent materials. This combined approach enabled accurate dealing with different optical and thermophysical properties of solid and liquid phases as well as with the absorption, emission, and reflection of the thermal radiation at the solid-liquid interface, as was shown in the present paper. Moreover, being based on the fixed grid, the approach does not need adaptation of meshes to the solid-liquid interface shape and therefore, interpolation of field variables in every iteration of solving procedure seems unnecessary.

It was proved that the proposed method can be effectively used for the solution of problems formulated in different coordinate systems. The numerical model was applied to two different geometrical configurations, i.e., two-dimensional Cartesian and axisymmetric cases with different thermophysical and optical properties in solid and liquid phases. The test cases with complex fixed boundaries reveal the good accuracy of the presented method, whereas simulation with complex moving boundaries and opaque, absorbing, emitting, and reflecting diffusively solid-liquid interface show the capabilities and potential application area of the presented method. Three combinations of optical properties, i.e., semitransparent solid phase and opaque liquid phases, opaque solid phase and semitransparent liquid phase, and semitransparent both phases were considered during the simulations of solidification process. Effects of the optical parameters such as the conduction-radiation parameter and the optical thickness of the layer on temperature distribution in the solidified system, solidification rate, and on the solid-liquid interface shape were studied. The results of our numerical calculations reveal strong influence of the thermal radiation on solidification process of semitransparent materials. It was found, that depending on configuration of the optical properties of the phases, strong internal thermal radiative cooling decreases temperature in solid or bulk liquid, respectively,

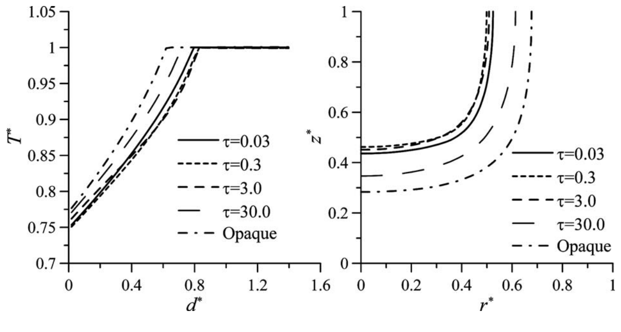

Fig. 11 Temperature distributions along line d^* (left) and front locations (right) for varying τ for case C: semitransparent both phases

and leads to higher or lower rate of solidification. The most pronounced radiative cooling was observed for small value of the conduction-radiation parameter and for the optical thickness close to unity.

The presented model is still being developed. Reflection and refraction of thermal radiation at the solid-liquid interface, anisotropy of properties of the solid phase, thermosolutal convection, and macrosegregation are planned to be included to better simulate real processes.

Acknowledgment

This paper was financially supported in part by the Polish Ministry of Science and Higher Education under Grant No. N N512 459736.

Nomenclature

I = radiation intensity, $\mathrm{W/m^2\ sr}$
K_a = absorption coefficient, 1/m
K_e = extinction coefficient, 1/m
K_s = scattering coefficient, 1/m
L_f = latent heat of melting, J/kg
L_x, L_y = dimension of two-dimensional computational domain, m
L_r, L_z = dimension of axisymmetric computational domain, m
T = temperature, K
T_m = melting temperature, K
V = interface velocity, m/s
c_p = specific heat, J/kg K
k = thermal conductivity, W/m K
n = refractive index
$\mathbf{n}$ = normal vector
q = density of heat flux, $\mathrm{W/m^2}$
$\mathbf{q}$ = heat flux vector, $\mathrm{W/m^2}$
r, z = axisymmetric coordinates
$\mathbf{s}$ = radiation direction vector
t = time, s
x, y, z = Cartesian coordinates
h = convective heat transfer coefficient, $\mathrm{W/m^2\ K}$
ε = surface emissivity
ϕ = azimuthal angle, rad
θ = polar angle, rad
ρ = density, $\mathrm{kg/m^3}$
σ = Stefan–Boltzmann constant, $\mathrm{W/m^2\ K^4}$
Φ = scattering phase function
ω = albedo
Ω = solid angle, sr

Subscripts

i = associated with interface
in = incident
l = liquid phase
out = emitted
r = associated with radiation
s = solid phase
w = wall
∞ = surroundings
z = solid or liquid phase

Superscripts

$*$ = nondimensional

References

[1] Prisniakov, V. F., and Gabrinets, V. A., 1995, "The New Conceptions for Design of Thermal Energy Storage for Solar Dynamic Plants," Acta Astronaut., **37**, pp. 7–10.
[2] Tsukada, T., Kakinoki, K., Hozawa, M., and Imaishi, N., 1995, "Effect of Internal Radiation Within Crystal and Melt on Czochralski Crystal Growth of Oxide," Int. J. Heat Mass Transfer, **38**, pp. 2707–2714.
[3] Abrams, M., and Viskanta, R., 1974, "The Effect of Radiative Heat Transfer Upon the Melting and Solidification of Semitransparent Crystals," ASME J. Heat Transfer, **96**, pp. 184–190.
[4] Chan, S. H., Cho, D. H., and Kocamustafaogullari, G., 1983, "Melting and Solidification With Internal Radiative Transfer—A Generalized Phase Change Model," Int. J. Heat Mass Transfer, **26**, pp. 621–633.
[5] Dorsey, N. E., 1968, *Properties of Ordinary Water Substance*, Hafner, New York.
[6] Knight, C. A., 1967, *The Freezing of Supercooled Liquids*, Van Nostrand, Princeton, NJ.
[7] Yao, C., Chung, B. T. F., and Wang, G.-X., 2002, "Mushy Zone Equilibrium Solidification of Semitransparent Layer Subject to Radiative and Convective Cooling," Int. J. Heat Mass Transfer, **45**, pp. 2397–2405.
[8] Mishra, S. C., Behera, N. C., Garg, A. K., and Mishra, A., 2008, "Solidification of a 2-D Semitransparent Medium Using the Lattice Boltzmann Method and the Finite Volume Method," Int. J. Heat Mass Transfer, **51**, pp. 4447–4460.
[9] Łapka, P., and Furmański, P., 2008, "Numerical Modeling of Solidification Processes of Semitransparent Materials Using the Enthalpy and the Finite Volume Methods," Heat Mass Transfer, **44**, pp. 937–957.
[10] Yao, C., Wang, G.-X., and Chung, B. T. F., 2000, "Nonequilibrium Planar Interface Model for Solidification of Semitransparent Radiating Materials," J. Thermophys. Heat Transfer, **14**, pp. 297–304.
[11] Wang, G.-X., Yao, C., and Chung, B. T. F., 2003, "Thermal Analysis on Planar Interface Stability in Solidification of Semitransparent Materials," J. Thermophys. Heat Transfer, **17**, pp. 193–198.
[12] Sokolov, P., Ibrahim, M., and Kerslake, T., 2000, "Computational Heat-Transfer Modeling of Thermal Energy Storage Canisters for Space Applications," J. Spacecr. Rockets, **37**, pp. 265–272.
[13] Yimer, B., 2000, "Multi-Dimensional Solidification With Internal Radiation and Temperature Dependent Properties," Energy Convers. Manage., **41**, pp. 343–352.
[14] Brandon, S., and Derby, J. J., 1991, "Internal Radiative Transport in the Vertical Bridgman Growth of Semitransparent Crystals," J. Cryst. Growth, **110**, pp. 481–500.
[15] Lan, C. W., and Tu, C. Y., 2001, "Three-Dimensional Simulation of Facet Formation and the Coupled Heat and Segregation in Bridgman Growth of Oxide Crystals," J. Cryst. Growth, **233**, pp. 523–536.
[16] Lan, C. W., and Chen, C., 2007, "Dynamic Three-Dimensional Simulation of Facet Formation and Segregation in Bridgman Crystal Growth," J. Cryst. Growth, **303**, pp. 287–296.
[17] Kobayashi, M., Hagino, T., Tsukada, T., and Hozawa, M., 2002, "Effect of Internal Radiative Heat Transfer on Interface Inversion in Chochralski Crystal Growth of Oxides," J. Cryst. Growth, **235**, pp. 258–270.
[18] Yuferev, V. S., Budenkova, O. N., Vasiliev, M., Rukolaine, S. A., Shlegel, V. N., Vasiliev, Ya. V., and Zhmakin, A. I., 2003, "Variation of Solid-Liquid Interface in the BGO Low Thermal Gradients Cz Growth for Diffuse and Specular Crystal Side Surface," J. Cryst. Growth, **253**, pp. 383–397.
[19] Jing, C. J., Hayashi, A., Kobayashi, M., Tsukada, T., Hozawa, M., Imaishi, N., Shimamura, K., and Ichinose, N., 2003, "Effect of Internal Radiative Heat Transfer on Spoke Pattern on Oxide Melt Surface in Czochralski Crystal Growth," J. Cryst. Growth, **259**, pp. 367–373.
[20] Jing, C. J., Ihara, S., Sugioka, K.-I., Tsukada, T., Kobayashi, M., Mito, M., and Yokoyama, C., 2007, "Global Analysis of Heat Transfer Considering Three-Dimensional Unsteady Melt Flow in CZ Crystal Growth of Oxide," J. Cryst. Growth, **307**, pp. 235–244.
[21] Lee, H., and Pearlstein, A. J., 2001, "Interface Shape and Thermally-Driven Convection in Vertical Bridgman Growth of Gallium Selenide: A Semiconductor With Anisotropic Solid-Phase Thermal Conductivity," ASME J. Heat Transfer, **123**, pp. 729–740.
[22] Udaykumar, H., Mittal, R., and Shyy, W., 1999, "Computation of Solid-Liquid Phase Fronts in the Sharp Interface Limit on Fixed Grids," J. Comput. Phys., **153**, pp. 535–574.
[23] Ye, T., Mittal, R., Udaykumar, H. S., and Shyy, W., 1999, "An Accurate Cartesian Grid Method for Viscous Incompressible Flow With Complex Immersed Boundaries," J. Comput. Phys., **156**, pp. 209–240.
[24] Byun, Y. D., Baek, S. W., and Kim, M. Y., 2003, "Investigation of Radiative Heat Transfer in Complex Geometries Using Blocked-Off, Multiblock, and Embedded Boundary Treatments," Numer. Heat Transfer, Part A, **43**, pp. 807–825.
[25] Kim, T.-K., and Lee, H., 1988, "Effect of Anisotropic Scattering on Radiative Heat Transfer in Two-Dimensional Rectangular Enclosures," Int. J. Heat Mass Transfer, **31**, pp. 1711–1721.
[26] Versteeg, H. K., and Malalasekera, W., 2007, *An Introduction to Computational Fluid Dynamics. The Finite Volume Method*, Pearson, Harlow, UK.
[27] Raithby, G. D., and Chui, E., 1990, "A Finite-Volume Method for Predicting a Radiant Heat Transfer in Enclosures With Participating Media," ASME J. Heat Transfer, **112**, pp. 415–423.
[28] Murthy, J. Y., and Mathur, S. R., 1998, "Radiative Heat Transfer in Axisymmetric Geometries Using Unstructured Finite-Volume Method," Numer. Heat Transfer, Part B, **33**, pp. 397–416.
[29] Baek, M. Y., Kim, M. Y., and Kim, J. S., 1998, "Nonorthogonal Finite-Volume Solutions of Radiative Heat Transfer in a Three-Dimensional Enclosure," Numer. Heat Transfer, Part B, **34**, pp. 419–437.
[30] Murthy, J. Y., and Mathur, S. R., 2000, "A Finite-Volume Scheme for Radiative Heat Transfer in Semitransparent Media," Numer. Heat Transfer, Part B,

37, pp. 25–43.

[31] Swaminathan, C. R., and Voller, V. R., 1992, “A General Enthalpy Method for Modelling Solidification Processes,” Metall. Trans. B, **23**, pp. 651–663.

[32] Salah, M. B., Askri, F., Jemni, A., and Nasrallah, S. B., 2006, “Numerical Analyses of Radiative Heat Transfer in Any Arbitrarily-Shaped Axisymmetric Enclosures,” J. Quant. Spectrosc. Radiat. Transf., **97**, pp. 395–414.

[33] Mishra, S. C., Lankadasu, A., and Beronov, K. N., 2005, “Application of the Lattice Boltzmann Method for Solving Energy Equation of a 2-D Transient Conduction-Radiation Problem,” Int. J. Heat Mass Transfer, **48**, pp. 3648–3659.

Heat Transfer Augmentation: Radiative-Convective Heat Transfer in a Tube With Fiber Array Inserts

Andreas Hantsch
e-mail: hantscha@mailserver.tu-freiberg.de

Ulrich Gross
e-mail: gross@iwtt.tu-freiberg.de

Institut für Wärmetechnik und Thermodynamik,
TU Bergakademie Freiberg,
G.- Zeuner-Str. 7,
09599 Freiberg, Germany

Andrew R. Martin[1]
Department of Energy Technology,
KTH,
Brinellvägen 68,
10044 Stockholm, Sweden
e-mail: andrew.martin@energy.kth.se

Gas-phase heat transfer plays a critical role in many high temperature applications, such as preheaters, combustors, and other thermal equipment. In such cases common heat transfer augmentation methods rely on the convective component alone to achieve improved internal performance. Radiatively assisted heat transfer augmentation has been suggested as a way to overcome limitations in convective-only enhancement. One example of such a technique is the fiber array insert; thermal radiation emitted by tube walls is captured by a large number of slender fibers, which in turn convect heat to the flowing fluid. Previous numerical studies have indicated that this technique represents a promising enhancement method warranting further investigation. This paper presents results from an experimentally based feasibility study of fiber array inserts for heat transfer augmentation in an externally heated duct. Fibers composed of 140 μm silicon carbide and 150 μm stainless steel were assembled in arrays with porosities around 0.98, and were tested for empty-tube Reynolds numbers ranging from 17,500 to 112,500 and wall temperatures from ambient up to 750°C. The arrays cause a significant pressure drop—roughly two orders of magnitude higher than the empty-tube case—but tube-side heat transfer coefficients were improved by up to 100% over the convective-only case in the low flow rate regime. The stainless steel fiber array exhibited similar heat transfer performance as the silicon carbide case, although pressure drop characteristics differed owing to variations in fluid-structure flow phenomena. Pressure drop data were roughly within the range of d'Arcy law predictions for both arrays, and deviations could be explained by inhomogeneities in fiber-to-fiber spacing. Heat transfer was found to depend nonlinearly on wall temperature and flow rate, in contrast to previously reported numerical data. [DOI: 10.1115/1.4000189]

1 Introduction

Heat transfer to and from gases like air or steam is a critical operation in many technical applications, especially in high temperature systems like preheaters for combustors or systems for recovering the enthalpy of exhaust gases. In these settings convection is the primary mode of heat transfer, since gases typically have low thermal conductivity and are transparent to infrared radiation. Enhancement techniques like fins and turbulence promoters are well known, although there are limits to the amount of augmentation or allowable pressure drop tradeoffs. Exploiting the radiative component for promoting heat transfer at higher temperatures (say 500°C or more) remains a promising area for the development of advanced heat exchange equipment. Seeding gas flow with radiatively absorbing particles is one approach; fluidized beds are another example. However in most cases the introduction of particles would risk damage to downstream components—near 100% particle separation is impractical—so a fixed porous insert would be preferred. The key is to design an insert that allows for radiative enhancement while minimizing frictional losses, which points to the need for extremely high-porosity media.

In the early 1990s, Im and Ahluwalia [1] proposed a fiber array concept for achieving radiative heat transfer augmentation in internal, high temperature flows. The concept is illustrated in Fig. 1; in short thermal radiation emitted by the heated walls is captured by a number of slender (approximately 100 μm) fibers, which in turn convect this energy to the flowing fluid. One-dimensional calculations were employed to determine the net heat transfer as a function of fiber material (SiC, SiO_2, Al_2O_3, and metals), fiber diameter, array porosity, and flowrate. Results indicated that the best enhancement would occur at lower porosities and higher wall temperatures, and that SiC and metals were the preferred fiber materials.

Martin and co-workers [2,3] conducted a two-dimensional numerical investigation considering the fiber array as a nongray porous media with prescribed permeability (so-called micro-macro modeling approach). The fact that an optimum in heat exchange effectiveness was found at a porosity of 0.96 (corresponding to an optical depth of about 6) demonstrated that low porosities were not necessary favored. Otherwise findings essentially confirmed those presented by Im and Ahluwahlia [1], including the importance to account for differences in local fiber-fluid temperatures (expressed as departure from local thermodynamic equilibrium).

Chen and Sutton [4] performed numerical calculations for investigating the heat transfer enhancement with porous media in a cylindrical duct. Their model had a porous core and a free fluid annular section. Both thermal and hydrodynamic boundary layers were not fully developed. A special integral equation was employed for solving the radiative heat transfer equation. Results showed that the convective and radiative Nusselt numbers are increased by 35% and 105%, respectively, with the porous insert compared with the case without porous inserts.

Clearly the fiber array concept merits experimental investigation based on the positive results of the above numerical studies.

---

[1] Corresponding author.

Contributed by the Heat Transfer Division of ASME for publication in the JOURNAL OF HEAT TRANSFER. Manuscript received October 30, 2008; final manuscript received August 22, 2009; published online December 2, 2009. Assoc. Editor: Yogesh Jaluria.

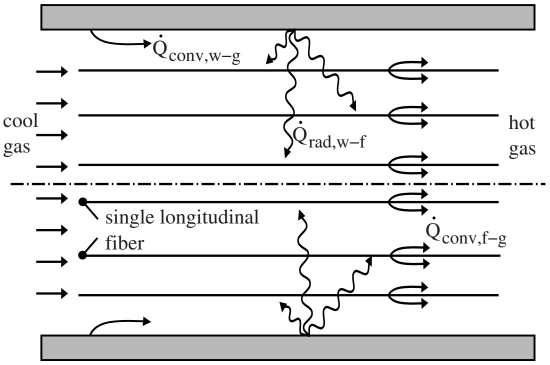

Fig. 1 Model of the system with heat fluxes

The objective of the present work is to design, build, and operate a test section for feasibility studies of high-porosity (0.98 and higher) fiber arrays composed of SiC and stainless steel. Aside from quantifying experimental heat transfer and pressure drop characteristics, this study sheds light on some of the practical issues experienced when assembling a fiber array.

2 Experiments

2.1 Test Rig. Measurements were conducted with a test rig shown in Fig. 2. The airflow was driven by a fan and its mass flow rate measured by an orifice plate. Afterwards, the air entered a settling chamber fitted with a mesh and a flow conditioner for dissipation of strong vortices. The core piece of the test rig was a heat exchanger tube made of Inconel 600 (emissivity $\epsilon = 0.5$) with an inner diameter of 42 mm. Measurements were conducted with two tubes of different lengths[2]—340 mm and 1000 mm. Essentially one can say that the shorter tube was used first in order to minimize the length of the array (challenging to install it for the first time) and to ensure that most of the section was heated. Later it was understood that the inlet geometry coupled with the short length meant that complexities at the entry inhibited fully developed flow to be obtained. A redesign to a longer tube was then employed, and calculations indicated that entry effects would be sufficiently reduced after approximately 15D (see Hantsch [5]). Due to the fact that the end faces were closed by plates fixing the fibers in the tube, the air flow had to enter and leave the tube through three apertures on each side. In the short tube, the heated section[3] was placed exactly in the middle between inlet and outlet (see Fig. 2(*b*)), and in the long tube the test section was located close to the outlet for offering a length of 650 mm ($\approx 15.5D$) for developing the air flow until entering it. The test section was built similar in both tubes. Four heaters were placed between the pressure taps (see Fig. 2(*b*)).

Perforated plates of sheet steel (EN 10270-3: 1.4319; hole diameter: 0.5 mm, hole density: 967660 m^{-2}) were mounted at the ends of each Inconel test section in order to form the fiber array. Fibers were threaded manually through the holes, forming a triangular pattern, and a temperature-resistant ceramic adhesive was used to fix the fibers in place. More details on the assembly can be found in Hantsch [5]. Two different materials were used as fibers: a composite of silicon carbide (SiC) with a carbon core; and stainless steel (EN 10270-3: 1.4310). Their characteristic properties are shown in Table 1. The supplier for the SiC fibers is Specialty Materials, Inc., Lowell, MA.

Table 1 Characteristic properties of fiber materials

Property	SiC	Steel
Diameter d, in mm	0.14	0.15
Young's modulus, in GPa	380	210
Density ρ, in $\mathrm{kg/m^3}$	3000	7850
Emissivity ϵ	0.93	0.65

2.2 Measurements and Evaluation

2.2.1 Measurement System. Temperature measurements were conducted with thermocouples type N whose voltages were converted into temperatures by a multimeter (Keithley 2701/7706, interfaced to PC via LABVIEW). Temperatures were measured at specific positions (see Fig. 2): gas temperatures at inlet and outlet of the tube; wall temperatures in the test section; and the ambient temperature. At the outlet of the tube, gas temperatures were measured over each of the three apertures and their values were averaged for determining the outlet temperature. The maximum difference of these three temperatures was 5–10°C, depending upon flowrate and temperature.

Pressure drop over the test section was measured with a transducer (Sensortechnics GmbH, Puchheim, Germany, PCL [6]) providing an analog signal which was converted into a pressure reading via a calibration curve. In the short tube, the pressure drop was measured with one tap on either side, whereas in the long tube three taps on either side were used for averaging the pressure information at the respective position. For calculating the mass flow rate, an orifice plate was used where the pressure drop and the pressure difference to ambient conditions were measured by a transducer (Sensortechnics, HCX [7]) and a water column, respectively. The ambient pressure was measured with a digital barometer (Weston Aerospace, Farnborough, UK, 7885 Digital Pressure Module [8])

Electrical power input was measured as the total input of four heaters with a power meter (Yokogawa, Electric Corp., Mitaka, Japan, WT130 [9]).

2.2.2 Further Quantities. For characterizing the flow regime, the Reynolds number is calculated via

$$\mathrm{Re} = \frac{\dot{m} L_{\mathrm{ch}}}{A \mu} \tag{1}$$

by using the hydraulic diameter as characteristic length scale

$$L_{\mathrm{ch}} = D_h = \frac{D^2 - nd^2}{D + nd} \tag{2}$$

and the free cross section

$$A = 0.25\pi(D^2 - nd^2) \tag{3}$$

where $\dot{m}$ is the mass flow rate, μ the dynamic viscosity, D the tube's inner diameter, n is the number of fibers, and d is their diameter. Heat transfer characteristics are determined with the Nusselt number:

$$\mathrm{Nu} = \frac{P_{\mathrm{in}} L_{\mathrm{ch}}}{\pi D L k(\langle t_w \rangle - \langle t_g \rangle)} \tag{4}$$

where k and $\langle t_g \rangle = 0.5(t_{\mathrm{out}} + t_{\mathrm{in}})$ are the thermal conductivity and averaged temperature of the gas, respectively, $\langle t_w \rangle = 1/3(t_{w1} + t_{w2} + t_{w3})$ is the averaged wall temperature, D is the inner tube diameter, and L is the length of the test section. L_{ch} is the characteristic length scale.

Based on the measured electrical power input, the total power input in the system can be calculated with

---

[2] Denoted below as short and long tubes, respectively.

[3] Denoted below as test section.

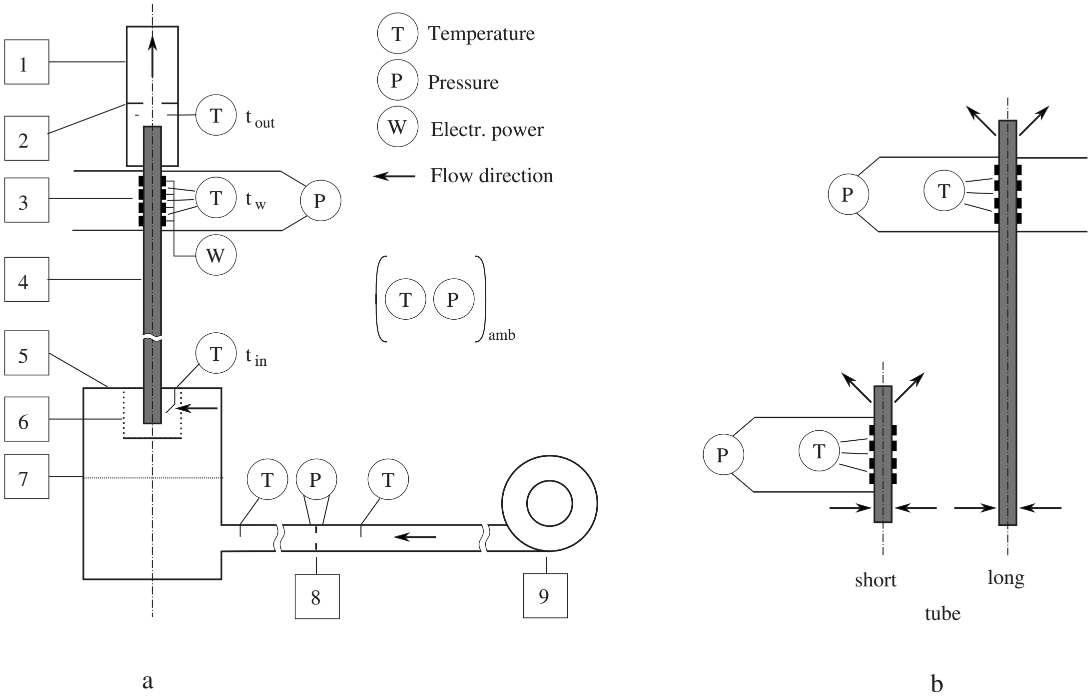

Fig. 2 Test rig and details of short and long tube; (*a*) Test rig: (1) Exhaust pipe, (2) orifice plate, (3) heaters, (4) heat exchanger tube, (5) settling chamber, (6) flow conditioner, (7) mesh, (8) orifice plate, (9) fan; (*b*): Positions of the test section in short and long heat exchanger tube

$$P_{\text{in}} = P_{\text{el}} - \dot{Q}_{\text{loss}} = \dot{m}[c_p(t_{\text{out}})t_{\text{out}} - c_p(t_{\text{in}})t_{\text{in}}] \tag{5}$$

where P_{el} is the electrical power, $\dot{Q}_{\text{loss}}$ are the heat losses, $\dot{m}$ is the mass flow rate, c_p is the specific heat capacity at constant pressure, and t_{in} and t_{out} are the gas temperatures at inlet and outlet of the tube, respectively.

The heat losses, depending on the wall temperature, are estimated separately by closing the tube and measuring the electrical power input. According to Eq. (5), the heat losses equal the electrical power input for stagnant conditions.

By using relations derived from Stokes flow analysis, Drummond and Tahir [10] devised explicit expressions for the permeability of longitudinally aligned cylinders, a logical basis for comparison to experimental results. Considering a triangular array, the share of solid phase is

$$\Psi_s = \frac{\pi}{2\sqrt{3}}\left(\frac{d}{l}\right)^2 \tag{6}$$

where d is the fiber's diameter and l is the distance of their centers. Assuming an ideal, homogeneous, and infinite array, the permeability in axial direction is then

$$K = \frac{d^2}{16\Psi_s}\left[\ln\left(\frac{1}{\Psi_s}\right) - 1.498 + 2\Psi_s - 0.5\Psi_s^2 - 0.002514\Psi_s^6\right] \tag{7}$$

By applying d'Arcy's law

$$\Delta p = \frac{\dot{m}\nu L}{AK} \tag{8}$$

where $\dot{m}$ is the mass flow rate, A is the free cross section, Eq. (3), K is the permeability, ν is the kinematic viscosity, and L is the length of the test section, one can calculate the pressure drop Δp. At higher mass flows inertia becomes important and has to be considered by using the Forchheimer equation:

$$\Delta p = \frac{\mu}{K}\langle u\rangle + b\rho\langle u\rangle^2 \tag{9}$$

where μ and ρ are the dynamic viscosity and density of gas, respectively, and b is an empiric constant (Note that b can also be considered to be a nonconstant parameter, as noted by Huang and Ayoub [11]. However, no attempt is made to further clarify b in this study due to the fact that only one porosity is considered.) The cross section averaged velocity $\langle u\rangle$ is calculated with the continuity equation

$$\langle u\rangle = \frac{\dot{m}}{\rho A} \tag{10}$$

where ρ is the density of the gas. By introducing the friction factor

$$f = \frac{2\Delta p}{\rho\langle u\rangle^2} \tag{11}$$

the hydrodynamical influence of the fibers can be shown.

2.2.3 Error Analysis. Measurement uncertainties are based on a confidence interval of 95%. For analyzing the data, the mean values and root-mean-square values are calculated. The total variance for a measured mean value is the sum of the variance of the device and two times the variance of the mean of the measurements. The uncertainties of the different measuring devices are shown in Table 2. This approach corresponds to type A given in NIST standards [12].

Table 2 Systematic uncertainties of the measurement devices

Device	Uncertainty
Pressure sensor mass flow	0.125% of full scale
Pressure sensor tube	0.32% of full scale
Pressure sensor ambient	0.1% of full scale
Thermocouple	$0.75\% T$
Power meter	$0.25\% P + 0.1\%$ range
Measurement of tube diameter	0.25 mm

The uncertainties of derived general quantities Φ' are calculated with an equation for the maximum uncertainty by using the linear part of the Taylor series. The absolute values of the partial deviations multiplied with the total uncertainty of the measured quantities, are then summed up:

$$\Phi' = \sum_i \left| \frac{\partial \Phi}{\partial \phi_i} \right| \phi_i' \qquad (12)$$

The uncertainty of the mass flow rate is calculated according to the equation given in ISO 5167 [13].

2.3 Experimental Procedure. Test series were performed at mass flow rates in the range of 0.010 to 0.065 kg/s and wall temperatures of 20–750°C. Measurements in the short tube were conducted with an array of 817 SiC fibers, and in the long tube with an array of 1250 SiC fibers and a second array with 1244 stainless steel fibers. In Table 3 the respective temperature-averaged Reynolds numbers are shown.

After setting the wall temperature, the system stabilized and finally the measurement was taken. During 5 min approximately 300 sets of readings were recorded and stored in an ASCII file. Averaging and calculation of the root-mean-square value was performed with a C++ program.

3 Results and Discussion

3.1 Pressure Drop Measurements. In Fig. 3 the friction factors are presented, depending on Reynolds number with the hydraulic diameter as characteristic length scale. In each diagram measurements with fibers as well as the theoretical friction factor according to d'Arcy, Eqs. (7) and (8), are shown. Measured values are normalized to 25°C and analytical values are calculated with properties at this temperature.

In Fig. 3(*a*) the friction factor of SiC fiber-filled tube is much lower than values predicted with the d'Arcy relation. Additional measurements with the empty short tube showed a pressure recovery in the flow direction, which indicates that the pressure measurement at the inlet of the test section is strongly affected by the entry vortex. Figure 3(*b*) shows the friction factor in the long tube with SiC and stainless steel fibers. It is obvious that their influence on the flow is roughly the same for low Reynolds numbers, but lower than predicted with d'Arcy's law. The SiC fibers show strong fluctuations, which are displayed separately in Fig. 4, and a lower friction factor from an apparent transition zone at approximately $Re_{Dh} = 12{,}300$ onwards. Stainless steel fibers show this transition at higher Reynolds numbers, close to 16,800. The fact that SiC and steel arrays exhibited such different flow characteristics is not fully understood. Attempts to link transition to fluctuating flows via aeroelastic considerations were inconclusive. Other factors like fiber prestress or the fact that the SiC fibers were possibly not tensed as strong as the stainless steel fibers could possibly have played a role.

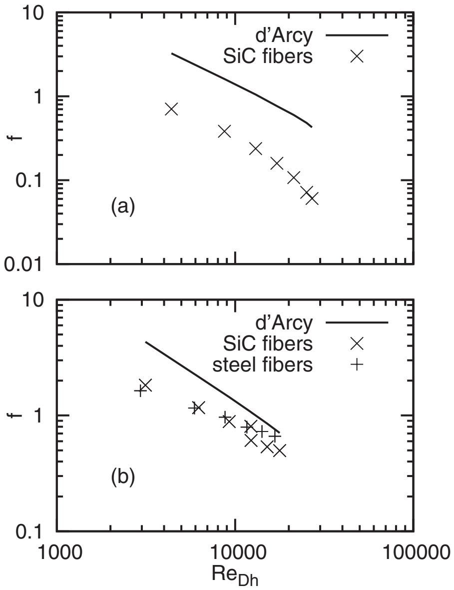

Fig. 3 Friction factor depending on Reynolds number with hydraulic diameter as length scale; (*a*) short tube with SiC fibers and (*b*) long tube with SiC and steel fibers

For distinguishing the permeability of the array, the Forchheimer equation, Eq. (9), is fitted to the pressure drop measurements (see Fig. 4) up to the so-called transition Reynolds number (12,300 for SiC and 16,800 for steel). In Table 4 the results are shown. By calculating the d'Arcian Reynolds number, with $\sqrt{K_{\text{measured}}}$ as length scale, one comes to the conclusion that the flow is in the non-d'Arcy regime, with $Re_{\sqrt{K}} > 750 \gg 1$. Another finding relates to the fact that measured permeability is one order of magnitude higher than the theoretical permeability. This effect can be explained by considering that Drummond and Tahir [10] assumed an infinite, ideal, and homogeneous array of rigid parallel cylinders. Since the arrays are limited in size, with a higher local porosity close to the wall and nonuniformities in fiber spac-

Table 3 Temperature-averaged Reynolds numbers of the test series based on the respective hydraulic diameter

	Re_{D_H}			
$\dot{m}$			Long tube	
(kg/s)	Empty	Short tube SiC	SiC	Steel
0.010	17,500	4680	3370	3200
0.020	34,700	9320	6710	6390
0.030	52,000	13,960	10,050	9550
0.040	69,300	18,600	13,400	12,720
0.050	86,500	23,250	16,750	15,900
0.060	103,800	27,890	20,100	19,080
0.065	112500	30,220	–	–

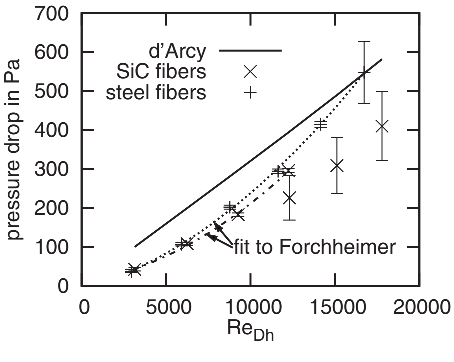

Fig. 4 Pressure drop depending on Reynolds number based on hydraulic diameter in the long tube with SiC and stainless steel fibers

Table 4 Theoretical and measured permeabilities and their square roots of the arrays fitted into Forchheimer equation

	Short	Long	
	SiC	SiC	Steel
$K_{\text{theoretical}}$ in 10^{-7} m^2	3.23	2.24	2.13
K_{measured} in 10^{-7} m^2	50.6	38.1	30.5
b_{measured}	−0.052	0.37	0.26
$\sqrt{K_{\text{theoretical}}}$ in 10^{-3} m	0.57	0.47	0.46
$\sqrt{K_{\text{measured}}}$ in 10^{-3} m	2.25	1.95	1.75
d in 10^{-6} m	140	140	150
l in 10^{-3} m	1.25	1.09	1.09

ing, it is obvious that the array is nonideal. Furthermore, buckling effects can locally increase the distance of fibers and hence the measured characteristic length. Additionally it should be mentioned that the short tube's array has an annular section of approximately 3 mm width.

3.2 Heat Transfer Measurements. Heat transfer measurements were designed to distinguish the influence of the fibers on total heat transfer. The results of selected mass flow rates are shown in Fig. 5. The Nusselt number, for better comparison being based on the inner tube diameter, is plotted versus the averaged wall temperature.

In the short tube, Fig. 5(*a*), the heat transfer for the empty tube shows the highest performance since the heat transfer is dominated by convection due to the entry vortex. By inserting the fibers, the flow is obstructed and therefore the convective heat transfer reduced. Only for low mass flow rates and high wall temperatures the loss of convection is compensated by radiation. By comparing these results with those obtained by Im and Ahluwalia [1], one can see that they also show the trend of nonlinear increase with higher wall temperatures.

In the long tube, Figs. 5(*b*) and 5(*c*), the Nusselt number with fibers, SiC and stainless steel, respectively, exceeds in any measured point the Nusselt number of the empty tube. Contrary to the findings of Im and Ahluwalia [1], which suggested that the heat transfer is independent of the Reynolds number, the experimental measurements show a strong dependence on Reynolds number. Im and Ahluwalia assumed the flow to be laminar for Reynolds numbers based on inner tube diameter below 100,000, and therefore the Nusselt number was constant. The measurements have shown that the Nusselt number increases with Reynolds number, but the difference to the empty case decreases, because of forced convection.

Due to the transition to strongly fluctuating flow, the heat transfer is affected. This can be seen in Fig. 5(*b*) at mass flow rate 0.06 kg/s, where at low wall temperatures, the Nusselt number is higher than at high wall temperatures. This effect is caused by strong convection at low system temperatures. By increasing the temperature, the viscosity increases also and eventually the strong fluctuations diminish at highest wall temperature. Hence the convection is reduced also, but from approximately 550°C on, the radiation compensates the missing convection and the Nusselt number rises again.

By comparing the results of SiC and stainless steel, one comes to the conclusion that the Nusselt number of SiC fibers is only slightly higher than the Nusselt number of stainless steel fibers. This effect has previously been shown by Im and Ahluwalia [1] who presented radiative heat transfer coefficients depending on the radiative properties of different fiber materials. By taking into account that the material for SiC fibers is approximately thirty times more expensive than the material for stainless steel fibers, it is obvious that further research shall be concentrated on steel fibers.

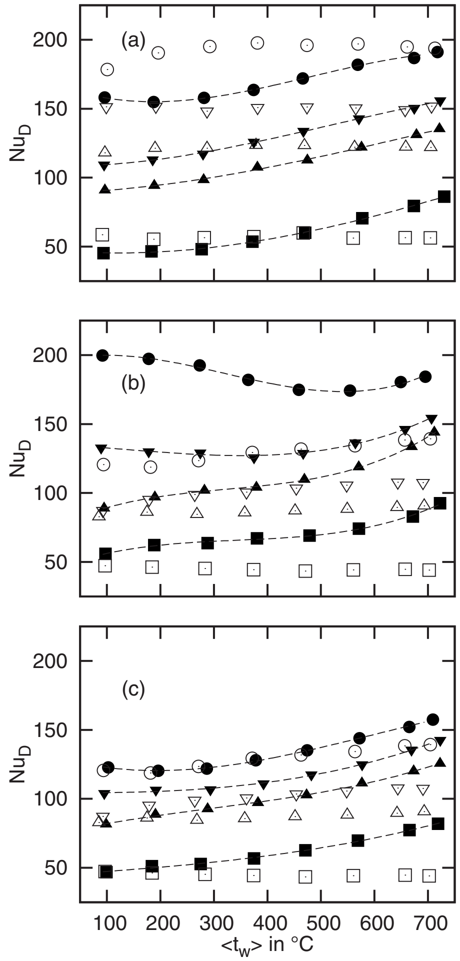

Fig. 5 Nusselt number depending on averaged wall temperature: (*a*) Short tube with SiC fibers, (*b*) long tube with SiC fibers, and (*c*) long tube with stainless steel fibers; with $\dot{m}=0.06$ kg/s (○), $\dot{m}=0.04$ kg/s (▽), $\dot{m}=0.03$ kg/s (△), and $\dot{m}=0.01$ kg/s (□). Empty symbols are used for the empty tube and filled symbols are used for the same mass flow rate in the fiber-filled tube.

4 Conclusion

Experiments were performed for investigating the influence of a fiber array insert on the heat transfer and pressure drop in an externally heated tube. Measurements in the short tube show that the heat transfer is dominated by convection in both cases, with and without fibers. Due to the fact that the fibers interfere with normal convective process, the radiative-convective heat transfer with fibers is only higher than in the empty tube from wall temperatures of 500°C upwards and for low mass flow rates. Pressure data demonstrate that the flow is strongly affected by an entry vortex at the tube inlet. By using a longer tube, a thermally and hydrodynamically developed flow could be established in the test section. The pressure drop is obviously higher than in the case without fibers but lower than expected with d'Arcy's law. Determinations of the permeabilities and characteristic length scales of the arrays—SiC and stainless steel—show that they are one order of magnitude higher than expected. This effect occurs because of nonideal traits (e.g., nonuniform fiber-to-fiber spacing, and channeling effects).

Heat transfer enhancement by radiation with fiber array inserts is clearly demonstrated. Depending on the mass flow rate and wall temperature, the heat transfer with SiC fibers is up to 100% greater than heat transfer without them. With stainless steel fibers the enhancement is only little lower. Hence, stainless steel fibers should be the material of choice for further investigations, since they are relatively cheap and additionally less brittle and easier to handle than SiC fibers. Further work should focus on developing models for calculating the pressure drop and radiative-convective heat transfer with fibers, and measuring heat transfer at even higher wall temperatures. Additionally, more detailed investigations of fluid-solid aeroelastic interactions are of interest. In summary fiber arrays show strong potential for significant augmentation of gas-phase heat transfer, and it will be exciting to see if this method will find applications in real thermal equipment.

Acknowledgment

Financial support from the EC Research Infrastructure Action under the FP6 "Structuring the European Research Area" Program, within the SUSPOWER project, is gratefully acknowledged. The authors would like to thank Mr. Gerhard Schlund and Mr. Rene Stahlschmidt for their collaboration.

Nomenclature

A = cross section in m^2
b = empiric constant
c_p = specific heat capacity at constant pressure in J/(kg K)
d = fiber diameter in m
D = inner tube diameter in m
D_h = hydraulic diameter in m
k = thermal conductivity in W/(mK)
K = permeability in m^2
l = distance between centers of fibers in m
L = length in m
$\dot{m}$ = mass flow rate in Kg/s
n = number of fibers
p = pressure in N/m^2
P = power in W
$\dot{Q}$ = heat rate in W
t = temperature in °C
u = velocity in m/s

Greek Letters

μ = dynamic viscosity in kg/(ms)
ν = kinematic viscosity in m^2/s
ϕ, Φ = general quantities
Ψ_s = fraction of solid material in porous media

Dimensionless Numbers

f = friction factor: $f = \frac{2\Delta p}{\rho \langle u \rangle^2}$
Re = Reynolds number: $\mathrm{Re} = \frac{uL_{\mathrm{ch}}}{\nu}$
Nu = Nusselt number: $\mathrm{Nu} = \frac{hL_{\mathrm{ch}}}{k}$

Subscripts

amb = ambient
ch = characteristic, generic length
conv = convective
el = electrical
f = fiber
g = gas
in = inside, inlet
loss = losses
out = outlet
rad = radiative
t = test section
w = wall

References

[1] Im, K. H., and Ahluwalia, R. K., 1994, "Radiative Enhancement of Tube-Side Heat Transfer," Int. J. Heat Mass Transfer, **37**, pp. 2635–2646.
[2] Martin, A. R., 1997, "Multiscale Modeling of Heat Transfer Enhancement With Fiber Array Inserts," Ph.D. thesis, University of Florida, Gainesville, FL.
[3] Martin, A. R., Saltiel, C., Chai, J., and Shyy, W., 1998, "Convective and Radiative Internal Heat Transfer Augmentation With Fiber Arrays," Int. J. Heat Mass Transfer, **41**, pp. 3431–3440.
[4] Chen, X., and Sutton, W. H., 2005, "Enhancement of Heat Transfer: Combined Convection and Radiation in the Entrance Region of Circular Ducts With Porous Inserts," Int. J. Heat Mass Transfer, **48**, pp. 5460–5474.
[5] Hantsch, A., 2008, "Heat Transfer Augmentation: Radiative-Convective Heat Transfer in a Tube With Fibre Array Inserts," KTH Report EGI/EKV 776.
[6] Sensortechnics GmbH, 2005, PCL Series, Miniature Temperature Compensated Low Pressure Sensors Data Sheet.
[7] Sensortechnics GmbH, 2004, HCX Series, Fully Signal Conditioned Pressure Transducer Data Sheet.
[8] Weston Aerospace Corp., 2005, 7885 Digital Pressure Module Data Sheet.
[9] Yokogawa Electrical Corp., 1998, WT110/WT130, Digital Power Meter, User's Manual, 3rd ed.
[10] Drummond, J. E., and Tahir, M. I., 1984, "Laminar Viscous Flow Through Regular Arrays of Parallel Solid Cylinders," Int. J. Multiphase Flow, **10**, pp. 515–540.
[11] Huang, H., and Ayoub, J., 2008, "Applicability of the Forchheimer Equation for Non-Darcy Flow in Porous Media," SPE J., **13**, p. 112–122.
[12] National Institute of Standards and Technology, 1994, "Guidelines for Evaluating and Expressing the Uncertainty of NIST Measurement Results," Technical Note No. 1297, Washington, DC.
[13] International Standard Organization, 2003, "Measurement of Fluid Flow by Means of Pressure Differential Devices Inserted in Circular Cross-Section Conduits Running Full," ISO-5167:2003 (E).

Transient Radiation and Conduction Heat Transfer in Glass Sheets by the Thin Layer Approximation

Georges El Hitti[1]
e-mail: georges.el_hitti@mines-paristech.fr

Maroun Nemer

Khalil El Khoury

Mines ParisTech,
Center for Energy and Process Studies (CEP),
CNRS FRE 2861,
60 Boulevard Saint-Michel,
F-75272 Paris Cedex 06, France

This paper is devoted to the simulation of 3D transient radiation and conduction heat transfer occurring inside thin glass sheets undergoing high temperature processing. The glass is considered as an absorbing, emitting, and nonscattering medium. The zonal method is used to establish the governing radiation transfer model. Direct exchange areas are calculated by the flux planes approximation. The thin layer approximation (TLA) is then introduced for increasing CPU efficiency. Three different numerical integration schemes made possible by the TLA are presented. Comparisons are made, with calculations performed using the finite volume method (FVM). The transient coupled energy equation is solved by a full implicit control volume method using the incomplete Cholesky conjugate gradient method. The heat transfer analysis of a glass sheet residing inside a hot rectangular enclosure is studied. Results obtained by the zonal method, with or without the TLA, are in close agreement with those obtained by the FVM. CPU requirements for radiative heat transfer analysis of the zonal method with TLA are, depending on the numerical integration scheme used, between 8 and 23 times smaller than those of the zonal method without TLA. The difference between the results of the different models never exceeds 4%. The zonal method with the TLA offered significant improvements in CPU time when compared with the original zonal method with similar or acceptable accuracy. [DOI: 10.1115/1.4000228]

Keywords: zonal method, finite volume method, thin layer approximation, coupled heat transfer, glass

1 Introduction

Recently, considerable effort is being invested in the study of heat transfer inside glass sheets undergoing high temperature processing such as forming for windscreen production, tempering for toughened glass production, or annealing to relieve internal stresses. The reasons behind these studies are to increase the efficiency of glass processing, which, regardless of recent advances in computer engineering, remains heavily reliant on the skills and diligence of the operator.

Solving the coupled radiative-conductive problem requires solving the radiative transfer equation (RTE), as well as the energy equation. Over the years, numerous numerical techniques were developed to provide a quantitative assessment of radiation effect. The most common ones being: the spherical harmonics method [1], the discrete ordinates method [2], the finite volume method (FVM) [3], the discrete transfer method [4], the Monte Carlo method [5], and the zonal method [6]. Recent developments in computer processing power have made it possible to apply the above methods for fairly complex applications. Once radiative heat transfer is assessed, the energy equation can be solved.

Asllanaj et al. [7] used a FVM based on a cell vertex scheme combined with a modified exponential scheme for solving the radiative transfer equation (RTE) in 2D high temperature molten glass. The transient radiation-conduction energy equation was solved using the FVM [7]. Lentes and Siedow [8] simulated radiative heat transfer in 3D glasses and glass melts using an improved diffusion approximation method, particularly adapted for nongray calculations. Siedow et al. [9] later applied the method to determine the temperature along flat glass thickness during tempering. Frattolillo et al. [10] used a FVM to perform a 3D simulation of transient radiation-conduction and convection heat transfer during the forming of flat glass sheets for automotive windscreen production. Virgone et al. [11] used a first order spherical harmonics method for the description of radiative heat transfer, and a control volume method for the discretization of the coupled radiation-conduction problem. Van der Linden [12] developed the algebraic ray tracing method for the analysis of radiative heat transfer in glass like semitransparent media.

The aim of this paper is to propose an efficient method for radiative heat transfer analysis for glass sheets undergoing forming, tempering, annealing, or any similar high temperature processing. The zonal method developed by Hottel and Cohen [13], and later expanded by Hottel and Sarofim [14] to include isotropic nongray media, is used to establish the governing radiation transfer model. One of the many advantages of the method is that solid angles are directly integrated when solving the RTE, thus eliminating false scattering and ray effect. In this method, an enclosure is decomposed into a number of isothermal volume and surface elements. Radiative heat exchange inside the enclosure is represented by total exchange areas (TEAs), which are deduced from direct exchange areas (DEAs). The simplicity of the zonal method resides in its ability to directly correlate temperature and heat flux without ever passing by the radiative intensity. Employment of the zonal method is generally restricted to applications where radiative properties are independent of temperature, thereby requiring the calculation of TEAs only once.

The flux planes approximation is used for DEA calculation. Glass is considered as an absorbing, emitting, and nonscattering

---

[1] Corresponding author.

Contributed by the Heat Transfer Division of ASME for publication in the JOURNAL OF HEAT TRANSFER. Manuscript received October 31, 2008, final manuscript received March 20, 2009; published online December 3, 2009. Assoc. Editor: Yogesh Jaluria.

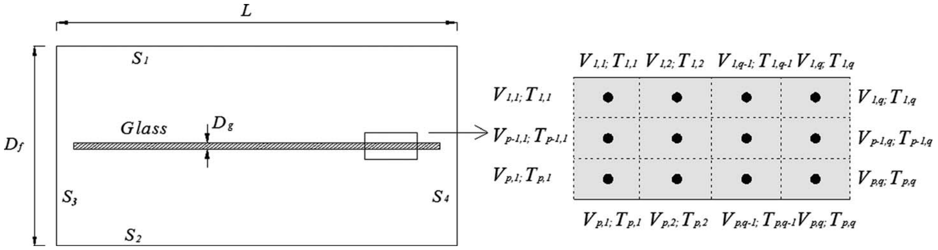

Fig. 1 Simple schematic 2D representation of a standard processing furnace: processing enclosure (left), and discrete physical model of glass (right)

medium. The thin layer approximation (TLA) is then introduced for increasing CPU efficiency. The TLA makes benefit of the extremely thin thickness of glass sheets compared with their surface area to reformulate new equations for DEA calculation. Different resolution schemes are proposed and tested for solving the new DEA equations. The different models are then used for DEA calculation and coupled radiative-conductive heat transfer analysis in a glass processing furnace. Results are compared with others obtained using FVM. The coupled energy equation is solved by a full implicit control volume method using an incomplete Cholesky conjugate gradient method (ICCG).

A drawback of the zonal method is that it is not compatible with CFD modeling. When using the zonal method in applications where fluid mechanics and convective heat transfer are not negligible, a macroscale fluid dynamics modeling, such as the pressurized zonal method, is sometimes used [15]. Macroscale fluid dynamics offer reasonable accuracy when estimating simple fluid dynamics phenomena and overall flow distribution. Nevertheless, convective heat transfer and fluid mechanics are not considered in the applications since the aim of this paper is to present the TLA method for radiative heat transfer.

2 Physical Model and Governing Equations

A simple schematic 2D representation of a standard processing furnace is presented in Fig. 1. A glass sheet of large surface area and very small thickness with respect to the furnace dimensions ($L_g/D_g \gg 1$ and $D_f/D_g \gg 1$) resides inside the hot enclosure. In such furnaces, glass sheets are heated primarily by radiation, to high temperatures ($\sim 600°\mathrm{C}$) where processing, such as forming, tempering, or annealing, takes place. The enclosure is filled with air, which is totally transparent, and therefore, does not participate in radiation.

In order to apply the control volume method for heat transfer analysis, the glass is divided into n control volumes in thickness, and m control volumes in length. Each control volume is represented by a single isothermal node of specific physical and optical characteristics. The transient energy equation in a 2D participating media for combined conduction and radiation, and absence of convection and inter heat generation, is

$$\rho c_p \frac{\partial T}{\partial t} = \frac{\partial}{\partial x}\left(k\frac{\partial T}{\partial x}\right) + \frac{\partial}{\partial y}\left(k\frac{\partial T}{\partial y}\right) - \nabla \cdot q_r \tag{1}$$

In a fully implicit discrete format, assuming all properties inside the medium are constant, the energy conservation equation for glass control volume lc, becomes

$$\begin{aligned}\Delta x_{cl}\rho_{lc}c_{p,lc}\frac{T_{lc}^{n} - T_{lc}^{n-1}}{t_n - t_{n-1}} &= \sum_{p=0}^{p=1} \frac{1}{\Delta x_{l\to l+1-2p,c}} k_{ij}^{n}(T_{l+1-2p,c}^{n} - T_{l,c}^{n}) \\ &+ \sum_{p=0}^{p=1} \frac{1}{\Delta x_{l,c\to l+1-2p}} k_{ij}^{n}(T_{l,c+1-2p}^{n} - T_{l,c}^{n}) - \phi_{lc,r}^{n}\end{aligned} \tag{2}$$

where $\phi_{ij,r}^{n}$ contains radiative heat transfer for control volume lc. Extension of Eq. (2) to 3D geometries is straightforward, and therefore, will not be presented in this paper.

A major difficulty in coupled radiation-conduction heat transfer is solving for ϕ_r^n. If a zonal method is used, TEAs are calculated prior to the resolution of the energy equation. Physically, TEAs represent the total fraction of radiative energy emitted by one element, and absorbed by another. TEAs remain unchanged, and need only be calculated once if all radiative properties are independent of temperature. $\phi_{ij,r}^{n}$ is then deduced from TEAs and Stefan–Boltzmann's law.

3 Radiative Transfer Model

3.1 Zonal Method. In the zonal method, the RTE is written in terms of irradiation and radiosity. A nonisothermal enclosure is divided into a set of discrete isothermal surface elements and volume elements. Each discrete element is assumed as having homogeneous radiosity and irradiation. The incoming heat flux or irradiation at surface element i and volume element j are given, respectively, as

$$H_i = \frac{1}{A_i}\left(\sum_{j=1}^{N} (\overline{s_i s_j} J_j) + \sum_{j=1}^{M} (\overline{s_i g_j} J_{bg,j})\right) \tag{3}$$

$$H_g = \frac{1}{4\kappa_g V_g}\left(\sum_{j=1}^{N} (\overline{g_g s_j} J_j) + \sum_{j=1}^{M} (\overline{g_g g_j} J_{bg,j})\right) \tag{4}$$

where $\overline{s_i s_j}$, $\overline{g_i s_j}$, and $\overline{g_i g_j}$ are surface-surface, volume-surface, and volume-volume DEA, respectively. The general equations for surface-surface, volume-surface, and volume-volume DEAs are, respectively

$$\overline{s_i s_j} = \int_{A_i}\int_{A_j} \frac{\tau_{ij}|\hat{n}_i \,.\, \vec{r}||\hat{n}_j \,.\, \vec{r}|}{\pi r^4} dA_i dA_j \tag{5}$$

$$\overline{g_i s_j} = \int_{V_i}\int_{A_j} \frac{\kappa_i \tau_{ij}|\hat{n}_j \,.\, \vec{r}|}{\pi r^3} dV_i dA_j \tag{6}$$

$$\overline{g_i g_j} = \int_{V_i}\int_{V_j} \frac{\kappa_i \kappa_j \tau_{ij}}{\pi r^2} dV_i dV_j \tag{7}$$

If i and j are separated by h media of different radiative properties, then τ_{ij} becomes

$$\tau_{ij} = e^{-\sum_{m=1}^{h} \kappa_m L_m} \tag{8}$$

with L_m as the distance inside the medium m of absorptivity κ_m.

According to Fig. 2, Eq. (5) can also be expressed in terms of angular integrals as

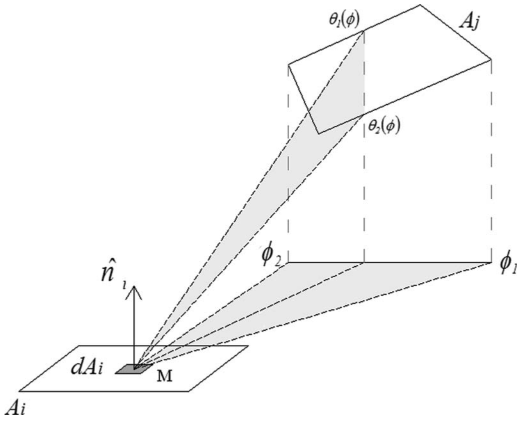

Fig. 2 Radiative exchange between two surfaces

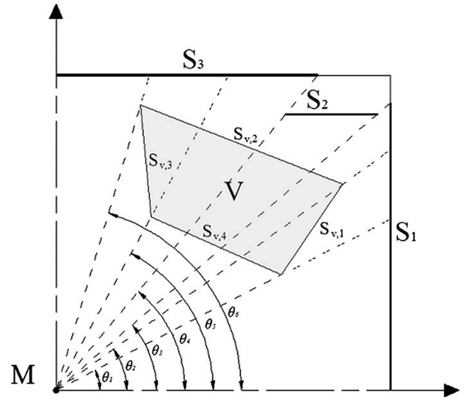

Fig. 4 Geometric example of a flux plane projection onto a quarter of a plane

$$\overline{s_i s_j} = \int_{A_i} \int_{\phi_1}^{\phi_2} \int_{\theta_1(\phi)}^{\theta_2(\phi)} \tau_{ij} \sin\theta \cos\theta d\theta d\phi dA_i \tag{9}$$

Equations (1) and (2) are applicable when the semitransparent media separating the surfaces of the enclosure have indices of refraction, very close to unity. This is practically the case for most gases. However, when a semitransparent media such as glass is present, important phenomena result from the nonunity of its refractive index. The most significant ones being reflection and refraction of radiation at its interface, as presented in Fig. 3.

Refraction causes radiation to bend when entering or leaving a glass sheet. The distance (L'_m) traversed inside a glass sheet after refraction can be deduced from Snell's law as

$$L'_m = \frac{\cos\alpha}{\sqrt{1 - \dfrac{\sin^2\alpha}{n_g^2}}} L_m \tag{10}$$

In order to compensate for multiple reflections inside glass sheets that are caused by the change in refractive indices, the trasmittance in Eq. (8) is multiplied by a factor, which takes into account multiple reflections inside the glass sheets [16]. If b glass sheets separate S_i from S_j, the modified transmittance τ' becomes

$$\tau'_{ij} = e^{-\sum_{m=1}^{h} \kappa_m L'_m} \prod_{m=1}^{h} \left(\frac{1-\rho_m}{1+\rho_m} \cdot \frac{1-\rho_m^2}{1-\tau^2\rho_m^2} \right) \approx e^{-\sum_{m=1}^{h} \kappa_m L'_m} \prod_{m=1}^{h} \left(\frac{1-\rho_m}{1+\rho_m} \right) \tag{11}$$

Equation (9) is solved according to the flux planes approximation for DEA calculation. The flux plane approximations are discussed in details by Ferrand [17], and will only be briefly repeated in this paper. In Fig. 4, the hemisphere surrounding point M of A_i is decomposed into a finite number of solid angles $\delta\omega_k(k=1,N_\Phi)$, each wedged between two quarter planes normal to A_i, and forming an angle $\delta\Phi_k$ between each other. Radiative flux leaving M in the direction of solid angle $\delta\omega_k$ is then considered to be concentrated in the bisector plane of $\delta\omega_k$. The flux planes approximation equation, for surface-surface DEA calculation, expressed in angular integration form, becomes

$$\overline{s_i s_j} = \frac{1}{N_\Phi} \int_{A_i} \sum_{k:\Phi_1 \le \Phi \le \Phi_2} \int_{\theta_{1,k}}^{\theta_{2,k}} \tau'_{ij} \sin\theta \cos\theta d\theta dA_i \tag{12}$$

where $\theta_{1,k}$ and $\theta_{2,k}$ are the limits of A_j in the direction of the bisector plane. Both integrals in Eq. (12) are solved by Gaussian quadrature.

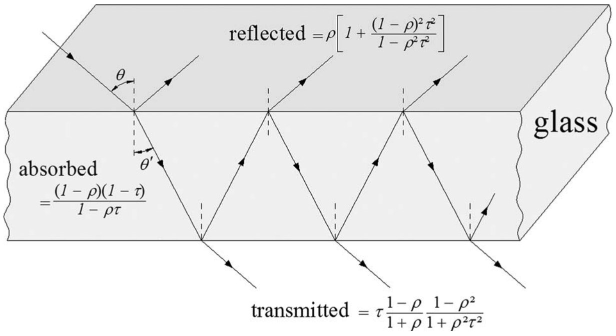

Fig. 3 Absorption, reflection, refraction, and transmission of incident radiation on a glass sheet

An example of a flux plane projection is presented in Fig. 4. S_1, S_2, and S_3 constitute the enclosure around point M in the direction of flux plane Φ_k. V is a semitransparent medium delimited by four fictive surface elements: $S_{v,1}$, $S_{v,2}$, $S_{v,3}$, and $S_{v,4}$.

Ferrand [17] then used tabulated view factors formulated by Yuen and Takara [6] as reference values for validation of the flux plans method, since the authors claim an error of no more than 1% between their tabulated values and exact solution.

Volume-surface and volume-volume DEAs are deduced by applying energy balance equations on the surface elements delimiting the volume elements [18]. By superposition, the energy balance equations for volume-surface and volume-volume DEAs are given by

$$\overline{s_i g_j} = \sum_{p:g_j \text{ delimiting surfaces}} (\overline{s_i s_{p,\text{outward}}} - \overline{s_i s_{p,\text{inward}}}) \tag{13}$$

$$\overline{g_i g_j} = \sum_{p:g_i \text{ delimiting surfaces}} (\overline{s_{p,\text{outward}} g_j} - \overline{s_{p,\text{inward}} g_j}) \tag{14}$$

DEAs between opaque surfaces and fictive surfaces delimiting discretized volume elements are calculated by Eq. (12).

Assuming all elements are gray, a net energy balance on surface element i or volume element g yields

$$Q_i = \varepsilon_i A_i E_{b,i} - \varepsilon_i \sum_{j=1}^{N} \overline{s_i s_j} J_j - \varepsilon_i \sum_{j=1}^{M} \overline{s_i g_j} J_{g,j} = \sigma \sum_{j=1}^{N} \overline{S_i S_j} (T_i^4 - T_j^4) + \sigma \sum_{j=1}^{M} \overline{S_i G_j} (T_i^4 - T_j^4) \tag{15}$$

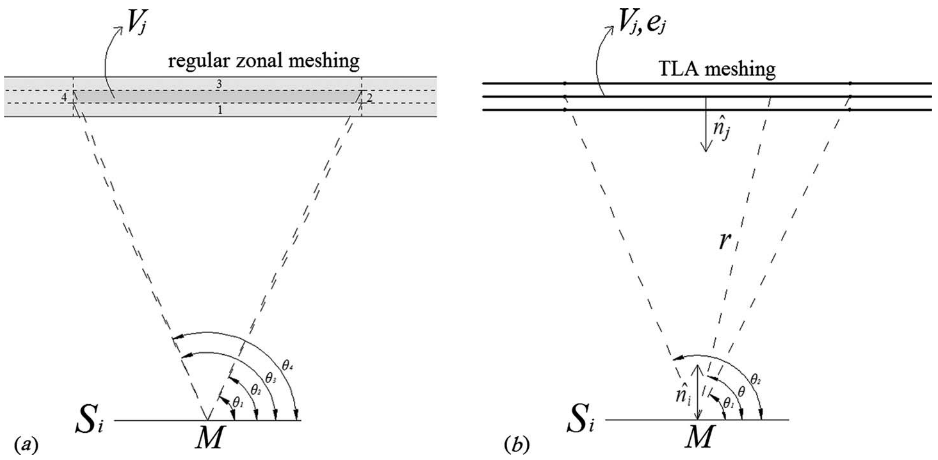

Fig. 5 DEA calculation between S_k and V_j: (a) regular meshing, and (b) ITL meshing

$$Q_g = 4\kappa_g V_g E_{b,g} - (1-\omega_g)\sum_{j=1}^{N} \overline{g_g s_j} J_j + (1-\omega_g)\sum_{j=1}^{M} \overline{g_g g_j} J_{g,j}$$
$$= \sigma\sum_{j=1}^{N} \overline{G_g S_j}(T_g^4 - T_j^4) + \sigma\sum_{j=1}^{M} \overline{G_g G_j}(T_g^4 - T_j^4) \tag{16}$$

where $\overline{s_i s_j}$, $\overline{G_i S_j}$, and $\overline{G_i G_j}$ are surface-surface, volume-surface, and volume-volume TEA, respectively. TEAs are deduced from DEAs by the plating algorithm developed by Edwards [19]. The algorithm uses a set of recursion relations that allows the transfer factors to be obtained from the view factors in N consecutive plating steps (where N is the number of reflective surfaces). The plating algorithm is easily coded, and occupies less memory space than the widely used matrix inversion techniques for calculation of total transfer factors. The plating algorithm also saves CPU time in executing parametric studies. Cai [20] generalized the algorithm for enclosures delimited by diffusive or semitransparent surfaces, and containing absorbing-emitting/nonscattering medias. The algorithm was further extended in Ref. [21] for applications containing semitransparent media with a reflective interface.

The plating algorithm considers that reflection is always diffused in nature. This is obviously not true for glass and most polished surfaces, nevertheless, in most closed enclosures lacking narrow channels, collimated irradiation, and beam channeling, it is sufficient to evaluate heat fluxes, assuming purely diffused reflectors [1].

For the processing furnace of Fig. 2, the radiative source term $\phi_{cl,r}^{n}$ for control volume cl becomes

$$\phi_{cl,r} = Q_{cl,r} = \sigma\sum_{s=1}^{N} \overline{G_{cl} S_s}(T_{cl}^4 - T_s^4) + \sigma\sum_{p=1}^{M} \overline{G_{cl} G_p}(T_{cl}^4 - T_p^4) \tag{17}$$

3.2 Thin Layer Approximation. Figure 5 displays a surface element S_i, exchanging heat by radiation with a semitransparent volume element V_j. Applying Eqs. (12) and (13) for calculating the DEA between S_i and V_j in the flux plane of Fig. 5(a) yields

$$(\overline{s_i g_j})_{M,\phi_k} = \int_{\theta_{1,k}}^{\theta_{4,k}} \tau'_{ij_1} \sin\theta \cos\theta d\theta - \int_{\theta_{1,k}}^{\theta_{2,k}} \tau'_{ij_2} \sin\theta \cos\theta d\theta$$
$$- \int_{\theta_{2,k}}^{\theta_{3,k}} \tau'_{ij_3} \sin\theta \cos\theta d\theta - \int_{\theta_{3,k}}^{\theta_{4,k}} \tau'_{ij_4} \sin\theta \cos\theta d\theta \tag{18}$$

Volume elements generated for zonal discretization of glass sheets are usually parallelogramic shaped, with very small thickness to length ratio. This type of discretization is adopted for better representation of temperature variations inside glass sheets while keeping the number of volume elements to a minimum. Consequently, $\theta_{1,k} \approx \theta_{2,k}$ and $\theta_{2,k} \approx \theta_{3,k}$, and therefore, the second and fourth integrals on the right side of Eq. (18), become insignificant when compared with the other terms of the equation, and can be neglected.

The TLA takes advantage of this particularity of zonal glass sheets meshing, in order to propose a new geometric representation of glass volume elements for DEA calculation. Instead of using parallelogramic-shaped volume elements for zonal glass sheets discretization, the TLA utilizes absorbing, emitting, and nonscattering isothermal semitransparent surfaces, each having distinctive radiative properties with a designated thickness. Figure 5(b) displays the TLA of a fragment of a glass sheet. By this approach, a glass mesh becomes represented by a single semitransparent surface, instead of six fictive surfaces delimiting a parallelogramic-shaped volume. The new equation for calculating the DEA between S_i and V_j becomes

$$(\overline{s_i g_j})_{M,\phi_k} = \int_{\theta_{1,k}}^{\theta_{2,k}} \tau'_{ij} \xi_j \sin\theta \cos\theta d\theta \tag{19}$$

where ξ_j, the equivalent emittance of semitransparent surface j, is defined as

$$\xi_j = 1 - \tau_j \tag{20}$$

with

$$\tau_j = e^{-\sum_{m=1}^{h} \kappa_m L'_m} = e^{-\kappa_j e_j / |\hat{n}_j . \hat{r}(\theta)| \cdot \cos\alpha / \sqrt{1 - \sin^2 \alpha / n_g^2}} \tag{21}$$

In the regular zonal method, the plating algorithm is alone, capable of treating multiple reflections inside glass sheets. However, when the TLA is used, the equivalent emittance must be multiplied by a correction factor [16] that accounts for multiple refections inside glass. Consequently, Eq. (20) becomes

$$\xi_j = \frac{(1-\rho_j)(1-\tau_j)}{1-\rho_j \tau_j} \tag{22}$$

Solving Eq. (19) is much simpler than solving Eq. (18), and involves a fewer number of numerical integrations. Another advantage of the TLA is that errors caused by numerical roundoffs during calculation of distances traversed in very thin glass volume elements are reduced by direct deduction of those distances from the designated thickness of the corresponding semitransparent surfaces.

Using the same reasoning as before, the new formulation for volume-volume DEAs becomes

$$(\overline{g_i g_j})_{M,\phi_k} = \int_{\theta_{1,k}}^{\theta_{2,k}} \tau'_{ij}\xi_i\xi_j \sin\theta\cos\theta d\theta \tag{23}$$

Three different resolution schemes are proposed for solving Eqs. (18) and (20):

CAL 1: Eqs. (19) and (23) are solved using Gauss quadratures.

CAL 2: τ and ξ of Eq. (22) are considered constant, and global mean values are calculated beforehand for each semitransparent surface. A global transmittance (τ_g) and global emittance (ξ_g) are defined for each semitransparent surface. Incident radiative flux coming from direction (Φ,θ), around an elementary solid angle $(d^2\omega)$ of a semitransparent surface j, is given by

$$d^2q^i = q^i\frac{d^2\omega}{2\pi} = \frac{q^i}{2\pi}\sin\theta d\theta d\phi \tag{24}$$

where q^i, the total incident heat flux onto semitransparent surface j, is considered to be isotropic.

Combining Eqs. (11) and (24), the transmitted flux becomes

$$d^2q^t = d^2q^i\tau_j = \frac{q^i}{2\pi}e^{-\sum_{m=1}^{h}\kappa_m L'_m}\prod_{m=1}^{h}\left(\frac{1-\rho_m}{1+\rho_m}\right)\sin\theta d\theta d\phi \tag{25}$$

The global transmittance τ_g for semitransparent surface j is then obtained by integrating Eq. (25) over the entire hemisphere surrounding it, and then dividing it by the total incident heat flux q^i as

$$\tau_{g,j} = \frac{q^t}{q^i} = \frac{1}{2\pi}\int_0^{2\pi}\int_0^{\pi/2}\tau_j\sin\theta d\theta d\phi = \int_0^{\pi/2}\tau_j\sin\theta d\theta \tag{26}$$

The global emittance for semitransparent surface j is then directly obtained by

$$\xi_{g,j} = \frac{(1-\rho_{g,j})(1-\tau_{g,j})}{1-\rho_{g,j}\tau_{g,j}} \tag{27}$$

In Eqs. (19) and (23), ξ is replaced by ξ_g, which is not a function of θ, and therefore, can be moved to the outside of the integrals. In addition, in an enclosure containing only semitransparent or opaque surfaces, τ_{ij} can now be expresses as the product of the global transmittance of the media separating element i and element j

$$\tau'_{ij} = \prod_{m=1}^{h}\tau_{g,h}\prod_{l=1}^{b}\left(\frac{1-\rho_l}{1+\rho_l}\right) \tag{28}$$

Combining Eqs. (19), (23), and (28), $(\overline{s_i g_j})_{M,\phi_k}$ and $(\overline{g_i g_j})_{M,\phi_k}$ finally become

$$(\overline{s_i g_j})_{M,\phi_k} = \tau'_{ij}\xi_{g,j}\int_{\theta_{1,k}}^{\theta_{2,k}}\sin\theta\cos\theta d\theta = \frac{\tau'_{ij}\xi_{g,j}}{2}\int_{\theta_{1,k}}^{\theta_{2,k}}d(\sin^2\theta)$$
$$= \frac{\tau'_{ij}\xi_{g,j}}{2}(\sin^2\theta_{2,k} - \sin^2\theta_{1,k}) \tag{29}$$

$$(\overline{g_i g_j})_{M,\phi_k} = \tau'_{ij}\xi_{g,i}\xi_{g,j}\int_{\theta_{1,k}}^{\theta_{2,k}}\sin\theta\cos\theta d\theta = \frac{\tau'_{ij}\xi_{g,i}\xi_{g,j}}{2}\int_{\theta_{1},k}^{\theta_{2,k}}d(\sin^2\theta)$$
$$= \frac{\tau'_{ij}\xi_{g,i}\xi_{g,j}}{2}(\sin^2\theta_{2,k} - \sin^2\theta_{1,k}) \tag{30}$$

Equations (29) and (30) are then calculated analytically for each flux plane without the need for any numerical integrations.

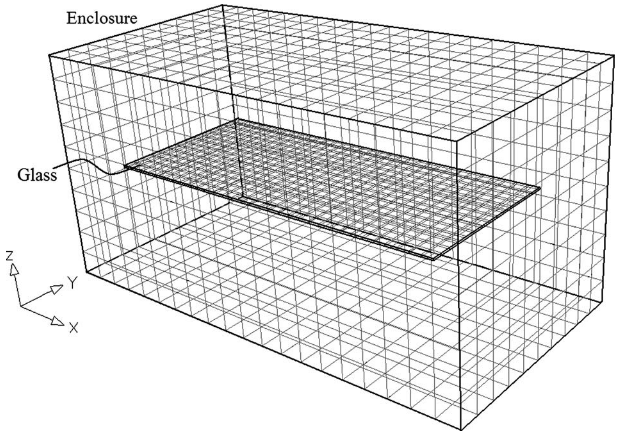

Fig. 6 Glass processing furnace analysis model

CAL 3: is very similar to CAL 2, except that $\xi_{g,j}$ in Eqs. (29) and (30) is replaced by

$$(\xi_j)_{M,\phi_k} = 1 - \frac{1}{2}\left(\frac{1-\tau_{j,\theta_1}}{1-\rho_j\tau_{j,\theta_1}} + \frac{1-\tau_{j,\theta_2}}{1-\rho_j\tau_{j,\theta_2}}\right) \tag{31}$$

For all three cases (CAL 1, CAL 2, and CAL 3), the reflectivity used for the plating algorithm of a semitransparent surface j is calculated by integrating the reflectivity of a thin glass sheet over the entire hemisphere

$$\rho_{\text{average}} = \int_0^{\pi/2}\rho_j\left(1 + \frac{(1-\rho_j^2)\tau_j^2}{1-\rho_j^2\tau_j^2}\right)\sin\theta d\theta \tag{32}$$

4 Results and Analysis

4.1 Radiative Transfer in a Glass Processing Furnace. The present methods for radiative heat transfer analysis are first applied to calculate the radiative heat transfer of a flat rectangular glass sheet ($L=0.8$ m, $W=0.35$ m, $H=0.004$ m) residing inside a 3D enclosure ($1\times0.5\times0.5$ m^3), as shown in Fig. 6. The medium surrounding the glass sheet is air, which is totally transparent and does not participate in radiation. The inner surfaces of the enclosure are black and cold (300 K), except for its upper part, which is black and at a constant temperature (T_{Hot}) of 1500 K. The absorption coefficient of glass is set at 500 m^{-1}. Glass is considered having a refractive index equal to 1. The zonal model includes 1000 surface elements for the enclosure, and 1344 volume elements delimited by 9236 fictive surface elements for the glass. The glass sheet is meshed 32 times in length (x-axis), 14 times in width (y-axis), and 3 times in thickness (z-axis). For the TLA, the 1344 glass volume elements are replaced by 1344 semitransparent surfaces. Throughout the rest of the article, the regular zonal analysis model designates using the flux planes approximation without TLA.

Results obtained using the different radiation calculation methods presented in this paper are compared with others obtained using the FVM. The FVM model is composed of 764,052 tetrahedral or hexahedral elements and 179,047 nodes, of which 23,142 hexahedrons and 31,624 nodes are for glass meshing. Most of the elements created for the FVM analysis model are for meshing the transparent atmosphere inside the enclosure. An angular grid of 20×8 discrete directions (20 azimuthal directions, and 8 polar directions) is used. All calculations were performed on a 2.00 GHz personal computer.

Figure 7 shows the computed steady state dimensionless temperatures and heat flux divergence across the glass sheet for the various numerical models used. Steady state results are obtained in the absence of conduction. Furthermore, convective heat trans-

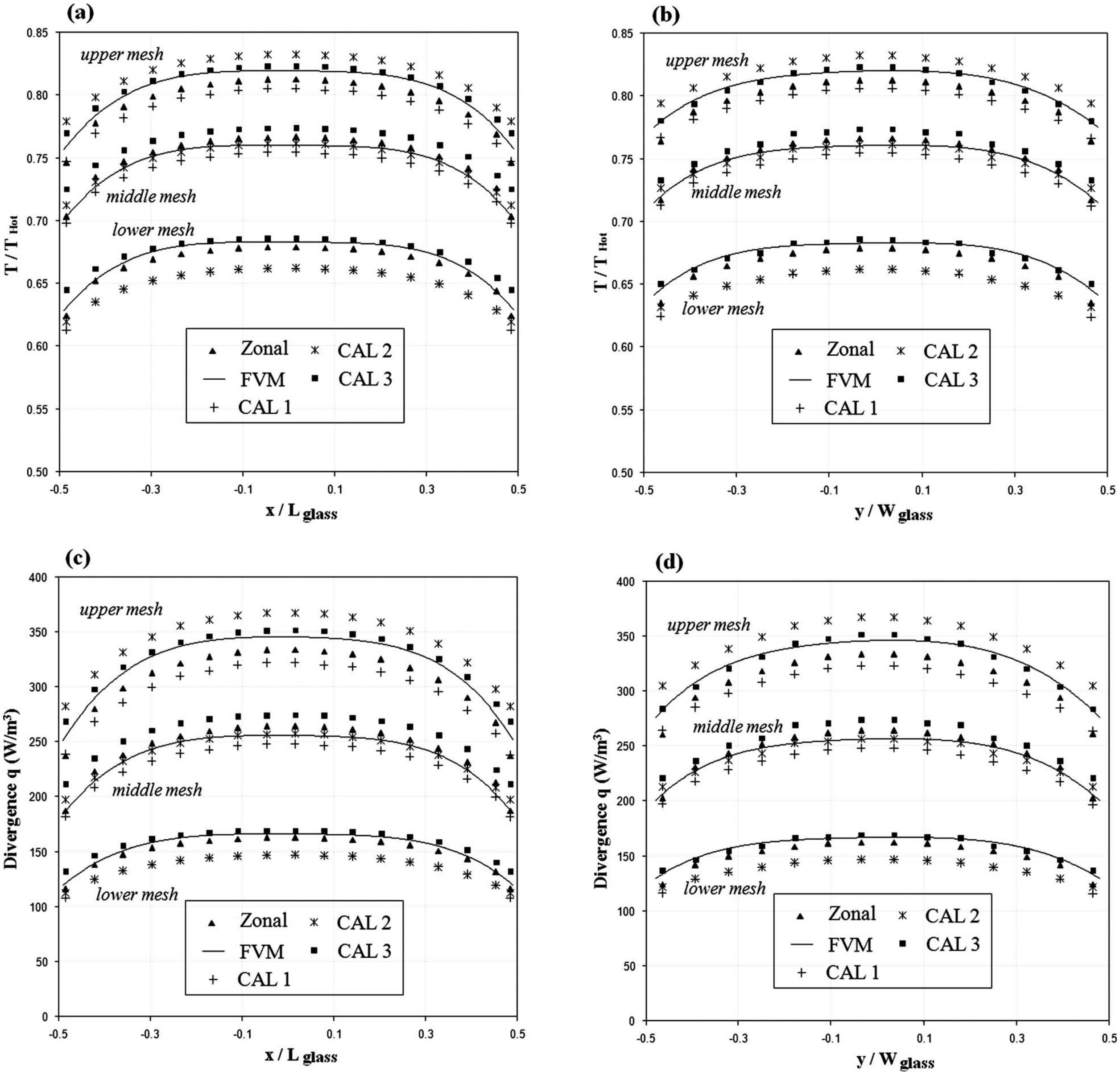

Fig. 7 Comparisons for steady state calculation: (*a*) glass dimensionless temperature along centerline *x*, (*b*) glass dimensionless temperature along centerline *y*, (*c*) heat flux divergence along centerline *x*, and (*d*) heat flux divergence along centerline *y*

fer, as well as fluid mechanics, are not considered since the purpose of the example is to highlight the TLA method for radiative heat transfer. Figure 7, demonstrates that for the application under consideration, all the models used yield very similar results. The difference between the results of all the models never exceeds 4% for the dimensionless steady state temperature. As expected, the glass temperature across the *z*-axis varies considerably. The glass upper mesh layer, which is in direct exposure to the hot surface, has a much higher temperature than the other two mesh layers.

The CPU time for calculation of the glass processing furnace are presented in Table 1. The steady state temperatures obtained by the FVM model are used as the reference values for error

Table 1 CPU time and errors for a glass processing furnace simulation—steady state example

	Zonal	TLA-CAL 1	TLA-CAL 2	TLA-CAL 3
	CPU time (s)			
DEA	1445.2	140.1	64.8	93.6
Steady state calculation	9.2	9.4	9.3	9.4
Total steady state	1454.4	149.5	74.1	103
Average error (%)	0.91	3.11	1.64	0.66

Table 2 CPU time and errors for a glass processing furnace simulation—transient example

	Zonal	TLA-CAL 1	TLA-CAL 2	TLA-CAL 3
	CPU time (s)			
DEA	247.3	31.7	13.2	16.2
Transient simulation	3.3	2.1	2.1	2.1
Average error (%)	0.78	1.13	1.76	1.54

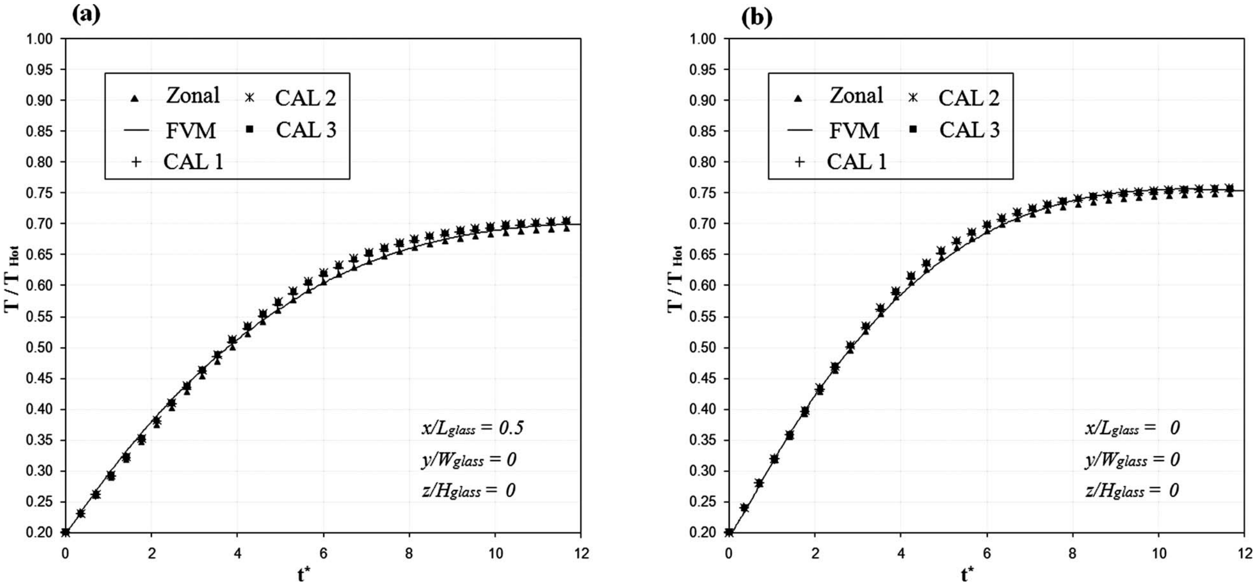

Fig. 8 Dimensionless glass temperature as a function of dimensionless time: (*a*) $x/W_{glass}=0.5$, $y/H_{glass}=0$, and $z/L_{glass}=0$; (*b*) $x/W_{glass}=0$, $y/H_{glass}=0$, and $z/L_{glass}=0$

estimation. Without the TLA, the CPU time required for DEA calculation using the flux planes approximation is 1445 s. It should be noted that CPU time for DEA calculations by all three models of the TLA are remarkably faster than that of the flux planes approximation. CPU time for DEA calculation is divided by a factor 10 with the CAL 1 model, 23 with the CAL 2 model, and 15 with the CAL 3 model. Both CAL 2 and CAL 3 do not include any numerical quadrature, and are therefore much faster than the other models. CAL 2 is the least demanding model for DEA calculation, nevertheless, the results obtained using CAL 2 are similar to those obtained by the other models. The maximum difference between CAL 1 and the FVM never exceeds 3.7%. It is expected that the total CPU time reduction can be more significant if more elements are employed for the simulation.

4.2 Transient Coupled Radiation-Conduction Heat Transfer. The same model of Fig. 6 is used for transient radiation and conduction heat transfer analysis. However, this time, the glass sheet is meshed only once in thickness (z-axis). The zonal model now includes 3676 fictive surfaces for the glass, while the TLA-zonal model includes 448 semitransparent surfaces. The refraction index of glass is 1.5, while its reflectivity is considered isotropic and equal to 7%. The inner surface of the enclosure is black and cold (300 K), except for its upper part, which is black and at a constant temperature (T_{Hot}) of 1500 K. Initially, the glass sheet is at 300 K. A dimensionless time parameter ($t^* = \kappa^2 \cdot \alpha \cdot t$, where α is the thermal diffusivity) is defined for calculation. A dimensionless time step of $\Delta t^* = 0.03$ is used throughout calculation.

A summary of the calculation is presented in Table 2. The transient dimensionless temperatures of the glass obtained by the different numerical models are shown in Fig. 8. Figure 8 demonstrates that all five models yield very close results throughout the simulation. When compared with the zonal method, the CPU time for DEA calculation is divided by a factor 8 with the CAL 1 model, 19 with the CAL 2 model, and 15 with the CAL 3 model.

5 Conclusions

The TLA was introduced in order to reduce the CPU time associated with the DEA calculation for radiative-conductive heat transfer analysis for high temperature processing furnaces. Three different resolution schemes, made possible by the TLA, were proposed.

The TLA was then applied for the radiative heat transfer of a glass processing furnace. The coupled energy equation was solved by a full implicit control volume method using the ICCG method. Steady state and transient results were compared with those obtained by the popular FVM, and a regular zonal method employing the flux planes approximation for DEA calculation. The TLA reduced the CPU time for the DEA calculation for the glass processing furnace by 87–96% when compared with the regular zonal method.

Several directions to improve this model are currently underway: Anisotropic scattering and specular reflection represent important phenomena that should be included in the model for a more compete analysis. In addition, a wide band model will be included for the nongray radiative properties of glass. Thereafter, a main endeavor to go further would be to use the model for an actual glass processing furnace, and compare the numerical approach to experimental results.

Nomenclature

A = area (m^2)
c_p = heat capacity (J/kg K)
D_f = height of furnaces (m)
D_g = thickness of glass (m)
e = designated thickness of a semitransparent surface (m)
E_b = blackbody emissive power ($\mathrm{W/m}^2$)
$\overline{g_i g_j}$ = volume-volume direct exchange area (m^2)
$\overline{G_i G_j}$ = volume-volume total exchange area (m^2)
H = irradiation ($\mathrm{W/m}^2$)
J = radiosity ($\mathrm{W/m}^2$)
k = thermal conductivity (W/m K)
L = length of furnace (m)
L_m = distance traversed in medium (m)
M = total number of volume elements
N = total number of surface elements
N_Φ = number of flux planes
q = heat flux ($\mathrm{W/m}^2$)
Q = heat rate (W)
r = distance between two differential elements (m)
S = surface area (m^2)
$\overline{s_i s_j}$ = surface-surface direct exchange area (m^2)

$\overline{S_iS_j}$ = surface-surface total exchange area (m^2)
$\overline{s_ig_j}$ = surface-volume direct exchange area (m^2)
$\overline{S_iG_j}$ = surface-volume total exchange area (m^2)
t^* = dimensionless time
T = temperature (K)
V = volume (m^3)
Δx = spatial discretization step (m)
Δt = dimensionless time step
α = angular variable (rad)
α = thermal diffusivity (m^2/s)
ε = emissivity
ξ = equivalent emittance defined in Eq. (17)
Φ = angular variable (rad)
κ = absorption coefficient (m^{-1})
θ = angular variable (rad)
ρ = density (kg/m^3)
ρ = reflectivity
τ = transmittivity
τ' = modified transmittivity
ω = solid angle (sr)
ω_g = scattering albedo

Subscripts

c, l, p, and q = element index

Superscripts

i = incident
t = transmitted
n = time step number

References

[1] Modest, M. F., 2003, *Radiative Heat Transfer*, 2nd ed., Academic, New York, Chaps. 6 and 15.
[2] Fiveland, W. A., 1987, "Discrete-Ordinates Method for Radiative Heat Transfer in Isotropically and Anisotropically Scattering Media," ASME J. Heat Transfer, **109**(3), pp. 809–812.
[3] Raithby, G. D., 1999, "Discussion of the Finite-Volume Method for Radiation, and Its Application Using 3-D Unstructured Meshed," Numer. Heat Transfer, Part B, **35**(4), pp. 389–405.
[4] Versteeg, H. K., Henson, J. C., and Malalaserka, W., 2003, "An Adaptive Angular-Quadrature for the Discrete Transfer Method Based on Error Estimation," ASME J. Heat Transfer, **125**(2), pp. 301–311.
[5] Nisipeanu, E., and Jones, P. D., 2003, "Monte Carlo Simulation of Radiative Heat Transfer in Coarse Fibrous Media," ASME J. Heat Transfer, **125**(4), pp. 748–752.
[6] Yuen, W. W., and Takara, E. E., 1997, "The Zonal Method: A Practical Solution Method for Radiative Transfer in Non-Isothermal Inhomogeneous Media," Annu. Rev. Heat Transfer, **8**, pp. 153–215.
[7] Asllanaj, F., Feldheim, V., and Lybaert, P., 2007, "Solution of Radiative Heat Transfer in 2-D Geometries by a Modified Finite Volume Method Based on a Cell Vertex Scheme Using Unstructured Triangular Meshes," Numer. Heat Transfer, Part B, **51**(2), pp. 97–119.
[8] Lentes, F. T., and Siedow, N., 1999, "Three-Dimensional Radiative Heat Transfer in Glass Cooling Processes," Glass Sci. Technol., **72**(6), pp. 188–196.
[9] Siedow, N., Crosan, T., Lochegnies, D., and Romero, E., 2005, "Application of a New Method for Radiative Heat Transfer to Flat Glass Tempering," J. Am. Ceram. Soc., **88**(8), pp. 2181–2187.
[10] Buonanno, G., Dell'Isola, M., Frattolillo, A., and Giovinco, G., 2005, "Thermal Analysis of a Glass Bending Furnace," Appl. Therm. Eng., **25**, pp. 2108–2121.
[11] Virgone, J., Depecker, P., Meyer, M., and Fredholm, A., 1996, "Modélisation Thermique de L'opération de Formage à Chaud de Feuilles de Verre," Rev. Gen. Therm., **35**(410), pp. 125–140.
[12] Van der Liden, B., 2002, "Radiative Heat Transfer in Glass: The Algebraic Ray Tracing Method," Ph.D. thesis, Eindhoven University of Technology, Eindhoven.
[13] Hottel, H. C., and Cohen, E. S., 1958, "Radiant Heat Exchange in a Gas Filled Enclosure: Allowance for Nonuniformity of Gas Temperature," AIChE J., **4**, pp. 3–14.
[14] Hottel, H. C., and Sarofim, A. F., 1967, *Radiative Transfer*, McGraw-Hill, New York.
[15] Haghighat, F., Li, Y., and Megri, A. C., 2001, "Development and Validation of a Zonal Model—POMA," Build. Environ., **36**, pp. 1039–1047.
[16] Siegel, R., and Howell, J., 2002, *Thermal Radiation Heat Transfer*, 4th ed., Taylor & Francis, New York, Chap. 18.
[17] Ferrand, L., 2003, "Modélisation et Expérimentation des Fours de Réchauffage Sidérurgiques Equipés de Brûleurs Régénératifs à Oxydation sans Flamme," Ph.D. thesis, Ecole de Mines de Paris, Paris, France.
[18] Emery, A. F., Johansson, O., and Abrous, A., 1987, "Radiation Heat Transfer Shape Factors for Combustion Systems," Fundamentals and Applications of Radiation Heat Transfer, **72**, pp. 119–126.
[19] Edwards, D. K., 1986, "The Plating Algorithm for Radiation Script-F Transfer Factor," ASME J. Heat Transfer, **108**(1), pp. 237–238.
[20] Cai, W., and El Khoury, K., 1996, "Radiative Heat Transfer Model in Industrial Enclosures by Ray-Tracing," *Proceedings of the Fourth International Symposium on Heat Transfer*, Beijing, China.
[21] Hitti, E. L., Nemer, G., Khoury, M., El, K., and Clodic, D., 2007, "Modified Zonal Method for Thin Solid Semi-Transparent Media With Reflective Boundary," *Proceedings of the ASME-JSME Heat Transfer Conference*, Vancouver.

Atsushi Sakurai
Department of Mechanical and Production Engineering,
Niigata University,
Ikarashi 2-nocho 8050,
Niigata 950-2181, Japan
e-mail: sakurai@eng.niigata-u.ac.jp

Shigenao Maruyama
Institute of Fluid Science,
Tohoku University,
Katahira 2-1-1,
Sendai 980-8577, Japan
e-mail: maruyama@ifs.tohoku.ac.jp

Koji Matsubara
e-mail: matsu@eng.niigata-u.ac.jp

Takahiro Miura
e-mail: f07b100f@mail.cc.niigata-u.ac.jp

Department of Mechanical and Production Engineering,
Niigata University,
Ikarashi 2-nocho 8050,
Niigata 950-2181, Japan

Masud Behnia
Dean of Graduate Studies,
University of Sydney,
Sydney, New South Wales, 2006, Australia
e-mail: m.behnia@usyd.edu.au

An Efficient Method for Radiative Heat Transfer Applied to a Turbulent Channel Flow

The purpose of this paper is to consider a possibility of the independent column approximation for solving the radiative heat fluxes in a 3D turbulent channel flow. This simulation method is the simplest extension of the plane-parallel radiative heat transfer. The test case of the temperature profile was obtained from the direct numerical simulation. We demonstrate the comparison between the 3D radiative transfer simulation and the independent column approximation with an inhomogeneous temperature field and optical properties. The above mentioned results show the trivial discrepancies between the 3D simulation and the independent column approximation. The required processing time for the independent column approximation is much faster than the 3D radiative transfer simulation due to the simple algorithm. Although the independent column simulation is restricted to simple configurations such as channel flow in this paper, wide application areas are expected due to the computational efficiency. [DOI: 10.1115/1.4000240]

Keywords: radiative heat transfer, independent column approximation, turbulent channel flow

1 Introduction

The interaction between the radiative heat transfer and the turbulent fluid flow is of interest in various engineering fields. In particular, the combined heat transfer within an enclosure composed of participating media plays a key role for combustion engineering, fire safety science, and many other applications [1,2]. In large-scale phenomena such as combustion in a gas turbine or smoke and fire movement in a building, turbulent flow and radiative heat transfer significantly influence the temperature field, the flow pattern, and hence, the chemical reactions. The simulations at high temperature processes require an ability to predict the thermal radiation field, otherwise inaccurate predictions are unavoidable.

In order to predict these phenomena, a large number of numerical and experimental studies have been conducted for many years [3–8]. Song and Viskanta [9] pointed out the importance of the turbulence/radiation interaction (TRI). Li and Modest [10] showed the importance of the TRI in turbulent diffusion jet flames. Tesse et al. [11] have performed the Monte Carlo modeling for radiation in a turbulent sooty flame. Coupled radiation and turbulent multiphase flow in an aluminized solid propellant rocket have been conducted to investigate effects of particles of temperature fluctuations with the Lagrangian approach [12]. The effect of radiative heat transfer also becomes important when it is combined with natural convection. Fusegi and Farouk [13] have investigated laminar and turbulent natural convection-radiation heat transfer in an enclosure composed of a participating medium. Yucel et al. [14] have studied the phenomena in a square cavity. Dehghan and Behnia [15] have studied the combined natural convection, conduction, and radiation in a discretely heated open cavity.

Direct numerical simulation (DNS) in a three-dimensional (3D) turbulent channel flow is one of the basic subjects in heat transfer researches [16–18]. Detailed turbulent flow structure and/or heat transfer mechanisms have been investigated to provide guidance for model development such as electronics cooling, heat exchangers, and atmospheric heat diffusion. Accurate descriptions of turbulence by themselves are complex. This has often resulted in the neglect of radiative heat transfer in turbulent fluid flow to avoid the additional complexity of solving the radiative transfer equation (RTE).

The nonlinear dependence of the radiative heat transfer on temperature coupled with the fluctuations in temperature tends to enhance radiative transfer. Several researchers have reported the large amount of enhancement from the TRI effect. Wu et al. [19] was the first to study the TRI for an idealized turbulent premixed flame using the DNS coupled with a photon Monte Carlo method for the solution of the RTE. The DNS coupled with a photon Monte Carlo method is used to isolate and quantify the TRI effects. Generally, these combined numerical simulations are computationally quite expensive.

The purpose of this paper is to consider a possibility of the independent column approximation (ICA) for solving the radiative heat fluxes in a 3D turbulent channel flow. The ICA is the

---

Contributed by the Heat Transfer Division of ASME for publication in the Journal of Heat Transfer. Manuscript received December 15, 2008; final manuscript received April 1, 2009; published online December 9, 2009. Assoc. Editor: Yogesh Jaluria.

simplest extension of the plane-parallel radiative heat transfer. It ignores the net horizontal photon transport, but includes horizontal inhomogeneities in scalar parameters. This approach has originated at remote sensing applications and atmospheric sciences [20,21]. Although the ICA ignores 3D radiative effects, the algorithm is quite simple; therefore, it is feasible to considerably decrease computational costs and to apply for practical problems. The plan of this paper is as follows. Section 2 describes the numerical methods of the 3D and the ICA radiative transfer models. Section 3 shows the physical modeling of a 3D turbulent channel flow. Section 4 discusses the results of a radiative transfer simulation using the 3D simulation and the ICA. Finally Sec. 5 summarizes the conclusions derived from this paper.

2 Numerical Methods

To directly ascertain the 3D radiative effects, the model can be run in the 3D simulation and the ICA [20]. Secs. 2.1 and 2.2 explain the radiative heat transfer models. Sec. 2.1 describes the 3D radiative transfer model, and the description in Sec. 2.2 is the ICA.

2.1 3D Radiative Transfer Model. In the present study, the discrete ordinates radiation element method (DOREM) is used for representing the 3D radiation field. The detailed formulation of the DOREM is available in Ref. [22]. The radiation element method was originally developed by Maruyama and Aihara [23]. The method can be readily applied to the complex 3D systems with unstructured mesh elements, which contain specular surfaces, diffuse surfaces, nongray participating gases, and anisotropic scattering media [24–26]. Though the method is suitable for such applications, there was a need to improve the efficiency for applying it to large-scale phenomena. The DOREM has been developed to avoid the computational loads in computing with the original radiation element method. Here, the simple formulation of the DOREM is described as follows.

In the DOREM, the computational space is discretized using numerous radiation elements. Also the following assumptions are introduced to simplify the problem.

(1) Each radiation element is at a constant uniform temperature. The refractive index and the heat generation rate per unit volume are also constant and are uniform over the radiation element.
(2) Radiative intensities in a radiation element are constant for each discrete ordinate independent of its location in the element.

With these assumptions, the RTE can be solved as follows. If the source function is known or assumed to be known, the radiative intensity can be formally integrated from a point $s'=0$ at the wall to point $s'=s$ inside the medium, so that it can be expressed as

$$I_{\mathrm{in},\lambda}(\boldsymbol{r}_s,\hat{\boldsymbol{s}}) = I_{\mathrm{bw},\lambda}\exp\left(-\int_0^s \beta_\lambda ds'\right) + \int_0^s S_\lambda(\boldsymbol{r},\hat{\boldsymbol{s}})\exp\left(-\int_{s'}^s \beta_\lambda ds''\right)\beta_\lambda ds' \qquad (1)$$

where $I_{\mathrm{bw},\lambda}$ is the intensity emitted into the medium from the boundary wall, $I_{\mathrm{in},\lambda}$ is the incoming intensity to the element i, $\boldsymbol{r}_s$ is the position vector of the entering point on the surface of the radiation element, and S_λ is the spectral radiative source function. The backward ray tracing method is used to calculate Eq. (1). Normally, the rays are traced backward from the surface of the element i to the boundary. Equation (1) has consistency even though a ray is traced near the edge of the element due to the assumptions that the radiative intensity and the source function are constant. When a ray hits the boundary, the integration of intensity from the element i to the boundary is completed.

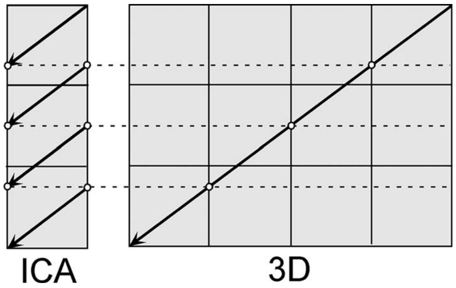

Fig. 1 The schematic diagram demonstrating the mechanisms for the 3D simulation and the ICA is described. Gray squares represent participating media elements. Arrows represent photon trajectory. Dashed line shows the effect of the periodic horizontal boundary for ICA.

The radiative intensity and the source function are constant in the element, and thus the outgoing radiative intensity $I_{\mathrm{out},\lambda}$ from the element i is defined as [22]

$$I_{\mathrm{out},\lambda}(\hat{\boldsymbol{s}}) = I_{\mathrm{in},\lambda}(\boldsymbol{r}_s,\hat{\boldsymbol{s}})\exp(-\beta_\lambda\overline{s}) + S_\lambda(\boldsymbol{r},\hat{\boldsymbol{s}})[1-\exp(-\beta_\lambda\overline{s})] \qquad (2)$$

The averaged thickness $\overline{s}\equiv V/A(\hat{\boldsymbol{s}})$ of the radiation element in the direction $\hat{\boldsymbol{s}}$ is introduced, in which V and A are the volume of the element and the projected cross section of the element from the direction $\hat{\boldsymbol{s}}$, respectively. The radiative intensity I_λ can be obtained by the geometric mean of incoming and outgoing radiative intensities.

The DOREM solves the RTE in each element and integrates radiative intensities along discrete ordinates. The concept of integrated radiative intensities from the surface of a certain radiation element to walls is basically similar to the discrete transfer method [27]. However, the DOREM has to first calculate the effective radiation area of each radiation element, then incoming radiative intensities to the radiation element are integrated. The DOREM focuses on the radiation element, resulting in the procedure that is appropriate to include the anisotropic scattering phase function and to predict the divergence of the radiative heat flux accurately.

Once the intensities in the element have been determined, the divergence of the radiative heat flux can be found as

$$q_x = \int_0^\infty \left[\beta_\lambda(1-\omega_\lambda)\left(4\pi I_{b,\lambda}(\boldsymbol{r}_i) - \sum_{l=1}^{n} I_\lambda(\boldsymbol{r}_i,\hat{\boldsymbol{s}}_l)W_l\right)\right]d\lambda \qquad (3)$$

where $\boldsymbol{r}_i$ is the barycentric vector of the radiation element i and W_l is the angular weight. The DOREM algorithm is stable and fast. The method can implement a full-spectrum radiative heat transfer analysis using nongray gas models. Also, the DOREM code is feasible to deal with multidimensional problems. The ICA algorithm described in Sec. 2.2 basically uses a 1D plane-parallel radiative transfer; thus, the DOREM code can be easily applied to the ICA code.

2.2 Independent Column Approximation. The ICA [20] is the simplest extension of plane-parallel radiative heat transfer. It ignores net horizontal photon transport, but includes horizontal inhomogeneities in scalar parameters. Figure 1 shows the comparison between the 3D simulation and the ICA. It represents the schematic demonstration of the photon trajectory. In the ICA, plane-parallel computations are essentially performed at each element and a photon is constrained to a horizontally homogeneous column. After a photon enters the top of the model, the photon remains in the same column as it traverses in the vertical direction. When the photon hits the boundary of the column, it moves at the opposite position at the column boundary, consequently

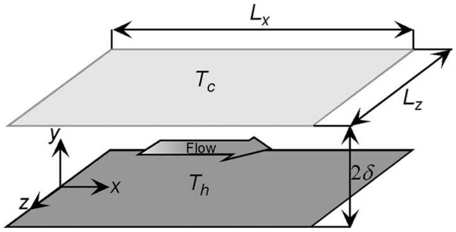

Fig. 2 Computational domain and coordinate system

creating a periodic boundary condition inside each column. By comparison, the 3D photon trajectory is shown at the right hand side of Fig. 1. The integrations of the optical path length are the same for both models. The 3D ray tracing for the photon trajectory experiences each participating media element ($N_x \times N_y \times N_z$ elements) in the entire computational domain. On the other hand, the ICA computes only $N_x \times N_z$ elements because the 1D plane-parallel radiative transfer simulations are conducted with the y-direction along each column. The ICA method requires horizontal periodicity due to the computational scheme. This is one of the limitations. The objective of this study is to show the numerical efficiency for calculating the local divergence of the radiative heat flux with the ICA. Although the ICA ignores 3D radiative effects, the algorithm is quite simple. Thus, it is feasible to considerably decrease the computational costs.

3 Physical Modeling

Temperature field data in a 3D turbulent channel flow is derived from the DNS [16]. Here, the simple description of creating a physical model is available. The computational domain and the coordinate system are shown in Fig. 2. The streamwise, the wall-normal, and the spanwise coordinates are denoted by x, y, and z. The present DNS treats the fully developed turbulent flow in a channel between the heated and the cooled walls. All the turbulence statistics including presented values were confirmed to agree with the existing literatures (for example, see Ref. [18]), and our numerical results were thus validated. This is the usual case of the two-dimensional heat transfer from the wall where the wall is uniformly heated at constant temperatures. The periodic boundary condition is applied for x- and z-directions for velocity and temperature fields. Numerical conditions taken in this paper are listed Table 1. The uniform grid mesh is used in x- and z-directions with nonuniform grid spacing in the y-direction (finer grid points are used near the boundary walls). Symbol δ is the half-length between the top and the bottom walls. The radiative transfer models use the various characteristic optical thicknesses using the parameter δ. The DNS, which we used to obtain the temperature profile, dealt with air flows; therefore, the larger optical thicknesses ($\tau_L > 10$) are somewhat artificial. However, it is important to know the optical thickness sensitivity with the parametric study. Spectral dependence is not taken into account for simplicity.

Figure 3 shows the snapshot of the instantaneous nondimensional temperature $T^* = (T - T_c)/(T_h - T_c)$, which is derived from the DNS data. The DNS computations were conducted for Prandtl number $\mathrm{Pr} = 0.71$. Here, the Reynolds number Re is based on the channel half-width and the frictional velocity. This Reynolds number was set equal to 150, and the Reynolds number scaled by the mean velocity and the channel width was 4530. The mean temperature changes monotonically over the width of the channel. The temperature fluctuation has peaks near the walls where turbulent velocity is intensified. The temperature fluctuation also shows a peak in the channel center where the turbulence length scale increases, moving away from the wall. To scrutinize the effects of the 3D and the ICA radiative transfer models, the radiative transfer simulation in this paper does not directly consider the turbulent flow using the DNS. The inclusion of flow simulations will be a part of our future research.

Table 1 Computational condition

L_x / δ	7.8
L_z / δ	3.5
Number of grid ($N_x \times N_y \times N_z$)	$64 \times 61 \times 64$
Optical thickness ($\tau_L = \beta_L L = 2\beta_L \delta$)	1–50

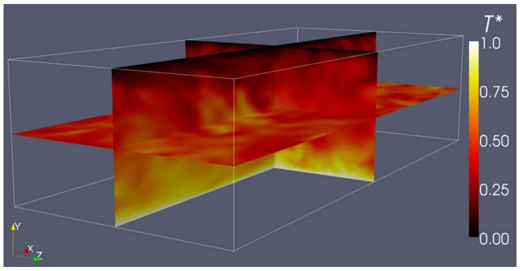

Fig. 3 Instantaneous temperature field in turbulent channel flow

The nondimensional temperature at the top boundary ($y = 2\delta$) and at the bottom boundary ($y = 0$) are set to $T^* = 0$ and 1, respectively. These walls are assumed to be isothermal black, and they are called cold and hot walls, for radiative transfer simulation. The periodic boundary condition is also applied for x- and z-directions for the 3D radiative transfer. All the radiative transfer simulations are carried out using a $64 \times 61 \times 64$ computational grid. The ray tracing at the 3D simulation and the ICA uses the S_8 discrete ordinates [1]. The Monte Carlo simulation requires a large number of photons to obtain reliable solutions depending on the optical thickness. The Monte Carlo results often provide benchmark solutions; however, in general, Monte Carlo is computationally expensive. On the other hand, the radiative transfer simulations employed here do not depend on the optical thickness and do not require a large number of rays for tracing the photon trajectory. Thus, these methods are suitable for practical engineering applications due to computational costs.

4 Results and Discussions

4.1 1D Plane-Parallel Test. It is necessary to validate these models using the simplest way before radiative transfer simulations are performed using the real temperature profile. A good place to start validating the models is with the well-understood 1D plane-parallel test. When the uniform nondimensional temperature in a participating medium is set to $T^* = 0$ instead of using the real temperature distribution shown in Fig. 3, the physical model becomes a 1D plane-parallel nonscattering gray medium problem. Thus, the exact solution of the RTE can be readily derived [1]. The real radiative gases should be rigorously treated as a nongray medium. However, it is important to show the validity of this numerical method by the simplest case. When a method is valid in gray media, it is easy to extend it to nongray radiative transfer conditions.

Figure 4 shows the comparison between the exact solutions, the 3D simulation, and the ICA results for the nondimensional divergence of the radiative heat flux with varying optical thicknesses. In the case of $\tau_L = 1$, the entire participating medium is heated because the emissive power from the hot wall is easy to transport to the cold wall. With increasing optical thickness, the radiative heat fluxes attenuate quickly near the hot wall. Although a small discrepancy can be found because the ICA ignores the 3D horizontal photon transport, the 3D and the ICA results show good agreement with the exact solutions.

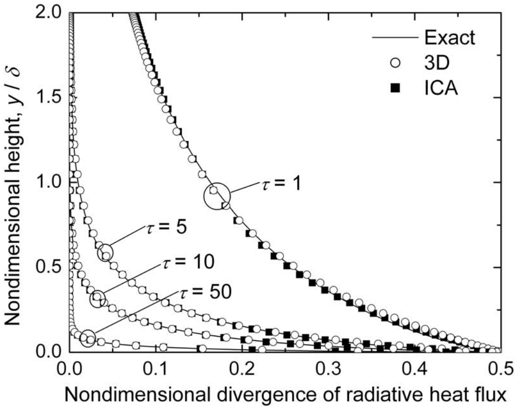

Fig. 4 Comparison between the exact solutions, the 3D simulation, and the ICA results for a 1D plane-parallel medium

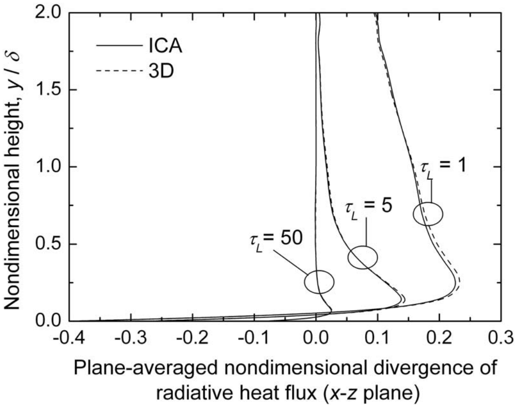

Fig. 6 Plane-averaged nondimensional divergence of radiative heat flux distributions with a homogeneous medium

4.2 3D Homogeneous Test. The next two series of tests show differences between the 3D simulation and the ICA using a real temperature profile in the turbulent channel flow. This first problem deals with a 3D homogeneous optical thickness medium. All horizontal elements are given the uniform optical properties. The purpose of this case study is to identify and explain the potential errors obtained in computing the divergence of the radiative heat flux using plane-parallel assumptions for the ICA.

Presented in this section are the nondimensional divergences of radiative heat flux distributions for the 3D model and the differences between the 3D simulation and the ICA computations on the contour surface where $T^* = 0.5$ is shown in Fig. 5. Here, the average location (y) of the distribution is about half of the height ($y = \delta$). Even the uniform emissive powers are emitted at the contour surface, the incident radiations from the surrounding medium depend on the locations. In the case of $\tau_L = 1$, the emissive powers from the hot wall propagates longer than the optically thick case. The upper parts of the contour surface are heated because the emissive powers are relatively low, additionally, the incident radiations from the surrounding medium can transport from the hot walls. The lower parts are vice versa. As shown in this figure, the ICA slightly underestimates the radiative heating effect on upper parts of the contour surface and the radiative cooling effect on lower parts compared with 3D radiative transfer simulations.

Figure 6 shows the plane-averaged nondimensional divergence of radiative heat flux distributions (x-z plane) with a homogeneous

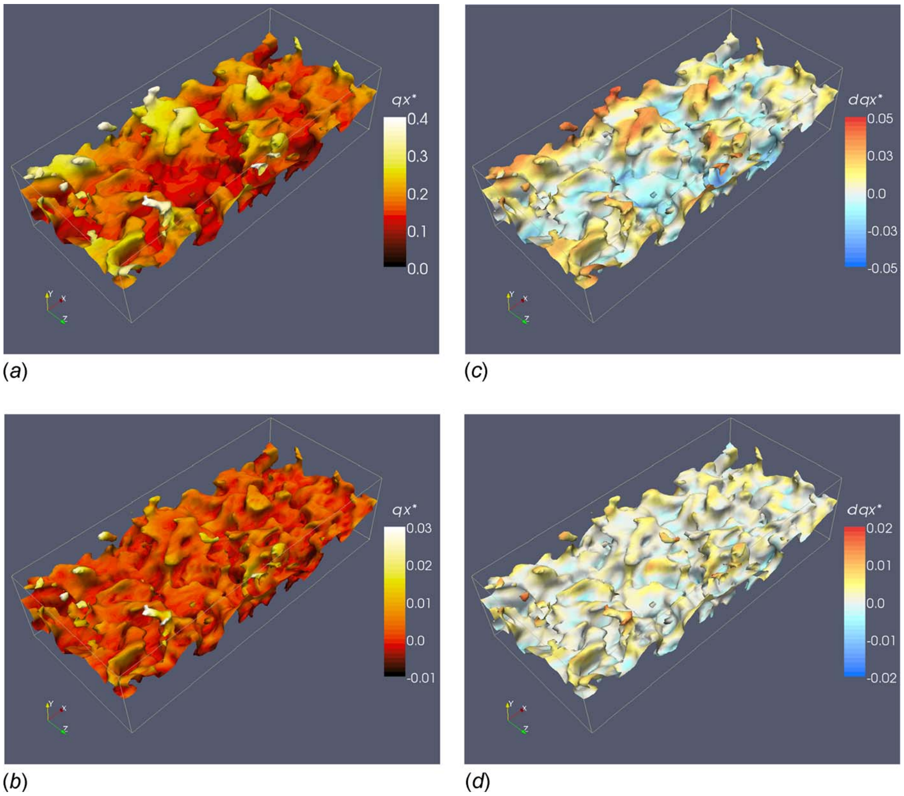

(*a*) (*c*)

(*b*) (*d*)

Fig. 5 Nondimensional divergence of radiative heat flux distributions on the contour surface at $T^* = 0.5$ in a homogeneous medium. (*a*) and (*c*) show the results from 3D radiative transfer simulations. (*b*) and (*d*) show the difference between the 3D and the ICA simulations in the case of $\tau_L = 1$ and $\tau_L = 50$.

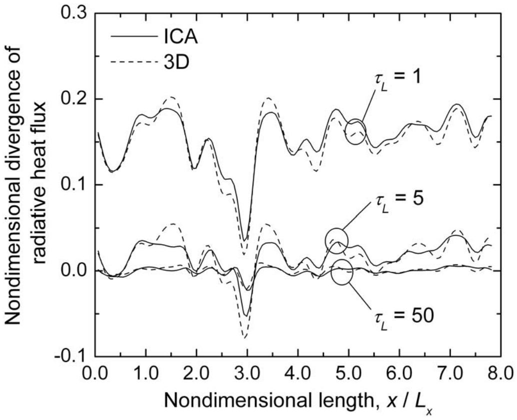

Fig. 7 Nondimensional divergence of radiative heat flux distributions with homogeneous medium along the horizontal line at $y=\delta$ and $z=L_z/2$

medium. The ICA results underestimate the radiative heating effect at $y=0.25-1.00$ region. Figure 7 shows the nondimensional divergence of radiative heat flux distributions with a homogeneous medium along the horizontal line at $y=\delta$ and $z=L_z/2$. The ICA results underestimate about 0.1 radiative heating at $x=1.5$ and 3.5 regions, and also about 0.03 radiative cooling at $x=3.0$. This is due to the fact of neglecting the 3D horizontal photon transport in the ICA. However, these discrepancies between the 3D and the ICA radiative simulations are not substantial for a practical engineering problem.

4.3 3D Inhomogeneous Test. This second problem deals with a 3D inhomogeneous optical thickness medium. All horizontal elements are given different optical properties. We assume that the optical properties depend on the local medium temperature as $\beta=\beta_L T^*$, where $\beta_L=\tau_L/2\delta$. It means the higher temperature medium is given optically thick properties and vice versa. The purpose of this case study is to identify and explain the potential errors obtained in computing the divergence of the radiative heat flux within an inhomogeneous medium using plane-parallel assumptions for the ICA. Realistic physical modeling often requires an inhomogeneous medium; thus, it is useful to provide valuable information.

Figure 8 shows the nondimensional divergence of radiative heat flux distributions and the differences between the 3D simulation and the ICA within an inhomogeneous medium on the contour surface at $T^*=0.5$. The 3D and the ICA results show a similar tendency even when the radiative transfer simulation is conducted under the inhomogeneous medium situation.

Figure 9 shows the plane-averaged nondimensional divergence of radiative heat flux distributions with an inhomogeneous medium. Because of the relatively low optical thickness near the cold wall, the emissive powers from the hot wall can propagate longer than the homogeneous medium situation; therefore, radiative heating effects are large in the case of an inhomogeneous medium. The ICA results slightly underestimate the radiative heating effect. The phenomenon has a similar behavior as the homogeneous medium situation. Figure 10 shows the nondimensional divergence of radiative heat flux distributions with an inhomogeneous medium along the horizontal line at $y=\delta$ and $z=L_z/2$. The ICA results underestimate about 0.05 radiative heating at $x=1.5$ and 3.5 in the case of three optical thicknesses.

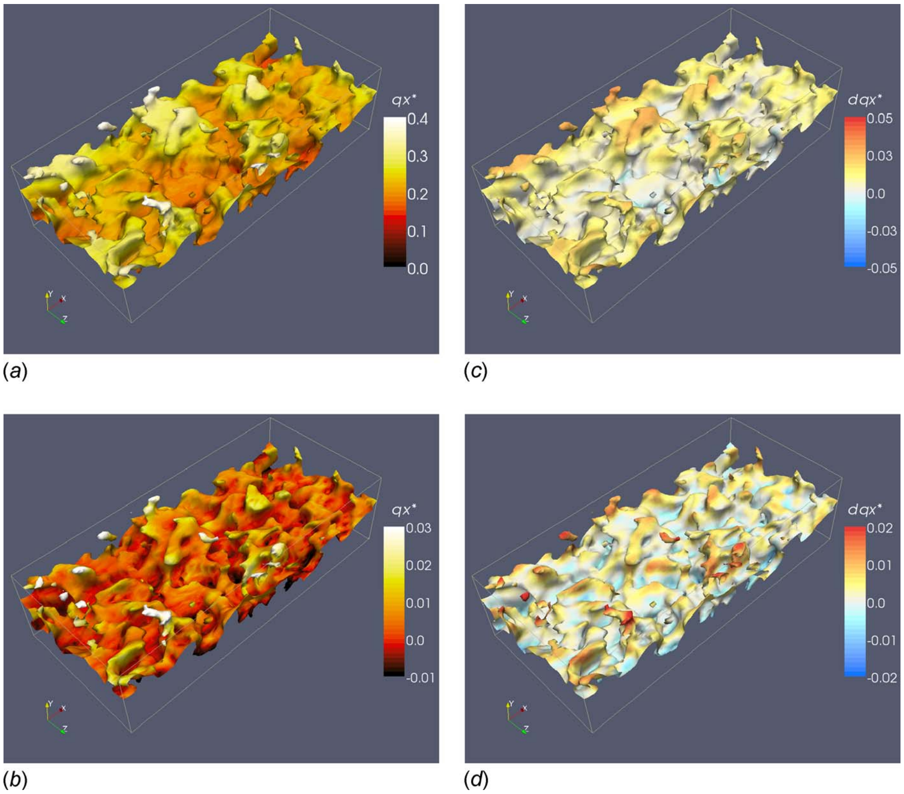

(*a*) (*c*)

(*b*) (*d*)

Fig. 8 Nondimensional divergence of radiative heat flux distributions on the contour surface at $T^*=0.5$ in an inhomogeneous medium. (*a*) and (*c*) show the results from 3D radiative transfer simulations. (*b*) and (*d*) show the difference between the 3D and the ICA simulations in the case of $\tau_L=1$ and $\tau_L=50$.

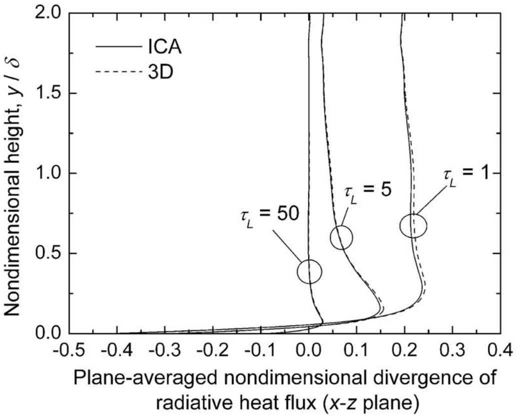

Fig. 9 Plane-averaged nondimensional divergence of radiative heat flux distributions with an inhomogeneous medium

Even in the case of the inhomogeneous medium, the differences between the 3D simulation and the ICA are not large. For 3D radiative transfer simulations, photons are not constrained within single columns like the ICA; therefore, they reach the optically thick part of an inhomogeneous medium more readily through the 3D photon transport. The photons in the ICA experiences only vertical optical properties, resulting in the general underestimation of radiative fluxes compared with the 3D simulation. If a single column has large optical thicknesses and the surrounding media have small ones, the ICA has a possibility to overestimate radiative fluxes. In the case of a strongly scattering medium, photons may be a result in strong radiative interactions three-dimensionally; therefore, the ICA simulation should be carefully used in such a case. However, this is beyond the scope of this paper. Even in a nonscattering medium, the derived results from the 3D and the ICA exhibit a good agreement in a three-dimensionally inhomogeneous medium.

To summarize the above mentioned results, the domain-averaged divergence of radiative heat fluxes is introduced. The definition is as follows:

$$\overline{q_x} = \frac{\sum_{i=1}^{N} q_{x,i} V_i}{V} \tag{4}$$

where N is the total number of elements, V_i is the volume of the discretized element, and V is the total volume of the computational domain. The results are shown in Table 2 with varying optical thicknesses. Generally the ICA results underestimate the radiative transfer even in the entire domain. In the case of $\tau_L = 1$ and 5, the differences are trivial (1–7%) in both of the homogeneous and the inhomogeneous medium situations. Radiative transfer simulations in the case of $\tau_L > 10$ are generally more difficult compared with the optically thin case. The discrepancies (about 26%) between the ICA and the 3D simulations in the case of $\tau_L = 50$ seem to be larger than the case of $\tau_L = 1$. Since the domain-averaged values are quite smaller than the case of $\tau_L = 1$, we believe that these differences are acceptable for practical engineering problems.

Table 2 Domain-averaged divergence of the radiative heat flux

Homogeneous medium	τ_L	ICA	3D	Difference (%)
	1	0.1443	0.1459	1.1060
	5	0.0305	0.0315	3.1566
	10	0.0124	0.0130	4.8941
	50	0.0008	0.0010	16.3665
Inhomogeneous medium	τ_L	ICA	3D	Difference (%)
	1	0.1957	0.1996	1.9542
	5	0.0541	0.0557	2.9704
	10	0.0222	0.0237	6.6768
	50	0.0017	0.0023	26.2829

The required processing time is only in the vicinity of 10 s for the ICA radiative transfer simulation on a personal computer (Pentium $4^{®}$ CPU, 3.2 GHz). Conversely for the 3D radiative transfer simulation the required processing time is in the vicinity of 650 s by the same computer. This resulted in a considerable decrease in the computational cost. Although the ICA simulations are restricted to simple configurations such as channel flows in this paper, wide application areas are expected due to the computational efficiency.

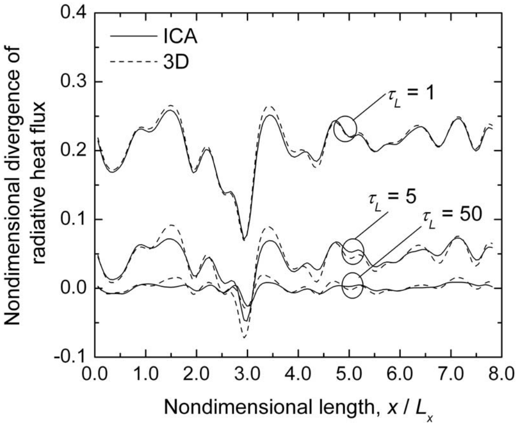

Fig. 10 Nondimensional divergence of radiative heat flux distributions with an inhomogeneous medium along the horizontal line at $y=\delta$ and $z=L_z/2$

5 Conclusions

A possibility of the independent column approximation for solving the radiative heat fluxes in a 3D turbulent channel flow has been described. This simulation method is the simplest extension of the plane-parallel radiative heat transfer. The test case of the nonisothermal temperature profile was obtained from the direct numerical simulation. Conclusions are summarized as follows:

(1) We have demonstrated the comparison between the 3D radiative transfer simulation and the independent column approximation with a well-understood 1D plane-parallel problem with varying optical thicknesses. Both the radiative transfer simulations have shown good agreement with the analytical solutions.

(2) The two series of tests have shown the differences between the 3D simulation and plane-parallel approximation using a real temperature profile in the turbulent channel flow. The first problem deals with a 3D homogeneous optical thickness. All horizontal elements are given uniform optical properties. The second one deals with a 3D inhomogeneous optical thickness medium. We assume that the optical properties depend on the local medium temperature. In these two series of tests, the divergence of radiative heat fluxes on the contour surface at an intermediate temperature, on plane-averaged and on a horizontal line are calculated. The above mentioned results have shown the trivial discrepancies between the 3D simulation and the independent column approximation.

(3) We have shown the domain-averaged divergence of radiative heat fluxes. In the case of $\tau_L = 1$, the errors are only 1–2%. And in the case of $\tau_L = 50$, they are about 16 $\sim$26%. Radiative transfer simulations in an optically thick medium are generally more difficult compared with an optically thin case. We believe that these differences are acceptable for practical engineering problems.

(4) The processing time for the ICA model is in the vicinity of 10 s as compared with 650 s for the 3D radiative transfer simulation model resulting in a considerable decrease in the computational cost. Although the independent column approximation simulations are restricted to simple configurations such as channel flows in this paper, wide application areas are expected due to the computational efficiency.

Nomenclature

A = surface area (m^2)
A^R = effective radiation area (m^2)
I = radiative intensity (W/m^2 sr)
I_b = blackbody intensity (W/m^2 sr)
L = length (m)
N = number of elements
Pr = Prandtl number
q_x = divergence of the radiative heat flux (W/m^3)
$\boldsymbol{r}$ = position vector
Re = Reynolds number
$\hat{\boldsymbol{s}}, \hat{\boldsymbol{s}}'$ = unit direction vector
S = radiative source function (W/m^2 sr)
$\overline{s}$ = averaged thickness of the radiation element (m)
T = temperature (K)
V = volume (m^3)
W_l = quadrature weight

Greek Symbols

β = extinction coefficient (m^{-1})
δ = channel half-width (m)
κ = absorption coefficient (m^{-1})
λ = wavelength (μm)
τ = optical thickness
τ_L = optical thickness $L = 2\delta$
ω = single scattering albedo

Subscripts

c = cold
h = hot
in = incoming
out = outgoing
x, y, z = streamwise, wall-normal, and spanwise coordinates
* = normalized by T_c and T_h

References

[1] Modest, M. F., 2003, *Radiative Heat Transfer*, 2nd ed., Academic, New York.
[2] Maruyama, S., 2004, *Light Energy Engineering*, Yoken-do, Tokyo, in Japanese.
[3] Mazumder, S., and Modest, M. F., 1999, "Turbulence-Radiation Interactions in Nonreactive Flow of Combustion Gases," ASME J. Heat Transfer, **121**, pp. 726–729.
[4] Velusamy K., Sundararajan T., and Seetharamu K. N., 2001, "Interaction Effects Between Surface Radiation and Turbulent Natural Convection in Square and Rectangular Enclosures," ASME J. Heat Transfer, **123**(6), pp. 1062–1070.
[5] Zheng, Y., Barlow, R. S., and Gore, J. P., 2003, "Spectral Radiation Properties of Partially Premixed Turbulent Flames," ASME J. Heat Transfer, **125**, pp. 1065–1073.
[6] Ridouane E. H., and Hasnaoui M., 2006, "Effect of Surface Radiation on Multiple Natural Convection Solutions in a Square Cavity Partially Heated From Below," ASME J. Heat Transfer, **128**(10), pp. 1012–1021.
[7] Paul, M. C., 2008, "Performance of the Various S_n Approximations of DOM in a 3D Combustion Chamber," ASME J. Heat Transfer, **130**, p. 072701.
[8] Husain, A., Baig, M. F., and Varshney, H., 2009, "Turbulent Rotating Rayleigh–Benard Convection: Spatiotemporal and Statistical Study," ASME J. Heat Transfer, **131**, p. 022501.
[9] Song, T. H., and Viskanta, R., 1987, "Interaction of Radiation With Turbulence: Application to a Combustion System," J. Thermophys. Heat Transfer, **1**, pp. 56–62.
[10] Li, G., and Modest, M. F., 2003, "Importance of Turbulence-Radiation Interactions in Turbulent Diffusion Jet Flames," ASME J. Heat Transfer, **125**(5), pp. 831–838.
[11] Tesse, L., Dupoirieux, F., and Taine, J., 2004, "Monte Carlo Modeling of Radiative Transfer in a Turbulent Sooty Flame," Int. J. Heat Mass Transfer, **47**(3), pp. 555–572.
[12] Duval, R., Soufiani, A., and Taine, J., 2004, "Coupled Radiation and Turbulent Multiphase Flow in an Aluminised Solid Propellant Rocket Engine," J. Quant. Spectrosc. Radiat. Transf., **84**(4), pp. 513–526.
[13] Fusegi, T., and Farouk, B., 1989, "Laminar and Turbulent Natural Convection-Radiation Interactions in a Square Enclosure Filled With a Nongray Gas," Numer. Heat Transfer, Part A, **15**(3), pp. 303–322.
[14] Yucel, A., Acharya, S., and Williams, M. L., 1989, "Natural-Convection and Radiation in a Square Enclosure," Numer. Heat Transfer, Part A, **15**(2), pp. 261–278.
[15] Dehghan, A. A., and Behnia, M., 1996, "Combined Natural Convection-Conduction and Radiation Heat Transfer in a Discretely Heated Open Cavity," ASME J. Heat Transfer, **118**(1), pp. 56–64.
[16] Matsubara, K., Kobayashi, M., and Maekawa, H., 1998, "Direct Numerical Simulation of a Turbulent Channel Flow With a Linear Spanwise Mean Temperature Gradient," Int. J. Heat Mass Transfer, **41**, pp. 3627–3634.
[17] Matsubara, K., Kobayashi, M., Sakai, T., and Suto, H., 2001, "A Study on Spanwise Heat Transfer in a Turbulent Channel Flow—Education of Coherent Structures by a Conditional Sampling Technique," Int. J. Heat Fluid Flow, **22**(3), pp. 213–219.
[18] Kasagi, N., Tomita, T., and Kuroda, A., 1992, "Direct Numerical Simulation of Passive Scalar Field in a Turbulent Channel Flow," ASME J. Heat Transfer, **114**, pp. 598–606.
[19] Wu, Y., Haworth, D. C., Modest, M. F., and Cuenot, B., 2005, "Direct Numerical Simulation of Turbulence/Radiation Interaction in Premixed Combustion Systems," Proc. Combust. Inst., **30**(1), pp. 639–646.
[20] Cahalan, R. F., Ridgway, W., Wiscombe, W. J., Gollmer, S., and Harshvardhan, 1994, "Independent Pixel and Monte Carlo Estimates of Stratocumulus Albedo," J. Atmos. Sci., **51**(24), pp. 3776–3790.
[21] O'Hirok, W., and Gautier, C., 1998, "A Three-Dimensional Radiative Transfer Model to Investigate the Solar Radiation Within a Cloudy Atmosphere. Part 1: Spatial Effects," J. Atmos. Sci., **55**, pp. 2162–2179.
[22] Maruyama, S., Sakurai, A., and Komiya, A., 2007, "Discrete Ordinates Radiation Element Method for Radiative Heat Transfer in Three-Dimensional Participating Media," Numer. Heat Transfer, Part B, **51**, pp. 121–140.
[23] Maruyama S., Aihara T., 1997, "Radiation Heat Transfer of Arbitrary Three-Dimensional Absorbing, Emitting and Scattering Media and Specular and Diffuse Surfaces," ASME J. Heat Transfer, **119**(1), pp. 129–136.
[24] Maruyama, S., and Guo, Z. X., 1999, "Radiative Heat Transfer in Arbitrary Configurations With Nongray Absorbing, Emitting, and Anisotropic Scattering Media," ASME J. Heat Transfer, **121**(3), pp. 722–726.
[25] Guo, Z. X., and Maruyama, S., 2001, "Prediction of Radiative Heat Transfer in Industrial Equipment Using the Radiation Element Method," ASME J. Pressure Vessel Technol., **123**(4), pp. 530–536.
[26] Sakurai, A., Maruyama, S., Sakai, S., and Nishikawa, T., 2005, "The Effect of Three-Dimensional Radiative Heat Transfer in Cloud Fields Using the Radiation Element Method," J. Quant. Spectrosc. Radiat. Transf., **93**(1–3), pp. 79–87.
[27] Lockwood, F. C., and Shah, N. G., 1981, "A New Radiation Solution Method for Incorporation in General Combustion Prediction Procedures," *Proceedings of the Combustion Institute*, pp. 1405–1414.

A Parametric Case Study in Radiative Heat Transfer Using the Reverse Monte-Carlo Ray-Tracing With Full-Spectrum *k*-Distribution Method

Xiaojing Sun
e-mail: minipaula@msn.com

Philip J. Smith[1]
e-mail: philip.smith@utah.edu

Department of Chemical Engineering,
Institute for Clean and Secure Energy,
University of Utah,
Salt Lake City, UT 84112

A combined method of reverse Monte-Carlo ray-tracing with full-spectrum k-distribution (FSK) for computing the radiative heat transfer is applied to an extreme nonhomogeneous case (both temperature and gas mixture composition vary with positions) with an absorbing, emitting media. The parameter studies of the scaled FSK (FSSK) and correlated FSK (FSCK) methods for the case, such as g point resolution, mesh resolution, reference states, and integration quadratures, are carried out. The results from the FSSK and FSCK are only affected by the chosen reference states and are not sensitive to other parameters.

[DOI: 10.1115/1.4000232]

Keywords: Monte-Carlo ray-tracing, radiative heat transfer, full-spectrum k-distribution

1 Introduction

Monte-Carlo ray-tracing (MCRT) is a statistical method in which the history of bundles of photons (or rays) is traced as they travel through the enclosure. The MCRT has been studied and applied to radiation heat transfer by many researchers [1–4]. It has the advantage over conventional radiative transfer equation (RTE) solvers (discrete ordinate method (DOM), spherical harmonic, etc.) of having a low cost of implementation. It also has the reputation of handling thermal radiation from real gas mixture and particulates with almost no approximation [5]. The recently developed full-spectrum *k*-distribution (FSK) method by Modest [6] reorders the irregular absorption coefficient into smooth *k*-distributions and carries out the spectral integration over the *g* space. The FSK method achieves line-by-line (LBL) accuracy for homogeneous media with only a tiny fraction of LBL's computational cost [6].

In this technical brief, we present a combined method of the reverse Monte-Carlo Ray-Tracing (RMCRT) method for solving the RTE and the FSK method for spectral radiative properties. In order to verify the code's ability for a three-dimensional problem, this one-dimensional problem is calculated in a three-dimensional domain. The performance of this combined method is demonstrated by sample calculations in a multidimensional, inhomogeneous, nongray gas mixture problem. The results are compared with LBL calculations.

2 RMCRT Method

The MCRT method can be carried out with either the forward MCRT (FMCRT) or the reverse MCRT (RMCRT). The RMCRT is based on the principle of reciprocity in radiative transfer theory as described by Case [7]. In RMCRT, instead of tracing how much energy a ray has lost to its path, the amount of *incoming* intensity along a path that contributes back to the origin (where the ray is emitted) is traced. Thus, the process of tracing a ray only updates the original emitting location, which makes the update relatively independent of other locations. Therefore, the RMCRT method can explicitly obtain solutions for the domain of interest without the need for the solution on the entire domain. This is a great advantage in a domain decomposition parallelization strategy.

We used a revised RMCRT equation for incoming intensity I of element k, similar to Walters and Buckius [1]

$$I_{i,k} = \int_0^{l_k} I_{b,cv}[T(l')]\kappa(l')\exp\left[-\int_{l'}^{l_k}\kappa(l'')\mathrm{d}l''\right]\mathrm{d}l' + I_{o,\mathrm{sur}}(T_w)\exp\left(-\int_{l_w}^{l_k}\kappa(l')\mathrm{d}l'\right) \quad (1)$$

The divergence of heat flux and surface heat fluxes are then readily obtained from

$$\nabla\cdot q_{k,cv} = 4\pi\left(\kappa_{k,cv}I_{o,k} - \frac{\kappa_{k,cv}}{N}\sum_{n=1}^{N} I_{i,k,n}\right) \quad (2)$$

$$\mathbf{q}_{k,\mathrm{sur}} = \pi\left(I_{o,k} - \frac{\alpha_{k,\mathrm{sur}}}{N}\sum_{n=1}^{N} I_{i,k,n}\right) \quad (3)$$

3 FSK Method

The FSK has been developed and constantly improved by Modest and co-workers [8–10] in recent years. Full-Spectrum Correlated-*k* method (FSCK) and FSSK have been developed by Modest co-workers [6,8–10].

For FSCK, the governing RTE equation [6] is

$$\frac{dI_g}{ds} = k(T_0,\phi,g_0)[a(T,T_0,g_0)I_b(T) - I_g] - \sigma_s\left(I_g - \frac{1}{4\pi}\int_{4\pi} I_g(\hat{s}')\Phi(\hat{s},\hat{s}')d\Omega'\right) \quad (4)$$

with the boundary conditions

$$I_g = I_{wg} = \epsilon_w a(T_w,T_0,g_0)I_{bw} + (1-\epsilon_w)\frac{1}{\pi}\int_{\hat{n}\cdot\hat{s}<0} I_g|\hat{n}\cdot\hat{s}|d\Omega \quad (5)$$

Here

$$I_g = \frac{I_k}{f(T_0,\boldsymbol{\phi_0},k)} = \frac{\int_0^\infty I_\eta\delta(k-\kappa_\eta(\eta,\boldsymbol{\phi_0}))\mathrm{d}\eta}{f(T_0,\boldsymbol{\phi_0},k)} \quad (6)$$

$$g_0(T_0,\boldsymbol{\phi_0},k) = \int_0^k f(T_0,\boldsymbol{\phi_0},k)\mathrm{d}k \quad (7)$$

$$a(T,T_0,g_0) = \frac{f(T,\boldsymbol{\phi_0},k)}{f(T_0,\boldsymbol{\phi_0},k)} = \frac{\mathrm{d}g(T,\boldsymbol{\phi_0},k)}{\mathrm{d}g_0(T_0,\boldsymbol{\phi_0},k)} \quad (8)$$

In $k(T_0,\phi,g_0)$, T_0 is the temperature at which the Planck function $I_{b\eta}(T_0)$ is evaluated and ϕ is the mixture state at which the absorption coefficient κ_η is evaluated.

For FSSK, the governing RTE equation [6] is

---

[1] Corresponding author.

Contributed by the Heat Transfer Division of ASME for publication in the JOURNAL OF HEAT TRANSFER. Manuscript received October 31, 2008; final manuscript received April 22, 2009; published online December 3, 2009. Assoc. Editor: Yogesh Jaluria.

$$\frac{dI_g}{ds} = k(T,\phi,g)[a(T,T_0,g_0)I_b(T) - I_g] - \sigma_s\left(I_g - \frac{1}{4\pi}\int_{4\pi} I_g(\hat{s}')\Phi(\hat{s},\hat{s}')d\Omega'\right) \tag{9}$$

where

$$k(T,\phi,g) = k(T,\phi_{\mathbf{0}},g)u(\phi,\phi_{\mathbf{0}}) = k(T_0,\phi,g_0) = k(T_0,\phi_{\mathbf{0}},g_0)u(\phi,\phi_{\mathbf{0}}) \tag{10}$$

In $k(T,\phi,g)$, T is the temperature at which the Planck function $I_{b\eta}(T)$ is evaluated, ϕ is the mixture state at which the absorption coefficient κ_η is evaluated, and u is the scaling function.

Modest and Zhang [9] suggested the implicit relation for scaling functions in FSSK.

$$\int_0^\infty I_{b\eta}(T_0)\exp[-\kappa_\eta(\eta,\phi)L_m]\mathrm{d}\eta = \int_0^\infty I_{b\eta}(T_0)\exp[-\kappa_\eta(\eta,\phi_{\mathbf{0}})u(\phi,\phi_{\mathbf{0}})L_m]\mathrm{d}\eta \tag{11}$$

i.e., forcing correct evaluation of radiation leaving from a homogeneous slab equal in width to the mean beam length L_m.

For both FSSK and FSCK to be coupled with RMCRT, I_b in Eq. (1) is simply replaced by aI_b for both media and boundaries and κ in Eq. (1) is replaced by κu for FSSK.

Finally, the total intensity is integrated over g space from 0 to 1

$$I = \int_0^\infty I_\eta d\eta = \int_0^1 I_g dg_0 \tag{12}$$

4 Parameter Case Study

The simulation error from RMCRT-FSK comes from many sources: the mesh resolution of the spatial domain, the number of rays, the ray's stopping criteria, the random number generator, resolution of the g-space spectral domain, the integration quadrature (because k is an exponentially monotonically increasing function of g and larger k plays an important role in the final intensity, we tend to concentrate more g in the $0.9 < g < 1$ region), the database for generating k-distribution (HITEMP [11], HITRAN [12], or CDSD-1000 [13]), the reference state (temperature and composition) in FSSK and FSCK.

4.1 Problem Statement. This nonhomogeneous case is described by Solovjov and Webb [14]. We study one-dimensional parallel plates with gray diffuse surfaces at $T_w = 1000$ K and $\epsilon = 0.8$. The plates are separated by $L = 1$ m. The medium between the plates is a nongray, nonscattering gas mixture. The composition of this gas mixture is divided into three uniform sections as follows:

1. $T_g = 1000$ K; $Y_{H_2O} = 0.2$; $Y_{CO_2} = 0.1$; $Y_{CO} = 0.03$ if $x \in [0, 0.35]$ m
2. $T_g = 1500$ K; $Y_{H_2O} = 0.4$; $Y_{CO_2} = 0.2$; $Y_{CO} = 0.06$ if $x \in [0.35, 0.65]$ m
3. $T_g = 1000$ K; $Y_{H_2O} = 0.2$; $Y_{CO_2} = 0.1$; $Y_{CO} = 0.03$ if $x \in [0.65, 1]$ m

This is an extreme scenario with sharp temperature and composition gradients between different sections.

4.2 Simulation Conditions. To verify this combined method for three-dimensional problems, this one-dimensional problem is simulated in a three-dimensional domain with mirror side walls. Two mesh resolutions are studied: $20 \times 20 \times 60$ and $40 \times 40 \times 120$. Both FSCK and FSSK for nonhomogeneous media are applied. This case has nonhomogeneity in both temperature and gas compositions but with constant ratio of gas composition. Four reference states have been examined following the suggestions by Modest and co-workers [9,15]

1. (Tref1000cold) $T_{\mathrm{ref}} = 1000$ K, $Y_{H_2O} = 0.2$, $Y_{CO_2} = 0.1$, $Y_{CO} = 0.03$
2. (Tref1500hot) $T_{\mathrm{ref}} = 1500$ K, $Y_{H_2O} = 0.4$, $Y_{CO_2} = 0.2$, $Y_{CO} = 0.06$
3. (Tref1240cold) $T_{\mathrm{ref}} = 1240$ K, $Y_{H_2O} = 0.2$, $Y_{CO_2} = 0.1$, $Y_{CO} = 0.03$
4. (Tref1240hot) $T_{\mathrm{ref}} = 1240$ K, $Y_{H_2O} = 0.4$, $Y_{CO_2} = 0.2$, $Y_{CO} = 0.06$

Both 12 and 128 abscissas are used in g space. Because this problem is symmetric only half of the domain is simulated. For all these different conditions, 1000 rays emitted from each control volume, proved to produce adequate convergence.

4.3 Mesh Resolution. The $40 \times 40 \times 120$ mesh resolution produces the same results as those from a $20 \times 20 \times 60$ mesh resolution. Thus the $20 \times 20 \times 60$ mesh resolution has reached mesh convergence and is applied to all cases below.

4.4 FSSK and FSCK. FSCK and FSSK are carried out according to Eqs. (4) and (9), respectively, for each reference state. In the following, a_{hot} and a_{cold} indicate the stretching factor a for the hot middle and cold outer section, respectively; u_{hot} and u_{cold} indicate the scaling function u for the hot middle and cold outer section, respectively. The stretching factor a is needed for both FSCK and FSSK in Eqs. (4) and (9) and is calculated from Eq. (8). The scaling function u is only needed for FSSK in Eq. (9), and is calculated from Eq. (11) by setting L_m. For this particular case with 1 m slab gap, the geometric mean beam length L_m can be approximated to be 1.76 m [16].

For the reference state designated as Tref1000cold, $k(T_{\mathrm{ref}}, \phi_{\mathrm{ref}}, g_0)$ and $k(T = 1500\ K, \phi_{\mathrm{ref}}, g)$ are needed for a_{hot} in FSSK and FSCK, $k(T_{\mathrm{ref}}, \phi(1500\text{ K section}), g_0)$ is needed in the RTE for all sections and u_{hot} in FSSK, where $k(T_{\mathrm{ref}}, \phi(1500\text{ K section}), g_0)$ indicates the absorption coefficient is evaluated at the 1500 K middle section state (both the temperature and the composition) and with the Planck function evaluated at the same gas composition but at $T = 1000$ K, $a_{\mathrm{cold}} = 1$, a_{hot} is calculated from Eq. (8), and $u_{\mathrm{cold}} = 1$, $u_{\mathrm{hot}} = 4.1686$ is calculated from Eq. (11).

For the reference state designated as Tref1500hot, $k(T_{\mathrm{ref}}, \phi_{\mathrm{ref}}, g_0)$ and $k(T = 1000\ K, \phi_{\mathrm{ref}}, g)$ are needed for a_{cold} in FSSK and FSCK, $k(T_{\mathrm{ref}}, \phi(1000\text{ K section}), g_0)$ is needed in the RTE for all sections and u_{cold} in FSSK, a_{cold} is calculated from Eq. (8), $a_{\mathrm{hot}} = 1$, and $u_{\mathrm{cold}} = 0.3420$ is calculated from Eq. (11), $u_{\mathrm{hot}} = 1$.

For the reference state designated as Tref1240cold and Tref1240hot, $k(T_{\mathrm{ref}}, \phi_{\mathrm{ref}}, g_0)$, $k(T = 1000\ K, \phi_{\mathrm{ref}}, g)$, and $k(T = 1500\ K, \phi_{\mathrm{ref}}, g)$ are needed for a_{hot} and a_{cold} in FSSK and FSCK, $k(T_{\mathrm{ref}}, \phi(1000\text{ K section}), g_0)$ and $k(T_{\mathrm{ref}}, \phi(1500\text{ K section}), g_0)$ are needed for the RTE and u_{hot}, u_{cold} in FSSK, both a_{cold} and a_{hot} are calculated from Eq. (8), and for Tref1240cold, $u_{\mathrm{cold}} = 0.87367$, $u_{\mathrm{hot}} = 3.039176$; for Tref1240hot, $u_{\mathrm{cold}} = 0.388639$, $u_{\mathrm{hot}} = 1.33659$ is calculated from Eq. (11).

Figures 1 and 2 showed that the absorption coefficients after scaling are very close.

For any given reference state, FSCK outperformed FSSK as shown later in Fig. 3. This may due to the absorption coefficient of this gas mixture at these reference states are more correlated than scaled.

4.5 Reference State. To test the impact of the reference states, FSSK and FSCK calculations are carried out at the four reference states mentioned above. Mazumder and Modest [15] demonstrated that for a gas mixture that is nonhomogeneous in

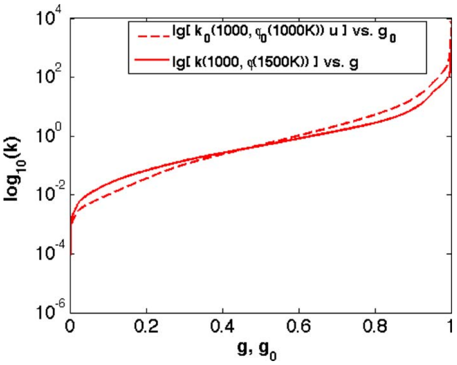

Fig. 1 absorption coefficient comparison after scaling for FSSK-Tref1000cold with $u=4.1686$

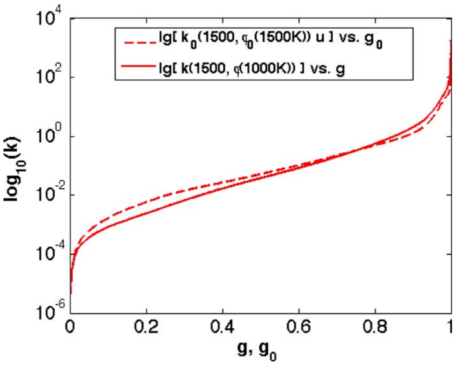

Fig. 2 Absorption coefficient comparison after scaling for FSSK-Tref1500hot with $u=0.3420$

both temperature and composition, if the ratio of components of the gas mixtures is constant, the resulting k-distributions with the same reference temperature have identical profiles. Thus, identical results from respective FSSK and FSCK computations are expected at Tref1240hot and Tref1240cold reference states.

Results are shown in Fig. 3 from the FSSK and FSCK simulations at all four reference states with 12 g-abscissas using GAUCHEB quadrature scheme. Both FSSK-Tref1240cold and FSSK-Tref1240hot outperformed FSSK-Tref1000cold and FSSK-Tref1500hot at the peaks and both returned identical results as expected. Figure 3 shows that FSSK-Tref1500hot outperformed FSSK-Tref1000cold at the lower peak in divergence of heat flux while FSSK-Tref1000cold outperformed FSSK-Tref1500hot at the higher peak. Two potential reasons for this are (1) the reference states. FSSK-Tref1500hot did better in the middle hot region where the property state is the same as the reference state; due to the same reason, FSSK-Tref1000cold did better in the outer cold region and (2) the scaling function's quality for different reference states varies. Figures 1 and 2 show that in $0.9 < g < 1.0$ region, the scaled k from the reference state Tref1500hot is closer to the original k than the k from Tref1000cold.

To test the second hypothesis above, the GAULEG quadrature, where g is distributed more evenly across 0 to 1, was applied to FSSK. As shown in Fig. 4, FSSK-Tref1500hot and FSSK-Tref1000cold obtained results that were independent of quadrature schemes.

All models produced large discrepancies from the LBL computation at the middle hot region. FSCK-Tref1000cold performed slightly better in the middle section than all other reference states. While in the outer sections, all four reference states with FSCK obtained virtually identical results. Based on the observation from Mazumder and Modest [15] and the FSSK results discussed above, it was expected that FSCK-Tref1500hot would perform better for the middle section, while FSCK-Tref1000cold would perform better at the outer section. This might also be explained by the long distance nature of radiative heat transfer.

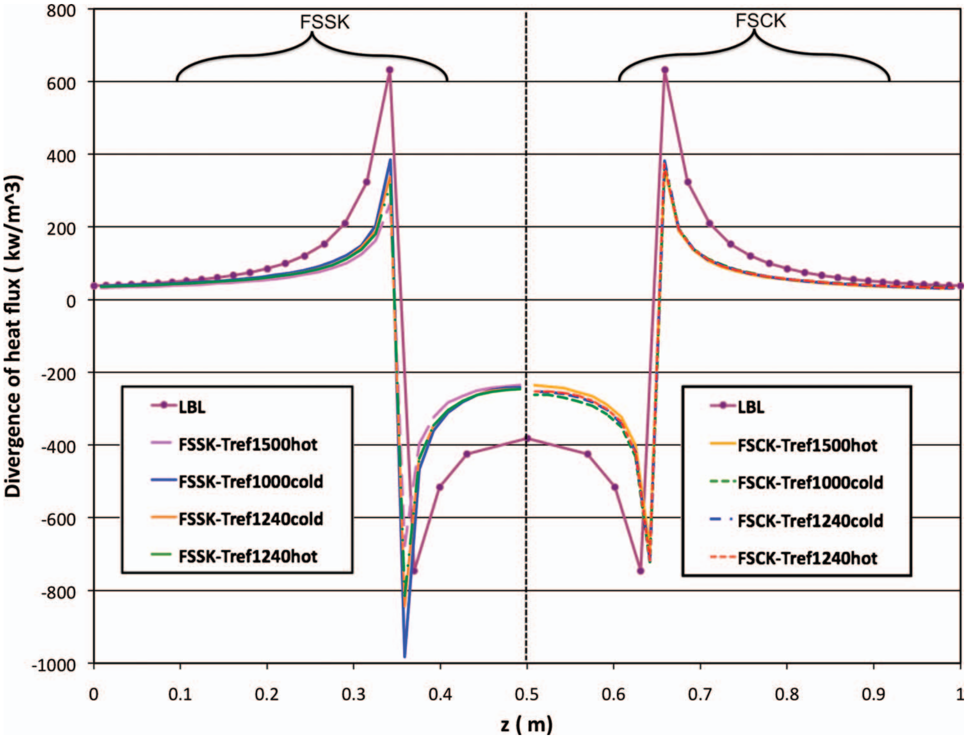

Fig. 3 FSSK and FSCK at different reference states with 12 g GAUCHEB ($\alpha=2.5$) quadrature in the nonhomogeneous medium case

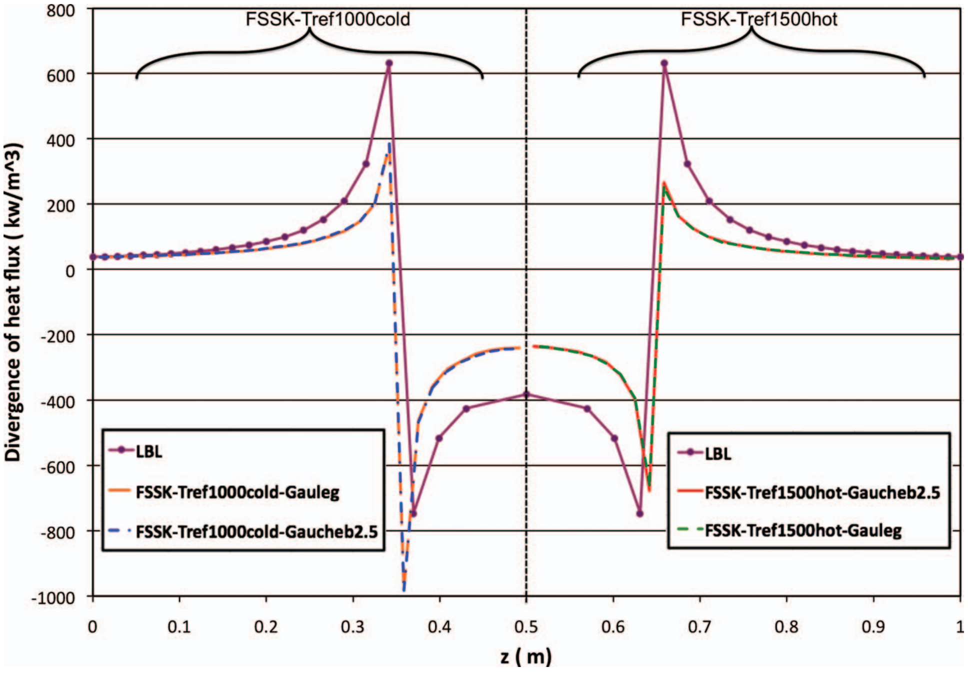

Fig. 4 FSSK with different quadrature schemes in the nonhomogeneous medium case with 12 g points

4.6 Quadrature Selection. The GAULEG scheme has symmetric weights, while GAUCHEB allows a finer resolution in $0.9 < g < 1.0$ region by setting a switching factor $\alpha = 2.5$. This switching is valuable for optically thin media. Equations (4) and (9) are applied to solve for I_g at 12 abscissas for the quadrature, respectively. The total intensity is then integrated from,

$$I = \sum_{i=1}^{12} w_i I_{g_i} \tag{13}$$

Because each homogeneous section is small and is an optically thin medium, the g-abscissas chosen from GAUCHEB was expected to better represent the spectral domain. GAUCHEB was applied for all four reference conditions. In order to verify the explanation of performances of the quadrature selections, GAUCHEB and GAULEG quadratures are applied to FSSK-Tref1500hot, FSSK-Tref1000cold with 12 g-abscissas. Figure 4 shows that these two quadratures obtained virtually identical results when holding other conditions constant.

4.7 Number of g Points. Both 12 and 128 g-abscissas for FSSK, FSCK at different reference states were applied. The results obtained from 128 g-abscissas are identical to the results from 12 g when holding other conditions constant. Thus, for these cases discretization of the g space into 12 abscissas was adequate for both quadrature schemes.

5 Conclusions

A combined Method RMCRT-FSK is applied to an extreme nongray, nonhomogeneous case. Parameter studies of the resolution of g space, mesh resolution, reference states and integration quadratures are carried out. The study showed that FSSK and FSCK are only slightly affected by the chosen reference state and are not sensitive to other parameters. The results from FSSK and FSCK computations produced sever errors as large as 35%. These errors are due to two reasons:

1. The sharp gradients in both compositions and temperatures between the layers;
2. The assumptions in FSSK and FSCK that the absorption coefficients are scaled or correlated.

Acknowledgment

The authors acknowledge Dr. Solovjov and Dr. Webb for their original data contributions and Dr. Modest for his academic advice. The authors also gratefully acknowledge the financial support from the Department of Energy Lawrence Livermore National Laboratory under Grant No. B524196 through the Center for the Simulation of Accidental Fires and Explosions (C-SAFE).

Nomenclature

Symbols

a = stretching factor for FSCK and FSSK
f = k-distribution
g = the quadrature points in FSK
I = radiative intensity
L = gap distance, (m)
l = distance of a ray it travels
N = number of rays
n = iteration number
q = radiative heat flux, $(\mathrm{W/m^2})$
s = geometric path length
$\hat{\mathbf{s}}$ = unit vector into a given direction
T = temperature, (K)
u = scaling function for FSSK
x, y, z = cartesian coordinates

Greek Symbols

α = the surface absorption coefficient, or the switching factor in GAUCHEB quadrature
ϵ = emittance or emissivity
η = wave number
κ = absorption coefficient, $(\mathrm{m^{-1}})$
Φ = scattering phase function
ϕ = the gas mixture state
σ_s = scattering coefficient, $(\mathrm{m^{-1}})$

Subscripts

b = blackbody property
cv = control volume
η = wave number
i = incoming
k = index of a calculation element
n = iteration number, or integral order
o = outgoing
P = Planck-mean property
ref = reference state property
σ = Stefan–Boltzmann constant is 5.670×10^{-8} $(\mathrm{W/m^2\,K^4})$
sur = surface element
w = wall, boundary property

References

[1] Walters, D. V., and Buckius, R. O., 1992, "Rigorous Development for Radiation Heat Transfer In Nonhomogeneous Absorbing, Emitting, and Scattering Media," Int. J. Heat Mass Transfer, **35**(12), pp. 3323–3333.

[2] Farmer, J. T., and Howell, J. R., 1998, "Comparison of Monte Carlo Strategies for Radiative Transfer in Participating Media," Adv. Heat Transfer, **31**, pp. 333–429.

[3] Wang, A., and Modest, M. F., 2006, "Photon Monte Carlo Simulation for Radiative Transfer in Gaseous Media Represented by Discrete Particle Fields," ASME J. Heat Transfer, **128**(10), pp. 1041–1049.

[4] Wang, A., and Modest, M. F., 2007, "An Adaptive Emission Model for Monte Carlo Simulations in Highly Inhomogeneous Media Represented by Stochastic Particle Fields," J. Quant. Spectrosc. Radiat. Transf., **104**, pp. 288–296.

[5] Howell, J. R., 1998, "The Monte Carlo Method in Radiative Heat Transfer," ASME J. Heat Transfer, **120**, pp. 547–560.

[6] Modest, M. F., 2003, *Radiative Heat Transfer*, 2nd ed., Academic Press, Burlington, MA.

[7] Case, K. M., 1957, "Transfer Problems and the Reciprocity Principle," Rev. Mod. Phys., **29**(4), pp. 651–663.

[8] Modest, M. F., 2003, "Narrow-Band and Full-Spectrum *k*-Distribution for Radiative Heat Transfer—Correlated-*k* vs. Scaling Approximation," J. Quant. Spectrosc. Radiat. Transf., **76**(1), pp. 69–83.

[9] Modest, M. F., and Zhang, H., 2002, "The Full-Spectrum Correlated-*k* Distribution for Thermal Radiation From Molecular Gas Particulate Mixtures," ASME J. Heat Transfer, **124**(1), pp. 30–38.

[10] Modest, M. F., and Riazzi, R. J., 2005, "Assembly of Full-Spectrum *k*-Distributions From a Narrow-Band Database; Effects of Mixing Gases, Gases and Nongray Absorbing Particles, and Mixtures With Nongray Scatters in Nongray Enclosures," J. Quant. Spectrosc. Radiat. Transf., **90**, pp. 169–189.

[11] Rothman, L., Camy-Peyret, C., Flaud, J.-M., Gamache, R., Goorvitch, D., Goldman, A., Hawkins, R., Schroeder, J., Selby, J., and Wattson, R., 2000, "HITEMP. The High-Temperature Molecular Spectroscopic Database," J. Quant. Spectrosc. Radiat. Transf..

[12] Rothman, L. S., Jacquemart, D., Barbe, A., Chris Benner, D., Birk, M., Brown, L. R., Carleer, M. R., Chackerian, Jr., C., Chance, K., Coudert, L. H., Dana, V., Devi, V. M., Flaud, J.-M., Gamache, R. R., Goldman, A., Hartmann, J.-M., Jucks, K. W., Maki, A. G., Mandin, J.-Y., Massie, S. T., Orphal, J., Perrin, A., Rinsland, C. P., Smith, M. A. H., Tennyson, J., Tolchenov, R. N., Toth, R. A., Vander Auwera, J., Varanasi, P., and Wagner, G., 2005, "The *HITRAN* 2004 Molecular Spectroscopic Database," J. Quant. Spectrosc. Radiat. Transf., **96**, pp. 139–204.

[13] Tashkun, S. A., Perevalov, V. I., Teffo, J.-L., Bykov, A. D., and Lavrentieva, N. N., 2003, "CDSD-1000, the High-Temperature Carbon Dioxide Spectroscopic Databank," J. Quant. Spectrosc. Radiat. Transf., **82**, pp. 165–196.

[14] Solovjov, V. P., and Webb, B. W., 2000, "SLW Modeling of Radiative Transfer in Multi-Component Gas Mixtures," J. Thermophys. Heat Transfer, **65**, pp. 655–672.

[15] Mazumder, S., and Modest, M. F., 2002, "Application of the Full Spectrum Correlated-*k* Distribution Approach to Modeling Non-Gray Radiation in Combustion Gases," Combust. Flame, **129**, pp. 416–438.

[16] Hottel, H. C., and Sarofim, A. F., 1968, *Radiative Transfer*, McGraw-Hill, New York.

Green's Function Approach to Nonlinear Conduction and Surface Radiation Problems

Matthew R. Jones

Vladimir P. Solovjov

Department of Mechanical Engineering,
Ira A. Fulton College of Engineering and Technology,
Brigham Young University,
Provo, UT 84602-4201

An exact approach for solving both transient and steady state conduction and surface radiation problems is presented. The method is based on the use of Green's function, and the temperature field is obtained by solving an integral equation. This is in contrast to the approach presented in radiative heat transfer texts in which temperature profiles are obtained from the simultaneous solution of coupled integral and differential equations. The analysis presented in this paper provides insight into the solution of this important class of problems. The method is illustrated by solving two representative problems. The first problem considered is the steady state analysis of a radiating fin. The second problem considered is the transient analysis of a radiating target, which is used to determine the temporal response of radiation thermometers. [DOI: 10.1115/1.4000234]

Keywords: conduction, radiation, Green's function, radiating fins, radiation thermometry

1 Introduction

Conduction coupled with surface radiation occurs in a wide range of applications such as heat transfer in vacuum insulation systems, radiative heat flux gauges, and thermal management of spacecraft. Using Green's functions, an analytical treatment of the nonlinear problems arising in combined conduction—surface radiation problems is developed. This approach requires the solution of a single integral equation. Although this solution procedure requires the use of a numerical quadrature algorithm, the quadrature can, in principle, be performed to any arbitrary degree of precision. Therefore, the solution is exact.

The Green's function approach is contrasted with the approach originally developed by Sparrow et al. [1] and outlined in radiative transfer texts [2–4] in which steady state temperature profiles are obtained from the simultaneous solution of coupled differential and integral equations. These texts discuss the steady state interaction between surface radiation and one-dimensional conduction for spectrally varying radiative surface properties and a wide range of geometries and irradiation conditions. Fewer studies have considered transient problems. Crosbie and Viskanta [5] solved for the transient temperature distributions in a plate subjected to combined convection and radiation.

The treatment of both steady and transient problems is considered through the analysis of two case studies. First, the steady state analysis of annular radiating fins is considered. In a spacecraft's thermal control system, heat is collected by a circulating fluid and transferred via conduction to the fin surface [2,6]. The size and weight of the radiating surfaces dominate the design of most thermal control systems [6], so extensive efforts have been made to develop tools necessary to design and optimize radiating fins [7–9]. The second problem considered is the transient analysis of a radiating target, which is being developed to assess the temporal response of radiation thermometers. Radiation thermometers can be deployed unobtrusively, and they respond rapidly to fluctuations in the temperature of the target. These features present opportunities to incorporate radiation thermometers in real time control systems that improve process productivity and product quality.

2 Case Study 1—A Radiating Fin

An extension of the annular fin problem posed by Chambers et al. [8] and illustrated in Fig. 1 is the basis for the first case study. Heat from the spacecraft's coolant system is conducted via a high conductivity rod to the fin where it diffuses radially outward and is radiated to space. The base temperature is fixed at T_b, temperature gradients in the z-direction are neglected and the tip is adiabatic. It is assumed that the fin is coated with a spectrally selective surface, and the effect of solar heating is included in the analysis.

With these assumptions, the application of an energy balance to the fin gives the following model:

$$\frac{1}{\rho}\frac{d}{d\rho}\left(\rho\frac{d\theta}{d\rho}\right) = -\gamma[Q-\tilde{\varepsilon}\theta^4], \quad \theta(1)=1, \quad \left.\frac{d\theta}{d\rho}\right|_{\rho=\rho_o}=0 \qquad (1)$$

This model shows that the radial temperature profile depends on four dimensionless parameters.

(1) The profile number γ, which a measure of the importance of radiation from the fin relative to conduction through the fin.

(2) The solar heating parameter Q, which is the absorbed solar flux normalized by the emissive power that would be emitted by the fin if it were isothermal at the base temperature.

(3) The normalized total emittance $\tilde{\varepsilon}(\rho)$, which is the ratio of the temperature dependent total emittance at ρ normalized by the emittance at the base temperature.

(4) An aspect ratio, which characterizes the geometry of the fin. The aspect ratio is equal to the dimensionless outer radius of the fin ρ_o.

2.1 Solution Based on a Green's Function Method. While Green's functions have been used extensively to solve problems involving heat conduction [10], their use in problems involving radiation has been limited [11]. Following the solution procedure outlined in Ref. [10], the temperature profile in the fin is given by

$$\theta(\rho) = 1 + \frac{\gamma Q}{2}\left[\rho_o^2 \ln\rho - \frac{\rho^2-1}{2}\right] - \gamma\left[\int_1^\rho \rho' \ln\rho' \tilde{\varepsilon}(\rho')\theta^4(\rho')d\rho' + \ln\rho \int_\rho^{\rho_o} \rho' \tilde{\varepsilon}(\rho')\theta^4(\rho')d\rho'\right] \qquad (2)$$

Equation (2) is solved using the method of successive approximations [2]. An initial estimate for the temperature profile is substituted into the right hand side of Eq. (2), and the integrals are evaluated. The numerical integration was performed using the right end point rule with 200 equal increments in ρ. A grid refinement study indicated these results to be exact to four significant figures, and the final solution is insensitive to the initial estimate.

The use of an under-relaxation technique was required for the iterative solution process to remain stable, so subsequent estimates of the dimensionless temperature profile were obtained from a weighted sum of the previous estimate and the right hand side of Eq. (2)

Contributed by the Heat Transfer Division of ASME for publication in the JOURNAL OF HEAT TRANSFER. Manuscript received November 15, 2008; final manuscript revised May 14, 2009; published online December 4, 2009. Assoc. Editor: Yogesh Jaluria.

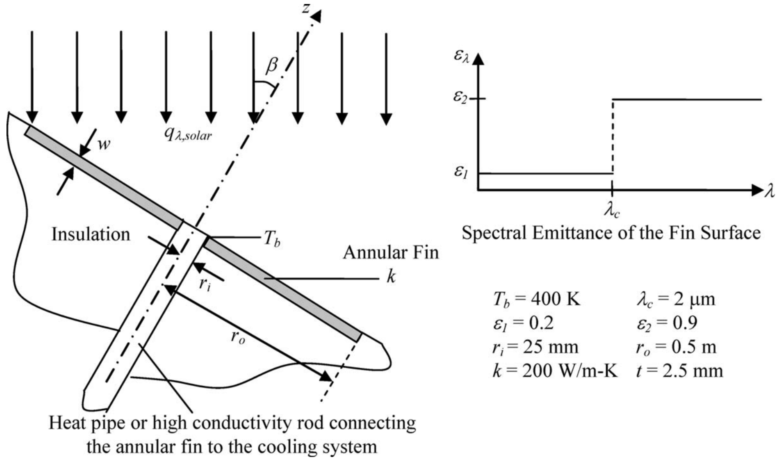

Fig. 1 Illustration of the radiating fin problem

$$\theta^i(\rho) = (1-\omega)\theta^{i-1}(\rho) + \omega\left\{1 + \frac{\gamma Q}{2}\left[\rho_o^2 \ln \rho - \frac{\rho^2 - 1}{2}\right] - \gamma\left[\int_1^\rho \rho' \ln \rho' \tilde{\varepsilon}\theta^{i-1^4} d\rho' + \ln \rho \int_1^\rho \rho' \tilde{\varepsilon}\theta^{i-1^4} d\rho'\right]\right\} \tag{3}$$

Typically, the relaxation factor ω was between 0.01 and 0.5.

The solution process was executed for a typical case based on the design parameters listed in Table 1, and the dimensionless radial temperature profiles obtained in the first three iterations are plotted in Fig. 2. Note the large discrepancy between the nonlinear and the linearized solutions. These results confirm the observation that calculations based on linearized solutions will contain significant errors [8].

Table 1 Dimensionless parameters for the parametric study

	γ	Q	ρ_o
Base case	4.82×10^{-3}	0.181	20
Range	10^{-4}–10^{-2}	0–0.95	5–30

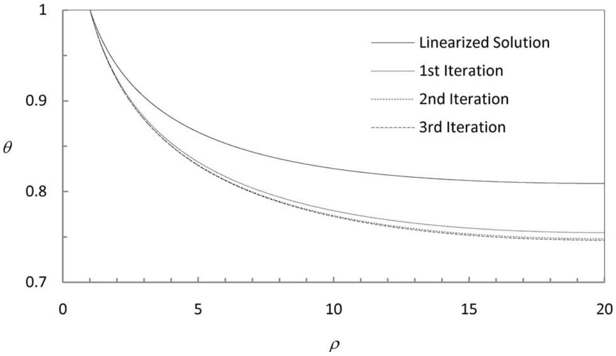

Fig. 2 Nondimensional radial temperature profile for the base case

2.2 Fin Performance Parameters. Fin efficiency is defined as the ratio of the heat rate from the base to the heat rate dissipated by the fin if it is isothermal at the base temperature

$$\eta_f = \frac{-2\pi r_i w k T_b \left.\dfrac{d\theta}{d\rho}\right|_{\rho=1}}{\varepsilon_b \sigma T_b^4 \pi (r_o^2 - r_i^2)} = \frac{2\int_1^{\rho_o} \rho' \tilde{\varepsilon}\theta^4 d\rho'}{\rho_o^2 - 1} - Q \tag{4}$$

Note that the fin efficiency is equal to the normalized, average emissive power minus the solar heating parameter.

Fin effectiveness is defined as the ratio of the heat rate leaving the base and the fin to the heat rate that would leave the base if the fin was not present. Clearly, the extra weight and complexity associated with a fin is only justified when the effectiveness is large. If the radiative properties of the base are equal to those of the fin, the effectiveness is

$$\varepsilon_f = \frac{\varepsilon_b \sigma T_b^4 \pi r_i^2 - 2\pi r_i w k T_b \left.\dfrac{d\theta}{d\rho}\right|_{\rho=1}}{\varepsilon_b \sigma T_b^4 \pi r_i^2} = 1 + \eta_f(\rho_o^2 - 1) \tag{5}$$

The performance parameters were calculated as functions of three of the governing parameters. Since $\tilde{\varepsilon}(\rho)$ does not vary significantly from 1, variations in this parameter were not considered. The ranges for the parametric study are listed in Table 1. The maximum value of the solar heating parameter occurs when the fin is oriented normal to the sun's rays and the solar absorptance is equal to the base emittance $Q_{\max} = T_s^4 R_s^2 / T_b^4 S^2 = 0.95$.

Figure 3(*a*) shows that the fin performance parameters decrease rapidly as γ increases. These results highlight the importance of designing an efficient path for heat conduction into the fin and show that contact resistance between the base and the fin will severely degrade performance. Figure 3(*b*) shows that if Q is large, the fin merely reradiates the absorbed radiation, and both the efficiency and effectiveness approach zero. Figure 3(*c*) show that the efficiency decreases and the effectiveness increases as the aspect ratio is increased. These results highlight the competing effects occurring as the surface area increases: More heat is dissipated from a larger surface, but the average emissive power decreases as the surface area increases. Since the weight of the fin increases as ρ_o^2, the incremental increases in the effectiveness do not justify increasing ρ_o beyond ~20.

3 Case Study 2—A Target for Measuring the Response Time of a Radiation Thermometer

3.1 Problem Formulation. A radiation thermometer senses the radiation emitted by a point on the target at one or more wavelengths and infers the temperature from these measurements based on Planck's law. In addition to the unobtrusiveness and

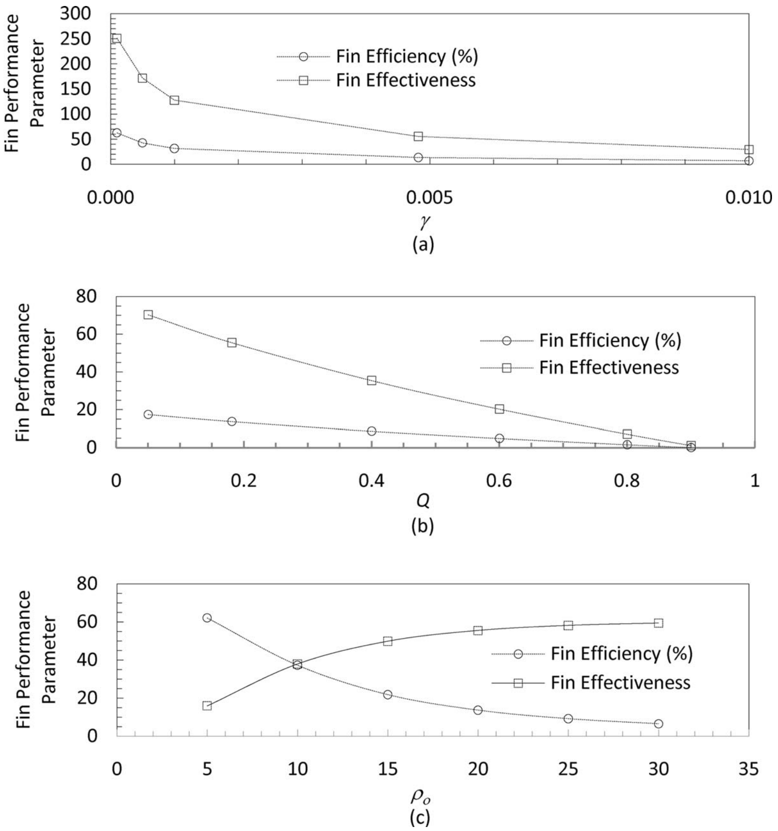

Fig. 3 Fin performance parameters as a function of (*a*) the profile number, (*b*) the solar heating parameter, and (*c*) the aspect ratio

rapid response of radiation thermometers, modern devices are highly sensitive, stable, and rugged. They generally do not require maintenance, so the long term cost of radiation thermometers compares favorably with conventional sensors. The use of radiation thermometers for process control is becoming increasingly common, and determining its response time is critical in the development of a radiation thermometer.

A proposed system for characterizing the response time of a radiation thermometer is illustrated in Fig. 4. The circular target is initially well insulated, and a heating element located on the circumference of the target brings the target to a uniform temperature T_b. Insulation covering the face of the target is removed, and the ability of the radiation thermometer to track temperature at the center of the target is assessed. Clearly, the usefulness of this system hinges on the accuracy of the model used to predict the time-dependent temperature profile at the center of the target. The target is constructed from a thin, highly conductive sheet, so temperature gradients are only significant in the radial direction. The surface is assumed to be diffuse and gray. Heat loss from the back of the target is neglected, and both convective and radiative exchanges occur on the face of the target. It is assumed that the convection coefficient is uniform over the face of the target, and the radiative exchange occurs between the face and large isothermal surroundings. A Green's function method is used to obtain an exact solution for the time-dependent temperature profile at the center of the target, and the solution is compared with the solution of a linearized problem.

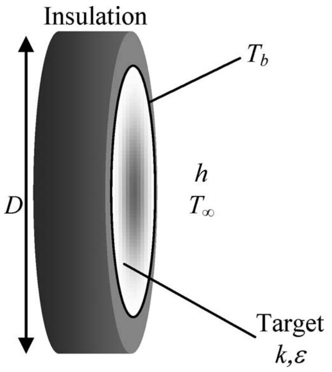

Fig. 4 Target used to assess the temporal response of a radiation thermometer

With these approximations, the application of an energy balance to the target gives the following model for its time-dependent radial temperature profile

$$\frac{1}{\rho}\frac{\partial}{\partial\rho}\left(\rho\frac{\partial\theta}{\partial\rho}\right)+\varphi=\frac{\partial\theta}{\partial\tau},\qquad \left.\frac{\partial\theta}{\partial\rho}\right|_{r=0}=0,\quad \theta(1,\tau)=0,\quad \theta(\rho,0)=0 \tag{6}$$

where the nonlinear source function is

$$\varphi=\frac{4D^2}{kw(T_b-T_\infty)}[\varepsilon\sigma(T^4(r,t)-T_\infty^4)+h(T(r,t)-T_\infty)] \tag{7}$$

3.2 Solution Based on a Green's Function Method. Again, following the procedure outlined in Ref. [10], the time-dependent temperature profile in the target is given by

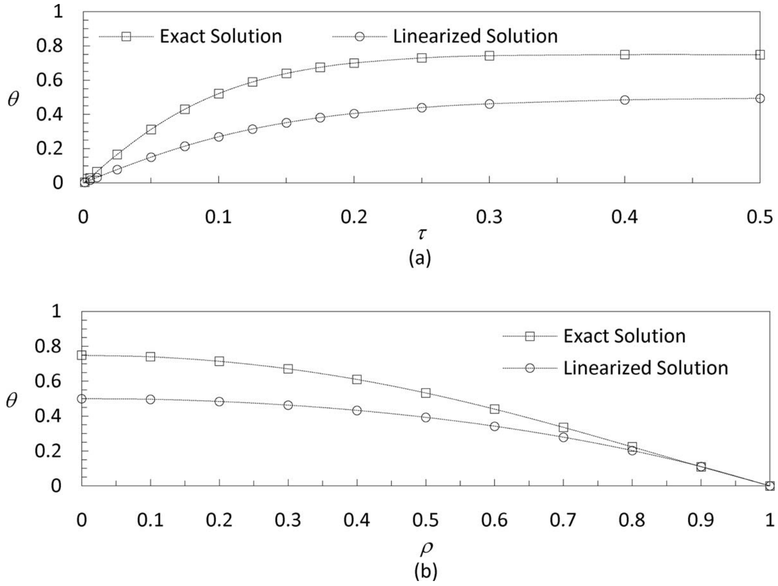

Fig. 5 Comparison between the exact and linearized temperature profiles (*a*) time-dependent temperature profile at the center of the target and (*b*) radial temperature profile at steady state

$$\theta(\rho,\tau) = 2\int_0^{\tau}\int_0^{1}\rho' H(\tau-\tau')\sum_{n=1}^{\infty}\frac{\lambda_n J_0(\lambda_n\rho')J_0(\lambda_n\rho)}{J_1^2(\lambda_n)}\exp\{-\lambda_n^2(\tau-\tau')\}\varphi(\rho',\tau')d\rho' d\tau' \tag{8}$$

where the eigenvalues are the roots of $J_0(\lambda_n)=0$. Eq. (8) is solved using the method of successive approximations with under-relaxation as described previously.

For comparison, it was assumed that $\varepsilon\sigma(T^4(r,t)-T_\infty^4)+h(T(r,t)-T_\infty)\approx h_L(T(r,t)-T_\infty)$, and the following linearized solution was obtained

$$\theta_L(\rho,\tau) = 2\text{Bi}\sum_{n=1}^{\infty}\frac{J_0(\lambda_n\rho)}{\lambda_n(\lambda_n^2+\text{Bi})J_1(\lambda_n)}[1-e^{-(\lambda_n^2+\text{Bi})\tau}] \tag{9}$$

3.3 Temperature Profiles in the Target. The time-dependent temperature profile of the center of the target is of particular interest, so the dimensionless temperature profiles obtained using the exact solution and the linearized solution are plotted in Fig. 5(*a*). The large discrepancy between the exact and the linearized solutions clearly show that a rigorous, nonlinear model is required to accurately predict the time-dependent temperature at the center of the target.

The steady state, radial temperature profiles are shown in Fig. 5(*b*). The discrepancy between the exact and linearized solutions is greatest at the center of the target. Again, these results show that the accurate prediction of the temperature field requires rigorous nonlinear modeling.

4 Summary

This paper presents an exact approach for solving the nonlinear diffusion problems, which result from the analysis systems involving coupled conduction and surface radiation. The Green's function solution method results in a single integral equation, whereas solution procedures described in radiative heat transfer literature require the numerical solution of coupled differential and integral equations. The case studies illustrate a process for obtaining exact solutions to this important class of problems.

Nomenclature

Bi = Biot number, $\text{Bi}=h_L D^2/4kw$
G = Green's function
H = heaviside step function
J = Bessel function
Q = solar heating parameter, $Q=\alpha_s T_s^4 R_s^2 \cos\beta/\varepsilon_b T_b^4 S^2$
R_s = radius of the sun
S = distance from the sun to the spacecraft
w = thickness of the fin or of the target

Greek Symbols

β = angle between the axis of the fin and the suns rays
$\tilde{\varepsilon}$ = normalized total emittance, $\tilde{\varepsilon}=\varepsilon(r)/\varepsilon_b$
ε_f = fin effectiveness
φ = dimensionless source function
γ = profile number, $\gamma=\varepsilon_b\sigma T_b^3 r_i^2/kw$
η_f = fin efficiency
λ_c = critical wavelength
λ_n = eigenvalues
θ = dimensionless temperature, $\theta=T/T_b$ for the fin or $\theta=(T_b-T)/(T_b-T_\infty)$ for the target
ρ = dimensionless radial coordinate, $\rho=r/r_i$ for the fin or $\rho=2r/D$ for the target
τ = dimensionless time, $\tau=4\alpha/D^2$
ω = relaxation factor

Subscripts

b = base
o = outer
i = inner

References

[1] Sparrow, E. M., Eckert, E. R. G., and Irvine, T. F., 1961, "The Effectiveness of Radiating Fins With Mutual Irradiation," J. Aerosp. Sci., **28**, pp. 763–772.
[2] Ozisik, M. N., 1973, *Radiative Transfer and Interactions With Conduction and Convection*, Werbel and Peck, New York.
[3] Modest, M. M., 2003, *Radiative Heat Transfer*, 2nd ed., Academic, Amsterdam.

[4] Siegel, R. S., and Howell, J. R., 2002, *Thermal Radiation Heat Transfer*, 4th ed., Taylor and Francis, New York.

[5] Crosbie, A. L., and Viskanta, R., 1968, "Transient Heating or Cooling of a Plate by Combined Convection and Radiation," Int. J. Heat Mass Transfer, **11**, pp. 305–317.

[6] Fraas, A. P., 1989, *Heat Exchanger Design*, 2nd ed., Wiley, New York.

[7] Callinan, J. P., and Berggren, W. P., 1959, "Some Radiator Design Criteria for Space Vehicles," ASME J. Heat Transfer, **81**, pp. 237–244.

[8] Chambers, R. L., and Somers, E. V., 1959, "Radiation Fin Efficiency for One-Dimensional Heat Flow in a Circular Fin," ASME J. Heat Transfer, **81**, pp. 327–329.

[9] Krikkis, R. N., and Razelos, P., 2004, "On the Optimization of Circular Radiating Fins With Fin-to-Fin and Fin-to-Base Radiant Interaction," ASME J. Heat Transfer, **126**, pp. 134–137.

[10] Beck, J. V., Cole, K. D., Haji-Sheikh, A., and Litkouhi, B., 1992, *Heat Conduction Using Green's Functions*, Hemisphere, Washington, DC.

[11] Siegel, R., 1999, "Transient Thermal Analysis of Parallel Translucent Layers by Using Green's Functions," J. Thermophys. Heat Transfer, **13**(1), pp. 10–17.